First Principles Investigations of Thermally Activated Processes in Pd-based Materials

A
thesis submitted
in partial fulfillment of the requirements for the degree of

DOCTOR OF PHILOSOPHY

by

Nandha Kumar V

Roll No.: 20123189

Indian Institute of Science Education and Research, Pune

2019

CERTIFICATE

Certified that the work incorporated in the thesis entitled **First Principles Investigations of Thermally Activated Processes in Pd-based Materials** submitted by **Nandha Kumar V** was carried out by the candidate, under my supervision. The work presented here or any part of it has not been included in any other thesis submitted previously for the award of any degree or diploma from any other University or institution.

Date: 18-04-2019

(Dr. Prasenjit Ghosh)
Thesis supervisor

Declaration

I declare that this written submission represents my ideas in my own words and where others ideas have been included, I have adequately cited and referenced the original sources. I also declare that I have adhered to all principles of academic honesty and integrity and have not misrepresented or fabricated or falsified any idea/data/fact/source in my submission. I understand that violation of the above will be cause for disciplinary action by the Institute and can also evoke penal action from the sources which have thus not been properly cited or from whom proper permission has not been taken when needed.

Date: 18-04-2019 (Nandha Kumar V)

Acknowledgements

I would like to thank my thesis supervisor, Dr. Prasenjit Ghosh for his constant support and guidance throughout the course and help in improving my scientific communication skills and research aptitude. I am thankful for my Research Advisory Committee (RAC) members: Dr. Chiranjib Majumder, Dr. Mukul Kabir and Dr. Arnab Mukherjee for their suggestions and useful comments to improve my research work. I thank Dr. Debabrata Chattaraj, BARC Mumbai, Dr. Sreekumar and his group, NCL Pune, Dr. Shabana Khan and her group for productive collaborations. My special thanks to Mr. Subrahmanyam Sappati for being a part in the encouraging discussions both scientific and personal life. I thank Mr. Avdhoot Datar for his help in writing FORTRAN codes. I am thankful to my labmates Subrahmanyam Sappati, Niharika Joshi, Vineet Kumar Pandey, Aswathi Mohan, Arti Shukla, Unmesh Mondal, Gautham Sharma and Amit Sahu for their valuable suggestions related to my research work and other scientific discussions. I thank my lab seniors, Dr. Saikat Chattopadhyay, Dr. Indu Kaul, Dr. Rahul Hardikar and Dr. Krishnakata Mondal for their valuable suggestions and discussions in the group meetings. I am thankful to all the IISER Pune friends.

I thank Prof. Jayant B. Udgaonkar and Dr. K. N. Ganesh, Director of IISER Pune, for providing excellent infrastructure and encouragement to do high-quality research. I thank Prof. M. Jeyakannan, Chair Chemistry, for keeping the department energetic. I am thankful to IISER Pune library for providing access to the scientific papers and books. I thank the IISER, Pune IT department especially Suresh Kumar, Goldi and Neeta for their help. I am thankful to the IISER, Pune administrative staff specially Mayuresh, Prabhakar, Nayana, Tushar and Anil Jadhav for their kind support.

I would like to thank Central for Development of Advanced Computing (CDAC), Pune, Super Computing Facility (SCF), BARC Mumbai, Dr. Prasenjit Sen, Harish-Chandra Research Institute, Allahabad and Tohoku University, Japan for providing computing facilities. I am thankful to Council of Scientific and Industrial Research (CSIR), India and IISER Pune for fellowship. I thank Department of Science and Technology, Science and Engineering Research Board (DST-SERB) for funding.

I am grateful to my parents Velankanni and Kanchana and my brothers Ramesh and Ragupathy for their love and support. I would like to thank Mr. P.P.S. Krishnan and his family for their consistent support and belief in me.

List of Publications

List of publications resulting from work presented in this thesis

1. Nandha Kumar, Prasenjit Ghosh, "Structure and stability of clean and adsorbate covered intermetallic PdGa surfaces: A first principles study", *Surf. Sci.*, **2016**, 644, 69-79.

2. Nandha Kumar, Prasenjit Ghosh, "Selectivity and Reactivity of Pd-Rich PdGa Surfaces toward Selective Hydrogenation of Acetylene: Interplay of Surface Roughness and Ensemble Effect", *J. Phys. Chem. C*, **2016**, 120 (50), pp 28654-28663.

3. Nandha Kumar, Debabrata Chattaraj, Prasenjit Ghosh, Chiranjib Majumder, "Microscopic insights into hydrogen permeation through a model PdCu membrane from first principles investigations" *J. Phys. Chem. C*, **2018**, 122 (24), pp 12920-12933.

4. Nandha Kumar, Indu Kaul, Debabrata Chattaraj, Prasenjit Ghosh, Chiranjib Majumder, "First principles investigation of growth of small Pd-Ga bimetallic clusters on MgO(100) surface" (manuscript accepted in Journal of Applied Physics).

List of publications from other works

1. Debabrata Chattaraj, Nandha Kumar, Prasenjit Ghosh, Chiranjib Majumder, Smruti Dash "Adsorption, dissociation and diffusion of hydrogen on the ZrCo surface and subsurface: A comprehensive study using first principles approach" *Applied Surface Science*, **2017**, 422, 394-405.

2. Pranav K. Gangadharan, Sreekuttan M. Unni, Nandha Kumar, Prasenjit Ghosh, Sreekumar Kurungot "Nitrogen-Doped Graphene with Three-Dimensional Architecture Assisted by Carbon Nitride Tetrapods as an Efficient Metal-Free Electrocatalyst for Hydrogen Evolution " *Chem Electro Chem*, **2017** 4, 1-11.

3. Neha Kathewad, Nandha Kumar, Rajarshi Dasgupta, Shiv Pal, Shabana Khan "Substituent effect: high quantum yield from PNP based dinuclear Au(I) complexes with strong intramolecular Au-Au interaction" (Manuscript accepted in Dalton Transaction).

Synopsis

A broad range of solid-state properties such as viscosity, ionic conductivity, mass transport etc., belong to the class of thermally activated processes. Thermally activated processes are those where the system requires to overcome an energy barrier when it moves from one potential energy basin to another. Computational studies of these processes are challenging because these involve large time scales that are typically of the order of milliseconds (due to barrier crossing) and are inaccessible by standard molecular dynamics simulations which are limited to microseconds. Hence, for theoretical investigations of activated processes, one needs to use a multi-scale approach and more advanced and sophisticated techniques.

In this thesis, we present the theoretical investigations of the activated processes in three different Pd-based materials. Based on the materials investigated, this thesis is divided into three parts. In the first part, we investigate the thermodynamic stability of the low indexed PdGa intermetallic surfaces and their reactivity and selectivity towards an important industrial reaction namely, the selective hydrogenation of acetylene to ethylene. In the second part, we present our results of structure and thermodynamic stability of small (up to tetramers) PdGa clusters adsorbed on two types of MgO(100) surfaces the clean one and one containing neutral oxygen vacancies. Moreover, we have investigated the elementary steps involved in the growth mechanism and nucleation kinetics of these clusters on the MgO surface. Further, we also discuss the possibility of stabilizing clusters with specific compositions by controlling the deposition rates and temperature. In the last part, we present the results of our study of the different microscopic processes involved in the solution-diffusion mechanism for hydrogen permeation through a PdCu membrane. We note that hydrogen permeation through the metallic membrane is one of the ways to purify hydrogen.

This thesis is divided into six chapters.

The first chapter (**Chapter-1**), contains a brief introduction about the activated processes and the classification of the different types of potential energy surfaces typically encountered. Additionally, we provide an overview of the different chapters in the thesis.

Chapter-2 describes the theoretical tools, i.e., density functional theory (DFT), density functional perturbation theory (DFPT), climbing image nudged elastic band (CI-NEB) method and graph theoretical kinetic Monte Carlo (GT-KMC) method used to investigate the activated processes. DFT calculations are performed to determine the ground state structures, electronic properties and total energy of a given system. DFPT is used to calculate the normal mode vibrational frequencies that are used in estimating the prefactor. The minimum energy path and the saddle points are estimated using CI-NEB method and the time evolution of the growth of the bimetallic clusters are estimated using the GT-KMC method.

Over the last decade, PdGa intermetallics are proposed to become a promising alternative catalyst for the semi-hydrogenation reaction due to their peculiar structure, high stability, high activity and very good selectivity. In **Chapter-3**, using *ab initio* density functional theory based calculations we have studied the structure and stability of clean and hydrogen covered low-indexed (100) and (110) surfaces of intermetallic PdGa. We find that for the clean (100) surface, the stability of the surface terminations is independent of the surface preparation condition. On the contrary, at least three different types of surface terminations can be stabilized for the (110) surface by tuning the surface preparation conditions. Upon adsorbing molecular and atomic hydrogen on these surfaces, it is found that: (a) at 450 K hydrogen adsorbs only at high hydrogen partial pressure and (b) the relative stability of the different surface terminations are unaffected by the presence of adsorbates.

Motivated by the experimental results that show the PdGa nanocrystallites act as highly selective and reactive catalyst for selective hydrogenation of acetylene to ethylene and our findings presented in Chapter-3, we have studied the mechanism and energetics of the above reaction on low indexed (100) and (110) PdGa surfaces using first-principles density functional theory based calculations, the results of which are presented in **Chapter-4**. We find that the energetically favorable (100) surface created by cleaving the crystal in the less dense region shows reasonably good selectivity and high reactivity. The reactivity

on this surface is comparable to that observed on Pd(111) surfaces. Since this surface termination is stable over a wide range of Ga chemical potential and hence is likely to occupy a substantial fraction of the surface area of PdGa nanocrystallites, we suggest this termination is responsible for the selectivity and reactivity exhibited by PdGa. In contrast to other surfaces where hydrogen adsorption and dissociation is followed by acetylene adsorption and hydrogenation, on this surface, we identify a novel reaction mechanism in which hydrogen dissociation occurs in the presence of acetylene. A careful analysis of the factors determining the selectivity shows that selectivity results due to an interplay between surface roughness and chemical nature of the reactive ensemble.

Industrial scale applications require the active catalyst to be supported on a stable, inert support. Typically the metal oxides are used as the support. In **Chapter-5**, we present our results for the structure and thermodynamic stability of small sized (up to 4 atoms) PdGa bimetallic clusters adsorption on MgO(100) surface studied by DFT. We also report the result of elementary steps involved in growth and the nucleation kinetics of these small clusters on the same surface studied within GT-KMC framework. Our calculations predict that binding energies and the formation energies of the clusters increase with cluster size. We find that the mixed bimetallic clusters on the surface are found to be more stable than that of the parent clusters, particularly clusters with 1:1 atomic ratio are the most stable ones. We find that all the clusters except Ga tetramer are highly mobile on the surface. At 300 K, all these clusters are kinetically stable, and the vacancy sites act as trapping center. Upon increasing temperature, Ga_2, Ga_3 and Pd_1Ga_2 clusters tend to escape from the vacancy site rather than decompose, whereas all other clusters tend to decompose rather than escaping from the vacancy site. The growth of the pure Pd and Ga clusters are heterogeneous, though the elementary reactions involved in the growth process for these two clusters are very different. When the bimetallic cluster are grown by depositing Pd and Ga adatoms with an equal deposition rate, the bimetallic clusters are formed in large proportion, especially clusters with 1:1 atomic ratio are found in the largest fraction. Further, clusters with desired stoichiometric ratios can be obtained in a significant fraction by varying the deposition rates of the Pd and Ga adatoms to the surface.

In **Chapter-6**, we present a systematic theoretical study of all the processes associated with the permeation of H through a model PdCu membrane. The surface of the membrane is modelled using the most stable (110) surface. The results show that the nuclear

quantum effects due to the light mass of the H atom can significantly affect the stability and the reaction rates. Based on a microkinetic model of the permeation process, we find that the permeation can be limited by diffusion of H in the membrane bulk or the reassociation of atomic H to form H_2 on the permeate side of the membrane depending on the operation temperature and membrane thickness. At typical operating conditions, for membranes thinner than 0.5 μm, the permeation at high temperature (T>500 K) is limited by surface processes, while at lower temperatures it can be either diffusion limited or reassociation limited.

Finally, in the last chapter (**Chapter-7**), we conclude this thesis by summarising the lessons learned from the studies presented and the possible avenue for the future research.

List of symbols

H	The Hamiltonian of a system
h	Plank's constant
M	Mass of the nucleus
m	Mass of the electron
Z	Atomic number
e	Charge of an electron
$\mathbf{R}$	Nuclear coordinates
$\mathbf{r}$	Electronic coordinates
ϵ_n	Energy eigenvalues
$\Psi_n(\mathbf{R}, \mathbf{r})$	Eigenfunctions
$\chi_n(\mathbf{R})$	Coefficients of the electronic states
$V_{ext}(\mathbf{r})$	External potential
$E_{xc}[n]$	Exchange-correlation energy
$n(\mathbf{r})$	Charge density
E_{Ewald}	Energy of the nuclear-nuclear interaction for a particular ionic configuration $\mathbf{R}$
$\mathbf{k}$	Wavevector
$\mathbf{G}$	Reciprocal lattice vector
r_c	Cut-off radius that separates the core and valence regions
l	Length of the reciprocal lattice vector
F	Force acting on the atoms
$\sigma^s_{\alpha\beta}$	Stress tensor
$\epsilon^s_{\alpha\beta}$	Strain tensor
$V_{\mathbf{R}}(\mathbf{r})$	Electron-nuclei interaction
k_{hTST}	Rate constant of an activated processes
ν_i^{init}	Normal mode frequencies of the system at mimima
ν_j^*	Normal mode frequencies of the system at saddle point
ΔE	Activation energy
k_B	Boltzmann's constant
T	Temperature

$\mathbf{F}_i^{NEB}$	The NEB force acting on image i
$\mathbf{F}_i^{\perp}$	The perpendicular force component
$\mathbf{F}_i^{S\parallel}$	The parallel force component
$\hat{\tau}$	Tangent along the NEB path
k	Spring constant
$P_i(t)$	Probability of finding the system at time t in state i
$\mathbf{s}$	Well-defined sites present in the lattice
$\mathcal{L}$	Graph representation of the lattice
$\mathcal{S}$	An index set contains all the sites on the lattice
$\mathcal{E}$	The subset containing the x- and y-coordinates of the sites
σ	State of each sites
$\mathcal{R}_\mathrm{k}$	Elementary step defined in a graph
$\mathcal{M}$	Subgraph isomorphism
u	Uniformly distributed random number
E_{ads}	Adsorption energy
$E_{Total}^{Slab+nX}$	Total energy of the slab with n adsorbates X
E_{Total}^{Slab}	Total energy of the clean slab
$E_{Total}^{H_2}$	Total energy of H_2 molecule in the gas phase
θ_{H_2}	Surface H_2 coverage
G	Gibbs free energy
E	Internal energy
P	Pressure
V	Volume
S	Entropy
n_i	Number of species of type i
μ_i	Chemical potential of species i
A	Surface area
ΔH_f	Enthalpy of formation
d_{rum}	degree of surface rumpling
d	Interplanar distances
n_e	Effective coordination number
$\rho(R)$	Atomic charge density of an isolated atom at a distance R
p_{H_2}	Partial pressure of hydrogen
R	Degree of surface roughness
E_{mix}	Mixing energy
$\Delta\rho$	Charge transfer
D	Diffusivity of hydrogen
α	The jump length of H

Q	Permeability of hydrogen
$K_s(T)$	Sievert's constant
I	Moment of inertia
J	Hydrogen flux through a membrane
l	Thickness of the membrane
X_s	Probability of subsurface site being occupied
θ_1	Probability of surface site being occupied
N_s	Density of the Pd atoms on the surface
N_b	Density of the Pd atoms in the bulk PdCu
N_{AA}	Concentration of the nearest neighbor occupied site pairs at the surface
z	Number of nearest neighbors
w	Pairwise interaction energy

Contents

List of Figures

List of Tables

Chapter 1

Introduction

A broad range of solid-state properties such as viscosity, ionic conductivity, mass transport etc., belong to the class of thermally activated processes. The activated processes in a material are essential for most of the interesting properties that make that material functioning. Microscopic structure of the material can significantly influence the macroscopic outcome of the thermally activated processes involving it. Catalysts and batteries are some examples of materials for which the activated processes govern the material properties. Catalysts are used to accelerate the rate of the reactions that are slow and have turn over frequencies less than 1 s^{-1}. A satisfactory battery material should charge on a time scale of minutes and discharge on a timescale of hours. [1]

Any process in which the system undergoes infrequent transitions from one stable state to another stable state, with long periods of idleness between such transitions, can be called as an activated process. Hence, these are also called "rare events". The timescale associated with an activated process typically varies between milliseconds to minutes and is an order of magnitude slower compared to atomic vibrations (typically of the order of femtoseconds to picoseconds). The long time between such transition is because the system is required to overcome an energy barrier in order to move from one state to another. [2] Figure 1.1 illustrates the occurrence of a rare event. In the Figure-1.1 there are three energy basins (labeled as A, B and C), each of which corresponds to a state of the system. The spacing between the contour lines in the Figure is assumed to be of the order of thermal energy. Suppose initially the system is in state B and wants to go to state C. The time evolution of the system is represented by the red lines. Most of the time the system will spend in basin B with the atoms oscillating about the minima with their vibrational energy before it crosses the barrier to get into the basin C. [2]

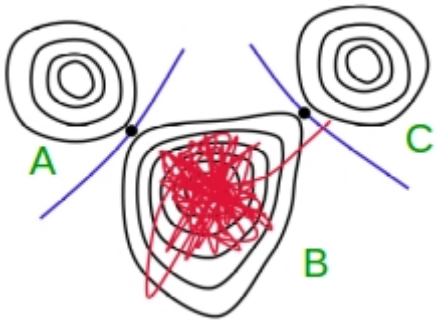

Figure 1.1: Schematic illustration of potential energy surface for an activated process. After a large number of vibrational periods, the trajectory captures one infrequent event where the system escapes from the initial potential energy basin to a new potential energy basin. The black dots are the saddle points. Adapted with permission from Ref.[2]

In order to study the time evolution of a system undergoing a "rare event" with standard molecular dynamic (MD) simulations, is impossible. This is because atomistic MD simulations are limited by femtosecond time step discretization. After every discrete time step, the forces on the atoms of the system need to be calculated, which is computationally expensive. Even neglecting the computational expenses of force calculation, with a billion times steps, the standard MD simulation is limited to microseconds. However, as mentioned before, the activated processes normally have a time scale of milliseconds to seconds. Hence, at least trillions of MD steps are required to capture one infrequent activated jump. For a proper understanding of the system, one needs to follow the time evolution over a span of time that includes several such infrequent events. Even with the best available supercomputers, it is impossible to compute so many MD time steps in a reasonable time. [1, 3]

A direct exploration of the potential energy surface (PES) is another approach to understand the mechanism, rate and timescale of the thermally activated processes in the materials. There are a number of computational methods available which can be used to explore the PES in part because of the different class of energy landscapes. Generally, the PESs are classified based on two properties, (1) smoothness of the energy landscapes and (2) knowledge about final state of the system, i.e., whether the final state of the system is known are it needs to be predicted over the course of time. Figure 1.2 shows some examples of the PESs based on the above-mentioned classifications. [1]

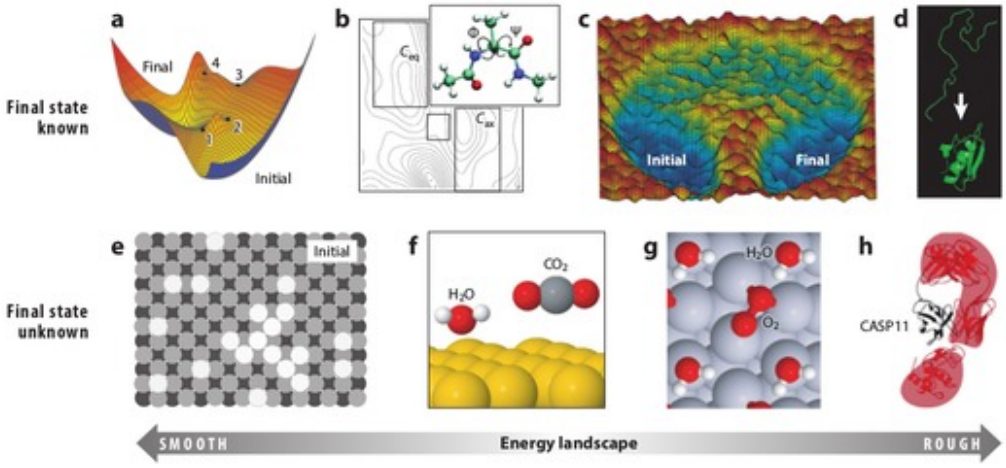

Figure 1.2: Classification of systems involving infrequent transitions based on the roughness of the PESs and the knowledge about the initial and final state of the systems. Depending on the roughness of the PESs, either the single-ended methods or double-ended methods are appropriate to study the reaction mechanism and rate of reaction of the system for which the final state is known (a-d). Systems presented in a) and b) can be studied using CI-NEB while systems presented in c) and d) require double-ended method like path sampling. Single-ended methods can be used to study the systems for which the final state is determined over the course of time. Systems having relatively smooth PESs (examples given in panel e and f) can be studied using kinetic Monte Carlo method and accelerated dynamics methods. Finding the reaction rates of the systems having rough PESs and the final state is predicted over the course of time (examples given in panel g and h), are challenging and are still an open area of research. Adapted with permission from Ref.[1]

Figure 1.2(a) shows an example of the simplest class of systems with a smooth energy landscape and the transition between a modest number of states. For this simplest system, the minimum energy path (MEP) between the reactants and the products can be determined by using methods such as climbing-image nudged elastic band (CI-NEB) method or closely related string method. Torsional rotation of a small peptide given in Figure 1.2(b) and a model two-dimensional potential presented in Figure 1.2(c) are the examples for the increasingly rough PES, for which no single point can capture the reaction mechanism and rate of the process. Sophisticated double-ended sampling methods are required to explore the PESs of these cases. Path sampling, discrete path sampling, forward flux sampling, transition interface sampling, milestoning and the finite temperature string are some examples of the double-ended methods. Protein folding to a known crystal structure is an example of the more complex PES with numerous local minima and long transition timescale. Exploring the PES of protein folding is challenging with even the best double-ended methods available. [1]

The other class of PES exploration is the initial state of the system is known and one might be interested in knowing what will happen to it over time. Figure 1.2(e) shows an initial state of the system where the metal adatoms are deposited on the support. Here, the questions that are typically asked are how these atoms will diffuse over the support? What will be the shape of the island formed? What are the conditions at which the cluster ripen? Additionally, the kinetic stability and the shape of the islands which one might be interested in knowing are not known at the beginning of the simulation. Figure 1.2(f) shows an example where a set of reactant molecules are adsorbed on a surface. What product will form and what will be the mechanism and the rate of the reaction are the questions of interest for these cases. Figure 1.2(g) shows an example of a surface reaction that is happening in the presence of solvent molecules. Understanding the problematic rough landscape is important in this case. Figure 1.2(h) shows an example of the most challenging PES exploration, for a given protein sequence finding how the protein folds over a long time on a support having a rough potential surface. [1]

In this thesis, we have studied three different types of activated processes on three kinds of Pd-based materials. In the first case, a catalytic reaction (selective hydrogenation of acetylene to ethylene) was studied on model PdGa low indexed surfaces, where the PES is similar to the one given in Figure 1.2(a). The second case, where the PES is similar to the example given in Figure 1.2(f), involves the study of the growth of bimetallic clusters (Pd and Ga) from individual metal atoms that are deposited on a model MgO(100) surface having 0.25 % of neutral vacancy sites. The elementary steps involved in the nucleation kinetics of the island formation is studied. Finally, we have studied, hydrogen permeation through a model PdCu membrane and the rate limited hydrogen flux is calculated within the one-dimensional mass transport model. The PES for this case is similar to the one given in Figure 1.2(c).

1.1 Theoretical tools

A number of theoretical tools are available with different levels of accuracy and computational cost to study the various physical and chemical processes. One needs to choose them depending on the type of processes and the length and time scales involved with them. All the above mentioned physical processes that have been investigated in this the-

sis involves bond formation and breaking. This requires an accurate description of the electronic structure and total energy of the system. Hence, it is necessary to treat the systems quantum mechanically. At the same time, the systems are of large size thereby making the calculations computationally expensive. Amongst the different computational methods that are available density functional theory (DFT) provides a reasonable balance between accuracy and the computational cost. Hence, in this thesis, we have used DFT to compute the total energies of the systems. The rates for the different activated processes have been computed within the harmonic transition state theory (HTST) as mentioned in Equation-2.38. For this, we need to estimate the activation barrier and the prefactor (that depends on the vibrational motion of the IS and TS). To compute the former, we have used the CI-NEB method while for the later we have used density functional perturbation theory (DFPT). The growth mechanism of the clusters involves accessing time scales that extends to a few seconds. Hence, these are studied using kinetic Monte Carlo (KMC) simulations. All the results presented in this thesis that involves DFT, DFPT and CI-NEB calculations were obtained using the Quantum ESPRESSO software. The KMC simulations were performed using the Zacros software.

1.2 Thesis outline

The rest of the thesis is organized as follows,

Chapter-2 includes a brief description of DFT used to calculate the electronic structure and the total energy of the system. It also includes a description of the practical aspects of the plane-wave implementation of DFT. Additionally, it also has a brief description of DFPT that was used to calculate the normal mode vibrations of the minima and the saddle points of the PES. It also includes a brief description of CI-NEB method used to estimate the saddle point and graph theoretical KMC method used to study the nucleation kinetics of the growth of bimetallic clusters.

Chapter-3 describes the structure and thermodynamic stability of clean and hydrogen covered low indexed (100) and (110) surfaces of intermetallic PdGa. The effect of hydrogen coverage on the stability is also studied. A correlation between the adsorption energy of hydrogen to the effective coordination number of the surface ensembles is presented.

Based on the energetics obtained from the ab-initio thermodynamics a surface phase diagram is constructed for the atomic and molecular hydrogen adsorbed on the (110) surfaces.

In **Chapter-4** we present the possible reaction mechanisms of selective hydrogenation of acetylene to ethylene on the stable low indexed (100) and (110) surfaces having different active surface ensembles. It also states the role of hydrogen diffusion on the catalytic surfaces to the reactivity and selectivity. Energetics of the various processes involved in the hydrogenation mechanism are analyzed to show an interplay of the surface roughness and the ensemble effect in dictating the selectivity.

The structure, electronic properties and thermodynamic stability of the small-sized PdGa clusters, up to tetramers on clean and neutral defect containing MgO(100) surface is presented in **Chapter-5**. The thermodynamic stability and formation of all the possible cluster compositions have been analyzed. Further, in this chapter, we have presented the results of our study on the elementary steps involved in the nucleation of bimetallic clusters on the MgO(100) surface. Factors affecting the growth mechanism of the clusters such as temperature, defect concentration, deposition rate, etc. are also analyzed. The possibility of growing clusters with a specific composition is also discussed.

Finally in **Chapter-6** we present the results of our study of the different microscopic processes involved in the solution-diffusion mechanism for the hydrogen permeation through a PdCu membrane. Based on the thermodynamic energetics a surface phase diagram is constructed for experimentally feasible ranges of temperature and hydrogen partial pressure. The kinetics related to the different processes involved in the solution-diffusion mechanism is analyzed as a function of membrane thickness, operating temperature, hydrogen partial pressure difference between the feed and the permeate side of the membrane and the rate-limiting steps are identified.

Chapter 2

Theoretical methods

2.1 Matter from first principles

2.1.1 The quantum mechanical problem of the structure of matter

Matter consists of a collection of interacting atoms, which may also be affected by the external field. This ensemble of particles can be in the gas phase or condensed phase; they could be homogeneous or heterogeneous. However, in all cases, one can unambiguously describe the system by a number of positively charged nuclei and negatively charged electrons interacting through Coulombic forces. The Hamiltonian (H) for such a system can be written as [4]

$$\begin{aligned} H = &-\sum_{I=1}^{N} \frac{\hbar^2}{2M_I}\nabla_I^2 - \sum_{i=1}^{n} \frac{\hbar^2}{2m}\nabla_i^2 + \frac{e^2}{2}\sum_{I=1}^{N}\sum_{I\neq J}^{N} \frac{Z_I Z_J}{|\mathbf{R}_I - \mathbf{R}_J|} \\ &+ \frac{e^2}{2}\sum_{i=1}^{n}\sum_{i\neq j}^{n} \frac{1}{|\mathbf{r}_i - \mathbf{r}_j|} - e^2 \sum_{I=1}^{N}\sum_{i=1}^{n} \frac{Z_I}{|\mathbf{R}_I - \mathbf{r}_i|}, \end{aligned} \tag{2.1}$$

where $\hbar = h/2\pi$, h being the Planck's constant. M_I and m are the masses of the I^{th} nucleus and electron respectively. e is the charge of an electron and Z_I is the atomic number of the I^{th} nuclei. $\mathbf{R} = \{\mathbf{R}_I\}, I = 1, 2, ...N$, is a set of N nuclear coordinates and $\mathbf{r} = \{\mathbf{r}_i\}, i = 1, 2, ...n$, is a set of n electronic coordinates. Since the electrons are fermions, the total electronic wavefunction must be antisymmetric with respect to exchange on any two electrons, while the nuclei can be fermions, bosons or distinguishable particles depending on the particular problem under investigation. In principle all the properties of the system can be derived by solving the time-independent Schrödinger

equation (SE):

$$H\Psi_n(\mathbf{R},\mathbf{r}) = \epsilon_n \Psi_n(\mathbf{R},\mathbf{r}), \tag{2.2}$$

where ϵ_n are the energy eigenvalues and $\Psi_n(\mathbf{R},\mathbf{r})$ are the corresponding eigenfunctions of the total system.

However, matter consists of a huge number of particles (of the order of Avogadro's number) which results in a very large number of degrees of freedom. For example, if the system comprised of N nuclei and n electrons, then the number of degrees of freedom is $3(N+n)$. Further the fact that electrons are Fermions and their wave function needs to be antisymmetric makes it more complicated. Additionally, the Coulomb interaction prevents separation of the electronic and nuclear degrees of freedom. For the above-mentioned reasons, it is impossible to solve Eqn. 2.2 within a full quantum mechanical framework. Hence several approximations need to be made to solve the above equation.

2.1.2 Adiabatic or Born-Oppenheimer approximation

The Born and Oppenheimer approximation was first introduced in 1927. It is based on the timescale associated with the motion of the nuclei and that of electrons. Born and Oppenheimer observed that the nuclei are very massive compared to electrons ($M_{proton}/m_{electron} = 1836$) and hence the timescale associated with the motion of electrons is much smaller compared to the timescale associated with the motion of nuclei. It is assumed that the electrons can almost instantly follow nuclear motion without change in their electronic states (adiabatically). This approximation is called the Born-Oppenheimer approximation. As a result, the first term in the Hamiltonian described in Eqn. 2.1 can be treated as a perturbation to H. This allows one to define the eigenfunctions of H in such a way that they depend parametrically on the nuclear positions $\mathbf{R}$. The eigenfunctions of the complete system can be written as the product of eigenfunctions of nuclei and electrons respectively.

$$\Psi(\mathbf{R},\mathbf{r}) = \sum_n \chi_n(\mathbf{R})\psi_n(\mathbf{R};\mathbf{r}) \tag{2.3}$$

where $\psi_n(\mathbf{R};\mathbf{r})$ defines a complete set of states for the electrons at each $\mathbf{R}$ and $\chi_n(\mathbf{R})$ are the coefficients of the electronic states. Using the above equation, the SE can be written as two coupled differential equations. The electronic Hamiltonian can be written in the

following form:

$$\Big(-\frac{\hbar^2}{2m}\sum_{j=1}^{n}\nabla_j^2 + \frac{e^2}{2}\sum_{i=1}^{n}\sum_{i\neq j}^{n}\frac{1}{|\mathbf{r}_i-\mathbf{r}_j|} - \sum_{i=1}^{n}\sum_{J=1}^{N}\frac{Z_J e^2}{|\mathbf{r}_i-\mathbf{R}_J|} + \frac{e^2}{2}\sum_{I=1}^{N}\sum_{I\neq J}^{N}\frac{Z_I Z_J}{|R_I-R_J|}\Big)\psi_n(\mathbf{R};\mathbf{r}) = E_n(\mathbf{R})\psi_n(\mathbf{R};\mathbf{r}) \tag{2.4}$$

where the term $\frac{e^2}{2}\sum_{I=1}^{N}\sum_{I\neq J}^{N}\frac{Z_I Z_J}{|R_I-R_J|}$, is only a constant and thus plays no role in the solution of the electronic problem. The nuclear Hamiltonian can be written in the following form:

$$\Big(-\sum_{I=1}^{N}\frac{\hbar^2}{2M_I}\nabla_J^2 + E_n(\mathbf{R})\Big)\chi_n(\mathbf{R}) = \epsilon\chi_n(\mathbf{R}) \tag{2.5}$$

Thus within the BO approximation the nuclei are subject to an effective potential $E_n(\mathbf{R})$ that is determined by the solution of the electronic problem. This results in decoupling of the vibrational DOF from the electronic DOF. $E_n(\mathbf{R})$ is also called the BO potential energy surface.

Now, the Eqn. 2.5 can be solved if $E_n(\mathbf{R})$ is known. However, the Eqn. 2.4 still contains the two-body Coulomb potential term. Hence solving this equation within a full quantum mechanical framework is still not possible. Therefore further approximations are needed.

2.1.3 Density functional theory

In 1964, Hohenberg and Kohn formulated and proved two theorems [5] in an attempt to provide an exact theory for a system of interacting particles that set up the foundation of the present day electronic structure calculations within the framework of density functional theory (DFT). [6] DFT can be applied to any system of interacting particles in an external potential $V_{ext}(\mathbf{r})$, including any problem of electrons and fixed nuclei. The hamiltonian for such system is written as,

$$\hat{H} = -\sum_i \frac{\hbar^2}{2m}\nabla_i^2 + \sum_i V_{ext}(\mathbf{r}_i) + \frac{e^2}{2}\sum_{i\neq j}\frac{1}{|\mathbf{r}_i-\mathbf{r}_j|}. \tag{2.6}$$

2.1.3.1 Hohenberg-Kohn theorems

Theorem 1: For any system of interacting particles in an external potential $V_{ext}(\mathbf{r})$, the potential $V_{ext}(\mathbf{r})$ is determined uniquely, except for a constant, by the ground state particle density $n_0(\mathbf{r})$.
Corollary 1: Since the hamiltonian is thus fully determined, except for a constant shift of the energy, it follows that the many-body wavefunctions for all states (ground and excited) are determined. *Therefore all properties of the system are completely determined given only the ground state density* $n_0(\boldsymbol{r})$.
Theorem 2: A *universal functional* for the energy $E[n]$ in terms of the density $n(\mathbf{r})$ can be defined, valid for any external potential $V_{\rm ext}(\mathbf{r})$. For any particular $V_{\rm ext}(\mathbf{r})$, the exact ground state energy of the system is the global minimum value of this functional, and the density $n(\mathbf{r})$ that minimizes the functional is the exact ground state density $n_0(\mathbf{r})$.
Corollary 2: The functional $E[n]$ alone is sufficient to determine the exact ground state energy and density. In general, excited states of the electrons must be determined by other means.

The first theorem establishes the one-to-one correspondence between $V_{ext}(\mathbf{r})$ and $n_0(\mathbf{r})$ i.e. a physical system of interacting particle is uniquely determined by its ground state density of these particles. The second theorem suggest that minimization of $E[n]$ with respect to $n(\mathbf{r})$ can give us the ground state energy and electron density which can be used to determine all the ground state properties of the material. These two theorems also suggest that if $n(\mathbf{r})$ is specified, all properties (e.g. kinetic energy, etc.) can be uniquely determined and hence each such properties, can be viewed as a functional of density. For a given external potential $V_{\rm ext}(\mathbf{r})$, the Hohenberg-Kohn energy functional (E_{HK}) is given by:

$$E_{HK}[n] = F[n] + \int V_{\rm ext}(\mathbf{r}) n(\mathbf{r}) d\mathbf{r}, \tag{2.7}$$

In the above equation, the functional $F[n]$ contains two terms, namely the kinetic energy of the electrons ($T[n]$) and the electron-electron interaction (E_{e-e}), thus it can be written as:

$$F[n] = T[n] + E_{e-e}. \tag{2.8}$$

As a result of HK theorem, the quantum mechanical problem of searching for the ground state properties of a system of interacting particles becomes enormously simple, since it replaces the traditional wavefunctions-based descriptions (which depend on $3N$ inde-

pendent variables, N being the number of electrons) with a much more tractable charge density based description (which depends only on three variables). However, the functional form of $F[n]$ is not known. The HK theorem proves that there exists a functional form $F[n]$ to describe the ground state properties of the system of interacting particles, but does not provide its actual form. In the next section, we have briefly described a practical way proposed by Kohn and Sham for finding this unknown functional.

2.1.3.2 Kohn and Sham ansatz

In 1965, Kohn and Sham (KS) came up with a idea to tackle the problem of unknown functional. [7] Their approach is to map the more complex many body problem of a system of interacting electrons onto a much simpler system of noninteracting electrons (for numerical treatment). The underlying assumptions are [6]:

1. The exact ground state density of the system of interacting particles can be represented by the ground state density of an auxiliary system of non-interacting particles.

2. The auxiliary Hamiltonian for single electron is chosen to have the usual kinetic energy operator and an effective local potential $V_{\text{eff}}(\mathbf{r})$ acting on an electron at point $\mathbf{r}$.

$$\hat{H}_{aux} = -\frac{\nabla^2}{2} + V_{\text{eff}}(\mathbf{r}) \tag{2.9}$$

Using these two ansatz, the KS has rewritten the HK functional as:

$$F_{KS}[n] = T_0[n] + E_H[n] + E_{xc}[n], \tag{2.10}$$

where $T_0[n]$ is the ground state kinetic energy of a system of non-interacting electrons as a function of its ground state charge density distribution. $E_{xc}[n]$ is the exchange-correlation energy and $E_H[n]$ is the Hartree energy, which is given by

$$E_H[n] = \frac{e^2}{2} \int \int \frac{n(\mathbf{r})n(\mathbf{r}')}{\mid \mathbf{r} - \mathbf{r}' \mid} d\mathbf{r} d\mathbf{r}', \tag{2.11}$$

the independent-particle kinetic energy T_0 is given by

$$T_0 = \frac{1}{2}\sum_i \int \mid \nabla\psi_i(\mathbf{r}) \mid^2 d\mathbf{r}. \tag{2.12}$$

Therefore, the KS total energy functional, $E_{KS}[n]$, is given by:

$$E_{KS}[n] = F_{KS}[n] + \int n(\mathbf{r})V_{\text{eff}}(\mathbf{r})d\mathbf{r}. \tag{2.13}$$

The variation of $E_{KS}[n]$ with the constraint that the total number of electrons in the system is kept fixed, leads to the same equation for a system of non-interacting electrons subject to an effective potential $V_{scf}(\mathbf{r})$. The functional form of system of noninteracting electrons is given by,

$$V_{scf}(\mathbf{r}) = V_{\text{ext}}(\mathbf{r}) + e^2 \int \frac{n(\mathbf{r}^{'})}{\mid \mathbf{r} - \mathbf{r}^{'} \mid} d\mathbf{r}^{'} + v_{xc}(\mathbf{r}), \tag{2.14}$$

where, the last term is the functional derivative of the exchange-correlation energy, can be written as:

$$v_{xc}(\mathbf{r}) \equiv \frac{\delta E_{xc}}{\delta n(\mathbf{r})}, \tag{2.15}$$

Thus, if V_{scf} is known, to find the ground state one needs to solve only the one electron Schrödinger equation:

$$\left(-\frac{\hbar^2}{2m}\nabla^2 + V_{scf}(\mathbf{r})\right)\psi_n(\mathbf{r}) = \epsilon_n\psi_n(\mathbf{r}). \tag{2.16}$$

where, $\psi_n(\mathbf{r})$ are the auxiliary Kohn-Sham orbitals. The charge density $n(\mathbf{r})$ is given by:

$$n(\mathbf{r}) = \sum_{n=1}^{N} \mid \psi_n(\mathbf{r}) \mid^2 . \tag{2.17}$$

Solving the one electron Schrödinger equation (Eqn. 2.16) gives the total energy. Figure 2.1 shows the procedure to solve the Eqn. 2.16 in a self consistent way.

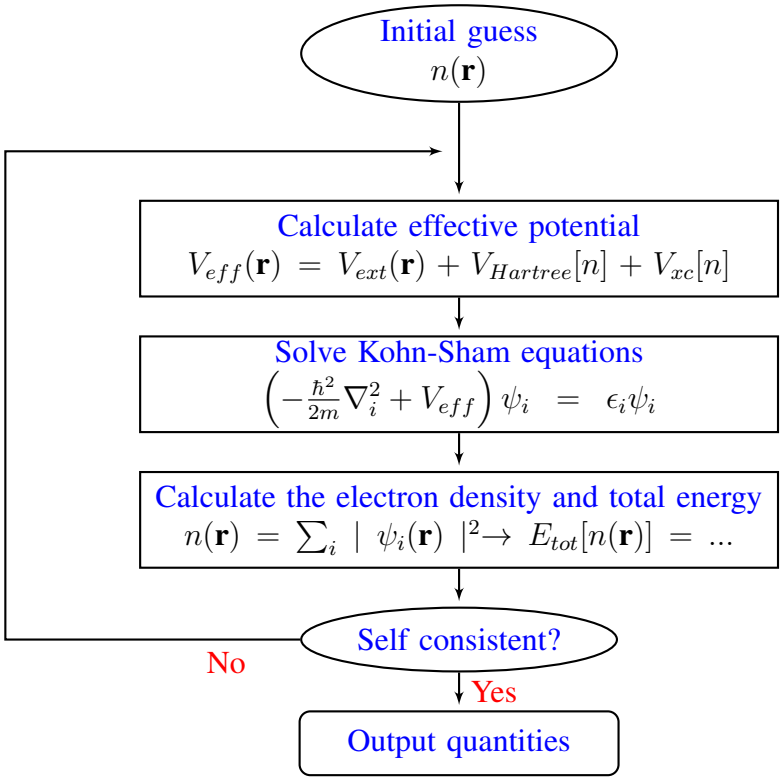

Figure 2.1: Self consistent loop used to solve the KS equations.

2.1.4 Exchange and correlation

The origin of exchange interaction is from Pauli's exclusion principle, which does not allow any two electrons to be in the same quantum state. Correlation is the effect of the presence of electrons on the motion of the other electrons. These many-body effects of a system of N electrons are incorporated through the calculation of the exchange-correlation functional. Both of the quantities are independent of the nuclei and depend only on the electron density. Hence, the exchange-correlation functional supposed to have a universal form dependent only on the electron density. The exchange-correlation energy can be expressed in the form,

$$E_{xc}[n] = \int n(\mathbf{r})\epsilon_{xc}([n](\mathbf{r}))d\mathbf{r}, \tag{2.18}$$

where, $\epsilon_{xc}([n](\mathbf{r}))$ is an energy per electron at point $\mathbf{r}$ that depends only upon the density $n(\mathbf{r})$ in some neighborhood of point $\mathbf{r}$. In the above expression the functional form of $\epsilon_{xc}([n](\mathbf{r}))$ is not known, hence, it is usually approximated. In principle, the accuracy of DFT is limited only the quality of approximation made for $\epsilon_{xc}([n](\mathbf{r}))$. The most commonly used approximations are the local density approximation (LDA) and the generalized gradient approximation (GGA).

2.1.4.1 Local density approximation

The assumptions made in the LDA approximation is that the exchange-correlation energy depends only on the local electron density and the local electron density is assumed to be homogeneous. The exchange-correlation energy is an integral over space where it is approximated that the exchange correlation energy at each point $\mathbf{r}$ is same as that of a homogeneous electron gas with the density of the system of interacting electrons at that point $\mathbf{r}$. The exchange-correction energy is given by:

$$E_{xc}^{LDA} = \int n(\mathbf{r})\epsilon_{xc}^{hom}(n(\mathbf{r}))d^3\mathbf{r}, \tag{2.19}$$

where $\epsilon_{xc}^{hom}(n(\mathbf{r}))$ is the exchange correlation density of a homogeneous electron gas at $\mathbf{r}$ with a density $n(\mathbf{r})$. Within LDA, the exchange-correlation potential (v_{xc}^{LDA}) is given by:

$$v_{xc}^{LDA}(\mathbf{r}) = \frac{\delta E_{xc}^{LDA}[n]}{\delta n(\mathbf{r})}. \tag{2.20}$$

In 1980 using Quantum Monte Carlo calculations Ceperley and Alder [8] had obtained an approximate form of ϵ_{xc}^{hom}, and later in 1981 Perdew and Zunger [9] parametrized it using a simple analytical form. The LDA approximation holds good for systems with a very small gradient of electron density, and it commensurately describes the properties of weakly correlated systems such as semiconductors and simple metals but fails to predict the electronic and structural properties adequately for strongly correlated systems such as transition metal oxides.

2.1.4.2 General gradient approximation

The GGA is an improved version to describe the exchange-correlation interaction, along with the local electron density it also takes into account the gradient of the electron density. The GGA assumes that at each point in space the E_{xc}^{GGA} is not only a functional of $n(\mathbf{r})$ but also of its gradient and higher derivatives. Within the GGA, the E_{xc}^{GGA} is given by:

$$E_{xc}^{GGA} = \int n(\mathbf{r})\epsilon_{xc}^{hom}(n(\mathbf{r}), \mid \nabla n(\mathbf{r}) \mid, \mid \nabla^2 n(\mathbf{r}) \mid d\mathbf{r}, ...). \tag{2.21}$$

The GGA predicts the binding energies, activation energies of chemical reactions and lattice constant of a large number of solids with a computational cost that is similar to that of a LDA calculation. However, the GGA is unable to provide a proper description of strongly correlated infinite solids. There are many flavours of the GGA exchange-correlation functional. The functionals developed by Becke (B88) [10], Perdew and Wang (PW91) [11] and Perdew, Burke and Ernzerhof (PBE) [12] are some of the most commonly used by computational material scientists. For all the calculations presented in this thesis, we have used the GGA based exchange-correlation functional proposed by Perdew, Burke and Ernzerhof (PBE). [12]

2.1.5 Total energy calculation

The total energy of a N electrons system is obtained from the eigenvalues obtained from the self consistent solution of the KS equations as,

$$E_{tot}[n] = \sum_{i=1}^{N} \varepsilon_i - \frac{1}{2}\int \frac{n(\mathbf{r})n(\mathbf{r}')}{\mid \mathbf{r} - \mathbf{r}' \mid} d\mathbf{r}' d\mathbf{r} + E_{xc}[n] - \int n(\mathbf{r})V_{xc}(\mathbf{r})d\mathbf{r} + E_{Ewald}. \tag{2.22}$$

where, E_{Ewald} is the energy of the nuclear-nuclear interaction for a particular ionic configuration **R**, evaluated using Ewald summation method [13–15]. Half of the Hartree energy is subtracted because of the double counting of electrons in the calculation of energy eigenvalues. The contribution to ε_i from exchange-correlation interaction ($\langle\psi_i \mid V_{xc} \mid \psi_i\rangle$) is not equal to E_{xc}. Hence in order to calculate E_{tot}, $\langle\psi_i \mid V_{xc} \mid \psi_i\rangle$ is subtracted and E_{xc} is added to it.

2.1.6 Basis

The KS equations are solved by expanding the wavefunctions in a basis. There are various types of basis sets available that can be used to expand the wave function, for example, Gaussian functions, plane waves, atomic orbitals or a mixture of two or more types of basis set. Bulk and surfaces of materials are composed of an infinite number of electrons moving in a static potential due to an infinite number of nuclei. The application of Bloch's theorem makes the plane waves an appropriate choice.

According to the Bloch's theorem, the eigenstates of the translational operators vary from one cell to another in the crystal with the phase factor. [6]

$$\hat{T}_n\psi(\mathbf{r}) = \psi(\mathbf{r} + \mathbf{T}_n) = e^{i\mathbf{k}.\mathbf{T}_n}\psi(\mathbf{r}), \tag{2.23}$$

where $\hat{T}_n$ is the translational operator. The eigenstates of any periodic operator, such as the Hamiltonian, can be chosen with definite values of **k** which can be used to classify any excitation of a periodic crystal. The eigenfunctions with a definite **k** can also be written as,

$$\psi_{\mathbf{k}}(\mathbf{r}) = e^{i\mathbf{k}.\mathbf{r}}u_{\mathbf{k}}(\mathbf{r}) \tag{2.24}$$

where $u_{\mathbf{k}}(\mathbf{r})$ is periodic ($u_{\mathbf{k}}(\mathbf{r} + \mathbf{T}_n) = u_{\mathbf{k}}(\mathbf{r})$). [6]

For all the DFT calculations we used a plane wave basis set, which has a form of $e^{i(\mathbf{k}+\mathbf{G}).\mathbf{r}}$, where **k** is the wavevector in the first Brillouin zone at which the KS equations are solved, and **G** is a reciprocal lattice vector. The discretization of the plane waves is done by applying the periodic boundary conditions. An energy parameter E_{cut} determines the size

of the basis set (i.e. the number of plane waves in the basis set) as

$$\frac{\hbar \mid \mathbf{k}+\mathbf{G} \mid^2}{2m_e} < E_{cut}. \tag{2.25}$$

In order to determine the value of E_{cut} used in a calculation, it needs to be converged to the desired accuracy to the quantity of interest.

The plane wave basis set provides three major advantages:

1. evaluation of forces becomes easy because of the absence of Pulay forces [16] since the basis is independent of atomic position. The forces can be evaluated using the Hellmann-Feynman theorem [6, 17],
2. controlling the quality of the basis by a single parameter
3. easy implementation in computer codes.

The disadvantage of using a plane wave is the requirement of a huge number of plane waves to expand the wavefunctions in the core region. In the core region, the core electron's wavefunctions are highly peaked, and the valence electron's wavefunctions have several oscillations. A pseudopotential can be used to avoid this problem.

2.1.7 Pseudopotentials

The chemical interaction of the atoms are primarily determined by the valence electrons. Hence, the electronic configuration of atoms can be divided into two parts, namely the 'core electrons' that are not participation in chemical bonding and 'valence electrons' that are the active participant in chemical bonding. The wavefunctions and the electron density of the core electrons are highly localized close to the nucleus. The energy eigenvalues corresponding to the core electrons are much lower (deeply buried) than the valence electrons. That is the primary reason for the core electrons being inactive in chemical bonding. It can be assumed that the core electrons are tightly bound to the nucleus, and their effect on the valence electrons can be described using a simple potential felt by the valence electrons. In this way, the actual potential experienced by the valence electrons can be replaced with a much simpler pseudopotential, i.e., the oscillations of the wavefunction of the valence electrons in the core region are replaced by a smooth function. Figure-2.2

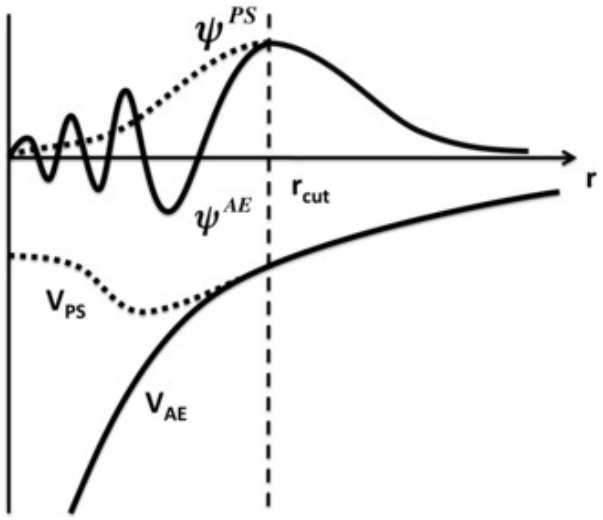

Figure 2.2: Schematic of all-electron and pseudo-electron potential and their corresponding wavefunctions. r_c is the cut-off radius that separates the core and valence regions. Adapted from Ref-[18]

shows the schematic of the pseudopotential. [18] This approximation simplifies the calculations in two ways: (1) it reduces the total number of electrons in an atom that needs to be considered to calculate the total energy of the system to the number of valence electrons in that atom. (2) it reduces the size of the basis set, since the valence electrons wavefunctions considered are free from nodes and sharp peak.

The pseudopotentials are constructed such that the all-electron and the pseudo wavefunctions match each other for $r > r_c$, where r is the radial distance from the center of the nucleus. Here, r_c is chosen such that the last node of the all-electron wavefunction lies within it. The pseudopotential is said to be transferable if the same pseudopotential of an atom can be used in different environments of that particular atom. The size of the basis set generally decreases with increasing r_c, while the transferability decreases. Two main types of the pseudopotentials widely used by the computational scientists are the norm-conserving and ultrasoft pseudopotentials.

In norm-conserving pseudopotentials, the transferability of the pseudopotential is ensured by keeping the norm of the pseudo-wavefunction in the core region to that of the norm of the all-electron wavefunction.

In the ultrasoft pseudopotentials, [19] the norm-conservation condition is relaxed that al-

lows one to use a very low energy cut-off (small sized basis sets). However, when the norm-conservation is relaxed, the orthonormality and the norm-conservation of the atomic orbitals are also lost. By considering a generalized eigenvalue problem, where a generalized orthogonality constraint is expressed in terms of an overlap operator, the issue of orthogonality can be solved. The norm-conservation problem can be solved by adding an augmentation charge that is localized within the core regions to the system's charge.

2.1.8 k-point sampling and smearing

Ideally, the numerical integrations should be carried out at an infinite number of k-points within the first Brillouin zone. For computational feasibility, one can use a finite number of k-points by choosing a set of special k-points to sample the reciprocal space appropriately. The method proposed by Monkhorst-Pack [20] is the most widely used one for the generation of a finite mesh of k-points. For all the calculations presented in this thesis we have used the same method. The k-points generated by this method are distributed uniformly through the reciprocal space as,

$$\mathbf{k}_j = x_{1j}\mathbf{b}_1 + x_{2j}\mathbf{b}_2 + x_{3j}\mathbf{b}_3 \tag{2.26}$$

where $\mathbf{b}_1, \mathbf{b}_2, \mathbf{b}_3$ are the reciprocal lattice vectors, and

$$x_{ij} = \frac{l_i}{n_j}, j = 1, 2, 3, ..., n_j \tag{2.27}$$

where l is the length of the reciprocal lattice vector, and n is an integer determining the number of points in the set.

For metals, the occupancy near Fermi surface can abruptly change, and that makes the sampling inadequate. Further, to capture the finite features of band crossing, that are common in metals a fine k-point mesh is needed. That makes the calculation computationally expensive. A slight broadening of the energy levels helps to describe the band crossing, and in that case, a moderate number of k-points are enough to describe the system adequately. A number of broadening schemes are available, such as Gaussian broadening [21], Methfessel-Paxton smearing [22], Marzari-Vanderbilt cold smearing [23], etc. For all the calculations presented in this thesis, we have used Marzari-Vanderbilt cold

smearing [23].

2.1.9 Calculation of forces and stresses

The forces acting on the atoms are calculated using the Hellmann-Feynman theorem [6, 17] as,

$$F_I = -\frac{\delta E(\mathbf{R})}{\delta \mathbf{R}_I} = -\langle \Psi(\mathbf{R}) \mid \frac{\delta E(\mathbf{R})}{\delta \mathbf{R}_I} \mid \Psi(\mathbf{R}) \rangle, \tag{2.28}$$

where $\Psi(\mathbf{R})$ are the electronic eigenstates of H_{BO} for a given configuration $\mathbf{R}$, F_I is the force acting on the I^{th} atom.

The advantage of this method is that it can extract the information of the force constants for the bond easily thus does not require the calculation the energies of the system at several configurations. There should be an additional term to Eqn. 2.28, corresponding to the Pulay force that is the derivative of the basis set with respect to the position of the ion. Since we are using the plane wave basis set, the derivative of the basis set with respect to the position of the ion is zero, and the Pulay force term vanishes.

The stress acting on the unit cell is calculated using the "stress theorem" proposed by Nielsen and Martin [24, 25]. The stress tensor, $\sigma^s_{\alpha\beta}$, is the derivative of total energy with respect to the strain tensor, $\epsilon^s_{\alpha\beta}$:

$$\sigma^s_{\alpha\beta} = -\frac{1}{\Omega}\frac{\delta E_{tot}}{\epsilon_{\alpha\beta}}, \tag{2.29}$$

where α and β are the Cartesian indexes and Ω is the volume of the unit cell.

2.2 Phonons from density functional perturbation theory

The phonons are the quasi-particles of lattice vibrations. The knowledge of the phonons of material can provide insights into the physical properties of that material that depends on the lattice-dynamical behavior such as vibrational spectra, structural stability of the material, specific heat, thermal expansion and lattice thermal conductivity etc. In 1954, Born and Huang developed the basic theory of lattice vibrations that were computationally

challenging at that time. [26] Over the years, the development of DFT, [5,7] DFPT [27,28] (based on linear response theory), enabled to perform *ab initio* calculations [29,30] of lattice vibrations for systems with a large number of atoms.

2.2.1 Lattice dynamics from electronic-structure theory

The adiabatic approximation enables to decouple the vibrational DOF from the electronic DOF (discussed in Section-2.1.2). The vibrational frequencies ω are determined by the eigenvalues of the Hessian matrix of the Born-Oppenheimer energy (also called the matrix of the inter-atomic force constants), scaled by their nuclear masses:

$$\det|\frac{1}{\sqrt{M_I M_J}}\frac{\partial^2 E(\mathbf{R})}{\partial \mathbf{R}_I \partial \mathbf{R}_J} - \omega^2| = 0. \tag{2.30}$$

The forces are given by the Hellmann-Feynman theorem as described in Section-2.1.9. The Hamiltonian depends on $\mathbf{R}$ via the electron-ion interaction that couples to the electronic degrees of freedom only through the electron charge density. The force acting on I^{th} nucleus is given by:

$$\mathbf{F}_I = -\int n_{\mathbf{R}}(\mathbf{r})\frac{\partial V_{\mathbf{R}}(\mathbf{r})}{\partial \mathbf{R}_I} d\mathbf{r} - \frac{\partial E_{Ewald}(\mathbf{R})}{\partial \mathbf{R}_I}, \tag{2.31}$$

where $V_{\mathbf{R}}(\mathbf{r})$ is the electron-nucleus interaction,

$$V_{\mathbf{R}}(\mathbf{r}) = -\sum_I \frac{Z_I e^2}{|\,\mathbf{r} - \mathbf{R}_I\,|}. \tag{2.32}$$

The Hessian of the BO energy surface appearing in Eqn. 2.30 is given by:

$$\begin{aligned}\frac{\partial^2 E(\mathbf{R})}{\partial \mathbf{R}_I \partial \mathbf{R}_J} &\equiv -\frac{\partial \mathbf{F}_I}{\partial \mathbf{R}_J} \\ &= \int \frac{\partial n_{\mathbf{R}}(\mathbf{r})}{\partial \mathbf{R}_J}\frac{\partial V_{\mathbf{R}}(\mathbf{r})}{\partial \mathbf{R}_J} d\mathbf{r} + \int n_{\mathbf{R}}(\mathbf{r})\frac{\partial^2 V_{\mathbf{R}}(\mathbf{r})}{\partial \mathbf{R}_I \partial \mathbf{R}_J} d\mathbf{r} + \frac{\partial^2 E_N(\mathbf{R})}{\partial \mathbf{R}_I \partial \mathbf{R}_J}.\end{aligned} \tag{2.33}$$

Eqn. 2.33 states that in order to calculate the Hessian of the BO surface one needs to calculate $n_{\mathbf{R}}(\mathbf{r})$ and its linear response to a distortion of the nuclear geometry $\partial n_{\mathbf{R}}(\mathbf{r})/\partial \mathbf{R}_I$.

DFT can be used to evaluate $n_{\mathbf{R}}(\mathbf{r})$ and $\partial n_{\mathbf{R}}(\mathbf{r})/\partial \mathbf{R}_I$ can be evaluated using DFPT.

2.2.2 Density-functional linear response

The electron response $\partial n_{\mathbf{R}}(\mathbf{r})/\partial \mathbf{R}_I$ appearing in Eqn. 2.33 can be obtained within the framework of DFPT. This is achieved by linearizing Eqns. 2.14, 2.16 and 2.17. Linearization of Eqn. 2.17 leads to

$$\Delta n(\mathbf{r}) = 2\mathrm{Re}\sum_{n=1}^{N} \psi_n^*(\mathbf{r})\Delta\psi_n(\mathbf{r}). \tag{2.34}$$

Variation of KS orbitals $\Delta\psi_n(\mathbf{r})$ is obtained by standard first-order perturbation theory:

$$(H_{SCF} - \epsilon_n) \mid \Delta\psi_n\rangle = -(\Delta V_{SCF} - \Delta\epsilon_n) \mid \psi_n\rangle, \tag{2.35}$$

where H_{SCF} is the unperturbed KS Hamiltonian and $\Delta\epsilon_n = \langle\psi_n \mid \Delta V_{SCF} \mid \psi_n\rangle$ is the first order variation of the KS eigenvalues. The first order correction to the self consistent potential ΔV_{SCF} is given by:

$$\Delta V_{SCF}(\mathbf{r}) = \Delta V(\mathbf{r}) + e^2 \int \frac{\Delta n(\mathbf{r}')}{\mid \mathbf{r} - \mathbf{r}' \mid} + \frac{dv_{XC}(n)}{dn}|_{n=n(r)}\Delta n(\mathbf{r}). \tag{2.36}$$

Eqns. 2.34, 2.35 and 2.36 form a set of self-consistent equations for the perturbed system, completely analogous to the KS equation in the unperturbed case, with the KS eigenvalue equation being replaced by the solution of a linear system. The value of $\partial n_{\mathbf{R}}(\mathbf{r})/\partial \mathbf{R}_I$ is then fed back to Eq. 2.33 to get the dynamical matrix.

The first order correction to a given eigenfunction of the Schrödinger equation is given by:

$$\Delta\psi_n(\mathbf{r}) = \sum_{m\neq n} \psi_m(\mathbf{r}) \frac{\langle\psi_m \mid \Delta V_{SCF} \mid \psi_n\rangle}{\epsilon_n - \epsilon_m}, \tag{2.37}$$

the summation is running over all the states of the system, occupied or empty. Thus, one needs to know the full spectrum of the KS Hamiltonian in order to explicitly compute the $\Delta\psi_n(\mathbf{r})$ from Eqn. 2.37. Moreover, extensive summations over conduction bands are needed. Both of these factors will make the calculations computationally expensive. Instead, only knowledge of the occupied manifold of the system is required to evaluate

$\Delta\psi_n(\mathbf{r})$ using Eqn. 2.35. Additionally, one can also exploit the availability of many efficient algorithms to numerically solve for the linear system. Therefore, in this way the computational cost of determining the density response to a single perturbation is of the same order as that needed to calculate the unperturbed ground state density.

The DFPT method holds good for systems with band gaps. However, for metals the presence of finite density of states at the Fermi level and the change in orbital occupation number that may occur when an infinitesimal perturbation is applied need to be taken into account.

2.3 Harmonic transition state theory

In the field of computational chemistry and material science, the rate of the activation process is calculated using harmonic transition state theory (HTST). The saddle points are the lowest-energy points that need to be crossed (locally) to escape the initial state. The single unstable mode at each saddle defines the local normal to the TS, and the TS is approximated as a hyperplane with a harmonic potential given by the N-1 remaining stable modes. [1] It is important to understand that the HTST is used to calculate the escape rate via each local channel characterized by a saddle point. The total rate of escape from the initial state can be approximated by summing over all escape channels. In this way, HTST can be viewed as approximating the TS by a set of hyperplanes passing through each saddle on the boundary of the initial state. Also, although it is common to hear the terms saddle point and transition state used interchangeably, this association is appropriate only in one dimension. In high-dimensional systems, the harmonic TS is the hyperplane that passes through the saddle with a normal along the unstable mode, and more generally in TST, the TS is an N-1-dimensional surface that divides the initial state from product states. According to HTST, the rate constant of an activated process is defined as, [1]

$$k_{hTST} = \frac{\Pi_{i=1}^{N} \nu_i^{init}}{\Pi_{j=1}^{N-1} \nu_j^{*}} exp^{-\left(\frac{\Delta E}{k_B T}\right)} \tag{2.38}$$

where ν_i^{init} and ν_j^{*} are the real normal mode vibrational frequencies of the system at IS and saddle point respectively, ΔE is the activation energy, k_B is Boltzmann constant and

[1] In this section N is the total number of degrees of freedom in the escape problem.

T is temperature.

2.4 Minimum energy path and saddle point estimation

Estimating the saddle point is challenging because the first order saddle point is minimum in all the directions except one direction alone which it is maximum. A number of methods are available for finding the saddle point and the MEPs. The drag method, CI-NEB method, the conjugate peak refinement (CPR) method, the ridge method, the Dewar, Healy and Stewart (DHS) method and dimer method are some of the examples for the methods used to estimate the saddle point. All the methods mentioned above involve maximization of one DOF while all other DOFs are minimized. The censorious issue is finding a good and effective way to identify which DOF needs to be maximized. [31] All the MEPs and saddle points presented in this thesis are estimated using CI-NEB method. [32]

2.4.1 Nudged elastic band (NEB) method

The NEB method can be used to estimate the MEP if initial and final state of the system is known. First, a path is constructed between the initial state and the final state using a string of images (replicas of the system) that are connected together with springs. Then, the images are relaxed towards the MEP using an optimization algorithms. If [$\mathbf{R}_0$, $\mathbf{R}_1$, $\mathbf{R}_2$, $\mathbf{R}_3$,..., $\mathbf{R}_N$] denotes the string of images with the initial ($\mathbf{R}_0$) and the final ($\mathbf{R}_N$) states are fixed, then the optimization algorithm will adjust the $N-1$ images towards the MEP. An objective function is constructed and minimized with respect to the $N-1$ intermediate images as, [31]

$$S(\mathbf{R}_1, ..., \mathbf{R}_N) = \sum_{i-1}^{N-1} E(\mathbf{R}_i) + \sum_{i-1}^{N} \frac{k}{2}(\mathbf{R}_i - \mathbf{R}_{i-1})^2 \tag{2.39}$$

The above expression imitates an elastic band made by $N-1$ beads and N springs having a spring constant k. This formulation has two major problems, 1) for curved regions of the MEP, the elastic band gets pulled off the MEPs by the spring forces and tends to cut corners due to the spring force perpendicular to the path and 2) the images close to the saddle point tend to slide down towards the initial and final state due to the parallel

component of the true force. Nudging (a force projection) helps to solve these problems.

In the force projection scheme, the potential forces are acting perpendicular to the band and the spring forces are acting parallel to the band. Based on these force projections the images are relaxed towards the MEP. The force projection is done by estimating the tangent along the path $\hat{\tau}$. The $\hat{\tau}$ is the unit vector pointing the neighboring image having higher energy. To avoid the abrupt change in the direction of $\hat{\tau}$ a linear interpolation is used between the higher energy neighboring images. This ensures no artificial kink developed along the path in the regions having high force. The NEB force acting on a image is the sum of the parallel and perpendicular force components and given by, [33]

$$\mathbf{F}_i^{NEB} = \mathbf{F}_i^{\perp} + \mathbf{F}_i^{S\parallel} \tag{2.40}$$

the perpendicular force component $\mathbf{F}_i^{\perp}$ can be calculated using the gradient of the energy as,

$$\mathbf{F}_i^{\perp} = -\nabla(\mathbf{R}_i) + \nabla(\mathbf{R}_i).\hat{\tau}_i\hat{\tau}_i \tag{2.41}$$

and the parallel force component $\mathbf{F}_i^{S\parallel}$ is defined as,

$$\mathbf{F}_i^{S\parallel} = k(|\mathbf{R}_{i+1} - \mathbf{R}_i| - |\mathbf{R}_i - \mathbf{R}_{i-1}|)\hat{\tau}_i \tag{2.42}$$

Figure-2.3 shows a schematic representation of how the force projection helps the NEB path to find the MEP.

2.4.1.1 The tangent estimation

The tangent $\hat{\tau}_i$ is estimated by the vector between the image i and the neighboring image $i \pm 1$ with higher energy and then normalized as, [31]

$$\hat{\tau}_i = \frac{\tau_i}{|\tau_i|} \tag{2.43}$$

where

$$\tau_i = \begin{cases} \mathbf{R}_{i+1} - \mathbf{R}_i & \text{if } E_{i+1} > E_i > E_{i-1} \\ \mathbf{R}_i - \mathbf{R}_{i-1} & \text{if } E_{i+1} > E_i > E_{i-1} \end{cases} \tag{2.44}$$

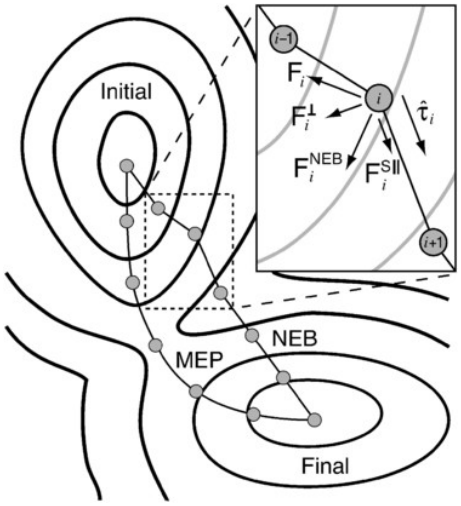

Figure 2.3: Schematic of the NEB used to estimate the MEP and the force projection. $\mathbf{F}_i$ is the unprojected force acting on image i, $\mathbf{F}_i^{S\|}$ is the spring force acting on image i, along the tangent $\hat{\tau}_i$ and $\mathbf{F}_i^{\perp}$ is the perpendicular force acting on image i. Figure taken from Ref.[30]

At the extrema along the MEP, either both of the neighboring images $i\pm1$ will have higher in energy (for minima) or both of the neighboring images $i \pm 1$ will have lower energy (for maxima). Hence, the tangent for an image at the extrema is estimated by a weighted average of the vectors to both of the neighboring images as, [31]

$$\tau_i = \begin{cases} (\mathbf{R}_{i+1} - \mathbf{R}_i)\Delta E_i^{max} + (\mathbf{R}_i - \mathbf{R}_{i-1})\Delta E_i^{min} & \text{if } E_{i+1} > E_{i-1} \\ (\mathbf{R}_{i+1} - \mathbf{R}_i)\Delta E_i^{min} + (\mathbf{R}_i - \mathbf{R}_{i-1})\Delta E_i^{max} & \text{if } E_{i+1} > E_{i-1} \end{cases} \tag{2.45}$$

where

$$\begin{aligned} \Delta E_i^{max} &= \max(|E_{i+1} - E_i|, |E_{i-1} - E_i|), \text{and} \\ \Delta E_i^{min} &= \min(|E_{i+1} - E_i|, |E_{i-1} - E_i|). \end{aligned} \tag{2.46}$$

2.4.1.2 Optimization methods

The NEB path is moved along the $\mathbf{F}^{\text{NEB}}$ to the MEP using an optimization algorithm. The optimization methods are limited by the force projections. The optimizer used to move the NEB path should follow the NEB force $\mathbf{F}^{\text{NEB}}$, rather than following the unprojected force. There are a number of optimization methods available; the Quantum ESPRESSO software [34] used to estimate the MEP offers five different methods, steepest descent

method (SD), quasi-Newton Broyden's second method (broyden), another variant of the quasi-Newton Broyden's second method (broyden2), velocity Verlet scheme (quick-min) and finite temperature Langevin dynamics (langevin). For all the NEB results presented in this thesis, we have used the quasi-Newton Broyden's second method (broyden).

2.4.1.3 Interpolation between the images

The images are interpolated to sketch the MEP and obtain a good estimate of the saddle point. Along with the energy of the images, the force acting along the band is also included in the interpolation. The interpolation is done by fitting each segment $[\mathbf{R}_i, \mathbf{R}_{i+1}]$ with a cubic polynomial, $ax^3 + bx^2 + cx + d$. The continuity in energy and the force at the ends of the band are enforced by the choice of the four parameters, that are given by, [31]

$$\begin{aligned} a &= \frac{2E_{i+1}-E_i}{R^3} - \frac{F_i+F_{i+1}}{R^2} \\ b &= \frac{3E_{i+1}-E_i}{R^2} - \frac{2F_i+F_{i+1}}{R} \\ c &= -F_i \\ d &= E_i \end{aligned} \tag{2.47}$$

where E_i and E_{i+1} are the energy of the initial and final states, and F_i and F_{i+1} are the forces along the path.

The NEB method provides a rough estimate of the MEP and does not provide the fair estimation of the TS. The highest energy image in the converged NEB can be away from the saddle point.

2.4.2 Climbing image nudged elastic band (CI-NEB) method

The CI-NEB method ensures the highest energy image in a path to be the saddle point, and it differs from the NEB method discussed above in one regard. In the CI-NEB method, the image having the highest energy in the path feels no spring forces. This highest energy image made to climb to the saddle point by applying a force along the tangent, [33]

$$\mathbf{F}_i^{CI} = \mathbf{F}_i - 2\mathbf{F}_i.\hat{\tau}_i\hat{\tau}_i \tag{2.48}$$

This ensures the highest energy image of a converged CI-NEB path to be the saddle point. The first order saddle point can be verified by calculating the normal mode frequencies.

2.5 Kinetic Monte Carlo method

The system spends a long time in one potential basin before it escapes from that basin. Hence, it can be assumed that the system retains no memory of how it got into that potential basin before escaping from there. In this way, each possible escape is independent of the potential energy basin visited by the system in the past. The system is performing Markov walk between the potential energy basins. The main idea behind the KMC simulation is the time evolution of this Markovian state to state dynamics. The time evolution is controlled by a master equation of Markovian form, [3]

$$\frac{dP_i(t)}{dt} = -\sum_{j \neq i} k_{ij} P_i(t) + \sum_{j \neq i} k_{ji} P_j(t) \tag{2.49}$$

where $P_i(t)$ and $P_j(t)$ are the probabilities of finding the system at time t in state i and j respectively. k_{ij} (k_{ji}) is the rate constant corresponding to a transition in which the system jumps from state i (j) to j (i).

2.5.1 Graph-theoretical Kinetic Monte Carlo framework

In this method, the possible reactions on a given lattice state is predicted by the application of graph theory. This GT-KMC method enables to represent any complex elementary reaction steps, which involve mono-dentate or multi-dentate species and any number of sites, which are connected in arbitrary neighboring pattern. In this method, the lattice is represented as a graph, which means a collection of sites which are connected in a specific pattern like a graph. The state of the lattice gives the information about the sites and their occupancy, i.e., which sites are occupied by which species. Any elementary reaction step is also represented by a graph with specific initial and final state. The graph representations of elementary reaction steps are mapped onto the lattice processes by solving the subgraph isomorphism problem. The lattice processes represent the reaction events that can occur on the lattice sites during the course of the simulation. Every such process

is assigned to a random occurrence time, and a priority list is created based on the random occurrence time. At each KMC step, the first process in the list is executed and the simulation time is updated, along with the lattice states and the energetics reflecting the occurrence of that event. The priority list is also updated for the new lattice state based on the lattice processes of the new state, and the whole procedure is repeated. This above procedure results in a stochastic trajectory that contains complete information about the lattice state at all the time. This trajectory also contains the information about the number of the species adsorbed and produced.

2.5.1.1 Lattice representation

Based on the type and position of the well defined reaction sites present in the catalytic surface, a lattice representation of the surface is constructed. Each one of the well defined sites s_i are represented by a three-element vector, where the first element denotes the type of the site s_i and the other two elements denote the x- and y-coordinates, [35]

$$\begin{aligned} &\mathbf{s_i} \in \{1, 2, 3, ..., S_T\} \times \mathbb{R}^2, \qquad \mathbf{i} \in \mathcal{S} = \{1, 2, 3, ..., S_L\}, \\ &\mathbf{s} = \{(s_{i,j})_{j=1}^{3}\}_{i=1}^{S_L} \end{aligned} \tag{2.50}$$

where $\mathcal{S}$ is an index set contains all the sites on the lattice and S_L is the number of these sites. The graph representation of the lattice $\mathcal{L}$ is given as,

$$\mathcal{L} = (\mathcal{S}, \mathcal{E}), \tag{2.51}$$

where $\mathcal{E}$ contains two element subsets of $\mathcal{S}$. $\mathcal{E}$ is the set of edges that show the connectivity of sites in the lattice-graph.

2.5.1.2 State of the system

The state of the system at a particular time depends on the occupancy of all the available sites, i.e., either a site s_i is occupied by a species k or it is empty. Each entity that exists on the lattice is labeled by an integer. Further, the state of each site is represented by a three-element vector $\sigma_\mathbf{i}$: the element corresponds to the label of the entity, the second element corresponds to the species number and the last third element corresponds to the subunit number occupying the site under consideration. An $S_L \times 3$ array defines the state

of the system σ, [35]

$$\begin{aligned} &\sigma_{\mathbf{i}} \in \{1,2,3,...,\mathrm{S_L}\} \times \{0,1,2,...,\mathrm{N_S}\} \times \{1,2,3,...,\max(\mathrm{d})\} \qquad \mathbf{i} \in \mathcal{S} \\ &\sigma = \{(\sigma_{\mathrm{i,j}})_{\mathrm{j=1}}^{3}\}_{\mathrm{i=1}}^{\mathrm{S_L}} \end{aligned} \tag{2.52}$$

where $\mathrm{N_S}$ is the number of different surface species and d is the number of sites being occupied by a species.

2.5.1.3 Elementary step representation

As a result of the rare event the state of the lattice will change. Similar to the sites represented in the lattice (Equation-2.50), the elementary step k involving $\mathrm{S_{R,k}}$ sites are assigned a site type, [35]

$$\xi_{\mathrm{k,i}} \subseteq \{0,1,2,3,...,\mathrm{S_T}\}, \qquad \mathrm{i} \in \Xi_{\mathrm{k}} = \{1,2,3,...,\mathrm{S_{R,k}}\} \tag{2.53}$$

where site type 0 corresponds to undefined site type involved in the elementary reaction step k and that site can be of any type. The elementary step (rare event) defined in a graph as,

$$\mathcal{R}_{\mathrm{k}} = (\Xi_{\mathrm{k}}, \mathcal{E}_{\mathrm{k}}). \tag{2.54}$$

The barrier corresponding to the elementary reaction step can be estimated using the CI-NEB method and the rate constant can be estimated within the HTST as described in Equation-2.38

2.5.1.4 Mapping to lattice processes

The basic idea is solving a subgraph isomorphism problem for the elementary reaction steps defined, in order to find out the lattice processes that are occurring. The lattice processes are mapping between the vertex sets of $\mathcal{R}_k$ and $\mathcal{L}$, [35]

$$\mathcal{M} : \Xi_{\mathrm{k}} \rightarrow \mathcal{S} \tag{2.55}$$

such that,

1. $\mathcal{M}$ is the subgraph isomorphism. For every pair p,q of neighboring sites in $\mathcal{E}_k$, there

exists a pair $\mathcal{M}$(p),$\mathcal{M}$(q) of neighboring sites in $\mathcal{E}$ of $\mathcal{L}$

$$\forall_{\substack{1\leq p\leq S_{R,k}\\ 1\leq q\leq S_{R,k}}} \{p,q\} \in \mathcal{E}_k \Longrightarrow \{\mathcal{M}(p), \mathcal{M}(q)\} \in \mathcal{E} \tag{2.56}$$

2. the sites type on the pattern p and the $\mathcal{M}$(p) on the lattice are the same,

$$s_{\mathcal{M}(p),3} = \mathcal{E}_{k,p} \qquad 1 \leq p \leq S_{R,k} \tag{2.57}$$

3. there is a mapping between the elementary reaction step entities and the lattice entities,

$$\mathcal{F} : \{1, 2, ..., N_{RE}\} \rightarrow \{1, 2, ..., N_E\} \tag{2.58}$$

such that,

$$\sigma_{\mathcal{M}(p),1} = \mathcal{F}(\sigma^{ini}_{k,p,1}) \qquad 1 \leq p \leq S_{R,k} \tag{2.59}$$

2.5.1.5 Event statistics

If a mapping is found, then there is a possibility for that elementary event i to occur in the future. The time taken for the occurrence of event i is calculated as, [35]

$$p(\tau_i) = k_i^{hTST}(t + \tau_i)\exp[-\int_0^{\tau_i} k_i^{hTST}(t + \tau_i')d\tau']. \tag{2.60}$$

In order to calculate the time for the occurrence of the next event, one needs to solve the equation,

$$\int_0^{\tau_i} k_i^{hTST}(t + \tau_i')d\tau' + ln(1 - u) = 0 \tag{2.61}$$

where u is a uniformly distributed random number $u \sim \mathcal{U}(0, 1)$. If the rate of the elementary step is time independent then,

$$\tau_i = \exp(k_i^{hTST}) \tag{2.62}$$

Hence, the time taken for the next event to occur,

$$\tau_i = -\frac{1}{k_i^{hTST}} ln(1 - u). \tag{2.63}$$

Figure-2.4 shows the flowchart of the basic steps in the time evolution of the system within

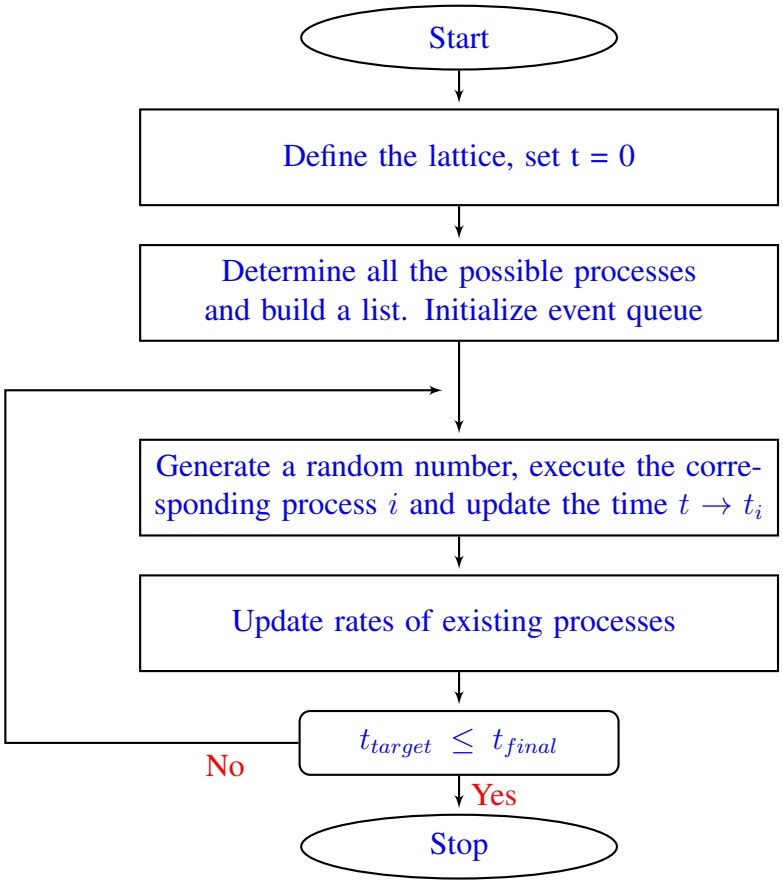

Figure 2.4: Flowchart showing the basic steps in the GT-KMC simulation.

the GT-KMC framework.

Chapter 3

Structure and Stability of Clean and Adsorbate Covered Intermetallic PdGa Surfaces

In this chapter, using *ab initio* density functional theory based calculations we have studied the structure and stability of clean and hydrogen covered low-indexed (100) and (110) surfaces of intermetallic PdGa. We find that for the clean (100) surface, the stability of the surface terminations is independent of the surface preparation condition. On the contrary, at least three different types of surface terminations can be stabilized for the (110) surface by tuning the surface preparation conditions. Upon adsorbing molecular and atomic hydrogen on these surfaces, it is found that: (a) at 450 K hydrogen adsorbs only at high hydrogen partial pressure ($> 10^6$ mbar) and (b) the relative stability of the different surface terminations are unaffected by the presence of adsorbates. The work presented in this chapter is published in *Surface Science*, **2016**, 644, 69-79.

3.1 Introduction

Intermetallic surfaces are interesting because of their use in technologically important areas like catalysis, magneto-optical films, microelectronics, etc. [36] Usually these surfaces are prepared from intermetallic compounds of two or more elements of which one is a transition metal. Among the intermetallics, PdGa has been of particular interest in the recent years because of its probable use as an efficient catalyst for selective hydrogenation of acetylene to ethylene. Armbrüster *et al.* showed that unlike the commercially used Pd catalysts for this reaction, [37] PdGa shows very high selectivity. [38] In order to understand the details of the reaction mechanism on PdGa, and in particular, the factors that contribute to it being highly selective, there have been efforts to characterize the low indexed PdGa surfaces. Using a combination of different surface science techniques like ultra-violet

photoelectron spectroscopies, scanning tunnelling microscopy (STM), etc. Rosenthal *et al.* showed that the stability of the (111) and $(\bar{1}\bar{1}\bar{1})$ surface terminations can be controlled by annealing the surfaces at different temperatures. [39] The works of Prinz *et al.* [40] and Krajčí *et al.* [41] suggest that for these surfaces the Pd and Ga rich three fold terminations are stable. Further, density functional theory (DFT) based calculations by Krajčí *et al.* suggest the pseudo-fivefold (210) surface as a possible catalytically active surface termination. [42] Recently, using STM, temperature programmed desorption studies and DFT, Prinz *et al.* showed that for the (111) and $(\bar{1}\bar{1}\bar{1})$ surfaces, the selectivity is strongly affected by structural differences in the arrangement of Pd atoms on these surfaces. [43] .

However, the other low indexed surfaces like the (100) and (110) are hardly studied. While the bulk truncated (100) surface is more or less flat (corrugation of only 0.07 Å), the bulk truncated (110) surface is highly corrugated and hence might affect the reactivity and selectivity of the PdGa catalyst if these are used for the selective hydrogenation of acetylene. Further, as mentioned in the previous paragraph, the selectivity, as well as the reactivity, is strongly affected by the microscopic details of the surface structure. In PdGa, particularly for the (110) surface, there is a rich variety of possible surface structures. In combination with the already existing understanding of the acetylene selective hydrogenation on the (210) and (111) surfaces, a detailed study of the same reaction on the other PdGa surfaces might provide useful insights to arrive to a correlation between the microscopic surface properties and the reactivity and selectivity. This can then be used for rational design of catalysts for the selective hydrogenation reactions.

To the best of our knowledge, the only experimental study related to the (110) surface is the investigation of its electronic properties by photoemission [44]. Recently Bechthold *et al.* used DFT to investigate the adsorption of hydrogen and CO on the (100), (110) and (111) surfaces. [45–48] However, they have used only one surface termination for the (100) and (110) surfaces and did not investigate the stability of the other possible terminations. Hence the question is how stable are the low indexed (110) and (100) surfaces? Are these also catalytically active for the selective hydrogenation reaction and if so how are the barriers and the reaction mechanisms compared to the (111) surfaces?

As a first step in answering these questions, a detailed investigation of the structure and stability of the different possible terminations of the clean (100) and (110) surfaces of

PdGa is carried out. It is also well known that the stability of the terminations can be altered in the presence of adsorbates. This will, in turn, affect their performance as a catalyst. In the acetylene hydrogenation reaction on these surfaces, the first step typically involves adsorption of molecular hydrogen and atomic hydrogen (after they are dissociated). Hence, the effect of adsorption of atomic and molecular hydrogen on the stability of the different surfaces terminations are also using *ab initio* thermodynamics.

The rest of the chapter is organised as follows: Section 3.2 contains the computational details and a description of the different terminations of the bulk truncated surfaces. We present our results and discuss their implications in Section 3.3. Finally we summarize them in Section 3.4.

3.2 Computational Details and Surface Models

3.2.1 Computational Details

We have used the Quantum Espresso software, [34] a plane wave based implementation of density functional theory, to solve the Kohn-Sham equations. The electronic exchange and correlation potential is described by the generalized gradient approximation (GGA) based parametrization of Perdew-Burke-Ernzerhof (PBE). [12] Ultrasoft pseudopotentials have been used to describe the electron-ion interactions. [19] A plane wave basis set was used with a kinetic energy cutoff of 30 Ry and 320 Ry for wavefunction and charge density respectively. For these cutoff values the total energy of the bulk PdGa is converged up to 10^{-4} Ry. Marzari-Vanderbilt smearing [23] with a smearing width of 0.01 Ry was used to speed up the convergence. Brillouin zone integrations were done with $8\times8\times8$ Monkhorst-Pack(MP) [20] k-point mesh for bulk PdGa and bulk Pd. A convergence test was carried out for the k-point mesh; with $8\times8\times8$ mesh the total energy of the bulk PdGa is converged to 10^{-4} Ry. For geometry optimization calculation the forces acting on atoms are converged up to 10^{-3} Ry/bohr.

To test the pseudopotentials used, we have calculated the lattice parameters of fcc bulk palladium, orthorhombic bulk gallium and simple cubic bulk PdGa and compared them with the previous experimental and theoretical results. The obtained results, reported in Table-3.1, are in excellent agreement with the experimental measurements [49–51] and

Table 3.1: Lattice constants of bulk Pd, bulk Ga and bulk PdGa.

System	lattice parameter (Å)		
	Calculated (GGA-PBE)		Experimental
	This work	Previous report	
fcc Pd	a=3.95	3.98[a], 3.95[b]	3.89[c]
orthorhombic Ga	a=4.52	-	4.51[d]
	b=4.50	-	4.49
	c=7.64	-	7.65
simple cubic PdGa	a=4.96	4.90[e]	4.90[f]

[a]Ref. 52, [b]Ref. 53, [c]Ref. 49, [d]Ref. 50, [e]Ref. 45 and [f]Ref. 51

previously computed values. [45, 52, 53]

3.2.2 Structure of Bulk PdGa and Bulk Truncated (110) and (100) Surfaces

Bulk PdGa belongs to the $P2_13$ space group [44] and has two enantiomorphic forms A and B, [51] whose atomic coordinates are related by inversion. The crystal structure of PdGa is simple cubic (lattice constant of 4.96 Å) with eight atoms (four Pd and four Ga) in the unit cell. The Pd and Ga atoms are located at Wyckoff positions ($4a$) with coordinates (u, u, u), (u+0.5, 0.5-u, -u), (-u, 0.5+u, 0.5-u) and (0.5-u, -u, 0.5+u). Our calculations yield $u_{Pd} = 0.142$ and $u_{Ga} = 0.843$. These are in excellent agreement with previous calculations [41, 42] and experimental results. [39] Each Pd (Ga) atom is surrounded by seven Ga (Pd) atoms forming a mono-capped trigonal prism. The coordination around Pd (Ga) and the Pd-Ga bond lengths are shown in Fig-3.1. The Pd-Ga bonds can be grouped into three categories based on their bond lengths. One short bond with a bond length of 2.57 Å, and two sets of slightly longer bonds (three each) with bond lengths of 2.61 and 2.75 Å. These bond lengths are slightly overestimated compared to the experimental values of 2.54, 2.57 and 2.71 Å respectively. [51]

Since the crystal is chiral; all the surface terminations exhibit two-dimensional chirality. However, unlike the (111) and ($\bar{1}\bar{1}\bar{1}$) surfaces, the (100) and ($\bar{1}00$) surfaces are equivalent. Same is true also for the (110) and ($\bar{1}\bar{1}0$) surfaces. In bulk PdGa, along the (100) direction, each layer has one Pd and one Ga atom. Further there are two inter planar distances of 1.00 Å and 1.48 Å (Fig-3.2(a)). Therefore, depending on where the crystal is cleaved,

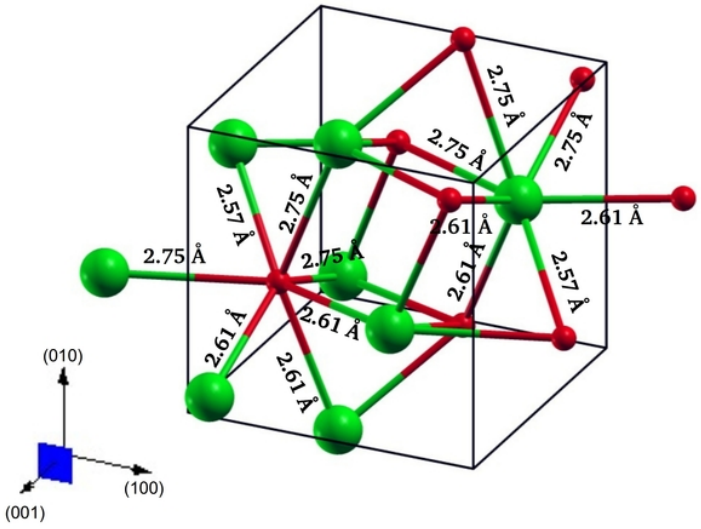

Figure 3.1: Unit cell of (1:1) PdGa and the coordination around Ga and Pd. Green (large) and red (small) spheres represent Pd and Ga atoms respectively.

there are two possible terminations which are labeled as PG_l and PG_h (Fig-3.2(a)). PG_l (PG_h) represents the surface that has been created by cleaving the crystal in the less dense (dense) region, where the inter planer distance is 1.48 Å(1.00 Å). The top view of the bulk truncated surfaces is shown in Fig-3.2(b-c). The (1×1) surface unit cell consists of two interpenetrating squares of Pd and Ga atoms. The bulk truncated layer is puckered with the Pd and Ga atoms separated vertically by 0.07 Å. For the PG_h termination, the Ga atoms are higher than the Pd atoms and vice versa for PG_l. The topmost Pd atom has two different Pd-Ga bond distances making it a two-dimensional chiral surface.

The stacking of PdGa in form A along the (110) direction is shown in Fig-3.3(a). Each layer may have either one Pd, or one Ga, or one Pd and one Ga atom (Fig-3.3(a)). Depending on the composition of the topmost layer and the one below it, there are six possible terminations. The proposed nomenclature for these different terminations depends on the number and type of atoms in the topmost layer and the one below it. Uppercase alphabets are used to represent atoms in topmost layers (P for Pd and G for Ga), and lowercase alphabets to represent atoms in the second layer (p for Pd and g for Ga). For example, Pp represents the (110) surface termination where there is only one Pd atom on both the topmost layer and the one below it (Fig-3.3(b)). Similarly, the other possible surface terminations for form A are Ppg, PGg, Gg, Gpg and PGp (Fig-3.3(c)-(g)). The crystal has

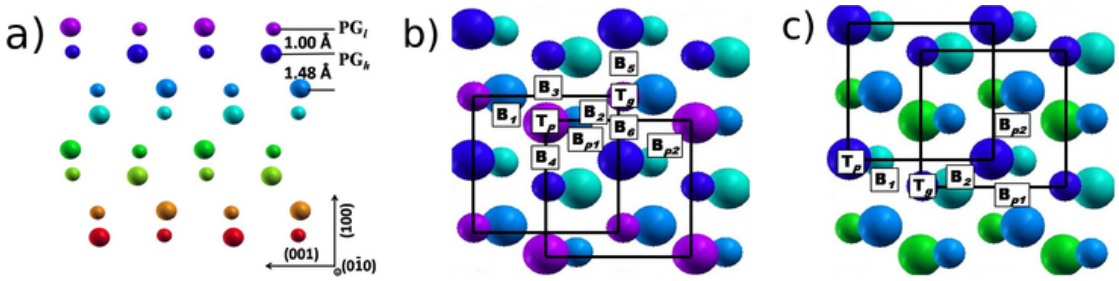

Figure 3.2: (a) Stacking of the layers along (100) direction in bulk PdGa and the bulk inter-planar distances. Top view of (b) PG$_l$ and (c) PG$_h$ terminations. The surface unit cell is marked by black squares. The larger spheres denote Pd atoms while the smaller ones denote Ga atoms. The different colours represent atoms at different heights. The sites considered for hydrogen adsorption are marked (refer to text for details regarding the labels of the sites).

no rotational or mirror symmetry along the (110) direction. So all the six terminations are chiral.

3.2.3 Surface Slab Model

For most of the low indexed surfaces of PdGa, not only the atoms in the topmost layer but also those several layers below it lack their bulk coordination number. For example in (110) surface even the atoms in the fourth layer below the surface are under-coordinated. Similarly for the (100) surfaces atoms up to two layers below the surface lack their bulk coordination number. Hence the surface relaxation effects might go several layers below the surface, thereby making it necessary to use thick slabs to model the surface.

The (100) surfaces are modeled using symmetric and stoichiometric slabs which are 24 layers thick. For the (110) surface, it is not possible to have stoichiometric and symmetric slabs for all possible terminations. Only the Ppg and Gpg terminations can be modeled with stoichiometric and symmetric slabs. The Ppg have been modeled with a slab of 36 layers. For the other terminations, the slab consists of two types of surfaces, of which one of them always have a PGg termination. We started off with a 36 layer thick slab having Pp and PGg terminations on either side. The other surfaces, have been created by sequentially removing atoms from the Pp surface layer. This results in slabs with 34, 33, 32 and 31 layers for PGg, Gg, Gpg and PGp terminations respectively. For all the surfaces, only one atom in the middle of the slab is kept fixed while all other atoms are relaxed. We ensured that the slabs are thick enough by checking that after relaxation, at least there are

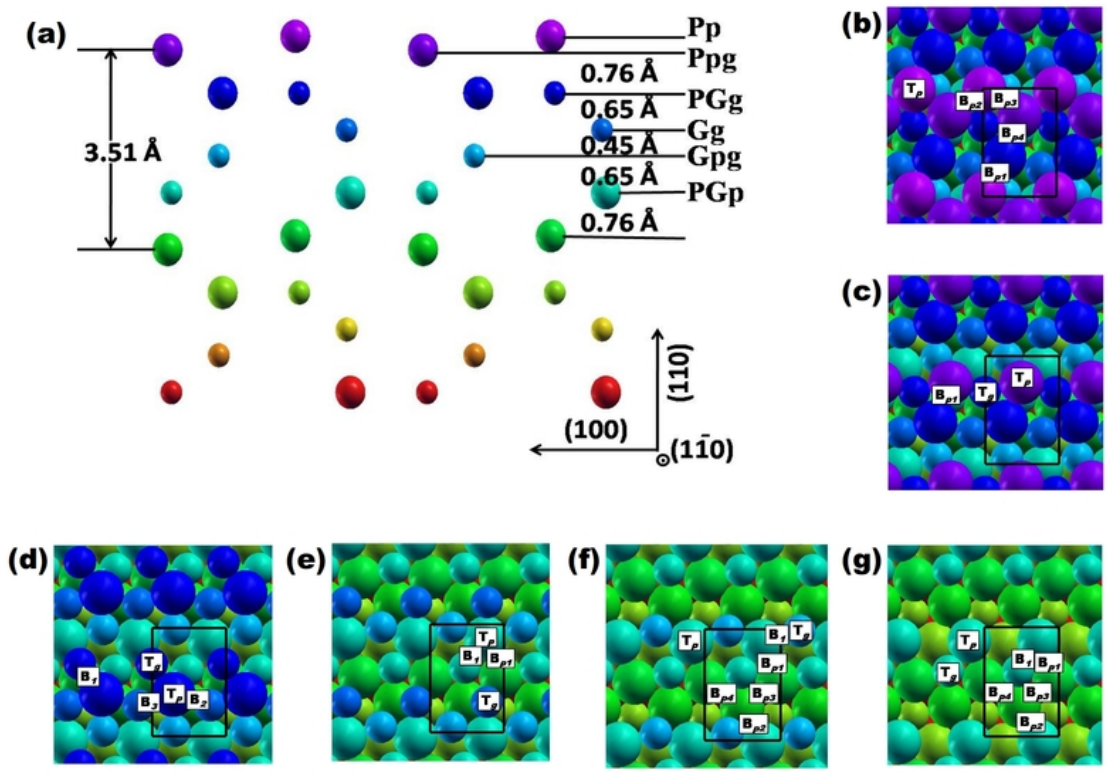

Figure 3.3: (a) Stacking of the layers along the (110) direction in bulk PdGa and the bulk inter planar distances. (b), (c), (d), (e), (f) and (g) show the top view of the Pp, Ppg, PGg, Gg, Gpg and PGp terminations respectively. The distance between Pp and Ppg (about 0.24 Å) is not shown in the figure for the sake of clarity. The surface unit cell is marked by black rectangles. The larger spheres denote Pd atoms while the smaller ones denote Ga atoms. The different colours represent atoms at different heights. The sites considered for hydrogen adsorption are marked (refer to text for details regarding the labels of the sites).

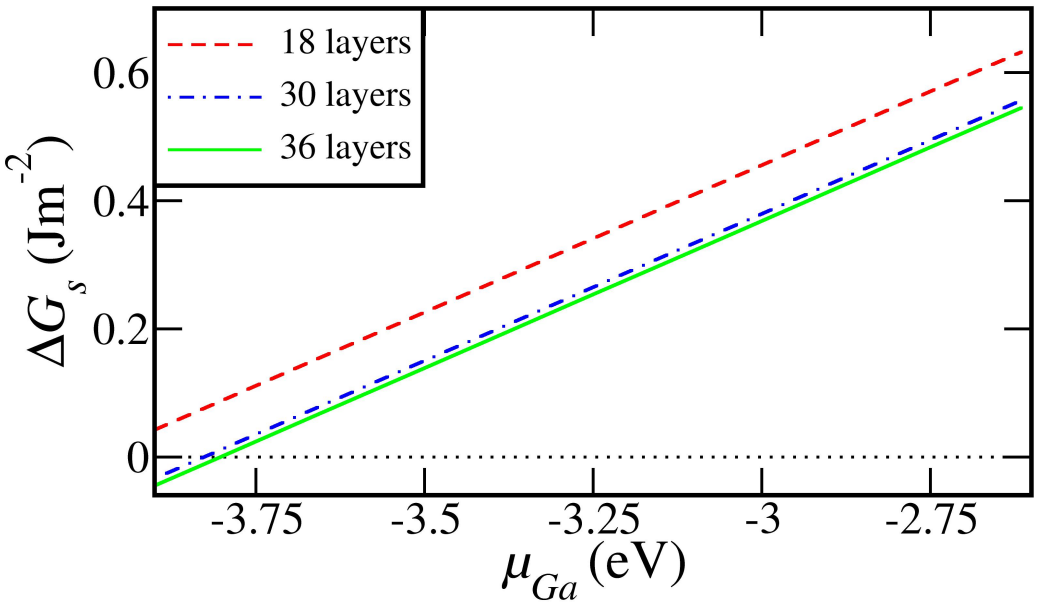

Figure 3.4: Relative surface energy as a function of μ_{Ga} for the three different thicknesses of Pp surface with respect to 32 layers thick Gpg surface termination (horizontal black dotted line).

eight layers which have inter-planar distances same as that of the bulk. The surface free energies are converged up to 10^{-2} Jm^{-2}. Figure 3.4 shows the convergence of relative surface energy of Pp surface with three different thicknesses with respect to 32 layers thick Gpg surface. A detailed procedure for calculating the relative surface free energy will be discussed in the next section (Section 3.2.4). To avoid the interactions between the periodic images of slabs a vacuum of 16 and 22 Å were used for (100) and (110) surfaces respectively. Brillouin zone integrations have been done using a $8\times8\times1$ k-point mesh for the (1×1) surface unit cell.

To study the adsorption of hydrogen on these surfaces using such thick slabs is computationally prohibitive. Hence to strike a balance between accuracy and computational cost, thinner slabs than what mentioned in the previous paragraph are used. The (100) PG_h and PG_l surfaces are modeled using stoichiometric slabs which are 13 and 12 layers thick. The bottom six layers are fixed at their bulk positions, and the top layers are relaxed. Similarly, for PGg, Gg, Gpg, PGp, Pp and Ppg terminations the slabs that are used are off 22, 21, 20, 19, 18 and 17 layers thick respectively. The maximum difference between the surface energies of these surfaces computed with the thinner slab and that obtained from the thicker one is about 10^{-2} Jm^{-2}. To further check that the reduced slab thickness does

not affect the ordering of the stable adsorption sites, the binding energies of atomic H on the PG_l surface with both the thick and thin surfaces are calculated. For this particular termination the differences in binding energies of H on different sites are very small, and their relative stability will be sensitive to the accuracy of the calculations. For the most stable adsorption geometry for each surface termination, the binding energies obtained using thicker and thinner slabs differ at the most by 0.01 eV.

The H atom/molecule can adsorb either on the atop site or on a bridge site. Depending on the type of atoms involved in a particular adsorption site, these are classified as on top of Pd (T_p) or Ga (T_g), bridge between Pd-Ga (B_i), and bridge between Pd-Pd (B_{pi}). The subscript i denotes the different number of inequivalent sites of a given type. The possible adsorption sites on the (100) and (110) surfaces are shown in Fig-3.2(b-c) and 3.3(b-g) respectively. The binding energy (E_{ads}) of the adsorbates on these surfaces is defined as:

$$E_{ads} = E_{Total}^{Slab+nX} - E_{Total}^{Slab} - yE_{Total}^{H_2} \tag{3.1}$$

where $E_{Total}^{Slab+nX}$, E_{Total}^{Slab} and $E_{Total}^{H_2}$ are the total energies of the slab with n adsorbates, clean slab and H_2 molecule in the gas phase respectively. X can be a H atom or a hydrogen molecule. In the above equation $y = n$ if X is hydrogen molecule. If X is a H atom then $y = \frac{n}{2}$.

3.2.4 *Ab initio* Atomistic Thermodynamics

Stability of different surfaces, both clean and in the presence of adsorbates, can be determined based on their surface free energies. For the surfaces considered in this study, since there are many terminations where the slabs are either nonstoichiometric or not symmetric with respect to inversion, the number of atoms of Pd and Ga is different in different slabs. Moreover, the number of adsorbate species on the surfaces also vary depending on their coverage. Hence the surface free energy has been calculated within the grand-canonical ensemble (GCE). In the GCE, assuming that the surface is in equilibrium with the adsorbates, the Gibbs free energy (G) is given by:

$$G = E + PV - TS - \sum_i n_i \mu_i \tag{3.2}$$

where P, V, T and S are the pressure, volume, temperature and entropy respectively. n_i and μ_i are the number and the chemical potential of the i^{th} species ($i \in$ Pd, Ga, X) respectively. E is the internal energy of the system and is obtained from the DFT calculations. In order to apply these concepts, one needs to clearly distinguish between what is considered as "system" and that which is to be its "surroundings". In this work we have taken the *fixed chemical potential* viewpoint in which the system consists of surfaces and any molecules attached to them. The rest of the world beyond them constitutes the surroundings. Now to a fair approximation, the entropy of the system is more or less negligible, since it consists only of vibrational and configurational contributions. Further, the PV term can also be neglected because the considered systems are solid slabs. The surface free energy as a function of the chemical potentials of Pd and Ga, temperature (T) and adsorbate partial pressures (p) is given by,

$$G_{slab} = E_{slab} - n_{Ga}\mu_{Ga} - n_{Pd}\mu_{Pd} - n_X\mu_X(T,p) \tag{3.3}$$

where, G_{slab} is the sum of the Gibbs surface energy of both the surfaces of the slab, E_{slab} is the total energy of the slab, n_i and μ_i are the number of atoms and the chemical potential respectively of the i^{th} species in the slab.

For the clean surfaces (in the absence of any adsorbates X, i.e., $n_X = 0$ in Eqn.3.3) that can be modelled by symmetric and stoichiometric slabs, $\frac{G_{slab}}{2}$ gives the absolute value of the surface free energy. For the other surfaces, we have calculated their stability relative to that of stoichiometric Gpg termination, for which the absolute value of the surface free energy can be calculated. The difference between their Gibbs free energy (ΔG_s) of two surfaces is given by:

$$\Delta G_s = \frac{1}{A}\left(G^{surf}_{slab} - G^{ref}_{slab}\right) \tag{3.4}$$

where, A is the area of the unit cell.

Similar argument also applies for the adsorbate covered surfaces. Hence combining equations 3.3 and 3.4 one can write ΔG_s as:

$$\Delta G_s(T,p) = \frac{1}{A}(E_{slab} - E^{ref}_{slab} - \Delta n_{Ga}\mu_{Ga} - \Delta n_{Pd}\mu_{Pd} - n_X\mu_X(T,p)) \tag{3.5}$$

where Δn_i is the difference between the number of atoms of the i^{th} species in the two

slabs and E^{ref}_{slab} is the total energy of the reference slab, which in this case is the one with Gpg termination.

The chemical potentials of Pd and Ga depend on the experimental conditions and it is not possible to exactly define them. However, the allowed range of the chemical potentials is given by,

$$\mu^{bulk}_{PdGa} = \mu^{bulk}_{Pd} + \mu^{bulk}_{Ga} + \Delta H_f \tag{3.6}$$

where, μ^{bulk}_{PdGa} is the cohesive energy of bulk PdGa per formula unit, μ^{bulk}_{Pd} is the cohesive energy of bulk Pd, μ^{bulk}_{Ga} is the cohesive energy of bulk Ga, and ΔH_f is the enthalpy of formation of bulk PdGa per formula unit. The cohesive energies of bulk Pd and bulk Ga obtained from our calculations are, μ^{bulk}_{Pd} = -3.68 eV and μ^{bulk}_{Ga} = -2.62 eV. These are in reasonably good agreement with previously reported computed values (μ^{bulk}_{Pd} = -3.69 eV, μ^{bulk}_{Ga} = -2.78 eV) and the experimental measurements (μ^{bulk}_{Pd} = -3.52 eV, μ^{bulk}_{Ga} = -2.48 eV). [40] The calculated value of the enthalpy of formation of bulk PdGa per formula unit (ΔH_f=-1.31 eV), is in excellent agreement with earlier theoretical report of -1.37 eV [40] and is slightly underestimated compared to the experimental value of -1.48 eV. [54] Assuming the sources of Pd and Ga are in equilibrium with PdGa, the upper boundary of the chemical potential of one of the constituent species can be set to its individual bulk value. Now, the allowed range of the chemical potential of Pd and Ga are,

$$\mu^{bulk}_{Pd} + \Delta H_f \leq \mu_{Pd} \leq \mu^{bulk}_{Pd} \tag{3.7}$$

$$\mu^{bulk}_{Ga} + \Delta H_f \leq \mu_{Ga} \leq \mu^{bulk}_{Ga}. \tag{3.8}$$

In eqn-3.7 (eqn-3.8) when the value of the chemical potential of Pd (Ga) in PdGa is same as that in bulk Pd (bulk Ga), the surfaces are prepared in Pd (Ga) rich environment, while if $\mu_{Pd} = \mu^{bulk}_{Pd} + \Delta H_f$ ($\mu_{Ga} = \mu^{bulk}_{Ga} + \Delta H_f$), the surfaces are prepared in Ga (Pd) rich environment.

The chemical potential of the adsorbed species (X) can be obtained from the following relationship:

$$\mu_X = \frac{1}{n_X}(H - TS) \tag{3.9}$$

where H is the enthalpy. The values of entropy at standard pressure can be extracted from the CRC Handbook. [55] However, for enthalpy, only the change in enthalpy in going

from absolute zero temperature to several finite temperatures $[\Delta H(0 \longrightarrow T, p^\circ)]$ at p° are reported in the CRC Handbook. Hence $H(T, p^\circ)$ can be obtained using the following relation,

$$H(T, p^\circ) = H(0, p^\circ) + \Delta H(0 \longrightarrow T, p^\circ), \tag{3.10}$$

where $H(0, p^\circ)$ can be obtained from DFT calculations. The variation of μ_X with T and p is given by:

$$\mu_X(T, p) = \mu_X(T, p^\circ) + k_B T ln(p/p^\circ) \tag{3.11}$$

3.3 Results and Discussion

3.3.1 Structure and Energetics of the Clean (100) and (110) Surfaces

Experimental results revealed no segregation of atoms on these surfaces [39,44]. From the relaxed geometries, it is found that lateral relaxation of the surface atoms are very small, while their vertical relaxations are large.

For the PG_l/PG_h terminations of the (100) surface the relaxation effects are significant down to seven/four layers below the surface (Table 3.2). The change in the inter planar distances of the relaxed surface with respect to that of the bulk terminated ones are given by $d^{rel}_{i,j} = \frac{\Delta d_{i,j}}{Z_{i,j}}$, where $\Delta d_{i,j} = d^i_{avg} - d^j_{avg}$, refers to the spacing between two layers of the relaxed surface and $Z_{i,j}$ represents the bulk interlayer spacing between the i^{th} and j^{th} layers. In their bulk truncated form, the surface layers are also rumpled. The surface rumpling (d_{rum}) is given by $d_{rum} = \frac{\Delta Z}{Z_{1,2}}$, where $\Delta Z = z^{(1)}_{Pd} - z^{(1)}_{Ga}$ refers to the spacing of Pd and Ga atoms in the top layer. For the bulk truncated PG_l and PG_h surfaces, the d_{rum} are 7.53 and -5.04 % respectively. Due to the difference in the electronegativities of Pd and Ga, the Pd and Ga atoms relax in opposite directions. While the Pd atoms move towards the surface, the Ga atoms move further away. This results in an increase of d_{rum} to -13.97 % on the PG_h termination. For PG_l, the effects of surface relaxations are more drastic. Here the d_{rum} not only decreases after relaxation but also changes sign ($d_{rum} = -1.39$ %) resulting in the Ga atoms being exposed while the Pd atoms just 0.01 Å below them.

Like their (100) counterpart, the (110) surfaces also show relaxation effects that are large and sensitive to the type of termination (Table 3.2). For the Pp, Ppg, PGg and Gg terminations, the relaxation effects go deep down to eleven layers below the surface, while for the

Table 3.2: % change in inter planer distances of the different surface terminations after relaxation compared to their bulk values. Positive and negative values indicate an increase and a decrease in the inter planer distances respectively after relaxation.

Surface	% change in inter planer distance												
	$d_{1,2}$	$d_{2,3}$	$d_{3,4}$	$d_{4,5}$	$d_{5,6}$	$d_{6,7}$	$d_{7,8}$	$d_{8,9}$	$d_{9,10}$	$d_{10,11}$	$d_{11,12}$	$d_{12,13}$	$d_{13,14}$
(100) PG_l	-25.45	9.73	-7.84	2.24	-3.05	1.31	-1.09	0.00	0.00	0.00	0.00	0.00	0.00
(100) PG_h	-13.03	14.33	-5.11	3.16	0.00	0.00	0.00	0.00	0.00	0.00	0.00	0.00	0.00
(110) Pp	12.12	-35.89	-28.46	37.80	12.82	-2.08	-11.73	-4.02	8.64	-4.81	-1.34	0.00	0.00
(110) Ppg	-37.19	-23.15	-1.29	21.35	5.67	-19.88	-6.52	4.05	7.34	-3.68	0.00	0.00	0.00
(110) PGg	-50.91	27.56	4.59	15.95	-30.31	-5.42	2.90	7.37	-3.40	0.00	0.00	0.00	0.00
(110) Gg	-45.14	1.53	-12.11	14.77	13.73	-9.63	-2.12	2.60	3.41	0.00	0.00	0.00	0.00
(110) Gpg	0.00	-4.74	-16.78	0.00	8.45	-9.67	1.39	-1.17	8.51	-5.74	0.00	0.00	0.00
(110) PGp	-15.15	18.48	-28.08	34.33	-19.36	-2.43	0.00	0.00	0.00	0.00	0.00	0.00	0.00

Gpg and PGp, significant surface relaxation effects are observed till seven layers below the surface. Except for Pp and Gpg terminations, for all the other terminations, there is a contraction of the interplanar distances between the top two surface layers ($d_{1,2}$). For the Pp termination there is an increase in $d_{1,2}$, and for Gpg $d_{1,2}$ remains unchanged compared to that of the bulk value.

The computed surface energies of PG_l and PG_h are 1.02 Jm^{-2} and 1.32 Jm^{-2} respectively. This shows that the PG_l termination is more stable than PG_h since the former is more densely packed compared to the latter.

For the stoichiometric Ppg and Gpg terminations of the (110) surfaces, the obtain the surface free energies are 1.29 Jm^{-2} and 1.14 Jm^{-2} respectively. The results suggest that the Gpg termination is more stable than the Ppg one. For the non-stoichiometric terminations, the surface free energies are plotted with respect to that of Gpg as a function of μ_{Ga} using Eqn. 3.5. The plots are shown in Fig. 3.5. Three stable terminations can be identified over the whole range of Ga chemical potential: (a) the PGp termination has the highest stability up to $\mu_{Ga} = -3.49$ eV, (b) for $-3.49 \leq \mu_{Ga} \leq -3.15$ eV the Gpg is the most stable one and (c) for $-3.15 \leq \mu_{Ga} \leq -2.62$ eV it is the Gg termination that is thermodynamically favorable. Moreover, based on the composition of the second layer for each surface termination, the six different (110) surfaces can be clubbed into three groups, namely (i) Gpg and Ppg where the second layer consists of both Pd and Ga atoms, (ii) PGp and Pp where there are only Pd atoms in the second layer, and (iii) Gg and PGg where there are only Ga atoms in the second layer. The relative stability of the terminations in each of these groups remain same over the complete range of μ_{Ga}. In (i), (ii) and (iii) the most stable terminations are Gpg, PGp and Gg respectively suggesting that presence of Ga atoms in the surface layer plays an important role in stabilizing these surfaces.

Within the allowed range of μ_{Ga} , depending on surface preparation conditions at least three different terminations can be stabilized along (110) surface direction. To find the most stable surface termination one needs to calculate μ_{Ga} corresponding to bulk PdGa. Using the recipe suggested in Ref. [40] the value of μ_{Ga} is estimated for the (110) surface under the assumptions that: (a) the sources of Pd and Ga are in equilibrium with kink units of the crystal and (b) the energy of the kink units is given by the energy difference between slabs with a proximate number of layers.

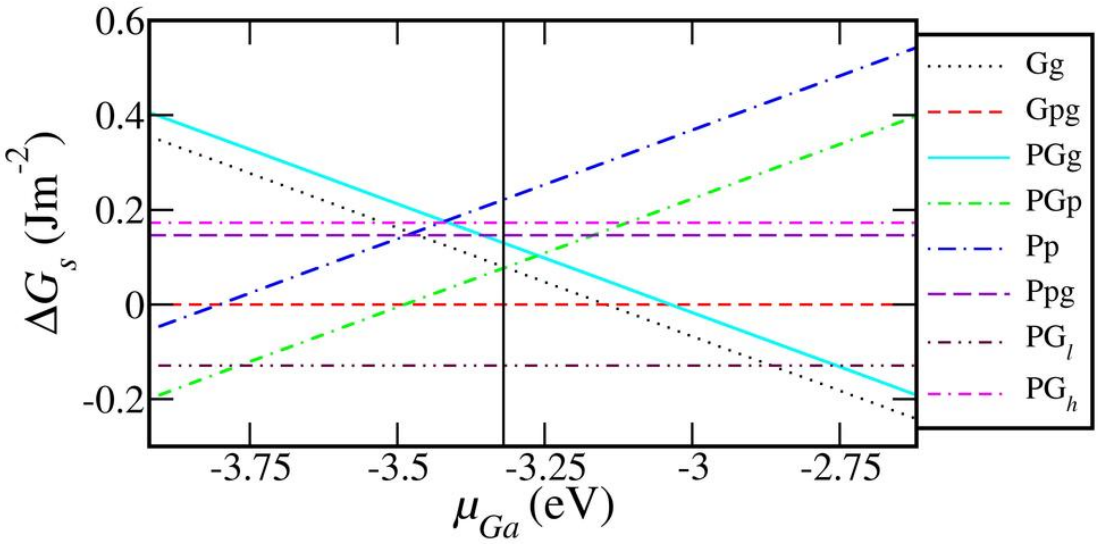

Figure 3.5: Relative surface energy as a function of μ_{Ga} for the different terminations of clean (110) and (100) surfaces with respect to that of the clean Gpg surface termination.

The surface is made up of layers that consist of one or more Pd and/or Ga units (kink units) stacked in a specific sequence. One complete repeating sequence is equal to one stoichiometric bulk unit. Hence, the sum of all the kink units in a complete sequence is equal to one bulk unit.

$$\sum_{1}^{n} \mu_k^X = \mu_{PdGa}^{bulk} \tag{3.12}$$

where n is the number of layers in one complete repeating sequence, X is the kink unit. For PdGa(110) surface n is six and X can be either one Pd or one Ga or one Pd and Ga, depending on the surface termination.

Assuming the source of the Pd and Ga are in equilibrium with the kink units and the energy cost for removing the kink unit to be equal to the kink energy, the value of the chemical potential of Pd and Ga can be uniquely determined. For example, the topmost layer of Pp has one Pd atom. Removing that Pd is equal to kink energy of Pp(μ_k^{Pp}) and will be given by

$$\mu_k^{Pp} = E_{slab}^{Pp} - E_{slab}^{Ppg} \tag{3.13}$$

where E_{slab}^{Pp} and E_{slab}^{Ppg} are the total energy of the Pp and Ppg surfaces respectively. Since one Pd atom is removed, this can be equated to Pd chemical potential. However, the kink

energy depends on the local chemical interaction of the kink unit. The topmost layer of Ppg termination also has one Pd atom, but μ_k^{Ppg} will be different from μ_k^{Pp} since the topmost Pd atom in Pp surface is bonding with three Ga atoms while the topmost Pd atom in Ppg surface is binding with four Ga atoms. To account for this, the kink energy is averaged over all possibility of a particular kink in one complete repeating sequence.

The relationship between $\mu_{Ga/Pd}$ and the change in energy upon removal of a kink unit (μ_k) is given by:

$$2\mu_{Pd} = \mu_k^{Pp} + \mu_k^{Ppg} \tag{3.14}$$

$$2\mu_{Ga} = \mu_k^{Gg} + \mu_k^{Gpg} \tag{3.15}$$

$$2\mu_{Pd} + 2\mu_{Ga} = \mu_k^{PGg} + \mu_k^{PGp}, \tag{3.16}$$

and the kink energies are related to the bulk energies as:

$$\mu_k^{Pp} + \mu_k^{Ppg} + \mu_k^{Gg} + \mu_k^{Gpg} + \mu_k^{PGg} + \mu_k^{PGp} = \mu_{PdGa}^{bulk}. \tag{3.17}$$

The estimated value of μ_{Ga} is about -3.32 eV. At this value of Ga chemical potential, it is seen that the Gpg termination of the clean surface to be stable.

To get an idea of the relative stability of the (110) and (100) surfaces, the surface free energy of the (100) surfaces with respect to that of the Gpg termination of the (110) surface are plotted in Fig. 3.5. For $-3.77 \leq \mu_{Ga} \leq -2.86$ eV the PG_l termination of the (100) surface is the most stable than that of the (110) one . For other values of μ_{Ga}, it is the (110) surface with PGp (under Pd rich growth condition) and Gg terminations (Ga rich growth condition) that are stable. It should be noted that these surfaces are even more stable than the Pd(111) surfaces.

In the B20 structure of PdGa, the (210) plays the role of the (110) surface of B2 compounds. Hence, the surface energies of the different (110) terminations of PdGa are compared with that of (210). Based on the values of the surface free energy of the (210) surface reported by Krajčí *et al.* [56], it is found that surface energies of the stoichiometric Ppg and Gpg terminations of the (110) surface are 0.21 and 0.06 Jm^{-2} higher than that of the (210) surface. In contrast, the most stable PGp (Gg) termination under Pd (Ga)-rich conditions has a surface energy which is about 0.14 Jm^{-2} lower than that of the (210). This

suggests that by tuning the surface preparation/growth conditions, particularly when one is using wet synthesis methods where the preparation conditions can be easily varied by simply changing the solvents or solvent mixtures, one can stabilize a desired termination of the (110) surface.

3.3.2 Adsorption of Hydrogen Molecule on (100) and (110) Surfaces

As a first step to study the reactivity of these surfaces the adsorption of molecular and atomic hydrogen on these surfaces at adsorbate coverages of 0.25, 0.50, 0.75 and 1.00 ML (1 ML is defined as one adsorbate atom/molecule in the (1×1) surface unit cell) are studied.

To determine the most stable adsorption geometry of molecular hydrogen on these surfaces we have considered several possible adsorption sites that are shown in Fig. 3.2 and 3.3 for the (100) and (110) surfaces respectively. The preferred adsorption sites and the corresponding adsorption energies, Pd-H distances and H-H bond length after adsorption at 0.25 ML H_2 coverage are reported in Table 3.3.

The calculations show that hydrogen molecule does not bind on the Ga rich Gg and Gpg terminations of the (110) surface. On the Gg termination, hydrogen molecule does not bind due to the unavailability of a binding site (hydrogen binds only to the Pd atoms, and for this termination, the first Pd atom is in the third layer from the surface). On the Gpg surface, there is a sub-surface Pd atom that is exposed. For this case, the adsorption of hydrogen is found to be endothermic, the H_2 interacts to the Pd atom with Pd-H distance of 1.86 Å and E_{ads} =0.08 eV/H_2 molecule. During the relaxation process, the subsurface Pd atom is pulled up by the hydrogen molecule by about 0.18 Å compared to the clean relaxed surface. To understand why molecular hydrogen binds endothermically on this surface, energy decomposition analysis was performed. The total binding energy can be decomposed into energy gained by the interaction of H_2 with the surface (Δ_1), the energy cost involved in distorting the clean surface (Δ_2) and the molecule in its gas phase (Δ_3) due to adsorption. Δ_2 (Δ_3) is given by the differences in energy of the relaxed clean surface (relaxed H_2 in gas phase) with that of the clean surface in the same geometry after adsorbing H_2 (H_2 in gas phase but in the same geometry as it was when adsorbed on the surface). Δ_1 is given by the differences in the total energy of the relaxed surface

after hydrogen adsorption with the sum of the total energies of the clean surface and the molecule in the gas phase, the latter two being in their adsorption geometry. It is found that the total energy cost of distorting the surface (i.e. pulling out the sub-surface Pd atom and exposing it so that H_2 can bind) and the activation of the H_2 molecule (H-H bond length becomes 0.84 Å), i.e., $\Delta_2 + \Delta_3$, is 0.25 eV while Δ_1 = -0.17 eV, resulting in an endothermic binding of H_2 on this surface termination.

For the other surface terminations of the (110) surface and the PG_h and PG_l terminations of the (100) surface, it is found that the H_2 molecule binds to a single Pd atom on the surface with the H-H molecular axis lying horizontally. We have also tried putting hydrogen molecule on the other adsorption sites. However, after relaxation, the molecule either desorbs or moves to the top site. From Table 3.3 it is seen that in general the binding energy of hydrogen molecule on all the surfaces is very weak, the binding energy varying from -0.15 to -0.32 eV/H_2 molecule. Among them, the binding energy is strongest on the (110) Pp and PGp termination. For all the cases the hydrogen molecule is activated, the H-H bond length varying from 0.81-0.83 Å, compared to that of 0.75 Å in the gas phase. The Pd-H bond lengths vary between 1.84 -1.93 Å.

At this point it would be interesting to compare these binding energies with that on other PdGa surfaces. As reported by Krajčí *et al.* and Prinz *et al.* the binding energy of H_2 on PdGa(111) and PdGa($\bar{1}\bar{1}\bar{1}$) surfaces are -0.25 and -0.29 eV respectively. [43, 56] It is found that the strength of the Pd-H bonds on the Pp and PGp terminations of (110) surface is comparable to those on the (111) and ($\bar{1}\bar{1}\bar{1}$) terminations, while it is slightly weaker on the other surface terminations of the (110) and (100) surfaces. For all the cases where hydrogen binds on the (110) and (100) surfaces, the hydrogen binding energies are much stronger compared to that on the PdGa(210) surface (-0.04 eV). [42]

In order to understand and quantify the correlation of the E_{ads} with the surface structure we have calculated the coordination number of the Pd atoms which are exposed on the creation of the surfaces. However, the nominal coordination number does not take into account the changes in bond length during relaxation or effect of strain. Hence we have calculated the effective coordination number ($n_e(i)$) of the i^{th} Pd atom. This is defined as: [57]

$$n_e(i) = \frac{\sum_j \rho_j^{at}(R_{ij})}{\sum \rho_{Pd}^{at}(R_{bulk})} \tag{3.18}$$

Table 3.3: Binding energy (E_{ads}), Pd-H (d_{Pd_1-H}, d_{Pd_2-H}) , H-H (d_{H-H}) bond lengths of H_2 on (110) and (100) surfaces at 0.25 ML hydrogen coverage. Pd_1 and Pd_2 denote the Pd atoms in the surface layer and the one below it respectively.

Surface:termination	Adsorption site	E_{ads} (eV/H_2)	d_{Pd_1-H} (Å)	d_{Pd_2-H} (Å)	d_{H-H} (Å)
(110):Pp	T_p	-0.32	1.86, 1.88	-	0.82
(110):Ppg	T_p	-0.19	1.92, 1.93	-	0.81
(110):PGg	T_p	-0.14	1.84, 1.85	-	0.83
(110):Gpg	T_p	0.08	-	1.86, 1.86	0.84
(110):PGp	T_p	-0.27	1.88, 1.88	-	0.81
(100):PG_h	T_p	-0.19	1.86, 1.86	-	0.82
(100): PG_l	T_p	-0.15	1.90, 1.92	-	0.81

where $\rho_j^{at}(R_{ij})$ is the atomic charge density of an isolated atom as a function of R, and the sum is taken over all the neighboring "j" atoms around the surface Pd atom i. R_{ij} is the distance between atom i and j, and R_{bulk} is the nearest neighbor Pd-Pd distance in bulk Pd. For bulk Pd, the effective coordination number becomes equal to the nominal coordination number of 12. In bulk PdGa the effective coordination number of a Pd atom is found to be 15.5, which is far greater than the nominal coordination number of seven because of strong covalent bonding between Pd and Ga. A comparison of the effective coordination number of the Pd atoms (before and after relaxation) with that of the nominal coordination number is given in Table 3.4. Similar to bulk PdGa, the effective coordination number of the Pd atoms is much larger than the nominal one. Further, the overall effect of the relaxations on the bulk truncated surfaces is also captured in the change in the effective coordination number obtained for the relaxed surfaces in comparison with that of the bulk truncated ones. As the surfaces are created, the surface Pd atoms have a reduced coordination number compared to that in bulk. During the relaxation process, the surface Pd and Ga atoms come closer to maximize their coordination number and hence there is an increase in the value of n_e. However, the reverse is observed for the Pd atom present in the third layer of PGp surface, i.e., n_e decreased after relaxation. This anomaly is attributed to the increase in the inter-planar spacing between second and third layers (about 0.1 Å), making that Pd atom more under coordinated than the bulk truncated one. Comparing the n_e of the Pd atoms on the different surface terminations, it is found that the Pd atoms in PGp and Pp are highly under coordinated while those on the Gg and PGg have an effective coordination number close to that of bulk PdGa. The variation of E_{ads} with effective coordination number at 0.25 ML coverage for the thermodynamically favorable adsorption sites are plotted in Fig. 3.6(a). It is found that the strength of binding of the molecule (adsorption energy) on the surfaces decreases with an increase in effective

Table 3.4: Nominal and effective coordination numbers (CN) of Pd atoms present in few top layers of the (110) and (100) surfaces. 1st layer denotes the topmost surface layer.

Surface	Nominal CN	n_e	
		Bulk truncated	Relaxed
Pp			
1st layer	3	7.7082	10.5449
2nd layer	4	7.7965	11.3821
3rd layer	5	11.2420	13.4844
Ppg			
1st layer	4	7.7964	12.1281
2nd layer	5	11.2420	13.6201
PGg			
1st layer	5	11.2420	14.2744
Gg			
3rd layer	6	13.0088	13.7687
4th layer	6	13.7378	14.5935
Gpg			
2nd layer	5	11.2420	12.2486
3rd layer	5	11.9709	12.8358
4th layer	6	12.7881	13.4739
PGp			
1st layer	3	6.9792	10.9073
2nd layer	5	11.9709	13.5773
3rd layer	5	12.7881	12.4801
PG$_l$			
1st layer	5	10.2923	13.3263
2nd layer	6	13.7378	14.1220
PG$_h$			
1st layer	4	9.4751	12.1687
2nd layer	6	13.0088	13.8316

coordination number of the Pd atom to which the molecule binds.

The change in the adsorption energy of the hydrogen molecule on these surfaces as a function of hydrogen coverage is calculated. The results are shown in Fig. 3.6(b). It is found that there is hardly any change of E_{ads} as a function of H_2 coverage. The H_2 molecules are quite far apart (the smallest distance between two hydrogen molecules at 1.0 ML coverage is 4.15 Å) so that they do not interact with each other.

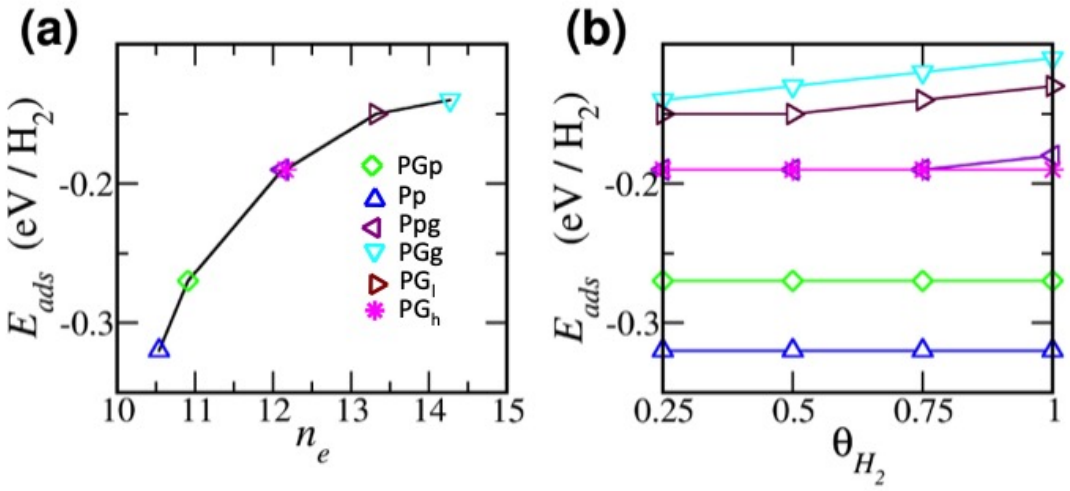

Figure 3.6: Molecular hydrogen: (a) variation of binding energy at 0.25 ML H_2 coverage with effective coordination number n_e and (b) binding energy change as a function of H_2 coverage. Green diamond, blue up triangle, violet left triangle, cyan down triangle and magenta star denote the PGp, Pp, Ppg, PGg and PG_h terminations respectively. The lines connecting the symbols are a guide to the eye.

3.3.3 Adsorption of Atomic Hydrogen on (100) and (110) Surfaces

Atomic hydrogen can bind at several possible sites on all the different surface terminations that we have considered in this work. Only for those cases where the H remains on the adsorption sites after relaxation, the energetics and the adsorption geometries are reported in Tables 3.5 (for the (100) surface) and 3.6 (for the (110) surface). For other possible sites, after geometry optimization, H either desorbs or moves to one of those reported in Tables 3.5 and 3.6 .

With respect to the total energy of H_2 in the gas phase, the binding of atomic H on all the sites of (100) PG_l surface termination is endothermic suggesting that dissociation of H_2 on this surface is thermodynamically unfavourable. On the PG_h surface, atomic H binds exothermically only on the bridge site between a Pd atom on the surface layer and the layer below it (B_{p2} site in Fig-3.2) with an adsorption energy of -0.12 eV/H at 0.25 ML coverage. The adsorption geometry is different compared to molecular hydrogen where the latter prefers to bind on the top site. The Pd-H distances between the H atom and the surface and sub-surface Pd atoms are 1.76 and 1.80 Å respectively.

On the Ga rich Gg and Gpg terminations of the (110) surface the H binds endothermically

Table 3.5: Binding energies with respect to H_2 (E_{ads}) and H (E_{coh}), Pd-H, Ga-H bond lengths and tilt angles of atomic H on PG_l and PG_h surfaces at 0.25 ML coverage. Pd_1, Pd_2 are the Pd atoms in the top most and the next layer respectively. Tilt angle denotes the angle Pd_1-H bond makes with the surface normal.

PG_l						
Adsorption site	B_1	B_2	B_3	B_5	B_{p1}	B_{p2}
E_{ads} (eV/H)	0.20	0.22	0.32	0.26	0.21	0.09
E_{coh} (eV/H)	-2.06	-2.04	-1.94	-2.00	-2.05	-2.16
Pd_1-H (Å)	1.76	1.73	1.66	-	1.77	1.80
Pd_2-H (Å)	-	-	-	1.72	1.83	1.79
Ga_1-H (Å)	1.82	1.80	-	-	-	-
Ga_2-H (Å)	-	-	2.05	1.81	-	-
Tilt angle (°)	47.50	50.15	51.79	31.76	70.96	76.50
PG_h						
Adsorption site	T_g	T_p	B_1	B_2	B_{p1}	B_{p2}
E_{ads} (eV/H)	0.48	0.17	0.06	0.10	0.04	-0.12
E_{coh} (eV/H)	-1.78	-2.09	-2.20	-2.16	-2.22	-2.38
Pd_1-H (Å)	-	1.60	1.75	1.74	1.76	1.76
Pd_2-H (Å)	-	-	-	-	1.79	1.80
Ga_1-H (Å)	1.58	-	1.79	1.80	-	-
Tilt angle (°)	-	30.11	40.02	46.88	80.63	79.29

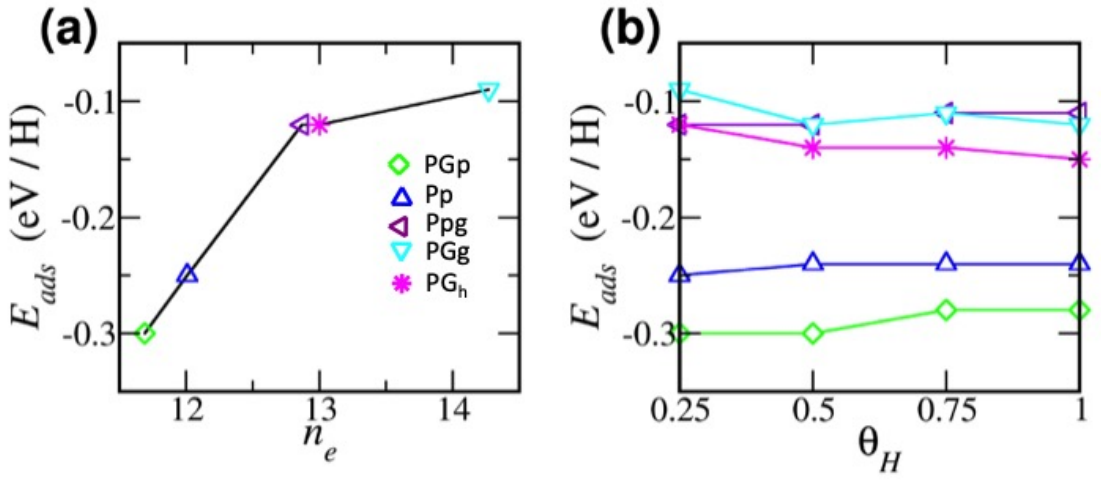

Figure 3.7: For atomic H: (a) variation of binding energy at 0.25 ML coverage with effective coordination number n_e and (b) binding energy as a function of H coverage. Green diamond, blue up triangle, violet left triangle, cyan down triangle and magenta star denote the PGp, Pp, Ppg, PGg and PG_h terminations respectively. The solid lines are a guide to the eye.

Table 3.6: Binding energies with respect to molecular (E_{ads}) and atomic H (E_{coh}), Pd-H, Ga-H bond lengths and tilt angles of atomic H on (110) surfaces at 1.00 ML coverage. The subscripts 1, 2, 3 to Pd indicate the positions of the Pd atoms as one goes from surface to the bulk. Tilt angle denotes the angle Pd_1-H or Ga_1-H bonds make with the surface normal.

Adsorption site	E_{ads} (eV/H)	E_{coh} (eV/H)	Pd_1-H (Å)	Pd_2-H (Å)	Pd_3-H (Å)	Ga_1-H (Å)	Tilt angle (°)
Pp							
B_{p1}	-0.28	-2.54	1.78	-	1.76	-	72.41
B_{p2}	-0.04	-2.30	1.75	1.74	-	-	66.52
B_{p3}	-0.08	-2.34	1.75	1.78	-	-	59.84
B_{p4}	-0.09	-2.35	-	1.79	1.77	-	72.38
Ppg							
B_{p1}	-0.11	-2.37	1.78	1.79	-	-	69.63
PGg							
T_p	0.01	-2.25	1.60	-	-	-	17.74
T_g	0.31	-1.95	-	-	-	1.58	13.34
B_1	0.12	-2.14	1.76	-	-	1.79	47.90
B_2	-0.12	-2.38	1.75	-	-	1.80	81.59
B_3	0.03	-2.23	1.73	-	-	1.83	51.56
Gg							
T_g	-0.03	-2.26	-	-	-	1.57	17.03
B_1	0.21	-2.05	-	-	1.75	1.89	47.99
B_{p1}	0.17	-2.09	-	1.79	1.75	-	41.11
Gpg							
B_{p1}	0.06	-2.20	-	1.75	1.83	-	69.90
B_{p2}	0.00	-2.26	-	1.75	1.81	-	73.83
B_{p3}	0.25	-2.01	-	1.78	1.80	-	61.47
B_{p4}	0.09	-2.17	-	1.82	1.82	-	56.51
PGp							
T_g	0.61	-1.65	-	-	-	1.60	22.25
B_1	0.29	-1.97	1.73	-	-	1.78	43.55
B_{p1}	-0.03	-2.29	1.73	1.79	1.84	-	70.80
B_{p2}	-0.29	-2.55	1.75	-	1.85	-	91.31
B_{p3}	-0.15	-2.41	-	1.82	1.84	-	59.70
B_{p4}	0.16	-2.10	-	1.80	1.84	-	58.86

to the bridge sites involving Pd atoms in the subsurface layers. On the other (110) surface terminations it prefers to bind in the bridge configurations only. The details of the energetics and the bond lengths for hydrogen adsorption on (110) surface terminations are given in Table-3.6. The binding is strongest on the B_{p1} (B_{p2}) site of the Pp (PGp) termination with an adsorption energy of -0.28 eV/H (-0.29 eV/H). Similar to molecular hydrogen, the adsorption energy of atomic H decreases as the effective coordination number of the Pd atom increases (Fig-3.7(a)). The adsorption energy of the H atom is almost independent of H coverage (Fig-3.7(b)).

3.3.4 Thermodynamic Analysis

In order to investigate whether the relative stability of the different surface terminations changes in presence of hydrogen (as a function of hydrogen partial pressure and temperature) under different surface preparation conditions (i.e. as a function of Ga chemical potential) the thermodynamic analysis was performed as described in Section 3.2.4. The change in Gibbs free energy (ΔG_s) of the surfaces at different hydrogen coverages with respect to the clean Gpg termination, as a function of the H chemical potential and Ga chemical potential was calculated. Some representative plots of ΔG_s as a function of μ_H on (110) surfaces are shown in Fig. 3.8(a-c) for molecular hydrogen and (d-f) for atomic hydrogen at μ_{Ga} of -3.92 eV (Pd rich condition), -3.27 eV (intermediate) and -2.62 eV (Ga rich condition). The complete phase diagram as a function of μ_H and μ_{Ga} is shown in Fig. 3.9(a) and (b). The μ_H has been converted to hydrogen partial pressures at 450 K; this corresponds to the temperature at which maximum catalytic activity was observed for selective hydrogenation of acetylene on PdGa. [58, 59]

From the phase diagram it is found that at low hydrogen partial pressure, for all values of Ga chemical potential, the clean surfaces are thermodynamically more stable than the ones with adsorbates. At Ga rich conditions, i.e., -3.15$\leq$ μ_{Ga} $\leq$-2.62 eV, the clean Gg surface termination is always stable independent of the H partial pressure. This is because on this surface either the adsorbates do not bind or they bind endothermically. At Pd rich conditions, $\mu_{Ga} \leq -3.49$ eV, the clean PGp surface is the most stable one till the H partial pressure is 5×10^6 mbar. As the H partial pressure is increased, the hydrogen covered PGp surfaces stabilize preferentially over the clean one, even though on the Pp termination the binding energies of the atomic and molecular hydrogen are similar to that of the PGp one.

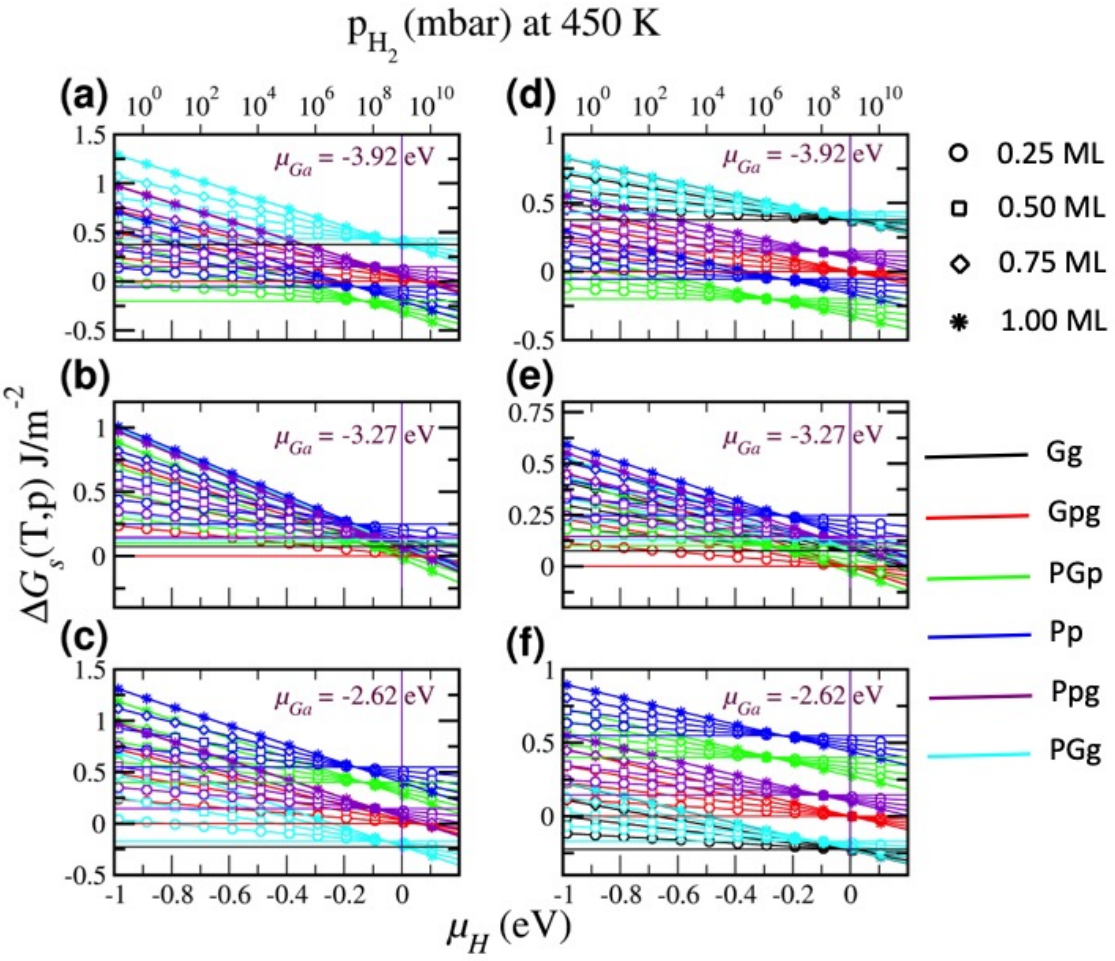

Figure 3.8: Surface free energy change for molecular hydrogen (a-c) and atomic hydrogen (d-f) adsorbed on PdGa (110) surfaces as a function of hydrogen partial pressure at different values of μ_{Ga}. Circle, square, diamond and star represent the hydrogen coverages of 0.25 ML, 0.50 ML, 0.75 ML and 1.00 ML respectively. Black, red, green, blue, violet and cyan lines represent Gg, Gpg, PGp, Pp, Ppg and PGg terminations respectively. The molecular hydrogen does not bind to the Gg surface and hence there are no black lines in panel (a), (b) and (c).

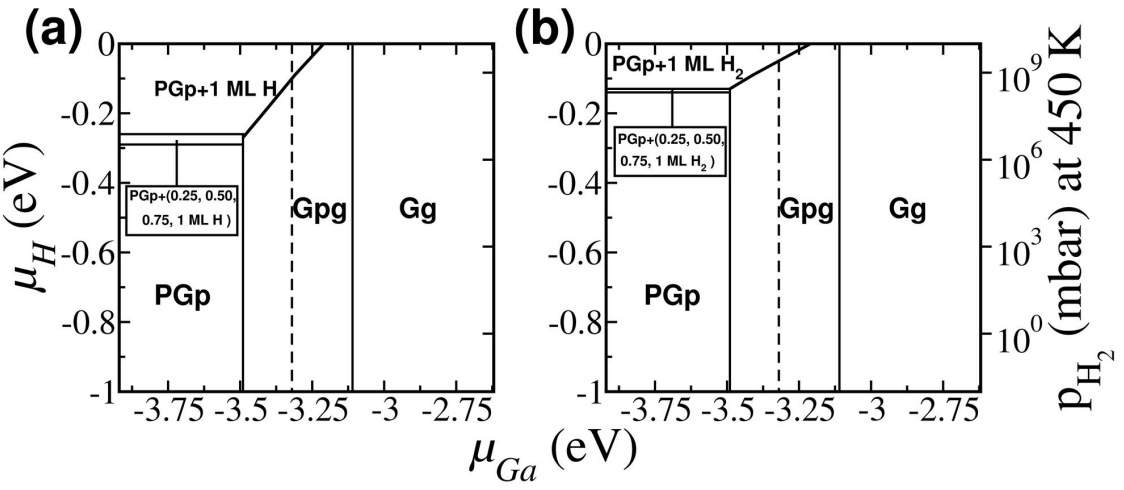

Figure 3.9: Surface phase diagram of (a) atomic and (b) molecular hydrogen adsorbed on PdGa (110) surfaces.

The latter termination is stabilized, because, for the clean surface the PGp termination is more stable compared to Pp and after adsorbing H_2/H, the amount of energy gained by the Pp surface is not large enough to reverse the stability. At intermediate values of Ga chemical potential ($-3.21 \leq \mu_{Ga} \leq$-3.15) and high hydrogen partial pressures ($p_{H_2} \geq 5 \times 10^6$ mbar), there is a transition from the hydrogen covered PGp surface to the clean Gpg surface. From this, we conclude that in order to have reactive PdGa(110) surfaces, one needs to prepare the surfaces at Pd rich growth conditions. The results further suggest that the PGp is the most stable reactive termination of the (110) surface and hydrogen dissociation will be possible at high hydrogen partial pressures.

Similar analysis on the PG_l and PG_h terminations of the (100) surface shows that for hydrogen molecule, the H_2 covered PG_l surface is most stable one when the hydrogen partial pressure is greater than 3.2×10^8 mbar (Fig. 3.10(a)). For atomic H, at all relevant hydrogen partial pressures, the clean PG_l surface is the most stable one (Fig. 3.10(b)).

Usually the surfaces are prepared by cleaving large single crystals. Gille *et al.* showed that it is possible to cleave the crystal to expose all the low indexed surfaces, namely (100), (110) and (111). [60] However, if one wants to prepare nanostructured PdGa using wet synthesis techniques, then the facets that will be exposed will depend on the surface energies and the reaction conditions (chemical potential of Ga or Pd). For example, Armbruster *et al.* [38] prepared nanostructured PdGa in Ga rich condition, the Pd:Ga ratio

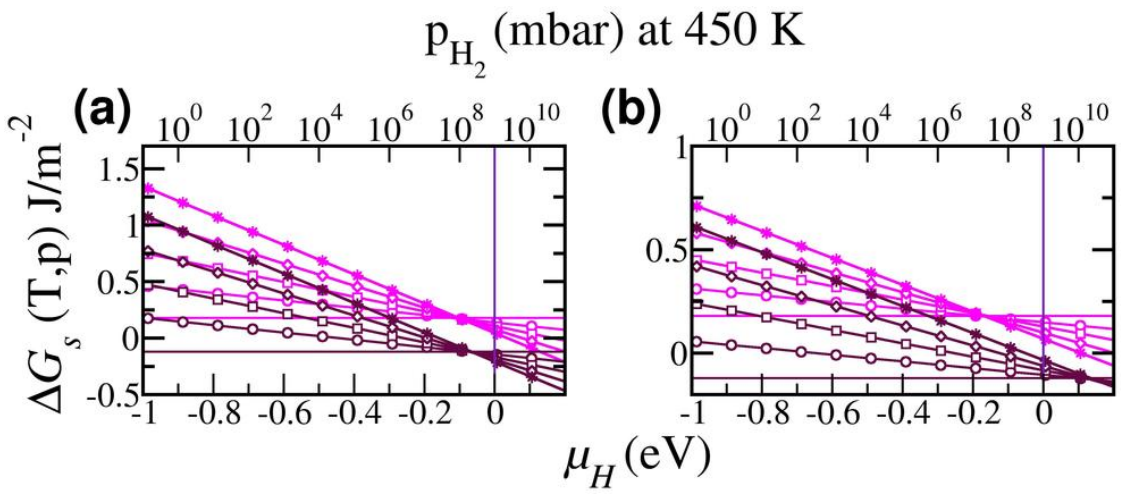

Figure 3.10: Surface free energy change for (a) molecular hydrogen and (b) atomic hydrogen adsorbed on the PG_l and PG_h terminations of the PdGa (100) surfaces as a function of hydrogen chemical potential. Circle, square, diamond and star represent the hydrogen coverages of 0.25 ML, 0.50 ML, 0.75 ML and 1.00 ML respectively. Magenta and maroon lines represent PG_h and PG_l terminations respectively.

being 1:1.1. Depending on the exact value of μ_{Ga} either the PG_l termination of the (100) surface or the Gg termination of the (110) surface will be stable among the (100) and (110) surfaces. As mentioned earlier, for the (110) surface μ_{Ga}=-3.32 eV is the relevant chemical potential. From the phase diagram in Fig. 3.9 it is seen that the hydrogen covered PGp surfaces will be stabilized for the above-mentioned value of Ga chemical potential only at extremely high hydrogen partial pressures. Hence, in order to make PdGa with the more reactive PGp termination exposed, one needs to remove the Ga atoms from the stable Gpg terminations.

3.4 Summary

In summary, the structure and stability of the (100) and (110) surfaces of intermetallic PdGa are investigated using DFT. The results show that for the clean (100) surface the most stable surface termination is PG_l, independent of the conditions under which the surface is prepared. This implies that if one wants to modify these surfaces, one needs to resort to methods like chemical etching or milling coarser crystalline samples. On the other hand in the case of (110) surface at least three possible surface terminations, namely

PGp, Gpg and Gg, can be stabilized by tuning the surface preparation condition.

The study of the adsorption of hydrogen molecule and atoms on these surfaces show that both atomic and molecular hydrogen binds exothermically on the Pd rich terminations of the (110) surface. In contrast, on (100) surface, while binding of the hydrogen molecule is thermodynamically favorable, that of atomic hydrogen is unfavorable. The phase diagram shows that the presence of adsorbates on the surface does not alter the stability of the surface terminations for both these surfaces. Since binding of atomic hydrogen is thermodynamically unfavorable on the (100) surface, the results suggest that if these surfaces are catalytically active, the reaction mechanism will be different from the conventional one where hydrogen first adsorbs on the surface, followed by dissociation.

Chapter 4

Selectivity and Reactivity of Pd Containing Low Indexed PdGa Surfaces Towards Selective Hydrogenation of Acetylene: Interplay of Surface Roughness and Ensemble Effect

In this chapter, using first principles based density functional theory based calculations, the mechanism and energetics of the selective hydrogenation of acetylene are studied on low indexed (100) and (110) PdGa surfaces. The energetically favorable (100) surface created by cleaving the crystal in the less dense region shows reasonably good selectivity and high reactivity. The reactivity on this surface is comparable to that observed on Pd(111) surfaces. Since this surface termination is stable over a wide range of Ga chemical potential and hence is likely to occupy a substantial fraction of the surface area of PdGa nanocrystallites, this termination is responsible for the selectivity and reactivity exhibited by PdGa. In contrast to other surfaces where hydrogen adsorption and dissociation is followed by acetylene adsorption and hydrogenation, on this surface, a novel reaction mechanism is identified in which hydrogen dissociation occurs in the presence of acetylene. A careful analysis of the factors determining the selectivity shows that selectivity results due to an interplay between surface roughness and chemical nature of the reactive ensemble. The work presented in this chapter is published in *J. Phys. Chem. C*, **2016**, 120 (50), pp 28654-28663. [1]

[1] Reprinted with permission from *J. Phys. Chem. C*, **2016**, 120 (50), pp 28654-28663. Copyright ©2016, American Chemical Society.

4.1 Introduction

Catalysts for many heterogeneous chemical reactions need to exhibit high reactivity and selectivity. One such industrially important reaction is the selective hydrogenation of acetylene to ethylene that is used to remove traces of acetylene present in ethylene. The latter is used as a feedstock for polymerization reaction and the acetylene contained in it poisons the polymerization catalyst. Usually Pd is used as a catalyst for the selective hydrogenation reaction. [37, 61] Though Pd shows high reactivity; it exhibits poor selectivity. [62] The reason for this has been attributed to several factors: (a) the strong binding energy of ethylene on Pd, (b) large capacity of Pd to store atomic H and (c) fast diffusion rate of atomic H from bulk to the surface. All these factors combined facilitates further hydrogenation of ethylene to ethane, thereby resulting in loss of selectivity of the Pd catalyst.

Hence there are efforts to design catalysts with high reactivity and selectivity. [63] Bimetallic alloys made by substituting atoms in the crystal of a host lattice with a different atom have been extensively explored as an alternative to Pd catalysts. For example, alloying Pd with less reactive metals like Ag and Pb results in significant improvement in the selectivity. [37, 64–66]. Alloying modifies the electronic structure of the host catalyst, thereby resulting in different catalytic properties. However, the two major problems of bimetallic catalysts are: (a) limited tunability of electronic properties of the host because the combinations are limited to elements with similar electronic properties and (b) stability, i.e., they easily phase segregate at high reaction temperatures thereby losing all their catalytic properties.

In contrast to bimetallic alloys, intermetallic compounds (e.g. Pd-Ga compounds with a wide range of stoichiometry) has gained a lot of attention over the last decade as an alternative catalyst for the selective hydrogenation reaction. [38, 67, 68]. These are different from the bimetallic alloys in several aspects, namely bonding is partially covalent, a complex crystal structure in comparison with the closed pack structure of the elements, etc. These result in significantly different electronic structures and thus different catalytic properties and enhanced stability. Although it is experimentally well established that they show enhanced selectivity, [38, 59, 67–71] till date there is not enough atomistic understanding of the reason behind this.

Usually, the concept of "site isolation", where the active material is embedded in a matrix of a non-reactive one, is used to explain the enhanced reactivity and selectivity of the catalysts made from PdGa intermetallic compounds. [72–74]. Although this might suppress undesired side reactions like oligomerization, this does not explain the better selectively. For example, on the polar $(\bar{1}\bar{1}\bar{1})$ surface, the reactive ensemble consists of a Pd triad (Pd_3) while that on the (111) surface is it the Pd monomers (Pd_1). The reactive sites are well separated from each other (by more than 5 Å for Pd_3 and 7 Å for Pd_1). Based on the concept of "site isolation", one would expect that both surfaces should show similar selectivity. However, recent studies by Prinz *et al.* using a combination of scanning tunneling microscopy (STM) and density functional theory (DFT) showed that the Pd_3 ensemble shows far better selectivity than the Pd_1. [43]. This indicates that there are other factors, apart from the isolation of the active sites that determine the reactivity and selectivity. Prinz *et al.* have attributed the chemical composition of the ensemble (3 Pd atoms for Pd_3 versus a single Pd atom on Pd_1) to be a determining factor for selectivity. Detailed DFT based studies by Krajčí *et al.* on the (210) surface showed that while the reactivity results from the activation of acetylene and vinyl strongly bound to the Ga atoms, the selectivity is due to the weak binding of ethylene on top of transition metals only. [42] Their results also suggest that the atomistic scenario is different and more complicated than the "site isolation" concept.

Typically the performance of a catalyst depends on the surface roughness and the chemical composition of the active sites (ensemble effect). It would be interesting and informative (from the rational catalyst design perspective) to have a microscopic understanding of how surface roughness and ensemble effects affect the reactivity and selectivity of the PdGa intermetallics based catalysts for selective hydrogenation of acetylene to ethylene. In order to do so, one needs to study the detailed reaction mechanism on several surfaces having a wide variety of active ensembles and different degree of roughness. Thanks to the complex structure of PdGa, there are several possible surface terminations for the different exposed PdGa surfaces. However, the stable surface composition depends on the chemical environment in which they are prepared (Ga or Pd chemical potentials). This study focuses on, how the ensemble effects and surface roughness affect the reactivity and selectivity of the Pd containing surface terminations that are stable over a wide range of Ga chemical potential and are the most probable facets to be exposed in experiments. Although there are studies available for reaction mechanisms on the different (111), $(\bar{1}\bar{1}\bar{1})$, (210) sur-

faces, there is hardly any study available on the (100) and (110) surfaces. The only study available is the acetylene hydrogenation on the (110) surface, reported by Bechthold and coworkers. [75] However, from the previous chapter, it is found that the surface termination on which they have done their studies is thermodynamically unfavourable. It should be noted that based on simulation of cleavage experiments by Krajčí and Hafner, the (100) surfaces are the most exposed ones over a wide range of Ga chemical potential. [41, 76]

In this work, mechanisms of the selective hydrogenation of acetylene to ethylene is studied in detail on the most stable terminations of (100) and (110) surfaces. For the (100) surface, the termination created by cleaving the crystal in the region where the bulk interplanar distance is 1.48 Å (PG_l) is considered. For the (110) surface, the termination where there is a Pd and a Ga atom in the top layer and a Pd atom in the second layer (PGp surface) is considered. These specific terminations are chosen because these are the most stable ones predicted by the calculations (previous chapter). [77]. Further, the role of surface roughness and ensemble effects is also elucidated in determining the reactivity and selectivity of these model catalysts. To achieve this the reaction mechanism is studied on another surface namely (100)PG_h, created by cleaving the crystal at the dense region (bulk interplanar distance of 1.00 Å). In the PG_h and PG_l surfaces, the active ensemble is a Pd-Ga dimer. However, the surface roughness of PG_h termination (created by cleaving the crystal at more dense region) is expected to be higher than that of PG_l termination (created by cleaving the surface at less dense region). Hence a direct comparison between these two surfaces will elucidate the role of surface roughness on the reactivity and selectivity.

The rest of the chapter is divided as follows: Section 4.2 contains the computational details. In section 4.3.1 we describe the geometry and thermodynamic stability of the different reaction intermediates on the above-mentioned surfaces. Section 4.3.2 contains the details of the reaction mechanism. In Section 4.3.3 we elucidate the role of surface ensemble and roughness on the selectivity and reactivity exhibited by these surfaces. Finally, we conclude in Section 4.4.

4.2 Methods and Computational details

All the calculations were performed using Quantum Espresso software, [34] a plane wave based implementation of density functional theory. The electronic exchange and correlation potential is described by the Perdew-Burke-Ernzerhof (PBE) based parametrization of the generalized gradient approximation (GGA) . [12] Electron-ion interactions are described by ultrasoft pseudopotentials. [19] A plane wave basis set is used with a kinetic energy cutoff of 30 Ry and 320 Ry for wave function and charge density respectively. Marzari-Vanderbilt smearing, [23] with a smearing width of 0.01 Ry was used to speed up the convergence. Brillouin zone integrations were done with a 4×4×1 Monkhorst-Pack k-point mesh. [20]

All three surfaces are modeled with a 2×2 super-cell, PG_l and PG_h surfaces have cell dimensions of 9.93×9.93 Å, and PGp surface has a cell dimension of 9.93×14.05 Å. The PGp, PG_h and PG_l surfaces were modeled with 19, 13 and 12 layer slabs respectively. For all the slabs the bottom six layers are fixed at their bulk position, and the rest of the layers are relaxed. To avoid the interactions between the periodic images of the slabs, a vacuum of 12 Å is used along the normal to the surface. Other details of the computational parameters and the surface models are described in the previous chapter.

The stability of the reactants and the products on these surfaces is given by the adsorption energy and is defined as:

$$E_{ads} = E_{total}^{slab+adsorbates} - E_{total}^{slab} - E_{total}^{adsorbates}. \tag{4.1}$$

In the above equation $E_{total}^{slab+adsorbates}$ is the total energy of the slab with reactants adsorbed on it, E_{total}^{slab} is the total energy of the clean surface and $E_{total}^{adsorbates}$ is the total energy of the reactants in their gas phase. The reactants can be hydrogen, acetylene and ethylene. $E_{total}^{adsorbates}$ was calculated by placing the reactant molecule in a cubic box with sides of length 18 Å. For the hydrogen molecule, H-H bond length is calculated to be of 0.75 Å and binding energy of -4.52 eV. These values are in reasonably good agreement with experimental reports of 0.74 Å and -4.75 eV. [78] Table-4.1 shows a comparison of the C-C and C-H bond lengths and bond angle ($\angle_{C-C-H}$) obtained for the reactants with those reported in the literature. The computed results are also in excellent agreement with the experimental reports. [79]

Table 4.1: Comparison of bond lengths and bond angles of H_2, C_2H_2 and C_2H_4 in gas phase obtained with those measured experimentally.

Molecule	Bond / Angle	Bond length (Å) / angle (°)	
		This study	Experimental report
H_2	d_{H-H}	0.75	0.74 [78]
C_2H_2	d_{C-C}	1.21	1.20 [79]
C_2H_2	d_{C-H}	1.07	1.06 [79]
C_2H_4	d_{C-C}	1.33	1.33 [79]
C_2H_4	d_{C-H}	1.09	1.08 [79]
C_2H_4	$\angle_{C-C-H}$	121.7	121.4 [79]
C_2H_4	$\angle_{H-C-H}$	116.6	117.2 [79]

The reaction barriers were computed using the climbing image nudged elastic band (CI-NEB) method. [32, 80] The number of images used for the different paths depends on the complexity of the path and varies between 7 and 27. The force acting on each image was converged up to 0.05 eV/Å.

4.3 Results and Discussion

4.3.1 Adsorption of reactants

As a first step to understand the activity and selectivity of the (110) and (100) surfaces towards hydrogenation of acetylene to ethylene the adsorption of the reactants on the PGp, PG_h and PG_l surfaces is studied.

4.3.1.1 H_2 and H+H adsorption

As reported in the previous chapter, [77] for all the surfaces considered in this study the most stable adsorption site for the molecular hydrogen is on top of the surface Pd atoms. Hydrogen molecule binds to the surfaces in an activated form (H-H bond length of about 0.81 Å) with binding energies of -0.27, -0.19 and -0.15 eV on PGp, PG_h and PG_l respectively. The Pd-H bond distances vary between 1.86 and 1.91 Å. It should be noted that Prinz *et al.* have reported similar values for adsorption of H_2 on Pd_3 and Pd_1 ensembles

Table 4.2: Comparison of adsorption/coadsorption energies (in eV) of some important reaction intermediates on the surfaces considered in this study with those reported on other PdGa surfaces in literature.

	Adsorption energy (eV)					
	This study			lit. report		
	PG_l	PG_h	PG_p	(210) [42]	(111)Pd_1 [43]	($\bar{1}\bar{1}\bar{1}$)Pd_3 [43]
H_2	-0.15	-0.19	-0.27	-0.05	-0.29	-0.25
H + H	0.23	-0.28	-0.60	-0.13	-0.51	-1.01
C_2H_2	-0.42	-0.56	-0.66	-1.14	-0.61	-1.17
C_2H_2 + H + H	-0.24	-0.72	-1.19	-1.08	-1.12	-2.18
C_2H_4	-0.52	-0.61	-0.72	-0.47	-0.73	-0.85

of the threefold (111) PdGa surfaces. [40, 43]. However, on the (210) surface Hafner and coworkers found the adsorption energy to be only -0.05 eV. [42]

For the case of dissociated hydrogen (co-adsorption of two atomic H) the lowest energy configuration is the one in which the hydrogen atoms are on the Pd-Pd bridge site. Of the two Pd atoms that form the bridge site, one of the Pd atoms is in the topmost layer while the second one is in the second (PG_l, PG_h) or third layer (PGp). [77] The binding of atomic hydrogens is exothermic on PGp and PG_h surfaces with -0.60 and -0.28 eV binding energies. In contrast, on PG_l coadsorption of atomic H is endothermic with a binding energy of about 0.23 eV. It should be noted that the adsorption energy on PGp is similar to that found by Prinz *et al.* on Pd_1 and is much weaker compared to that of -1.01 eV on Pd_3. [43] The binding energy on PG_h is similar to that observed on the (210) surface. [42]

4.3.1.2 C_2H_2 adsorption

Among the different possible adsorption geometries of acetylene on the PdGa surfaces considered in this study; acetylene prefers to bind to the topmost Pd atom on all the three surfaces in a π-configuration. The most stable adsorption geometries and the metastable configurations for the adsorption of C_2H_2 on the three surfaces are shown in Figure 4.1. Compared to the gas phase geometry, where the molecule is linear, upon adsorption on the surface it undergoes structural distortion. For example, the C-C-H bond angle deviates from 180° in the gas phase to 157-161° on the surfaces. This suggests a rehybridization of carbon atoms from sp towards sp^2. Upon adsorption, on the surfaces, the C-C triple bond of acetylene is activated, with bond lengths varying between 1.24-1.25 Å on the sur-

faces compared to that of 1.21 Å in the gas phase. The acetylene binding energies on the PGp, PG_h and PG_l surfaces are -0.66, -0.56 and -0.42 eV respectively. While the acetylene adsorption configurations and binding energies on these surfaces are similar to those observed on the Pd_1 ensemble of the (111) PdGa surface, they are significantly different from what has been observed on the $(\bar{1}\bar{1}\bar{1})$ and (210) PdGa surfaces [42, 43], and on the (111) Pd surface. [64,81,82] On the $(\bar{1}\bar{1}\bar{1})$ PdGa surface and the Pd(111) surface acetylene adsorbs in an asymmetric π/di-σ bonding with a much larger binding energies of -1.17 eV and -1.78 eV respectively. On (210) surface, acetylene binds in a bridge position between two Ga atoms in a triangular tile or diagonally across a rectangular tile between a Ga and a Pd atom with a binding energy of -1.14 eV. [42, 76]

In addition to above mentioned stable configurations of acetylene on the (100) and (110) surfaces, other configurations with similar energies are also found. It should be noted that also on the PdGa(111) surfaces, several energetically similar configurations were observed that are manifested in the course of the fast rotation of the acetylene molecule. [43] The results suggest that on the (100) and (110) surfaces it is expected that similar rotations of acetylene will be observed.

To understand the chemical interactions between the surface atoms and acetylene, the density of states of the combined system projected on the d-states of the surface Pd atom and the acetylene molecular orbitals are plotted (Figure 4.2). Also shown are the PDOS of the surface Pd for the clean surfaces and the acetylene molecule in the gas phase. Upon acetylene adsorption, an overall shift of the DOS of the surface Pd atom for all the surfaces towards lower energy is observed, suggesting a donation of electrons from the molecule to the surface.

For all the surfaces, the DOS of C_2H_2 adsorbed on the surface has sharp peaks at around -15, -10 and -8 eV. These correspond to the unperturbed MO arising from the σ-backbone orbitals ($\sigma_{CH}, \sigma^*_{CH}$, and σ_{CC}) of acetylene. Additionally, new features are comprising of three broad peaks (two at around -5.0 eV and one at around -2.0 eV) below the Fermi energy and one at about 3.0 eV above the Fermi energy. In the gas phase, acetylene has two degenerate highest occupied orbitals (HOMO) that have a π-bonding character (π_z and π_y) and two degenerate lowest energy unoccupied orbitals (LUMO) with a π-antibonding character (π^*_z and π^*_y). Upon adsorption on the surfaces in the π-configuration, these

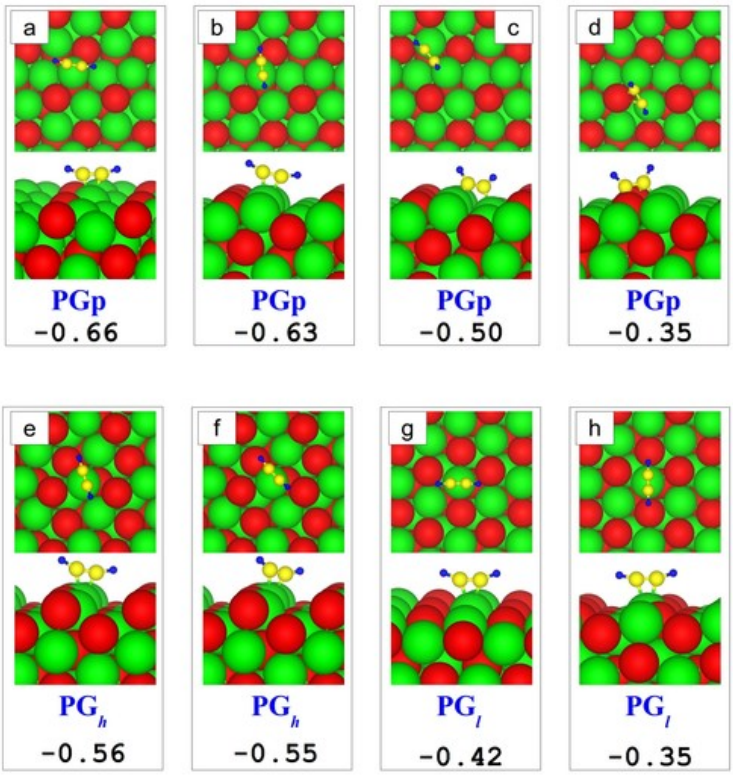

Figure 4.1: Summary of the minimum energy adsorption geometries of C_2H_2 on PGp, PG_h and PG_l surfaces. (a), (e) and (g) are the most stable configurations for the adsorption of C_2H_2 on PGp, PG_h and PG_l surfaces respectively. (b)-(d) are metastable configurations for the adsorption of C_2H_2 on PGp surface. (f) and (h) are the metastable configurations for the adsorption of C_2H_2 on PG_h and PG_l surfaces respectively. Green, red, yellow and blue balls represent Pd, Ga, C and H atoms respectively. The binding energies are given in eV.

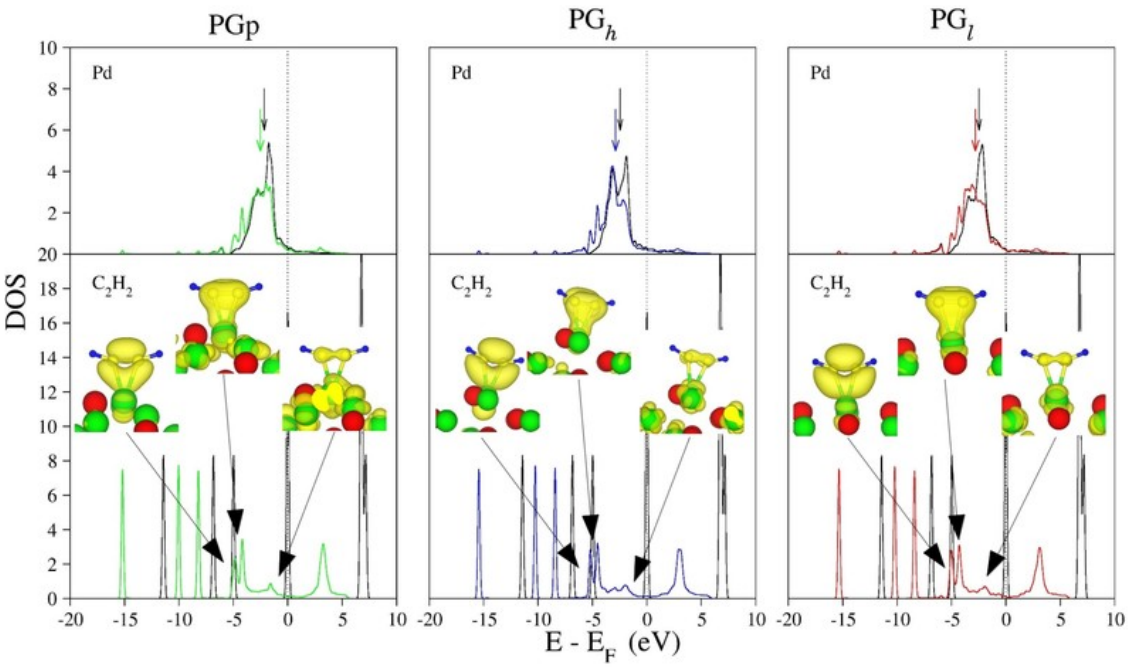

Figure 4.2: PDOS for Pd and acetylene before and after adsorption.Green, blue and red represents the PDOS of PGp, PG$_h$ and PG$_l$ surface after C_2H_2 adsorption and black represents the PDOS of clean surface and gas phase C_2H_2. For the clean and C_2H_2 adsorbed surfaces the Fermi is set at 0 and for the gas phase C_2H_2 the HOMO is set at 0. The d band center is marked as down pointing arrows with above mentioned colors. The wave functions corresponding to the broad bonding peaks at around -4.8, -4.2 and -2.0 eV are given, which are coming because of the interaction of C_2H_2 with the surface.

frontier orbitals hybridize with the Pd-d states and give rise to the above mentioned four new states. Out of these four peaks, the one that is lowest in energy (at about -4.8 eV) corresponds to the bonding interactions between the π_z of the molecule with that of the Pd-d_{z^2}. The second peak at around -4.2 eV is due to the antibonding state formed due to the hybridization of the acetylene π_y with the Pd-d_{zy}. The third occupied state (anti bonding) closest to the Fermi energy at about -2.0 eV is due to the hybridization of the π_y^* with the Pd-d_{zy}. The fourth state at about 3.0 eV above the Fermi energy is due to hybridization of π_z^* with the Pd-d. The fact that one of the empty antibonding orbitals of acetylene gets occupied suggests that there is back-donation of electrons from the surface to the molecule.

Next, the co-adsorption of acetylene and dissociated hydrogen on the surface is presented. Since this is the starting point of the hydrogenation reaction, this state should have enough

thermodynamic stability so that the surface adsorbed hydrogen can react with the adsorbed acetylene to form the vinyl intermediate. The calculations show that co-adsorption of acetylene and dissociated hydrogen is exothermic on all the surfaces. The largest binding energy was predicted on the PGp surface (-1.19 eV). On PG_h and PG_l the adsorption energies are respectively -0.72 and -0.24 eV. It should be noted that the stability of the co-adsorbed dissociated H and acetylene on PG_l is lower than that of the acetylene alone on the surface. This is due to the endothermic adsorption of the H atoms on this surface. Krajčí and Hafner reported similar endothermic adsorption of dissociated hydrogen on pseudo fivefold (210) surface. [42]

4.3.1.3 C_2H_4 adsorption

Similar to that of C_2H_2, various adsorption sites are considered for the C_2H_4 to find the most stable adsorption structure on these surfaces. Figure 4.3 shows the lowest energy configurations of ethylene on these three surfaces. On all the three surfaces, the molecule adsorbs in a π-configuration. There is considerable deviation of the molecule from its planar structure. The binding of ethylene is strongest on PGp surface with a binding energy of -0.72 eV, followed by that on PG_h and PG_l surfaces with binding energies of -0.61 eV and -0.52 eV respectively. It should be noted that the binding energies of ethylene on these surfaces are similar to what is reported on the (111) and (210) surfaces of PdGa. [42, 43] However this is smaller than the binding energy (-0.85 eV) observed on Pd(111) surface. [64, 65] Upon adsorption on the surface, ethylene is slightly activated with C-C double bond lengths increasing to 1.38 Å.

Figure-4.4 shows the PDOS for C_2H_4 adsorbed on PGp, PG_h and PG_l. Unlike acetylene, ethylene in its gas phase has only one HOMO and LUMO having π-bonding (π) and π-antibonding (π^*) character respectively. The five other occupied orbitals below HOMO are due to the σ-bonding and arise from combinations of 4 C-H and one C-C sigma bond. Upon interacting with the surface the lowest three molecular orbitals at around -12.0, -8.0 and -5.0 eV remain unperturbed and only shift to lower energy values of about -15.0, -11.0, -8.0 eV. The HOMO-2 and HOMO-1 of the molecule comprising of a combination of the C-H and C-C σ orbitals hybridize weakly with the Pd-d states. While the hybridization with HOMO-2 involves the formation of a bonding type state, hybridization with HOMO-1 results in the antibonding type state. In addition to these, new broad features

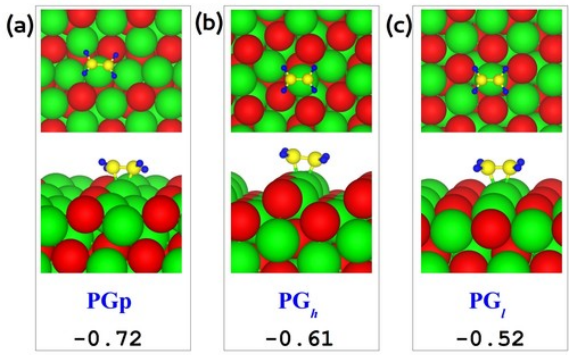

Figure 4.3: Summary of minimum energy adsorption geometries of C_2H_4 on PGp, PG_h and PG_l surfaces. Color code same as Figure-4.1

are found in between -5.0 to -1.0 eV resulting from hybridization of the molecular π states with that of Pd-d. For example, the state at -4.0 eV represents bonding configuration of π with Pd-d. The empty peak at about 3.0 eV is due to the hybridization of the π^* states with Pd-d.

4.3.1.4 Co adsorption of C_2H_3 and H

Vinyl is formed as an intermediate after the first hydrogenation of acetylene takes place. On the PGp surface, the active site is a triad comprising of a Ga atom and two Pd atoms that are about 0.7 and 0.14 Å below the Ga atom. In contrast, the active sites on the PG_l and PG_h surfaces is a diad formed of a Pd and a Ga atom. While in the former the Pd and Ga atoms are almost at the same height, in the latter the Pd atom is about 0.21 Å below the exposed Ga atom. In PG_h the Pd atom is connected to another Pd atom that is about 1.21 Å below the Pd atom, thus forming a quasi-triad. In order to determine the most stable co-adsorption geometry several possible configurations are considered, in which the two C atoms of vinyl can bind in different configurations, namely atop Pd, bridge between Pd and Ga and bridge between two Pd atoms, depending on the surface on which they are binding. All the co-adsorption geometries and their energy relative to the most stable configuration for PG_l, PG_h and PGp surfaces are respectively given in Figure 4.5-4.7.

On the PGp surface, the C atom of CH binds to the surface through a bridge between the Ga atom and the Pd atom (0.14 Å below the Ga atom). The Pd-C and the Ga-C bond lengths are 2.25 and 2.00 Å respectively. The C atom belonging to CH_2 is about

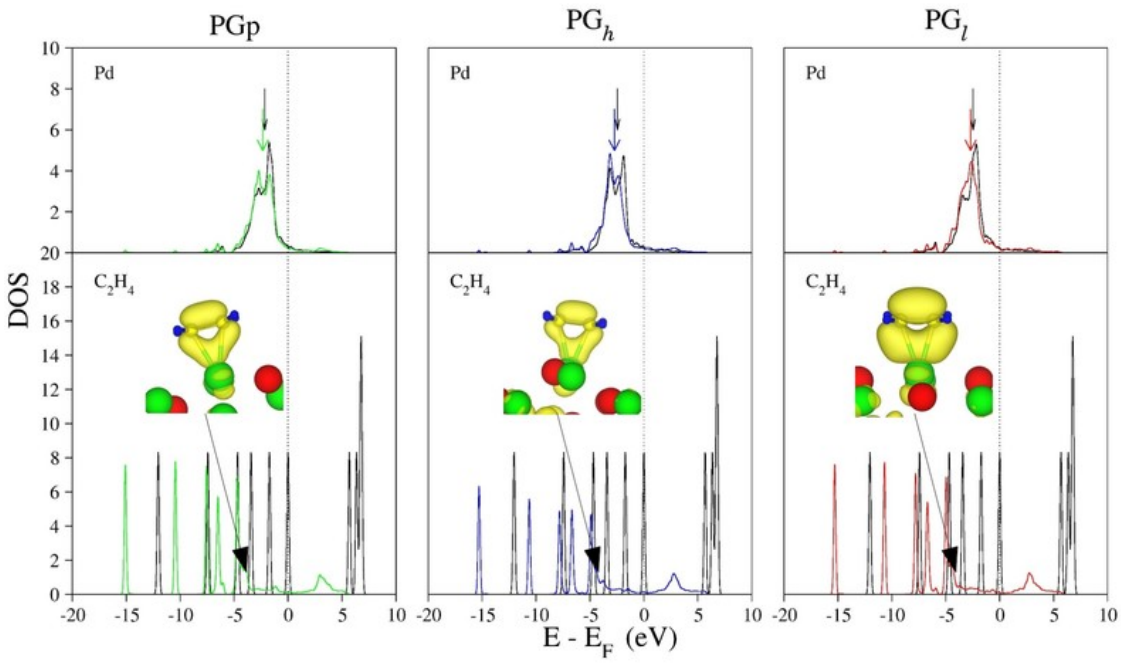

Figure 4.4: PDOS for Pd and ethylene before and after adsorption.Green, blue and red represents the PDOS of PGp, PG$_h$ and PG$_l$ surface after C_2H_4 adsorption and black represents the PDOS of clean surface and gas phase C_2H_4. For the clean and C_2H_4 adsorbed surfaces the Fermi level is set at 0 and for the gas phase C_2H_4 the HOMO is set at 0. The d band center is marked as down pointing arrows with above mentioned colors. The wave functions corresponding to the broad bonding peaks at around -4.6 eV is given, which is coming because of the interaction of C_2H_4 with the surface.

2.35 Å away from the Pd atom. The H atom is in a bridge position between two Pd atoms, of which one of them is part of the triad while the second one is about 1 Å below the surface. This configuration has co-adsorption energy of -0.85 eV with respect to co-adsorbed acetylene and dissociated hydrogen. Depending on the position of H atom, there are three more metastable configurations that are about 0.16, 0.16 and 0.25 eV higher in energy than the one reported above (see Figure-4.7 (b), (c) and (d)). The configurations in which the CH carbon binds atop Pd atom with a σ bond are also considered. However, these are about 0.49 and 0.86 eV higher in energy than the lowest energy configuration.

On PG$_h$ and PG$_l$ surfaces, in the most stable configuration of the co-adsorption of vinyl and H, the carbon of CH binds to the surface through a bridge site between topmost Pd and Ga. The H atom is in a bridge position between two Pd atoms, of which one of them is part of the triad while the second one is about 1.2 Å below the surface for PG$_h$ and 1.0

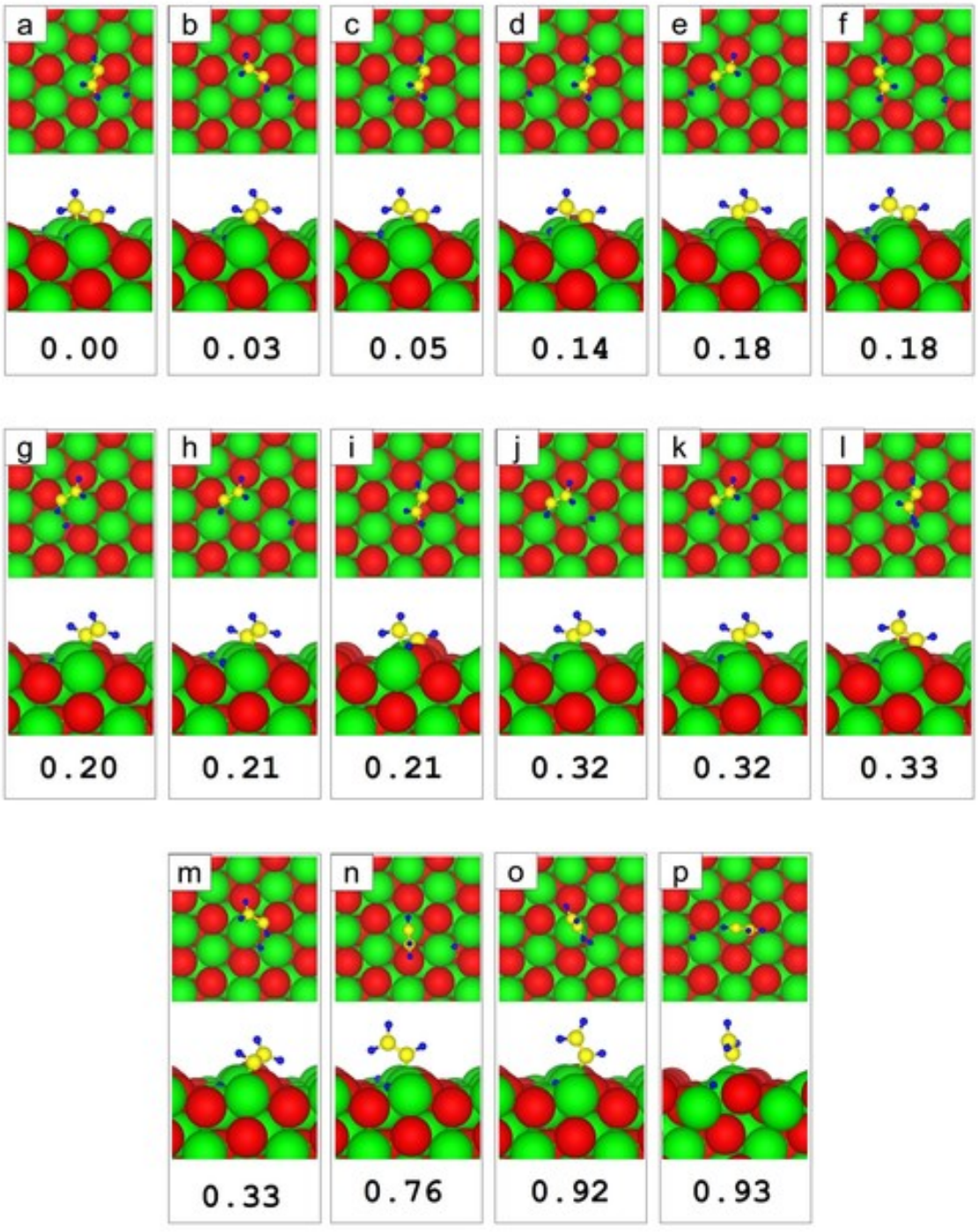

Figure 4.5: Summary of the minimum energy adsorption geometries of C_2H_3 on PG_l surface. The color codes are the same as Figure-4.1. The relative energies are given with respect to the most stable adsorption configuration.

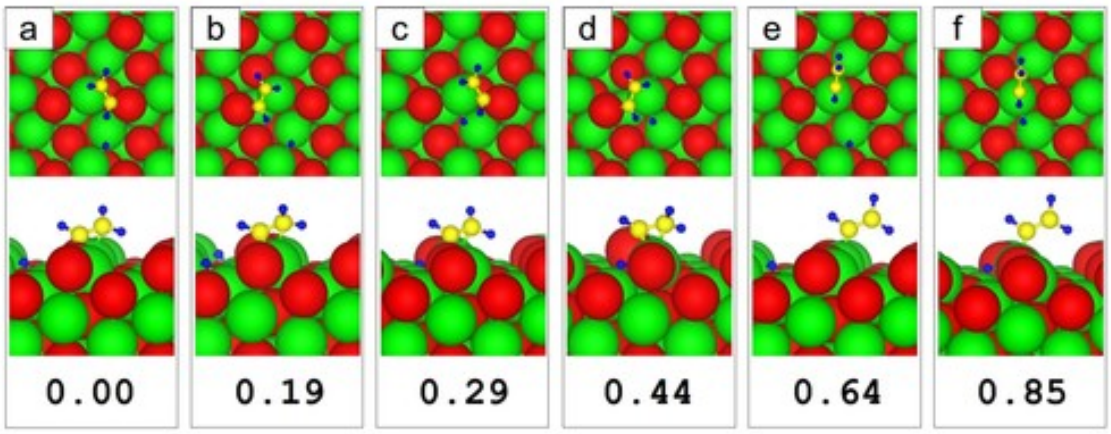

Figure 4.6: Summary of the minimum energy adsorption geometries of C_2H_3 on PG_h surface. The color codes are the same as Figure-4.1. The relative energies are given with respect to the most stable adsorption configuration.

Å below the surface for PG_l. The co-adsorption energies on these surfaces are found to be -1.52 and -1.63 eV respectively for PG_h and PG_l surfaces.

4.3.2 Hydrogenation mechanism

To determine the hydrogenation mechanism and the associated barriers, and thereby understand the reactivity and the selectivity of these model catalysts the reaction pathways are studied on these surfaces. Since it has already been shown that coke formation has large barriers (about 6.5 eV) on the PdGa surfaces, [75] the coke formation is not considered in the reaction pathway studies. Unlike Pd(111) where hydrogen dissociates spontaneously, [83, 84] on the PdGa surfaces hydrogen dissociation is an activated process. [43] Moreover, with the active sites well separated from one another, the reactants bind at larger distances from each other than the simple metal surfaces. [43] Hence, the barriers associated with the dissociation of hydrogen and the diffusion of the dissociated hydrogen atoms to the metastable state also need to be considered. Hence, on all the surfaces considered in this study the hydrogen dissociation and diffusion mechanism is included in the reaction profile.

On the PGp and PG_h surfaces the Horiuti-Polanyi mechanism is considered to study acetylene hydrogenation. In this acetylene adsorbs on these surfaces covered with hydrogen

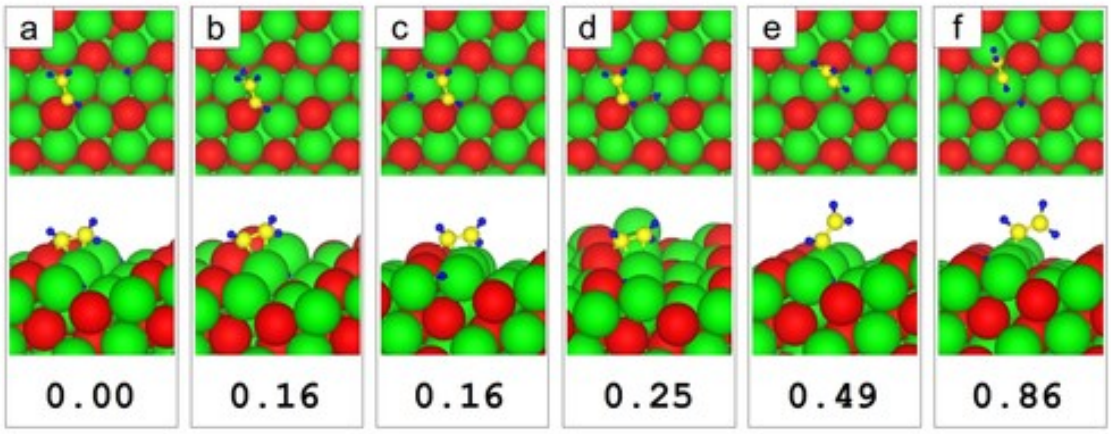

Figure 4.7: Summary of the minimum energy adsorption geometries of C_2H_3 on PGp surface. The color codes are the same as Figure-4.1. The relative energies are given with respect to the most stable adsorption configuration.

atoms. The H atoms then diffuse to acetylene. This is followed by hydrogenation. However, on PG_l the adsorption of atomic H is endothermic. This implies that the adsorbates might not have enough thermodynamic stability for the reaction to occur. However, in contrast, the co-adsorption of molecular hydrogen and acetylene is thermodynamically favorable on PG_l. Hence it is assumed that on PG_l hydrogen dissociation is preceded by co-adsorption of acetylene and molecular hydrogen. This is followed by hydrogen dissociation, diffusion and further hydrogenation.

4.3.2.1 Hydrogenation mechanism on PG_l

The energetics of the complete reaction mechanism is shown in Figure 4.8.
Hydrogen dissociation: Since on PG_l the hydrogen dissociation reaction is endothermic by about 0.33 eV; a novel pathway is considered in which the hydrogen dissociation is preceded by coadsorption of acetylene and molecular hydrogen (the coadsorption energy being -0.56 eV). Hydrogen dissociation from this coadsorbed configuration is endothermic by about 0.32 eV and involves a barrier of about 0.49 eV. The H-H bond length at the TS is about 1.52 Å. After dissociation, the H atoms bind to the Pd-Ga bridge sites. However, both these bridge sites share a common Pd atom. The reaction path is shown in Figure A.1 of Appendix A.

Vinyl formation: For the hydrogenation of C_2H_2 to C_2H_3 two possible paths are consid-

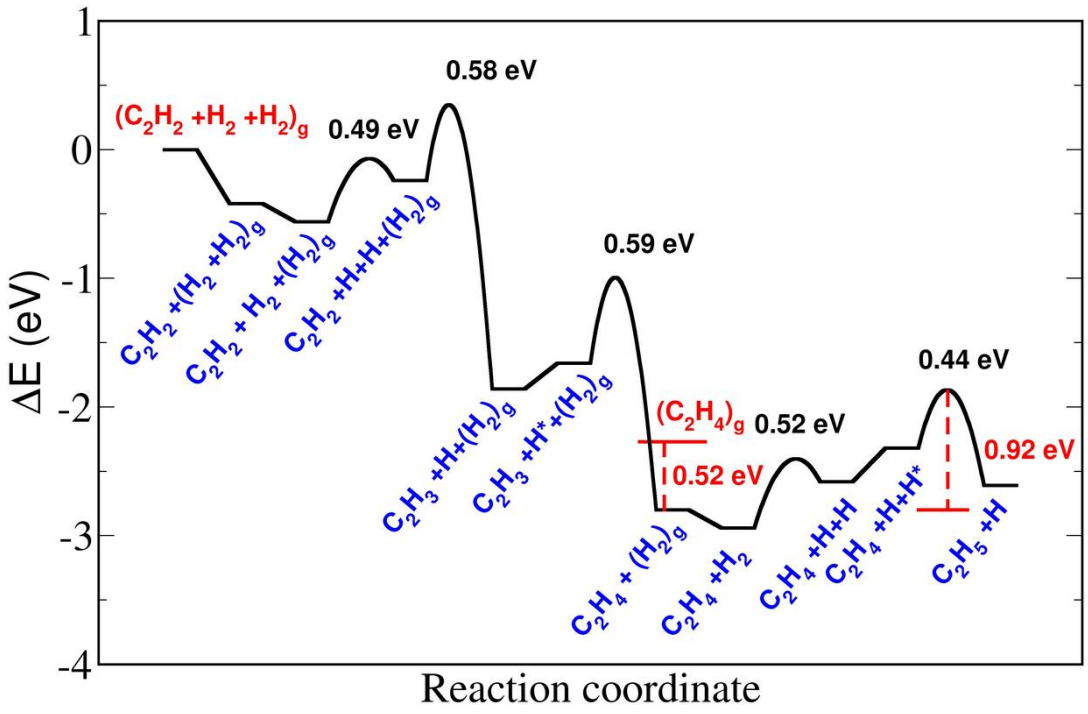

Figure 4.8: Computed energies and the barriers starting from gas phase reactants to the products on PG_l surface for selective hydrogenation of acetylene. "H*" represents metastable hydrogen diffusion steps. The subscript "g" represents the molecule in gas phase. Red line corresponds to the ethylene desorption.

ered. In the first path (Figure A.2 in Appendix A) the H diffuses from the most stable adsorption site to a metastable state where one of the H atoms is closer to acetylene. This metastable state is 0.15 eV endothermic. The diffusion of H to this metastable state requires overcoming a barrier of 0.33 eV. The subsequent hydrogenation to vinyl is associated with a barrier of 0.43 eV and results in a total reaction barrier of 0.58 eV with respect to the most stable co adsorption configuration of acetylene and dissociated hydrogen atoms. The hydrogenation primarily involves a rotation of C_2H_2 such that it is properly oriented with respect to the H atom. This is followed by transfer of the H atom from the Pd-Pd bridge site to the Pd atom to which acetylene is bound. In the transition state, the distance between this H atom and the C atom closest to it is about 1.60 Å. The $\angle_{C-C-H}$ is decreased to 146.2° compared to that of 160.3° in the initial state. Once the vinyl is formed, the molecule undergoes a barrierless rotation to the final state.

In the second path (Figure A.3 in Appendix A) the initial state is a metastable configuration in which the acetylene molecule is rotated by 90° compared to the most stable initial state for the first path. In this case, the H atom is already sufficiently close to the acetylene molecule for the hydrogenation to occur. The hydrogenation proceeds through the transfer of atomic H from the Pd-Pd bridge site to the Pd atom to which acetylene is adsorbed followed by formation of vinyl. This reaction path involves a barrier of about 0.52 eV. However, in this case, it is assumed that the rotation of acetylene molecule from the lowest energy configuration to the initial state of this pathway is barrierless. Moreover, this metastable state is about 0.35 eV higher in energy compared to the most stable co-adsorption configuration of acetylene and dissociated H, resulting in endothermic co-adsorption of the reactants on the surface with respect to the gas phase energies of acetylene and molecular hydrogen and the clean surface. Hence, the reaction going through this metastable state might result in desorption of the reactants from the surface even before the reaction is complete due to the insufficient thermodynamic stability of the reactants. Hence the first path will be the most probable one, and that has been given in the reaction profile (Figure-4.8).

Ethylene formation: Further hydrogenation of C_2H_3 to C_2H_4 is exothermic, lowering the energy of the system by about 0.94 eV. Four possible paths are considered. The reaction profiles for these paths are shown in Figure A.4-A.7 of Appendix A. Out of these, in the minimum energy pathway, the hydrogenation is preceded by diffusion of H to vinyl result-

ing in a metastable configuration that is about 0.20 eV higher in energy. In this metastable configuration, the carbon atom of the CH group of vinyl is bound to a Pd-Ga bridge, and the H atom is in a Pd-Pd bridge. The Pd-Ga and Pd-Pd bridge sites share a common Pd atom. Based on the previous calculations (where the hydrogen diffusion barriers are not significantly affected by the presence of other adsorbates) of hydrogen diffusion on this surface, it is expected that the diffusion barrier will be of the order of 0.3 eV. The hydrogenation is associated with a concerted transfer of the H from the bridge site to the common Pd atom and reorientation of the vinyl molecule such that the CH group moves towards the Ga atom and the CH_2 group binds to the same Pd atom. In the transition state, the Pd-C (C of CH_2) distance is about 2.21 Å compared to that of 2.44 Å in the initial state. This process involves a barrier of about 0.59 eV. Thus the total barrier (hydrogen diffusion and hydrogenation) for this reaction step is about 0.79 eV.

Once ethylene is formed, then it can either desorb from the surface that makes the surface selective towards semi-hydrogenation reaction or it may remain on the surface for further hydrogenation to ethane; the surface thereby losing its selectivity. Coke formation and other side reactions are highly unlikely due to the large barriers associated with those processes. Hence, it could be assumed that desorption of ethylene and further hydrogenation of ethylene to ethyl are the only competing processes. Desorption of the ethylene is a unimolecular reaction; it depends on the surface coverage of ethylene. While hydrogenation of ethylene is a bimolecular reaction; it depends on the surface coverage of ethylene and hydrogen. However, at equilibrium, the surface coverage of ethylene is much higher (feed) compared to the surface hydrogen coverage. Hence, the hydrogenation of ethylene depends only on the surface coverage of hydrogen. The ethylene is further hydrogenated to ethyl when desorption barrier of ethylene is larger than hydrogenation barrier or desorbed from the surface when desorption barrier is smaller than hydrogenation barrier. For a surface to exhibit high selectivity, the hydrogenation barrier should be sufficiently large compared to the desorption barrier. The energy difference between ethyl formation hydrogenation barrier and ethylene desorption barrier determines selectivity of the catalytic surface ($\Delta E_{selectivity} = \Delta E^{C_2H_5 formation}_{hydrogenation} - \Delta E^{C_2H_4}_{desorption}$).

Coadsorption of ethylene and H: Further hydrogenation requires the co-adsorbed C_2H_4 and atomic H. Since the hydrogen dissociation on this surface is endothermic, this should also be considered while calculating the hydrogenation barrier. The co-adsorption of

molecular hydrogen and ethylene stabilizes the reactants by 0.14 eV compared to that of ethylene adsorbed on the surface and hydrogen molecule in the gas phase. However, co-adsorption of ethylene and dissociated H on this surface is about 0.22 eV endothermic compared to that of ethylene adsorbed on the surface and hydrogen molecule in the gas phase. The hydrogen dissociation involves a barrier of about 0.52 eV (Figure A.8 in Appendix A).

Ethyl formation: For ethyl formation, the hydrogen atom needs to diffuse and reach near ethylene, resulting in a metastable state. Assuming that the diffusion barrier is not significantly effected by the presence of ethylene, the metastable state was found to be 0.26 eV higher in energy compared to that of the initial state in which the H atoms are far away from the molecule. From this metastable state, the conversion to ethyl follows similar mechanisms as observed on the other surfaces. The barrier for this is about 0.44 eV. The reaction pathway is shown in Figure A.9 of Appendix A. In comparison with the ethylene adsorbed on the surface and hydrogen in the gas phase, the effective barrier for further hydrogenation is 0.92 eV. In contrast, the desorption barrier of ethylene is 0.52 eV. Hence for this surface $\Delta E_{selectivity}$ is about 0.40 eV.

4.3.2.2 Hydrogenation on PGp and PG$_h$

The reaction profiles on the PGp and PG$_h$ surfaces are summarized in Figure-4.9.

H_2 dissociation and diffusion of atomic H: The complete reaction pathways and energy profiles for hydrogen dissociation and diffusion on PGp and PG$_h$ are given in Figure A.10 and A.11 respectively. The dissociation barriers on the PGp and the PG$_h$ surfaces are about 0.56 and 0.49 eV respectively. These barriers are comparable with those found on other PdGa terminations. In the transition state, the H-H distances are about 1.65 Å and 1.52 Å. After dissociation, the H atoms go to the closest metastable state that is a local minimum in the potential energy surface. From there they diffuse to the most stable minima. The diffusion of the hydrogen atoms on the surface is also an activated process. On the PGp surface, the diffusion barrier is high (0.43 eV and similar to the dissociation barrier). On the PG$_h$ there are two possible diffusion pathways: (a) where the hydrogen atom on the crest moves through the trough and (b) the H atom in the trough moves along the trough through a local minimum. For the former, the barrier is about 0.20 eV while for

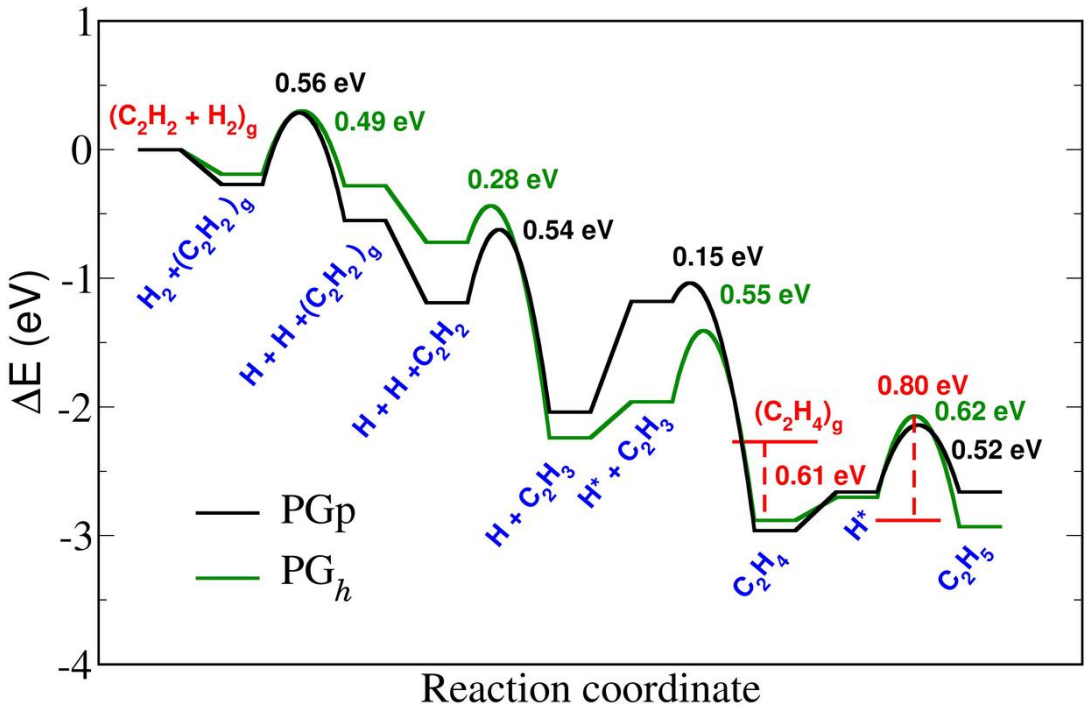

Figure 4.9: The energy barriers and reaction energies starting from gas phase reactants to the products on PGp and PG_h surfaces for selective hydrogenation of acetylene. "H*" represents metastable hydrogen diffusion steps. The subscript "g" represents the molecules in gas phase. Red line corresponds to ethylene desorption.

the later it is about 0.16 eV. It should be noted that these barriers are comparable with the barriers of 0.50 and 0.42 eV reported for (210) surface of PdGa and PdAl respectively. [42]

Vinyl formation: Hydrogenation of acetylene to vinyl is exothermic on both these surfaces. A correlation between the reaction barrier and the reaction exothermicity is found: the higher the exothermicity, the lower the barrier. For example, on PGp where the reaction is exothermic by about 0.85 eV, the barrier is about 0.54 eV, while on PG_h where the reaction is exothermic by about 1.52 eV, the hydrogenation barrier is only 0.28 eV. The energetics and the reaction profile for PGp and PG_h are shown in Figure A.12 and A.13 respectively. Even though on both these surfaces the acetylene molecule is adsorbed atop the surface Pd atom that also forms the bridge site for the dissociated H atom, the details of the reaction pathway are different on the two surfaces. On PGp, the full reaction can be divided into two parts. First, the hydrogenation takes place where the H atom moves primarily and binds to acetylene. The d_{Pd-H} distance and the $\angle_{C-C-H}$ are decreased to 1.76 Å and 145.4° at the transition state compared to that of 1.81 Å and 161.2° in the initial state. The vinyl formed is in a metastable state in which C_2H_3 is in a σ-bonded conformation on top of the Pd atom. The vinyl formed undergoes rotation to reach the lowest energy configuration. This involves a barrier of about 0.14 eV. In contrast on the PG_h surface, the molecule is not aligned properly to interact with the H atom. Hence on this surface, the acetylene molecule first undergoes rotation to properly reorient itself followed by the hydrogenation. The reaction barrier is primarily associated with the rotation of the molecule. At the transition state, the π bonded C_2H_2 rotates along the bond, thereby making a new σ bond with topmost Ga. The d_{Pd-H} distance is slightly increased to 1.81 Å (from 1.79 Å in the initial state) and the $\angle_{C-C-H}$ is decreased to 150.3° from that of 160.5° in the initial state.

Vinyl to ethylene formation: The next step is the hydrogenation of vinyl to ethylene. On both these surfaces, the second hydrogen atom is away from vinyl. Hence for the reaction to proceed, the hydrogen needs to diffuse on the surface and come close to vinyl. On PGp this process happens through two metastable states denoted as MS1 and MS2 (Figure A.14 in Appendix A).

The diffusion of H from the initial state (IS) to MS2 is endothermic by 0.86 eV and involves two barriers. The barrier for diffusion of H from IS to MS1 is about 0.52 eV while

the second diffusion barrier is about 0.60 eV. It should be noted that this barrier is similar to what is observed in the diffusion of atomic H in the absence of acetylene. The hydrogen diffusion is also accompanied with a reorientation of the π bonded C_2H_3 to atop σ bonded geometry on Pd. The hydrogenation involves a barrier of 0.15 eV and is primarily due to rotation of the vinyl. However, on PG_h first the H diffuses from the most stable site to a metastable site in which H is close to the C_2H_3 (Figure A.15 in Appendix A). This is slightly endothermic by 0.28 eV and has a barrier of 0.36 eV. The H diffuses from one crest to the next through the trough. The subsequent hydrogenation requires overcoming a barrier of 0.55 eV with respect to MS1. This barrier is primarily associated with the rotation of the ethylene molecule to the π-configuration. The overall reaction barrier compared to the IS is about 0.83 eV.

Ethylene to ethyl formation: Ethyl formation on PGp is weakly endothermic (0.30 eV) while on PG_h the reactants and products have similar energies. The energetics and the reaction profile for PGp and PG_h are shown in Figure A.16 and A.17 respectively. Similar to the hydrogenation of vinyl to ethylene, further hydrogenation of ethylene to ethyl is a two-step process involving diffusion of H to ethylene followed by subsequent hydrogenation. On PGp, the barrier for the former is about 0.56 eV while on PG_h it is about 0.30 eV. The subsequent hydrogenation barriers with respect to the metastable state on PGp and PG_h are 0.52 and 0.55 eV respectively. Both on PGp and PG_h the total barrier with respect to the initial state is about 0.82 and 0.80 eV. The ethylene desorption barriers on these surfaces are 0.72 and 0.61 eV respectively on PGp and PG_h. This gives $\Delta E_{selectivity}$ values of 0.10 and 0.19 eV on PGp and PG_h.

4.3.3 Reactivity and selectivity

After presenting the results of selective hydrogenation of acetylene to ethylene on the stable terminations of the low-indexed (100) and (110) PdGa surfaces in the previous sections, here we compare the results with those reported in the literature on the (111) surface terminations containing Pd atoms. Also, we elucidate the role of surface roughness and ensemble effects on the selectivity and reactivity.

Table-4.3 shows a comparison of the obtained reaction barriers and selectivity along with those reported in the literature. Selectivity (ΔE) has been calculated as the difference

between the barrier involved in the formation of ethyl from ethylene and the desorption barrier of ethylene. $\Delta E > 0$ indicates that the surface shows selectivity. Amongst the surfaces considered in this study, the (100)PG$_l$ surface shows the highest selectivity with $\Delta E = 0.40$ eV. This is only 0.21 eV lower than that of what is observed by Prinz *et al.* on the $(\bar{1}\bar{1}\bar{1})$Pd$_3$ surface. [43] It should be noted that, over a wide range of Ga chemical potential (even under Ga rich condition), the (100)PG$_l$ surface is theoretically predicted to be one of the most probable exposed facets in the PdGa crystallites grown. [41, 76, 77] Hence this surface termination may also be responsible for the high selectivity exhibited by PdGa nanocrystallites. [38]

The reactivity of the different surface terminations are determined by the barrier of the rate-limiting step. On all the three surfaces considered in this study and the (111)Pd$_1$ surface, the rate-limiting step for hydrogenation is vinyl to ethylene formation, with (111)Pd$_1$ surface having the largest barrier of 1.10 eV. In contrast, on the $(\bar{1}\bar{1}\bar{1})$Pd$_3$ that shows best selectivity, the rate-limiting step is acetylene to vinyl formation with a barrier of 1.04 eV. However, the (100)PG$_l$ surface, that shows reasonably good selectivity, has the lowest barrier for the rate-limiting step (0.79 eV for vinyl to ethylene formation) amongst all the Pd containing surfaces considered in this study and reported in the literature. Hence this surface termination is a probable candidate for the selective hydrogenation of acetylene to ethylene with high reactivity and selectivity.

Unlike transition metal surfaces that are typically close-packed and smooth, the PdGa surfaces are open and have a lot of corrugation and roughness. In order to understand the correlations between surface structure and roughness, and the selectivity and reactivity the root mean square roughness (R) is calculated, that is given by:

$$R = \sqrt{\frac{1}{N}\sum_{i=1,N}(z_i - < z >)^2}, \tag{4.2}$$

where N denotes the number of exposed atoms in a given termination, z_i is the vertical position of the i^{th} atom and $< z >$ is the mean of the vertical position and is given by $< z >= \frac{1}{N}\sum_{i=1,N} z_i$. A value of $R = 0$ implies that the surface is perfectly smooth while larger the value of R, more is the surface roughness. The values of R for the different surfaces containing Pd are given in the second column of Table-4.3. Among these surfaces, PG$_l$ with R =0.37 Å is the smoothest one and PG$_h$ with R =0.65 Å is the roughest one.

Table 4.3: Comparison of the barriers (in eV) for primary reaction steps as a function of surface roughness (R) on different Pd containing PdGa surfaces predicted by DFT.

Surface	R (Å)	Reaction Barrier (eV)				
		H_2* → H* +H*	C_2H_2* + H* → C_2H_3*	C_2H_3* + H* → C_2H_4*	C_2H_4* + H* → C_2H_5*	$\Delta E_{selectivity}$
(100)PG_l	0.37	0.49	0.58	0.79	0.92	+0.40
($\bar{1}\bar{1}\bar{1}$)Pd_3 [43,56]	0.47	0.55, 0.61	1.04, 0.81	0.80, 0.19	1.30, 0.54	+0.61, +0.06
(111)Pd_1 [43,56]	0.53	0.72, 0.78	0.80, 0.60	1.10, 0.31	0.90, 0.69	+0.17, -0.04
(110)PGp	0.61	0.56	0.54	1.01	0.82	+0.10
(100)PG_h	0.65	0.49	0.28	0.83	0.80	+0.19
Pd(111) [56,64]	0.00	-	0.68	0.88	0.78	-0.56

Figure 4.10 shows the plot of selectivity (green line with squares) as a function of R. While geometry optimizations are performed for all the surfaces and relaxed coordinates are taken to calculate R, the barriers for Pd_3 and Pd_1 are taken from Ref. [43].

Since selectivity depends on the ethylene desorption barrier and barrier for ethyl formation; these two quantities are also plotted in Figure 4.10. It is usually expected that as the surface roughness increases (implying more under coordinated surface atoms) the ethylene desorption barrier (primarily a measure of how strongly ethylene is bound to the surface) should increase. Similar trends are found except for PG_h, which shows a lower desorption barrier. It should be noted that the desorption barrier on PG_h is lowest amongst Pd_3, Pd_1 and PGp and is slightly more than PG_l. This behaviour can be rationalised by carefully looking into the chemical composition of the surface ensemble. Both in PG_h and PG_l the surface ensemble constitutes of Pd and Ga present in the 1:1 ratio; this being same as that in bulk. Hence these surfaces show lowest desorption barrier amongst the surfaces considered in this comparison, showing the importance of the ensemble effect. However, between PG_h and PG_l (both with the same ensemble), the surface roughness comes into play and the former surface with a larger degree of roughness has a larger desorption barrier.

In contrast to ethylene desorption, the ethylene hydrogenation barrier on all the surfaces except $(\bar{1}\bar{1}\bar{1})Pd_3$ are very similar. To understand this behavior the energy components determining the ethylene hydrogenation barrier are analysed. Ethylene hydrogenation barrier depends on two energy components: (a) endothermicity of the diffusion of H towards ethylene and (b) hydrogenation barrier of ethylene to ethyl. Both these quantities are also plotted in Figure 4.10. The latter has no significant change with the increase in R. R increases from 0.37 to 0.65 Å as one moves from PG_l to PG_h while the barrier for hydrogenation of ethylene to ethyl ranges from 0.44 eV to 0.62 eV. Unlike the hydrogenation barrier, the endothermicity, given by the difference between the most stable adsorption geometry of ethylene on the surface and hydrogen molecule in the gas phase with that of the metastable coadsorption configuration in which one of the H atoms are closest to ethylene, shows a non-monotonous behaviour. It increases from PG_l to Pd_3 (largest value of 0.80 eV) and again monotonically decreases from Pd_3 to PG_h (lowest value of 0.18 eV). As reported by Armbruster and coworkers, the unusually large value for Pd_3 is due to the fact that in the metastable state, the H atom binds to the Pd atom that is about 1.43 Å below

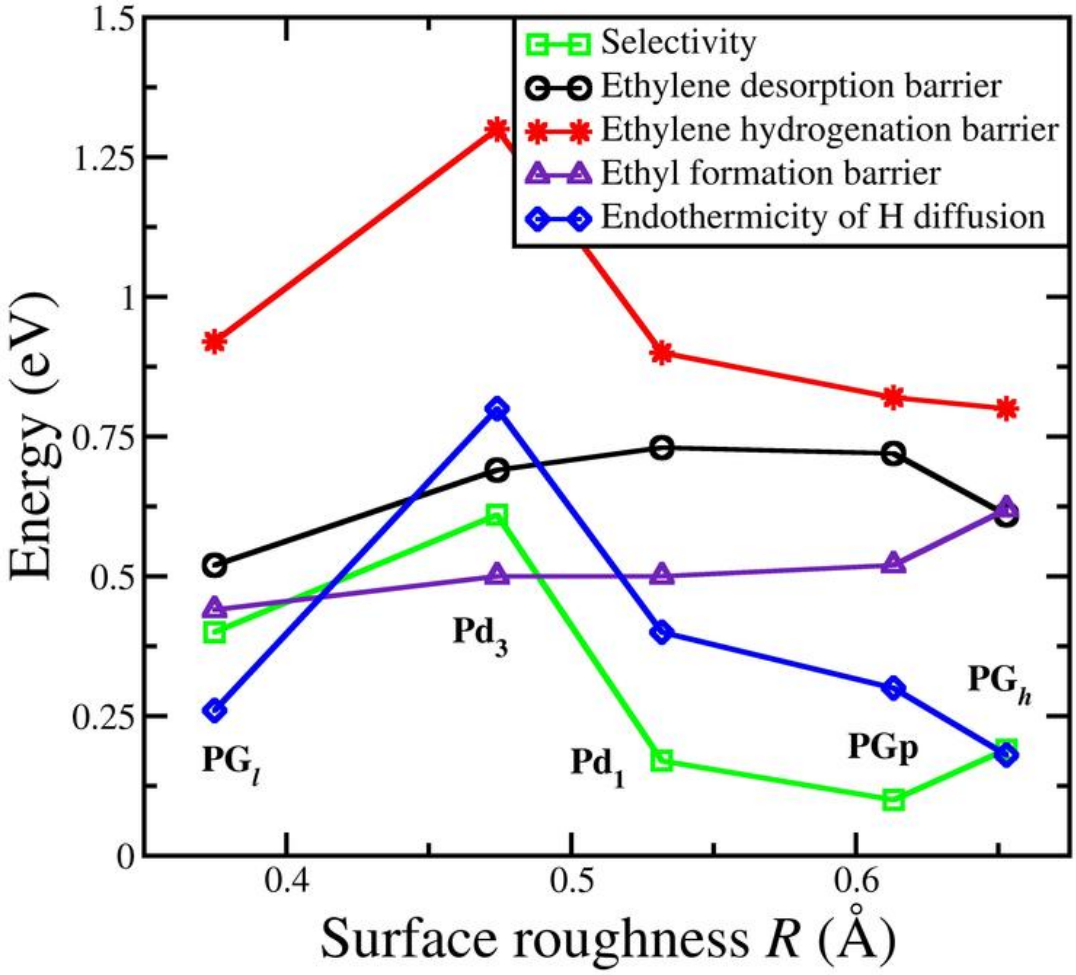

Figure 4.10: Selectivity ($\Delta E_{selectivity}$) (green line with open squares), ethylene desorption barrier (black line with open circles), ethylene hydrogenation barrier (red line with star), ethyl formation barrier (indigo line with open triangle) and endothermiticity of H diffusion (blue line with open diamond) as a function of surface root mean square roughness (R).

the surface Pd triad. This analysis shows the interplay between the surface roughness and ensemble effect in determining the selectivity of the catalyst.

4.4 Summary

In summary, the reactivity and selectivity of the (100)PG_l, (100)PG_h and (110)PGp surfaces are studied towards selective hydrogenation of acetylene. From these studies, the PG_l termination of the (100) surface, which is energetically favourable and will occupy a significant proportion of the surface area in PdGa nanocrystallites over a wide range of Ga chemical potential, is found to exhibit high reactivity and selectivity. Further on this surface, a novel reaction mechanism is found, in which hydrogen dissociation is preceded by coadsorption of acetylene and molecular hydrogen.

A detailed analysis of the factors determining the selectivity of the different low indexed Pd containing surfaces shows that the selectivity is determined by the interplay between surface roughness and ensemble effect.

Chapter 5

Growth of Small Pd-Ga Bimetallic Clusters on MgO(100) Surface

In this chapter, we present our results for the structure and thermodynamic stability of small sized (up to 4 atoms) PdGa bimetallic clusters adsorption on MgO(100) surface studied by DFT. We also report the result of elementary steps involved in the growth and nucleation kinetics of these small clusters on the same surface studied within the GT-KMC framework. Our calculations predict that the binding and formation energies of the clusters increase with cluster size. The mixed bimetallic clusters on the surface are found to be more stable than the parent clusters, particularly, clusters with 1:1 atomic ratio have the highest stability. We find that all the clusters except Ga tetramer are highly mobile on the surface. At 300 K, all these clusters are kinetically stable, and the vacancy sites act as trapping sites. Upon increasing temperature, Ga_2, Ga_3 and Pd_1Ga_2 clusters tend to escape from the vacancy site than decompose, whereas all other clusters tend to decompose rather than escape from the vacancy site. The growth of the pure Pd and Ga clusters is heterogeneous though the elementary reactions involved in the growth process for these two clusters are very different. When the bimetallic clusters are grown by depositing Pd and Ga adatoms with an equal deposition rate, the bimetallic clusters are formed in large proportion especially clusters with 1:1 atomic ratio are found in the highest fraction. Further, clusters with desired stoichiometric ratios can be obtained in a significant fraction by varying the deposition rates of the Pd and Ga adatoms to the surface.

5.1 Introduction

Small metal nanoparticles supported on oxide surfaces have many interesting properties and technological applications, especially in the area of catalysis, magnetic nanostruc-

tures, and photonic devices. [85–88] Their size, that in turn affects their electronic properties, strongly influences their functionality. For example, it has been shown that the activity and selectivity of a metal nanocatalyst can be improved by modifying its electronic properties through variation of its size. [89] In addition to tuning their properties by varying their size, forming bimetallic clusters by adding another metallic component provides an extra degree of freedom (variation of composition) to alter the properties and functionalities of these supported clusters.

Amongst the different metallic clusters, Pd cluster on MgO (100) surface has been extensively studied both experimentally and theoretically as a model system for the metal clusters on the oxide support. [87, 90–92] During the last decade, in addition to the pure Pd clusters, there are efforts to understand the structure and stability of the palladium-based bimetallic clusters on MgO surface. [93–97] In most of the cases the d block metals were taken as the second metal. Pasti *et al.* demonstrated that the stability of the Pd based bimetallic clusters depends on the substituting element. [93] Additionally, in some cases, the structure of the clusters also depends on the substituting element. [95–97]. Using DFT calculations Heard *et al.* showed that the thermodynamically most stable composition could also vary depending on the type of metal atoms added to the Pd. [94] The main disadvantage of the d block metal based bimetallic alloy catalysts is that they often phase segregate due to the very small value of thermodynamic mixing energy. In addition to that, one can not have control over the active site ensembles in the case of alloy catalyst.

The other possibility is making the bimetallic catalyst with Pd and p block metals. Pd is known to form stable intermetallic compounds with the third group metals. In particular, with Ga, it forms PdGa intermetallic compound, which shows unusually high selectivity and reactivity towards selective hydrogenation of acetylene to ethylene. [38, 43, 59, 69] A recent study from our group shows that formation of small (up to 4 atoms) PdGa clusters is possible in the gas phase and the reactivity of the gas phase clusters strongly depends on the cluster size and the Ga concentration. [98] However, for realistic applications, the clusters need to be on support. Hence it is imperative that we understand the stability and the formation mechanism of these clusters on a support. Therefore, in this work, we have studied the structure and stability (thermodynamics) and the growth process (kinetics) of small PdGa clusters on a commonly used MgO support.

The rest of the chapter is organized as follows: Section-5.2 describes the computational methods used, the thermodynamic energetics analyzed and the GT-KMC framework used to study the time evolution of the growth of the bimetallic clusters. In section-5.3.1 we present our results for the adsorption of Pd, Ga, PdGa clusters on the clean MgO (100) surface and F-centers thereof. Section-5.3.2 presents the discussion of the thermodynamic stability of these clusters. Section-5.3.3 discuss the thermodynamics of the different processes involved in the formation of the cluster. In section-5.3.4 we present our results for the diffusion of Pd, Ga, PdGa clusters on clean MgO (100) surface. Section-5.3.5 presents the discussion of the thermodynamic and kinetic stability of the cluster nucleus. Section-5.3.6 discuss the kinetic Monte Carlo simulation results for the nucleation of these clusters. Finally, we conclude in section-5.4.

5.2 Methods and Computational details

We have used the Quantum ESPRESSO software, [34] a plane wave based implementation of density functional theory, to solve spin-polarized Kohn-Sham equations. The electronic exchange and correlation potential was described by the generalized gradient approximation (GGA) as parametrized by Perdew-Burke-Ernzerhof (PBE). [12] Ultrasoft pseudopotentials was used to describe the electron-ion interactions. [19] We used a plane wave basis set with a kinetic energy cutoff of 35 Ry, and charge density cutoff of 400 Ry. Marzari-Vanderbilt smearing [23] with a smearing width of 0.002 Ry was used to speed up the convergence. Brillouin zone integrations were done at Gamma point.

The diffusion barriers were computed using the climbing image nudged elastic band (CI-NEB) method. [32, 80] Depending on the complexity of the diffusion path the number of images for a given path varies between 9 and 25. The forces acting on each image are converged up to 0.05 eV/Å.

5.2.1 Surface and adsorption model

To study the adsorption structures of Pd, Ga and PdGa clusters on a support, we have used the MgO(100) surface as a substrate. The latter was modelled by a four-layer slab of which the bottom two layers were fixed to the bulk interplanar separation while the top

two layers were relaxed. Since we are interested in the interaction of the clusters with the support, we have used a (4×4) surface supercell such that the minimum distance between the periodic images of the cluster is about 8 Å, thereby ensuring negligible interaction between them. Moreover, along the direction normal to the surface, we have used a vacuum of about 14 Å to avoid the interaction between the periodic images of the surface slab along that direction. Further, the oxide surfaces are usually prone to O vacancies. One oxygen from the topmost layer of this supercell was removed to create an F-center. Assuming one metal atom per surface oxygen, this corresponds to a defect concentration of 1.1 $\times 10^{15}$ cm^{-2}.

The thermodynamic stability of the clusters on the surface with respect to the gas phase clusters are calculated using the adsorption energies (E_{ads}):

$$E_{ads} = E_{Pd_xGa_y/MgO} - E_{MgO} - E_{Pd_xGa_y} \tag{5.1}$$

where, $E_{Pd_xGa_y/MgO}$ is the total energy of Pd_xGa_y cluster adsorbed on MgO slab, E_{MgO} is the total energy of the clean MgO slab or one with a F-center. $E_{Pd_xGa_y}$ is the total energy of Pd_xGa_y cluster in gas phase, which are calculated by taking Pd_xGa_y cluster in a cubical box with sides 15 Å long. x and y are the number of Pd and Ga atoms in the cluster respectively. The adsorption energy calculated using the above equation gives the energy gain if the clusters are first prepared in the gas phase and deposited on the MgO surface. This is important to understand the stability of the clusters obtained by the size-selective deposition.

Stability of the small clusters which are grown on the MgO support by vapor deposition method was explained by the binding and formation energies of the cluster. Binding energy of N atom cluster ($N = x + y$) on the MgO support was calculated as,

$$E_{bind} = E_{Pd_xGa_y/MgO} - E_{MgO} - xE_{Pd} - yE_{Ga} \tag{5.2}$$

where, E_{Pd} and E_{Ga} are the energy of the Pd and Ga atoms in the gas phase, which were calculated by taking one metal atom in a cubical box with sides having a length of 15 Å.

The formation energy of the clusters on MgO terrace was calculated as,

$$E_{form} = E_{Pd_xGa_y/MgO} + (N-1)E_{MgO} - x(E_{Pd/MgO}) - y(E_{Ga/MgO}) \tag{5.3}$$

where, all the terms in the right hand side are the total energies of the respective systems. The above equation describes the amount of energy released when an N atom cluster is formed starting from x number of Pd and y number of Ga atoms which are adsorbed on MgO terrace.

Further, to compare the stability of the bimetallic clusters with their parent clusters the energy of mixing was calculated as,

$$E_{mix} = E_{Pd_xGa_y/MgO} - (\frac{x}{N}E_{Pd_N/MgO} + \frac{y}{N}E_{Ga_N/MgO}) \tag{5.4}$$

In all the above expressions $N = x + y$, N vary from 1 to 4 ($0 \leq x, y \leq N$). All the terms present in the right-hand side are the total energies of the respective system. E_{mix} gives the energy gain due to the formation of the bimetallic cluster on MgO, which are formed by taking atoms from the metallic parent clusters of the same size which are already stabilized on MgO.

In order to understand the chemical interaction between the clusters and the support we have computed the charge transfer between the surface and the cluster. The charge transfer is given by,

$$\Delta\rho = \rho_{Pd_xGa_y/MgO} - \rho_{MgO} - \rho_{Pd_xGa_y} \tag{5.5}$$

where, $\rho_{Pd_xGa_y/MgO}$ is the charge density of Pd_xGa_y cluster adsorbed on MgO surface, ρ_{MgO} and $\rho_{Pd_xGa_y}$ are respectively the charge density of MgO surface and Pd_xGa_y cluster with the same geometry.

5.2.2 Kinetic Monte Carlo simulations

The energetics (both thermodynamics and diffusion barriers) obtained from the DFT calculations are employed as inputs to a graph-theoretical kinetic Monte Carlo (GT-KMC) framework to study the growth mechanism and sintering kinetics. All the GT-KMC calculations were done using Zacros software. [35, 99] This GT-KMC method enables us to

represent any complex elementary reaction step involving mono-dentate or multi-dentate species and any number of sites that are connected in an arbitrary pattern. In this method, the lattice is represented as a collection of sites which are connected in a specific pattern like a graph. The state of the lattice gives the information about the sites and their occupancy i.e., which sites are occupied by which species. Any elementary reaction step is also represented by a graph with specific initial and final state. The graph representation of elementary reaction steps are mapped onto the lattice processes by solving the subgraph isomorphism problem. The lattice processes represent the reaction events that can occur on the lattice sites during the course of the simulation. Every such process is assigned to a random occurrence time and a priority list is created based on the random occurrence time. At each KMC step, the first process in the list is executed and the simulation time is updated, along with the lattice states and the energetics reflecting the occurrence of that event. The priority list is also updated for the new lattice state based on the lattice processes of the new state, and the whole procedure is repeated. This procedure results in a stochastic trajectory that not only contains complete information about the lattice state at all the time but also the information about the number of the species adsorbed and produced.

The rate constant of the reaction steps are estimated using the harmonic approximation of the transition state theory as,

$$k_{hTST} = Ae^{-(E^* - E^{init})/k_B T} \tag{5.6}$$

where the prefactor A has been calculated as,

$$A = \frac{\Pi_{i=1}^{3N} \nu_i^{init}}{\Pi_{i=1}^{3N-1} \nu_i^*} \tag{5.7}$$

where ν_i^{init} is the harmonic modes of the initial state and ν_i^* is the stable modes at the saddle point. The normal mode frequencies are calculated using density functional perturbation theory (DFPT) as implemented in Quantum Espresso software. [27]

To study the growth mechanism of the clusters, the MgO(100) surface was modeled with a 100×100 two-dimensional lattice with periodic boundary condition in the xy plane. The fractional coordinates for the position of O and Mg atoms in the unitcell are (0,0) and (0.5, 0.5) respectively. This lattice corresponds to a substrate size of 30×30 nm^2, consist

of 10000 substrate oxygen sites. At the start of the simulation 25 oxygen vacancies were created at random positions, which corresponds to the experimentally determined value of 0.25%. [92] The atoms are deposited at a rate of 5.33×10^{-4}ML/s, which is the typical experimental deposition rate. 170 elementary reaction steps were accounted in the KMC model, which include the diffusion of the cluster on the terrace, formation and decomposition of the clusters on the terrace and at the defect site. A complete list of the reaction steps used in the KMC simulations is given in Appendix B. Each simulation was done with five different random seeds and the average quantities are presented in the results section.

The prefactors for the diffusion of the Pd, Ga and PdGa clusters on the MgO terrace are explicitly calculated as described in Equation-5.7. However, the prefactor and barriers for the formation and decomposition of the clusters on the MgO terrace and at the F-center are approximately estimated. To explain the approximations, we refer to the case of formation/dissociation of a dimer on the surface as shown schematically in Figure 5.1.The Figure 5.1(a) shows the schematic representation of the formation of the dimer on the surface involving three sites. Initially sites 1 and 3 are occupied by metal adatoms (left panel of Figure 5.1(a)) while site 2 is empty. During the formation one of the atoms move; let us assume that the atom at site 1 diffuses to site 2 to form a dimer with the atom already present at site 3 (right panel of Figure 5.1(a)). Since diffusion of the adatom determines the formation of the dimer in this case, the prefactors to compute the rate of formation are taken to be the same as that for the diffusion process. Similarly for the larger clusters, where the diffusing species can be either adatoms or smaller sized clusters, we consider the prefactor of the diffusing species. The barriers for these processes are also assumed to be the same as those of the diffusion barrier of the diffusing species.

For the cluster dissociation (the dimer in this example), we consider that in the initial state, the dimer occupies sites 1 and 2 while site 3 is empty (left panel of Figure 5.1(b)). During the decomposition process, the atom of the dimer at site 2 detaches and diffuses to site 3. The final state is the dimer dissociated to two monomers; the atoms are occupying sites 1 and 3 (right panel of Figure 5.1(b)). For this case also the prefactors for the rate of dissociation have been assumed to be the same as those of the diffusion. Further the decomposition barrier is assumed to be the sum of the thermodynamic barrier (energy cost to break the bonds between the dimer to form monomers) and the diffusion barrier of the

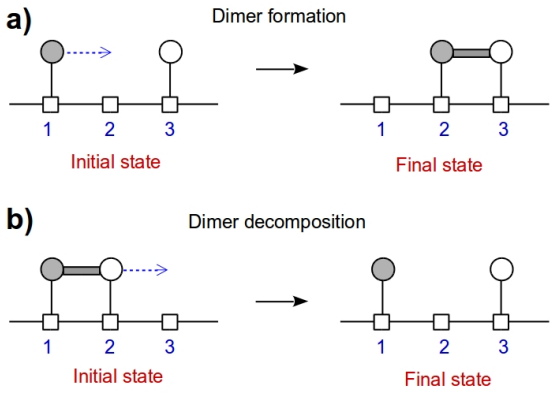

Figure 5.1: Schematic representation of the formation and decomposition of dimer cluster on the surface. The squares represent the adsorption sites present in the surface, and the circles represent the metal atoms.

moving adatom. For the larger clusters, those of the mobile fragment replace the diffusion prefactors and barriers.

5.3 Results and Discussion

5.3.1 Adsorption of small clusters on MgO(100) terrace and F-center

A small amount of neutral oxygen vacancies are present when the oxide surfaces are created. Experiments had shown that these oxygen vacancies act as a nucleation center for the formation of the cluster islands. Hence, studying the structure and energetics of the small clusters adsorbed on MgO terrace and at the vacancy sites are necessary to understand the growth of the small clusters on the oxide surface.

5.3.1.1 Adatoms

To study the stable adsorption geometries for Pd and Ga adatoms on MgO terrace three adsorption sites are considered, top of surface O, top of Mg and the hollow site between two Mg and two O ions. The adatoms are placed directly on top of the vacancy site to study the adsorption at the vacancy site.

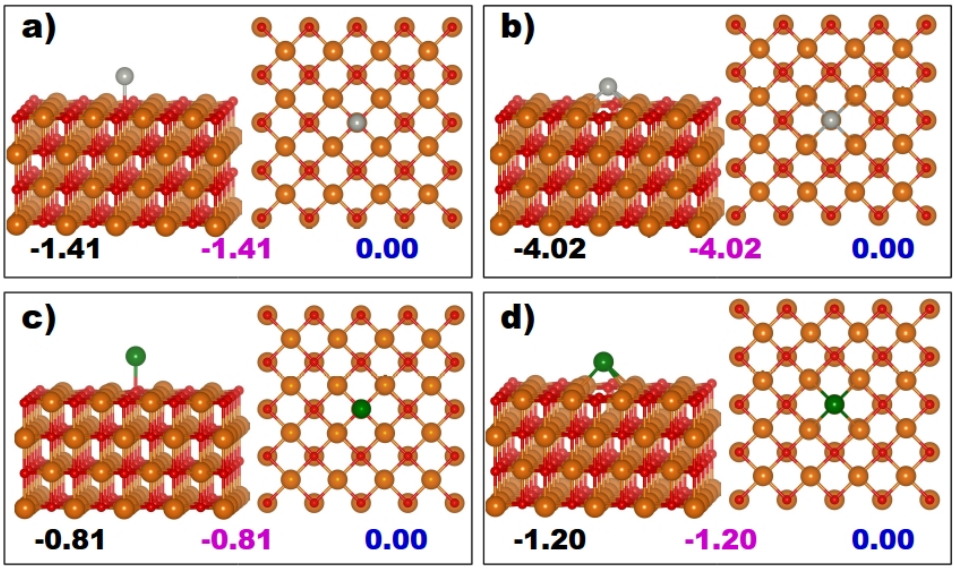

Figure 5.2: a) Pd and c) Ga adatoms adsorbed on MgO (100) terrace. b) Pd and d) Ga adatoms adsorbed at the vacancy site. Pd, Ga, Mg and O are respectively represented by gray, green, orange and red balls. The values given in black, magenta and blue respectively are the E_{ads}, E_{bind} and E_{form} in eV.

Pd: Pd adatom on MgO terrace is the most thoroughly studied system to explore the interaction of metal cluster with oxide surface. The Pd adatom binds on top of the surface O ion with a Pd-O distance of 2.08 Å and adsorption energy of -1.41 eV (Figure 5.2(a)). The electronic ground state for an isolated Pd atom is [Kr]$4d^{10}5s^{0}$, thus non-magnetic. We find that the Pd adatom remains non-magnetic after adsorption on the surface. To understand the chemical interaction between the Pd adatom to the surface we have computed the charge transfer plots that are shown in Figure 5.3(a). We see a charge depletion along the Pd-O bond axis and charge accumulation on the Pd atom. A Bader charge analysis shows a charge transfer of about 0.26 e^{-} from the surface to the Pd adatom. The charge transfer from the surface to the Pd adatom is a robust prediction of the DFT calculations. The literature reports of charge transfer computed using Bader atom-in-molecule analysis for the Pd adatom adsorbed on MgO support varies between 0.15 e^{-} to 0.19 e^{-}, while the same calculated using Mulliken population analysis varies between 0.2 e^{-} to 0.3 e^{-}. [91] Further, the chemical interaction between the surface and the Pd adatom have also been analyzed by the projected density of states(PDOS) and the wavefunction corresponding to the highest occupied molecular orbital (HOMO) and lowest unoccupied molecular orbital (LUMO). As a result of the chemical interaction between the Pd atom to the surface,

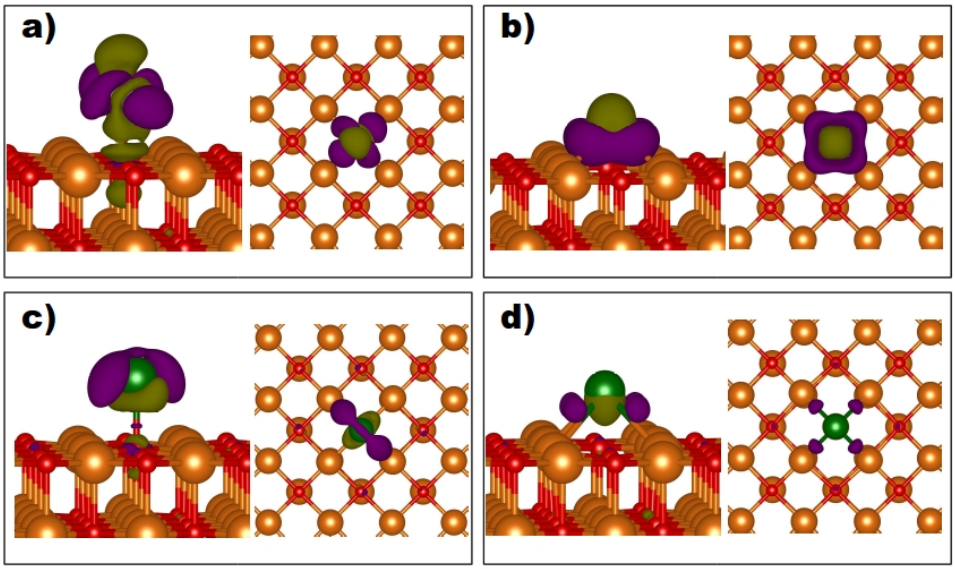

Figure 5.3: Isosurfaces of charge density differences showing the charge transfer from surface to metal adatoms. a) Pd and c) Ga adatoms adsorbed on MgO (100) terrace. b) Pd and d) Ga adatoms adsorbed at the vacancy site. Pd, Ga, Mg and O are respectively represented by gray, green, orange and red balls. Violet and olive lobes respectively represent the charge accumulation and charge depletion. The isovalue used to represent the charge density is 0.03 $e^{-}/Å^{3}$.

there is a stabilization (destabilization) of HOMO (LUMO). The stabilization of HOMO and the destabilization of LUMO is found to be 0.30 eV and 0.70 eV respectively. The HOMO of the system is predominantly localized on the Pd atom showing the features of d_{z^2} orbital with some minor contribution from the surface oxygen atoms, while the LUMO has features of anti-bonding type orbital along the Pd-O bond axis (see Figure-5.4).

In contrast to the clean surface, the binding of Pd adatom to the F-center is much stronger (Figure 5.2(b)) with an adsorption energy of -4.02 eV. The very strong binding of Pd adatom to the vacancy site is attributed to the high amount of charge transfer of 1.91 e^{-} from the vacancy site to the Pd adatom. Figure 5.3(b) shows the isosurfaces of charge density differences for Pd adatom binding to the F-center. We see that the charge is accumulated along the Pd-Mg bond and there is a charge depletion at the Pd and the vacancy site. Similar to the adsorption of Pd adatom on the clean MgO surface, the Pd adatom remains nonmagnetic after adsorption to the neutral oxygen vacancy site. After binding to the F-center, the HOMO is stabilized by about 0.16 eV, and the LUMO is destabilized by about 1.80 eV. In contrast to the binding of Pd adatom to the clean surface for which

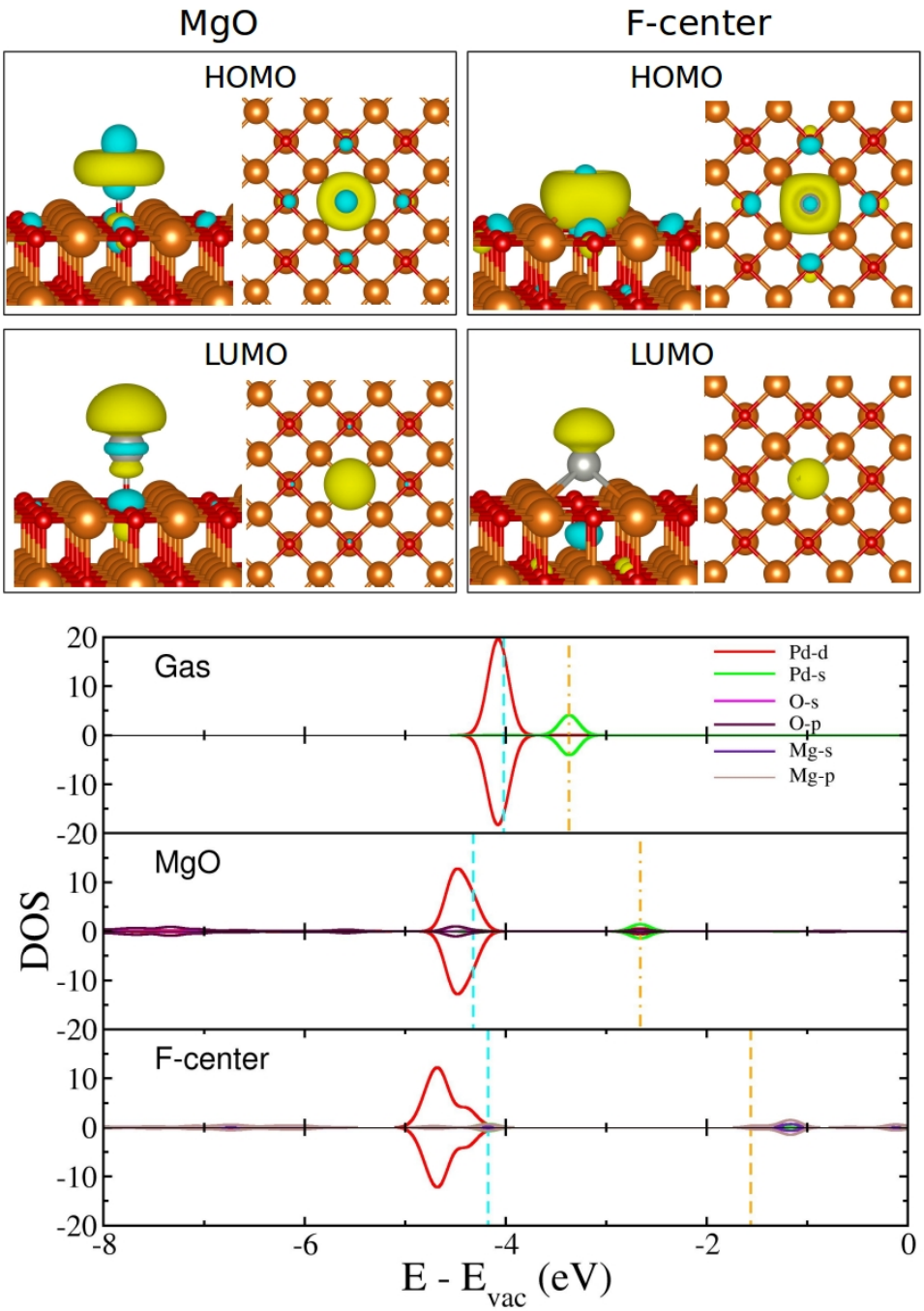

Figure 5.4: The highest occupied molecular orbitals (HOMO) and lowest unoccupied molecular orbitals (LUMO) of Pd adatom adsorbed at the clean MgO surface and the F-center. Yellow and cyan color isosurfaces denote the positive and negative part of the wavefunctions. Pd, Mg and O are represented by gray, orange and red color balls respectively. The density of states projected on the atomic orbitals of the Pd, O and Mg. Cyan and orange color vertical lines are the positions of the HOMO and LUMO respectively. E_{vac} is the electrostatic potential in the vacuum region. The color code of the isosurfaces are the same for all the other figures unless specified.

the HOMO is primarily coming from the Pd d orbital, for the Pd adatom binding to the vacancy site, the d orbitals are more stabilized and the Pd s orbitals are getting occupied. The HOMO has mainly comprised of Pd s orbitals with a very small contribution from the surface oxygen atoms surrounding the vacancy site. However, the LUMO is coming from the Pd atom and the vacancy site (see Figure-5.4). The predicted adsorption geometries and the binding energies for adsorption of Pd adatom to the clean MgO surface and the vacancy site are consistent with the previous reports. [91, 100–104] We note that the binding of Pd at the vacancy site is about -2.61 eV more stable compared to the binding on the terrace, which supports the experimental observations of the vacancy sites acting as the nucleation site for the growth of Pd clusters.

Ga: In the most stable geometry on the MgO terrace the Ga adatom binds on top of the O ion with a Ga-O distance of 2.15 Å (Figure 5.2(c)) and has a binding energy of -0.81 eV. The binding geometry for the Ga adatom on the MgO surface is very similar to that of d-block metals such as Ni, Cu and Pd. [102, 105] However, it has a lower binding energy value compared to that of Pd (-1.41 eV) and Ni (-1.24 eV) and a relatively higher binding energy compared to the binding of Cu adatom (-0.34 eV) on MgO surface. The ground state electronic configuration for an isolated Ga atom is [Ar]$4s^2 4p^1$; thus it has a magnetic moment of 1.00 μ_B. After adsorption, the Ga adatom remains magnetic with a magnetic moment of 1.00 μ_B. The degeneracy between the Ga $4p$ orbitals is removed, both HOMO and LUMO are coming from the same spin channels (down spin). Both HOMO and LUMO are mainly coming from Ga showing the unhybridized p orbital like features (Figure-5.5). The weak binding of Ga adatom to the MgO surface is in accordance with the small amount of charge transfer of 0.11 e^- from the surface to the Ga adatom, and we note that the same is about 0.26 e^- for the case of Pd adatom binding to the MgO surface. Figure 5.3(c) shows the isosurfaces of the charge density differences for the Ga adatom adsorbed to the MgO surface. Similar to the Pd adatom, for the Ga adatom we see that there is charge depletion along the Ga-O bond axis and charge accumulation at the Ga adatom. The Ga adatom binding to the hollow site is slightly less stable by 0.06 eV relative to the most stable site (Figure-C.1 of Appendix C). At the hollow site, Ga-O and Ga-Mg distances are found to be 2.62 and 2.78 Å respectively.

Unlike the Pd adatoms which are strongly bound to the F-center, the Ga adatoms bind to the F-center (Figure 5.2(d)) with an adsorption energy of -1.19 eV. This is about -0.38 eV

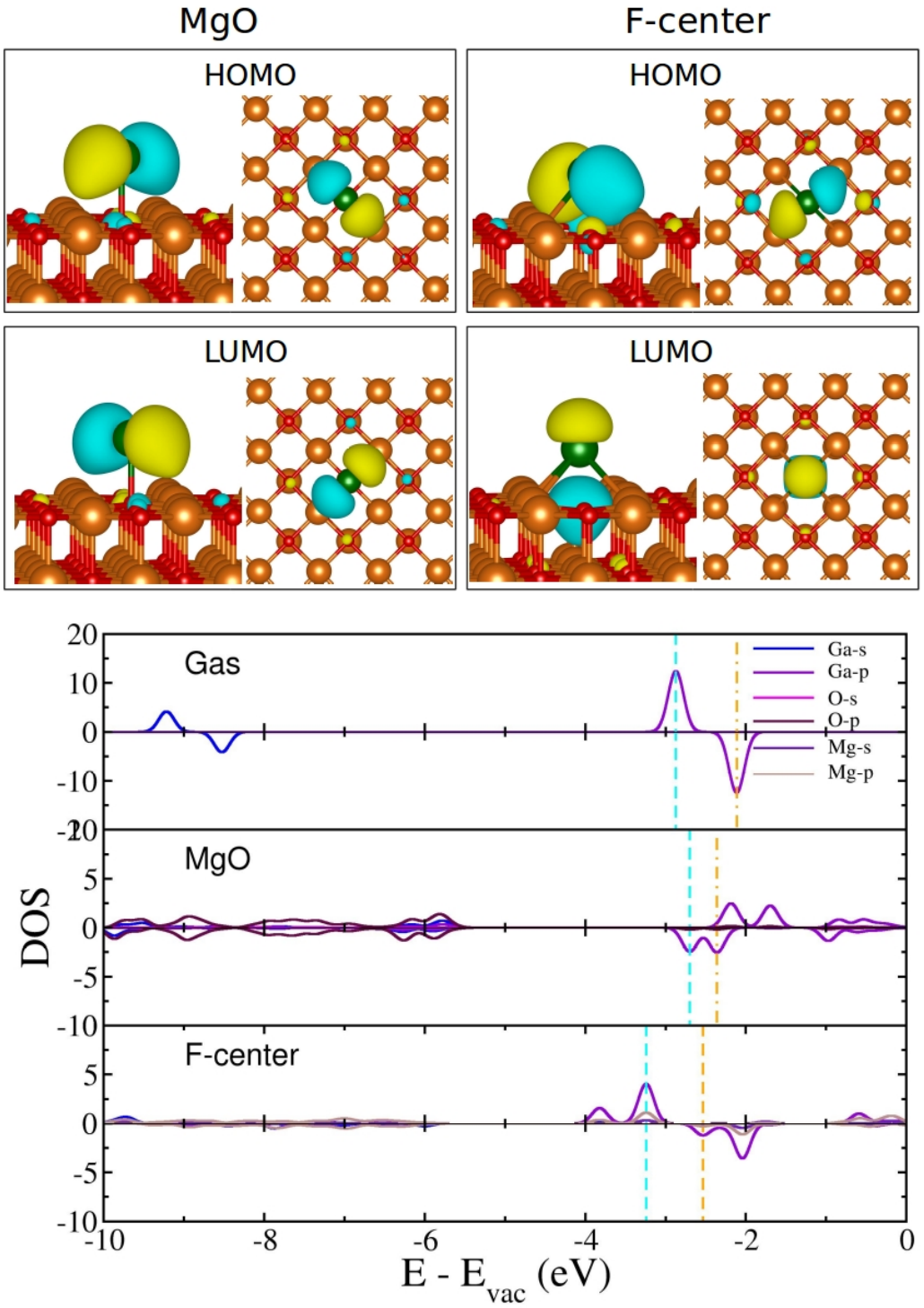

Figure 5.5: The HOMO and LUMO of Ga adatom adsorbed at the clean MgO surface and the F-center. The density of states projected on the atomic orbitals of the Ga, O and Mg. The color code is the same as Figure-5.4.

more stable compared to the Ga adatom binding to the terrace site. Further, unlike the Ga adatom binding to the clean MgO which has retained the gas phase magnetic moment of 1.00 μ_B, the Ga adatom binding at the F-center has a high magnetic moment of 3.00 μ_B. We have also done a calculation by freezing magnetic moment on the Ga atom to be 1.00 μ_B. However, we find that this configuration is about 0.26 eV less stable compared to the configuration with Ga adatom having a magnetic moment of 3.00 μ_B. Analysis of the projected DOS shows that the HOMO and LUMO of the Ga adatom binding to the F-center is coming from different spin channels (HOMO from up spin and LUMO from down spin). Similar to the Pd adatom binding to the F-center, also for Ga adatom binding to the F-center a large amount of charge (about 1.74 e^-) is transferred from the vacancy site to the Ga adatom. A charge accumulation along the Ga-Mg bond and a charge depletion at the Ga atom and the vacancy site is also seen. We do not find any direct correlation between the charge transfer and the adsorption energy if we consider both the adatoms binding to the clean MgO and to the F-center together. However, considering only the adatoms binding to the clean MgO surface, we see a direct correlation between the adsorption energy to the amount of charge transfer. The adsorption energy increases with increasing the amount of charge transfer from the surface to the metal adatom. Similarly, a direct correlation is seen between the charge transfer to the adsorption energy for the adatoms binding to the F-center.

Based on the adsorption energies we envisage that the Pd adatoms are strongly trapped at the vacancy site, and these sites act as the nucleation site for the growth of Pd clusters, in contrast to Pd adatoms which are strongly bound to the vacancy sites, the Ga adatoms are weakly bound at the vacancy site. The vacancy site may act as the nucleation site for the growth of Ga clusters due to the slightly more thermodynamic stability (about -0.38 eV). However, the nucleation processes will strongly depend on the diffusion barrier on the terrace and escape barriers from the vacancy sites.

5.3.1.2 Dimers

We have three possible compositions for the dimers, namely Pd_2, Ga_2 and Pd_1Ga_1. These are formed by adding one Pd or Ga adatom to the Pd or Ga adatom already adsorbed on the terrace and vacancy site. From the previous section, we find that the favorable adsorption site for the metal atoms is the O site and the hollow site. Hence, to study the

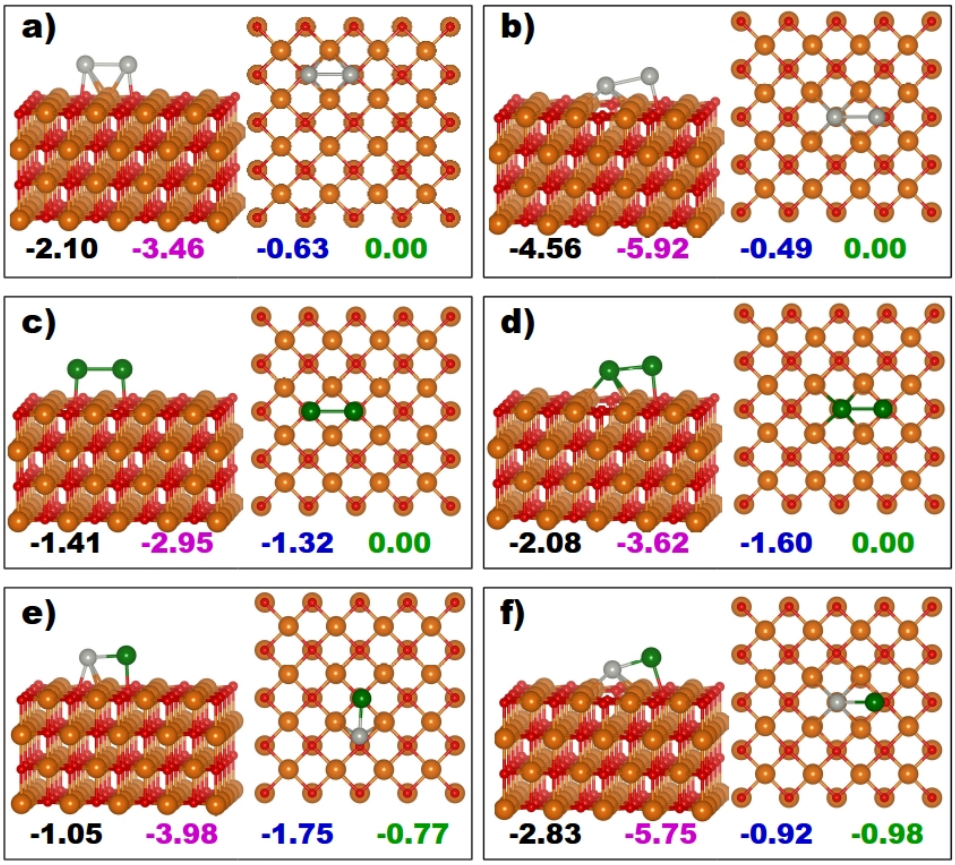

Figure 5.6: a)Pd_2, c)Ga_2 and e)Pd_1Ga_1 clusters adsorbed on MgO(100) terrace. b)Pd_2, d)Ga_2 and f)Pd_1Ga_1 clusters adsorbed at the vacancy site. Pd, Ga, Mg and O are represented by gray, green, orange and red balls respectively. The values given in black, magenta, blue and green respectively are the E_{ads}, E_{bind}, E_{form} and E_{mix} in eV.

stable adsorption sites for the dimers on the MgO terrace, they are placed on the surface such that at least one atom is on any one of these sites. In the case of vacancy site, one Pd or Ga adatom is added to the Pd or Ga adatom already adsorbed at the vacancy site. We have considered both horizontal and vertical orientations of the dimers on the surface.

Pd_2: On MgO terrace, Pd dimer binds in a horizontal geometry on top of two neighboring surface O (Figure 5.6(a)). The adsorption energy calculated with respect to the most stable gas phase geometry is found to be -2.10 eV. Moreover, the binding energy of Pd_2 on MgO terrace is calculated to be -3.46 eV, which is in good agreement with the previous report of -3.28 eV. [91] The Pd_2 is magnetic in the isolated gas phase and has a magnetic moment of 2.00 μ_B. [98] The Pd_2 adsorbed to the MgO surface is also magnetic with a magnetic

moment of 2.00 μ_B. The Pd-Pd and Pd-O distances for the Pd_2 binding to the MgO surface are found to be 2.59 Å and 2.19 Å respectively. Using PW91 functional, with non-spin polarized DFT calculations Xu *et al.* [91] has predicted a Pd-Pd and Pd-O distance of 2.81 Å and 2.12 Å for the dimer cluster adsorbed to the MgO surface. In order to understand the deviation in the predicted Pd-Pd and Pd-O bond distances we have calculated the energy of the Pd_2 in the singlet electronic state, and we find exactly the same bond distances as reported by Xu *et al.* However, we find that this non-magnetic structure is about 0.16 eV less stable than the most stable magnetic structure. As a result of the cluster surface interaction, the Pd-Pd bond is weakened, which is seen from the increase in the Pd-Pd bond length from the gas phase value of 2.40 Å. The formation energy of Pd_2 is found to be -0.63 eV. Bader charge analysis shows a net charge transfer of 0.39 e^- from the surface to the Pd_2. This is slightly overestimated compared to the value of 0.30 e^- reported by Xu et al. [91] Figure 5.7(a) shows the charge density isosurfaces of charge differences for the Pd_2 adsorbed at the MgO surface. Similar to the Pd adatom adsorbed on the MgO surface, for the Pd_2 cluster, there is charge depletion along the Pd-O bond axis and charge accumulation at the Pd atoms. For the gas phase Pd_2, both HOMO and LUMO are coming from the same spin channel. While for the Pd_2 adsorbed at the MgO surface, the HOMO and LUMO are coming from two different spin channels. The HOMO is coming from the up spin channel. The majority of the HOMO is located at the Pd-Pd bond and shows features like the bonding orbital. Meanwhile, the wavefunction corresponding to LUMO, that is coming from down spin channel is primarily localized on the Pd atoms and has an anti-bonding character (Figure-5.8). The anti-bonding type LUMO, suggesting that adding more electronic charge to the Pd_2 will weaken the Pd-Pd bond. The other stable structures of Pd_2 adsorbed at the clean MgO surface are given in Figure-C.2 of Appendix C.

Similar to the terrace site, at the vacancy site also the Pd dimer binds in a horizontal geometry. In this geometry, one of the Pd atoms is binding to the F-center while the other Pd binds on top of the neighboring O site with a Pd-Pd distance of 2.72 Å (Figure 5.6(b)). In contrast to the adsorption of Pd_2 at the clean MgO, the Pd_2 in the most stable geometry at the F-center is found to be nonmagnetic. We have also calculated the energy of the cluster by restricting the magnetic moment on the Pd_2 to be 2.00 μ_B. However, this structure is about 0.40 eV less stable compared to the most stable non-magnetic structure. Bader charge analysis shows about 2.12 e^- net charge transfer from the surface to the

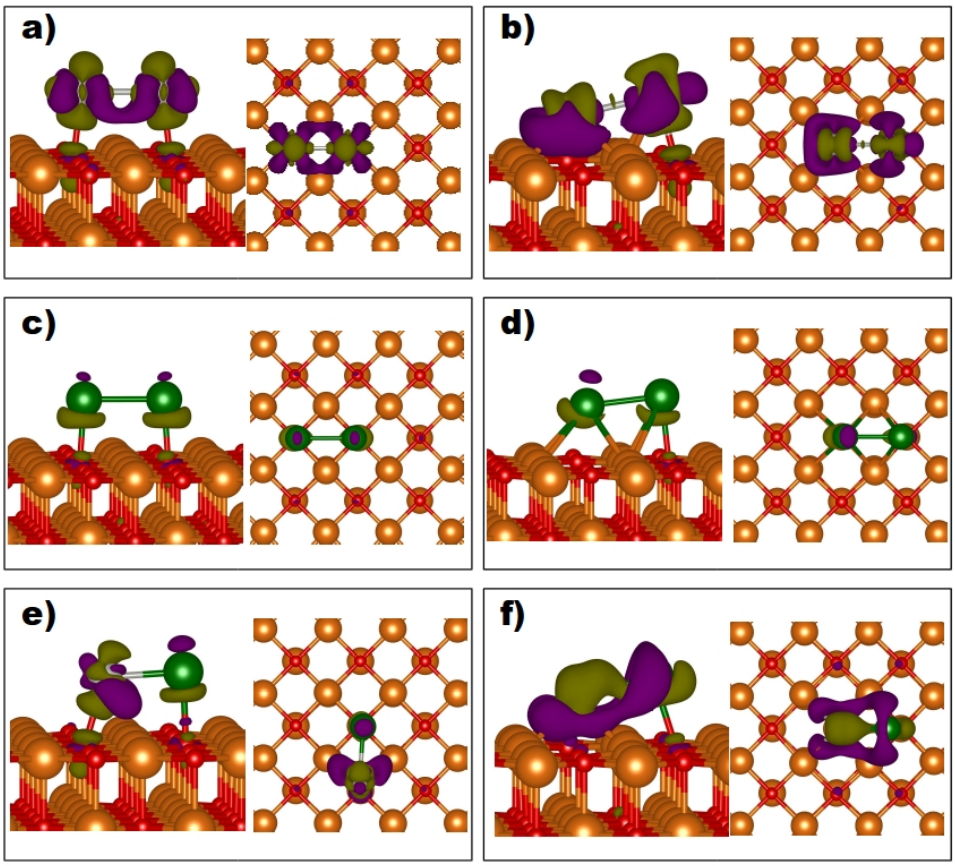

Figure 5.7: Isosurfaces of charge density differences showing the charge transfer from surface to dimer clusters. a) Pd_2, c) Ga_2 and e)Pd_1Ga_1 clusters adsorbed on MgO (100) terrace. b) Pd_2, d) Ga_2 and f)Pd_1Ga_1 clusters adsorbed at the vacancy site. The color code and the isovalue are same as Figure 5.3.

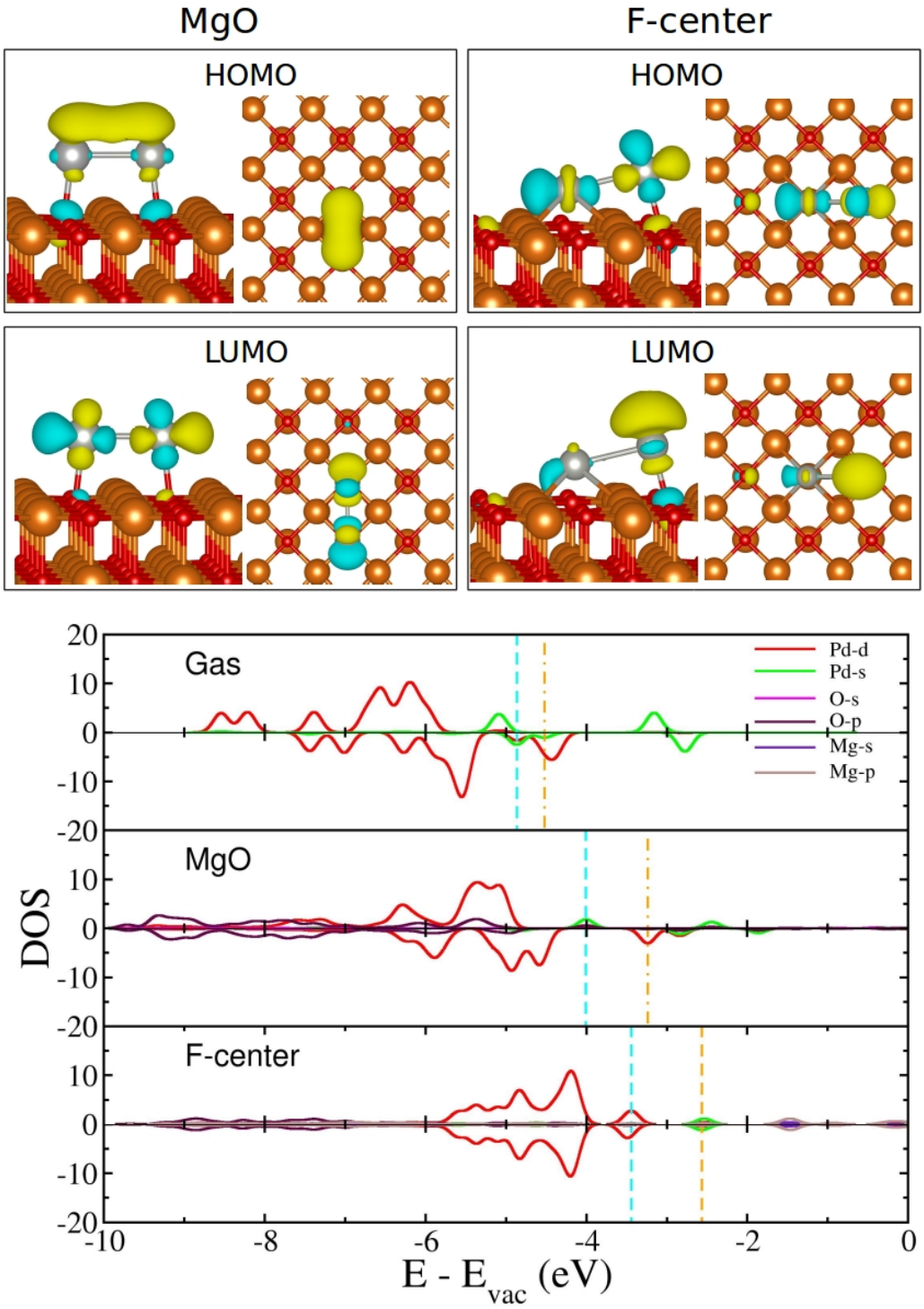

Figure 5.8: The HOMO and LUMO of Pd_2 adsorbed at the clean MgO surface and the F-center. The density of states projected on the atomic orbitals of the Pd_2. The color code is the same as Figure-5.4.

Pd_2. Unlike clean MgO surface, the charge transfer is non-symmetric with respect to the Pd atoms. The Pd atom binding to the vacancy site gains a charge of 1.75 e^- while the Pd atom binding to the O site gains only about 0.37 e^-. Figure 5.7(b) shows the isosurfaces of the charge density differences for the Pd_2 binding at the F-center. The majority of the HOMO is found on both of the Pd atoms and showing features like anti-bonding type orbitals while the majority of the LUMO is localized on the Pd atom binding on top of the oxygen site with a small contribution from the Pd atom binding to the vacancy site (see Figure-5.8). The adsorption, binding and formation energies for the Pd_2 cluster at the F-center is found to be -4.56 eV, -5.92 eV and -0.49 eV respectively. The calculated energetics suggest that the formation of Pd dimer on the MgO terrace is slightly (about -0.14 eV) thermodynamically more stable than the formation of Pd dimer at the vacancy site. However, the low values of the formation energy of the Pd dimer on the MgO terrace and the vacancy site suggest that the dimer clusters will dissociate into adatom at the elevated temperature, which is in good agreement with the kinetic Monte Carlo predictions by the Xu *et al.* [106] The other stable structures of Pd_2 adsorbed at the F-center are given in Figure-C.2 of Appendix C.

Ga_2: The most stable adsorption geometry for the Ga dimer on MgO terrace is similar to that found for the Pd_2 on MgO. The two Ga atoms are sitting on top of two adjacent O sites with Ga-Ga and Ga-O distance of 2.72 and 2.22 Å respectively (Figure 5.6(c)). Similar to Pd dimer, also for the Ga_2 the Ga-Ga bond distance increase from 2.44 Å in the gas phase to 2.72 Å on the MgO support. The Ga_2 binding to the MgO surface has a magnetic moment of 2.00 μ_B, which is same as the magnetic moment on the gas phase Ga_2. [98] Bader charge analysis shows a net charge transfer of 0.18 e^- from the surface to the Ga_2 (each of the Ga atoms gain 0.09 e^-). Figure 5.7(c) shows the charge density difference isosurfaces for the Ga_2 adsorbed at the clean MgO surface. Similar to the Pd_2 adsorbed at the MgO surface, there is a depletion along the Ga-O bond axis and a charge accumulation on the Ga atoms. The HOMO is coming from the down spin channel, and the LUMO is coming from the up spin channel. Both HOMO and LUMO are primarily located along the Ga-Ga bond showing a bonding orbital like features (Figure-5.9) suggesting that adding more electron to the Ga_2 cluster will strengthen the Ga-Ga bond. The adsorption, binding and formation energies for this geometry are found to be -1.41 eV, -2.95 eV and -1.32 eV respectively. We note that the formation energy of the Ga_2 (-1.32 eV) is much higher compared to the Pd_2 (-0.63 eV). The high value of formation energy

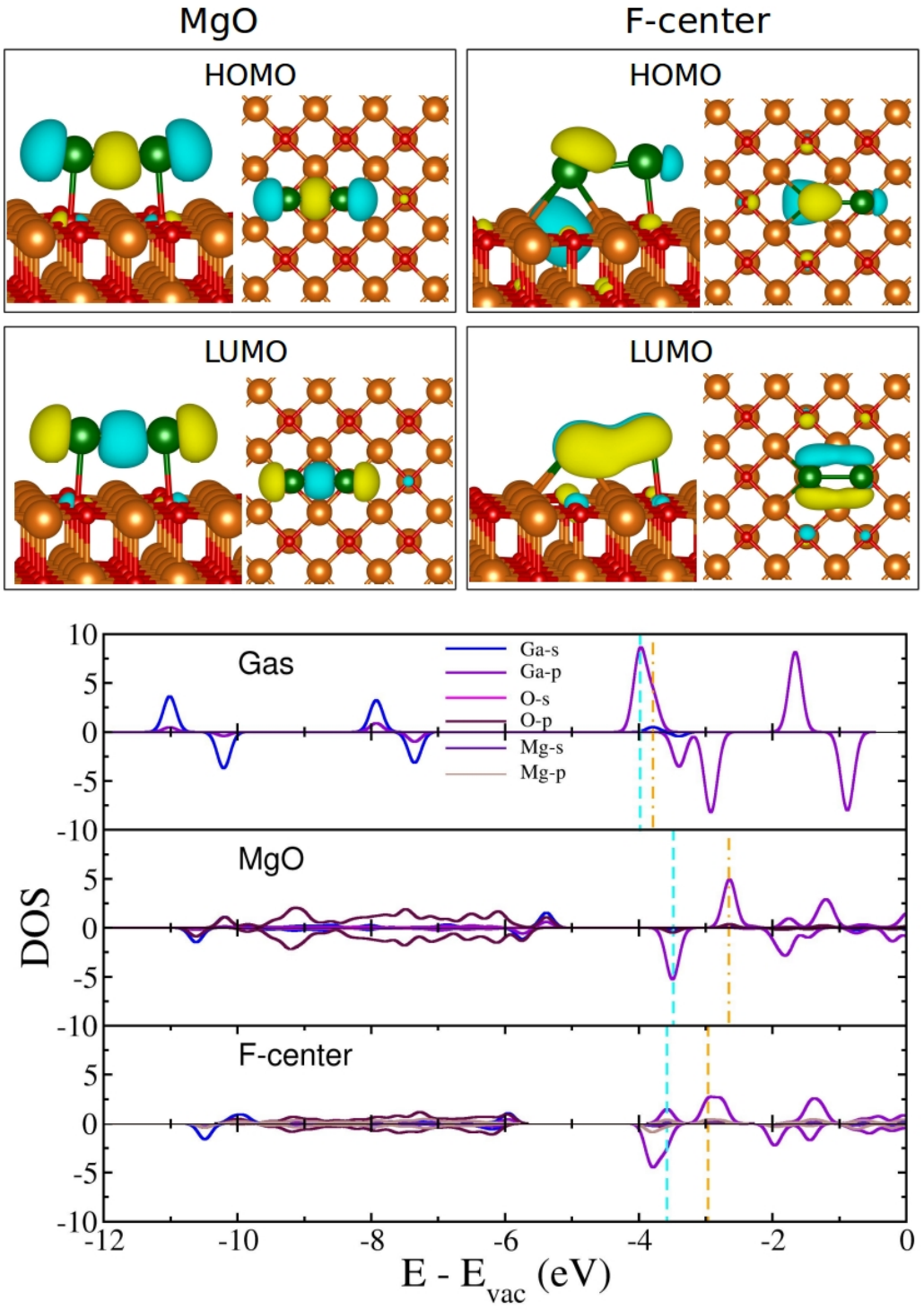

Figure 5.9: The HOMO and LUMO of Ga_2 adsorbed at the clean MgO surface and the F-center. The density of states projected on the atomic orbitals of the Ga_2. The color code is the same as Figure-5.4.

for the Ga_2 suggest that the Ga-Ga interaction is stronger than Pd-Pd interaction. The strong Ga-Ga bond suggests that the dissociation of Ga_2 on the MgO terrace will take place at a relatively high temperature than the Pd_2 dissociation on the MgO terrace. In the second most stable structure, two Ga atoms are adsorbed on two neighboring hollow sites with a Ga-Ga bond distance of 2.96 Å. This structure is about 0.44 eV less stable than the most stable structure. The other stable structures for the Ga_2 on the MgO surface are given in Figure-C.3 of Appendix C.

The structure for the Ga_2 cluster binding to the defect site (Figure 5.6(d)) is the same as the structure of Pd_2 cluster at the defect site. The Ga_2 binding to the F-center has a magnetic moment of 2.00 μ_B. Bader charge analysis shows a net charge transfer of 1.68 e^- from the surface to the Ga_2 cluster. However, the Ga atom sitting on top of the vacancy site has a charge gain of 1.66 e^- while the Ga binding to the O site has only a very small charge gain of 0.02 e^-. Figure 5.7(d) shows the isosurfaces of the charge density differences for the Ga_2 binding to the F-center. Unlike Ga_2 binding to the clean MgO for which the HOMO and LUMO are coming from different spin channels, for Ga_2 binding to the F-center both HOMO and LUMO are coming from up spin channel only (Figure-5.9). The majority of the HOMO is located at the Ga atom sitting on top of the vacancy site while the majority of the LUMO is located along the Ga-Ga bond showing features like lateral π type bonding orbital. The Ga-Ga bond length, adsorption energy, binding energy and formation energy of the Ga_2 at the F-center is found to be 2.61 Å, -2.08 eV, -3.62 eV and -1.60 eV respectively. We note that in contrast to the formation of the Pd dimers that are thermodynamically more favorable at the terrace sites compared to the vacancy site, the formation of Ga dimers is thermodynamically more favorable at the vacancy site. However, the thermodynamic energy difference between a Ga dimer on the MgO terrace site to the vacancy site is about -0.67 eV, suggesting that the Ga dimers are also weakly bound to the vacancy site and might escape from the vacancy site before they dissociate. For other stable structures of Ga dimer at the F-center see Figure-C.3 of Appendix C.

Pd_1Ga_1: In its most stable geometry both Pd and Ga atoms are sitting on top of two neighboring surface O site with Pd-O and Ga-O distance of 2.29 and 2.26 Å respectively, where the Pd is pulled towards the Ga atom by adjusting its position (Figure 5.6(e)). Igor *et al.* also reported a similar geometry for the adsorption of Pd_1Ru_1, Pd_1Rh_1 and Pd_1Ir_1 dimers on the MgO(100) surface. [107] Similar to the pure Pd and Ga dimers, as a re-

sult of cluster-substrate interaction the Pd-Ga bond length is increased to 2.39 Å, from the gas phase value of 2.29 Å. The Pd_1Ga_1 cluster has a magnetic moment of 1.00 μ_B in the isolated gas phase. [98] We find that Pd_1Ga_1 adsorbed on the clean MgO surface also has the same value of the magnetic moment. Bader charge analysis shows a net charge transfer of about 0.29 e^- from the surface to the Pd_1Ga_1 cluster. However, the Pd atom is gaining about 0.24 e^- while the Ga atom is gaining about 0.05 e^-. We note that the charge transfer to the Pd atom is larger than that of Ga atoms, which is consistent with the charge transfer for the parent clusters. Figure 5.7(e) shows the isosurfaces of charge density differences for the Pd_1Ga_1 cluster adsorbed on the clean MgO surface. Similar to the other dimers for Pd_1Ga_1 there is charge depletion along the metal-oxygen bond. However, in contrast to the other dimers for Pd_1Ga_1 there is a charge accumulation between the Pd and the surface Mg suggesting that there is new bond formation between the Pd and Mg. The Pd atom slightly moved towards Ga due to this bonding of Pd with Mg. Further analysis shows that the majority of the HOMO and LUMO are located at both Pd and Ga atoms showing features like anti-bonding type orbitals. While the HOMO is coming from down spin channel, the LUMO is coming from the up spin channel (Figure-5.10). The adsorption, binding and formation energies of Pd_1Ga_1 corresponding to this most stable structure are calculated to be -1.05 eV, -3.98 eV and -1.75 eV respectively. A high value of the formation energy suggests that the dissociation of Pd_1Ga_1 will occur at high temperature compared to the pure dimer clusters. The high formation energy is attributed to the strong hybridization between the Pd-s and Ga-p states. [98] A negative value of E_{mix} calculated using Equation-5.4 for Pd_1Ga_1 (about -0.77 eV), suggests that the formation of a mixed dimer is thermodynamically more stable than the formation of the Pd and Ga dimers on the MgO terrace. Other metastable structures are presented in Figure-C.4 of Appendix C.

In the most stable geometry of Pd_1Ga_1 cluster at the F-center, the Pd atom sits on the F-center, and the Ga atom is binding to the neighboring O site with a Pd-Ga distance of 2.47 Å (Figure 5.6(f)). Similar to the clean MgO surface, the Pd_1Ga_1 cluster binding at the F-center also has a magnetic moment of 1.00 μ_B. Bader charge analysis shows a net charge transfer of 1.97 e^- from the surface to the Pd_1Ga_1 cluster. However, the Pd atom sitting on top of the oxygen vacancy has a high charge gain of 1.57 e^- and the Ga atom sitting on top of the O site has a charge gain of 0.40 e^-. The charge density differences presented in Figure 5.7(f) show the charge depletion along the Pd-Ga σ bond axis and charge accumu-

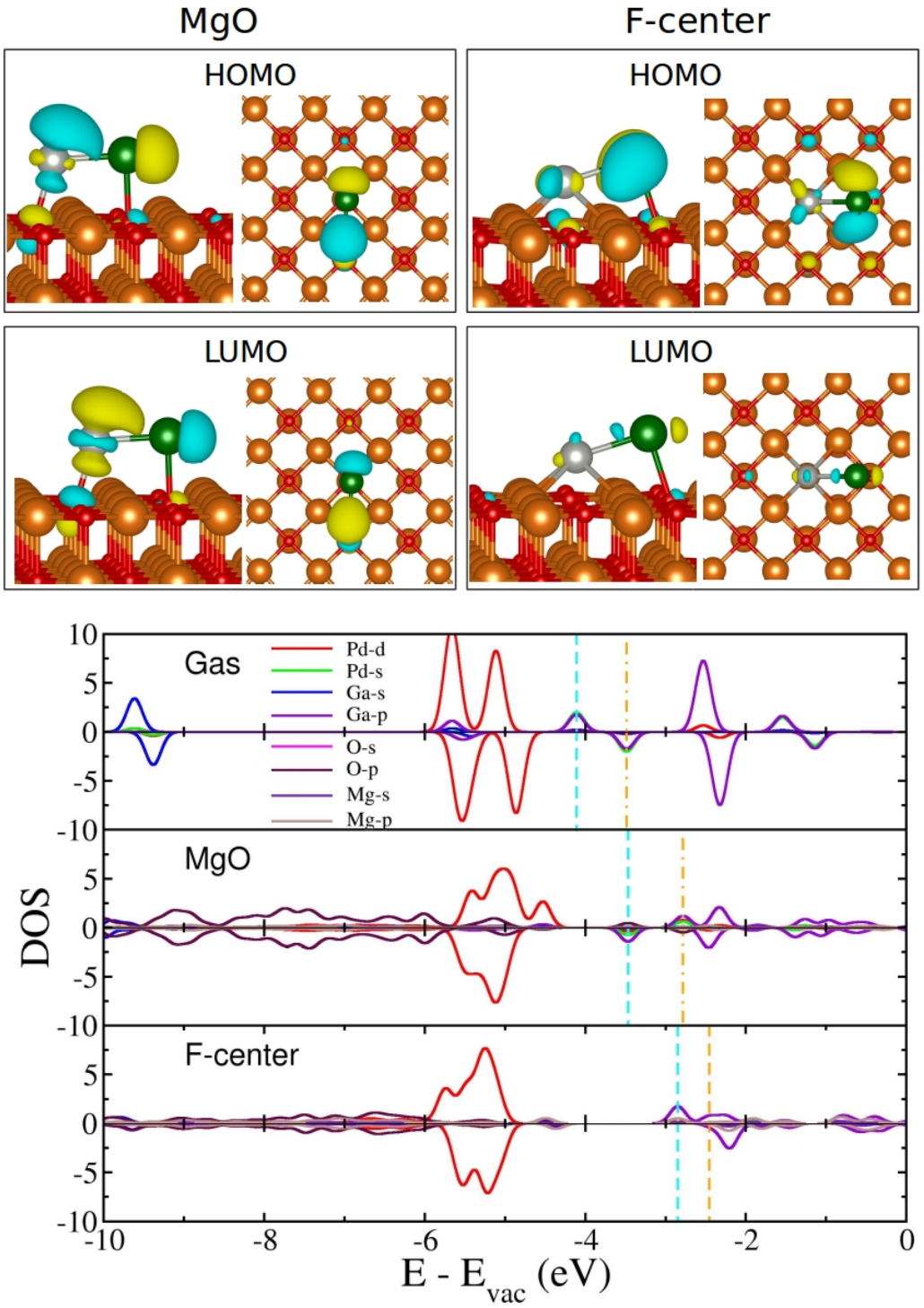

Figure 5.10: The HOMO and LUMO of Pd_1Ga_1 adsorbed at the clean MgO surface and the F-center. The density of states projected on the atomic orbitals of the Pd_1Ga_1. The color code is the same as Figure-5.4.

lation at the Pd and Mg atoms surrounding the vacancy site. Additionally, there is some charge accumulation around Pd-Ga like lateral π bonding. Both HOMO and LUMO are coming from up spin channel (Figure-5.10). The majority of the HOMO is located on the Ga atom showing unhybridized p orbital like features, while the LUMO is located on both Pd and Ga atoms. The adsorption, binding and formation energies for Pd_1Ga_1 at the vacancy site are found to be -2.83 eV, -5.75 eV and -0.91 eV respectively. The relatively low value of the formation energy at the vacancy site is attributed to the binding geometry. At the terrace, in addition to the Pd-O bonding interaction, the $4d$ orbital of Pd interact with the $2s$ orbital of surface Mg. Due to this additional bonding interaction, the Pd atom is slightly pulled towards the hollow site. Hence, the formation energy is large at the terrace. However, the Ga atom binding to the surface O has no suitable orbitals to make bonding interaction with the surface Mg. Hence, when the Pd atom is strongly bound to the vacancy site, and the Ga atom is moving towards Pd there is no bond formation between Ga and Mg atoms. Hence, the formation energy is low for the formation of Pd_1Ga_1 at the F-center. This is also reflected in their increased bond distances compared to the binding on the terrace. Other stable structures for the Pd_1Ga_1 cluster binding to the F-center are given in Figure-C.4 of Appendix C.

5.3.1.3 Trimers

A trimer was formed by adding one Pd or Ga atom to the dimer clusters. Depending on the type of atom added and the existing dimer, we have four possible compositions for the trimer clusters, namely Pd_3, Ga_3, Pd_1Ga_2 and Pd_2Ga_1. Similar to dimers, both horizontal and vertical orientations are considered to study the adsorption of trimers on MgO terrace and at the F-center.

Pd_3: Pd trimer binds to the MgO terrace in a triangular geometry, in which two of the Pd atoms binding with the surface oxygen with the O-Pd distance of 2.19 Å and the third Pd is about 4.42 Å away from the surface (Figure 5.11(a)). After the trimer binds to the surface, the Pd-Pd bond length of the atoms interacting with the surface increases from the gas phase value of 2.49 Å to 2.60Å. The magnetic moment on the isolated gas phase Pd_3 cluster is 2.00 μ_B. [98] The Pd_3 binding to the MgO surface also has a magnetic moment of 2.00 μ_B. Bader charge analysis shows a net charge transfer of about 0.40 e^- from the surface to the Pd_3 cluster. However, the charge transfer to the Pd atoms interacting with the

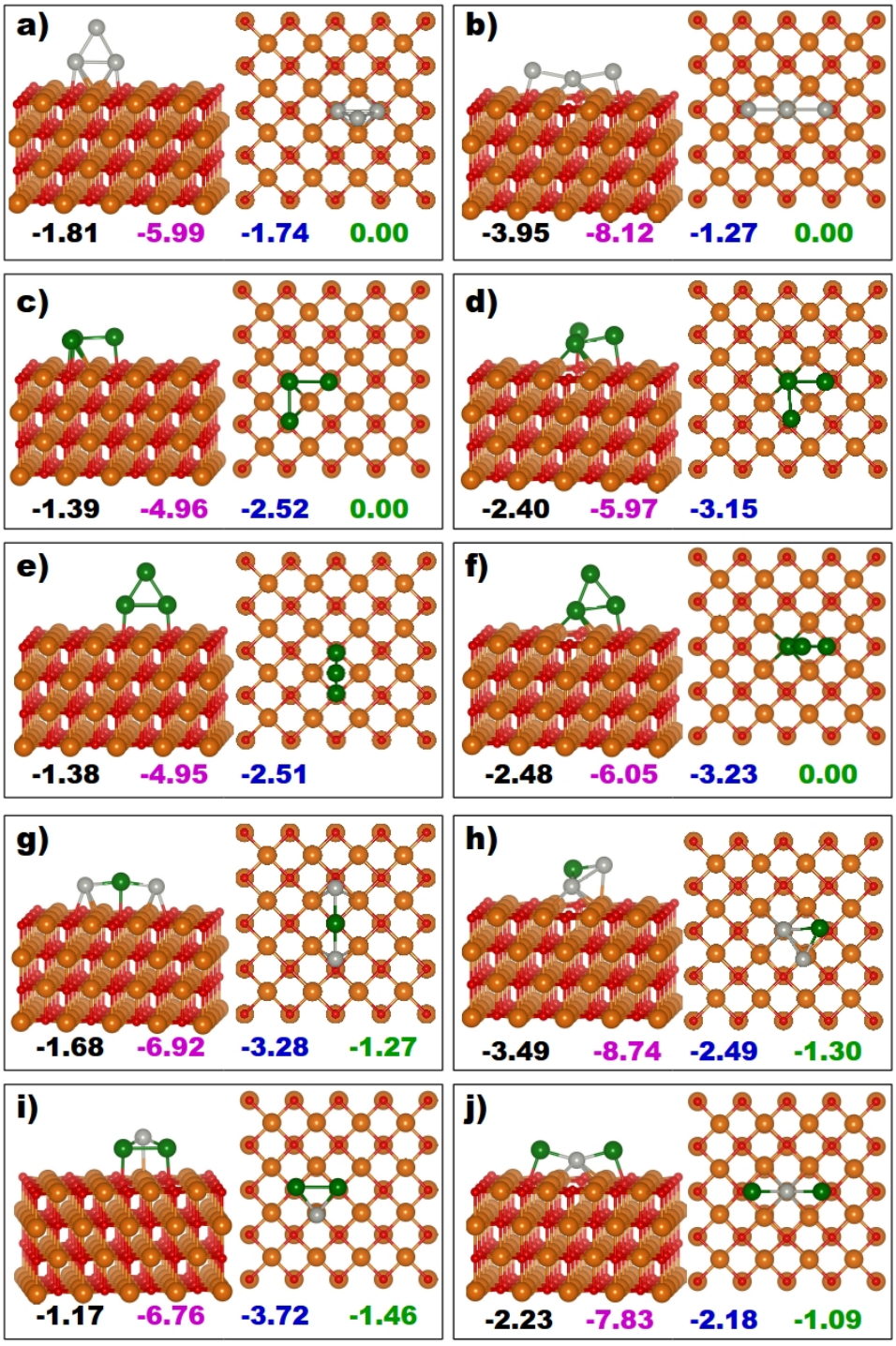

Figure 5.11: a)Pd_3, c)Ga_3(I), e)Ga_3(II), g)Pd_2Ga_1 and i)Pd_1Ga_2 clusters adsorbed on MgO(100) terrace. b)Pd_3, d)Ga_3(I), f)Ga_3(II), h)Pd_2Ga_1 and j)Pd_1Ga_2 clusters adsorbed at the vacancy site. The color code is same as Figure 5.6.

surface oxygen sites are about 0.11 e^- and to the top Pd is about 0.18 e^-. Figure 5.12(a) shows the isosurfaces of charge density differences for the Pd_3 binding to the clean MgO surface. Both HOMO and LUMO of Pd_3 adsorbed at the MgO surface are coming from down spin channel (Figure-5.13). The HOMO is localized at the two Pd atoms interacting with the surface oxygen site showing an anti-bonding like features, while the majority of the LUMO is located at the top Pd atom with some small contribution from the other Pd atoms. The binding energy of Pd trimer on the MgO terrace is calculated to be -5.99 eV, which is in good agreement with the reported value of -5.72 eV. [91] The adsorption and formation energies for Pd trimer are calculated to be -1.81 eV and -1.74 eV respectively. Other stable structures of Pd_3 adsorbed at the clean MgO surface are given in Figure-C.5 of Appendix C.

A linear structure is found to be the most stable structure for the Pd trimer at the vacancy site, in which the central Pd sits on the vacancy site and the other two Pd atoms sit on top of the O sites on either sides of the vacancy (Figure 5.11(b)) with a Pd-Pd bond distance of 2.64 Å. In contrast to the Pd_3 adsorbed at the clean MgO surface, the Pd_3 binding at the F-center is found to be nonmagnetic. A Bader charge analysis shows about 2.32 e^- net charge transfer from the surface to the Pd_3 cluster. The Pd atom sitting on top of the vacancy site gains a charge of about 1.42 e^-, while each of the Pd atoms sitting on top of O sites gain a charge of 0.45 e^-. Figure 5.12(b) shows the isosurfaces of charge density differences for the Pd_3 binding to the F-center. The HOMO is located on all three Pd atoms while the LUMO is localized only on the Pd atoms sitting on top of the O site (Figure-5.13). The calculated binding energy of -8.12 eV for the Pd_3 cluster at the F-center is in good agreement with the reported value of -8.08 eV. [91] The adsorption and formation energies of Pd_3 cluster at the F-center is calculated to be -3.95 eV and -1.27 eV respectively. The low formation energy is due to the structural deformation. The other stable geometries for Pd_3 cluster adsorbed at the F-center are given in Figure-C.5 of Appendix C.

Ga_3: For Ga trimer on the terrace, we find two different structures which are energetically similar. We note that also in gas phase the Ga trimer has two different stable structures namely, equilateral triangle (spin doublet) and an isosceles triangle (spin quartet). [98] In the first structure, here onwards mentioned as Ga_3(I), the Ga_3 binds horizontally on MgO terrace in a "L" shaped geometry, in which all the three Ga adatoms are sitting on top of three neighboring O sites (Figure 5.11(c)). This structure is symmetric with respect to the

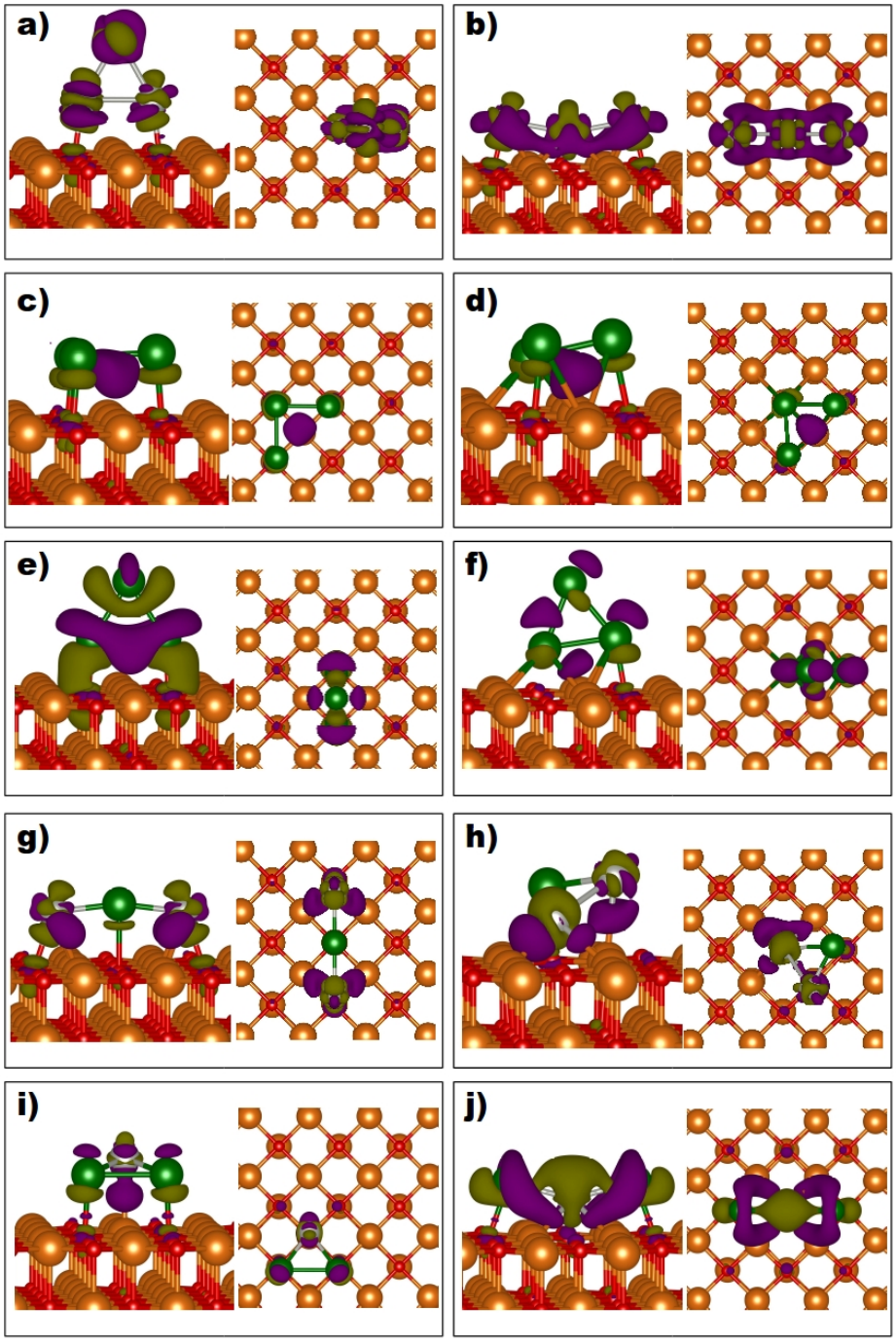

Figure 5.12: Isosurfaces of charge density differences showing the charge transfer from surface to trimer clusters. a)Pd_3, c)Ga_3(I), e)Ga_3(II), g)Pd_2Ga_1 and i)Pd_1Ga_2 clusters adsorbed on MgO(100) terrace. b)Pd_3, d)Ga_3(I), f)Ga_3(II), h)Pd_2Ga_1 and j)Pd_1Ga_2 clusters adsorbed at the vacancy site. The color code and the isovalue are same as Figure 5.3.

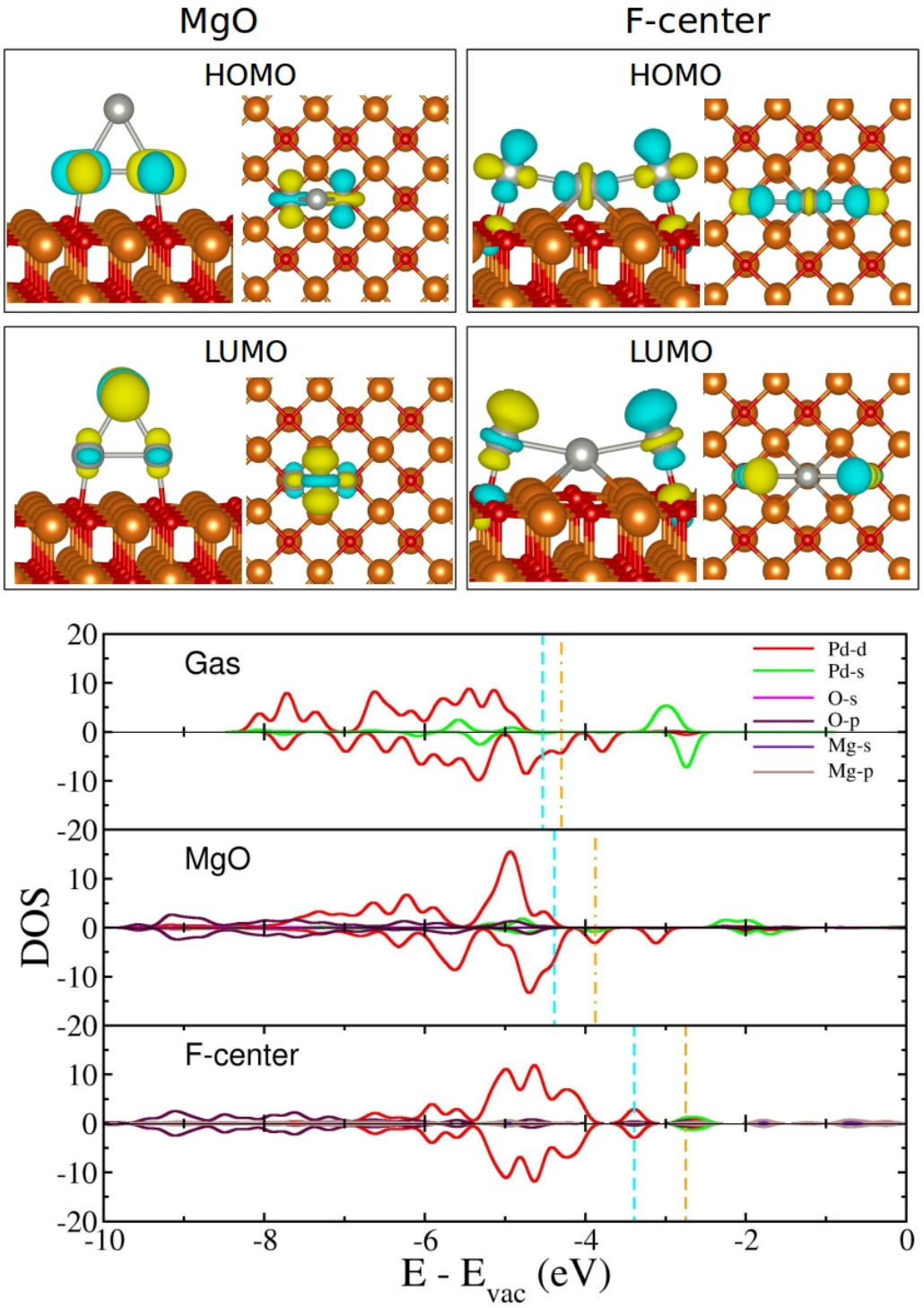

Figure 5.13: The HOMO and LUMO of Pd_3 adsorbed at the clean MgO surface and the F-center. The density of states projected on the atomic orbitals of the Pd_3. The color code is the same as Figure-5.4.

central Ga atom, and each of the Ga-Ga bond lengths is about 2.66 Å. The Ga-Ga bond length in this structure is slightly larger than that of the gas phase bond length of 2.58 Å (isosceles triangular structure). [98] The O-Ga bond for the center Ga is 2.22 Å, which is slightly smaller compared to the other O-Ga bond(2.29 Å). The Ga_3(I) adsorbed on the MgO terrace has a magnetic moment of 1.00 μ_B. A Bader charge analysis shows a net charge transfer of 0.24 e^- from the surface to the Ga_3(I). Among the three Ga atoms, the central one has a charge gain of 0.06 e^- while each of the other two Ga atoms has a charge gain of 0.09 e^-. Figure 5.12(c) shows the isosurfaces of the charge density differences for the Ga_3(I) adsorbed on the MgO terrace. We find a charge depletion at the Ga-O bond similar to the dimer, while the charge accumulation is found at the center of three Ga atoms. Both HOMO and LUMO are coming from up spin channel (Figure-5.14). Further analysis of the wavefunctions corresponding HOMO shows that the HOMO is spread over all the Ga atoms and also shows features of bonding type orbital. Similar to the HOMO, the LUMO is also spread over all three Ga atoms, however showing features like anti-bonding type orbital suggesting that adding more electron to the cluster will weaken the Ga-Ga bond. The adsorption, binding and formation energies for this structure are found to be -1.39, -4.96 and -2.52 eV respectively.

In the second structure, here onwards mentioned as Ga_3(II), the isosceles triangular Ga_3 horizontally binds on the MgO terrace (Figure 5.11(i)). The binding energy obtained for this structure (-4.95 eV) is almost the same as the first structure. In this structure, only two Ga atoms are bound with the surface with a Ga-O distance of 2.13 Å and Ga-Ga distance of 2.71 Å. The third Ga is about 4.24 Å vertically away from the surface, and the Ga-Ga distances are found to be 2.51 Å. Similar to Ga_3(I), the Ga_3(II) adsorbed on the MgO terrace also has a magnetic moment of 1.00 μ_B. However, Bader charge analysis of Ga_3(II) adsorbed on the MgO terrace shows net charge transfer of 0.21 e^- from the surface to the Ga_3(II). This value is slightly lower compared to the value of 0.24 e^- for the adsorption of Ga_3(I) on MgO terrace. The charge gain on the Ga atoms interacting to the surface is about 0.16 e^- while third Ga loses about 0.11 e^-. Figure 5.12(e) shows the isosurfaces of the charge density differences for the Ga_3(II) adsorbed on the MgO terrace. Similar to Ga_3(I), also for Ga_3(II) adsorbed on the MgO terrace, both HOMO and LUMO are coming from up spin channel (Figure-5.15). The majority of the HOMO is located on the cluster, and the wavefunctions are spread over all three Ga atoms. However, the LUMO is located on the Ga atoms interacting with the surface and shows features like bonding orbital. The

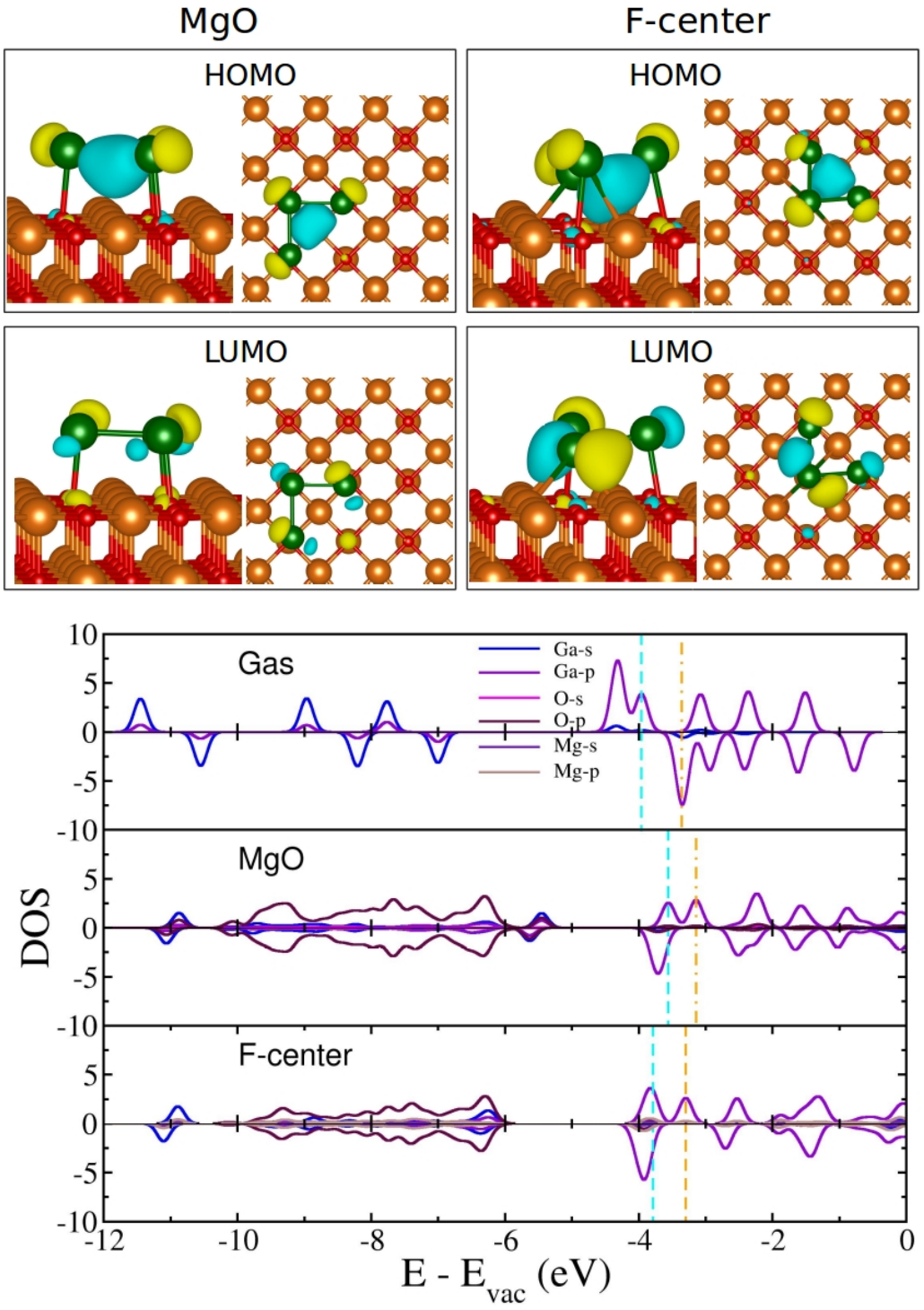

Figure 5.14: The HOMO and LUMO of Ga_3(I) adsorbed at the clean MgO surface and the F-center. The density of states projected on the atomic orbitals of the Ga_3(I). The color code is the same as Figure-5.4.

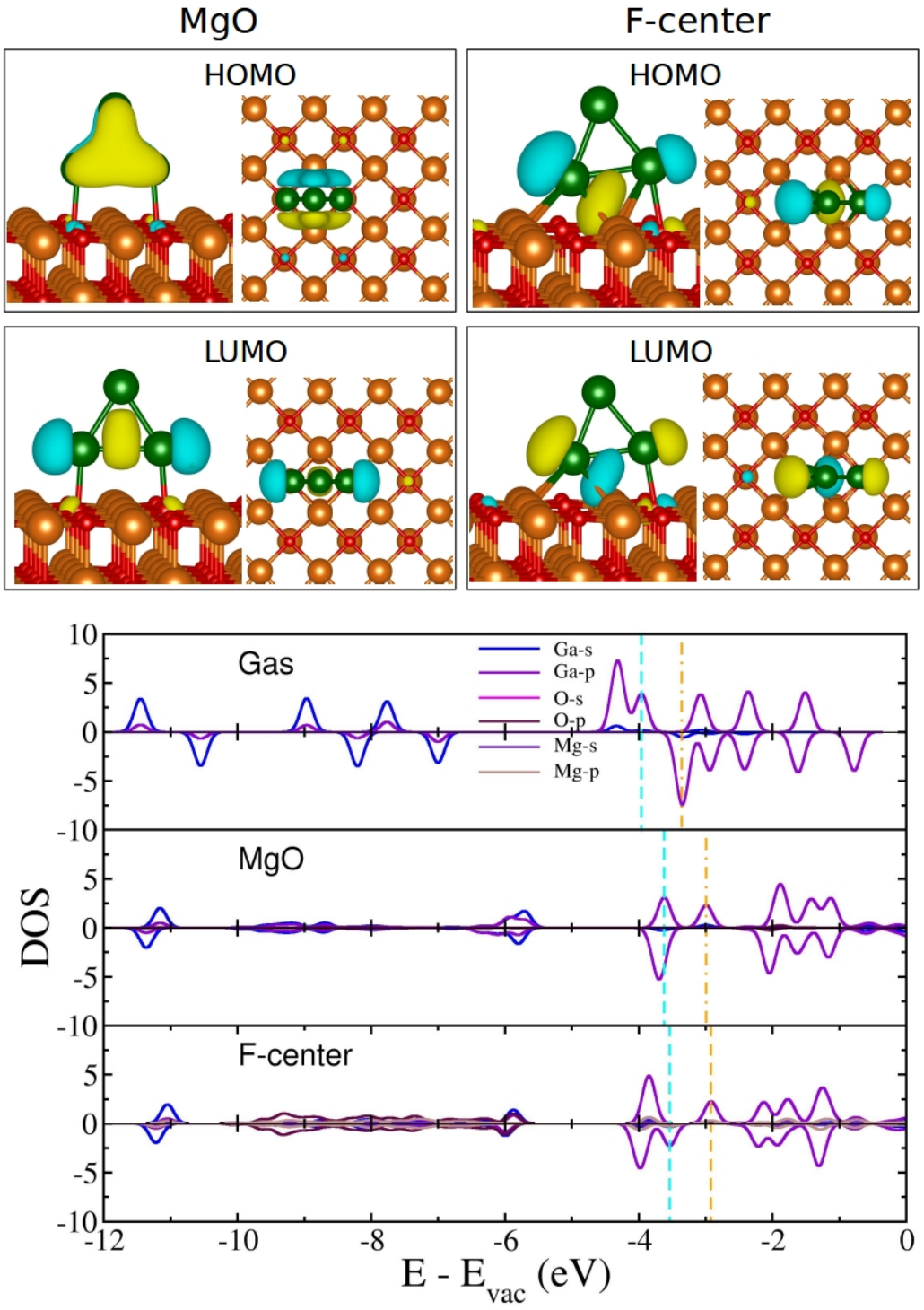

Figure 5.15: The HOMO and LUMO of Ga_3(II) adsorbed at the clean MgO surface and the F-center. The density of states projected on the atomic orbitals of the Ga_3(II). The color code is the same as Figure-5.4.

bonding orbital like LUMO suggests that adding more electron to the cluster will increase the Ga-Ga bond strength. We note that the adsorption energy (-1.38 eV) of the Ga_3(II) on MgO terrace is very similar to that of Ga_2 on MgO terrace (-1.41 eV). This is because in both the cases only two Ga atoms are interacting with the surface. For Ga_3(I) adsorption on the MgO, one would expect the adsorption energy to be larger than these values since all three Ga atoms are binding to the surface. However, the Ga_3(I) also has similar adsorption energy (-1.39 eV) on the MgO terrace. To understand why Ga_3(I) and Ga_3(II) have similar adsorption energies, we have performed energy decomposition analysis. The adsorption energy can be decomposed into ($E_{ads} = \Delta E_1 + \Delta E_2 + \Delta E_3$) energy gained by the interaction of Ga_3 with the MgO surface (ΔE_1), the energy cost involved in distorting the clean MgO surface (ΔE_2) and the Ga_3 in its gas phase (ΔE_3) due to adsorption. For Ga_3(I) adsorption on the MgO terrace, the ΔE_1, ΔE_2 and ΔE_3 are respectively found to be -1.72 eV, 0.27 eV and 0.06 eV while the same for the Ga_3(II) adsorption on the MgO terrace are found to be -1.79 eV, 0.36 eV and 0.05 eV respectively. The energy decomposition analysis shows that the energy cost involved in distorting the clean MgO surface (ΔE_2) and the Ga_3 in its gas phase (ΔE_3) due to adsorption are very low compared to the energy gained by the interaction of Ga_3 with the MgO surface (ΔE_1). Moreover, ΔE_1 is similar for both Ga_3(I) and Ga_3(II). The adsorption energy for Ga_3(I) and Ga_3(II) are similar due to the similar amount of charge transfer. Other stable geometries for the Ga_3 adsorbed on the MgO terrace are given in Figure-C.6 of Appendix C.

The triangular configuration Ga_3(II), with the cluster lying vertically on the surface, is found to the most stable structure for the Ga_3 bound to the vacancy site. Among three Ga atoms one sits on the F-center, the second one sits on top of neighboring O site, and third Ga is vertically away from the surface (Figure 5.11(f)). In comparison to the Ga_3(II) binding to the clean MgO terrace, the longer Ga-Ga bond distance decreases from 2.71 Å to 2.53 Å, while the shorter Ga-Ga bond distance slightly increases from 2.51 Å to 2.58 Å. However, the magnetic moment on the Ga_3(II) binding to F-center is found to be 1.00 μ_B which is same as Ga_3(II) adsorbed on the MgO terrace. A Bader charge analysis shows a net charge transfer of 1.76 e^- from the surface to the Ga_3(II). Similar to the Ga dimer binding at the F-center, Ga sitting on top of the vacancy site has a large amount of charge gain of 1.74 e^-, and the other Ga atoms have a small charge gain of 0.02 e^-. Figure 5.12(f) shows the isosurfaces of the charge density differences. Unlike Ga_3(II) adsorbed on the MgO terrace, where both HOMO and LUMO are coming from the up spin channel, for

Ga_3(II) adsorbed at the F-center the HOMO is coming from the down spin channel while the LUMO is coming from the up spin channel (Figure-5.15). We see that for Ga_3(II) adsorbed at the F-center, the majority of the HOMO is localized at the Ga atoms binding to the surface. The shape of the LUMO is also same as the HOMO; however, the signs of the lobes are switched. The adsorption, binding and formation energies of Ga_3(II) at the vacancy site are found to be -2.48, -6.05 and -3.23 eV respectively.

The "L" shaped geometry Ga_3(I) lying horizontally on the surface and bound to the F-center (Figure 5.11(d)), in which the central Ga bind to the vacancy site and other two Ga atoms bind on top of two O sites, is found to be 0.08 eV less stable compared to the previous geometry. Similar to Ga_3(II), the Ga_3(I) adsorbed at the F-center also has a magnetic moment of 1.00 μ_B. A Bader charge analysis shows a net charge transfer of 1.85 e^- from the surface to the Ga_3(I). Figure 5.12(d) shows the isosurfaces of the charge density differences. Similar to the Ga_3(I) adsorption on the MgO terrace also for the Ga_3(I) at the F-center, we see charge accumulation in the middle of all the three Ga atoms. Further, both HOMO and LUMO are coming from the up spin channel (Figure-5.14). The HOMO is spread over all three Ga atoms with features indicating bonding type orbital while the LUMO shows features like anti-bonding type orbital. Other metastable structures for Ga trimer cluster at the F-center are presented in Figure-C.6 of Appendix C.

Pd_2Ga_1: The Pd rich Pd_2Ga_1 cluster can be formed in two possible ways: (1) adding a Ga adatom to the Pd dimer adsorbed on the MgO terrace and (2) adding a Pd adatom to the Pd_1Ga_1 cluster adsorbed on the MgO terrace. The most stable structure for Pd_2Ga_1 in the gas phase is an isosceles triangle. However, a linear structure is only about 0.03 eV less stable than the lowest energy triangular one in the gas phase. In the linear structure, Ga is in the center and the Pd atoms occupy the sides with Pd-Ga distance of 2.30 Å. In both the structures the cluster has a magnetic moment of 1.00 μ_B. [98] In the most stable configuration of Pd_2Ga_1 on MgO terrace (Figure 5.11(g)), we find that the cluster lies horizontally with the Ga and Pd atoms occupying the atop O site. The Pd-Ga bond distance is found to be 2.37 Å, which is slightly elongated compared to the gas phase bond distance of 2.30 Å. However, this is about 0.6 Å smaller than that of two neighboring O-O distance. From the results of Pd_1Ga_1 clusters on the MgO terrace, we have seen that due to the additional bonding interaction between Pd and the surface Mg, the Pd atom is slightly pulled towards the Ga atom. Similarly, for Pd_2Ga_1 adsorption on MgO, both the

Pd atoms are about 0.6 Å pulled towards Ga. Similar to the gas phase cluster, the Pd_2Ga_1 adsorbed on the MgO also has a magnetic moment of 1.00 μ_B. Due to the interaction between the cluster and the surface about 0.52 e^- charge is transferred from the surface to the Pd_2Ga_1. Each of the Pd atoms is gaining about 0.26 e^- while Ga has no net charge gain. Figure 5.12(g) shows the isosurfaces of the charge density differences. We see that there is charge depletion along the Ga-O bond and charge accumulation between the Pd and the surface Mg atoms. Further analysis of the DOS shows that similar to the gas phase clusters, [98] the HOMO is coming from the up spin channel and the LUMO is coming from the down spin channel (Figure-5.16). The majority of the HOMO is located on the Pd atoms showing features like an anti-bonding type orbital. The shape of the LUMO is the same as the HOMO; however, the sign for the orbital lobes are reverted. The adsorption energy, binding energy and the formation energy of this geometry are calculated to be -1.68, -6.92 and -3.28 eV respectively. Other stable geometries of the Pd_2Ga_1 cluster on MgO terrace are given in Figure-C.7 of Appendix C.

The most stable geometry for the adsorption of Pd_2Ga_1 at the F-center is triangular geometry. In the most stable geometry, one of the Pd atoms occupies the vacancy site while the other Pd sits on top of neighboring Mg and the Ga atom sits on top of the neighboring O site (Figure 5.11(h)). After adsorption of Pd_2Ga_1 to the F-center, the Pd-Pd bond length is slightly increased from the gas phase value of 2.63 Å to 2.68 Å while the two Pd-Ga bond distances increased from 2.37 Å each to 2.39 Å and 2.56 Å. [98] Similar to the gas phase, Pd_2Ga_1 adsorbed at the F-center has a magnetic moment of 1.00 μ_B. The Bader charge analysis shows that a charge of 2.00 e^- transferred from the surface to the cluster. The Pd atom occupying the F-center has a large amount of charge gain of 1.52 e^- and the other Pd has a charge gain of 0.36 e^-, while the Ga has a small charge gain about 0.12 e^-. Figure 5.12(h) shows the isosurfaces of the charge density differences for the adsorption of Pd_2Ga_1 to the F-center. Figure-5.16 shows the DOS and the wave functions corresponding to the HOMO and LUMO of Pd_2Ga_1 adsorbed at the F-center. The HOMO is coming from the down spin channel while the LUMO is coming from the up spin channel. Both HOMO and LUMO are spread over all the metal atoms in the cluster showing the features like anti-bonding type orbitals. The adsorption, binding and formation energies for the Pd_2Ga_1 at the F-center is found to be -3.49eV, -8.74 eV and -2.49 eV respectively. Other possible structures for the Pd_2Ga_1 clusters at the F-center are given in Figure-C.8 of Appendix C.

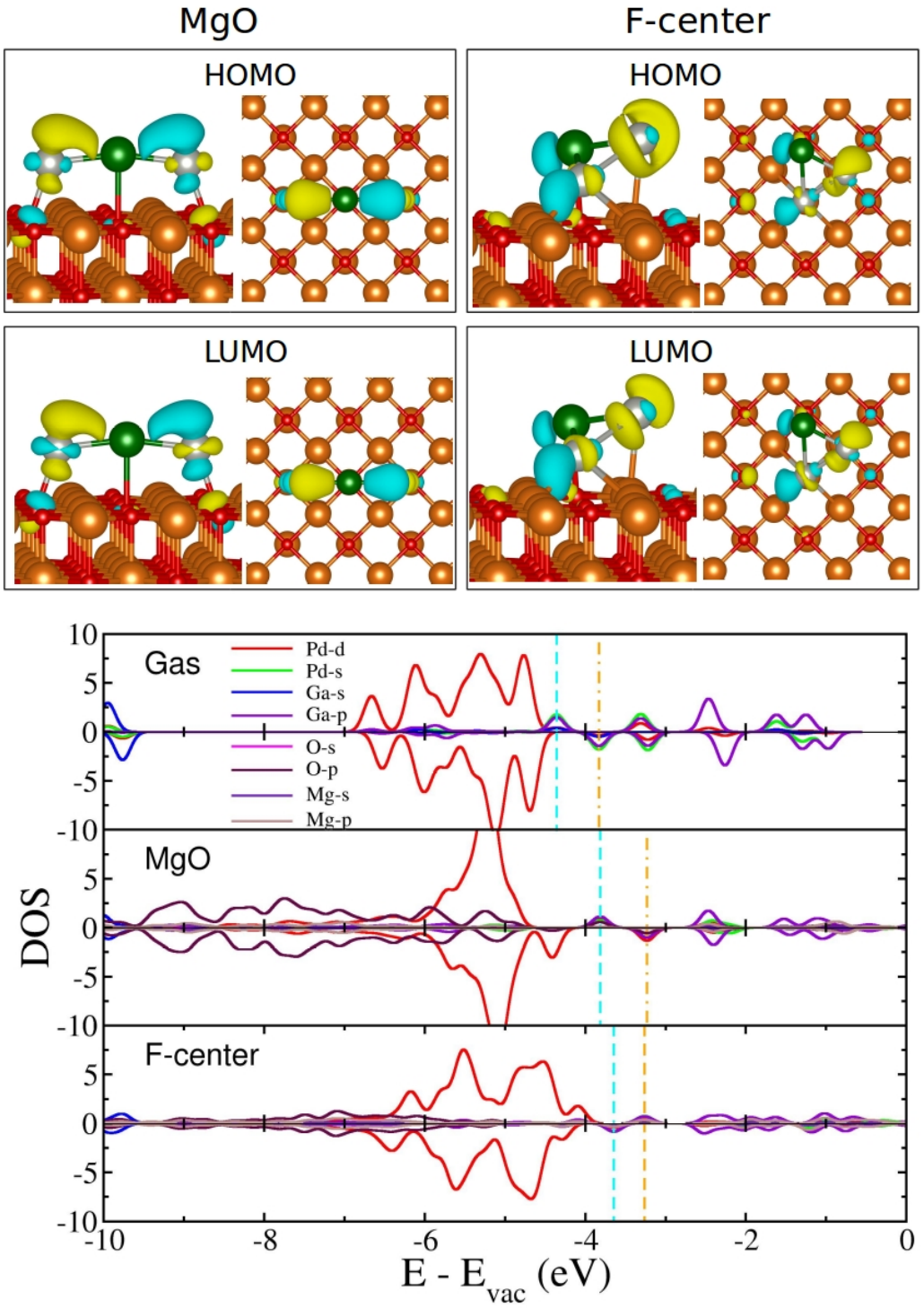

Figure 5.16: The HOMO and LUMO of Pd_2Ga_1 adsorbed at the clean MgO surface and the F-center. The density of states projected on the atomic orbitals of the Pd_2Ga_1. The color code is the same as Figure-5.4.

Pd_1Ga_2: Similar to Pd_2Ga_1 clusters, the Ga rich Pd_1Ga_2 clusters can also be formed in two different ways: (1) adding a Ga adatom to the Pd_1Ga_1 cluster adsorbed on the MgO terrace and (2) adding a Pd adatom to the Ga dimer adsorbed on the MgO terrace. In the gas phase, the structure of Pd_1Ga_2 is an isosceles triangle and the cluster is nonmagnetic. Similar to the gas phase geometry, an isosceles triangular structure was found to be the most stable geometry for the Ga rich Pd_1Ga_2 cluster adsorbed on MgO terrace (Figure 5.11(i)) with a binding energy of -6.76 eV. In this geometry, the two Ga adatoms bind on top of two surface O sites while the Pd atom binds on top of Mg atom which is attached to the O atoms on which the Ga atoms are sitting. In comparison to the Ga atoms, the Pd is slightly away from the surface, which is clear from the Pd-Mg and Ga-O distance of 2.78 and 2.24 Å respectively. The Ga-Ga bond distance is slightly decreased from the gas phase value of 2.84 Å to 2.82 Å while the Pd-Ga bond distance is slightly increased from 2.37 Å to 2.41 Å. Similar to the gas phase cluster, Pd_1Ga_2 adsorbed on the MgO terrace also nonmagnetic. A Bader charge analysis shows a net charge transfer of 0.24 e^- from the surface to the Pd_1Ga_2. While the Pd atom gains a charge of about 0.16 e^-, the Ga atoms gain about 0.04 e^- each. Similar to the Pd_2Ga_1, the charge gain on the Pd atom in the Pd_1Ga_2 also large as compared to the pure Pd clusters. Moreover, for the Ga rich Pd_1Ga_2 the charge gain is larger than that of Pd_2Ga_1 suggesting that with increasing the amount of Ga in the cluster the charge gain on the Pd increases. The charge density difference isosurface shows the charge gain around the Pd atom and the charge depletion around Ga atoms (Figure 5.12(i)). Figure-5.17 shows the wavefunctions corresponding to the HOMO, LUMO and the DOS for the Pd_1Ga_2 adsorbed on the MgO terrace. The majority of the positive lobes of the HOMO is localized around Pd while the negative lobes are around the Ga atoms. However, the majority of the LUMO is localized along the Ga-Ga bond and shows features like bonding type orbital. The adsorption and formation energy for the Ga rich Pd_1Ga_2 cluster were respectively calculated to be -1.17 eV and -3.72 eV. For other stable structures of Pd_1Ga_2 cluster on MgO terrace see Figure-C.9 of Appendix C.

In the most stable structure for Pd_1Ga_2 cluster at the F-center (Figure 5.11(j)), the Pd occupies the vacancy site and the two Ga atoms bind to the two sides it and sitting on top of O site. Similar to the gas phase, the Pd_1Ga_2 binding to the F-center is also non-magnetic. The Pd-Ga bond length increased to 2.43 Å compared to the gas phase value of 2.37

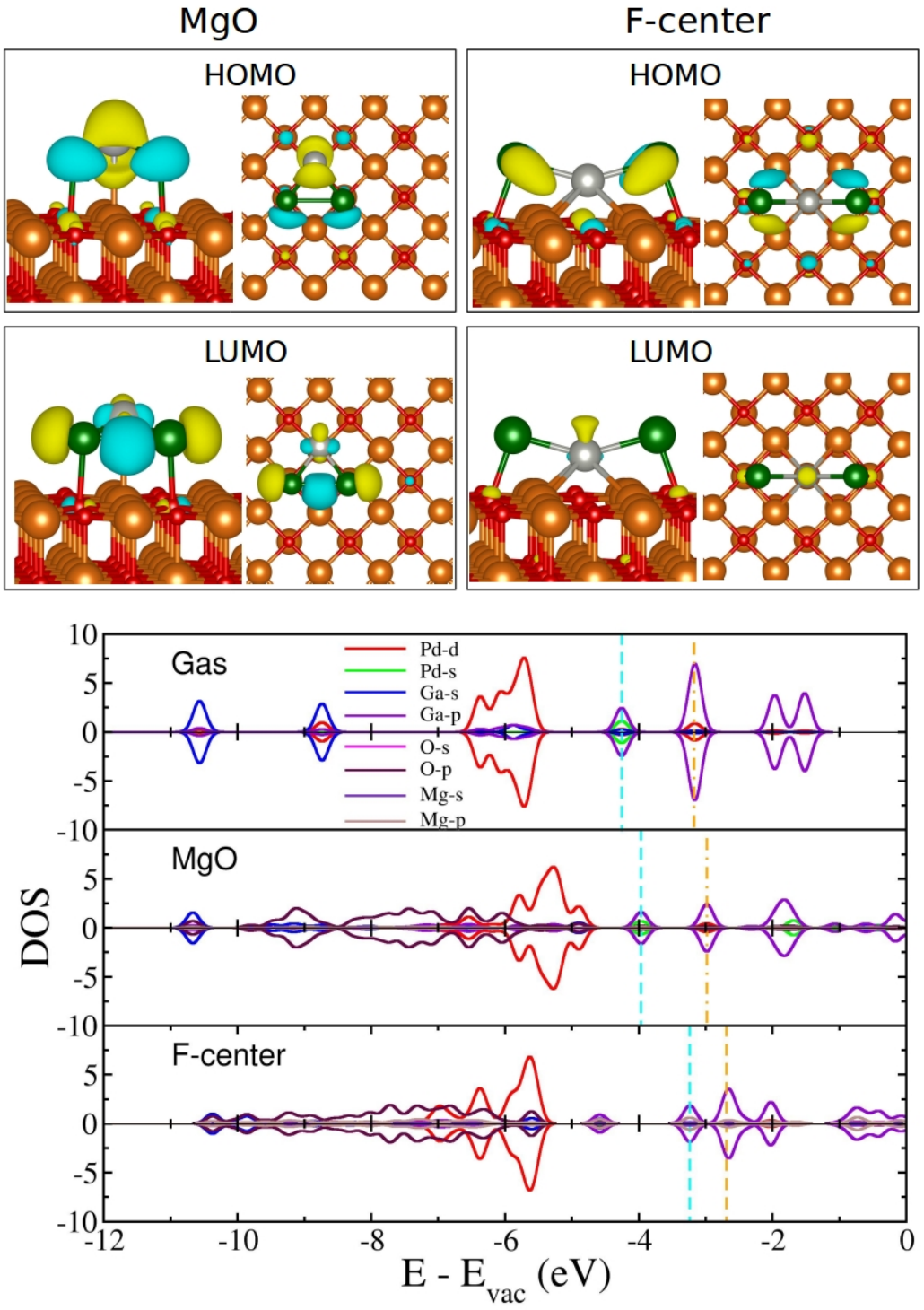

Figure 5.17: The HOMO and LUMO of Pd_1Ga_2 adsorbed at the clean MgO surface and the F-center. The density of states projected on the atomic orbitals of the Pd_1Ga_2. The color code is the same as Figure-5.4.

Å, while the Ga-Ga distance increased from 2.84 Å to 4.69 Å. A Bader charge analysis shows a net charge transfer of 2.06 e^- from the surface to the Pd_1Ga_2 cluster. However, the Pd atom gains about 1.34 e^- while each of the Ga atoms gains about 0.36 e^-. Figure 5.12(j) shows the isosurfaces of charge density differences for the Pd_1Ga_2 adsorbed at the F-center. Further, analysis of the wavefunctions corresponding to the HOMO, LUMO and DOS for Pd_1Ga_2 adsorbed at the F-center shows that most of the HOMO is localized around the Ga atoms while the LUMO is more localized around the Pd atom (Figure-5.17). The adsorption, binding and formation energies are respectively calculated to be -2.23, -7.83 and -2.18 eV. For other metastable structures of Pd_1Ga_2 clusters at the F-center see Figure-C.10 of Appendix C.

5.3.1.4 Tetramers

A tetramer was formed by adding one Pd or Ga atom to the existing trimer clusters. Depending on the type of atom added and the existing trimer, we have five possible compositions for the tetramer clusters, namely Pd_4, Ga_4, Pd_3Ga_1, Pd_2Ga_2 and Pd_1Ga_3. For all the clusters both 2D flat structures and 3D tetrahedral structures are considered to study the adsorption on both MgO terrace and F-center.

Pd_4: The 3D tetrahedron structure is found to be the most stable geometry for Pd_4 adsorbed on MgO terrace (Figure 5.18(a)). Three Pd atoms bind to the surface to form the base triangle, and the fourth one sits on top of it. Among the three Pd atoms forming the base triangle one Pd atom sits on top of O site while the other two Pd atoms bind to two neighboring O atoms; however, these Pd atoms are shifted laterally by about 0.7 Å with respect to the atop O position. In the gas phase structure, three Pd atoms form an equilateral triangle with the Pd-Pd distance of 2.67 Å, and the fourth Pd sits on top of the base triangle. All other Pd-Pd bonds are of same distance of 2.58 Å. [98] However, on the MgO terrace, the base triangle is isosceles with two Pd-Pd bond distances of 2.63 Å, and the third one is about 2.88 Å. Moreover, the Pd-Pd distances with the fourth Pd atom are 2.60 Å, 2.60 Å and 2.62 Å respectively. The binding energy of Pd tetramer on MgO is calculated to be -9.15 eV. The obtained stable geometry and the calculated binding energy are consistent with the previous reports. [90, 91] The Pd_4 adsorbed on MgO terrace has a magnetic moment of 2.00 μ_B, which is same as the magnetic moment on the isolated gas phase cluster. [98] A Bader charge analysis shows that as a result of the chemical in-

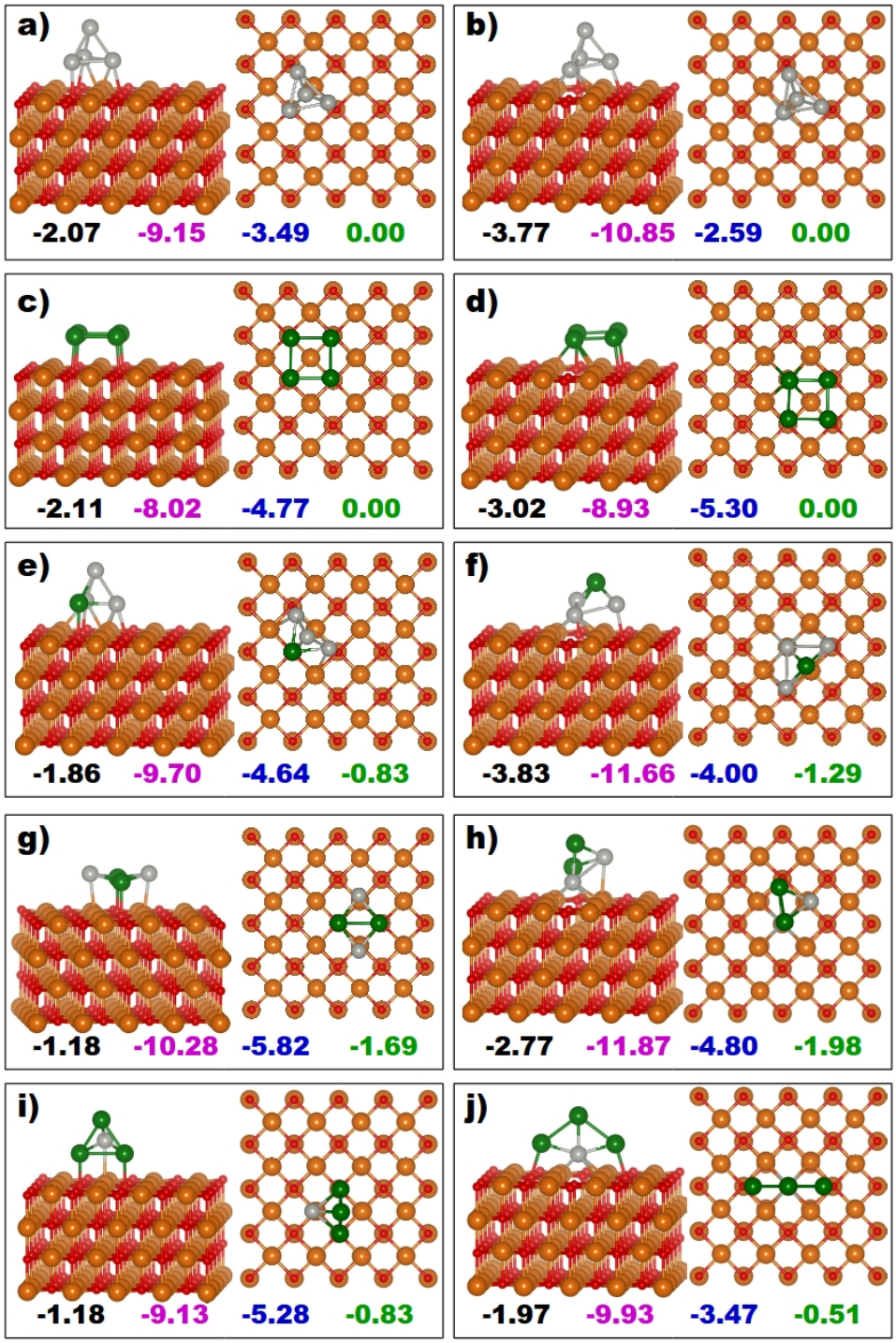

Figure 5.18: a)Pd_4, c)Ga_4, e)Pd_3Ga_1, g)Pd_2Ga_2 and i)Pd_1Ga_3 clusters adsorbed on MgO(100) terrace. b)Pd_4, d)Ga_4, f)Pd_3Ga_1, h)Pd_2Ga_2 and j)Pd_1Ga_3 clusters adsorbed at the vacancy site. The color code is same as Figure 5.2.

teraction between the Pd_4 and MgO surface about 0.53 e^- charge is transferred from the surface to the Pd_4. Among the four Pd atoms, one sitting on top of O site has a charge gain of 0.07 e^-, other two equivalent Pd atoms on the base have a charge gain of 0.12 e^-, and the fourth Pd has a charge gain of 0.22 e^-. Figure 5.19(a) shows the isosurfaces of the charge density differences for the Pd_4 adsorbed on the MgO terrace. Both HOMO and LUMO of the Pd_4 adsorbed on MgO terrace are coming from up spin channel (Figure-5.20) and have contributions from the Pd d orbitals. The HOMO is localized around the Pd atoms of the base triangle while the LUMO is spread over all the Pd atoms. The adsorption and formation energy of Pd_4 on MgO terrace is calculated to be -2.07 and -3.49 eV respectively. Other stable structures for the Pd_4 adsorbed on MgO terrace is given in Figure-C.11 of Appendix C.

The most stable configuration of Pd_4 at the F-center is also found to be a 3D tetrahedron structure (Figure 5.18(b)). Similar to Pd_4 binding to the MgO terrace, also for Pd_4 adsorption on the F-center, the base triangle is an isosceles triangle with Pd-Pd distances of 2.63 Å, 2.63 Å and 2.92 Å. Moreover, the Pd-Pd distances with the fourth Pd are about 2.57 Å, 2.57 Å and 2.81 Å respectively. Unlike other small Pd clusters which are nonmagnetic at the F-center, the Pd_4 adsorbed at the F-center has a magnetic moment of 2.00 μ_B. The nonmagnetic structure is about 0.07 eV less stable compared to the magnetic structure. A Bader charge analysis shows a net charge transfer of 2.20 e^- from the surface to the Pd_4. Figure 5.19(b) shows the isosurfaces of the charge density differences for the Pd_4 adsorbed at the F-center. Similar to other small Pd clusters the Pd atom binding to the vacancy site has a larger charge gain (1.48 e^-) than the other Pd atoms (0.23, 0.23 and 0.26 e^- respectively). Both HOMO and LUMO are coming from the up spin channel (Figure-5.20). The HOMO is primarily located on the Pd atom binding to the vacancy site and the fourth Pd sitting on top of the base triangle. In contrast, the LUMO is spread over all the four Pd atoms. The adsorption, binding and formation energies for Pd_4 cluster at the F-center are calculated to be -3.77 eV, -10.85 eV and -2.59 eV respectively, which is consistent with the previous theoretical prediction. [91]

Ga_4: The most stable geometry for Ga tetramer on MgO terrace is a 2D square planar structure (Figure 5.18(c)), in which four Ga atoms are sitting on top of four neighboring surface O sites with a Ga-O distance of 2.29 Å and Ga-Ga distance of 2.68 Å. The obtained Ga-Ga bond length for the Ga tetramer on the support is slightly larger compared to the

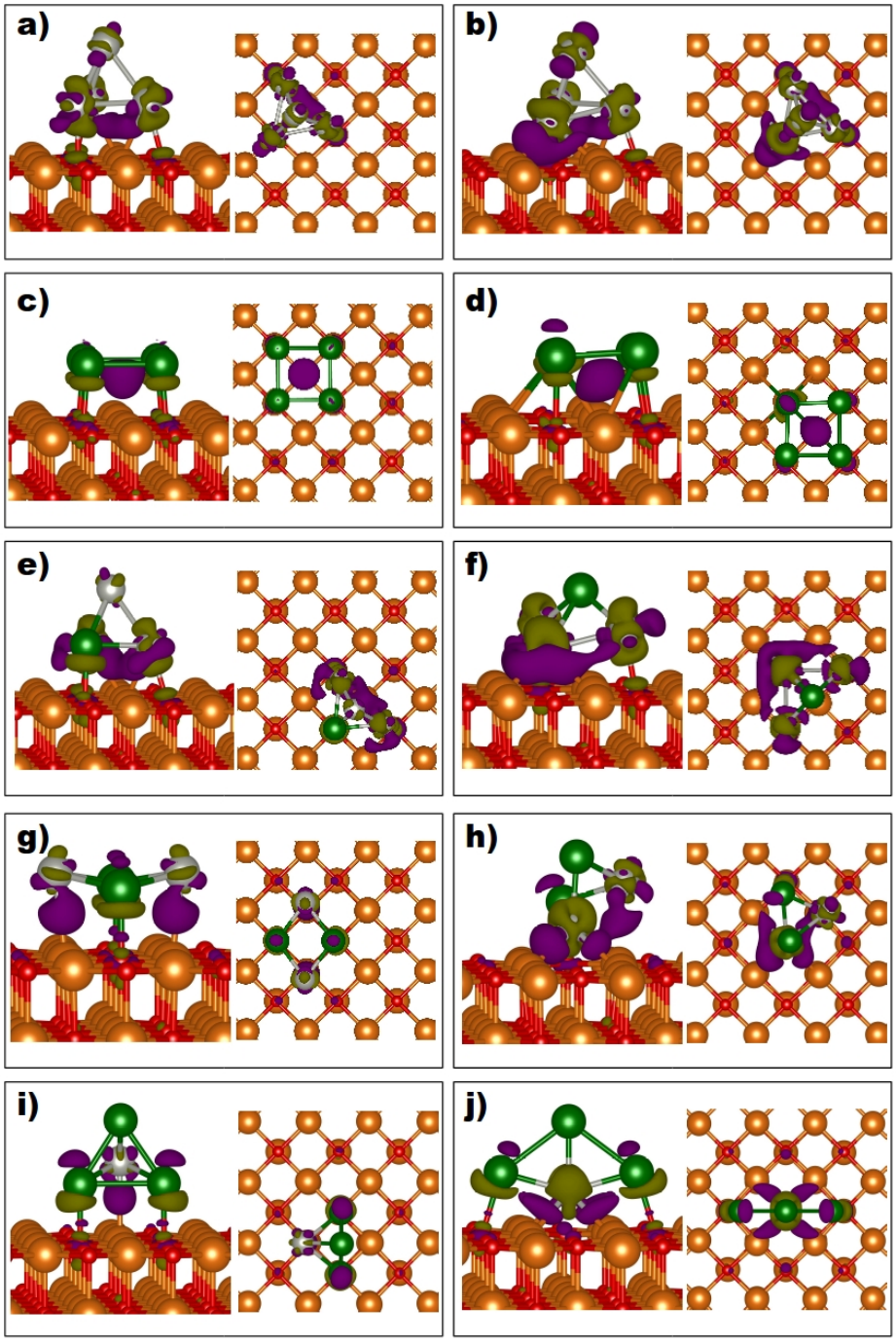

Figure 5.19: Isosurfaces of charge density differences showing the charge transfer from surface to tetramer clusters. a)Pd_4, c)Ga_4, e)Pd_3Ga_1, g)Pd_2Ga_2 and i)Pd_1Ga_3 clusters adsorbed on MgO(100) terrace. b)Pd_4, d)Ga_4, f)Pd_3Ga_1, h)Pd_2Ga_2 and j)Pd_1Ga_3 clusters adsorbed at the vacancy site. The color code and the isovalue are same as Figure 5.3.

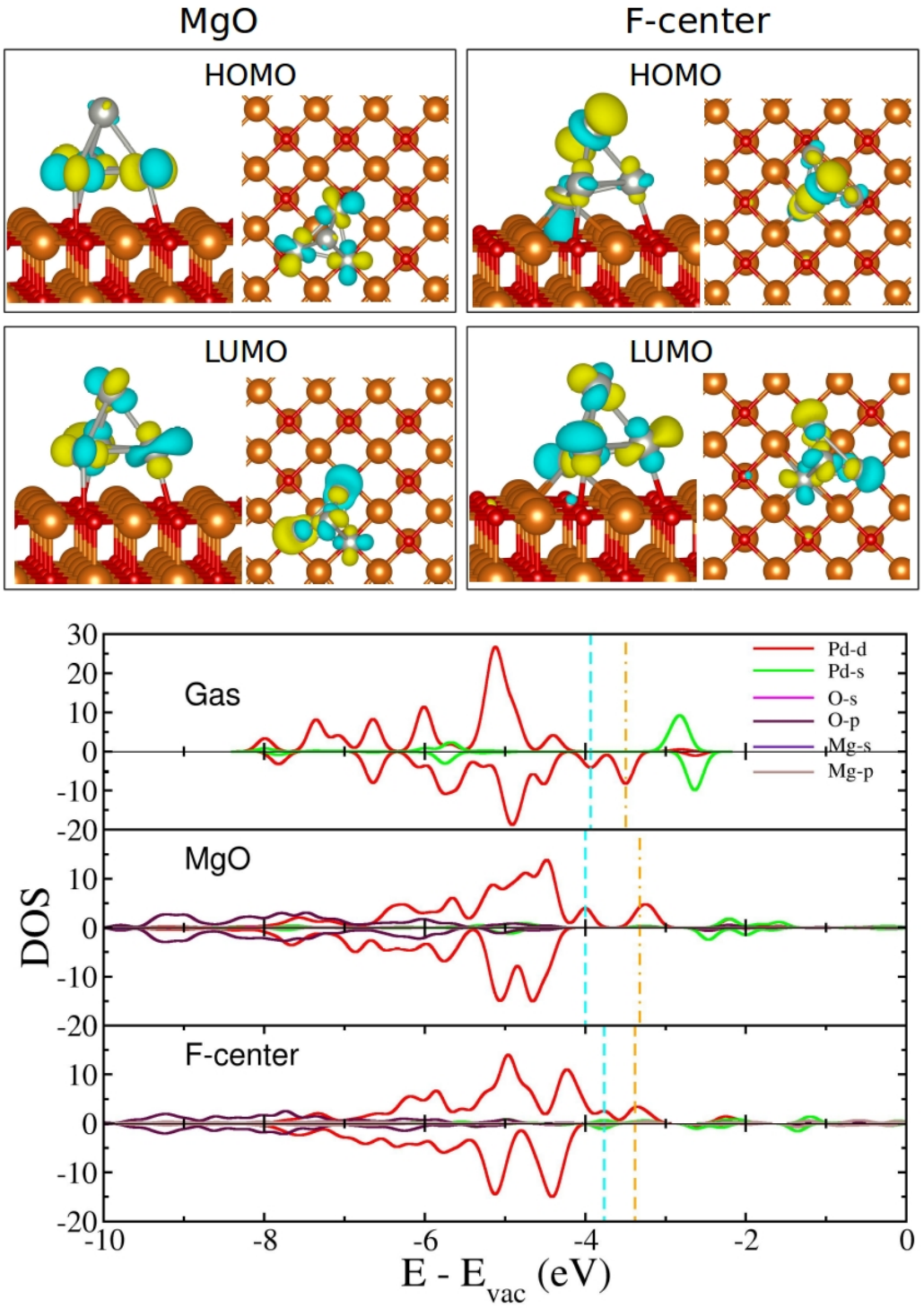

Figure 5.20: The HOMO and LUMO of Pd_4 adsorbed at the clean MgO surface and the F-center. The density of states projected on the atomic orbitals of the Pd_4. The color code is the same as Figure-5.4.

gas phase value of 2.61 Å. Unlike other small Ga clusters, those have non-zero magnetic moment both in the gas phase as well as adsorbed on MgO terrace; the Ga tetramer adsorbed on MgO is found to be nonmagnetic where as the gas phase cluster has a magnetic moment of 2.00 μ_B. [98] We have also considered a magnetic structure for Ga tetramer on MgO terrace by restricting the magnetic moment on the cluster to be 2.00 μ_B, however, during relaxation, the square planar geometry becomes a rhombus structure and is about 1.00 eV less stable than the nonmagnetic structure. A Bader charge analysis shows a net charge transfer of 0.34 e^- from the surface to the Ga_4. Isosurfaces of the charge density differences (Figure 5.19(c)) show charge depletion along the Ga-O bond and charge accumulation at the center of the Ga_4 cluster, which is consistent with the other small Ga clusters adsorbed on the MgO terrace. Majority of the HOMO and LUMO are coming from Ga p states and are evenly spread over all the Ga atoms (Figure-5.21). The adsorption energy, binding energy and the formation energies of Ga tetramer on MgO terrace are found to be -2.11, -8.02 and -4.77 eV respectively. Other metastable structures of Ga_4 on MgO terrace are given in Figure-C.12 of Appendix C.

The most stable structure for the Ga_4 cluster at the vacancy site is found to be a 2D planar kite-like structure (Figure 5.18(d)). Among the four Ga atoms, one Ga occupies on the vacancy site, and the other three Ga atoms sit on top of three O sites. The Ga-Ga bond distances for the Ga atoms binding to the Ga atom sitting on the vacancy site are equal and found to be -2.57 and the same with the diagonally opposite Ga are also found to be equal and are about 2.64 Å. Similar to the adsorption on the MgO terrace, the Ga_4 adsorbed at the F-center is also non-magnetic. As a result of the chemical interaction between the Ga_4 and the MgO surface about 1.79 e^- charge is transferred from the surface to the Ga_4. Among the four Ga atoms, the one occupying the vacancy site has a charge gain of 1.43 e^-, the one which is diagonally opposite to this Ga has a charge gain of 0.10 e^- and each of the other two Ga atoms has a charge gain of 0.13 e^-. Figure 5.19(d) shows the isosurfaces of the charge density differences for the Ga_4 adsorbed at the F-center. Unlike the Ga_4 adsorbed on the MgO terrace where the HOMO and LUMO is delocalized over all the four Ga atoms, for Ga_4 adsorbed at the F-center, the HOMO is localized primarily around the Ga atom binding to the vacancy site while the LUMO is localized on the Ga atom which is diagonally opposite to the Ga atom on the vacancy site (Figure-5.21). The adsorption, binding and the formation energies for Ga_4 cluster at F-center are calculated to be -3.02 eV, -8.93 eV and -5.30 eV respectively. Other metastable structures for Ga_4

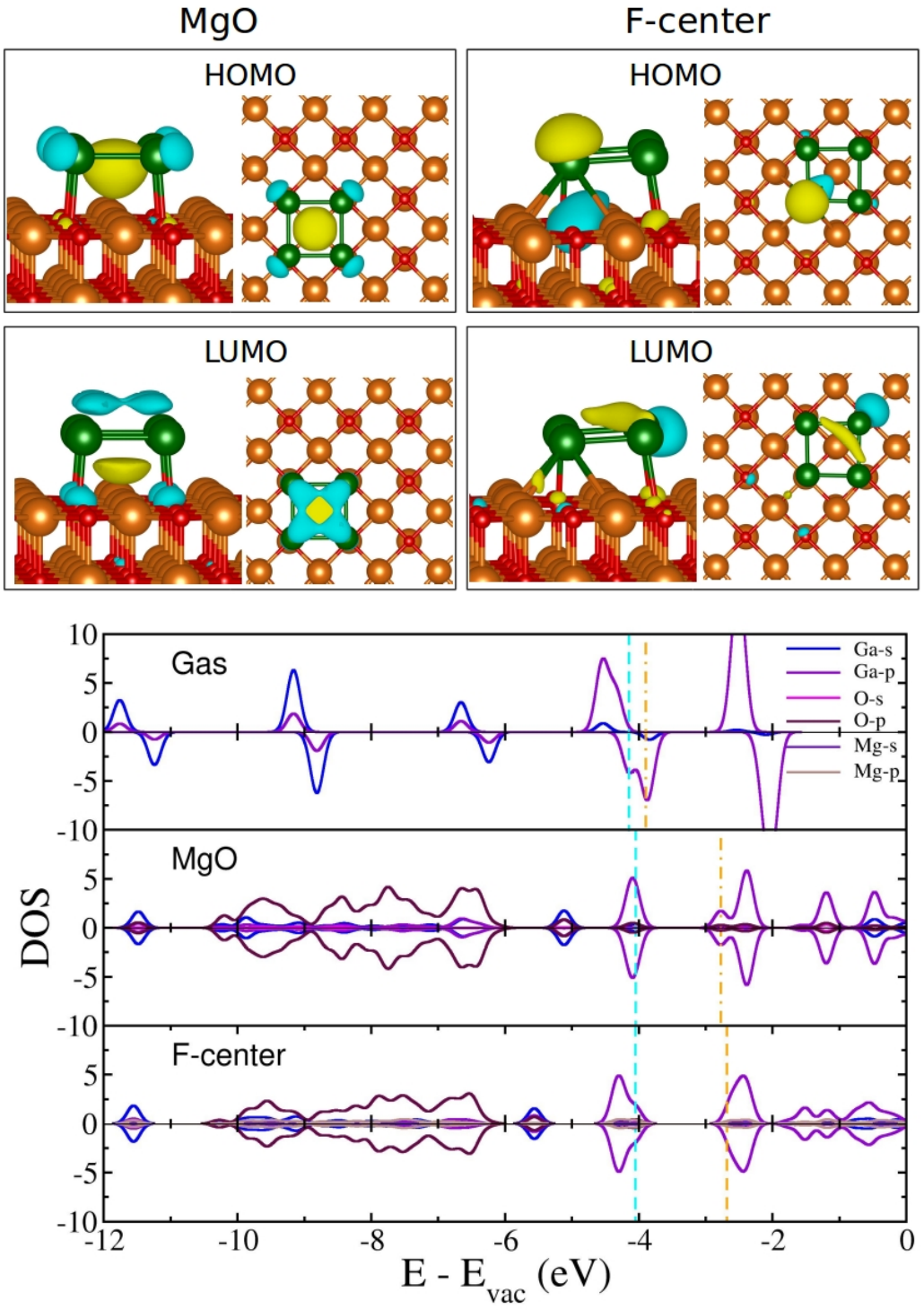

Figure 5.21: The HOMO and LUMO of Ga_4 adsorbed at the clean MgO surface and the F-center. The density of states projected on the atomic orbitals of the Ga_4. The color code is the same as Figure-5.4.

adsorbed at the vacancy site are given in Figure-C.12 of Appendix C.

Pd_3Ga_1: The most stable structure for Pd_3Ga_1 in the gas phase is a 3D tetrahedron. Three Pd atoms make an equilateral triangle with Pd-Pd distances of 2.56 Å, and the Ga atom sits on top of the Pd triangle. All the Pd-Ga bonds are of equal length and found to be 2.59 Å. [98] In the most stable structure of Pd_3Ga_1 on the MgO terrace, the Pd_2Ga_1 face is binding to the surface, and third Pd atom sits on top of it (Figure 5.18(e)). After binding to the surface, the Pd-Pd bond lengths are increased, and the Pd-Ga bonds are shortened. The Pd-Pd bond length between the Pd atoms interacting with the surface is found to be 3.11 Å while the same between the Pd atoms binding to the surface and the third Pd is found to be 2.65 Å. The Pd-Ga bond distance for the atoms interacting with the surface is found to be 2.44 Å. The Ga atom binds to the third Pd with a Pd-Ga distance of about 2.46 Å. The Pd_3Ga_1 adsorbed on the MgO terrace has a magnetic moment of 1.00 μ_B which is same as the magnetic moment on the gas phase cluster. [98] A Bader charge analysis shows a net charge transfer of 0.50 e^- from the surface to the Pd_3Ga_1. The two Pd atoms which are interacting to the surface gain about 0.25 e^- each, the third Pd gains about 0.08 e^- while Ga is loosing about 0.08 e^-. Figure 5.19(e) shows the isosurfaces of the charge density differences for the Pd_3Ga_1 adsorbed on the MgO terrace. The HOMO for this complex is coming from the up spin channel and is primarily located on the Ga atom and the third Pd atom which is sitting on top of the Pd_2Ga_1 base triangle. However, the LUMO is coming from down spin channel and is primarily localized on all three Pd atoms (Figure-5.22). The adsorption, binding and formation energies of Pd_3Ga_1 on MgO terrace are found to be -1.86, -9.70 and -4.64 eV respectively. Other stable structures of Pd_3Ga_1 cluster on MgO terrace are given in Figure-C.13 of Appendix C.

In contrast to the clean surface where the Pd_2Ga_1 face is interacting to the surface, at the F-center the Pd_3Ga_1 interacts through Pd_3 face (Figure 5.18(f)). Three Pd atoms bind to the surface in a "L" shaped geometry with a Pd-Pd bond distance of 2.79 Å. Among these three Pd atoms, one sits on top of the vacancy site while the others occupy the atop O sites. The Ga atom sits on top of these three Pd atoms with Pd-Ga bond distances of 2.36 Å, 2.36 Å and 2.67 Å respectively. Similar to the adsorption of Pd_3Ga_1 on MgO terrace, the Pd_3Ga_1 adsorbed at the F-center has a magnetic moment of 1.00 μ_B. As a result of the chemical interaction between the surface and the Pd_3Ga_1, about 2.21 e^- is transferred from the surface to Pd_3Ga_1. The Pd binding to the vacancy site gains about

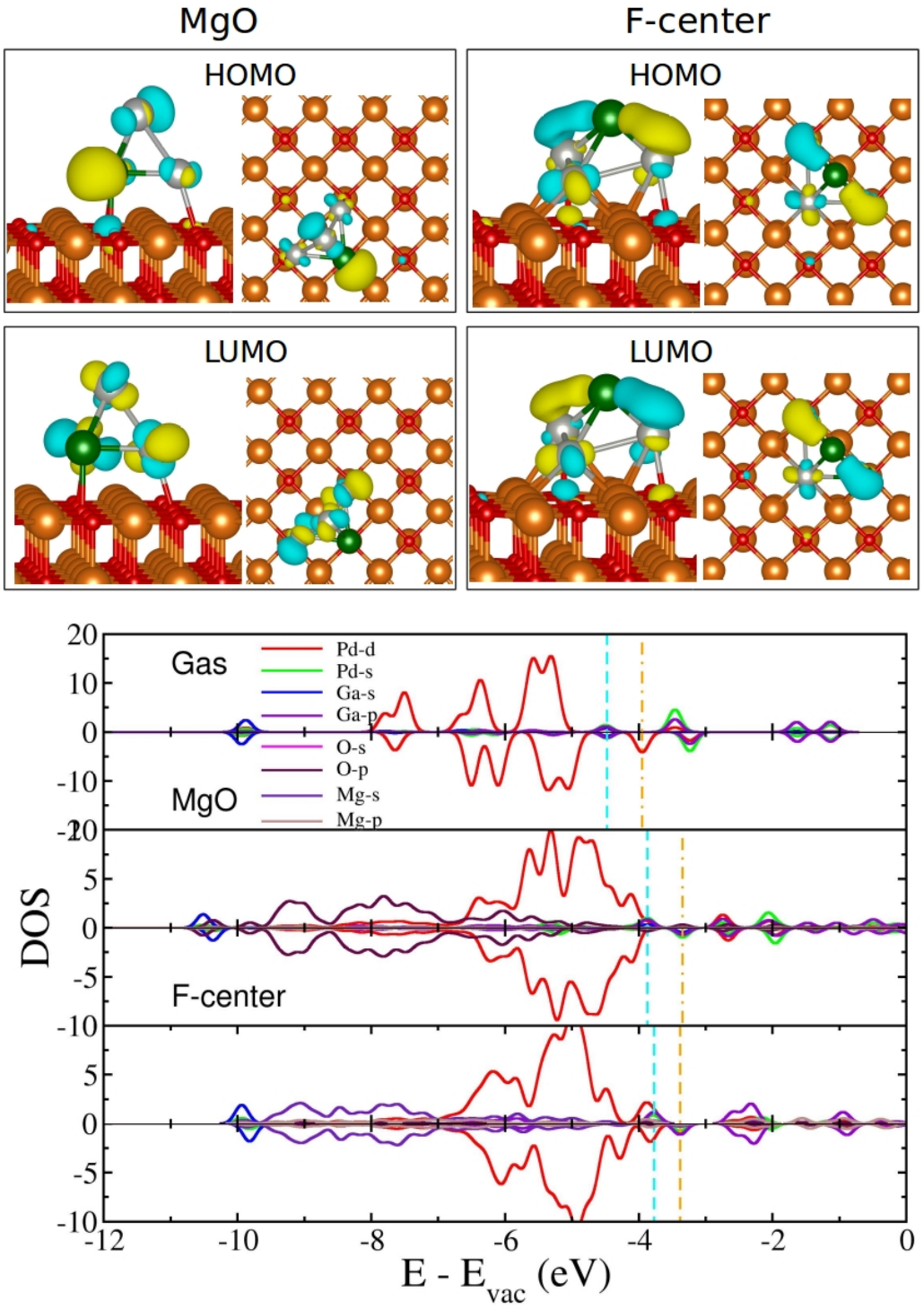

Figure 5.22: The HOMO and LUMO of Pd_3Ga_1 adsorbed at the clean MgO surface and the F-center. The density of states projected on the atomic orbitals of the Pd_3Ga_1. The color code is the same as Figure-5.4.

1.58 e^-, and other two Pd atoms gain about 0.27 e^- each while the Ga atom gains about 0.09 e^-. Figure 5.19(f) shows the isosurfaces of the charge density differences for the Pd_3Ga_1 adsorbed at the F-center. The HOMO of the Pd_3Ga_1-F-center complex is coming from the up spin channel and the LUMO is coming from the down spin channel (Figure-5.22). However, the HOMO is primarily localized along the Pd-Ga bond and at the Pd binding to the vacancy site. The LUMO also has features similar to that of HOMO. The adsorption, binding and formation energies for this structure are calculated to be -3.83 eV, -11.66 eV and -4.00 eV respectively. For other metastable structures of Pd_3Ga_1 cluster at the F-center see Figure-C.14 of Appendix C.

Pd_2Ga_2: The structure of Pd_2Ga_2 in the gas phase is a 2D planar structure. The cluster substrate interaction between Pd_2Ga_2 cluster and MgO terrace leads to the puckering of the structure of Pd_2Ga_2. The Ga atoms bind to the surface O site with the Ga-O distance of 2.23 Å while the Pd atoms bind to the Mg site with a Pd-Mg distance of 2.74 Å (Figure 5.18(g)). Due to the puckering, the Pd atoms are lifted above the Ga atoms by 0.4 Å. Moreover, the Pd-Ga bond lengths after adsorption to the MgO terrace is found to be 2.42 Å which is slightly longer than the gas phase value of 2.39 Å. [98] Similar to the gas phase cluster, the Pd_2Ga_2 adsorbed on the MgO terrace is also found to be nonmagnetic. A Bader charge analysis shows a net charge transfer of about 0.32 e^- from the surface to the Pd_2Ga_2. However, each of the Pd atoms is gaining about 0.20 e^- while each of the Ga atoms is loosing about 0.04 e^-. Figure 5.19(g) shows the isosurfaces of the charge density differences for the adsorption of Pd_2Ga_2 on the MgO terrace. Similar to the previously discussed small clusters, the Pd_2Ga_2 on the MgO terrace also shows charge depletion along Ga-O bond and charge accumulation along the Pd-Mg bond. The majority of the HOMO is localized on the Pd atoms while the majority of the LUMO is localized on the Ga atoms with some small contribution from the Pd atoms (Figure-5.23). The adsorption, binding and the formation energies for Pd_2Ga_2 on MgO terrace are found to be -1.18, -10.28 and -5.82 eV respectively. Other stable structures of Pd_2Ga_2 cluster on MgO terrace are given in Figure-C.15 of Appendix C.

In contrast to the gas phase and adsorption on the clean MgO surface, the structure of Pd_2Ga_2 on the F-center is found to be a distorted tetrahedron (Figure 5.18(h)). The cluster interacts with the surface through a Pd_2Ga_1 face. One of the Pd atoms sits on top of the vacancy site, and the other Pd sits on top of the neighboring Mg site with a Pd-Mg

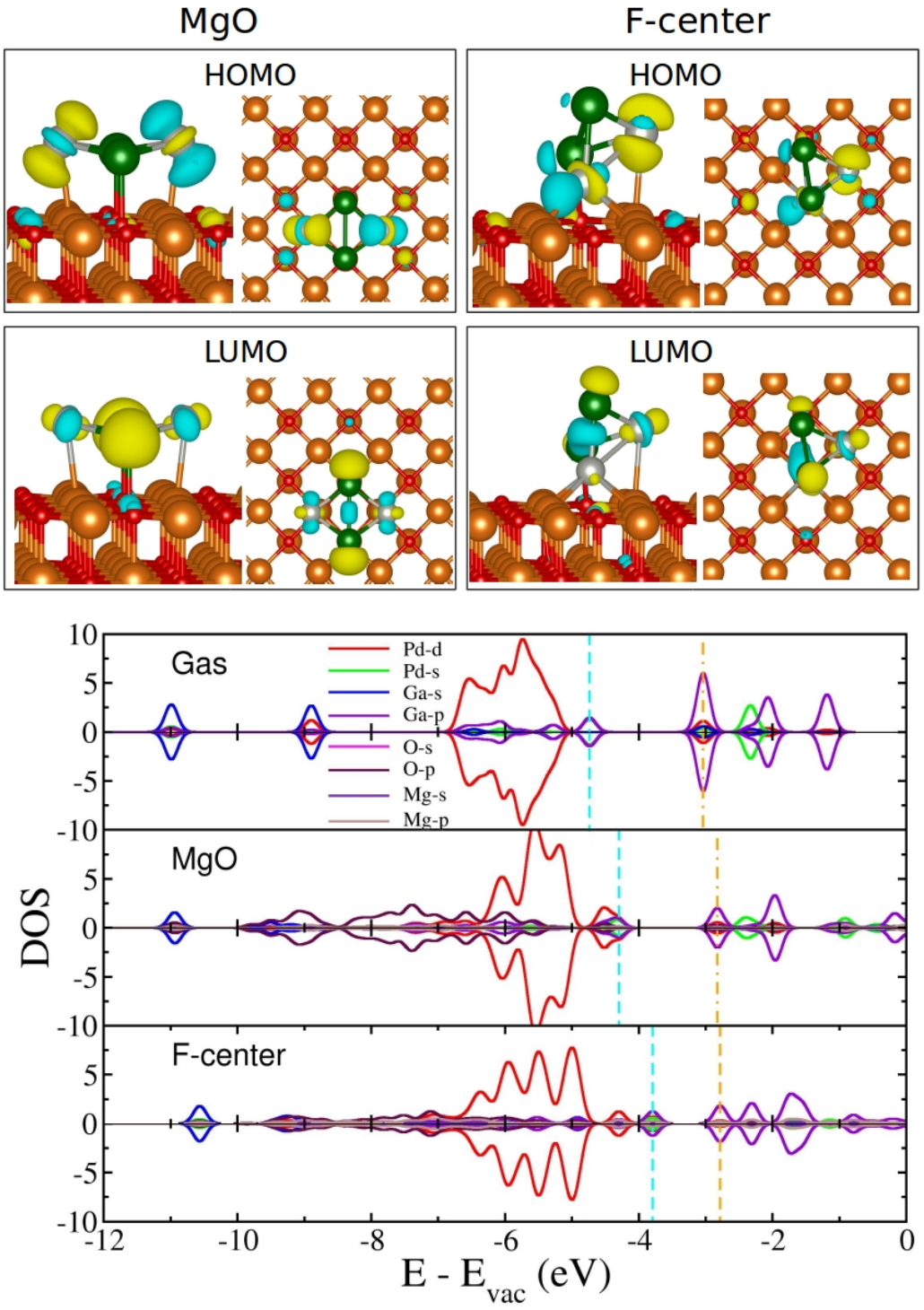

Figure 5.23: The HOMO and LUMO of Pd_2Ga_2 adsorbed at the clean MgO surface and the F-center. The density of states projected on the atomic orbitals of the Pd_2Ga_2. The color code is the same as Figure-5.4.

distance of 2.91 Å, and the Ga atom sits on top of the neighboring O site with a Ga-O distance of 2.29 Å. The Pd-Pd bond distance is found to be 2.84 Å, the Pd-Ga distance with the Pd sitting on top of vacancy site is found to be 2.55 Å and the same with the Pd sitting on top of Mg is found to be 2.44 Å. The other Ga atom sits on top of the Pd atom binding to the vacancy site with a Pd-Ga distance of 2.48 Å. Similar to the clean MgO surface, the Pd_2Ga_2 adsorbed on the F-center is also nonmagnetic. A Bader charge analysis shows a net charge transfer of 2.01 e^- from the surface to the Pd_2Ga_2. Among these, the Pd atom binding to the vacancy site gains about 1.53 e^- and the Pd atom sitting on top of Mg gains about 0.33 e^-. Moreover, the Ga binding to the surface gains about 0.10 e^- and the other Ga atom gains about 0.05 e^-. Figure 5.19(h) shows the isosurfaces of the charge density differences for the Pd_2Ga_2 adsorbed on the F-center. Further analysis of the wavefunction corresponding to the HOMO and LUMO shows that majority of the HOMO is coming from the Pd atoms and majority of the LUMO is coming from the Ga atoms (Figure-5.23). The adsorption, binding and formation energies for Pd_2Ga_2 cluster at the F-center are found to be -2.77 eV, -11.87 eV and -4.80 eV respectively. The other stable structures of Pd_2Ga_2 cluster adsorbed at the F-center are shown in Figure-C.16 of Appendix C.

Pd_1Ga_3: Similar to the Pd_4 and Pd_3Ga_1 clusters the most stable structure for Pd_1Ga_3 on MgO terrace is also a tetrahedron (Figure 5.18(i)). In the gas phase, three Ga atoms form an equilateral base triangle with Ga-Ga bond distance of 2.79 Å, and the Pd atom sits on top of the base triangle with Pd-Ga distance of 2.46 Å. [98] However, Pd_1Ga_3 interacts with the MgO terrace through a Pd_1Ga_2 face. The Ga atoms of the base triangle bind to the surface O sites with the Ga-O distance of 2.15 Å and with a Ga-Ga distance of 2.99 Å. The Pd atom sits on top of the Mg site with a Pd-Mg distance of 2.92 Å and Pd-Ga distance of 2.50 Å. The third Ga atom sits on top of the base triangle with Ga-Ga distance of 2.72 Å and Pd-Ga distance of 2.48 Å. Similar to the gas phase cluster, Pd_1Ga_3 adsorbed on the MgO terrace has a magnetic moment of 1.00 μ_B. A Bader charge analysis shows a net charge transfer of 0.27 e^- from the surface to the Pd_1Ga_3. The Pd atom gains about 0.15 e^-, and each of the two Ga atoms interacting to the surface O is gaining about 0.08 e^- while the other Ga atom is loosing about 0.04 e^-. The isosurfaces showing the charge density differences for the charge transfer in Pd_1Ga_3 adsorbed on the MgO terrace is given in Figure 5.19(i). Similar to other bimetallic clusters binding to the MgO terrace, also for the Pd_1Ga_3 we see charge depletion along the Ga-O bonds and charge accumulation

around the Pd-Mg bond. The adsorption, binding and formation energies for Pd_1Ga_3 on MgO terrace is found to be -1.18eV, -9.13 eV and -5.28 eV respectively. For other stable structures of Pd_1Ga_3 on MgO terrace see Figure-C.17 of Appendix C.

In contrast to the gas phase tetrahedral structure, Pd_1Ga_3 binds to the F-center in a vertical planar geometry. The most stable geometry of the Pd_1Ga_3 cluster bound to the F-center is shown in Figure-5.18(j). In the most stable geometry, the Pd atom occupies the vacancy site, and two Ga atoms bind to two O sites that are at two sides of the Pd, and the third Ga atom is sitting on top of the Pd atom. The Pd-Ga bond distances are of 2.48 Å, 2.48 Å and 2.46 Å respectively and both the Ga-Ga bond distances are found to be equal which is about 2.98 Å. Similar to the MgO terrace, Pd_1Ga_3 adsorbed at the F-center also has a magnetic moment of 1.00 μ_B. As a result of the chemical interaction between the cluster and the surface about 1.97 e^- charge transfers from the surface to the Pd_1Ga_3. However, the Pd atom is gaining about 1.59 e^- while the Ga atoms interacting with the surface O are gaining about 0.17 e^- each and the third Ga atom is gaining about 0.04 e^-. Figure 5.19(j) shows the isosurfaces of charge density differences for the Pd_1Ga_3 adsorbed at the F-center. Similar to other small bimetallic clusters, also for the Pd_1Ga_3 adsorbed at the F-center we see charge depletion along the Ga-O bond and charge accumulation along the Pd-Mg bond. Both HOMO and LUMO are coming from the up spin channel, while the HOMO is located along the Pd-Ga bond for the Ga atom sits on top of the Pd, and the LUMO is located along the Pd-Ga bond of the Ga atoms sitting on top of the O sites (Figure-5.24). The adsorption, binding and formation energies for this structure is calculated to be -1.97 eV, -9.93 eV and -3.47 eV respectively. Other stable structures of Pd_1Ga_3 tetramer clusters at the vacancy sites are given in Figure-C.18 of Appendix C.

5.3.2 Trends in the Stability of the clusters

In this section, we discuss the trends in the thermodynamic stability of the clusters on the MgO terrace and at the F-centre. Figure-5.25(a) shows the adsorption energy of the parent Pd and Ga clusters as a function of the number of atoms. While the Pd adatom is strongly trapped at the F-centre, it binds relatively weakly on the terrace. The binding energy of the latter is about 2.61 eV lower. As the cluster size grows, the interaction between the surface (both the terrace and at the F-centre) and the cluster weakens. This is because of the strong Pd-Pd interaction compared to the Pd-O interaction. The reduction of the

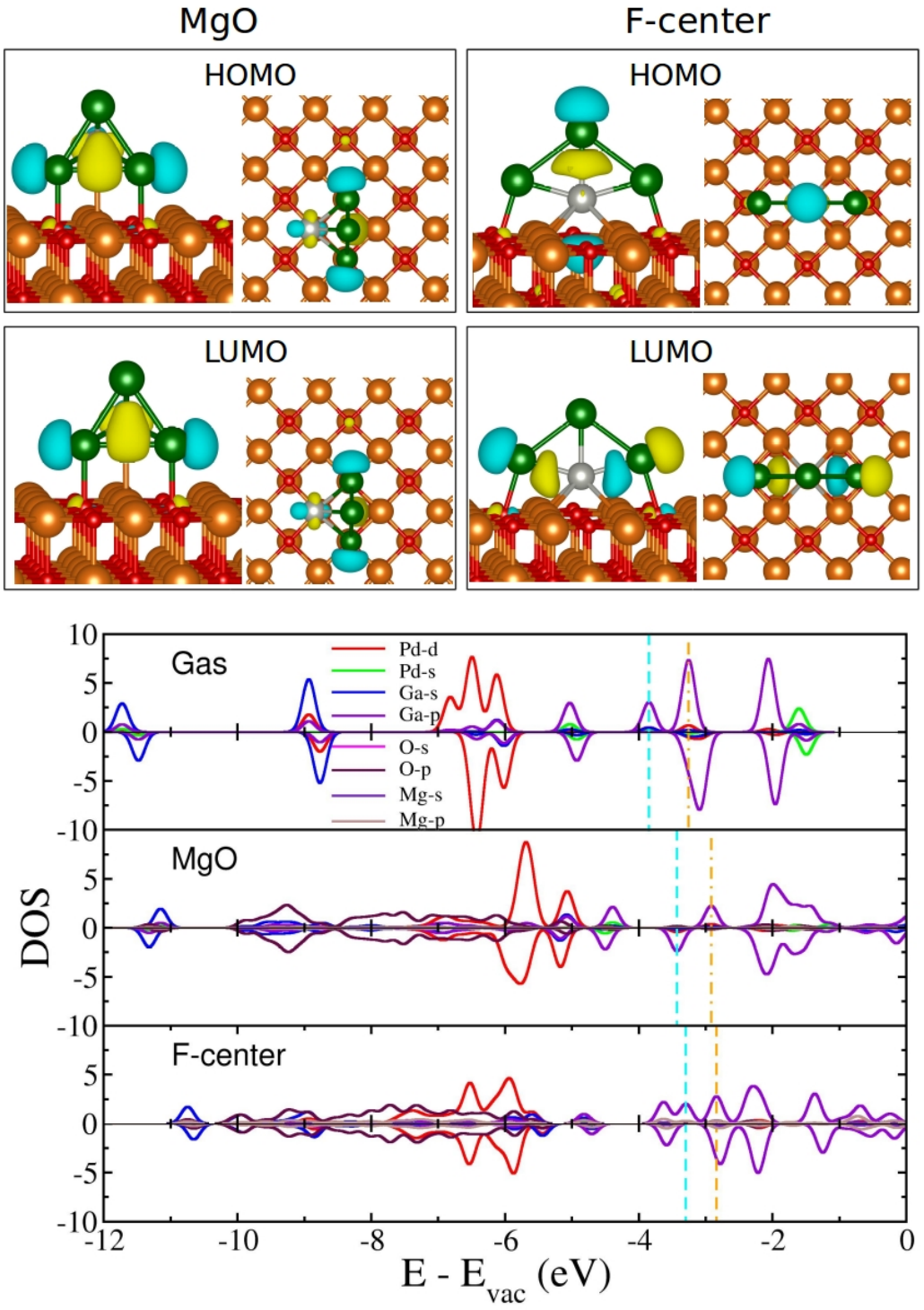

Figure 5.24: The HOMO and LUMO of Pd_1Ga_3 adsorbed at the clean MgO surface and the F-center. The density of states projected on the atomic orbitals of the Pd_1Ga_3. The color code is the same as Figure-5.4.

Table 5.1: Adsorption, binding, formation and mixing energies of Pd_xGa_y clusters on MgO terrace. d_{Pd-Pd}, d_{Pd-Ga} and d_{Ga-Ga} for the Pd_xGa_y clusters adsorbed on MgO terrace.

Cluster	E_{ads} (eV)	E_{bind} (eV)	E_{form} (eV)	E_{mix} (eV)	d_{Pd-Pd} (Å)	d_{Pd-Ga} (Å)	d_{Ga-Ga} (Å)	Magnetic moment (μ_B)	Charge transfer ($\Delta\rho$)
Monomer									
Pd_1	-1.41	-1.41	0.00	-	-	-	-	0.00	0.26
Ga_1	-0.81	-0.81	0.00	-	-	-	-	1.00	0.11
Dimers									
Pd_2	-2.10	-3.46	-0.63	0.00	2.59	-	-	2.00	0.39
Ga_2	-1.41	-2.95	-1.32	0.00	-	-	2.72	2.00	0.18
Pd_1Ga_1	-1.05	-3.98	-1.75	-0.77	-	2.39	-	1.00	0.29
Trimers									
Pd_3	-1.81	-5.99	-1.74	0.00	2.60, 2.58, 2.58	-	-	2.00	0.40
Ga_3 (I)	-1.39	-4.96	-2.52	0.00	-	-	2.66, 2.66	1.00	0.24
Ga_3 (II)	-1.38	-4.95	-2.51	0.01	-	-	2.71, 2.51, 2.51	1.00	0.21
Pd_2Ga_1	-1.68	-6.92	-3.28	-1.27	-	2.37, 2.37	-	1.00	0.51
Pd_1Ga_2	-1.17	-6.76	-3.72	-1.46	-	2.41, 2.41	2.82	0.00	0.24
Tetramers									
Pd_4	-2.07	-9.15	-3.49	0.00	2.63, 2.63, 2.88 2.60, 2.60, 2.62	-	-	2.00	0.53
Ga_4	-2.11	-8.02	-4.77	0.00	-	-	2.68, 2.68, 2.68, 2.68	0.00	0.34
Pd_3Ga_1	-1.86	-9.70	-4.64	-0.83	3.11, 2.65, 2.65	2.44, 2.44, 2.46	-	1.00	0.50
Pd_2Ga_2	-1.18	-10.28	-5.82	-1.69	-	2.42, 2.42, 2.42, 2.42	2.80	0.00	0.33
Pd_1Ga_3	-1.18	-9.13	-5.28	-0.83	-	2.50, 2.50, 2.48	2.99, 2.72, 2.69	1.00	0.27

Table 5.2: Adsorption, binding, formation and mixing energies of Pd_xGa_y clusters binding at F-center. d_{Pd-Pd}, d_{Pd-Ga} and d_{Ga-Ga} for the Pd_xGa_y clusters adsorbed at F-center.

Cluster	E_{ads} (eV)	E_{bind} (eV)	E_{form} (eV)	E_{mix} (eV)	d_{Pd-Pd} (Å)	d_{Pd-Ga} (Å)	d_{Ga-Ga} (Å)	Magnetic moment (μ_B)	Charge transfer ($\Delta\rho$)
Monomer									
Pd_1	-4.02	-4.02	0.00	-	-	-	-	0.00	1.91
Ga_1	-1.20	-1.20	0.00	-	-	-	-	3.00	1.74
Dimers									
Pd_2	-4.56	-5.92	-0.49	0.00	2.72	-	-	0.00	2.12
Ga_2	-2.08	-3.62	-1.60	0.00	-	-	2.61	2.00	1.68
Pd_1Ga_1	-2.83	-5.75	-0.92	-0.98	-	2.47	-	1.00	1.97
Trimers									
Pd_3	-3.95	-8.12	-1.27	0.00	2.64, 2.64	-	-	0.00	2.32
Ga_3 (I)	-2.40	-5.97	-3.15	0.08	-	-	2.57, 2.53	1.00	1.76
Ga_3 (II)	-2.48	-6.05	-3.23	0.00	-	-	2.58, 2.53, 2.58	1.00	1.85
Pd_2Ga_1	-3.49	-8.74	-2.49	-1.30	2.68	2.56, 2.39	-	1.00	2.00
Pd_1Ga_2	-2.23	-7.83	-2.18	-1.09	-	2.43, 2.43	-	0.00	2.06
Tetramers									
Pd_4	-3.77	-10.85	-2.59	0.00	2.62, 2.62, 3.05 2.75, 2.59, 2.59	-	-	0.00	2.20
Ga_4	-3.02	-8.93	-5.30	0.00	-	-	2.57, 2.57, 2.64, 2.64	0.00	1.79
Pd_3Ga_1	-3.82	-11.66	-4.00	-1.29	2.79, 2.79	2.67, 2.36, 2.36	-	1.00	2.21
Pd_2Ga_2	-2.77	-11.87	-4.80	-1.98	2.84	2.55, 2.48, 2.44, 2.44	2.92	0.00	2.01
Pd_1Ga_3	-1.97	-9.93	-3.47	-0.51	-	2.48, 2.48, 2.46	2.98, 2.98	1.00	1.97

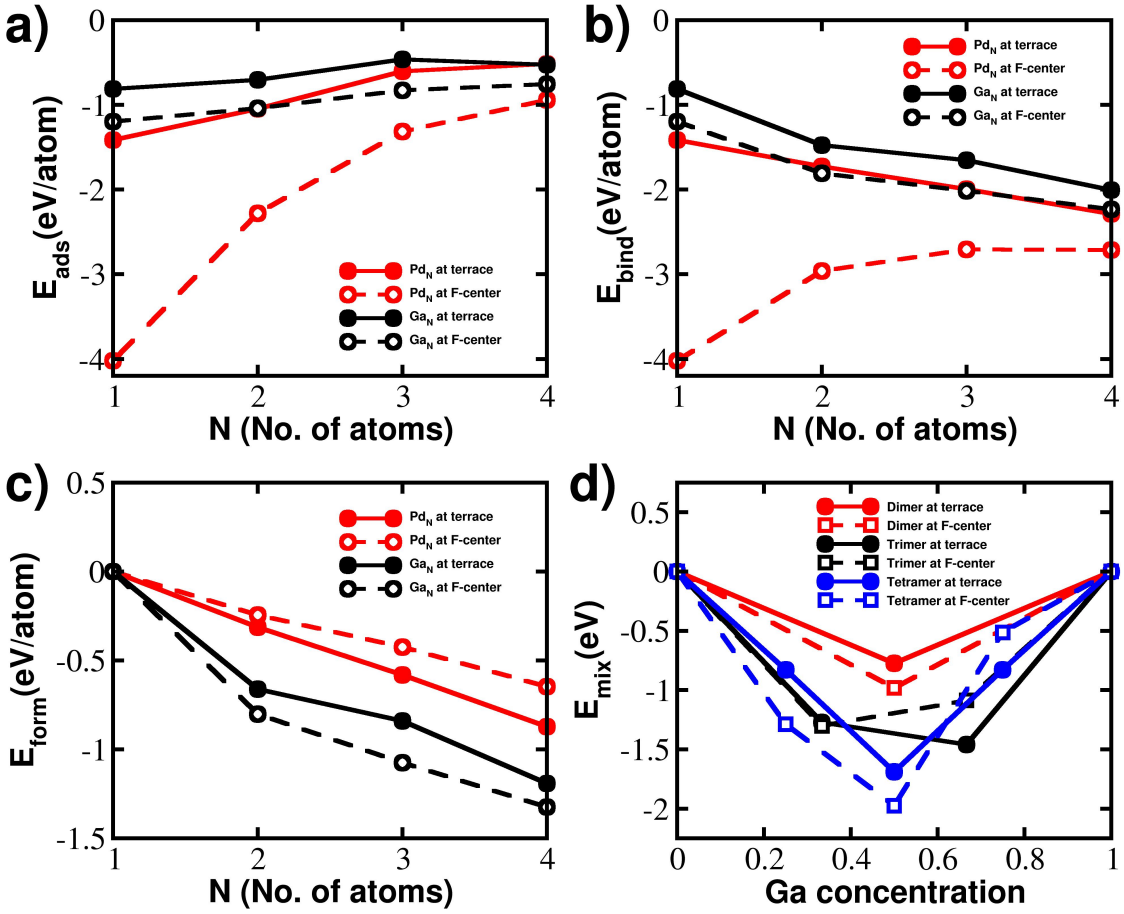

Figure 5.25: (a) Adsorption, (b) binding, (c) formation energies of pure Pd and Ga clusters as a function of cluster size and (d) energy of mixing for the bimetallic clusters as a function of Ga concentration.

adsorption energy of the cluster on the surface is more rapid at the F-centre (from -4.02 eV/atom for the adatom to -0.94 eV/atom for the tetramer) compared to that on the terrace (from -1.41 eV/atom for the adatom to -0.52 eV/atom for the tetramer). However, all the clusters up to the tetramers are more stable at the F-centre than on the terrace. These results show that compared to the trimers and tetramers, it would be extremely difficult to detach the small clusters (monomer and dimer) bound to the F-centre. In contrast to the Pd clusters, the interaction of the Ga adatom with the terrace and the F-centre is relatively weak. For all the Ga clusters considered in this study, they bind more strongly to the F-centre than on the terrace. Further, we observe a very small variation of the adsorption energy of the Ga clusters as a function of their size.

The formation energy calculated using Equation-5.3 presented in Figure-5.25(c) gives the amount of energy released when the cluster is formed starting from metal adatoms deposited on the surface, i.e. the thermodynamic stability of the cluster against decomposition to monomers. The results show that the formation energy of the simple metallic clusters (Pd and Ga) monotonously increases with an increase in the number of atoms. Formation of Pd clusters on the terrace is thermodynamically more stable than the formation at the defect site. However, this trend is reversed for the formation of Ga clusters; the Ga clusters are thermodynamically more stable at the defect site than on the terrace. The greater thermodynamic stability of the Ga clusters at the vacancy site is due to the stronger Ga-Ga interaction, and this is also seen from the shorter Ga-Ga distance for the Ga clusters at the F-center than on the terrace (see Table 5.1 and 5.2). From the energetics, we find that the formation of Ga clusters are thermodynamically more stable than the formation of the Pd clusters.

For the mixed clusters, for a specific size, more than one compositions are possible. For example, three compositions are possible for tetramer cluster (Pd_1Ga_3, Pd_2Ga_2, Pd_3Ga_1). In these mixed clusters, not only the size dependence but also the composition dependence are important since they may have different thermodynamic stability and different chemical properties. The stability of the mixed clusters is explained by the E_{mix} calculated using Equation-5.4. This gives the thermodynamic energy gain when a mixed cluster is formed by pulling atoms out from pure metallic clusters (of the same size as that of the mixed clusters) which are already deposited on the surface. All the mixed Pd_xGa_y clusters are more stable than the parent Pd_N and Ga_N clusters. For a given cluster size, E_{mix} is found to be maximum for the clusters with 1:1 atomic ratio of Pd and Ga (see Table-5.1 and 5.2). It also depends on the number of Pd-Ga bonds present in that particular geometry of the cluster. On terrace Pd_2Ga_2 cluster has maximum E_{mix} of -1.69 eV among tetramer clusters, which has four Pd-Ga bonds. However, the other two clusters Pd_3Ga_1 and Pd_1Ga_3 are having equal E_{mix} of -0.83 eV, since both of them are having three Pd-Ga bonds. The highest value of E_{mix}=-1.98 eV was found for the Pd_2Ga_2 cluster on the F-center. The results also show that in general the mixing energy for the Pd_xGa_y clusters on the F-center is higher than on the terrace except for the Ga rich clusters. The Ga rich clusters have low mixing energy due to the structural deformation.

5.3.3 Thermodynamics of formation of Pd, Ga and PdGa clusters

In order to understand the thermodynamics of the growth process, we assume that Pd/Ga adatoms are soft-landed on the surface. Once the adatoms landed on the terrace, the larger clusters may be formed either at the terrace or the F-centre. Table 5.3 and 5.4 shows all the pathways for the cluster formation. The energies of these reactions are also given. Formation of all the clusters are summarised in Figure 5.26.

The oxygen vacancy sites are generally believed to act as the nucleation site for the growth of small metal clusters. In accordance to this, we find that the binding energies of adatoms (both Pd and Ga) to the vacancy sites are greater than the binding energies on the MgO terrace. The Pd adatom is strongly trapped at the F-center, the difference in the binding energy for adsorption of Pd adatom to the F-center and the MgO terrace is found to be -2.60 eV (dark green dotted line in Figure 5.26). In comparison to the Pd adatoms, the Ga adatoms are weakly trapped at the F-center, the thermodynamic energy difference between the binding of Ga adatom to the F-center and to the MgO terrace is found to be -0.38 eV (red dotted line in Figure 5.26). Because of the low stability at the F-center, at elevated temperature, the Ga adatom trapped at the F-center may escape from the vacancy site depending on the barrier associated with this escape processes. However, the Pd adatoms are strongly trapped at the F-center and can act as the nucleation site at elevated temperature.

Metal adatoms deposited by vapor deposition method primarily land on the terrace of the oxide surface. If these adatoms are mobile on the terrace, the hop from one site to another until they meet another adatom or a small cluster on the terrace or a defect site. Clusters deposited by the size-selective deposition method will also undergo the above-mentioned processes if they are mobile on the surface. Hence, first, we report the diffusion of adatoms and small clusters on the MgO terrace. Diffusion of the Pd clusters on the MgO terrace is extensively studied, [90, 91, 100, 108] hence we report only the most favorable paths. For Ga and PdGa clusters, here we discuss only the path having the lowest diffusion barrier and the other paths are given in Appendix D.

Table 5.3: Summary of all the possible pathways of formation of clusters. F is vacancy site.

Cluster	Reaction step	ΔE (eV)
Pd/F	Pd + F $\rightarrow$ Pd_1/F	-2.60
Ga/F	Ga + F $\rightarrow$ Ga_1/F	-0.38
Pd_2	Pd_1 + Pd_1 $\rightarrow$ Pd_2	-0.63
Pd_2/F	Pd_2 + F $\rightarrow$ Pd_2/F	-2.47
Pd_2/F	Pd_1 + Pd/F $\rightarrow$ Pd_2/F	-0.49
Ga_2	Ga_1 + Ga_1 $\rightarrow$ Ga_2	-1.33
Ga_2/F	Ga_2 + F $\rightarrow$ Ga_2/F	-0.67
Ga_2/F	Ga_1 + Ga/F $\rightarrow$ Ga_2/F	-1.60
Pd_1Ga_1	Ga_1 + Pd_1 $\rightarrow$ Pd_1Ga_1	-1.75
Pd_1Ga_1/F	Pd_1Ga_1 + F $\rightarrow$ Pd_1Ga_1/F	-1.78
Pd_1Ga_1/F	Ga_1 + Pd/F $\rightarrow$ Pd_1Ga_1/F	-0.92
Pd_1Ga_1/F	Pd_1 + Ga_1/F $\rightarrow$ Pd_1Ga_1/F	-3.14
Pd_3	Pd_1 + Pd_2 $\rightarrow$ Pd_3	-1.12
Pd_3/F	Pd_3 + F $\rightarrow$ Pd_3/F	-2.14
Pd_3/F	Pd_2 + Pd/F $\rightarrow$ Pd_3/F	-0.65
Pd_3/F	Pd + Pd_2/F $\rightarrow$ Pd_3/F	-0.78
Ga_3	Ga_1 + Ga_2 $\rightarrow$ Ga_3	-1.20
Ga_3/F	Ga_3 + F $\rightarrow$ Ga_3/F	-1.09
Ga_3/F	Ga_2 + Ga/F $\rightarrow$ Ga_3/F	-1.90
Ga_3/F	Ga + Ga_2/F $\rightarrow$ Ga_3/F	-1.62
Pd_1Ga_2	Pd_1 + Ga_2 $\rightarrow$ Pd_1Ga_2	-2.40
Pd_1Ga_2	Ga_1 + Pd_1Ga_1 $\rightarrow$ Pd_1Ga_2	-1.97
Pd_1Ga_2/F	Pd_1Ga_2 + F $\rightarrow$ Pd_1Ga_2/F	-1.07
Pd_1Ga_2/F	Ga_2 + Pd/F $\rightarrow$ Pd_1Ga_2/F	-0.86
Pd_1Ga_2/F	Ga_1 + Pd_1Ga_1/F $\rightarrow$ Pd_1Ga_2/F	-1.26
Pd_1Ga_2/F	Pd_1 + Ga_2/F $\rightarrow$ Pd_1Ga_2/F	-2.80
Pd_1Ga_2/F	Pd_1Ga_1 + Ga_1/F $\rightarrow$ Pd_1Ga_2/F	-2.66
Pd_2Ga_1	Pd_2 + Ga_1 $\rightarrow$ Pd_2Ga_1	-2.65
Pd_2Ga_1	Pd_1 + Pd_1Ga_1 $\rightarrow$ Pd_2Ga_1	-1.53
Pd_2Ga_1/F	Pd_2Ga_1 + F $\rightarrow$ Pd_2Ga_1/F	-1.82
Pd_2Ga_1/F	Pd_2 + Ga/F $\rightarrow$ Pd_2Ga_1/F	-4.08
Pd_2Ga_1/F	Pd_1 + Pd_1Ga_1/F $\rightarrow$ Pd_2Ga_1/F	-1.57
Pd_2Ga_1/F	Ga_1 + Pd_2/F $\rightarrow$ Pd_2Ga_1/F	-2.00
Pd_2Ga_1/F	Pd_1Ga_1 + Pd_1/F $\rightarrow$ Pd_2Ga_1/F	-0.74
Pd_4	Pd_1 + Pd_3 $\rightarrow$ Pd_4	-1.75
Pd_4	Pd_2 + Pd_2 $\rightarrow$ Pd_4	-2.24
Pd_4/F	Pd_4 + F $\rightarrow$ Pd_4/F	-1.70
Pd_4/F	Pd_3 + Pd_1/F $\rightarrow$ Pd_4/F	-0.84
Pd_4/F	Pd_2 + Pd_2/F $\rightarrow$ Pd_4/F	-1.47
Pd_4/F	Pd_1 + Pd_3/F $\rightarrow$ Pd_4/F	-1.31

Table 5.4: Summary of all the possible pathways of formation of clusters. F is vacancy site.

Cluster	Reaction step	ΔE (eV)
Ga_4	$Ga_1 + Ga_3 \rightarrow Ga_4$	-2.25
Ga_4	$Ga_2 + Ga_2 \rightarrow Ga_4$	-2.12
Ga_4/F	$Ga_4 + F \rightarrow Ga_4$/F	-0.91
Ga_4/F	$Ga_3 + Ga_1$/F $\rightarrow Ga_4$/F	-2.77
Ga_4/F	$Ga_2 + Ga_2$/F $\rightarrow Ga_4$/F	-2.37
Ga_4/F	$Ga_1 + Ga_3$/F $\rightarrow Ga_4$/F	-2.07
Pd_1Ga_3	$Ga_3 + Pd_1 \rightarrow Pd_1Ga_3$	-2.75
Pd_1Ga_3	$Ga_2 + Pd_1Ga_1 \rightarrow Pd_1Ga_3$	-2.21
Pd_1Ga_3	$Ga_1 + Pd_1Ga_2 \rightarrow Pd_1Ga_3$	-1.56
Pd_1Ga_3/F	$Pd_1Ga_3 + F \rightarrow Pd_1Ga_3$/F	-0.79
Pd_1Ga_3/F	$Pd_1Ga_2 + Ga_1$/F $\rightarrow Pd_1Ga_3$/F	-1.96
Pd_1Ga_3/F	$Pd_1Ga_1 + Ga_2$/F $\rightarrow Pd_1Ga_3$/F	-2.34
Pd_1Ga_3/F	$Pd_1 + Ga_3$/F $\rightarrow Pd_1Ga_3$/F	-2.46
Pd_1Ga_3/F	$Ga_3 + Pd_1$/F $\rightarrow Pd_1Ga_3$/F	-0.94
Pd_1Ga_3/F	$Ga_2 + Pd_1Ga_1$/F $\rightarrow Pd_1Ga_3$/F	-1.23
Pd_1Ga_3/F	$Ga_1 + Pd_1Ga_2$/F $\rightarrow Pd_1Ga_3$/F	-1.28
Pd_2Ga_2	$Pd_1 + Pd_1Ga_2 \rightarrow Pd_2Ga_2$	-2.10
Pd_2Ga_2	$Pd_2 + Ga_2 \rightarrow Pd_2Ga_2$	-3.87
Pd_2Ga_2	$Pd_2Ga_1 + Ga_1 \rightarrow Pd_2Ga_2$	-2.54
Pd_2Ga_2	$Pd_1Ga_1 + Pd_1Ga_1 \rightarrow Pd_2Ga_2$	-2.32
Pd_2Ga_2/F	$Pd_2Ga_2 + F \rightarrow Pd_2Ga_2$/F	-1.59
Pd_2Ga_2/F	$Pd_1Ga_2 + Pd_1$/F $\rightarrow Pd_2Ga_2$/F	-1.08
Pd_2Ga_2/F	$Ga_2 + Pd_2$/F $\rightarrow Pd_2Ga_2$/F	-3.00
Pd_2Ga_2/F	$Pd_2Ga_1 + Ga_1$/F $\rightarrow Pd_2Ga_2$/F	-3.75
Pd_2Ga_2/F	$Pd_2 + Ga_2F \rightarrow Pd_2Ga_2$/F	-4.80
Pd_2Ga_2/F	$Pd_1Ga_1 + Pd_1Ga_1$/F $\rightarrow Pd_2Ga_2$/F	-2.14
Pd_2Ga_2/F	$Pd_1 + Pd_1Ga_2$/F $\rightarrow Pd_2Ga_2$/F	-2.62
Pd_2Ga_2/F	$Ga_1 + Pd_2Ga_1$/F $\rightarrow Pd_2Ga_2$/F	-2.32
Pd_3Ga_1	$Pd_3 + Ga_1 \rightarrow Pd_3Ga_1$	-1.96
Pd_3Ga_1	$Pd_2 + Pd_1Ga_1 \rightarrow Pd_3Ga_1$	-2.26
Pd_3Ga_1	$Pd_1 + Pd_2Ga_1 \rightarrow Pd_3Ga_1$	-1.36
Pd_3Ga_1/F	$Pd_3Ga_1 + F \rightarrow Pd_3Ga_1$/F	-1.96
Pd_3Ga_1/F	$Pd_3 + Ga_1$/F $\rightarrow Pd_3Ga_1$/F	-4.47
Pd_3Ga_1/F	$Pd_2 + Pd_1Ga_1$/F $\rightarrow Pd_3Ga_1$/F	-2.45
Pd_3Ga_1/F	$Pd_1 + Pd_2Ga_1$/F $\rightarrow Pd_3Ga_1$/F	-1.51
Pd_3Ga_1/F	$Ga_1 + Pd_3$/F $\rightarrow Pd_3Ga_1$/F	-2.72
Pd_3Ga_1/F	$Pd_1Ga_1 + Pd_2$/F $\rightarrow Pd_3Ga_1$/F	-1.76
Pd_3Ga_1/F	$Pd_2Ga_1 + Pd_1$/F $\rightarrow Pd_3Ga_1$/F	-0.72

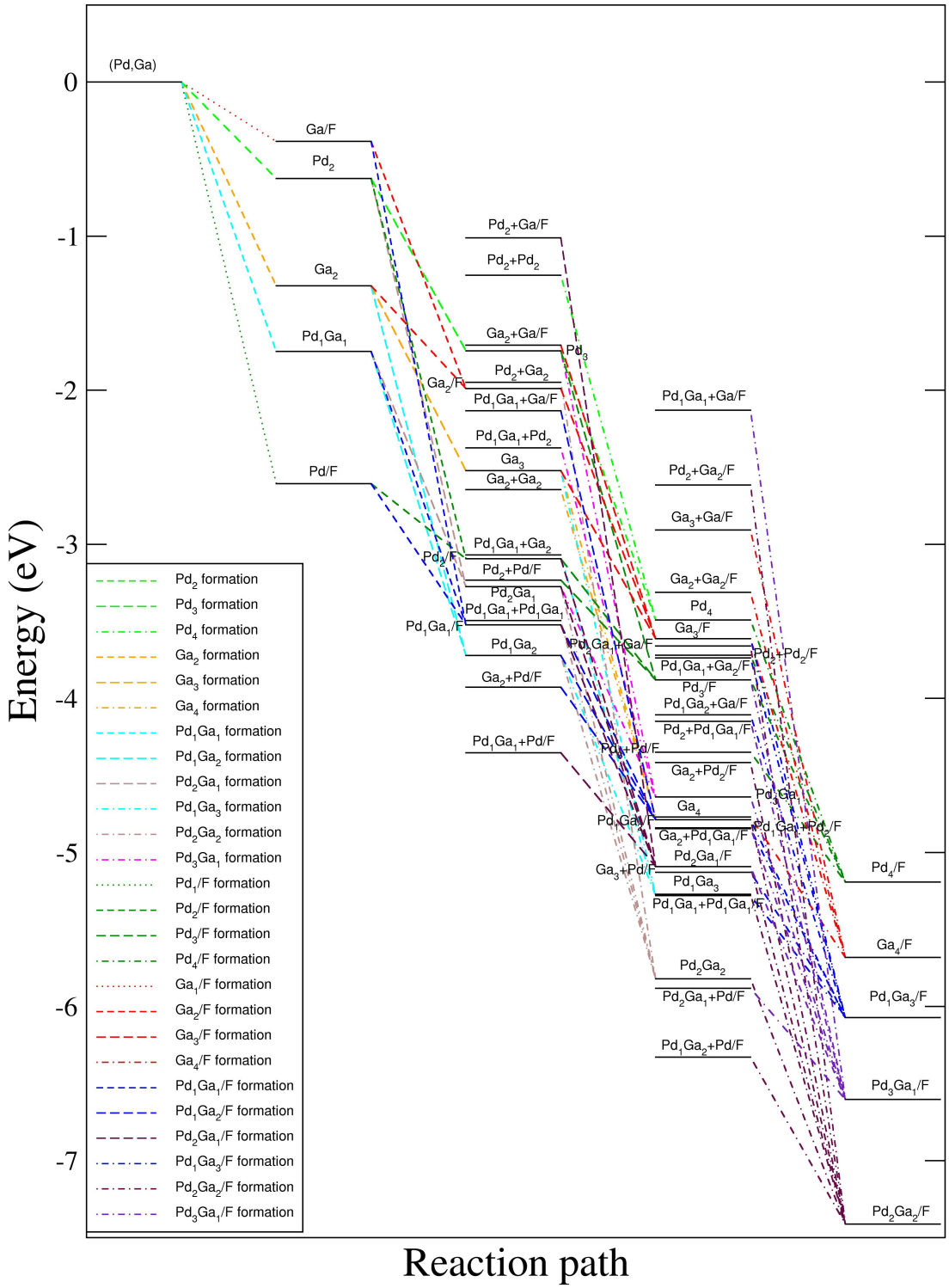

Figure 5.26: Thermodynamic energetics for the growth of small Pd, Ga and PdGa clusters on the MgO terrace and at the F-center.

5.3.4 Diffusion of small clusters on MgO (100) surface

5.3.4.1 Adatoms: Hopping mechanism of adatoms

Pd_1: The Pd adatom adsorbed on top of oxygen site of MgO terrace diffuses to the next neighboring oxygen site by direct hopping. The diffusion barrier associated with this process is found to be 0.40 eV. At the saddle point, the Pd adatom sits above the hollow site. The energy profile for the Pd adatom diffusion on the MgO terrace is shown in Figure 5.27(a). The top view of the geometries of the initial state, transition state and the final state are given as insets. We obtained an Arrhenius prefactor of 4.2×10^{11} s^{-1} from the Equation 5.7 for the Pd adatom hopping and the rate constant is estimated to be 9.0×10^4 s^{-1} at 300 K. A high value of the rate constant suggests that the Pd adatoms are quite mobile on the terrace. Our results for the Pd adatom diffusion on MgO terrace is consistent with the previous reports. [90, 91, 100, 106, 108, 109]

Ga_1: Similar to Pd adatom, Ga adatom also diffuses on the MgO terrace by direct hopping from one oxygen site to the neighboring oxygen site. At the saddle point, the Ga adatom sits on the hollow site. The diffusion barrier for the Ga adatom hopping on the MgO terrace is found to be 0.06 eV. The energy profile for the diffusion of Ga adatom on the MgO terrace, the top views of the initial state, transition state and the final state are given in Figure 5.27(b). Arrhenius prefactor for the Ga adatom diffusion on MgO is calculated to be 1.4×10^{12} s^{-1}. The rate constant at 300 K is estimated to be 1.4×10^{11} s^{-1}. We note that the Ga adatom is freely mobile on the surface and its diffusion rate is about 10^6 times faster than that of the Pd adatom diffusion. The very low activation energy for the Ga adatom hopping is attributed to the weak interaction with the support; thus, it is freely mobile on the support.

5.3.4.2 Dimers: Diffusion

Pd_2: The Pd_2 cluster diffuses on MgO terrace through partial dissociation and association mechanism, and this involves two steps. In the first step, the Pd dimer sitting on top of two neighboring oxygen sites partially dissociates to form an intermediate state where the Pd-Pd bond distance is increased from 2.81 Å at the initial state to 3.10 Å at the intermediate state. The partial dissociation involves a 45° clockwise rotation of the cluster. The barrier associated with the partial dissociation of the Pd dimer is calculated to be 0.44 eV. The

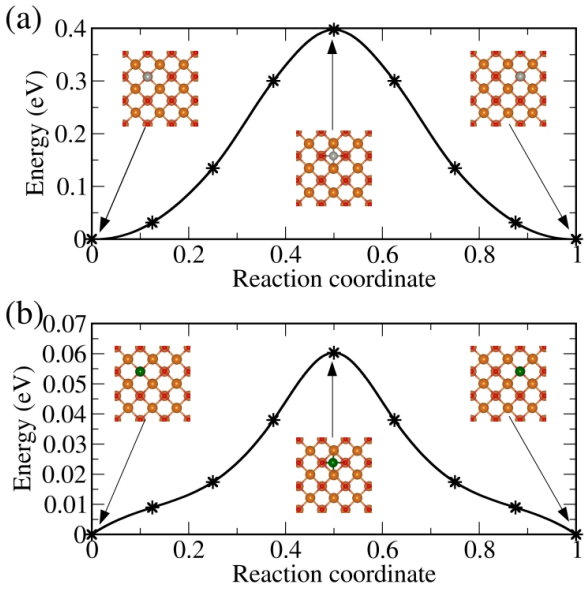

Figure 5.27: Diffusion of (a) Pd and (b) Ga adatoms on MgO(100) surface. Orange, red, gray and green color balls respectively represent Mg, O, Pd and Ga atoms. Top views of the initial state, saddle point and the final state are given as insets.

second step is the reverse of the first one; in this step, the partially dissociated Pd dimer reassociates to form the stable Pd dimer. This reassociation involves a 45° anti-clockwise rotation of the cluster. The barrier associated with the reassociation of the dimer is found to be 0.12 eV. The energy profile for this diffusion mechanism is shown in Figure-5.28(a). The rate constant for the diffusion of Pd dimer on the MgO at 300 K is found to be 1.9 $\times$ 10^4 s^{-1}. We note that the diffusion rates of Pd adatom and dimer are of similar order of magnitude, with the former diffusing slightly faster. Our results are in excellent agreement with those reported in the literature. [90, 91, 106, 108]

Ga_2: The Ga dimer sitting on top of two neighboring surface oxygen sites on MgO terrace diffuses to the next site through a sliding mechanism. For the dimer to slide on the surface, it needs to overcome a barrier of 0.45 eV. At the saddle point, both the Ga atoms are sitting above the hollow site with the Ga-Ga bond stretched to 2.96 Å from 2.72 Å at the initial state. Figure-5.28(b) shows the energy profile for the sliding mechanism of Ga dimers on MgO. The top view of the initial state, saddle point and the final state are given as insets. The rate of diffusion for the Ga dimer on MgO terrace is calculated to be 5.7 $\times$ 10^4 s^{-1} at 300 K. A high value of the rate constant for the Ga dimer on MgO terrace

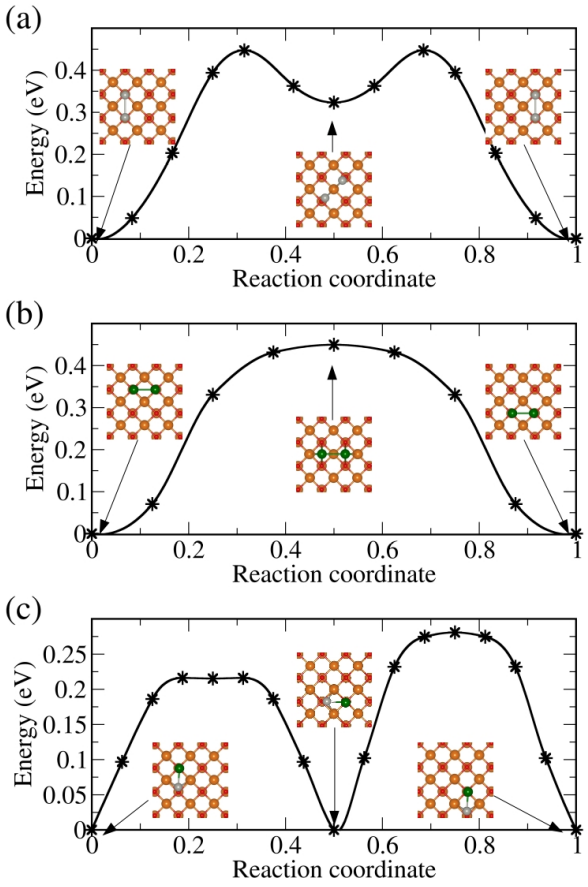

Figure 5.28: Diffusion of dimers on MgO surface. (a) Partial dissociation mechanism for Pd dimer, (b) sliding mechanism for Ga dimer and (c) walking mechanism for PdGa dimer. Orange, red, gray and green color balls respectively represent Mg, O, Pd and Ga atoms.

suggest that the Ga dimer is highly mobile on the MgO surface. While the Ga adatom is freely mobile on the MgO terrace, Ga dimer has a mobility that is similar to Pd dimer on the MgO terrace.

Pd_1Ga_1: The Pd_1Ga_1 cluster sitting on top of two oxygen sites on MgO terrace diffuses to the next site by walking mechanism. This walking mechanism involves two steps. The first step involves a 90° rotation of Pd_1Ga_1 about the Pd atom. The barrier associated with this rotation is about 0.22 eV. At the saddle point, the Pd atom occupies the oxygen atop site while the Ga atom sits on top of the surface Mg atom. However, only the Pd atom is interacting to the surface with a an O-Pd distance of 2.21 Å while the Mg-Ga distance is found to be 3.66 Å. This strengthens the Pd-Ga interaction with shortening of Pd-Ga bond length to 2.32 Å. In contrast to the pure dimers, for which the metal-metal bond distance increases at the saddle point compared with initial state, for bimetallic Pd_1Ga_1 we found a slight shortening of Pd-Ga bond at the saddle point (from 2.39 Å at the initial state to 2.32 Å at the saddle point). The second step is also a 90° rotation; however, in this step, the cluster rotates in the reverse direction about the Ga atom of the cluster. This 90° rotation involves a diffusion barrier of 0.28 eV. At this second saddle point, the Ga atom sits on top of the oxygen atom while the Pd sits on top of surface Mg. The Pd-Ga bond distance decreases to 2.35 Å at the saddle point from 2.39 Å at the initial state. The energetics for the diffusion of Pd_1Ga_1 is shown in Figure-5.28(c). The diffusion of Pd_1Ga_1 involves two distinct steps that are having two different barriers. In this situation one can assume that the slower step determines the overall diffusion rate. Since the second step is the slower one the barrier and the prefactor associated to this step is used as the overall barrier and prefactor to calculate the overall diffusion rate. The rate constant for the diffusion of Pd_1Ga_1 is calculated to be 1.5×10^7 s^{-1} at 300 K. The high rate constant suggests that the diffusion of bimetallic Pd_1Ga_1 cluster on MgO terrace is about 10^2 times faster than that of the parent Pd and Ga dimers.

5.3.4.3 Trimers: Diffusion

Pd_3: The Pd_3 cluster diffuses on MgO(100) surface through a two-step skating mechanism. Initially the Pd_3 is bound vertically to the terrace where two of the Pd atoms are on top of two surface oxygen atoms. In the first diffusion step, the cluster diffuses to an intermediate state (about 0.18 eV higher in energy than the most stable initial state) in

which the Pd atoms that are interacting with the surface are bound to two O atoms, the latter having an Mg atom between them. In order to reach this intermediate, the cluster rotates by about 45° about one of the Pd atoms anchored to the surface oxygen site. At the saddle point, the Pd atom that moves occupy the hollow site. This diffusion process has a barrier of 0.34 eV associated with it. In the second step, the cluster diffuses from the intermediate to the final state through further rotation of 45°. However, the rotation is in the reverse direction compared to that of the first step, and the Pd atom that was mobile in the previous step is now fixed while the fixed Pd atom in the previous step is now mobile. The diffusion barrier associated with this process is calculated to be 0.17 eV. The energy profile for the complete diffusion process for the Pd_3 cluster on the MgO terrace is shown in Figure 5.29(a). The rate constant for the diffusion of the Pd_3 cluster on the MgO terrace at 300 K is estimated to be 9.0×10^4 s^{-1}. Our calculated barrier of 0.34 eV for the Pd trimer walking on MgO terrace is in good agreement with the barrier of 0.30 eV reported by Barcaro *et al.* [100] However, Xu *et al.* reported a larger value of 0.48 eV, for the Pd trimer walking on MgO. [90, 91] Moreover, Xu *et al.* reported that a flipping mechanism for Pd trimer also have a similar barrier of 0.50 eV. However, we find a barrier of 0.43 eV for the flipping mechanism of Pd trimer on the MgO terrace (Figure-D.11 of Appendix D).

Ga_3: The diffusion of Ga trimer on the MgO surface occurs through a rolling mechanism involving four similar steps. In the initial state, all three Ga atoms are on top of three surface oxygen atoms making an 'L' shaped geometry. In the first step, the cluster moves to an intermediate (about 0.01 eV higher in energy than the initial state) where it is vertically on top of two surface O atoms and forms an isosceles triangle (Fig 5.29(b)). This involves a barrier of about 0.32 eV. In the next step, the Ga atom (that is not interacting with the surface) of this vertical cluster falls on the O atom at the other side. The barrier of "toppling" of this cluster is about 0.31 eV. The next two steps are similar to the first two. However, in this case, the orientation of the vertical cluster is rotated by 90 ° with respect to that observed in the first intermediate. The energy profile of the complete diffusion mechanism of Ga trimer cluster on MgO terrace is shown in Figure-5.29(b). Similar to Pd_1Ga_1 for this case also the overall rate constant is calculated using the barrier associated with the slower step and the corresponding prefactor. The rate constant for this diffusion process at 300 K is calculated to be 3.6×10^6 s^{-1}. We note that the rate of diffusion of Ga trimer on the MgO surface is about 10^2 times faster than the diffusion of Ga dimer.

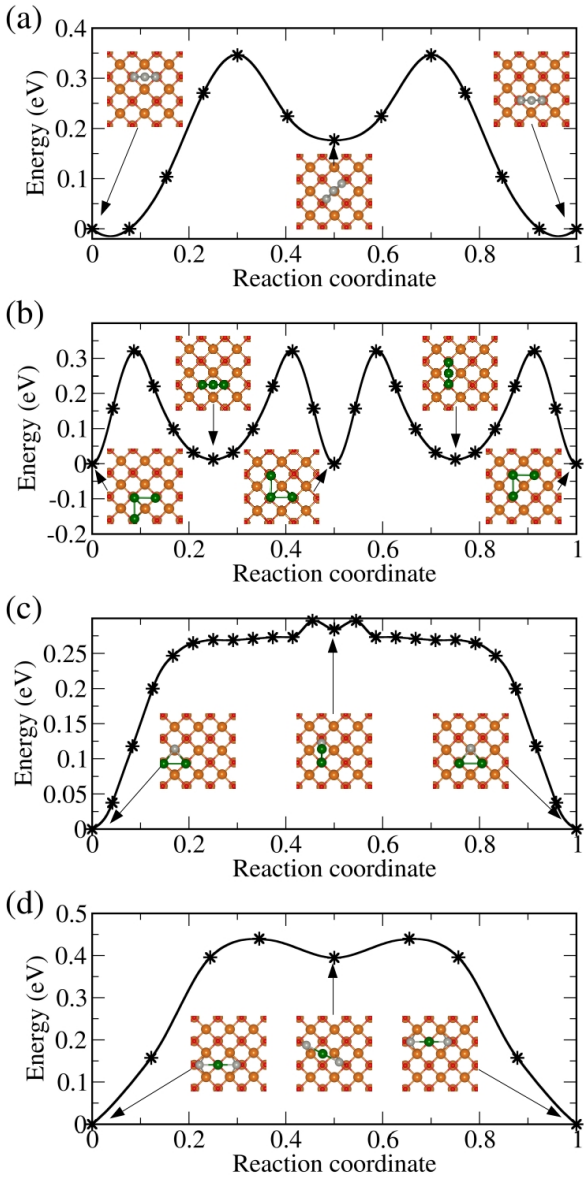

Figure 5.29: Diffusion of trimer on MgO surface. (a) Skating mechanism for Pd trimer, (b) rolling mechanism for the Ga trimer, (c) rolling mechanism for Pd_1Ga_2 cluster and (d) skating mechanism for the Pd_2Ga_1 cluster.

Pd_1Ga_2: In the initial state, Pd_1Ga_2 has a triangular structure and horizontally binds to the surface with two Ga atoms occupying the O sites and the Pd sits on Mg site. The lowest energy pathway for the diffusion of Pd_1Ga_2 clusters involves a transition from a horizontal configuration in the initial state to a vertical one at an intermediate state (0.28 eV higher in energy than the initial state). The barrier associated with this step is about 0.30 eV. In the next step the cluster rolls from the intermediate state to the final state, and for this process, the cluster requires to overcome a very small barrier of 0.02 eV. The energy profile for the diffusion of Pd_1Ga_2 clusters through rolling mechanism is given in Figure-5.29(c). The Pd_1Ga_2 clusters are freely mobile on the MgO terrace, the rate constant for the diffusion of Pd_1Ga_2 clusters at 300 K is calculated to be 4.0×10^9 s^{-1}.

Pd_2Ga_1: The Pd_2Ga_1 cluster diffuses on MgO terrace through skating mechanism, which involves two steps. Figure-5.29(d) shows the complete energy profile for the diffusion of Pd_2Ga_1 cluster on MgO through skating mechanism. In the initial state, all three atoms of the Pd_2Ga_1 cluster are sitting on top of the three surface oxygen sites, such that the Ga atom is at the center and both the Pd atoms occupy two sides. In the first step, one of the Pd atoms moves to the next neighboring oxygen site, and the Ga atom adjusts its position accordingly to form an intermediate state. At the intermediate state, the Ga atom occupies the hollow site. This intermediate state is 0.39 eV less stable than the most stable initial state. The Pd_2Ga_1 cluster requires to overcome a diffusion barrier of 0.44 eV for this process to occur. The second step is the mirror image of the first process, in this step, the Pd_2Ga_1 cluster at the intermediate step diffuses to the final state. This process has a very small barrier of 0.05 eV associated with it. The rate constant for the diffusion of Pd_2Ga_1 cluster on MgO terrace is calculated to be 4.0×10^6 s^{-1}. We note that the Pd rich Pd_2Ga_1 clusters are highly mobile on the MgO terrace and their mobility is comparable to that observed for the Ga trimer.

5.3.4.4 Tetramers: Diffusion

Pd_4: The Pd_4 clusters diffuse on MgO surface by following the rolling mechanism. In the initial state, one of the Pd atoms is sitting on top of the surface O site, and two of the Pd atoms are occupying the Mg-O bridge site. These three atoms make the base for the tetrahedron, and the fourth Pd atom is standing upright. In the first step, the cluster rolls to the next nearest site with a barrier of 0.41 eV. At the saddle point, two of the Pd

atoms are binding on top of two nearby surface oxygen sites and other two Pd atoms are standing upright thereby retaining the tetrahedron structure. Figure-5.30(a) shows the energy profile of this rolling mechanism of Pd_4 cluster diffusion on MgO terrace. The rate constant for the diffusion of Pd_4 clusters on MgO terrace is calculated to be 2.5×10^7 s^{-1} at 300 K. We note that among the Pd clusters considered in this study the diffusion of Pd_4 on the MgO terrace is the fastest process, this process is about 10^3 times faster than the diffusion of other Pd clusters on MgO terrace. Out results for the diffusion of Pd_4 on the MgO terrace is consistent with the previous reports. [90, 91, 106, 108]

Ga_4: The Ga_4 clusters also migrate trough the rolling mechanism on the MgO(100) surface. In the initial state, all the four Ga atoms are occupying the O site. The Ga_4 cluster sitting on top of four oxygen sites of the MgO terrace in a planar geometry rolls to the next sites retaining the planar geometry. At the saddle point, the cluster moves to a vertical position retaining the original square geometry. The Ga_4 cluster needs to overcome a barrier of 1.04 eV for this rolling process. The energy profile for the rolling mechanism of Ga_4 cluster on MgO terrace is given in Figure-5.30(b). The rate of diffusion of Ga_4 cluster on MgO terrace at 300 K is calculated to be 5.2×10^{-6} s^{-1}. We note that among the four atom clusters considered in this study the Ga_4 cluster has the slowest diffusion rate.

Pd_1Ga_3: In the initial state, the tetrahedron Pd_1Ga_3 cluster binding to the MgO surface through Pd_1Ga_2 face. The Pd_1Ga_3 cluster diffuses on MgO(100) surface by a combined clockwise-anticlockwise rotation of the cluster by 45 ° about one of the Ga atoms that are interacting with the surface. Figure-5.30(c) shows the energy profile of the diffusion process. The clockwise rotation to an intermediate involves a barrier of about 0.34 eV. The anticlockwise rotation of the cluster from this intermediate to the final one involves a barrier of about 0.23 eV. The overall diffusion barrier associated with sliding mechanism is calculated to be 0.56 eV. The rate constant for the Pd_1Ga_3 cluster diffusion on MgO(100) surface at 300 K is calculated to be 3.0×10^2 s^{-1}. We note that the calculated diffusion rate for Pd_1Ga_3 cluster on MgO terrace is about 10^5 times slower than that of Pd_4 cluster and about 10^8 times faster than that of Ga_4 cluster.

Pd_2Ga_2: The rhombus Pd_2Ga_2 binding to the surface such that the Ga atoms occupy the O sites and the Pd atoms occupy the Mg sites. Similar to Pd_1Ga_3, diffusion of Pd_2Ga_2 cluster on MgO(100) also involves a combined clockwise-anticlockwise rotation by 45 °.

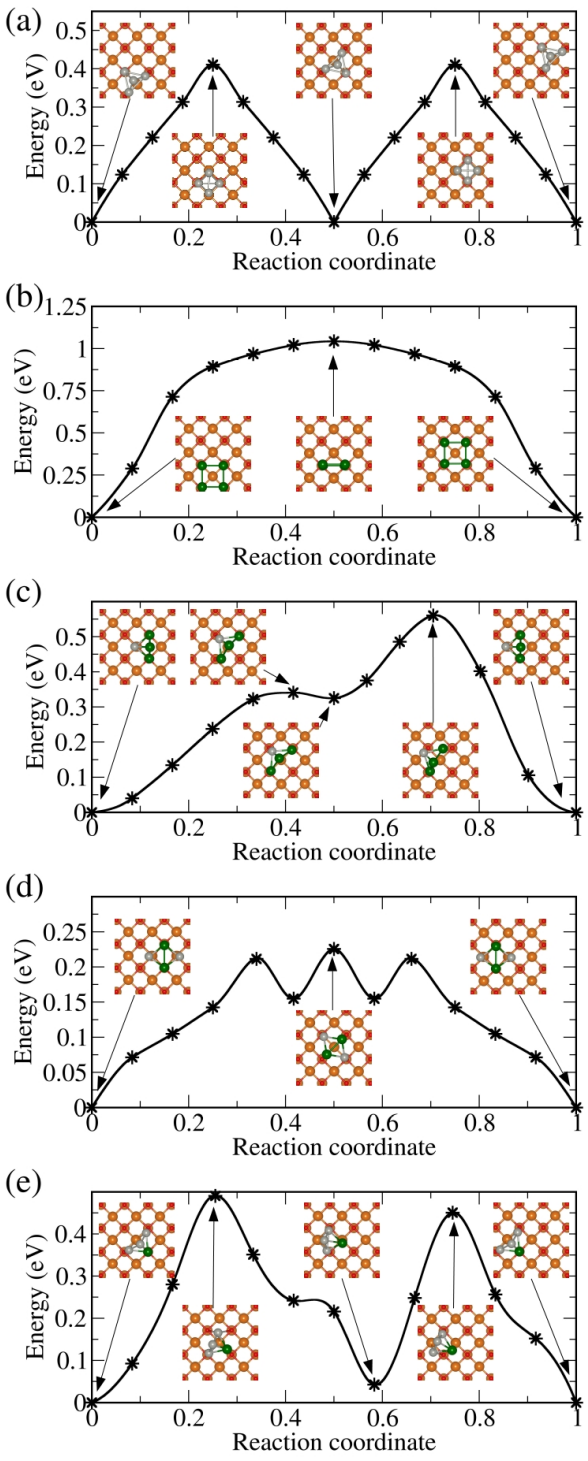

Figure 5.30: Diffusion of tetramer on MgO surface. (a) and (b) are the rolling mechanism of Pd_4 and Ga_4 respectively. (c), (d) and (e) are the sliding mechanism respectively for the Pd_1Ga_3, Pd_2Ga_2 and Pd_3Ga_1 clusters.

However, unlike Pd_1Ga_3, the whole Pd_2Ga_2 cluster rotates about the surface normal. After the first rotation, the cluster reaches a saddle point in which the mid-point of the Pd-Pd/ Ga-Ga bond is atop of Mg atom. The process involves a barrier of 0.22 eV. The rate of the Pd_2Ga_2 cluster sliding on MgO(100) terrace at 300 K is calculated to be 6.9×10^6 s^{-1}. The calculated diffusion rate for the Pd_2Ga_2 cluster is comparable to the Pd_4 cluster. The energy profile for this sliding mechanism of Pd_2Ga_2 cluster diffusion on MgO(100) is given in Figure-5.30(d).

Pd_3Ga_1: The Pd_3Ga_1 clusters also diffuse on MgO(100) surface by following a mechanism that is similar to that of Pd_1Ga_3 clusters. This also involves two steps in which the cluster rotates in the opposite direction in each step to slide. In the initial state, the Ga atom sitting on top of oxygen site and two Pd atoms on the bridge sites make the base triangle of the tetrahedron geometry, and the third Pd is sitting on top of the base triangle and connected with all three atoms. First, the cluster diffuses to an intermediate state in which both the Pd atoms of the base triangle sitting on top of the surface oxygen sites and the Ga atom is on top of the Mg site. This process has a diffusion barrier of 0.49 eV associated with it. In the next step, the cluster in the intermediate state diffuses to the next nearest stable site with a barrier of 0.45 eV. The energy profile of this diffusion mechanism is given in Figure-5.30(e). The rate of diffusion of Pd_3Ga_1 clusters on MgO surface at 300 K is calculated to be 1.1×10^4 s^{-1}.

Despite all three bimetallic tetramers diffuse on the MgO terrace by a combined clockwise-anticlockwise rotation of the cluster by 45 °, the diffusion barriers associated with the Pd rich Pd_3Ga_1 cluster and Ga rich Pd_1Ga_3 cluster is about 0.3 eV larger than that of barrier associated with the 1:1, Pd_2Ga_2 cluster. The low barrier associated with the Pd_2Ga_2 diffusion is attributed to the shape of the cluster. The rhombus structure allows the atoms in Pd_2Ga_2 cluster to rotate without going through the high energy hollow site. However, the Pd rich Pd_3Ga_1 (Ga rich Pd_1Ga_3) interact to the surface through the Pd_2Ga_1 (Pd_1Ga_2) face. The triangular face interacting to the surface must go through a transition state where one of the atoms occupy the hollow site.

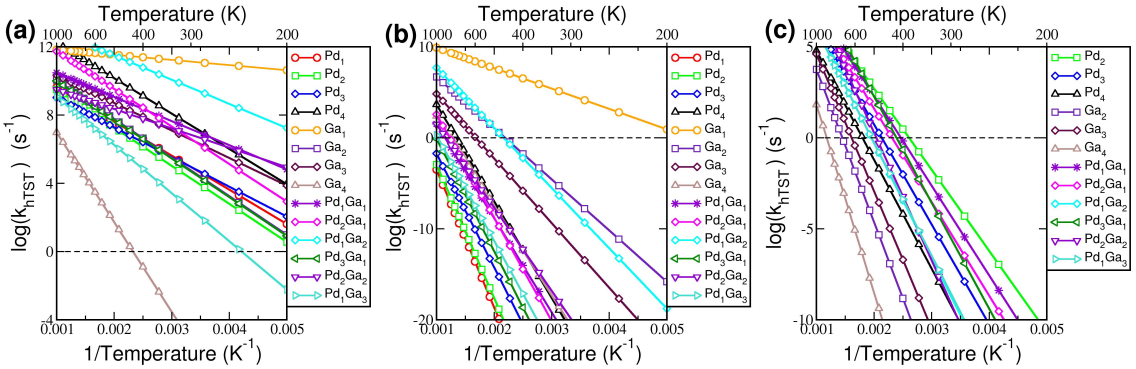

Figure 5.31: (a) log(k_{hTST}) for the diffusion of small clusters on MgO terrace for a temperature range of 200 K to 1000 K. (b) log(k_{hTST}) for the escape of clusters from vacancy site for a temperature range of 200 K to 1000 K. (c) log(k_{hTST}) for the decomposition of small clusters at the vacancy site for a temperature range of 200 K to 1000 K.

5.3.5 Cluster nucleation: Thermodynamic and kinetic stability

The metal clusters on MgO can nucleate either by heterogeneous nucleation or by homogeneous nucleation. In heterogeneous nucleation the metal cluster nucleates at the vacancy sites. The metal adatom hopping over the terrace gets strongly trapped at the vacancy site when it encounters a vacancy site. When a second metal atom comes in the vicinity of such metal adatom trapped at the vacancy site that also gets trapped. The metal cluster builds up at the vacancy site by the further addition of metal atoms which are diffusing over the terrace. In the homogeneous nucleation when a metal adatom encounters another adatom on the terrace, it forms an immobile or less mobile dimer. The less mobile clusters build up larger clusters by the addition of more adatoms which are diffusing on the terrace to it. This nucleation occurs homogeneously all over the terrace. The cluster nucleus should have enough thermodynamic and kinetic stability in order to use them to make a sintering resistive clusters.

A metal cluster on the oxide support is said to be thermodynamically stable if the energy of formation for that particular cluster from the constituent metal adatom deposited on the oxide surface is negative. We find that all the clusters reported in this study are thermodynamically stable and the clusters bound to the oxygen vacancy site are having a higher thermodynamic stability than the clusters bound to the MgO terrace.

A metal cluster deposited or formed on the oxide substrate is said to be kinetically stable

Table 5.5: Diffusion mechanisms and the required activation energy for clusters on MgO surface, corresponding Arrhenius prefactors and the diffusion rate at 300 K.

	Diffusion on terrace				Escape from F-center	Decomposition at F-center
Cluster	Diffusion mechanism	Barrier (eV)	ν (s^{-1})	k_{hTST} at 300 K (s^{-1})	k_{hTST} at 300 K (s^{-1})	k_{hTST} at 300 K (s^{-1})
Pd_1	Hopping	0.40	4.2×10^{11}	9.0×10^{4}	1.5×10^{-39}	-
Pd_2	Partial dissociation	0.44	5.3×10^{11}	1.9×10^{4}	6.8×10^{-38}	5.7×10^{-4}
Pd_3	Skating	0.34	5.9×10^{10}	9.0×10^{4}	1.2×10^{-31}	2.6×10^{-7}
Pd_4	Rolling	0.41	2.0×10^{14}	2.5×10^{7}	6.9×10^{-22}	6.5×10^{-10}
Ga_1	Hopping	0.06	1.4×10^{12}	1.4×10^{11}	4.6×10^{4}	-
Ga_2	Sliding	0.45	2.0×10^{12}	5.7×10^{4}	3.6×10^{-7}	1.5×10^{-16}
Ga_3	Rolling	0.32	8.7×10^{11}	3.6×10^{6}	1.8×10^{-12}	7.3×10^{-17}
Ga_4	Rolling	1.04	1.7×10^{12}	5.2×10^{-6}	2.6×10^{-21}	5.3×10^{-23}
Pd_1Ga_1	Skating	0.28	7.8×10^{11}	1.5×10^{7}	2.2×10^{-23}	5.2×10^{-5}
Pd_1Ga_2	Rolling	0.30	2.1×10^{14}	4.0×10^{9}	1.8×10^{-8}	2.0×10^{-9}
Pd_2Ga_1	Skating	0.44	8.7×10^{13}	4.0×10^{6}	1.2×10^{-24}	5.6×10^{-6}
Pd_1Ga_3	Sliding	0.56	7.8×10^{11}	3.0×10^{2}	1.6×10^{-27}	2.8×10^{-9}
Pd_2Ga_2	Sliding	0.23	4.3×10^{10}	6.9×10^{6}	1.3×10^{-20}	8.4×10^{-10}
Pd_3Ga_1	Sliding	0.49	1.9×10^{12}	1.1×10^{4}	1.1×10^{-29}	3.1×10^{-6}

if the cluster is immobile and non-decomposable at the reaction conditions. Figure 5.31(a) shows the log(k_{hTST}) for the diffusion of the small cluster on the MgO terrace as a function of the inverse of temperature. We find that the Ga adatoms are freely mobile on MgO terrace and the rate of diffusion for the Ga adatoms on MgO is more or less independent of the temperature due to the very small diffusion barrier (about 0.06 eV) associated with this process. Moreover, the Ga adatoms have highest diffusion rate among the clusters considered in this study. For all other clusters, the rate of diffusion significantly increases with increasing temperature. All the clusters except Ga tetramer are found to be highly mobile on the MgO terrace even at low temperatures such as 300 K. The high mobility of these clusters suggest that the small clusters deposited or formed on the MgO terrace are kinetically less stable and diffuse over the terrace until it finds a strong trapping site like vacancy site. However, the Ga tetramers deposited or formed on the MgO terrace are immobile at low temperatures and act as the cluster nucleus for the formation of larger clusters for temperatures below 440 K.

The clusters trapped at the oxygen vacancy site should not escape from the vacancy site to call it kinetically stable. The log(k_{hTST}) for the escape of small Pd, Ga and PdGa clusters from the oxygen vacancy site within a temperature range of 200 K to 1000 K is given in Figure 5.31(b) and the rate constant for the escape of Pd, Ga and PdGa clusters from the vacancy site at 300 K is given in Table 5.5. A positive value for log(k_{hTST}) signifies that the cluster can escape from the vacancy site within one second and a negative value means the cluster cannot escape from the vacancy in the time scale of second and may escape at longer time depending on the value. The diffusion of adatoms and smaller clusters are occurring in the millisecond timescale. Hence, an event that occurs beyond one second may not have any significant effect in the nucleation kinetics. For all the clusters the rate of escape increases with increasing temperature. We find that the Ga adatoms readily escape from the vacancy site even at a temperature as low as 200 K while the Pd adatoms are strongly trapped at the vacancy site and will not escape from the vacancy site even at a high temperature such as 800 K. In addition to the contrary behavior of the Ga and Pd adatoms, we also find that as the size of the Ga cluster increases the rate of escape from the vacancy site decreases. The escaping temperatures (T at which the rate constant for the escape becomes greater than 1) for the Ga_2, Ga_3 and Ga_4 clusters are respectively calculated to be 460, 600 and 800 K. In contrast to the Ga clusters, the Pd clusters are stable against the escape at least up to 1000 K, except the Pd tetramer for which the escape tem-

perature is calculated to be 760 K. Moreover, for the Pd clusters, the rate of escape from the vacancy site increases with increasing size of the cluster. These results suggest that for the Ga clusters the binding strength of the clusters to the oxygen vacancy site increases with the addition of more Ga adatom to the cluster while for the Pd clusters the binding strength of the clusters to the oxygen vacancy site decreases with the addition of more Pd adatoms to the cluster. The mixed clusters show the mixed behavior, the Pd_1Ga_2 cluster starts to escape from the vacancy site at a temperature of 480 K and the other clusters are stable against the escape up to 800 K.

A kinetically stable cluster bound to the vacancy site should not decompose into smaller fragments at the reaction conditions. Figure 5.31(c) presents the log(k_{hTST}) for the decomposition of small clusters at the oxygen vacancy site as a function of temperature and the k_{hTST} at 300 K is given in Table 5.5. The rate constant for decomposition of all the clusters considered in this study increases with increasing temperature. We find that for the Pd clusters as their size increase the rate of decomposition of the clusters decreases. A Pd_n cluster trapped at the vacancy site decompose into Pd_{n-1} adsorbed on the terrace and a Pd adatom trapped at the vacancy site. The decomposition temperatures (T at which the rate constant for the decomposition of the cluster becomes greater than 1) for Pd_2, Pd_3 and Pd_4 clusters are calculated to be 400, 480 and 560 K respectively. In contrast to the Pd clusters, Ga_n cluster trapped at the vacancy site decompose into Ga_{n-1} cluster trapped at the vacancy site and Ga adatom adsorbed on the MgO terrace. Moreover, the Ga clusters decompose at a higher temperature, the decomposition temperatures for Ga_2, Ga_3 and Ga_4 clusters are calculated to be 700, 640 and 800 K respectively. Due to the strong binding of Pd adatom to the F-center compared to the Ga adatom, the Pd_xGa_y cluster trapped at the vacancy site decompose into $Pd_{x-1}Ga_y$ adsorbed on the MgO terrace leaving a Pd adatom trapped at the vacancy site. The decomposition temperature for the mixed clusters is found to be higher than that of Pd_2 decomposition but lower than that of Ga_4 clusters decomposition. The decomposition temperatures for the Pd_1Ga_1, Pd_2Ga_1, Pd_1Ga_2, Pd_3Ga_1, Pd_2Ga_2 and Pd_1Ga_3 clusters are respectively found to be 420, 440, 520, 420, 500 and 520 K. We note that Ga_2, Ga_3 and Pd_1Ga_2 clusters tend to escape from the vacancy site than decompose, whereas all other clusters tend to decompose rather than escape from the vacancy site.

5.3.6 Growth of small clusters on MgO: KMC simulation results

The growth of the small clusters on the MgO (100) surface can be affected by various factors such as temperature, metal adatom deposition rate, defect concentration, type of metal atoms deposited, binding strength of clusters to the surface, mobility of the clusters on the terrace, thermodynamic and kinetic stability of the clusters etc. From the Section 5.3.5, we find that the small Pd, Ga, PdGa clusters are thermodynamically stable. However, these clusters are highly mobile on the surface, and their kinetic stability is significantly affected by the temperature. In order to understand the growth of these small clusters on the MgO terrace we have performed the KMC simulations. All the elementary reaction steps accounted for in the KMC simulations are given in Appendix B. In this work, we focused on the nucleation of cluster islands in the growth process. The formation of the stable nucleus is the critical process in the growth of the metal clusters; larger clusters can be formed by the addition of more adatoms to the cluster nucleus. Our KMC simulations carried out by employing the energetics of up to tetramer clusters can capture the cluster nucleation and island density qualitatively for temperatures below ripening temperature. We note that it is plausible to capture the size and shape of the cluster islands for temperatures above ripening temperature by including the energetics of clusters larger than tetramer clusters. However, the growth process is already complicated with 170 elementary reaction steps, and hence adding the energetics of larger clusters will drastically increase the complexity of the pathways and hence, the growth process above ripening temperature including the size and shape of the cluster islands will be studied in future work. In order to account for the trapping sites present in the MgO surface, about 0.25% of neutral oxygen vacancies (F center) are introduced. However, the MgO surface may also contain other types of vacancies like the charged vacancies (F^+ center), double vacancies and other complicated trapping sites. [110] Xu *et al.* had shown that adsorption of Pd adatom to the F^+ center weaker than that to the F center. Due to the weak surface metal atom interaction, the metal-metal interaction in the cluster binding at F^+ center is stronger compared to the cluster binding at the F center. [106] The stronger metal-metal interaction at the F^+ center increase the cluster decomposition temperature thus increase in the cluster ripening temperature. Before discussing the results of the bimetallic cluster, first, we present our results for the growth of pure Pd and Ga clusters on the MgO surface.

5.3.6.1 Growth of Pd clusters

Growth mechanism of Pd clusters on the MgO surface is extensively studied both experimentally and theoretically. [90–92, 100] Using variable temperature atomic force microscopy Haas *et al.* predicted that increasing the Pd adatom deposition rate speeds up the island formation while the number of Pd islands formed (island density) is constant. The estimated island density of 3×10^{12} cm^{-2} is equal to that of the defect concentration. [92] The authors also reported that the island density is constant up to 600 K and starts to decrease for temperatures above 600 K. The decrease in the cluster island density at high temperatures are attributed to the decomposition of Pd clusters initially formed at the vacancy sites.

The Pd adatoms randomly deposited on the MgO terrace diffuse over the terrace until they meet a vacancy site or another adatom or small cluster on the terrace. When a Pd adatom diffusing over the terrace encounters a vacancy site it gets strongly trapped there. Similarly, when a Pd adatom diffusing over the MgO terrace encounters a Pd adatom trapped at the vacancy site (Pd/F-center), that also gets trapped and forms a Pd dimer at the vacancy site. If the Pd adatom diffusing over the terrace meets another Pd adatom on the terrace before meeting a Pd/F-center complex, Pd dimer is formed on the terrace. The Pd dimer and other small clusters formed on the terrace are also diffusing over the terrace until they bind to the vacancy site. The larger clusters are build up at the vacancy site by adding the Pd adatom and the small clusters diffusing over the terrace.

Figure 5.32(a) shows the bare surface with no Pd adatom adsorbed. At very low temperature such as 200 K, the rate of diffusion of Pd adatom on the terrace is low ($k_{hTST} \sim 4$ s^{-1}) and adatoms deposited on the terrace start to form dimers as early as 3 seconds (see encircled region of Figure 5.32(b)). These dimers formed on terrace stay at the vicinity of where it is initially formed (encircled region of Figure 5.32(c)) until another Pd adatom encounters this dimer to form a trimer cluster (encircled region of Figure 5.32 (d)). Similar to the dimers, the trimers also stay close to where they were formed. Because of the low diffusion rate of dimer and trimer on the terrace, initially, a substantial amount of small Pd clusters are formed on the terrace (see Figure 5.32(e)). The cluster nucleation is observed all over the terrace, and small clusters are formed on the terrace even before all the vacancy sites are occupied at least by a Pd adatom. This initial nucleation before the tetramer formation follows homogeneous nucleation as defined in the beginning of Section 5.3.5.

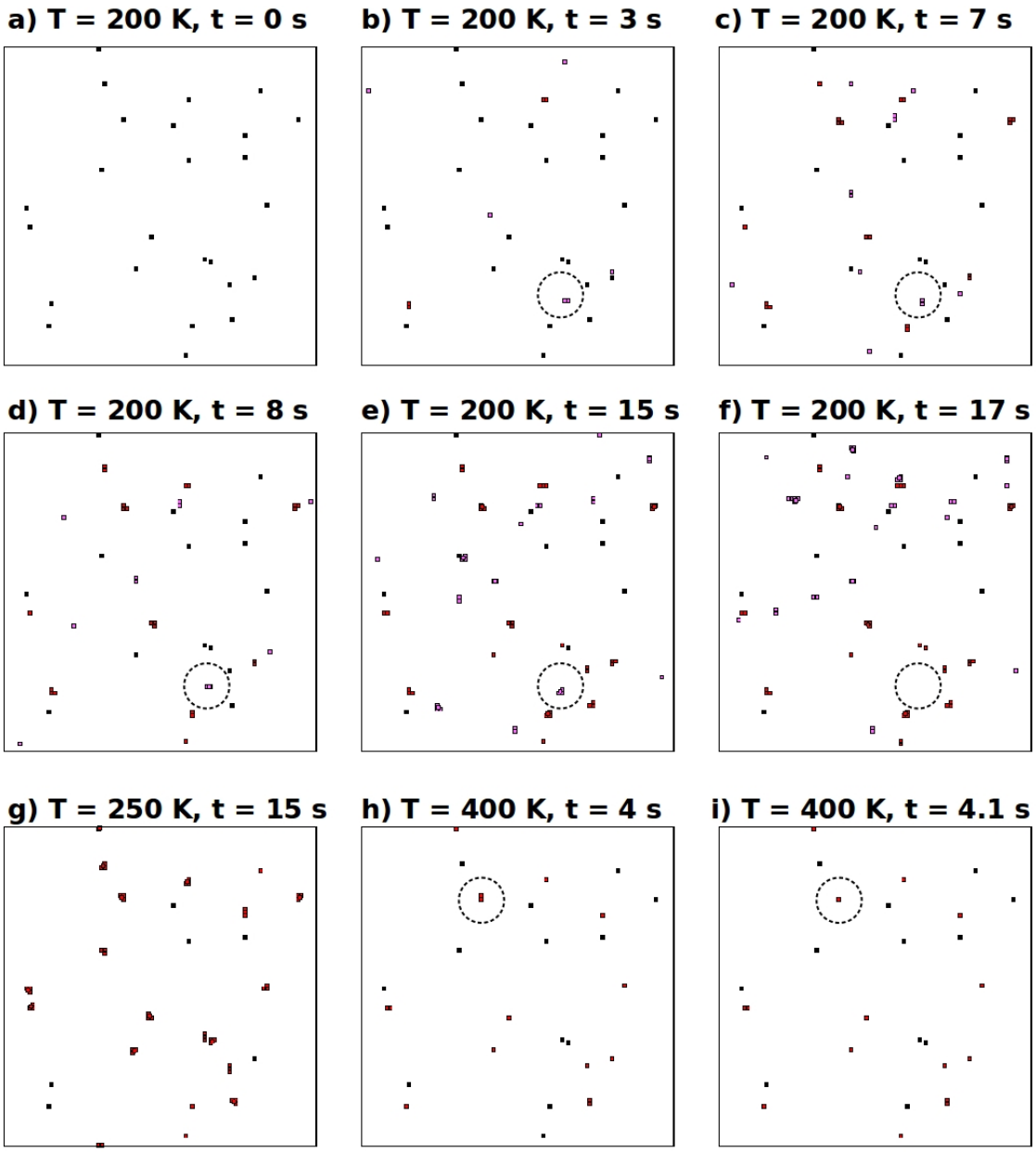

Figure 5.32: Growth of Pd clusters on MgO surface. Black filled squares represent the vacancy sites with no atom occupied. Magenta and red color filled squares represent Pd atoms adsorbed on the terrace and at the F-center respectively.

The tetramers that are formed on the terrace are highly mobile (see the disappearance of clusters from the encircled region in Figure 5.32(f)). Hence, these diffuse over the surface and bind to the vacancy site to build the large clusters. After equilibrium is established between the formation of small clusters on the terrace and at the vacancy site, the cluster growth changes from homogeneous nucleation towards heterogeneous nucleation. A slight increase in the temperature to 250 K, shifts the initial nucleation process towards the heterogeneous nucleation due to the significant increase in the rate of diffusion of Pd adatom on the terrace ($k_{hTST} \sim 10^3$ s^{-1}). At 250 K, the Pd adatoms randomly deposited on the terrace diffuse over the surface and get trapped at the vacancy site. No formation of small clusters at the terrace sites was seen up to 15 seconds (see Figure 5.32(g)), because of the high mobility of Pd adatoms. Before any dimer is formed on the terrace, the adatom gets trapped at the vacancy site. The clusters build on the adatoms trapped vacancy site by heterogeneous nucleation. This growth process is same up to 400 K.

The formation energy of -0.49 eV for the Pd dimer on the vacancy site is not strong enough to hold the cluster together at 400 K and above. At 400 K, the dimers initially formed at the F-center rapidly dissociate into monomers; these monomers diffuse on the terrace until they get irreversibly trapped at F-center. This continues till all the vacancies are occupied by a Pd adatom. Figure 5.32(h) shows the formation of Pd dimer at the vacancy site at 4.0 second (see the encircled region), and this dimer dissociates into monomers at 4.1 seconds (Figure 5.32(i)). As soon as all the vacancy sites are occupied after a quick equilibrium is established between the small mobile cluster on the terrace and those at the defects more stable trimer and tetramer clusters are formed at the F-center.

The cluster island density is calculated by counting all the clusters except the monomers adsorbed on the terrace and at the vacancy site. We obtained a island density of 3.6 $\times 10^{12}$ cm^{-2} at 200 K, and 2.7 $\times 10^{12}$ cm^{-2} for a temperature range of 225 K to 375 K. The calculated island density at 200 K is slightly higher than the experimentally reported value of 2.3 $\times 10^{12}$ cm^{-2} while the value obtained for the temperature range 225 K to 375 K is consistent with the experiment. The discrepancy in the calculated island density at 200 K with the experiment is due to the fact that we do not include the formation of clusters larger than the tetramer clusters. Hence, a tetramer formed on the terrace cannot bind to the vacancy site which is occupied by small clusters. These tetramers formed on the terrace are over counted, the island density calculated by neglecting these tetramers on

the terrace gave consistent value with the experiment (2.9 $\times 10^{12}$ cm^{-2}). Using DFT and KMC simulations, Xu *et al.* [106] reported that at 200 K the island density would be overestimated by 30% if the tetramers are assumed to be immobile. Moreover, the calculated island density and the growth process predicted for the formation of small clusters are consistent with the previous theoretical reports. [91, 106]

With a given enough Pd concentration and time the clusters at F-centers will grow larger. Using variable temperature atomic force microscopy Haas *et al.* showed that the ripening occurs at a high temperature such as above 600 K. [92] At this temperature the cluster nucleus (dimers, trimers and tetramers) formed at the F-center will decompose leaving a Pd adatom strongly trapped at the F-center. However, the very large clusters formed at the F-center will be stable against decomposition. In contrast to the experiment, Xu *et al.* predicted the ripening temperature for the Pd clusters at the F-center to be 400 K assuming that the decomposition temperature for the dimer binding at the F-center to be the ripening temperature. [106] We also see that the dimer dissociates at 400 K and our calculated ripening temperature of 400 K is in good agreement with the reports of Xu *et al.* Assuming the charged defects to be the nucleation sites, Xu *et al.* predicted the ripening temperature (560 K) close to the experimentally reported one. For an accurate prediction of the ripening temperature, one needs to model the MgO surface with exact proportion of the various defect sites present in the surface, which are further dependent on the surface preparation methods and conditions. However, we are interested in understanding the formation of the cluster nucleus at the MgO surface created with neutral vacancy site. The effect of the charged vacancies and other complex vacancies on the ripening temperature is the future scope of this work.

5.3.6.2 Growth of Ga clusters

The growth mechanism of the Ga clusters on the MgO surface is completely different from that of Pd clusters. Even at a very low temperature such as 200 K, the Ga adatoms are highly mobile on the MgO terrace ($k_{hTST} \sim 8$ s^{-1} at 200 K). Figure 5.33(a) shows the bare surface with no Ga adatom adsorbed. The Ga adatoms randomly deposited over the MgO terrace freely hops over the surface until it encounters a vacancy site. Due to very high mobility, as soon as the Ga adatom landed the terrace, it binds to the vacancy site. The encircled region in Figure 5.33(b) shows the Ga adatom binding to the vacancy site.

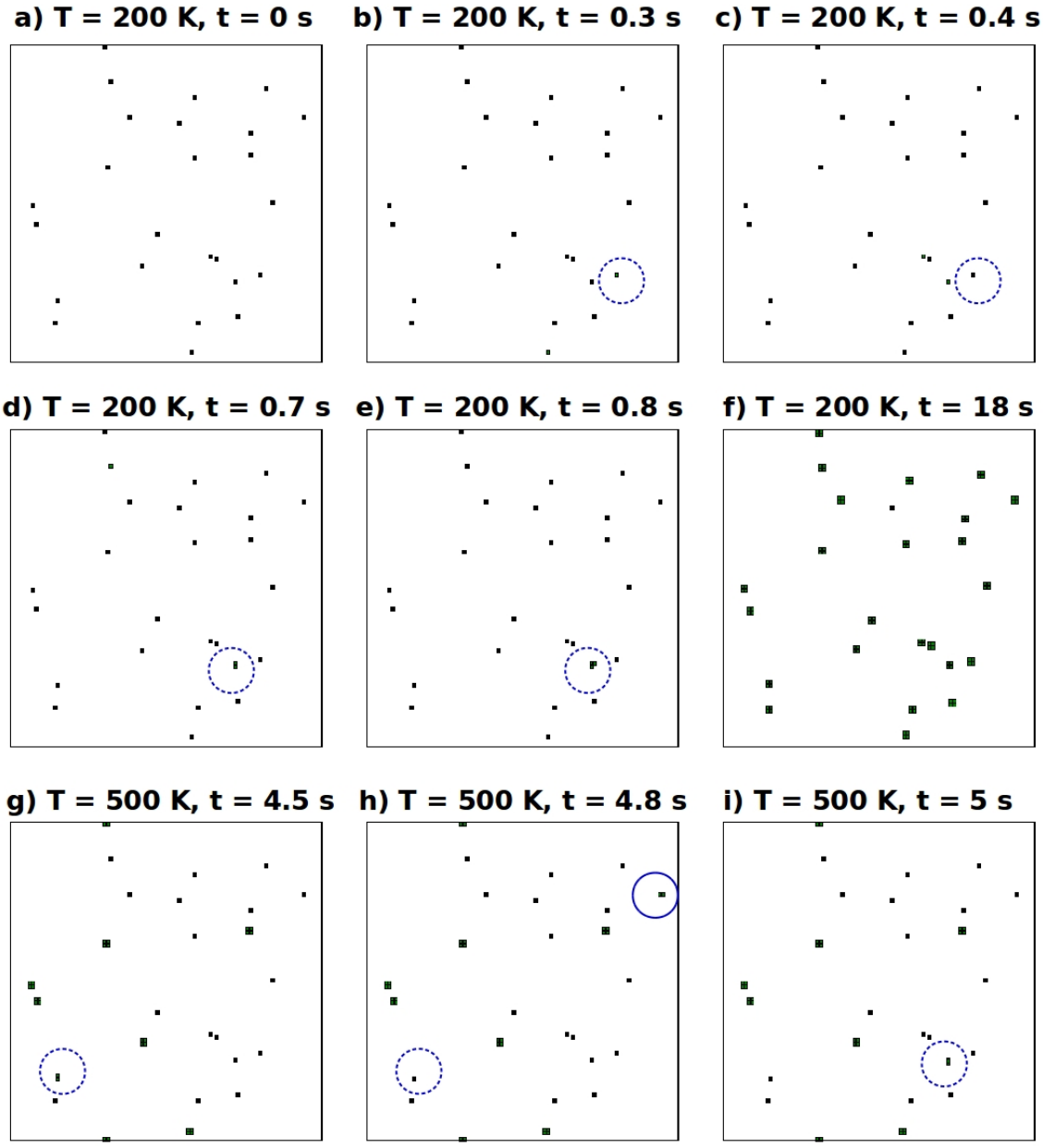

Figure 5.33: Growth of Ga clusters on MgO surface. Black filled squares represent the vacancy sites with no atom occupied. Green and dark green color represent Ga atoms adsorbed on the terrace and at the F-center respectively.

However, the binding energy of -0.39 eV for the Ga adatom on the oxygen vacancy site is not strong enough to hold the clusters at the vacancy site. The Ga adatom binding to the vacancy site readily escapes from the vacancy site ($k_{hTST} \sim 8$ s^{-1} at 200 K). The Ga adatom binding to the vacancy at 0.3 second (encircled region in Figure 5.33(b)) escaped at 0.4 second (the encircled region in Figure 5.33(c)). When a Ga adatom diffusing over the terrace encounters a Ga adatom bound to the vacancy site, a more stable Ga dimer is formed at the vacancy (encircled region in Figure 5.33(d)). Unlike the Ga adatom which readily escapes from the vacancy site, the Ga dimers are strongly bound to the vacancy and escape only at temperatures above 460 K. The large Ga clusters are build up by adding more number of Ga adatoms to the Ga dimer at the vacancy (encircled region in Figure 5.33(e)). The cluster nuclei are formed only at the vacancy sites, no cluster formation is seen on the terrace site (Figure 5.33(f)). The growth of Ga clusters at low temperature is happening through heterogeneous nucleation.

In contrast to the Pd dimer clusters adsorbed at the vacancy site in which the Pd atoms weakly bound and tend to dissociate into adatoms for temperatures above 400 K, the atoms in Ga dimers are strongly bound and tend to be stable up to 700 K. However, the Ga dimer is weakly bound at the vacancy site and tend to escape from the vacancy for temperatures above 460 K. The Ga adatom rapidly escape from the vacancy site for temperatures above 300 K, the rate constant for the escape of Ga adatom from the vacancy site at 300 K is calculated to be 4.6×10^4 s^{-1}. This very high escaping rate of Ga adatom from the vacancy sites becomes a limitation to study the growth at high temperatures.

The low barrier of a process becoming the limiting factor to the accesible time scale of the KMC simulation is commonly known as “the low barrier problem”. [2] One plausible solution to overcome this limitation is artificially increasing the barrier associated with the fastest process. However, increasing the barrier of the fastest process to that of the second fastest process will affect the qualitative depiction of the growth mechanism. For an accurate depiction of the growth mechanism, the fastest process should be reasonably well equilibrated under the conditions of interest. There is no straightforward way to test on how much the barrier can be increased so that the dynamic will not be spuriously affected by this artificial increase of barrier. However, it is safe to assume that the fastest process will be well equilibrated if it is kept at least 10 times faster than that of the second fastest process. The fastest and second fastest processes for the growth of Ga clusters are

diffusion of adatom and trimer respectively. Thus, the limitation is not coming from the fastest process. Moreover, artificially increasing the diffusion barrier of Ga adatom will decrease the mobility of the Ga adatom; consequently, that would lead to the formation of dimers and larger clusters on the MgO terrace. This makes the growth follow homogeneous nucleation. However, the growth of Ga clusters happens through heterogeneous nucleation. Thus, artificially increasing the barrier of Ga adatom diffusion will change the qualitative picture of the growth mechanism. Hence, diffusion barriers cannot be artificially increased. Since the escape of Ga adatom from the vacancy site is causing the low barrier limitation, this barrier can be artificially increased.

In order to study the growth of Ga clusters at high temperatures, the barrier associated to the Ga adatom escape from the vacancy site is artificially increased to 0.95 eV. We note that this barrier is smaller than the barrier of 1.12 eV associated with the escape of Ga dimer from the vacancy site and will not affect the qualitative description of the growth process. Figure 5.33(d) shows a snapshot taken after 4.5 seconds for the growth of Ga clusters at 500 K, where a Ga dimer is formed (see the dashed line encircled region). The Ga dimer formed at the vacancy site readily escapes and diffuses over the terrace. At 500 K, the Ga dimer is highly mobile on the surface. As soon as it escapes from one vacancy, it diffuses over the terrace and quickly binds to another vacancy. Figure 5.33(e) shows, a dimer formed at the vacancy site at 4.5 seconds escaped (see the dashed line encircled region) from the vacancy and binding to another vacancy site (see the solid line encircled region) after 4.8 seconds. The Ga dimer keeps escaping from the vacancy sites until a more stable Ga trimer is formed. Figure 5.33(e) shows the more stable Ga trimer (dashed line encircled region) formed after 5 seconds. The Ga adatoms and dimers escaping from the vacancy, diffuse on the terrace until they bind to the small clusters adsorbed at the vacancy site to build up a larger cluster. The nucleation of the Ga clusters at high temperature is also heterogeneous. At 600 K and above the Ga trimer formed on the vacancy site also start to escape from the vacancy. The Ga tetramer clusters start to escape from the vacancy site for temperatures above 800 K. For the Ga clusters, the ripening will occur for temperatures above 460 K (assuming that the cluster ripening occurs when Ga dimers start escaping from the vacancy site).

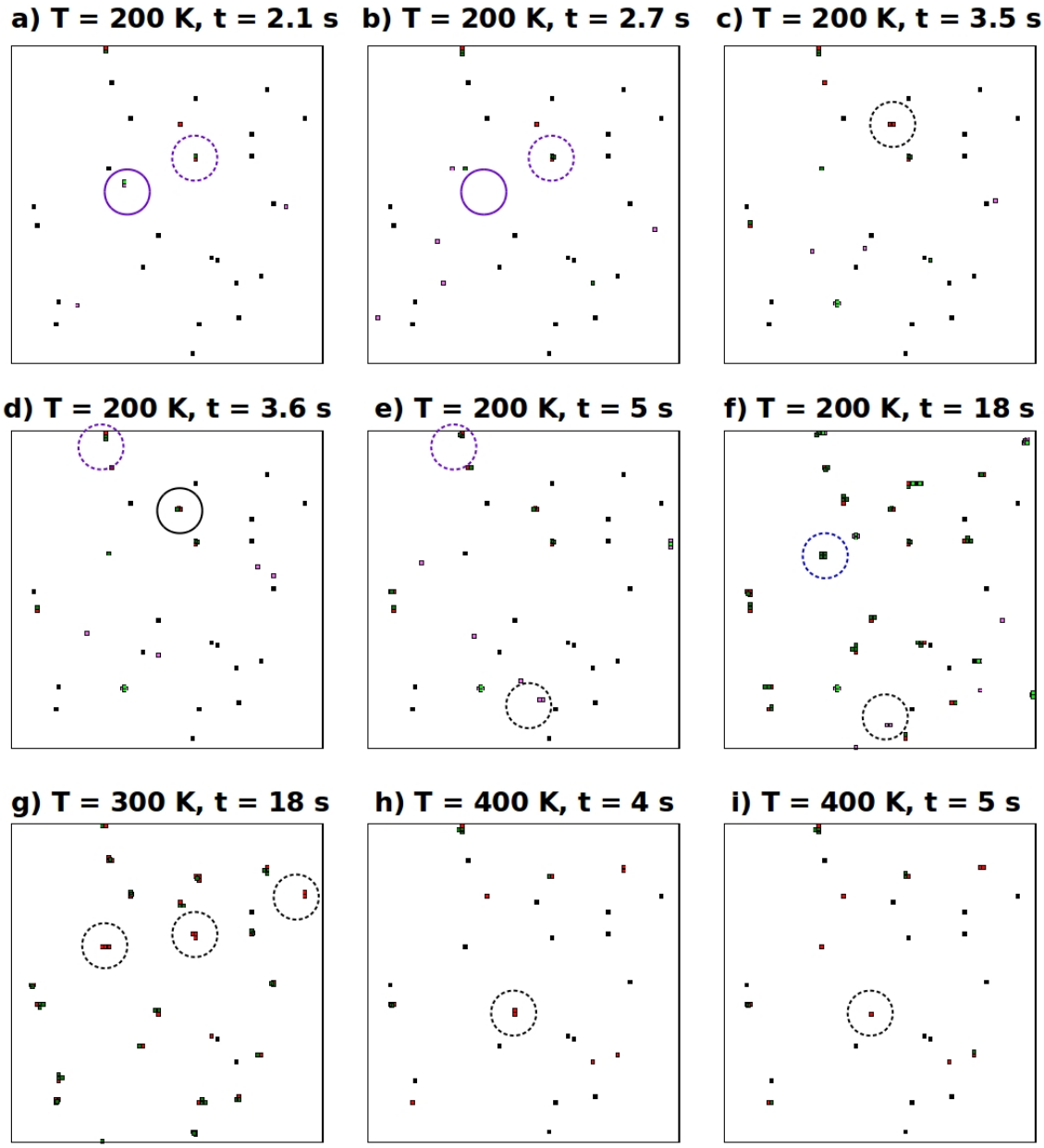

Figure 5.34: Growth of PdGa bimetallic clusters on MgO surface. Black squares represent the vacancy sites with no atom occupied. Magenta and red color filled squares represent Pd atoms adsorbed on the terrace and at the F-center respectively. Green and dark green color filled squares represent Ga atoms adsorbed on the terrace and at the F-center respectively.

5.3.6.3 Growth of PdGa clusters

From the section 5.3.6.1 and 5.3.6.2, we find that despite the heterogeneous nucleation the growth mechanism, the elementary reaction steps involved in the cluster nucleation for the pure Pd and Ga clusters are completely different from each other. In this section, we report the results for the growth mechanism of clusters when Pd and Ga adatoms are deposited on the surface with the same deposition rate. Upon landing on MgO terrace, the Ga adatoms freely hop over the surface until they meet another Ga or Pd adatom. In contrast, the Pd adatoms hop over the terrace until irreversibly trapped at the F-center. Moreover, a more stable PdGa dimer will be formed on the terrace when a freely mobile Ga adatom meets a slow-moving Pd adatom. Initially, the kinetically more favorable small sized Ga rich clusters will be formed in a significant fraction, since the Pd adatoms are strongly trapped at the F-center while the Ga adatoms are freely mobile. After a quick equilibrium between the clusters, thermodynamically most stable clusters with a 1:1 PdGa ratio will be formed.

At 200 K, the nucleation for the growth of pure Pd clusters and pure Ga clusters are homogeneous and heterogeneous respectively. When Pd and Ga adatoms are randomly deposited on the MgO terrace, there is a competition between homogeneous and heterogeneous nucleation. On the one hand, the slow-moving Pd adatoms diffuse over the terrace until it gets strongly trapped at the vacancy site. Because of its very high thermodynamic stability, the Pd adatoms at the vacancy site can act as nucleation centers for the formation of the small clusters. On the other hand, the freely mobile Ga adatoms hop over the surface sites on the terrace until it encounters a Pd adatom trapped at the vacancy site or a slow-moving Pd adatom on the terrace. The high thermodynamic stability of Pd adatoms trapped at the vacancy site and the high kinetic mobility of the Ga adatoms on the terrace results in the formation of bimetallic clusters at the vacancy sites. However, when a freely mobile Ga adatom meets a slow-moving Pd adatom, a small fraction of bimetallic clusters are also formed on the terrace (about 20%). These bimetallic clusters formed on the terrace diffuse over the terrace and merge with the Pd or a small bimetallic cluster adsorbed at the vacancy to build up a larger cluster. A snapshot taken from one of the trajectories after 2.1 seconds (Figure 5.34(a)) shows the formation of bimetallic PdGa dimer at the vacancy site (see the violet dashed line encircled region) and at the terrace (see the violet solid line encircled region). After 2.7 seconds, this bimetallic dimer formed on the terrace merged with the bimetallic dimer formed at the vacancy and a Pd_2Ga_2 is formed at the vacancy (see the disappearance of PdGa dimer from the violet solid line encircled

region and formation of larger bimetallic cluster in the violet dashed line encircled region in Figure 5.34(b)). The strongly trapped Pd adatoms at the vacancy act as holding site and the highly mobile Ga adatoms act as a building block for the formation of bimetallic clusters. The freely mobile Ga adatoms lead to the formation of Ga rich clusters. With given enough time and Pd atom concentration, part of the Ga rich clusters formed initially will be converted into most stable 1:1 clusters. The Ga rich Pd_1Ga_2 cluster grown at the vacancy site seen after 3.6 seconds (see the violet dashed line encircled region in Figure 5.34(d)) is converted into a most stable Pd_2Ga_2 cluster after 5.0 seconds (see the violet dashed line encircled region in Figure 5.34(e)). In addition to the bimetallic clusters, a small amount of pure metal clusters are also formed. The nucleation of pure Ga clusters are found to be occurring only at the vacancy sites, and about 3.6 % of pure Ga clusters are formed. The blue dashed line encircled region in Figure 5.34(f) shows the Ga tetramer formed at the vacancy. In contrast, the nucleation of pure Pd clusters are found to occur both on the terrace as well as at the vacancy site (about 8.8 % of pure Pd clusters are formed). The black dashed line encircled region in Figure 5.34(c) shows Pd dimer formed at the vacancy and the black dashed line encircled region in Figure 5.34(e) and (f) show the Pd dimer formed on the terrace. However, the Pd dimers are quickly converted into bimetallic clusters by the addition of freely mobile Ga adatom to it. The Pd dimer formed after 3.5 seconds (see the black dashed line encircled region in Figure 5.34(c)) is converted into a Pd_2Ga_1 after 3.6 seconds (see the black solid line encircled region in Figure 5.34(d)).

At 300 K, the Pd adatoms are also highly mobile on the MgO terrace, and hence the Pd adatoms deposited on the terrace quickly find the vacancy site. These Pd adatoms binding at the vacancy sites act as the nucleation center, the Ga and Pd adatoms diffusing over the terrace bind to this Pd/F-center complex to build up larger clusters. When a Ga adatom soft-landed on the terrace encounters this Pd/F-center complex, a bimetallic PdGa cluster is formed at the vacancy. Similarly, when a Pd adatom soft-landed on the terrace encounters this Pd/F-center complex, a Pd dimer is formed at the vacancy. Because of the high mobility of Pd and Ga adatoms, no cluster formation on the terrace was found. Larger clusters are formed at the vacancy by adding more Pd and Ga adatoms to the existing cluster. Due to the rapid escape of Ga adatoms form the vacancy, no formation of pure Ga clusters is found. In contrast, due to strong binding of Pd adatom to the vacancy site and high mobility of Pd adatom on the terrace about 9 % of pure Pd clusters are formed

at the vacancy sites. Figure 5.34(g) shows the snapshot of the lattice for the growth of clusters at 300 K after 18 seconds and the Pd clusters formed are encircled by a black dashed line. Upon increasing the temperature to 400 K, we find that the Pd dimers formed at the vacancy sites dissociate into adatoms. Figure 5.34(h) showing a Pd dimer trapped in a vacancy site at $t = 4$ seconds (the black dashed line encircled region) and the same cluster is dissociated into adatoms at $t = 5$ seconds (the black dashed line encircled region in Figure 5.34(i)). Hence, we envisage that the ripening of the clusters will occur at 400 K. However, for temperatures above 300 K, when the Pd and Ga atoms are deposited with equal deposition rate the formation of Pd clusters are only about < 10 %. Hence, the reduction in the island density will not be significant at 400 K. A slight increase in temperature ($T \sim 420$ K) is sufficient for the bimetallic clusters (Pd_1Ga_1 and Pd_3Ga_1) to decompose. Further increase in temperature up to 500 K will cause rapid ripening. At 500 K, most of the cluster nuclei tend to decompose (both pure metal clusters nuclei and bimetallic clusters nuclei).

In Figure 5.35(a) we present the calculated island density for the pure Pd, pure Ga and bimetallic PdGa clusters grown at 200, 250, 300 and 350 K. For all these temperatures the growth of the Ga clusters follows a heterogeneous nucleation mechanism. The calculated island density of 2.7 $\times 10^{12}$ cm^{-2} is more or less independent of the temperature. At 200 K, in contrast to the Ga clusters, the initial growth of the Pd clusters follows homogeneous nucleation. Due to the overcounting of cluster islands formed on the terrace, the calculated island density for the Pd clusters at 200 K is about 30% higher than that of Ga clusters. However, for temperatures above 250 K, the Pd clusters also exhibit heterogeneous nucleation, and the calculated island density is similar to that of Ga clusters. When a heterogeneous nucleating Ga and homogeneous nucleating Pd atoms are deposited at equal deposition rate at 200 K, a mixed behavior is seen. A small amount of (about 10%) clusters are formed on the terrace. For temperatures above 300 K, the growth of the PdGa clusters follows heterogeneous nucleation mechanism, and the calculated island density is consistent with that of Pd and Ga clusters.

Further, analysis of the cluster composition shows that irrespective of the temperature at which the clusters are grown, about 10 % of pure Pd clusters are formed (Table 5.6). In contrast, due to the high escape rate of Ga adatoms, the formation of the Ga clusters is decreasing with temperature. For temperatures above 300 K, no formation of pure Ga

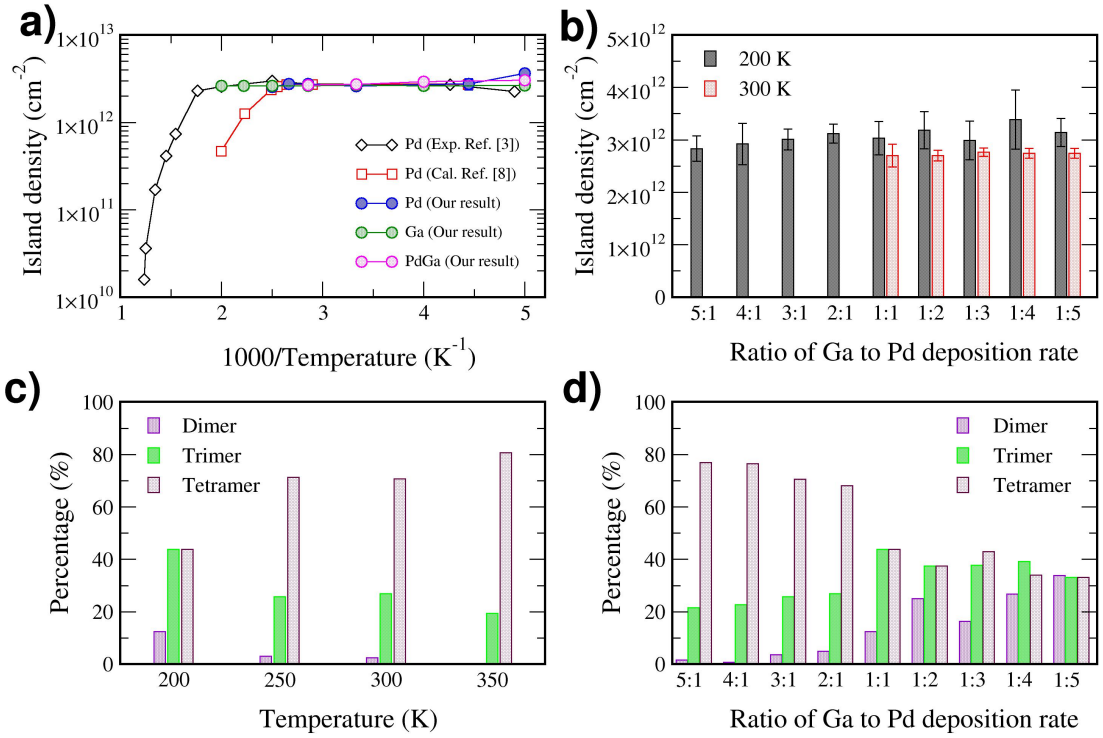

Figure 5.35: a) Estimated island density for the Pd, Ga and PdGa clusters along with the literature report for the island density of pure Pd cluster. b) Estimated island density for the various ratios of Ga to Pd deposition rate at 200 and 300 K. c) Size distribution of island density for the PdGa clusters grown at 200, 250, 300 and 350 K. d) Size distribution of island density for the various ratios of Ga to Pd deposition rate at 300 K.

Table 5.6: % of clusters formed for various temperatures when Pd and Ga adatoms are deposited with equal deposition rate

Temperature	% of clusters formed							
	Pure Pd	Pure Ga	Pd_1Ga_1	Pd_2Ga_1	Pd_1Ga_2	Pd_3Ga_1	Pd_2Ga_2	Pd_1Ga_3
200	8.8	3.6	5.1	22.6	18.2	7.3	20.4	13.9
250	5.3	1.5	2.3	2.3	23.5	14.4	26.5	24.2
300	8.9	0.0	1.6	4.9	21.1	12.2	34.1	17.1
350	9.2	0.0	0.0	0.0	18.5	16.0	34.5	21.8

clusters is seen. Despite the Pd rich clusters (Pd_2Ga_1 and Pd_3Ga_1) are having higher thermodynamic stability than their Ga rich counterpart (Pd_1Ga_2 and Pd_1Ga_3), irrespective of the growth temperature (up to 400 K), always the Ga rich clusters are formed in a larger percentage than the Pd rich clusters. This is because below the ripening temperature formation of a cluster with a particular composition depends on the kinetics of the building blocks. The freely mobile Ga adatoms build more Ga rich clusters than that of Pd rich clusters built by slow-moving Pd adatoms. However, with given enough concentrations of Pd and Ga adatoms for temperatures above 250 K, the thermodynamically most stable Pd_2Ga_2 cluster is formed in largest percentage.

5.3.6.4 Effect of Ga deposition rate on the cluster composition

The reactivity of the PdGa catalyst significantly depends on the chemical composition. [38] Further, the selectivity of the PdGa catalyst primarily depends on the active ensemble. [43, 77] Clusters of the same size with different composition might result in different reactivity and selectivity. [98] The bimetallic clusters are more effective in the reaction of hydrogen dissociation than the pure Pd clusters. [98] Hence, it is important to stabilize the clusters of a specific composition in order to use them effectively. One plausible way to obtain the clusters with the specific composition is controlling the rate of deposition of Pd and Ga adatoms. We have performed a series of KMC simulations by varying Ga to Pd deposition rate ratio for a range of 5:1 to 1:5. The calculated total island density for various Ga to Pd deposition ratios are presented in Figure 5.35(b). Due to the limitation of very high escape rate of Ga adatoms the island densities for the Ga rich deposition cannot be calculated. The island density calculated at 200 K is about 10 to 20 % higher than that calculated at 300 K. This is consistent with the homogeneous nucleation at 200 K and the heterogeneous nucleation at 300 K.

Next, we analyzed the composition of clusters formed for the different ratios of the Pd and Ga adatom deposition rates. In Table 5.7 and 5.8, we provide the composition of the clusters formed for the different ratios of Pd and Ga adatom deposition rate at 200 K and 300 K respectively. Our results show that if any one of the atoms deposited at least two times faster than the other atom, then pure clusters of faster depositing atoms are formed. However, still, a significant fraction of bimetallic clusters are formed even for the ratios as high as 5:1 suggesting that the formation of bimetallic clusters are more prompt to

Table 5.7: % of clusters formed at 200 K for various deposition rates of Pd and Ga clusters starting from Ga richness to Pd richness

Ratio of Ga to Pd deposition rate	% of clusters formed							
	Pure Pd	Pure Ga	Pd_1Ga_1	Pd_2Ga_1	Pd_1Ga_2	Pd_3Ga_1	Pd_2Ga_2	Pd_1Ga_3
5:1	0.0	52.1	1.6	0.0	18.2	0.0	9.1	19.0
4:1	0.0	34.1	0.0	0.8	21.2	0.0	12.9	31.1
3:1	0.0	30.1	2.9	2.9	19.8	0.0	20.6	23.5
2:1	2.1	17.0	2.8	7.1	19.8	2.8	24.1	24.1
1:1	8.8	3.6	5.1	22.6	18.2	7.3	20.4	13.9
1:2	26.4	0.0	11.8	18.0	11.1	11.1	16.7	4.9
1:3	33.3	0.7	5.9	13.3	10.4	19.2	13.0	3.7
1:4	50.3	0.6	4.6	19.0	5.2	11.1	7.8	1.3
1:5	46.5	0.0	8.4	16.9	4.2	16.9	5.6	1.4

Table 5.8: % of clusters formed at 300 K for various deposition rates of Pd and Ga clusters starting from Ga richness to Pd richness

Ratio of Ga to Pd deposition rate	% of clusters formed							
	Pure Pd	Pure Ga	Pd_1Ga_1	Pd_2Ga_1	Pd_1Ga_2	Pd_3Ga_1	Pd_2Ga_2	Pd_1Ga_3
1:1	8.9	0.0	1.6	4.9	21.1	12.2	34.1	17.1
1:2	28.5	0.0	2.4	3.3	11.4	21.1	24.4	8.9
1:3	34.4	0.0	0.8	0.8	6.4	30.4	23.2	4.0
1:4	42.7	0.0	1.6	3.2	4.0	33.9	12.1	2.4
1:5	54.0	0.0	0.8	2.4	4.0	24.2	13.7	0.8

occur. Moreover, deposition of Pd and Ga adatoms with an equal deposition rate gives the highest % of bimetallic clusters. However, clusters with various compositions are formed in small fractions. By altering the deposition rates the amount of clusters with the specific composition can be improved, but a large fraction of undesired pure metallic clusters will be formed.

Further analysis of the size distribution of the cluster nuclei formed for the growth of bimetallic clusters where the Pd and Ga atoms are deposited with equal rates at 200 K, 250 K, 300 K and 350 K are presented in Figure 5.35(c). The results show that at 200 K after the given enough time of 20 seconds the smaller clusters (dimers and trimers) are found in a higher percentage (about 56 %) compared to that of tetramers (about 44%). The multi-step growth process at 200 K is the reason for the formation of a high percentage of smaller clusters. A slight increase in temperature (250 K) shifts the formation of cluster nucleus from the multi-step process to the single-step growth process. The single-step growth process significantly improved the formation of tetramers (about 71%). The growth of cluster nuclei follows the single-step growth process up to ripening tempera-

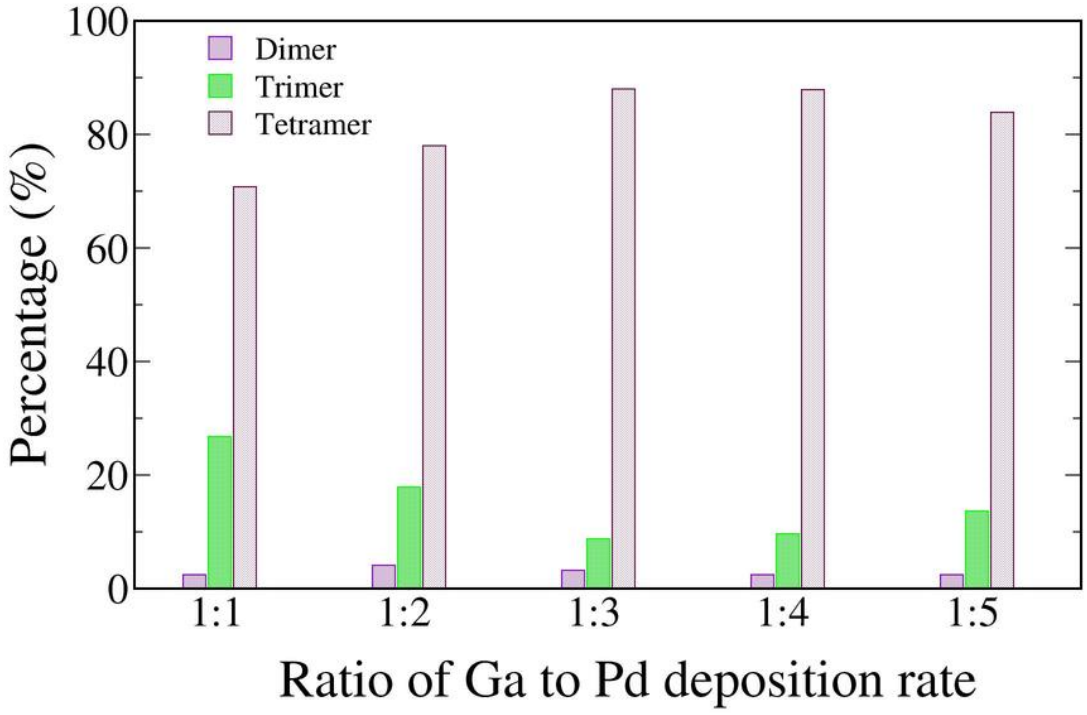

Figure 5.36: Size distribution of island density for the various ratios of the Ga to Pd deposition rate at 300 K.

ture. Hence, for a temperature range of 250 K to 400 K, a large percentage ($> 70\%$) of tetramers are formed.

The freely mobile Ga adatoms also shift the nucleus formation from the multi-step process to the single step process. Even at a very low temperature such as 200 K, at least double the times faster deposition of Ga adatoms to that of Pd adatoms deposition also produced about 70% of tetramers (Figure 5.35(d)). In contrast, the slow mobile Pd adatoms shift the nucleation process towards the multi-step growth process. At 200 K, equal rate or faster rate of Pd atoms deposition to that of Ga adatoms deposition leads to the formation of a high percentage of smaller clusters. At these conditions, only about $< 40\%$ of tetramers are formed. However, the formation of more stable tetramers for a faster Pd adatoms deposition rate can also be improved by shifting the nucleation process to single step growth process, ie., by increasing the temperature to 300 K. At 300 K, the formation of tetramers are about $> 70\%$ (Figure-5.36).

5.4 Conclusion

In summary, we have studied the structure and energetics of small (up to four atoms) Pd, Ga and PdGa bimetallic clusters on MgO(100) terrace and at the oxygen vacancy site. The adatoms (Pd and Ga) and dimers (Pd_2, Pd_1Ga_1 and Ga_2) preferably bind on top of surface O, and the larger clusters have a variety of structures like linear, planar and 3D. The interaction of the pure clusters with the substrate weakens as the size of the cluster increases. Adsorption cohesive energy of the clusters monotonously increases with an increase in cluster size except for the Pd cluster at the F-center. Further, we find that all the bimetallic clusters are more stable compared to that of the pure ones on the substrate. Among the various possible compositions of a particular sized cluster, the Pd rich clusters binding at the vacancy site are having higher thermodynamic stability than the Ga counterpart while the stability is reversed for the clusters binding on the terrace. In spite of this behavior the clusters with 1:1 atomic ratio of Pd and Ga have the highest stability among the mixed clusters binding to both at vacancy site and terrace. From the thermodynamics of the formation of the clusters, we found that for clusters with $N \geq 2$ and where Pd is involved, the cluster formation happens by a cluster of size $(N-1)$ diffusing and binding to a Pd adatom trapped at the F-centre.

Further, our calculations show that the small clusters at least up to tetramers are highly mobile on the surface except for the Ga tetramer. The mobility of the bimetallic clusters is similar to that of the Pd clusters, while the Ga adatom is highly mobile on these surfaces. Our results show that despite the heterogeneous nucleation the elementary reaction steps involved in the nucleation of Pd and Ga clusters are different from each other. At elevated temperatures, the Pd clusters formed at the vacancy site dissociate into smaller fragments while the Ga clusters escape from the vacancy. When the bimetallic clusters are grown by depositing Pd and Ga adatom, the thermodynamically more stable Pd adatom trapped at the vacancy site act as nucleate for the cluster growth and the freely mobile Ga adatom significantly influences the kinetic formation of the clusters. The highest fractions of the bimetallic clusters can be grown by depositing Pd and Ga adatoms with equal deposition rate. Further, the bimetallic PdGa clusters with the specific composition can be grown by altering the deposition rates of the Pd and Ga adatoms to the surface and temperature.

Chapter 6

Microscopic Insights into Hydrogen Permeation Through a Model PdCu Membrane

In this chapter, a systematic theoretical study of all the processes associated with the permeation of H through a model PdCu membrane is studied. The surface of the membrane is modelled using the most stable (110) surface. The results show that the nuclear quantum effects due to the light mass, the H atom can significantly affect the stability and the reaction rates. Based on a microkinetic model of the permeation process, we find that the permeation can be limited by diffusion of H in the membrane bulk or the reassociation of atomic H to form H_2 on the permeate side of the membrane depending on the operation temperature and membrane thickness. At typical operating conditions, for membranes thinner than 0.5 μm, the permeation at high temperature (T>500 K) is limited by surface processes, while at lower temperatures it can be either diffusion limited or reassociation limited. The work presented in this chapter is published in *J. Phys. Chem. C*, **2018**, 122 (24), pp 12920-12933. [1]

6.1 Introduction

Hydrogen is an important raw material in large-scale industrial processes to manufacture a diverse range of products from semiconductors to metal alloys to vitamins. [111] Moreover, H_2 is also perceived as an alternate source of energy. At an industrial scale hydrogen is produced primarily through steam reforming of light hydrocarbons, mainly methane, that results in the production of syngas (CO+H_2). The ratio of CO and hydrogen in syngas varies depending on the reaction conditions. Hence there is a need for a cheap and

[1] Reprinted with permission from *J. Phys. Chem. C*, **2018**, 122 (24), pp 12920-12933. Copyright ©2018, American Chemical Society.

efficient separation process.

Amongst the different hydrogen separation processes that are in use, those based on dense metallic membranes are one of the most efficient ones. Amongst the metal-based membranes, palladium has been regarded as a good hydrogen separation membrane material due to its high selectivity and permeability for hydrogen, and good thermal and mechanical stability. [112–115] Palladium membranes can be used in a membrane reactor for producing highly pure hydrogen (H_2) by shifting the equilibrium of hydrogenation or dehydrogenation reactions. Combination of the H_2 production reaction and its separation in the same unit results in higher yields and reduced operational costs. [116] However, pure Pd membrane has some limitations. Firstly, Pd is a precious metal with limited supply, which makes pure Pd membranes expensive. Secondly, pure Pd is susceptible to surface poisoning by several gases such as CO, CO_2, H_2S etc., which are present in the atmosphere. [117, 118] These impurities poison the catalytic surface and retard the flux by reducing the number of catalytic sites available for dissociative adsorption of hydrogen. Additionally, palladium membranes suffer hydrogen embrittlement due to $\alpha \rightarrow \beta$ phase transition below 573 K. [119] The hydride β phase has an expanded lattice (4.02 Å) compared to the α phase (3.89 Å). [120] Formation and growth of β phase during several cycles of operation induces strain in the system which causes embrittlement of the membrane. All these factors limit the use of Pd membranes for industrial applications.

The embrittlement due to the $\alpha - \beta$ phase transition can be suppressed by alloying Pd with other metals. [121] Alloying with metals often increases the permeability of palladium while at the same time enhancing its mechanical properties. [113] As a result, alloying strategies have been sought experimentally [122–125] and theoretically [126–130] to develop robust Pd-alloys with increased chemical stability and hydrogen permeability in aggressive environments. Binary alloys such as Pd-Cu, Pd-Ag and Pd-Au are more resistant to poisoning by contaminants such as H_2S, CO and CO_2. [131] However, H_2S reacts with palladium and palladium-silver alloy membranes by forming species like $Pd_{2.8}S$, Pd_4S and $Ag_{10}Pd_{10}S_5$, [117, 132, 133] which reduces the hydrogen flux and the mechanical stability of the membrane. Addition of Cu to Pd suppresses the critical temperature for hydrogen embrittlement, enhances the sulphur tolerance, and reduces the noble metal cost. [134] Hence, Pd-Cu alloys are being widely studied as plausible candidates for alloy based hydrogen separation membranes.

In spite of the above advantages of Cu based Pd alloys, there are some shortcomings. For example, hydrogen permeability decreases as the Cu content in the alloy increases, except for a narrow range of the BCC phase where the fastest diffusion of hydrogen is observed. [135] From the phase diagram of Pd-Cu system [136] it is clear that above 60 atom % of palladium it forms a disordered fcc phase. The overall permeability of hydrogen depends on the diffusivity and solubility of hydrogen in the metal/alloy. Addition of Cu to Pd decreases the lattice parameter which results in a decrease in the solubility of hydrogen in Pd-Cu alloy. [131] Thus it is diffusivity in Pd-Cu alloy which accounts for high permeability of hydrogen in the ordered bcc phase at room temperature. Using Density Functional Theory (DFT) based calculations and kinetic Monte Carlo (KMC) simulations, Kamakoti *et al.* had shown that the diffusion coefficient for interstitial H in the bcc phase of Pd-Cu alloy is not only two orders of magnitude faster than in the fcc phase (1.87×10^{-8} m^2/s in bcc vs. 3.69×10^{-10} m^2/s in fcc at 500 K) but also more than what is observed in pure palladium (2.65×10^{-9} m^2/s at 500 K). [131] Experimental studies by Piper [137] *et al.* showed that at room temperature diffusivity of H in bcc Pd-Cu is almost twice than that in the fcc phase. Rao *et al.* [123] has shown that hydrogen flux in the bcc phase of Pd-Cu membrane is higher than that of the fcc phase.

Several theoretical studies have been carried out in predicting hydrogen diffusion in binary Pd alloys. [128, 131, 138, 139] Kamakoti *et al.* carried out DFT studies to examine the binding sites, diffusion pathways, and diffusion activation energies for H diffusion in pure Pd and CuPd alloys with 50 atom % Pd. [138] In another work, Flecha *et al.* reported the solubility, diffusivity and permeation of interstitial H in fcc Pd-based binary and PdCu-based ternary alloys using DFT and cluster expansion methods. [129] Gao *et al.* performed the screening of B2 phase stabilizer in CuPd-based hydrogen separation membranes using the first-principles method. [140] The authors have calculated the enthalpy of formation without zero-point energy contributions as a screening parameter of a number of Pd-based alloys. They have also reported the electronic structure, elastic properties, electronegativities and solubility of those alloys. [140] Boes *et al.* experimentally measured the bulk-composition-dependent dissociative adsorption energy of hydrogen on CuPd alloy surfaces and modeled that using DFT. [141] Hu *et al.* studied the temperature dependent thermodynamic and mechanical properties of bulk $Pd_{50}Cu_{50}$ alloy using the first-principles method. [142]

In a dense metallic membrane, the hydrogen permeation occurs via the solution diffusion mechanism. [143] The solution-diffusion mechanism involves total of seven steps, which are (1) adsorption of raw gas (H_2 and undesired gas molecule) at the feeder side of the membrane surface, (2) dissociation of H_2 on the membrane surface, (3) penetration of H from surface to membrane bulk, (4) diffusion of H through the membrane, (5) diffusion of H from membrane bulk to the surface on the collector side of the membrane, (6) reassociation of H_2 molecule on the membrane surface and (7) desorption of H_2 from the collector side surface of the membrane. Most of the studies are focused either on processes involved on the surface or in the bulk of the material [131, 138, 144–148]. However, to have a complete understanding of the factors that affect the performance of the membrane, there is a need for a comprehensive study of all the above-mentioned processes. Hence, in this work, computational studies of the above mentioned seven fundamental processes related to hydrogen permeation through the bcc phase of Pd-Cu alloy is studied.

The rest of the chapter is divided as follows: In Section 6.2 we provide the computational details. Structure and stability of the clean surfaces are presented in Section 6.3.1. Section 6.3.2 contains the adsorption energetics and dissociation mechanism of hydrogen molecule on PdCu (110) surface. Structure and thermodynamic stability of atomic H adsorption on the PdCu (110) surface with various coverages, adsorption of H at the subsurface and binding of H inside bulk is presented in Section 6.3.3. We present the thermodynamic phase diagram of the hydrogen covered surfaces in Section 6.3.4. In Section 6.3.5 we describe the mechanism and the barriers associated with the diffusion of H inside bulk PdCu, on the surface and subsurface. Section 6.3.6 contains the energetics of reassociation mechanism for the formation of molecular hydrogen from two atomic H on PdCu (110) surface. In section 6.3.7 we present the temperature dependent kinetics of all the steps involved in the permeation process and analyse the rate limiting step in Section 6.3.8. Finally, in Section 6.4 we discuss all the steps involved in the hydrogen permeation process and conclude in Section 6.5.

6.2 Methods

6.2.1 Computational details

All the calculations were performed using the Quantum ESPRESSO software, [34] a plane wave based implementation of density functional theory to solve the Kohn-Sham equations. The electronic exchange and correlation potential is described by the generalized gradient approximation (GGA) based parameterization of Perdew-Burke-Ernzerhof (PBE). [12] Ultrasoft pseudopotentials were used to describe the electron-ion interactions. [19] To expand the wavefunction, a plane wave basis set with kinetic energy cutoff of 35 Ry, and charge density cutoff of 320 Ry were used. Brillouin zone integrations were done with Monkhorst-Pack (MP) k-point mesh. [20] Marzari-Vanderbilt smearing [23] with a smearing width of 0.005 Ry was used to speed up the convergence. The obtained lattice parameter of 3.02 Å for the bcc structure of bulk PdCu, with a converged 9×9×9 k-point mesh is slightly overestimated in comparison with the experimental value of 2.98 Å [149, 150] and very good agreement with the previous theoretical reported value of 3.03 Å. [151]

The climbing image nudged elastic band method (CI-NEB) [32, 80] was used to find out the minimum energy path (MEP), energy barriers and transition states. According to the complexity of the NEB simulation, the number of images employed in a given path varies from 5 to 17 images. Forces acting on each image are converged up to 0.05 eV/Å.

The rate constant of the reaction steps and the diffusion processes are estimated using the harmonic transition state theory as,

$$k_{hTST} = \frac{\Pi_{i=1}^{3N} \nu_i^{init}}{\Pi_{i=1}^{3N-1} \nu_i^{*}} exp^{-\left(\frac{\Delta E^q}{k_B T}\right)} \tag{6.1}$$

where, k_B is Boltzmann constant, T is temperature, ΔE^q is the zero point energy corrected activation barrier calculated as $\Delta E^q = \Delta E^c + \frac{1}{2}(\sum h\nu_i^* - \sum h\nu_i^{init})$ where ΔE^c is the classical activation barrier calculated using CI-NEB calculations. ν_i^{init} and ν_i^* are the stable harmonic modes at the initial state and saddle point respectively. The normal mode frequencies are calculated using density functional perturbation theory (DFPT) as implemented in Quantum Espresso software. [27]

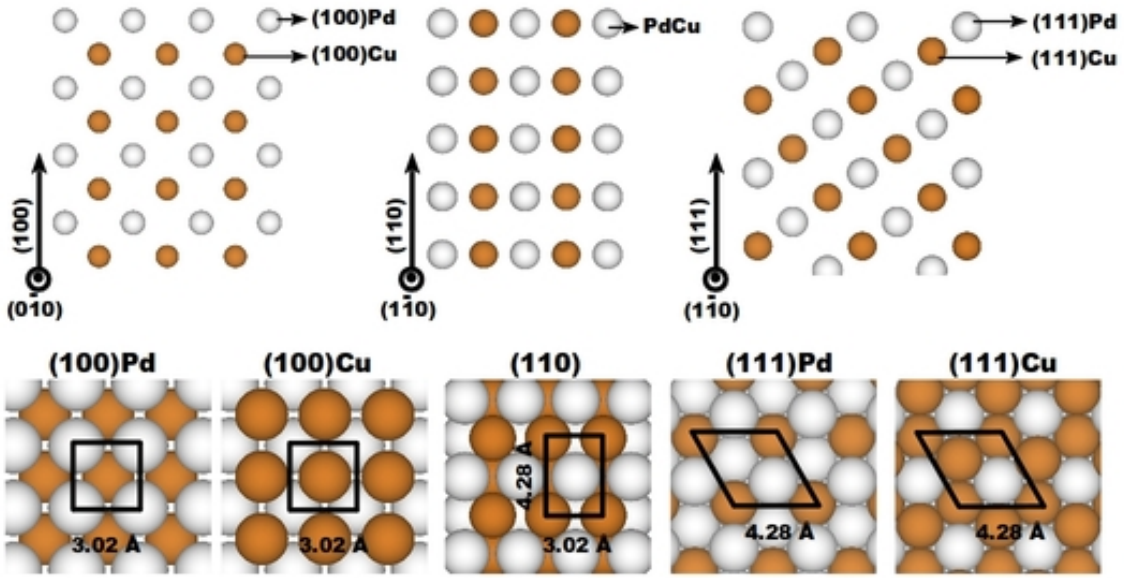

Figure 6.1: Staking of atoms in the low indexed (100), (110) and (111) surface direction of bcc PdCu and the top views of the possible surface terminations.

6.2.2 Surface model

Typically the low indexed surfaces have higher stability than the high indexed ones. Hence, in order to find the most stable surface termination of bcc PdCu the low indexed (100), (110) and (111) surfaces are considered. Among the low indexed surfaces, the atoms in (110) surface are densely packed with the largest nominal coordination number of 6, which is closest to the bulk value of 8. Along this direction each layer consists of two atoms (one Pd and one Cu) with a bulk interplanar distance of 2.14 Å. In contrast, along the (100) and (111) directions the atoms are less densely packed and are comprised of alternate layers of Pd and Cu atoms. Hence for these surfaces, there are two possible terminations, namely Pd or Cu terminated surface (see Fig.6.1). The bulk interplanar distances along (100) and (111) surface directions are 1.51 and 0.87 Å respectively.

The PdCu(110) surface was modeled with symmetric and stoichiometric slab where all the atoms are allowed to relax. To minimize the spurious interaction between the periodic images, 11 Å vacuum was used along the direction normal to the surface. In order to determine the optimal number of layers, the surface energy was calculated using slabs

with four, six and eight layers. The surface energy calculated using six layers (1.33 Jm^{-2}) remains unchanged as the number of layers in the slabs increase from six to eight layers. Hence, the (110) surface was represented with a six-layer slab for the rest of the calculations. The (100) and (111) surfaces are modeled with non-stoichiometric symmetric slabs. Following a similar strategy, we find that 11 layers are optimal for (100) and (111) surfaces. The (110) surface was found to be more stable than the (100) and (111) surfaces (More details are discussed in Section-6.3.1).

To study the surface and subsurface processes occurring on the PdCu membrane, the membrane was modeled with a slab representing the stoichiometric (110) surface. The (110) surface was chosen because this surface is found to be the most stable one. To study the adsorption, dissociation, diffusion and penetration of hydrogen a (3×2) supercell of (110) surface was considered. To maintain a balance between accuracy of the calculations and the computational cost, a six layer thick slab is considered, of which atoms in the bottom three layers are fixed at their bulk inter-planar distances and all other atoms are allowed to relax. Adsorption energies of hydrogen on the (110) surface is defined as,

$$E_{ads} = E_{slab+nX} - E_{slab} - yE_{H_2}, \tag{6.2}$$

where, $E_{slab+nX}$ is total energy of the slab with n number of hydrogen atom/molecule adsorbed on it, E_{slab} is total energy of the bare slab, E_{H_2} is total energy of the gas phase hydrogen molecule. The X can be either H atom or molecule. If X is hydrogen molecule then $y = n$, otherwise $y = \frac{n}{2}$. E_{H_2} was calculated by taking a H_2 molecule in a cubic-cell having a length of 15 Å. The H-H bond length is obtained as 0.75 Å with a binding energy of -4.52 eV. The calculated values are in good agreement with the experimentally reported values of 0.74 Å and -4.52 eV. [55] Zero point energy corrected adsorption energy was calculated as,

$$E_{ads}^{ZP} = E_{slab+nX} + \frac{1}{2}\sum h\nu_{slab+nX} - E_{slab} - yE_{H_2} - \frac{1}{2}\sum h\nu_{H_2} \tag{6.3}$$

6.2.3 Ab-initio thermodynamics

The stability of the different surface terminations (both clean surface and hydrogen covered surfaces) can be determined based on their respective surface free energies. Since the (100) and (111) surfaces are modeled with a nonstoichiometric symmetric slab, the num-

ber of Pd and Cu atoms are different in different slabs. Hence, the surface free energies need to be calculated within grand-canonical ensemble (GCE). In GCE, assuming that the surface is in equilibrium with the source, the Gibbs free energy is given by,

$$G = E + PV - TS - \sum_i n_i \mu_i \tag{6.4}$$

where, E is the internal energy obtained from the DFT calculation, P, V, T and S are the pressure, volume, temperature and entropy respectively. n_i and μ_i are respectively the number and chemical potential of species i ($i \in$ Pd, Cu, H). In the fixed chemical potential viewpoint, the system consists of the surface slab and the species bound to it and the surroundings consist of the rest of the universe. Since the surface is the solid slab, the PV term can be neglected. Further to a fair approximation, the entropy of the system is more or less negligible, since it consists primarily of configurational and vibrational contribution that are very small in solids. Now, the surface free energy of the hydrogen adsorbed surface slab as a function of chemical potentials of the constituents, temperature and hydrogen partial pressure is given by,

$$G^{surf}_{slab} = E^{surf}_{slab} - n_{Pd}\mu_{Pd} - n_{Cu}\mu_{Cu} - n_H \mu_H(T, p) \tag{6.5}$$

The surface free energy of the clean slab is given by,

$$G^{ref}_{slab} = E^{ref}_{slab} - n_{Pd}\mu_{Pd} - n_{Cu}\mu_{Cu} \tag{6.6}$$

To compare the relative stability of the hydrogen adsorbed surface to that of the clean surface, the change in the Gibbs free energy is calculated as,

$$\Delta G(T, p) = \frac{1}{A}\left(E^{surf}_{slab} - E^{ref}_{slab} - n_H \mu_H(T, p)\right) \tag{6.7}$$

where E^{surf}_{slab} is the total energy of the hydrogen adsorbed slab, E^{ref}_{slab} is the total energy of the clean slab and A is the surface area. Similarly, to compare the stability of the low indexed surfaces the surface free energy is calculated as,

$$G^{surf}_{slab} = \frac{1}{2A}\left(E^{surf}_{slab} - n_{Pd}\mu_{Pd} - n_{Cu}\mu_{Cu}\right) \tag{6.8}$$

The chemical potential of Pd and Cu can have any value depending on the experimental conditions, hence it is not possible to exactly define these values. However, the allowed range of the chemical potentials is given as,

$$\mu_{PdCu}^{bulk} = \mu_{Pd}^{bulk} + \mu_{Cu}^{bulk} + \Delta H_f \tag{6.9}$$

where, μ_{PdCu}^{bulk}, μ_{Pd}^{bulk} and μ_{Cu}^{bulk} are respectively the chemical potentials of bulk PdCu, bulk Pd and bulk Cu. ΔH_f is the enthalpy of formation of bulk PdCu. ΔH_f was calculated as, $\Delta H_f = E_{PdCu}^{bulk} - E_{Pd}^{bulk} - E_{Cu}^{bulk}$. All the terms in the right hand side are the total energies of the respective system. The calculated enthalpy of formation of bulk PdCu is -0.26 eV at 0 K. Assuming the sources of Pd and Cu are in equilibrium with PdCu, the upper boundary of the chemical potential of one of the constituent species can be set to its individual bulk value. Now, the allowed ranges of the chemical potential of Pd and Cu are given by,

$$\mu_{Pd}^{bulk} + \Delta H_f \leq \mu_{Pd} \leq \mu_{Pd}^{bulk} \tag{6.10}$$

$$\mu_{Cu}^{bulk} + \Delta H_f \leq \mu_{Cu} \leq \mu_{Cu}^{bulk}. \tag{6.11}$$

From the above equations, the allowed range of change in the chemical potential of Pd and Cu is derived as,

$$\Delta H_f \leq \Delta\mu_{Pd} \leq 0 \tag{6.12}$$

$$\Delta H_f \leq \Delta\mu_{Cu} \leq 0 \tag{6.13}$$

In this expression the value of $\mu_{Cu} = 0$ implies that the surface is prepared at Cu rich condition, while $\mu_{Cu} = \Delta H_f$ implies that the surfaces are prepared at Pd rich condition.

The chemical potential of hydrogen can be obtained from the following relationship:

$$\mu_H = \frac{1}{n}(H - TS) \tag{6.14}$$

where H is enthalpy. The values of entropy at standard pressure and the change in enthalpy going from absolute zero temperature to finite temperature $[\Delta H(0 \longrightarrow T, p^\circ)]$ at p° were taken from CRC handbook. [55] Hence $H(T, p^\circ)$ can be obtained using the following relation,

$$H(T, p^\circ) = H(0, p^\circ) + \Delta H(0 \longrightarrow T, p^\circ), \tag{6.15}$$

Table 6.1: % change in inter-planar distances after relaxation.

	(100)Pd	(100)Cu	(110)	(111)Pd	(111)Cu
z_{12}	-0.65	-3.09	-0.44	-8.48	-12.56
z_{23}	0.49	2.06	0.42	-11.62	-16.52
z_{34}	0.90	1.98	0.45	10.88	18.36

where $H(0, p^{\circ})$ can be obtained from DFT calculations. The variation of μ_X with T and p is given by,

$$\mu_H(T, p) = \mu_H(T, p^{\circ}) + k_B T ln(p/p^{\circ}) \tag{6.16}$$

6.3 Results and Discussion

6.3.1 Structure and stability of clean surfaces

After relaxation contraction and expansion of the interlayer distances are observed. The percentage change in the interlayer distances are calculated as $z_{ij} = \frac{d_{ij} - d'_{ij}}{d'_{ij}} \times 100$, where d_{ij} is the interlayer distance between i^{th} and j^{th} layer of the surface after relaxation and d'_{ij} is the same in the bulk truncated surface.The z_{ij} for the five surfaces considered in this study is given in Table-6.1. For all the surfaces the z_{12} show contraction while z_{23} of (100) and (110) surfaces show expansion. Moreover, in contrast to the densely packed (110) and (100) surfaces, the relaxation effects are significantly larger for the more open (111) surfaces.

Figure-6.2 shows the surface free energy as a function of the change in the chemical potential of copper ($\Delta\mu_{Cu}$) for various possible surface terminations of the low indexed surfaces of bcc PdCu calculated using Equation-6.8. For the non-stoichiometric (100) and (111) surfaces the relative stability depend on the Cu chemical potential ($\Delta\mu_{Cu}$). Over a very narrow range of $\Delta\mu_{Cu}$, from -0.26 to about -0.23 eV, the Pd terminated (100) and (111) surfaces are more stable than the corresponding Cu terminated ones. For the all other values of the $\Delta\mu_{Cu}$ the Cu terminated (100) and (111) surfaces are found to be more stable than their Pd terminated counterparts. Hence, it is unlikely that the Pd terminated surfaces will be formed under the experimental preparation conditions. For the allowed range of $\Delta\mu_{Cu}$ the Cu terminated (111) surface always has higher value of surface energy than the Cu-terminated (100) surface suggesting that the latter is more stable irrespective of surface preparation conditions. In contrast to the (100) and (111) surfaces, the stoichiometric

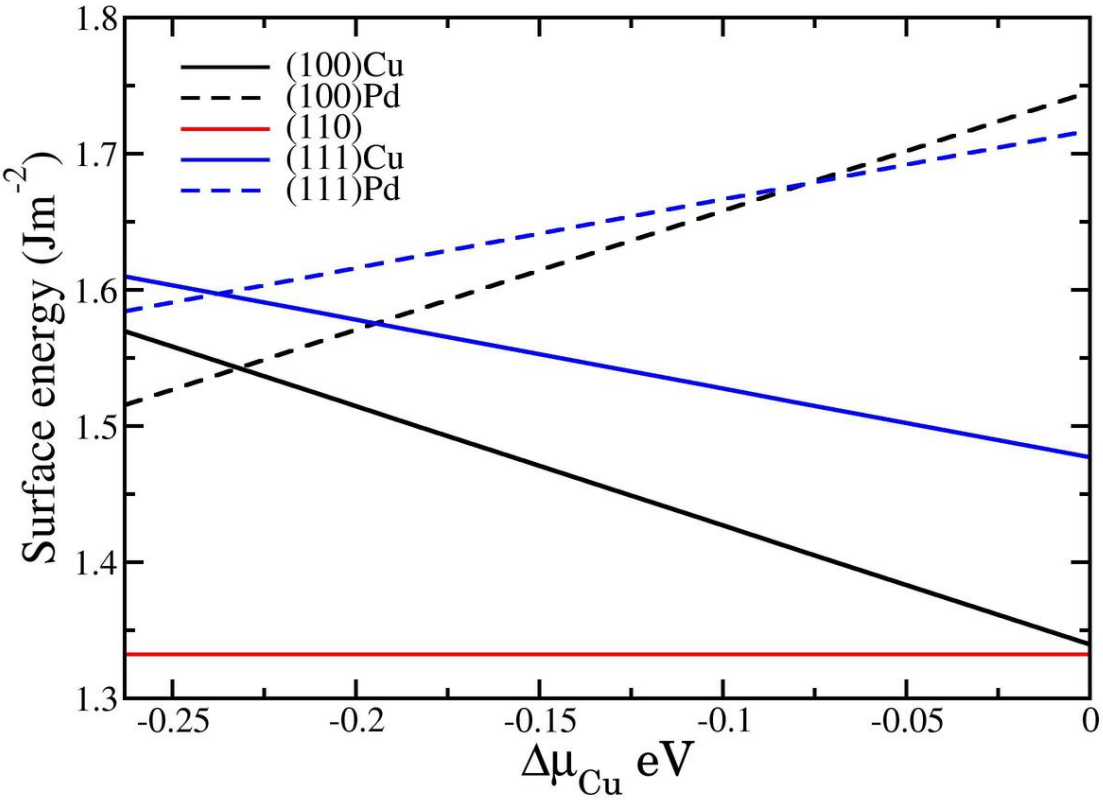

Figure 6.2: Surface free energy of various possible terminations of (100), (110) and (111) surface of bcc PdCu as a function of change in the chemical potential of copper ($\Delta\mu_{Cu}$).

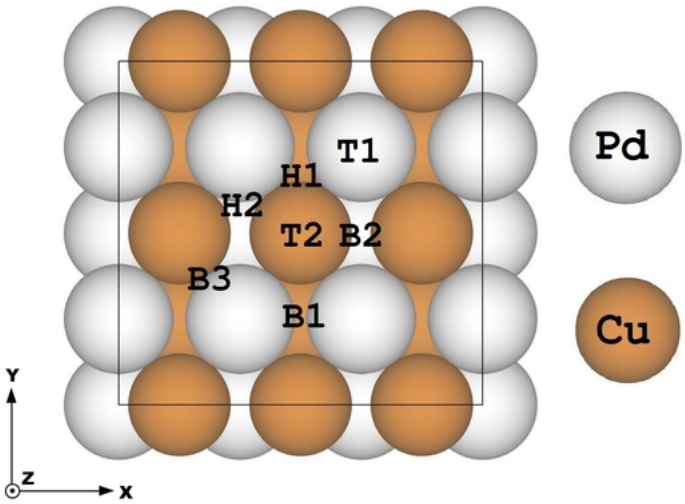

Figure 6.3: Top view of PdCu (110) surface. The adsorption sites considered for H adsorption are marked. T-ontop adsorption, B-bridge site connecting two atoms and H-hollow site connecting three atoms.

(110) surface has a surface energy of 1.33 Jm^{-2} and its surface stability is independent of the surface preparation conditions. Additionally, the (110) surface is found to be the most stable one for all the allowed values of $\Delta\mu_{Cu}$.

Since the (110) surface is the most stable surface for all the allowed values of $\Delta\mu_{Cu}$, it is more likely that under the experimental conditions these facets will be exposed. Hence, the (110) surface was chosen to study the processes involved in the H_2 permeation mechanism.

6.3.2 H_2 adsorption and dissociation on PdCu(110) surface

H_2 adsorption and dissociation on the membrane surface, are the first two steps in the solution diffusion mechanism. For a good hydrogen purification membrane, the hydrogen molecule should readily adsorb and dissociate on the membrane surface. Hence, first the adsorption and dissociation mechanism of H_2 molecule on PdCu(110) surface is studied. To find the most stable adsorption geometry for H_2 on (110) surface, H_2 molecule was placed over all the well-defined adsorption sites. Unlike the single metal system, two different top sites (Pd and Cu) are present on the PdCu (110) surface which is defined as the

T1 and T2 respectively. Similarly, there are three bridge sites denoted by B1, B2 and B3. B1 and B2 are the bridge sites between two Pd and two Cu atoms respectively, while B3 is the bridge site formed between a Pd and a Cu atom. In addition to the top and bridge sites the surface has two hollow sites: one formed by two Pd and one Cu atom (denoted by H1) and the second formed by one Pd and two Cu atoms (denoted by H2). All the sites are shown in Figure-6.3.

The topmost layer of the (3×2) supercell consists of six Pd atoms and six Cu atoms. The surface hydrogen coverage (θ_{H_2}) was defined as the number of H_2 molecule binding to the surface per surface Pd atom. With this definition, one H_2 molecule on a (3×2) supercell corresponds to θ_{H_2} = 0.16 ML. At this coverage, in the most stable adsorption geometry, the H_2 molecule binds on top of Pd (T1 site) in an activated form with an H-H bond length of 0.85 Å. In this adsorption configuration, H_2 binds to the surface Pd such that the molecular axis is parallel to the surface with palladium-hydrogen distance (d_{Pd-H}) of 1.79 Å. The adsorption energy for this configuration is found to be -0.35 eV, and the H-H bond length (d_{H-H}) is about 0.85 Å. The adsorption energy decreases to -0.23 eV after incorporating the zero point energy (ZPE) corrections. Opalka *et al.* also reported the same adsorption geometry for θ_{H_2}=0.25 ML on this surface and a surface H_2 distance of 1.9 Å. [152] In addition to the above-mentioned geometry H_2 also binds weakly (-0.01 eV binding energy) on top of Cu with d_{Cu-H} of 1.88 Å. The H_2 molecule placed on all other adsorption sites ends up in any one of the above mentioned top sites.

Since the adsorption of H_2 on top of the copper site is very weak, the hydrogen molecule adsorbed on T1 site is considered as the initial configuration to study the hydrogen dissociation (marked as IS in Figure-6.4). To find the final configuration, two H are placed at various possible adsorption sites like bridge and hollow sites. In the most stable geometry, the two H atoms are adsorbed on two nearby hollow sites (H1), which are formed by two Pd atoms and one Cu atom (marked as FS in Figure-6.4). The dissociative adsorption of two H atoms is about -0.77 eV thermodynamically more stable than that of adsorption of molecular hydrogen. A reaction pathway was established for H_2 dissociation starting from above mentioned initial and final configurations and the minimum energy path obtained from CI-NEB calculation is presented in Figure 6.4. The classical barrier for H_2 dissociation is estimated to be 0.27 eV, and this decreases to 0.15 eV after incorporating the quantum corrections. The d_{H-H}, which is about 0.85 Å in the initial state is stretched

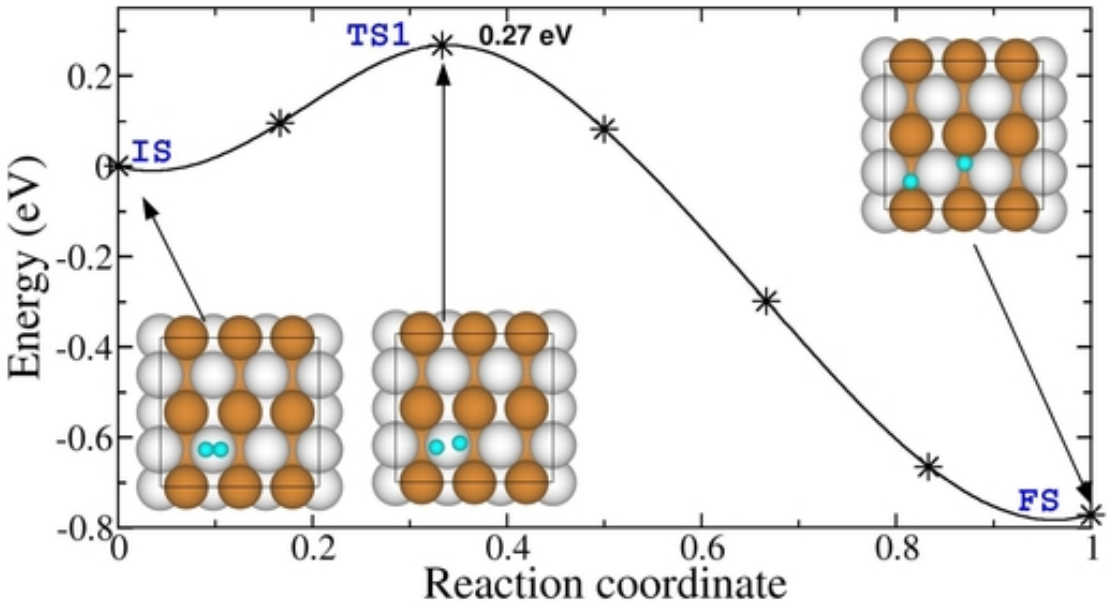

Figure 6.4: Energy profile of H_2 dissociation on PdCu(110) surface.

to 1.36 Å at the transition state. These results imply that the H_2 molecule will readily dissociate into atomic H on this surface; the rate constant for the H_2 dissociation at 300 K is estimated to be 2.02 $\times 10^{12}$ s^{-1}.

6.3.3 H adsorption on PdCu(110) surface, subsurface and bulk PdCu

6.3.3.1 Adsorption on surface at low coverage: θ_H = 0.16 ML

The H-atom coverage will have a strong influence on the adsorption energies associated with the various binding site on the surface. By adding one H atom at a time to the surface, first the adsorption site which has highest thermodynamic stability will be filled. To find the most stable adsorption site for the atomic hydrogen on PdCu(110) surface one H atom was placed over all adsorption sites shown in Figure-6.3. One H-atom in a supercell corresponds to the H coverage (θ_H) of 0.16 ML. Upon relaxation, the H atoms are found to be stable on T1, B1, H1 and H2 adsorption sites. The H atoms placed on other adsorption sites ended up in any one of the above-mentioned sites. The adsorption energies calculated using eq-6.2 are presented in Table.6.2. From this table, it is seen that adsorption

Table 6.2: Adsorption energies, d_{Pd-H} and d_{Cu-H} after H adsorbed on PdCu(110) surface at θ_H = 0.16

Adsorption site	E_{ads}/H (eV)	E_{ads}^{ZP}/H (eV)	d_{Pd-H} (Å)	d_{Cu-H} (Å)
T1	0.03	0.04	1.56	-
B1	-0.56	-0.53	1.74, 1.74	-
H1	-0.59	-0.55	1.77, 1.77	1.82
H2	-0.38	-0.35	1.74	1.79, 1.80
S1-Td	-0.05	-0.01	1.72, 1.77	1.78, 1.81
S2-Td	-0.09	-0.04	1.75, 1.75	1.78, 1.78
B-Td	-0.07	-0.02	1.75, 1.75	1.77, 1.77
B-Oh1	-0.03	-0.04	1.70	2.07
B-Oh2	-0.05	-0.10	2.06	1.74

of atomic hydrogen is exothermic for all available sites. The stability of the adsorbed H atom follows the following order: hollow > bridge > atop. The adsorption energy of H at the most stable adsorption site (H1 site) is found to be -0.59 eV/H. The next stable B1 bridge site is only 0.03 eV/H atom higher in energy than H1. Opalka *et al.* [152] reported adsorption energy of -0.52 eV for H adsorption on B1 site at θ_H = 0.25 ML. Adsorption on the T1 site, i.e., atop Pd, is endothermic with an adsorption energy of 0.03 eV/H.

6.3.3.2 H adsorption in subsurface at low H coverage: θ_H = 0.16 ML

Adsorption of H in the subsurface is an intermediate state for the diffusion of H from the surface to the bulk. Hence, it is important to understand the binding of H atom at the subsurface. The three inequivalent interstitial sites present in the subsurface (Figure 6.5) are two octahedral sites (Oh) and one tetrahedral site (Td). Of the two octahedral sites, the Oh-1 consists of four Cu atoms occupying the corners of a square and two Pd atoms occupying the axial position of the octahedron and vice versa for the second one (Oh-2). The tetrahedral site is formed by two Pd and two Cu atoms occupying the four corners of a tetrahedron. The subsurface adsorption sites are denoted with a prefix S1 and S2 corresponding to the first and second subsurface layer. At a low H concentration, the H in each of the first and second subsurface binds to the Td site with similar stability (-0.05 eV/H for S1-Td vs -0.07 eV/H for S2-Td). As a result of H binding, the tetrahedron is slightly expanded which is seen from the change in d_{Pd-Cu} (the d_{Pd-Cu} increases from 2.62 and 2.63 Å to 2.75 and 2.75 Å respectively for H binding to S1-Td and S2-Td site respectively). Binding of H to the subsurface is about 0.54 eV less stable in comparison

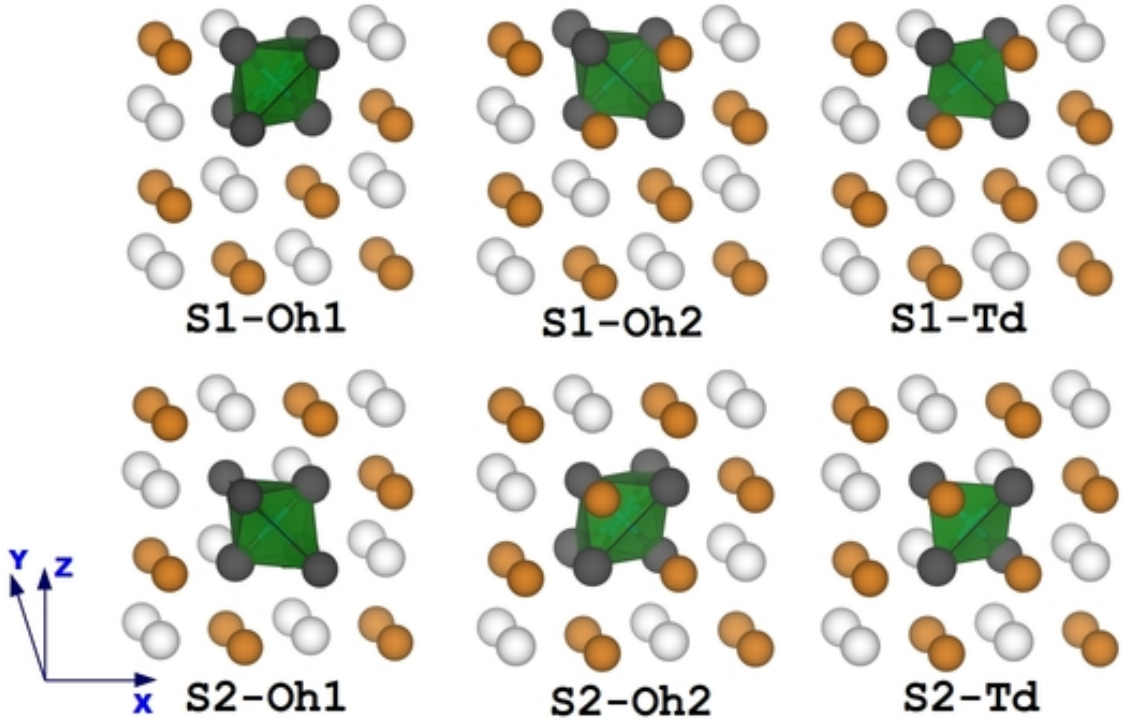

Figure 6.5: High symmetry interstitial sites in PdCu subsurface, considered for H adsorption. Oh- octahedral site, Td- tetrahedral site, S1- first subsurface and S2-second subsurface.

with the surface adsorption suggesting that at low H coverages (θ_H = 0.16 ML) the H preferably occupies the surface sites than the subsurface sites.

6.3.3.3 H adsorption at high H coverages: $\theta_H > 0.16$ ML

At higher H coverages the pre-adsorbed hydrogen can have a significant effect on the adsorption of the upcoming hydrogen. To study this, two H atoms are placed in a (3×2) supercell which corresponds to θ_H = 0.33 ML. On the (110) surface twelve distinct H1 sites are present (H1 site is the most stable binding site for H adsorption at θ_H = 0.16 ML). Of the two hydrogen atoms, one H is placed at any one of the most stable H1 sites. Among the remaining eleven H1 sites four sites are equivalent to four other sites by symmetry. Now, the other H atom can occupy any one of the seven possible H1 adsorption sites, and all these cases are considered. Figure-6.6(a) shows the adsorption energy as a function of H-H distance (d_{H-H}). For θ_H = 0.33 ML, the strength of H adsorption is more or less independent of the distance between them when the H atoms are more than 3 Å apart. The adsorption energies lie between -0.57 eV/H and -0.59 eV/H which is similar to that of the adsorption energy found for θ_H = 0.16 ML. However, when d_{H-H} is less than 3 Å the H adsorption is thermodynamically less stable. The obtained adsorption energy of -0.35 eV/H for the case where the d_{H-H} is 1.70 Å, which is relatively small compared to a value of -0.59 eV/H obtained at θ_H = 0.16 ML.

Till now for θ_H = 0.33 ML, the configurations in which both the H adsorbs only on the available H1 sites are considered. However, other possible combinations of sites are also there. To explore those, the adsorption energy was calculated by placing one H at the H1 site and other H at the H2 site. For this combination, the adsorption energy obtained (red filled circles) is more or less equal to the sum of adsorption energies of hydrogen adsorption to H1 and H2 site at θ_H = 0.16 ML. When the H atoms are placed very close to each other at two adjacent H1 and H2 sites, during the geometry optimization, the H placed at H2 site moves to the next nearest H2 site such that the $d_{H-H} > 3$ Å. However, for other combinations, for example, when one H was placed at the H1 or H2 site and the second one at B1 or T1 site, after relaxation, the H atom placed at the B1 or T1 site ended up occupying H1 or H2 site. The above results suggest that for $d_{H-H} > 3$ Å the hydrogen-hydrogen interaction is independent of the distance between them while the hydrogen-hydrogen interaction is repulsive when they are very close to each other.

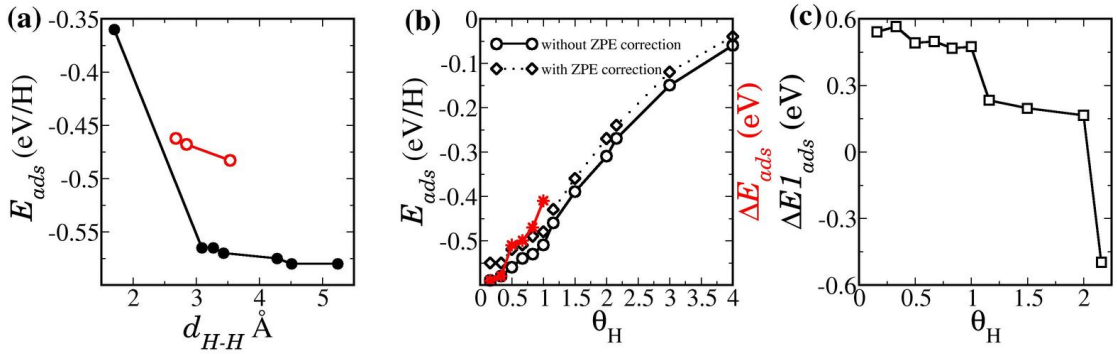

Figure 6.6: (a) Adsorption energy of H at θ_H = 0.33 ML on PdCu(110) as a function of d_{H-H} (black filled circles represent two H atoms are adsorbed on two H1 sites, red open circles represent one H adsorbed at H1 site and the other one adsorbed at H2 site). (b)Adsorption energy of H as a function of θ_H. Black open circles denote adsorption energy calculated using Eq.6.2, black open diamonds denote adsorption energy calculated using Eq.6.3 and red stars denote differential adsorption energy calculated using Eq.6.17. (c) Thermodynamic energy difference for a H adsorption between surface and subsurface.

Experiments such as advanced water gas shift membrane reactors (AWGSMR) are operated at high H_2 partial pressure. Moreover, H adsorption increases the stability of B2 phase, and the H solubility increases with increase in H_2 pressure. [152] Hence it is important to understand the adsorption behavior at higher θ_H. To address the effect of θ_H on the adsorption energy, H adsorption up to θ_H = 4 ML was studied. As seen previously, the H1 site is the most stable adsorption site, and the hydrogen-hydrogen interaction is negligible for $d_{H-H} > 3$ Å. Therefore, in order to find the thermodynamically favorable H adsorption configurations for atomic H up to θ_H = 1 ML, the H atoms are placed on the H1 site in such a way that between every two H atoms, $d_{H-H} > 3$ Å. For θ_H = 1.16 ML (seven H atoms are adsorbed in the surface supercell), six H atoms were placed on the six H1 sites and the seventh one can be either adsorbed at the H2 site ($d_{H-H} \sim 2.5$ Å) or it can be adsorbed at the H1 site ($d_{H-H} = 1.71$ Å). Both of these configurations are considered, and the configuration in which the H atom is adsorbed at the H2 site is about 0.20 eV more stable than the configuration in which all seven hydrogens are adsorbed at the H1 site.

For θ_H = 1.5 ML, the most stable configuration is the one in which six H atoms are placed at six H1 sites, and the remaining three H are placed at H2 sites. The configuration in which all the H atoms are placed at H1 sites is about 0.06 eV/H less stable than the previ-

ous one. Following a similar principle, i.e. to maximize the H-H distance on the surface, for θ_H = 2.0 ML, the most stable configuration is the one in which six H atoms are placed at six H1 sites, and six H atoms are placed at six H2 sites ($d_{H-H} \sim 2.5$ Å). If all the H atoms occupy the H1 site, it is about 0.11 eV/H less stable than the above configuration. To study the H adsorption at θ_H = 2.16 ML, one H atom was added to the most stable configuration of θ_H = 2.00 ML. Now, the upcoming H can occupy any one of the available surface sites (H1, H2 and T1) or the subsurface site. However, in all the surface sites the $d_{H-H} < 2$ Å and the H-H interaction will be repulsive. In the most stable configuration, the upcoming H occupies the first subsurface. The upcoming H occupying surface sites H1, H2 and T1 are 0.68, 0.53 and 0.50 eV less stable respectively than the most stable configuration. Therefore, for $\theta_H > 2.0$ ML, the subsurface sites start filling up. For example, for θ_H = 3.0 and 4.0 ML twelve H atoms adsorbed on the surface and the rest of the atoms are binding to the subsurface tetrahedron sites.

To understand the effect of H coverage on the adsorption energy more clearly the differential adsorption energy was calculated up to θ_H = 1 ML. The differential adsorption energy (ΔE_{ads}) was calculated as,

$$\Delta E_{ads} = E_{slab+nH} - E_{slab+(n-1)H} - \frac{1}{2}E_{H_2} \tag{6.17}$$

All the terms in the right-hand side of the equation are the total energies of the respective systems. Adsorption energy and differential adsorption energy of H as a function of θ_H is given in Figure 6.6(b). Both the adsorption energies and the differential adsorption energies are decreasing with an increase in θ_H. This suggests that the thermodynamic energy gain per H atom adsorption decreases when more and more H is adsorbed on the surface. Further, for the adsorption energy, the zero-point energy corrected values are also plotted. It should be noted that the trends in adsorption energy remain unaltered.

6.3.3.4 Hydrogen adsorption: surface vs subsurface

At θ_H = 0.16 ML, adsorption of H atom at the surface is about 0.54 eV more stable than the adsorption of H at the first subsurface. However, this scenario might change at the higher H coverages, hence to understand how the thermodynamic stability of the H binding to the subsurface changes with θ_H, the energy difference between the two configurations are

calculated, one of which has n H atoms on the surface and the second one with $(n-1)$ H atoms on the surface and one H atom at the subsurface. The above energy difference, $\Delta E1_{ads}$, is calculated using the following expression:

$$\Delta E1_{ads} = E_1 - E_2, \tag{6.18}$$

where E_1 is the energy of the system in which one H atom is binding to the first subsurface and all other H atoms are adsorbed at the surface and E_2 is the energy of the system in which all the H atoms are adsorbed at the surface. A positive value of $\Delta E1_{ads}$ means that the adsorption of hydrogen to the surface is thermodynamically more stable than the adsorption of hydrogen to the subsurface and vice versa for negative values. $\Delta E1_{ads}$ as a function of θ_H is plotted in Figure-6.6(c). The $\Delta E1_{ads}$ was calculated till θ_H =2.16 ML because based on the results presented in the previous subsection, at θ_H =2.16 ML, H atoms start occupying the subsurface sites. At the low value of θ_H, adsorption of H to the surface is thermodynamically more stable than subsurface and $\Delta E1_{ads}$ is almost independent of θ_H up to 1 ML. Above this coverage, it starts decreasing till 2.0 ML. Beyond 2.0 ML of H coverage $\Delta E1_{ads}$ becomes negative showing that the thermodynamic stability is reversed.

6.3.3.5 H absorption in bulk PdCu

Opalka *et al.* reported the H solubility in the B2 phase over a wide range of temperature and pressure. They found that the H solubility is at a maximum on the low Cu side of the B2 phase, exhibiting a maximum ratio of 0.033 H/metal at the 43.8 bar and 673 K operating condition. [152] To study the H absorption (interstitial solubility) in PdCu, the bulk B2 phase was modeled with 3×3×3 super-cell with one H absorbed in it. The H concentration (H/M = 0.018) with this model is within the solubility limit of H/M = 0.033. The H atom can occupy any one of the three inequivalent high symmetry interstitial sites present in bulk PdCu (Figure 6.7), i.e., two octahedral sites (Oh) and one tetrahedral site (Td). The interstitial binding sites present in bulk PdCu are denoted with a prefix B. Of the two octahedral sites, the B-Oh-1 (B-Oh-2) consists of four Cu (Pd) atoms occupying the corners of a square and two Pd (Cu) atoms occupying the axial position of the octahedron. The tetrahedral site (B-Td) is formed by two Pd and two Cu occupying the four corners of a tetrahedron.

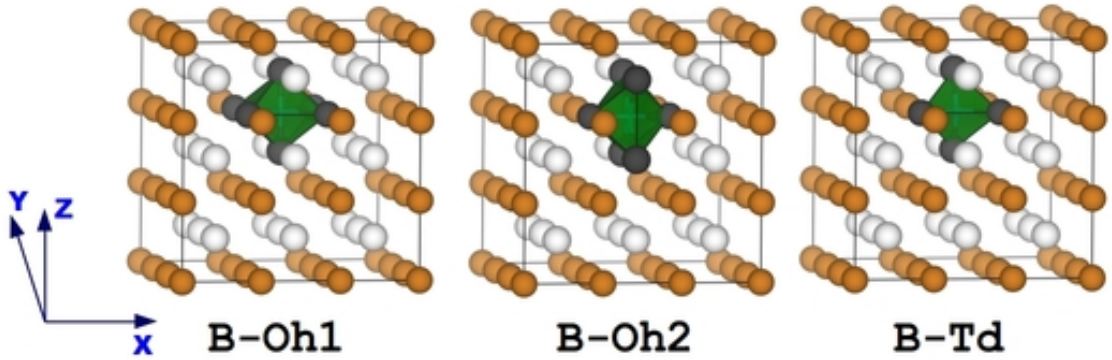

Figure 6.7: High symmetry interstitial sites in bulk PdCu, considered for H adsorption. Oh- octahedral site, Td- tetrahedral site.

Among these possible sites, the B-Td site is found to be most stable one with a binding energy value of -0.07 eV. Due to H incorporation, the tetrahedron is slightly expanded, and the volume expansion is estimated to be 5.93 % which is seen from the increase in Pd-Cu bond length (d_{Pd-Cu}) from 2.62 Å to 2.72 Å. In contrast, when the H is binding to the B-Oh-1 site, the octahedron is elongated along the Pd-Pd axis (d_{Pd-Pd} increases from 3.02 to 3.39 Å) and slightly contracted in the Cu plane (d_{Cu-Cu} decreases from 3.02 to 2.95 Å). Similarly, when the H is binding to the B-Oh-2 site, the octahedron is elongated along the Cu-Cu axis (d_{Cu-Cu} increases from 3.02 to 3.48 Å) and slightly contracted in the Pd plane (d_{Pd-Pd} decreases from 3.02 to 2.91 Å). Hydrogen binding to the B-Oh1 and B-Oh2 sites are respectively 0.04 and 0.02 eV less stable than the most stable B-Td site. The volume expansion after the H binding to B-Oh1 and B-Oh2 sites are estimated to be 5.82 % and 6.24 % respectively. It should be noted that the predicted binding sites and the binding energies are consistent with those reported in Ref. [131] and [152]. The binding energy of H at the most stable site in bulk PdCu is about 0.52 eV less stable than that of H at the most stable site on the surface suggesting that H atom prefers to stay on the surface than the bulk.

6.3.4 Thermodynamic analysis

To understand how the relative stability of the H covered surfaces change as a function of hydrogen partial pressure and temperature, the thermodynamic analysis was performed

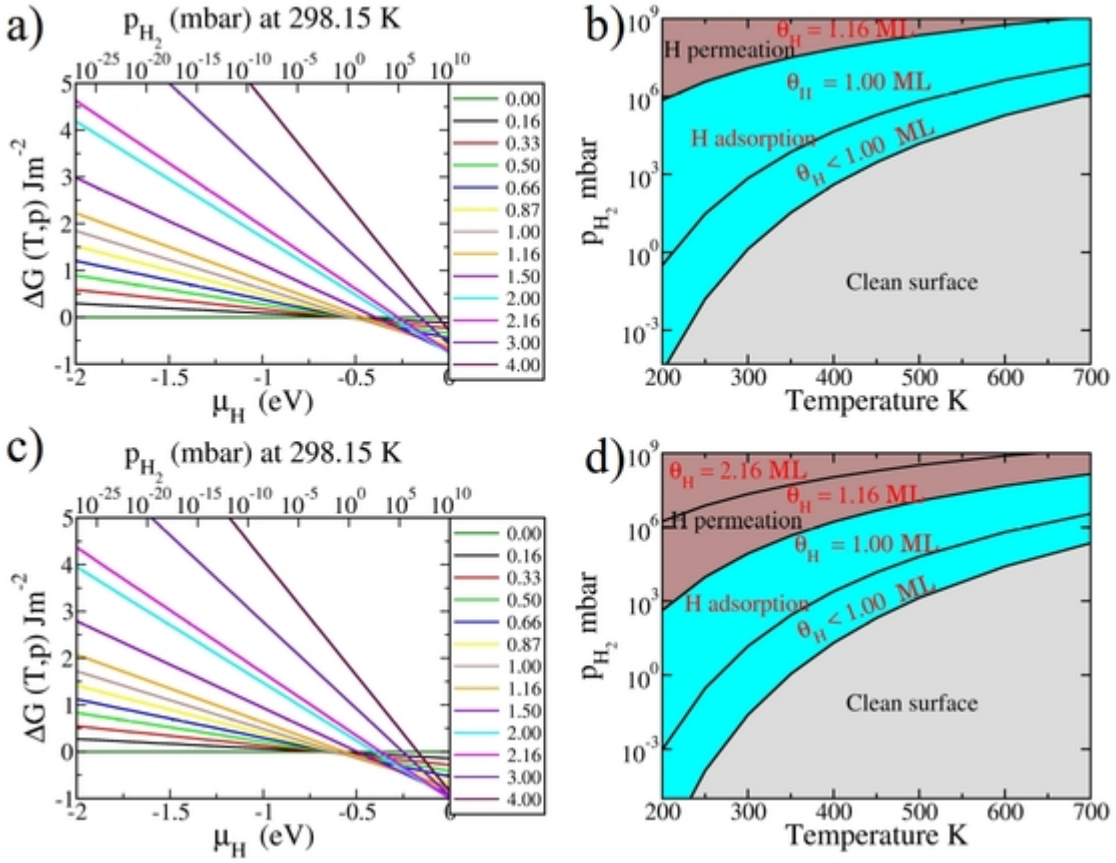

Figure 6.8: (a)Relative surface free energy as a function of μ_H at room temperature for the various θ_H. (b) Surface phase diagram of H adsorbed PdCu(110) surface. (c)Relative surface free energy calculated with quantum corrected energies as a function of μ_H at room temperature for the various θ_H. (d) Surface phase diagram of H adsorbed PdCu(110) surface constructed using quantum corrected energies.

as described in Section-6.2.3. The change in Gibbs surface free energy ($\Delta G(T,p)$) of the hydrogen adsorbed surfaces with respect to clean surface as a function of μ_H at room temperature is presented in Figure-6.8(a). From the phase diagram (Figure-6.8(a)) it is find that at room temperature the clean surfaces are thermodynamically more stable than the H adsorbed ones till 1 mbar hydrogen partial pressure. For a narrow range of hydrogen partial pressure (from 1 to 700 mbar) the H adsorbed surface with $0 \leq \theta_H \leq 1$ ML coexist. Further increase in hydrogen partial pressure to 1.2×10^7 mbar stabilizes $\theta_H = 1$ ML surface. Above 1.2×10^7 mbar of hydrogen partial pressure, the $\theta_H \geq 1$ML surfaces becomes thermodynamically more stable surfaces and the H atoms starts occupying the subsurface sites.

Similar analysis was carried out for a temperature range of 200 K to 700 K. Based on the most stable surface terminations over that temperature range a phase diagram was constructed as a function of hydrogen partial pressure and temperature, which is given in Figure-6.8(b). As the temperature increases from 200 K to 700 K the equilibrium boundary between the clean surface and hydrogen covered surface increases from 10^{-5} mbar to 10^{6} mbar suggesting that the clean surface will be stable over a wider range of hydrogen partial pressure as the temperature increases. This results in a decrease of the H adsorption window with a rise in temperature. At 200 K the hydrogen adsorption was found to be more stable in the range of hydrogen partial pressure from 10^{-5} mbar to 7.2×10^{5} mbar. However, this range reduces between 10^{6} mbar to 10^{9} mbar as the temperature is increased to 700 K.

A surface phase diagram was constructed including the zero point energy correction. When the quantum corrected energies are used the equilibrium is shifted to lower p_{H_2}. At room temperature the hydrogen covered surface becomes thermodynamically more stable than clean surfaces even at a low hydrogen partial pressure ($p_{H_2} > 10^{-2}$ mbar)(Figure-6.8(c)). For a narrow range of hydrogen partial pressure (from 10^{-2} to 15 mbar) the H adsorbed surface with $0 \leq \theta_H \leq 1$ ML coexist. Further increase in hydrogen partial pressure stabilizes the $\theta_H = 1$ ML surface, and it remains the most stable one up to 10^{5} mbar. Above 10^{5} mbar of hydrogen partial pressure, the $\theta_H \geq 1$ML surfaces becomes thermodynamically most stable, and the H atoms start occupying the subsurface sites. The phase diagram constructed based on the most stable surface termination over a temperature range of 200 K to 700 K is given in Figure-6.8(d). The equilibrium boundary between the hydrogen covered surface and clean surface increases from 10^{-7} mbar hydrogen partial pressure at 200 K to 10^{5} mbar at 700 K. Additionally, within the acceptable H partial pressure range, the surface with $\theta_H = 2.16$ ML is stable at high H_2 partial pressures. It should be noted that this is in contrast with what was found without incorporating the zero point energy (ZPE) corrections. This suggests the strong effect the ZPE have on the thermodynamics of this systems, in addition to that seen for the reaction barriers.

6.3.5 H diffusion on PdCu(110) surface, subsurface and inside bulk PdCu

6.3.5.1 H diffusion inside bulk PdCu

In this section, the H diffusion from one Td hole to near neighboring Td hole inside the bulk is studied. Two possible paths are considered; in the first path, the H occupying the Td site diffuses to the next nearest one through a $PdCu_2$ triangular face. The second path also similar to the first one, however in this path the H diffuses through a Pd_2Cu triangular face. The H atom can locally hop between the sites by following any one of the above-mentioned paths. However, the long-range diffusion is possible only by following both of these paths. [131] Hence, for good permeation the H atom should readily diffuse by both of these paths. The energetics for the H diffusion inside bulk PdCu by the above-mentioned paths are given in Figure 6.9. The results show that both these paths are having similar reaction barrier associated with them.

Due to significant quantum effects at low temperatures, the diffusion of hydrogen inside bcc metals are known to yield significantly different activation energies at low and high temperatures. [153] The predicted activation barriers for hydrogen diffusion are in very good agreement with the low temperature (below 350 K) experimental report of 0.03 eV inside bcc PdCu with 47 atom % Cu. Experiments by Piper for the diffusion of hydrogen inside bcc PdCu with 52.5 atom % Cu at moderately high temperatures (from 298 K to 406 K) yielded a somewhat larger barrier of 0.10 eV. [137] However, at high temperature (623 K to 673 K) Nayebossadri *et al.* reported a barrier of 0.06 eV for the diffusion of hydrogen in bcc PdCu with 53 atom % Cu. [154]

The theoretically predicted H diffusion barriers inside bcc PdCu reported in literature significantly vary depending on the methods used to estimate the barriers. Using the dimer method, Kamakoti and Sholl [131, 138] predicted that the diffusion barriers for the H diffusion inside bulk PdCu following first and second path are respectively to be 0.02 eV and 0.15 eV. It should be noted that the barrier reported by these authors for the second path is significantly larger than that of the first path. In another report, using lattice dynamics Opalka *et al.* predicted a significantly lower barrier of 0.07 eV for the diffusion of H by the second path. [152] Using CI-NEB method, Liu *et al.* predicted a diffusion barrier of 0.06 eV for the interstitial diffusion of H inside bcc PdCu. [155] Moreover, the barrier for

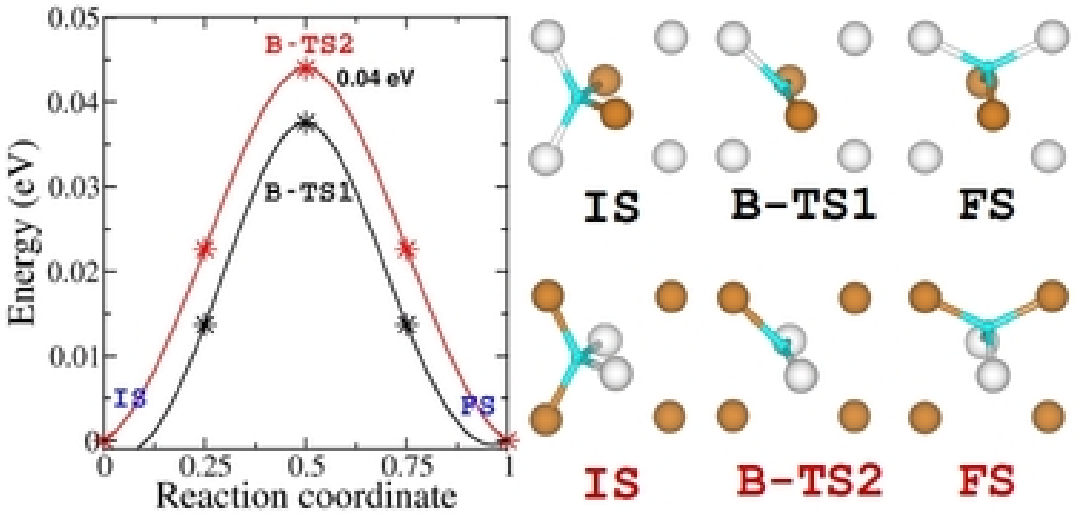

Figure 6.9: Energy profile of H diffusion from one Td site to near neighboring Td site inside bulk PdCu with two different path. Black and red respectively corresponds to the paths going through $PdCu_2$ and Pd_2Cu triangular transition states.

the interstitial diffusion of H inside bcc PdCu is significantly smaller than that observed in bulk Pd (0.21 eV) and the fcc PdCu phase (0.35 eV). [128, 139]

6.3.5.2 Diffusion of H on PdCu(110)

In addition to easy dissociation of H_2 on the PdCu alloy surface, the diffusion of H on the membrane surface and penetration of H from the surface to the subsurface are the important surface processes. For a good membrane, these processes should also readily occur. Hence, it is important to study the diffusion of H on the membrane surface to understand the surface processes in the solution-diffusion mechanism. Figure-6.10 shows the diffusion paths of H on PdCu(110) surface. Six possible paths were explored. First three paths are the diffusion of H from one H1 site to the next H1 site through three different saddle points. In the first path, H adsorbed at the most stable H1 site (binds to two Pd with d_{Pd-H} = 1.78 Å and one Cu with d_{Cu-H} = 1.83 Å) diffuses to the next H1 site through the B1 site. During this process, the Cu-H bond present in the initial state breaks and at the saddle point (marked as B1 in Figure-6.10) the H is binding to only two Pd atoms with a Pd-H distance of 1.74 Å. Finally, a new Cu-H bond is formed on the other side. The classical barrier associated with this process is 0.03 eV and slightly decreases to 0.01 eV after quantum correction. Because of the very small activation barrier, this

path is the most favorable path for H diffusion on (110) surface. The rate constant for this diffusion at 300 K is calculated to be 1.33 $\times 10^{12}$ s^{-1}. The second path is similar to the first one, however in this path two d_{Pd-H} bonds are breaking, and at the saddle point, the H is binding to Cu with a Cu-H bond length of 1.51 Å. Finally, two new Pd-H bonds are formed on the other side of the TS. The large barrier of 1.01 eV associated with this path makes it very unlikely to follow. The third path is also very similar to the first two paths. However, in this path, two bonds (one Pd-H bond and one Cu-H bond) are breaking. At the saddle point (marked as T1 in Figure-6.10), the H is binding to one Pd with a Pd-H distance of 1.56 Å. In the final state two new bonds (one Pd-H bond and one Cu-H bond) are formed. This path has a moderate diffusion barrier of 0.61 eV.

The fourth path involves two steps. In the first step, the H adsorbed at the most stable H1 site diffuses to the less stable H2 site with a barrier of 0.28 eV. At the H2 site, the H is binding to one Pd with Pd-H distance of 1.74 Å and two Cu atoms with Cu-H distance of 1.79 Å. In the next step, the H adsorbed at the H2 diffuses to the H1 site. Energetically the second step is equivalent to the first step and opposite in direction, hence only the first step is shown in Figure-6.10. This path has a diffusion barrier of 0.28 eV associated with this and slightly decreases to 0.27 eV after quantum correction. At the saddle point (marked as B3 in Figure-6.10) the H occupies the B3 bridge site (with d_{Pd-H} = 1.68 Å and d_{Cu-H} = 1.69 Å). The rate constant for this diffusion path at 300 K is calculated to be 1.27 $\times 10^{8}$ s^{-1}. In the last two paths (fifth and sixth), the H adsorbed at the H2 site (about 0.2 eV less stable than the H1 site) diffuses to the next H2 site. During the fifth path, two Cu-H bonds break and the saddle point for this diffusion process is the same as the saddle point T1. Finally, two new Cu-H bonds are formed on the other side. This path has a diffusion barrier of 0.41 eV. In the sixth path, one Pd-H bond breaks and at the saddle point the H is binding to two Cu with a Cu-H distance of 1.73 Å. The barrier associated with this process is 0.08 eV.

6.3.5.3 Diffusion of H from the surface to bulk

An important step in H permeation is the penetration of the surface H atoms to the subsurface. For a good permeation membrane, this process should have a small barrier. In this section, the kinetics of the diffusion of surface H to the subsurface is studied as a function of H coverage.

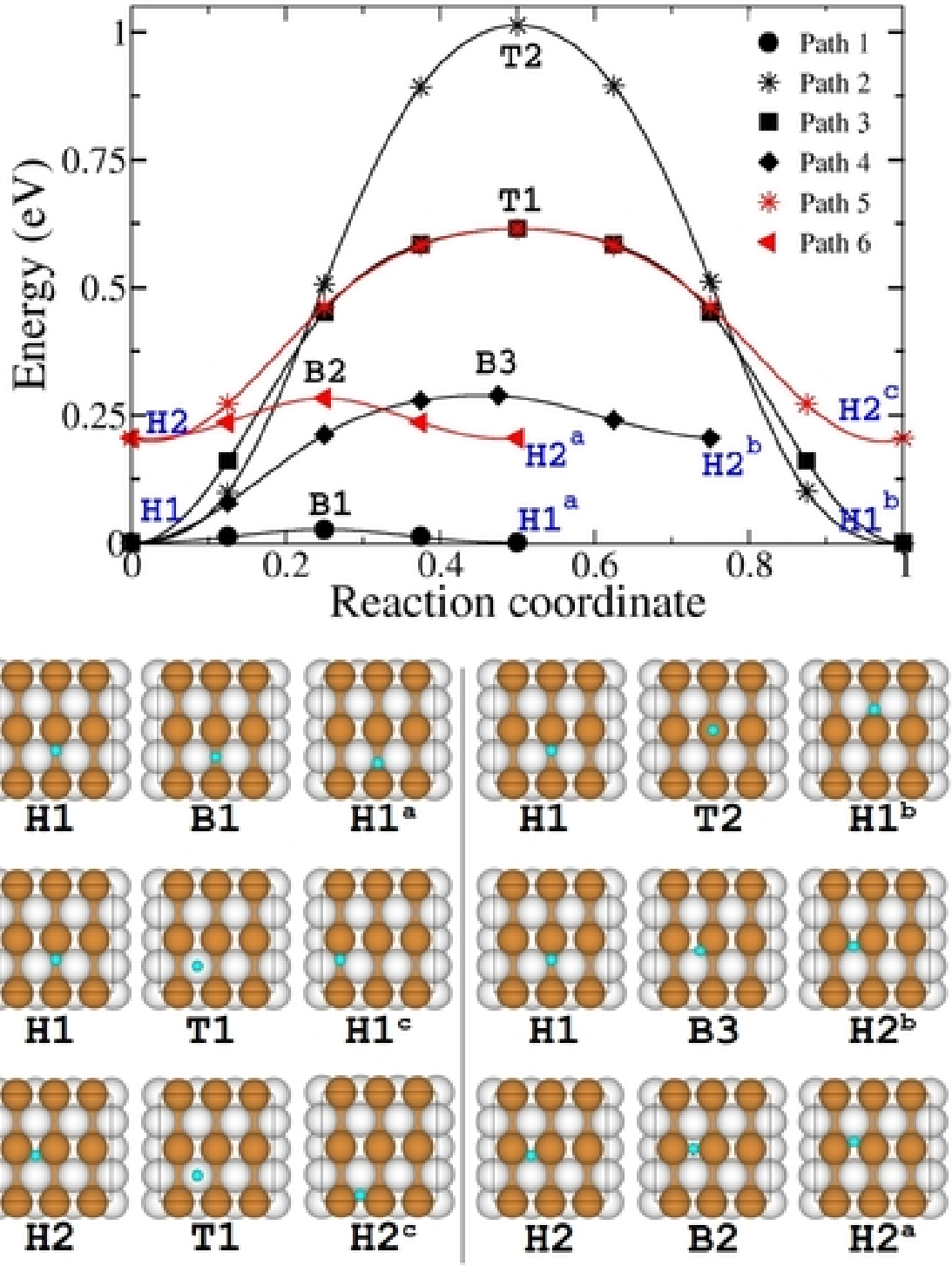

Figure 6.10: Energy profile of H diffusion on PdCu(110) surface.

A diffusion path was constructed in which the most stable adsorption configuration of H atom, i.e., one H atom ($\theta_H = 0.16$ML) adsorbed at the H1 site on the surface was considered as the initial state. In the final state, the H atom occupies the interstitial tetrahedral site of the first subsurface of PdCu (S1-Td). The H atom diffuses vertically from the surface to the first subsurface. The H diffusion path is shown in Figure 6.11. The diffusion barrier for this step is found to be 0.55 eV, and slightly decreases to 0.53 eV after quantum correction. This barrier is relatively larger than that of H diffusion barrier on the surface.

From Section-6.3.3.2, the thermodynamic energy difference for H adsorption between the surface to the subsurface, is significantly affected for $\theta_H > 1$ML. Hence, the effect of H coverages on the barrier associated with this diffusion process is also studied. To do so, three H coverages are considered, namely, 1 ML, 1.16 ML and 1.50 ML. These results show that the barrier associated with the penetration is significantly lowered (from 0.55 eV for θ_H = 0.16 ML to 0.26 eV for θ_H = 1.16 ML) as the θ_H increases above 1 ML. However, a further increase in θ_H to 1.50 ML has no significant effect in lowering the barrier. The reduction in the H penetration barrier at high H coverage can be attributed to the enhanced thermodynamic stability of the H at the subsurface sites at a higher value of θ_H.

After the H atom enters the subsurface, it readily diffuses further towards the bulk. In the next step, H diffuses from the first subsurface to the second subsurface. The two possible paths that have been investigated are shown in Figure 6.11. H diffuses from the first subsurface to the second subsurface through several transition states (labeled as TS1, TS2, TS3, TS4, TS5 and TS6 in Figure 6.11) and metastable states (labeled as S1-Td1, S2-Td1, S1-Td2 and S2-Td2 in Figure 6.11). The activation energies for these diffusions are calculated to be 0.06 and 0.07 eV respectively and decrease to 0.04 eV after quantum correction for both the cases. These values are relatively small compared to the diffusion barrier associated with the H diffusion from the surface to the first subsurface and very similar to that of H diffusion inside bulk PdCu. The above results indicate that once H atom penetrates into the first subsurface it can easily diffuse into the bulk.

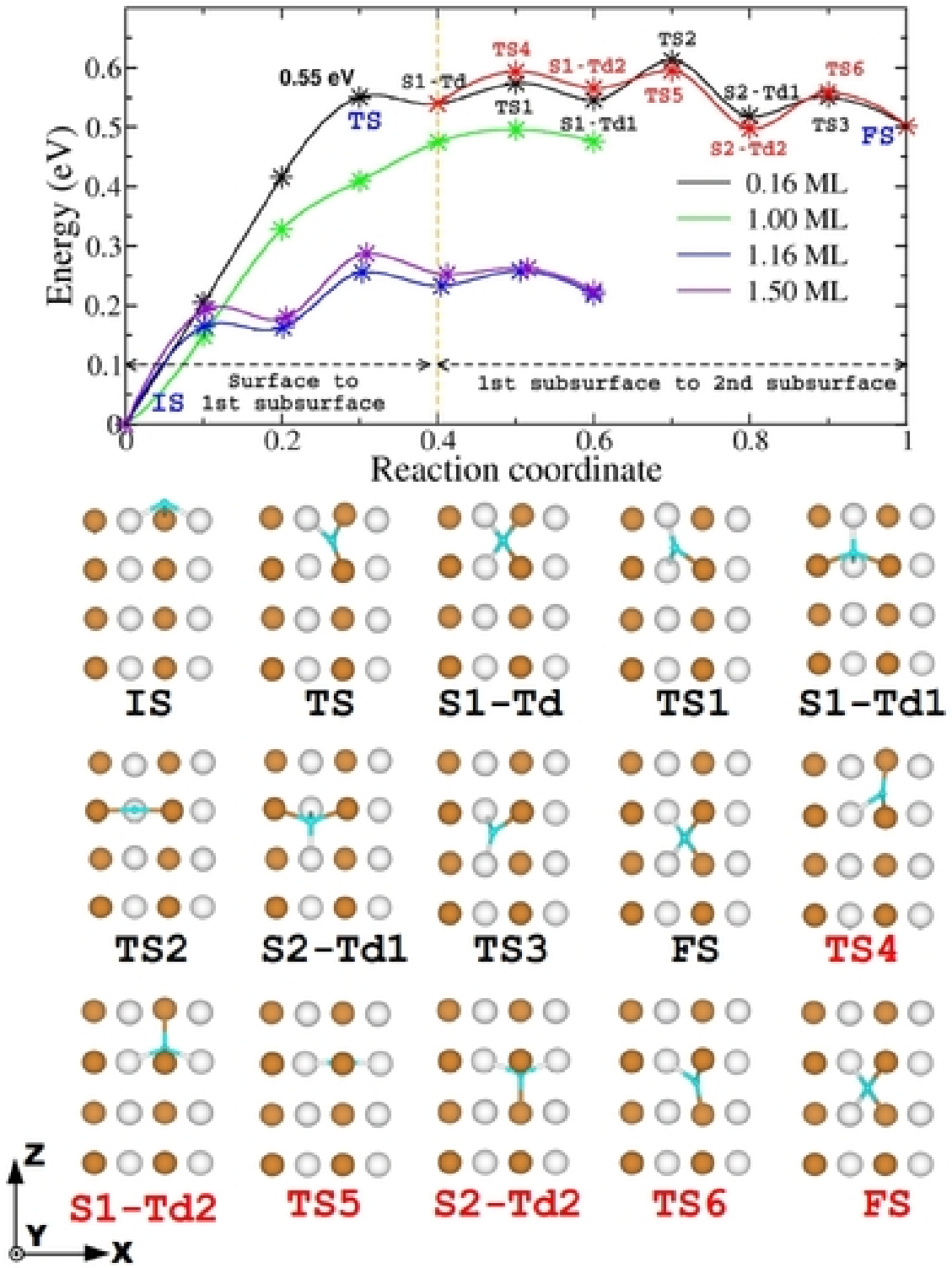

Figure 6.11: Energy profile of H penetration from PdCu(110) surface to the bulk.

6.3.6 H_2 reassociation energetics and kinetics

At the product side of the membrane surface first two H atoms combine to form H_2 molecule (H_2 reassociation) and then the desorption of H_2 from the surface produces pure H_2. The barrier required for the reassociation of H_2 molecule from two H atoms is the barrier corresponding to the reverse reaction of H_2 dissociation. Based on the results of the barrier calculation for H_2 dissociation at low H_2 coverages in Section-6.3.2, the classical barrier for the reverse reaction is estimated to be 1.04 eV and slightly decreases to 0.96 eV after quantum correction. This barrier is significantly large compared to the barrier corresponding to the forward reaction (0.15 eV). The rate constant for the reassociation of H_2 molecule on the surface at 300 K is calculated to be 2.50 $\times 10^{-1}$ s^{-1}.

However, in a realistic situation, it is expected that H_2 reassociation will take place in the presence of surface and subsurface H atoms. Hence the H_2 reassociation barriers might be affected by them. Therefore, the H reassociation barrier was calculated when there are H atoms in the subsurface as well as on the surface. To choose a reasonable coverage, the diffusion barriers of H atom from the subsurface to the surface is very small, and the thermodynamic energy gain for the system when the subsurface H atom diffuses out to the surface is large. This results in a very small amount of subsurface H on the product side of the membrane. From the calculations of H adsorption in Section-6.3.3.4, it is found that the lowest H coverage at which the H atoms start occupying the subsurface sites is about 2.16 ML (the surface is completely covered with H, and there is one H atom in the subsurface). Hence, this particular coverage was chosen to study H reassociation to form H_2.

Of the two possible pathways (Figure 6.12), in the most favorable one the H atoms at the nearby H1 and H2 sites recombine to form H_2 on the T1 site. The barrier for the same is about 0.47 eV (0.40 eV after zero point energy corrections). It should be noted that the barrier is reduced to almost half of that at low H coverage. The estimated rate constant at θ_H = 2.16 ML for reassociation of H_2 at 300 K (6.78 $\times 10^6$ s^{-1}) is about 10^6 times larger than the rate constant at θ_H = 0.16 ML.

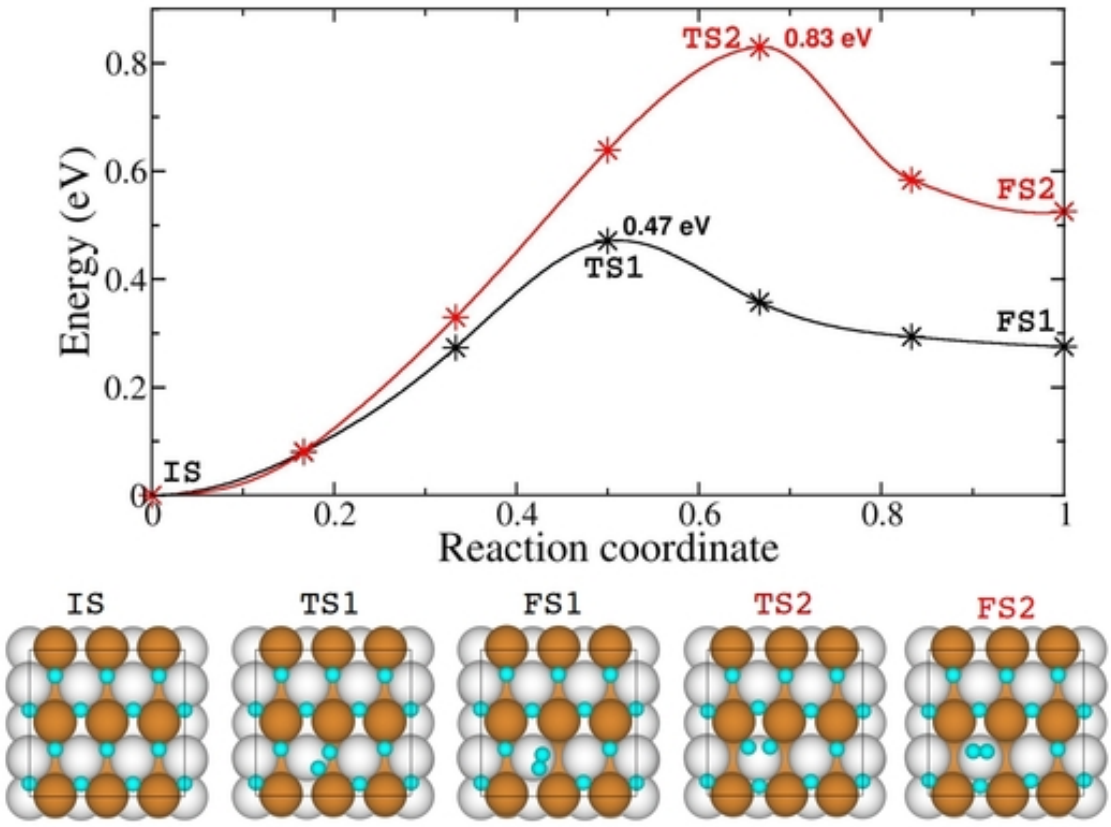

Figure 6.12: Energy profile of H reassociation to H_2 on PdCu(110) surface at θ_H = 2.16 ML.

Table 6.3: classical barriers (ΔE^c), quantum corrected barriers (ΔE^q), Arrhenius prefactor and rate constants calculated with the quantum corrected barriers (k_{hTST} at 300 K) of important processes of solution diffusion mechanism.

	ΔE^q (eV)	ΔE^c (eV)	Prefactor (s^{-1})	k_{hTST} at 300 K (s^{-1})
H_2 dissociation at θ_{H_2} = 0.16 ML	0.15	0.27	7.17×10^{14}	2.02×10^{12}
H_2 dissociation at θ_H = 1.00 ML	0.20	0.29	5.73×10^{13}	2.81×10^{10}
H_2 dissociation at θ_H = 2.16 ML	0.11	0.20	2.50×10^{12}	3.88×10^{10}
H diffusion on surface (path 1)	0.01	0.03	2.32×10^{12}	1.33×10^{12}
H diffusion on surface (path 2)	0.97	1.01	4.92×10^{13}	2.52×10^{-3}
H diffusion on surface (path 3)	0.59	0.61	1.77×10^{13}	2.32×10^{3}
H diffusion on surface (path 4)	0.27	0.28	4.81×10^{12}	1.27×10^{8}
H diffusion on surface (path 5)	0.39	0.41	1.46×10^{13}	3.49×10^{6}
H diffusion on surface (path 6)	0.03	0.08	1.12×10^{13}	2.95×10^{12}
H penetration at θ_H = 0.16 ML	0.53	0.55	1.57×10^{12}	2.13×10^{3}
H penetration at θ_H = 1.00 ML	0.45	0.50	6.24×10^{12}	1.64×10^{5}
H penetration at θ_H = 1.16 ML	0.24	0.26	3.40×10^{12}	2.69×10^{8}
H penetration at θ_H = 1.50 ML	0.27	0.29	3.52×10^{12}	8.73×10^{7}
H diffusion inside bulk (path 1)	0.02	0.04	9.63×10^{12}	4.69×10^{12}
H diffusion inside bulk (path 2)	0.02	0.04	7.03×10^{12}	1.32×10^{12}
H diffusion (bulk to surface)	0.01	0.02	3.60×10^{12}	2.35×10^{12}
Reassociation of H_2 at θ_{H_2} = 0.16 ML	0.96	1.04	3.87×10^{15}	2.50×10^{-1}
Reassociation of H_2 at θ_H = 1.00 ML	0.88	0.81	8.07×10^{14}	2.01×10^{1}
Reassociation of H_2 at θ_H = 2.16 ML	0.40	0.47	3.31×10^{13}	6.78×10^{6}

6.3.7 Temperature dependent kinetics

Table-6.3 presents the quantum corrected barrier and the rate constants of the above-mentioned steps involved in the permeation of H through this model PdCu membrane at 300 K. The temperature dependence of the rate constants for these processes is shown in Figure. 6.13. From Figure 6.13, it is found that the H diffusion from subsurface to bulk and within the bulk is almost independent of temperature because of very low diffusion barriers. At all temperatures considered in the plot, the rate determining steps are diffusion of atomic hydrogen from the surface to the subsurface on the feed side and the reassociation of atomic hydrogen to molecular hydrogen on the product side. However, for both these processes the rates depend significantly on the hydrogen coverages and temperature. The calculations suggest that a high H_2 partial pressure on the feed side and a high H coverage on the product side of the membrane surface significantly speed up these processes. Additionally, the two rate-limiting processes are significantly sped up at high temperatures suggesting that these membranes will act as efficient H permeable membrane at high temperatures.

Further, to compare the obtained results with those reported in the literature, the diffusion

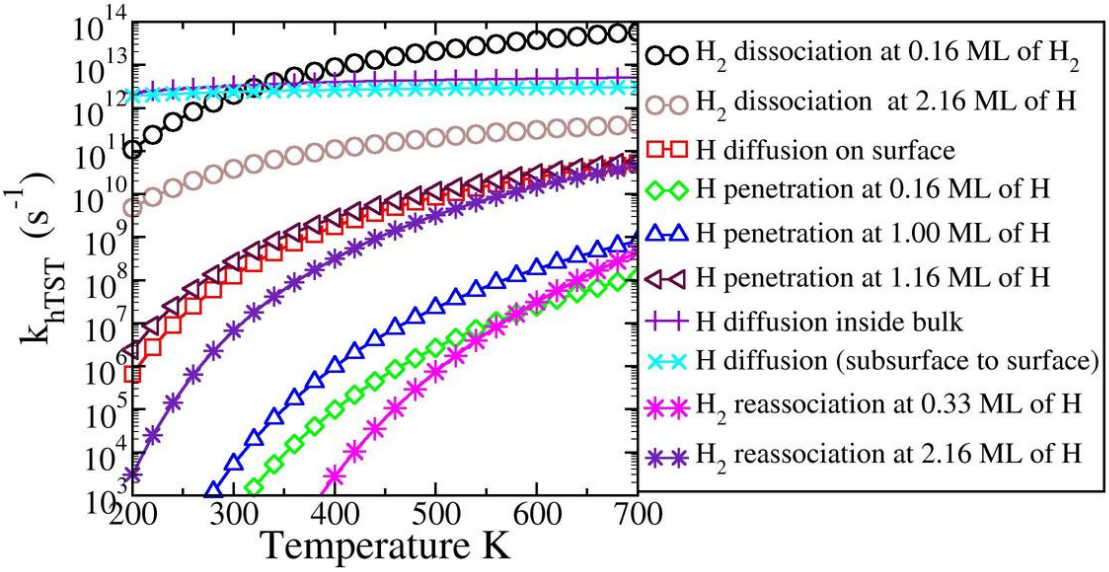

Figure 6.13: Rate constant for some important processes involved in the solution diffusion mechanism as a function of temperature.

coefficient (diffusivity) and permeability of H through the bulk of the membrane were calculated. The diffusion of hydrogen inside bulk PdCu could be described as random jumps between interstitial sites. However, only the diffusion along the direction of flow can help to maximize the hydrogen flow. The diffusivity of hydrogen along the direction of flow can be expressed as, [152, 155]

$$D = \left(\frac{n\alpha^2 k_B T}{6h}\right) exp\left(-\frac{\Delta E^q}{k_B T}\right), \tag{6.19}$$

where, n is the geometrical jump factor, which is 1 for the system considered in this study, α is the jump length, and k_B is the Boltzmann's constant. T, h and ΔE^q denote temperature, Planck's constant and the quantum corrected activation energy respectively. For the system considered in this study, α =1.5 Å and corresponds to the distance between two tetrahedral sites. Figure 6.14(a) shows the plot of diffusivity of H in the bulk of the membrane vs temperature as obtained for $Pd_{50}Cu_{50}$. For comparison, plots of diffusivity vs temperature for fcc-PdCu as well as bcc-PdCu (with compositions similar to that considered in this study and also with slightly different compositions) that had been reported in literature [131, 137, 152–154, 156] are reproduced in the same figure. In comparison with the diffusivities determined by Kamakoti *et al.* from their calculations, at low temperatures the diffusivity is overestimated. This is due to the reason that the barriers obtained

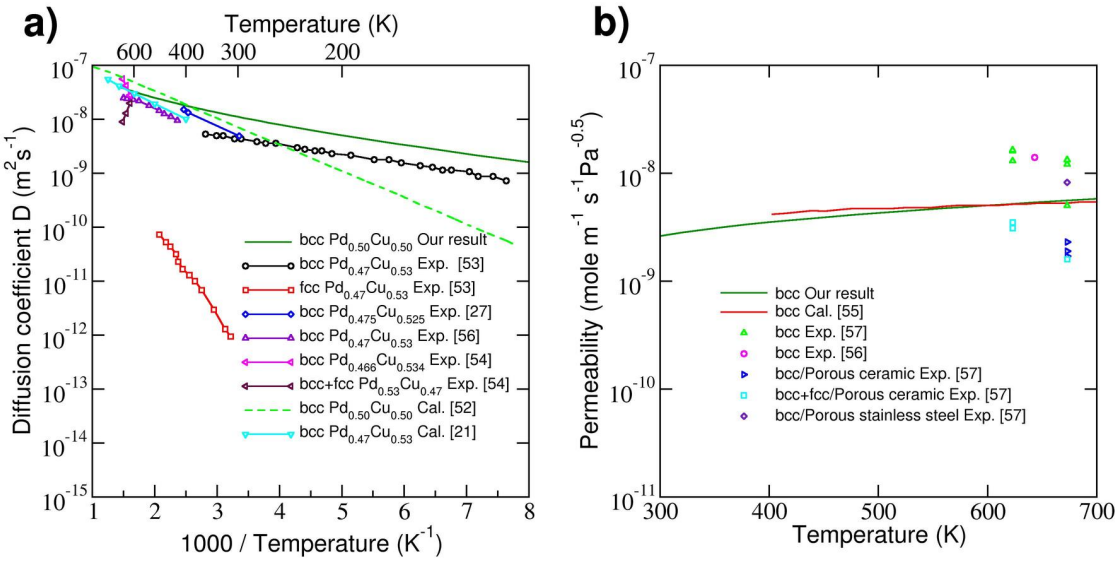

Figure 6.14: a) Diffusivity of hydrogen in bulk bcc PdCu. b) Hydrogen permeability in bcc PdCu. Experimental data and theoretical values reported in literature are also given for comparison.

in this study are lower than those reported in Ref [21]. However, the calculated diffusivity is in excellent agreement with the experimental reports over a broad temperature range, albeit they are slightly overestimated. For example, Piper [137] and Nayebossadri *et al.* [154] reported diffusivities of 1.52 $\times 10^{-8}$ m^{2}s^{-1} at 406 K and 2.8 $\times 10^{-8}$ m^{2}s^{-1} at 623 K respectively. In comparison, the obtained diffusivities at 406 K and 623 K are about 1.83 $\times 10^{-8}$ m^{2}s^{-1} and 3.42 $\times 10^{-8}$ m^{2}s^{-1} respectively.

The hydrogen permeability (Q) is typically used as a measure to understand the hydrogen permeation through the metallic membranes. It can be calculated as, [131, 155]

$$Q = \frac{1}{2} K_s(T) D \tag{6.20}$$

where, $K_s(T)$ is the Sievert's constant and D is the diffusivity. For dilute hydrogen concentration the hydrogen solubility obeys the Sieverts law and the value of Sievert's constant ($K_s(T)$) is calculated by equating the chemical potential of interstitial and gaseous hydrogen as, [131, 155]

$$K_s(T) = exp(\beta[\sum_i \frac{h\gamma_i}{4} - E_b - \frac{1}{2}\sum_i \frac{h\nu_i}{2}]) \frac{1}{\sqrt{\alpha}} \sqrt{1 - exp(-\beta \sum_i \frac{h\gamma_i}{2})} \frac{1}{\prod_i (1 - e^{-\beta h\nu_i})}, \tag{6.21}$$

$$\alpha = \left(\frac{2\pi m k_B T}{h^2}\right)^{\frac{3}{2}} \frac{4\pi^2 I (k_B T)^2}{h^2}, \tag{6.22}$$

$$\beta = \frac{1}{k_B T} \tag{6.23}$$

where γ_i is the vibrational frequency of H_2, E_b is the binding energy of H in bulk PdCu, ν_i is the vibrational frequency of interstitial H atom at PdCu, m and I are respectively the mass and moment of inertia of H_2. The hydrogen permeability calculated using Eq. 6.20 is shown in Figure 6.14(b). The Q increases from 2.6 $\times 10^{-9}$ mole m^{-1} s^{-1} $Pa^{-0.5}$ at 300 K to 5.8 $\times 10^{-9}$ mole m^{-1} s^{-1} $Pa^{-0.5}$ at 700 K. The computed values of Q are in very good agreement with the theoretical report of Liu *et. al.* [155] Experimentally the hydrogen permeability is estimated within the one-dimensional mass transport model using the measured hydrogen flux, assuming that the effect of surface processes are negligible. This assumption is true for the very thick membrane. The predicted value of 5.5 $\times 10^{-9}$ mole m^{-1} s^{-1} $Pa^{-0.5}$ at 673 K is in very good agreement with the experimentally reported value of 5 $\times 10^{-9}$ mole m^{-1} s^{-1} $Pa^{-0.5}$ at 673 K for a 100 μm thick membrane. [157] However, the hydrogen permeability reported for thin membranes supported on porous ceramics are smaller than this value. One plausible reason for the experimental observation of smaller hydrogen permeability of the very thin membrane is the significant effect of surface processes on the hydrogen permeation.

6.3.8 Rate limited flux prediction

So far the different factors that affect the hydrogen permeation are discussed. In this section, the rate-limiting processes and conditions for the hydrogen flux through a bcc PdCu membrane with (110) surface are analyzed. Since the rate constants corresponding to the hydrogen dissociation at the feed side and the diffusion from bulk to surface at the permeate side are very high compared to the other surface processes, those processes are not considered in this analysis.

6.3.8.1 Hydrogen diffusion inside bulk

The net hydrogen flux through a membrane with in one dimensional mass transport model is given by, [152, 156]

$$J_{diff} = \frac{Q}{l}(p_1^{0.5} - p_2^{0.5}) \tag{6.24}$$

where l is the thickness of the membrane, p_1 and p_2 are the hydrogen partial pressures on the feed side (upstream) and the permeate side (downstream) of the membrane respectively. The calculated hydrogen flux of 7.3 $\times 10^{-3}$ mole $m^{-2}s^{-1}$ for 100 μm thick membrane at 673 K, and $p_1 = 2$ bar and $p_2 = 1$ bar is in good agreement with the experimentally reported value of 6.5 $\times 10^{-3}$ $m^{-2}s^{-1}$ at the same conditions. Since the net hydrogen flux is inversely related to the membrane thickness, reducing the membrane thickness will increase in the hydrogen flux. The computed value of the hydrogen flux due to diffusion through the bulk as a function of temperature for membranes with varied thicknesses (100 μm, 20 μm, 1 μm and 0.5 μm) are shown in Figure 6.15.

6.3.8.2 Hydrogen penetration (surface to subsurface)

The net hydrogen flux from the surface of the feed side to the subsurface is decribed by, [158, 159]

$$J_{penet} = k_{penet}(1 - X_s)\theta_1 N_s N_b, \tag{6.25}$$

where k_{penet} is the rate constant associated with the penetration of hydrogen from the surface to the subsurface at the feed side of the membrane, X_s is the probability of the subsurface sites being occupied, θ_1 is the probability of surface sites being occupied, N_s is the density of Pd atoms on the surface and N_b is the density of Pd atoms in bulk PdCu. This mean field expression is accurate for $X_s << 1$, as it is in the metal alloy surfaces. At low hydrogen partial pressure, it is fair to assume that $X_s \sim 0$. Then Equation 6.25 becomes,

$$J_{penet} = k_{penet}\theta_1 N_s N_b. \tag{6.26}$$

where θ_1 depends on the partial pressure of hydrogen on the feed side. Typically, in experiments the feed side partial pressure is about 2 bar to 6 bar. [156, 157] From the surface phase diagram and the free energy plots (Figure 6.8), it is found that at that hydrogen partial pressure, the coverage of atomic H on the surface typically varies from about 0.16 ML ($\theta_1 = 0.08$) to about 1.5 ML ($\theta_1 = 0.75$). Hence, to get an upper and lower bound

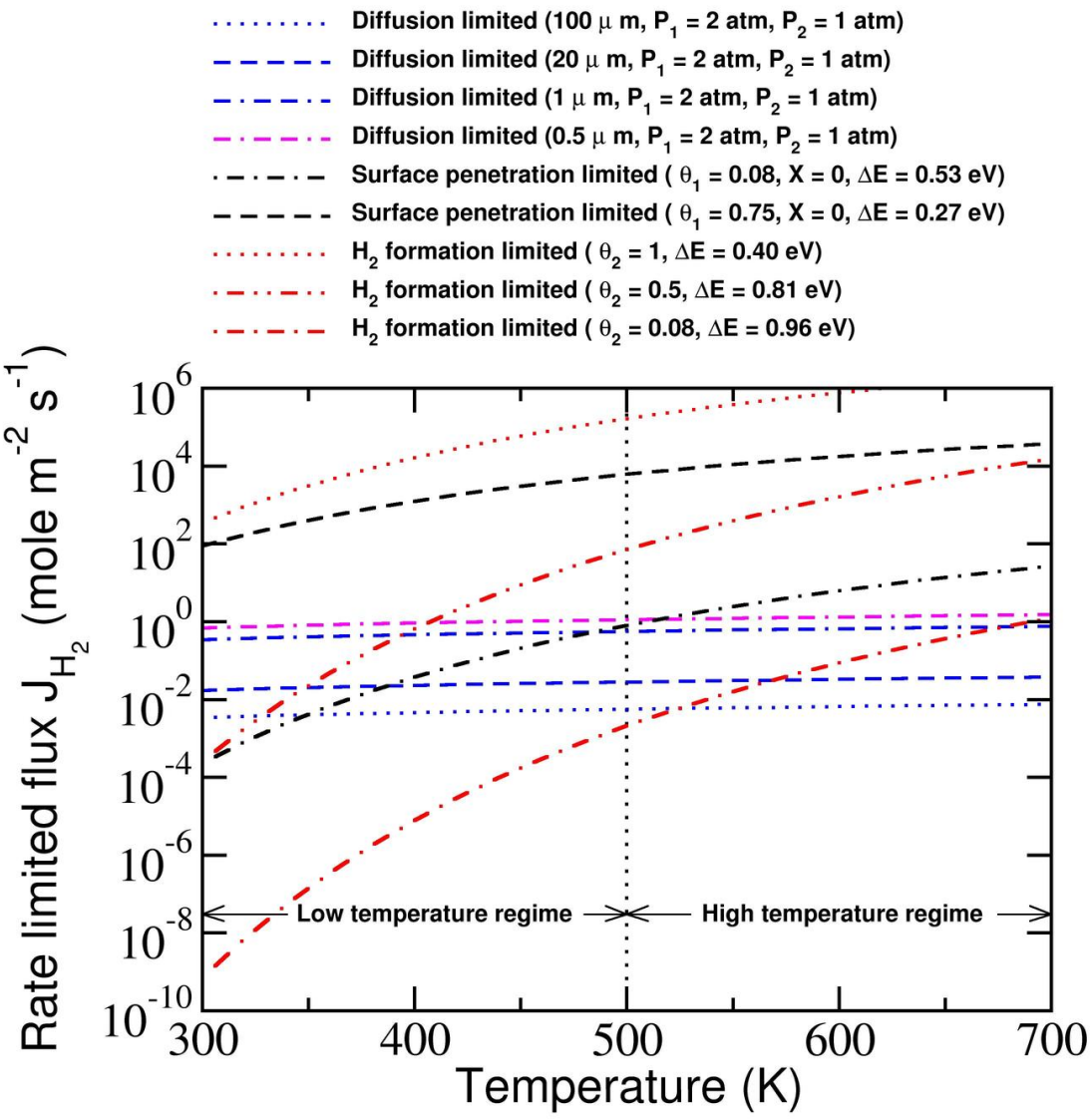

Figure 6.15: Rate limited hydrogen flux calculated at various conditions.

for the hydrogen flux due to penetration from surface to subsurface, J_{penet} was calculated for the above two values of θ_1. It should be noted that as mentioned in Section 6.3.5.3, the penetration barrier and in turn k_{penet} depends on the surface H coverage. While for $\theta_1 = 0.08$ it is 0.53 eV, for $\theta_1 = 0.75$ it reduces to 0.27 eV. For $\theta_1 = 0.08$, the J_{penet} increases from 2.28 $\times 10^{-4}$ mole m^{-2}s^{-1} at 300 K to 26.7 mole m^{-2}s^{-1} at 700 K (Figure 6.15). The net hydrogen flow calculated for $\theta_1 = 0.75$ is very high (87.9 mole m^{-2}s^{-1} at 300 K) compared to the value calculated for $\theta_1 = 0.08$ (2.28 $\times 10^{-4}$ mole m^{-2}s^{-1} at 300 K). Further, the upper limit of the net hydrogen flux (for θ_1 =0.75) increases from 87.9 mole m^{-2}s^{-1} at 300 K to 3.76 $\times 10^{4}$ mole m^{-2}s^{-1} at 700 K (Figure 6.15). The above finding suggest that at high pressure on the feed side, which typically is the case, the hydrogen penetration process may not be the rate limiting ones.

6.3.8.3 Molecular hydrogen formation

The net flux of hydrogen from the molecular hydrogen formation at the surface of the product side of the membrane is given by, [158]

$$J_{recom} = 2k_{H_2}N_{AA}, \tag{6.27}$$

where k_{H_2} is the rate constant for the H_2 formation and N_{AA} is the concentration of the nearest neighbor occupied site pairs at the surface. The N_{AA} can be calculated within quasi-chemical approximation as, [158]

$$N_{AA} = \frac{zN_s\theta_2}{2}\left(1 - \frac{2 - 2\theta_2}{\sqrt{1 - 4\theta_2(1-\theta_2)(1 - exp(-w/k_BT))} + 1}\right) \tag{6.28}$$

where z is the number of nearest neighbors on the surface (z=4 for the surface considered in this study), θ_2 is the probability of the surface sites on the permeate side to be occupied, and w is the pairwise interaction energy. The maximum possible net hydrogen flux for the hydrogen molecule formation can be obtained when all the available sites that are present on the surface are occupied by the H atom. By setting $\theta_2 = 1$ in Eq. 6.28, the upper limit for the net hydrogen flux was estimated as,

$$J_{recom} = k_{H_2}zN_s \tag{6.29}$$

At very high hydrogen coverage, the reaction barrier obtained for the formation of molecular hydrogen on PdCu(110) surface is 0.40 eV. The hydrogen flux calculated using this reaction barrier is shown in Figure 6.15. J_{recom} increases from 3.5 $\times 10^{2}$ mole $m^{-2}s^{-1}$ at 300 K to 2.3 $\times 10^{6}$ mole $m^{-2}s^{-1}$ at 700 K. However, $\theta_2 = 1$ corresponds to very high pressure on the permeate side. Generally the pressure at the permeate side is kept below 1 bar. Moreover, the thermodynamic analysis predicts that at 1 bar hydrogen partial pressure for temperatures above 500 K, the clean surfaces are thermodynamically more stable than the hydrogen covered surfaces. Hence, at conventional operating conditions of the membrane, i.e. T =500 K and $p_2 = 1$ bar, the hydrogen coverage at the permeate side is expected to be very low. At very low hydrogen coverages, the pairwise interaction energy can be assumed to be low, i.e. w can be approximated to be zero in Eq. 6.28 and the expression for J_{recom} hydrogen flux becomes,

$$J_{recom} = k_{H_2} z N_s \theta_2^2 \tag{6.30}$$

However, the barrier corresponding to the formation of hydrogen at low hydrogen coverage (0.96 eV) is much larger than at very high coverage (0.40 eV). Using the reaction barrier of 0.96 eV, the net hydrogen flux at $\theta_2 = 0.08$ was calculated. The calculated hydrogen flux increases from 7.01 $\times 10^{-10}$ mole $m^{-2}s^{-1}$ at 300 K to 1.25 mole $m^{-2}s^{-1}$ at 700 K.

Combining the above three important steps in the permeation process (Figure 6.15) and the phase diagram (Figure 6.8) that predicts the stability of the different hydrogen covered surfaces as a function of temperature and H_2 partial pressure, it is found that for a given value of the pressure difference between the feed and the permeate side, the rate-limiting step for hydrogen permeation is sensitive to temperature and thickness of the membrane. Below, the effect of different processes on hydrogen permeation is discussed, when $p_1 = 2$ bar and $p_2 = 1$ bar, the typical values of partial pressures under operational conditions. Usually, the partial pressure on the feed side is kept high, and from the calculations it is found that at high hydrogen partial pressures, the hydrogen coverage will be higher. From the coverage dependent studies of hydrogen penetration barrier (Section 6.3.5.3 and Figure 6.11), it is found that hydrogen penetration barrier is significantly reduced when the surface is covered with hydrogen, implying that J_{penet} will be high (black dashed line in Figure 6.15). Hence for hydrogen permeation, the penetration of the hydrogen from surface to subsurface is never a rate determining step at temperatures ranging between

300 to 700 K. Rather, it is the diffusion of hydrogen in the bulk of the membrane or the reassociation of hydrogen atoms on the permeate side of the membrane to form molecular hydrogen that limits the permeation process.

Based on the thermodynamic stability of the surfaces at the above-mentioned hydrogen partial pressures, the permeation can be divided into two regimes, namely the "high temperature" (500 to 700 K) and "low temperature" (300 to 500 K) regimes. At $T > 500$ K, the hydrogen coverage on the permeate side will be very low (Figure 6.8). Hence permeation limited by hydrogen formation on the permeate side is described by the red-dash-dotted line in Figure 6.15. In this temperature window, if the membrane thickness is less than 0.5 μm the permeation would be limited by reassociation on the permeate side. For membranes thicker than 0.5 μm, the rate-limiting step depends on the operating temperature and the thickness of the membrane. For example, for a 20 μm thick membrane, the permeation switches from reassociation limited to diffusion limited at 570 K.

In the "low temperature" regime, the surface coverage on the permeate side is high (typically about 1 ML). At this hydrogen coverage, the hydrogen reassociation barrier is reduced to 0.81 eV, and the hydrogen flux due to permeation limited by hydrogen formation on the permeate side is given by the red dash-dot-dot line in Figure 6.15. In this regime, even for membrane as thin as 0.5 μm the rate-limiting step can switch from diffusion limited to reassociation limited depending on the operation temperature and the thickness of the membrane.

6.4 Discussion

Based on the results in the previous section, the seven steps involved in the solution-diffusion mechanism, can be divided into two broad categories, (1) the surface processes and (2) the diffusion of hydrogen inside the membrane bulk. Hydrogen adsorption, dissociation and diffusion on the membrane surface and penetration from the surface to the subsurface are the surface processes that occur on the feed side of the membrane. Diffusion of H from bulk to the surface, reassociation of atomic H to molecular hydrogen and desorption of the H_2 molecule from the surface are the surface processes that occur on the product side of the membrane surface. Diffusion of H between the interstitial sites inside

the bulk is the process that occurs inside the bulk. A good membrane should ease both categories of processes, and that will depend on the thermodynamic stability of H on the surface, subsurface and inside bulk and the barriers associated with each of the diffusion processes.

The binding of H on the surface, subsurface and inside the bulk of a membrane should be moderately exothermic. Very strong binding of H to the membrane will lead to the formation of brittle hydrides. Weak binding of H to the subsurface and inside bulk (binding energy < 0.1 eV/H) and moderate binding to the surface (binding energy ~ 0.5 eV/H up to θ_H = 1 ML) makes the bcc PdCu to be a good candidate for hydrogen purification membrane material.

In addition to the thermodynamic stability, a good membrane material should also exhibit good permeability. The permeability of the membrane is generally addressed through the interstitial diffusion of H inside the bulk membrane. However, the surface processes like diffusion of H on the membrane surface, H penetration from surface to the bulk and H_2 formation at the product side of the surface can also have significant influence to the hydrogen permeability of the membrane, which as mentioned in the introduction, have not been considered in previous studies.

Considering the above mentioned surface and subsurface effects, while the H_2 molecule readily dissociate and diffuse on the membrane surface ($k_{hTST} \sim 10^8$ at 300 K), H penetration to the subsurface is very slow at low θ_H ($k_{hTST} \sim 10^3$ at 300 K). The penetration rate can be significantly improved to $k_{hTST} \sim 10^8$ by increasing the partial pressure of hydrogen, consequently increasing the θ_H. Once the H penetrates to the subsurface, it readily diffuses inside the bulk. The diffusion of H inside the bulk is about 10^3 times faster ($k_{hTST} \sim 10^{12}$ at 300 K) than the diffusion at the surface. The rate of diffusion of H from the subsurface to the product side of the surface is also similar to that of diffusion of H inside bulk. The formation of H_2 molecule on the product side of the surface is very slow ($k_{hTST} \sim 10^6$ at 300 K), and this is the slowest one among the important processes. However, high temperature and/or a reasonably large H coverage speeds up the H_2 formation.

Using a simple model of permeation of hydrogen through the membrane and neglecting

external mass transfer, at the conventional operational partial pressure difference between the feed and the permeate side of the membrane, the permeation process is not limited by penetration of hydrogen from surface to subsurface even for membranes as thin as 0.5 μm. Rather, the two relevant processes are (a) reassociation of atomic H to form molecule on the permeate side and (b) diffusion of hydrogen in the bulk of the membrane. Which of these two processes is the rate-limiting one for permeation depends on the operating temperature and the thickness of the membrane. For thick membranes at a higher temperature, it is the diffusion that acts as a rate-limiting step. However, for thin membranes (about 0.5 μm thick), it is the formation of H_2 from atomic hydrogen that acts as the rate-limiting step.

So far the discussion is focused on the hydrogen flux predicted for the most stable PdCu(110) surface. However, depending on the preparation conditions of the surfaces of the alloy, it might be possible that the surface texture might be different from the ideal (110) surface. For example, it is possible that defects, steps, etc. are present on the surface. Since in the experiments usually an average effect is measured, if the defect concentration on the (110) surface is low, then the above conclusions will hold true. This is because most of the membrane surface will be the ideal surface considered in this study. However, one needs to perform explicit calculations to verify the same and is beyond the scope of the present manuscript.

A comparison is made with the results obtained for the bcc phase of PdCu in this study with those of the fcc phase of PdCu that is reported in the literature. From their microkinetic model, Ling *et al.* found that for $Pd_{75}Cu_{25}$ (a) the relevant surface process that offers resistance to permeation is recombinative desorption of molecular hydrogen on the permeate side and (b) resistance associated with surface process plays a crucial role at temperatures lower than about 700 K for membranes that are 1 μm thick. In contrast, for bcc-$Pd_{50}Cu_{50}$ the relevant surface process is the formation of molecular hydrogen from atomic H on the surface of the permeate side of the membrane. Additionally, it is found that for the bcc $Pd_{50}Cu_{50}$ membranes at $500 < T < 700$ K and with thicknesses of 0.5 μm or less, the permeation is controlled by surface processes, while for thicker ones, the rate-limiting step depends on membrane thickness and operating temperature. Moreover, unlike the fcc-phase, at lower temperatures ($T < 500$ K), even for a thin membrane (thickness of 0.5 μm or less) the rate-limiting step for permeation can be diffusion or re-

association depending on the operational temperature.

6.5 Summary

In summary, the H permeation is studied through model PdCu membrane. Unlike other reports in the literature, all the relevant steps associated with the permeation process are studied. Additionally, the nuclear quantum effects due to the light mass of the H atom are incorporated through the ZPE corrections. Analysing the individual rate constants associated with the processes suggest that the rate-limiting steps for hydrogen permeation through this membrane are (i) diffusion of the surface H to the first subsurface on the feed side of the membrane and (ii) reassociation of H atoms to form H_2 at the collector side of the membrane. A hydrogen coverage and temperature dependence study of the kinetics of these two processes suggest that the rates associated with them can be significantly enhanced at large hydrogen coverages and high temperatures. Further, using a microkinetic model, the limiting net flux of hydrogen through the membrane was calculated. The flux calculations suggest that at typical operating pressures the permeation is not limited by penetration of H atoms from the surface to the subsurface. Rather the permeation can be either diffusion limited or limited by reassociation of atomic hydrogen to form molecular hydrogen on the permeate side. From the calculations it is found that for membranes thinner than 0.5 μm, H permeation is limited by the formation of molecular hydrogen on the permeate side of the membrane. For bcc-PdCu, the important surface process is different from fcc-PdCu; for the latter, it is recombinative desorption of hydrogen on the permeate side. For thicker membranes, the rate-limiting step for permeation can be either formation of molecular hydrogen or diffusion of atomic H in the bulk of the membrane. The transition from surface process limited permeation to bulk diffusion permeation depends on the operating temperature and thickness of the membrane. Additionally, the nuclear quantum effects of the H atom (manifested through the zero point energy corrections) affects the stability of the H covered surfaces and the reaction rates associated with the different diffusion, dissociation and reassociation processes significantly.

Chapter 7

Summary and Outlook

In summary, theoretical investigations of the activated processes in three different Pd-based materials are presented in this thesis. The first material investigated is the PdGa intermetallic surfaces. We have investigated the thermodynamic stability of the low indexed PdGa intermetallic surfaces and their reactivity and selectivity towards an important industrial reaction namely, the selective hydrogenation of acetylene to ethylene. The second one is the study of PdGa clusters supported on MgO(100) surface. We have presented our results of structure and thermodynamic stability of small (up to tetramers) PdGa clusters adsorbed on two types of MgO(100) surfaces the clean one and one containing neutral oxygen vacancies. We have also reported the results of our investigations on the elementary steps involved in the growth mechanism and nucleation kinetics of these clusters on the MgO surface. Further, we also discussed the possibility of stabilizing clusters with specific compositions by controlling the deposition rates and temperature. The last material we investigated is PdCu alloy. We have presented our results for the investigation of different microscopic processes involved in the solution-diffusion mechanism for hydrogen permeation through a PdCu membrane, one of the promising membrane materials to purify hydrogen.

We have investigated the structure, stability and reactivity of the PdGa intermetallic surfaces towards the semi-hydrogenation of acetylene to ethylene. In **Chapter-3** we show that for the clean (100) surface, the stability of the surface terminations is independent of the surface preparation condition. On the contrary, at least three different types of surface terminations can be stabilized for the (110) surface by tuning the surface preparation conditions. Upon adsorbing the molecular and atomic hydrogen on these surfaces, we find that both molecular and atomic hydrogen are weakly interacting with the surface. We also

find that the interaction energies are independent of surface hydrogen coverage. Using *ab initio* thermodynamic analysis we predicted that at 450 K hydrogen adsorbs only at high hydrogen partial pressure and the relative stability of the different surface terminations are unaffected by the presence of adsorbates. Further, we have also presented the mechanisms of the semi-hydrogenation reaction on the low indexed (100) and (110) surfaces and compared them with those reported in literature for the (111) surfaces in **Chapter-4**. We find that the energetically favorable (100) surface created by cleaving the crystal in the less dense region shows reasonably good selectivity and high reactivity. The reactivity on this surface is comparable to that observed on Pd(111) surfaces. Since this surface termination is stable over a wide range of Ga chemical potential and hence is likely to occupy a substantial fraction of the surface area of PdGa nanocrystallites. Based on the thermodynamic stability and reaction barriers calculated for the hydrogenation steps we propose this termination to be the responsible one for the selectivity and reactivity exhibited by PdGa. A careful analysis of the factors determining the selectivity shows that selectivity results due to an interplay between surface roughness and chemical nature of the reactive ensemble. We find that the ensemble effects are more significant than the so called "isolated active sites" in determining the selectivity. However, the number of surfaces investigated is only five, which is too small to make any solid conclusions. Surfaces of Pd_1Ga_2, Pd_2Ga_1 and Pd_3Ga_7 could offer rich variety of ensembles. Hence, a more detailed investigation of surfaces with different ensembles is required to clearly understand which factor is more important. Moreover, selectivity of a catalyst is an important criterion for most of the hydrogenation reactions. These surfaces can be explored for other partial hydrogenation reactions.

For the industrial scale applications, the active catalysts are generally supported on a stable, inert support. Typically the metal oxides are used as the support. In **Chapter-5** we have presented one such system; PdGa bimetallic clusters supported on MgO (100) surface. We have studied the structure and thermodynamic stability of small (up to 4 atoms) PdGa bimetallic clusters adsorption on MgO(100) surface using DFT. We also report the results of elementary steps involved in growth and the nucleation kinetics of these small clusters on the same surface studied within GT-KMC framework. The size and shape of the cluster islands plays crucial role in determining the activity of nano-catalysts. While our model can predict the nucleation kinetics it will not predict the size and shape of the large clusters made off more than 4 atoms since we have not included their energetics

because of the high complexity of the reaction steps involved in the growth kinetics. However, the prediction of size and shape of the large cluster islands can be done as a separate study in future. We find that the mixed bimetallic clusters on the surface are found to be more stable than that of the parent clusters, particularly clusters with 1:1 atomic ratio are found to be the most stable ones. We also find that all the clusters except Ga tetramer are highly mobile on the surface. At 300 K, all these clusters are kinetically stable, and the vacancy sites act as trapping center. Upon increasing temperature, Ga_2, Ga_3 and Pd_1Ga_2 clusters tend to escape from the vacancy site rather than decompose, whereas all other clusters tend to decompose rather than escaping from the vacancy site. Our calculations predict that the growth of the pure Pd and Ga clusters are heterogeneous, though the elementary reactions involved in the growth process for these two clusters are very different. We find that when the bimetallic cluster are grown by depositing Pd and Ga adatoms with an equal deposition rate, the bimetallic clusters are formed in large proportion, especially clusters with 1:1 atomic ratio are found in the largest fraction. Further, clusters with desired stoichiometric ratios can be obtained in a significant fraction by varying the deposition rates of the Pd and Ga adatoms to the surface. Once we have understood the growth and stability of these clusters on the support, it will be interesting to investigate their reactivity for selective hydrogenation reactions and compare them with those observed for the surface.

Finally in **Chapter-6**, we have presented a systematic theoretical investigation of all the processes associated with the permeation of H through a model PdCu membrane. The surface of the membrane was modelled using the most stable (110) surface. Our results show that the nuclear quantum effects due to the light mass of the H atom can significantly affect the stability and the reaction rates. Based on a microkinetic model of the permeation process, we find that the permeation can be limited by diffusion of H in the membrane bulk or the reassociation of atomic H to form H_2 on the permeate side of the membrane depending on the operation temperature and membrane thickness. Further, based on the thermodynamic stability of the hydrogen covered membrane surface the operating conditions are divided in to two regimes namely, high temperature regime and low temperature regime. At typical operating conditions, for membranes thinner than 0.5 μm, the permeation at high temperature regime (T$>$500 K) is limited by surface processes, while at low temperature regime (T$<$500 K) it can be either diffusion limited or reassociation limited. One of the limitations of the present study is that we have considered ordered ideal sur-

face of the PdCu alloy. However, depending on the surface preparation conditions it might be possible that the composition of the surface layers have significantly changed. Under such conditions, the rate limiting steps might be changed. Hence it would be interesting to explore the effect of surface structure on the above mentioned processes. Further as of now we have not considered the effect of impurities that are present on the hydrogen feed, for eg. CO, H2S, etc. on the surface processes. We believe that it would be interesting to investigate the effect of impurities on the different diffusion processes.

Appendix A

Reaction steps in the selective hydrogenation of acetylene on PdGa surfaces

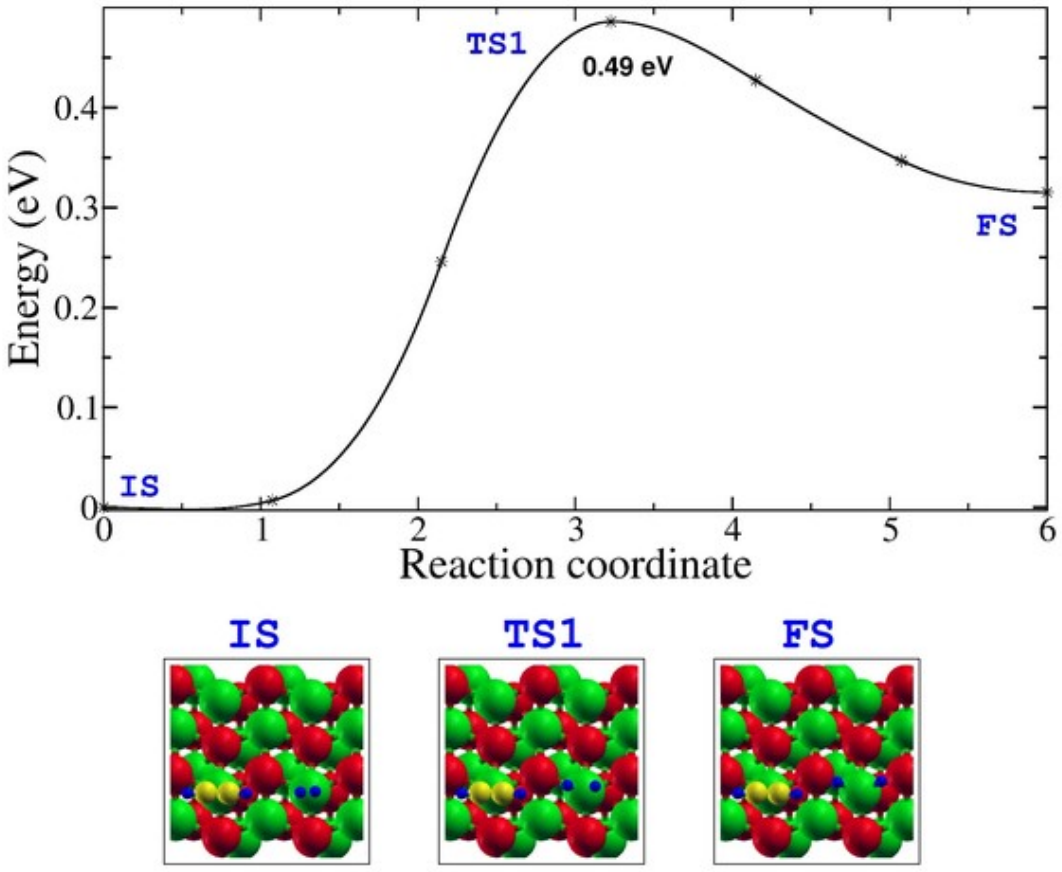

Figure A.1: $C_2H_2 + H_2 \rightarrow C_2H_2 + H + H$ on PG_l : The hydrogen dissociation is endothermic about 0.32 eV and has a barrier of 0.49 eV.

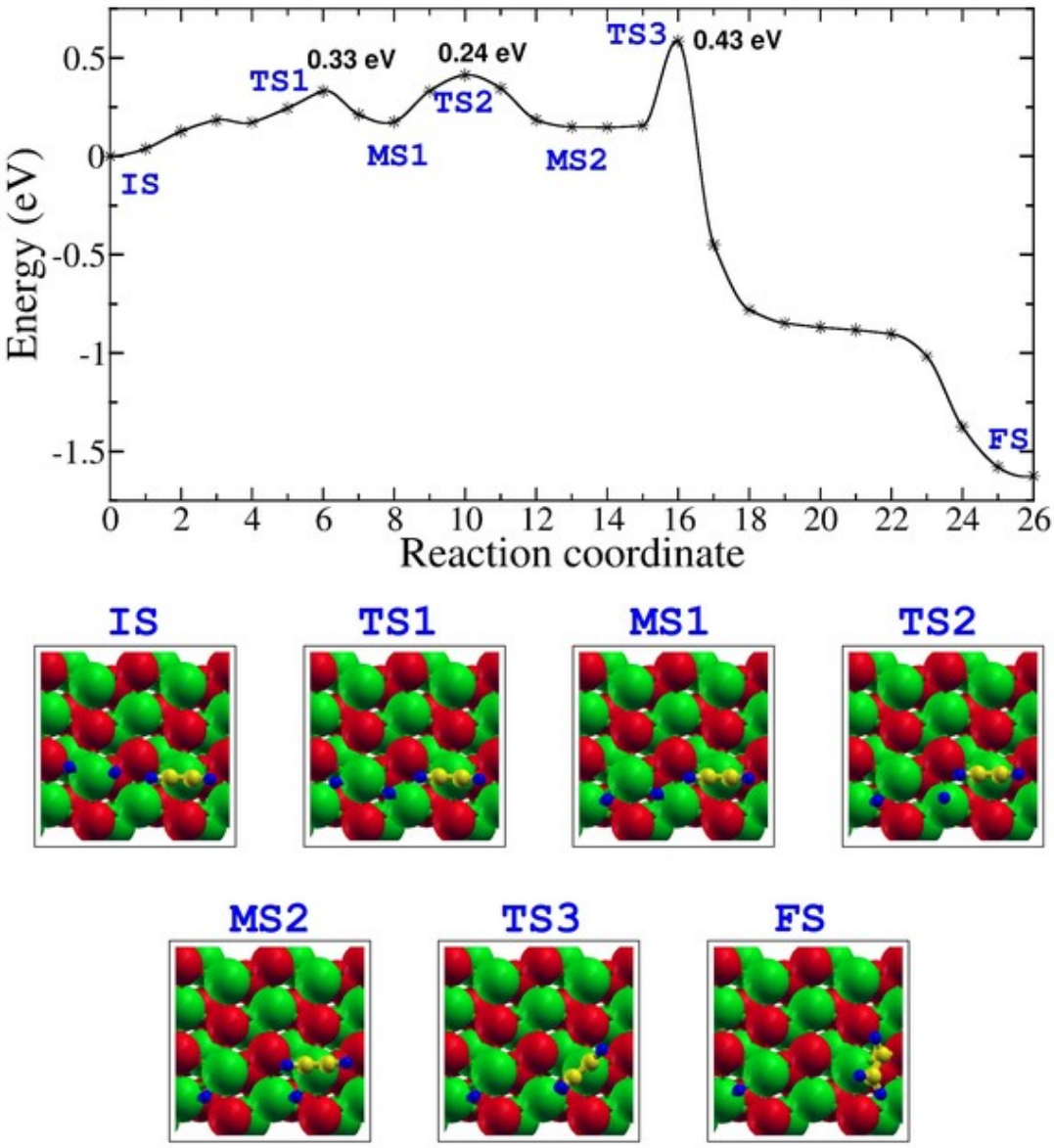

Figure A.2: C_2H_2 + H + H $\rightarrow$ C_2H_3 + H on PG_l; path1 : The first hydrogenation requires a precedent endothermic diffusion of hydrogen to a metastable MS2 state, which is 0.15 eV less stable than the most stable state. The hydrogen supplied from the metastable Pd-Pd bridge attacks the acetylene to give vinyl, this has a barrier of 0.43 eV which results a total reaction barrier to 0.58 eV.

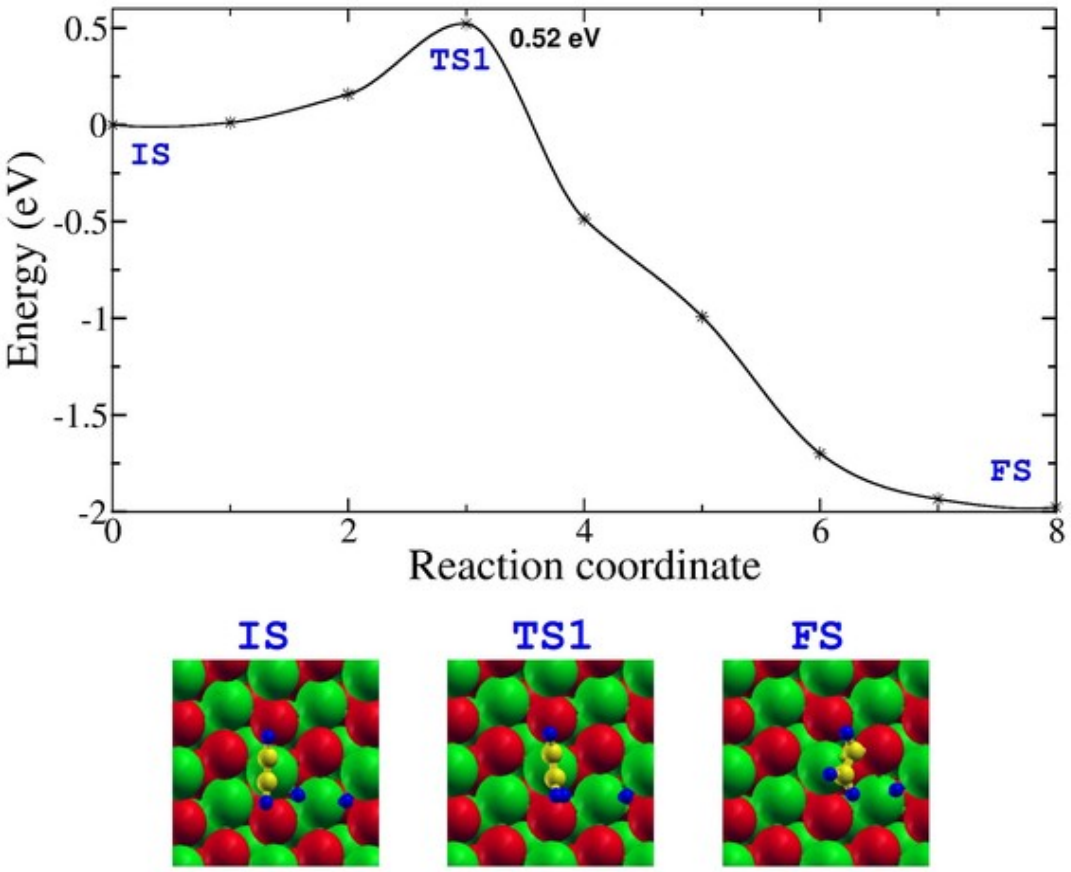

Figure A.3: C_2H_2 + H + H $\rightarrow$ C_2H_3 + H on PG_l; path2 : This is the next favorable path, this also requires a endothermic diffusion of hydrogen to the metastable position (not shown) which is 0.35 eV less stable than the most stable state. Hydrogen supplied from the metastable Bp1 state attacks the C_2H_2 to give C_2H_3, this has a barrier of 0.52 eV.

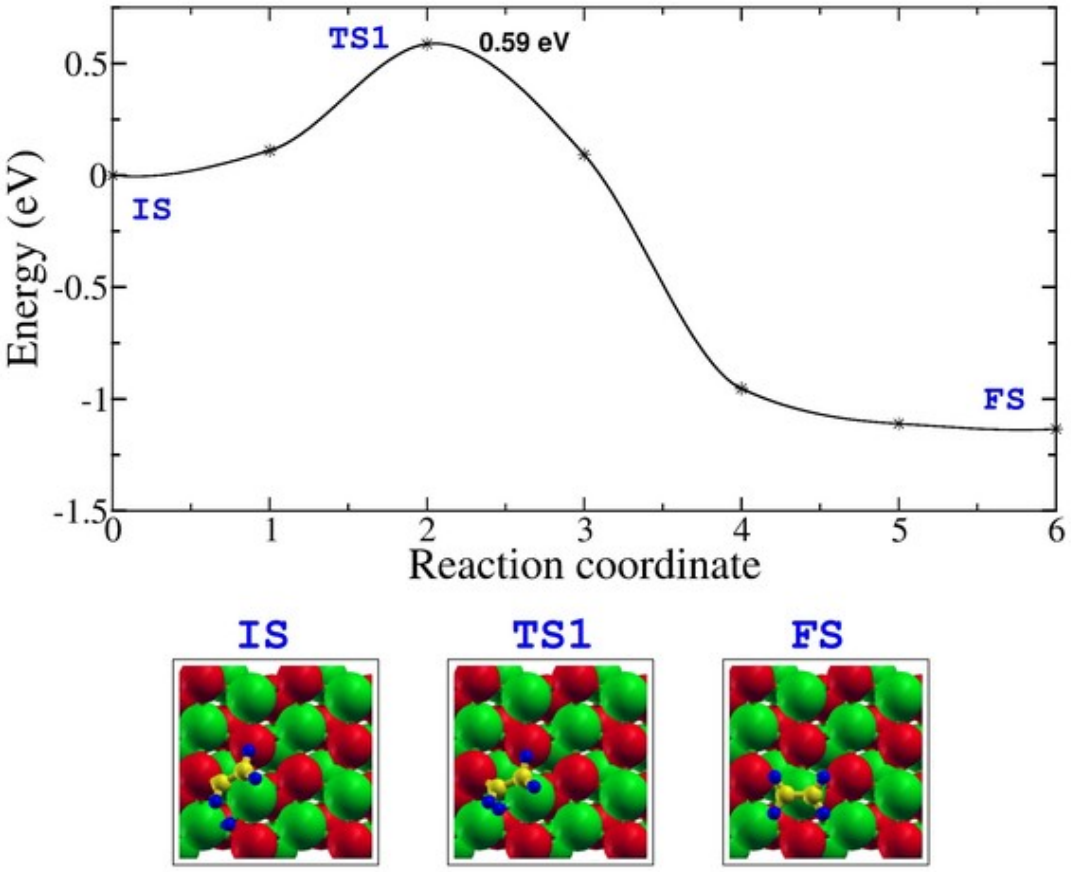

Figure A.4: C_2H_3 + H $\rightarrow$ C_2H_4 on PG_l; path1 : The hydrogenation of vinyl to ethylene on PG_l has a total reaction barrier of 0.79 eV. This path has the lowest reaction barrier. First the hydrogen endothermically diffuses from most stable Pd-Pd bridge to another metastable Pd-Pd bridge which is 0.20 eV less stable (not shown). Hydrogen supplied from the metastable state attacks the C_2H_3, this has a barrier of 0.59 eV.

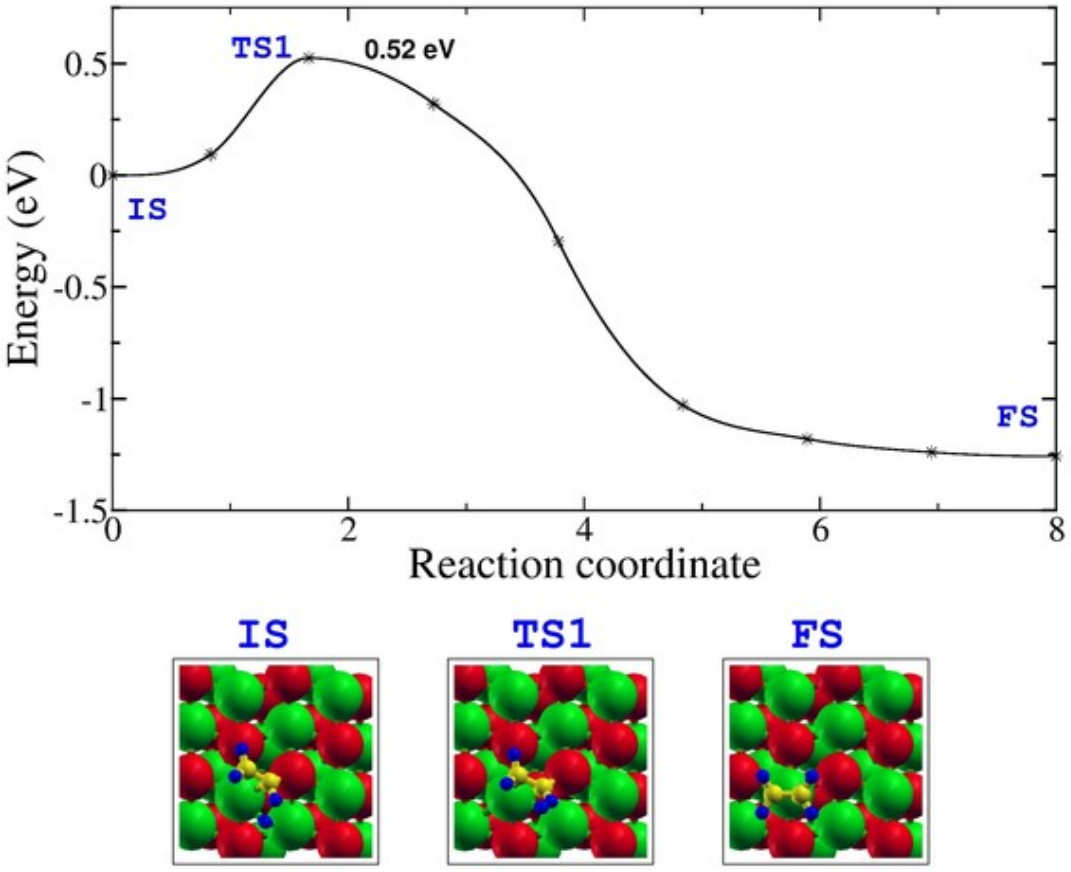

Figure A.5: C_2H_3 + H $\rightarrow$ C_2H_4 on PG_l; path2 : This is the next favorable path, this also requires a endothermic diffusion of hydrogen to the metastable position (not shown) which is 0.33 eV less stable than the most stable state. Hydrogen supplied from the metastable state attacks the C_2H_3 to give C_2H_4, this has a barrier of 0.52 eV.

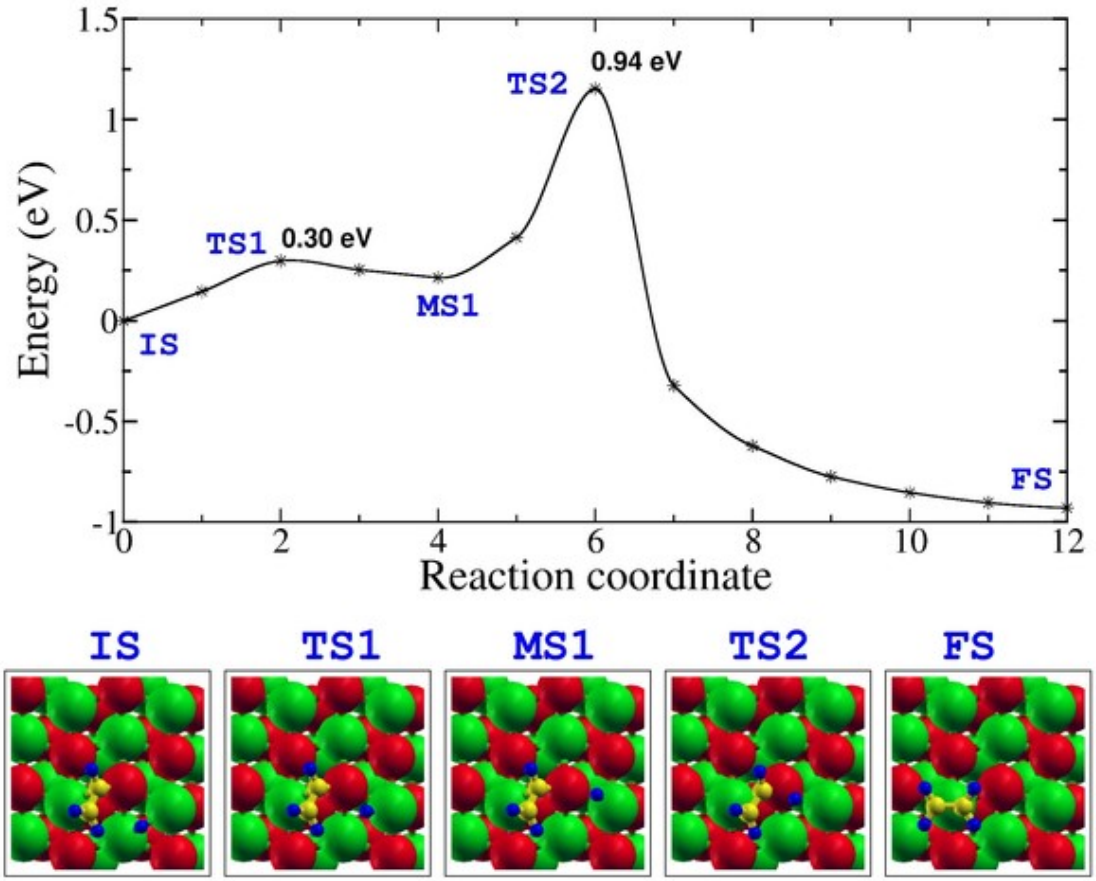

Figure A.6: C_2H_3 + H $\rightarrow$ C_2H_4 on PG_l; path3 : This path is rare to follow, has a total reaction barrier of 1.15 eV. The hydrogen at the most stable site diffuses to the metastable state (labeled as MS1) which is 0.21 eV endothermic and has a diffusion barrier of 0.30 eV. The hydrogen at the metastable state attacks the C_2H_3 to give C_2H_4, this has a high barrier of 0.94 eV.

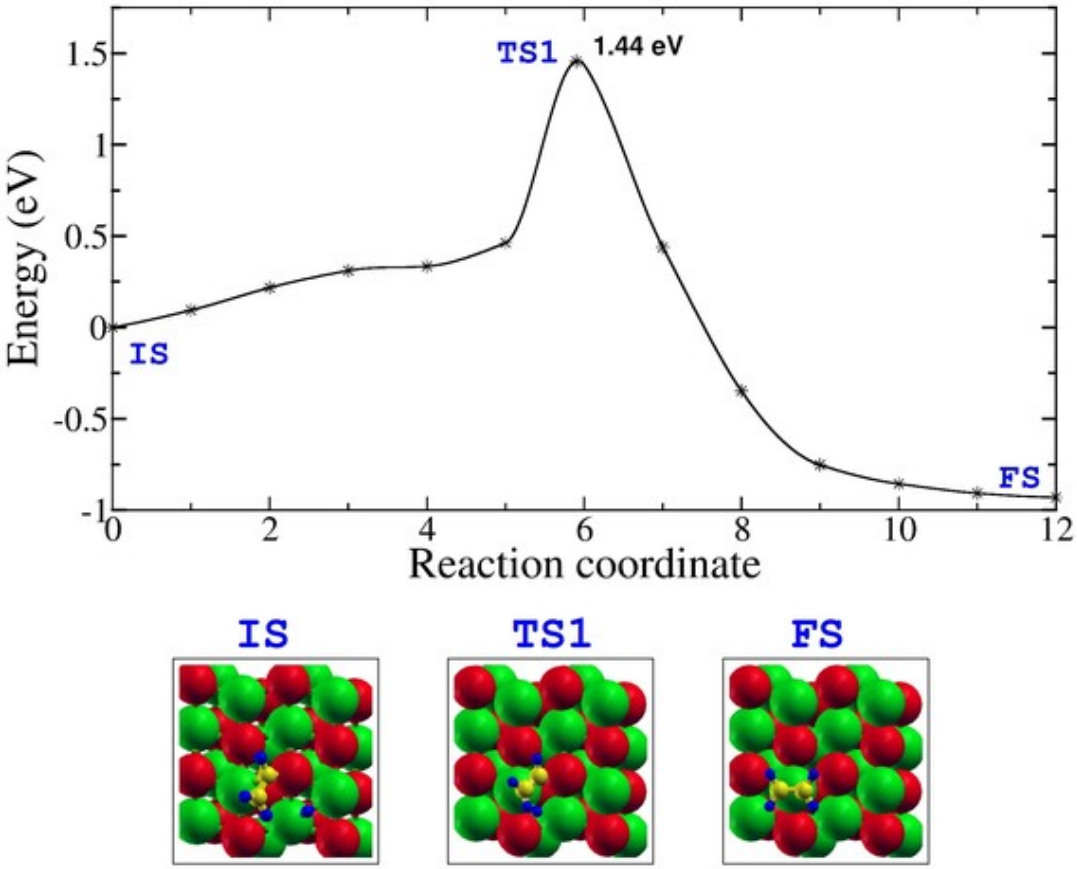

Figure A.7: C_2H_3 + H $\rightarrow$ C_2H_4 on PG_l; path4 : This path also has very high reaction barrier, not likely to follow. The hydrogen at the most stable state directly attacks the C_2H_3. This results in a very high reaction barrier of 1.44 eV.

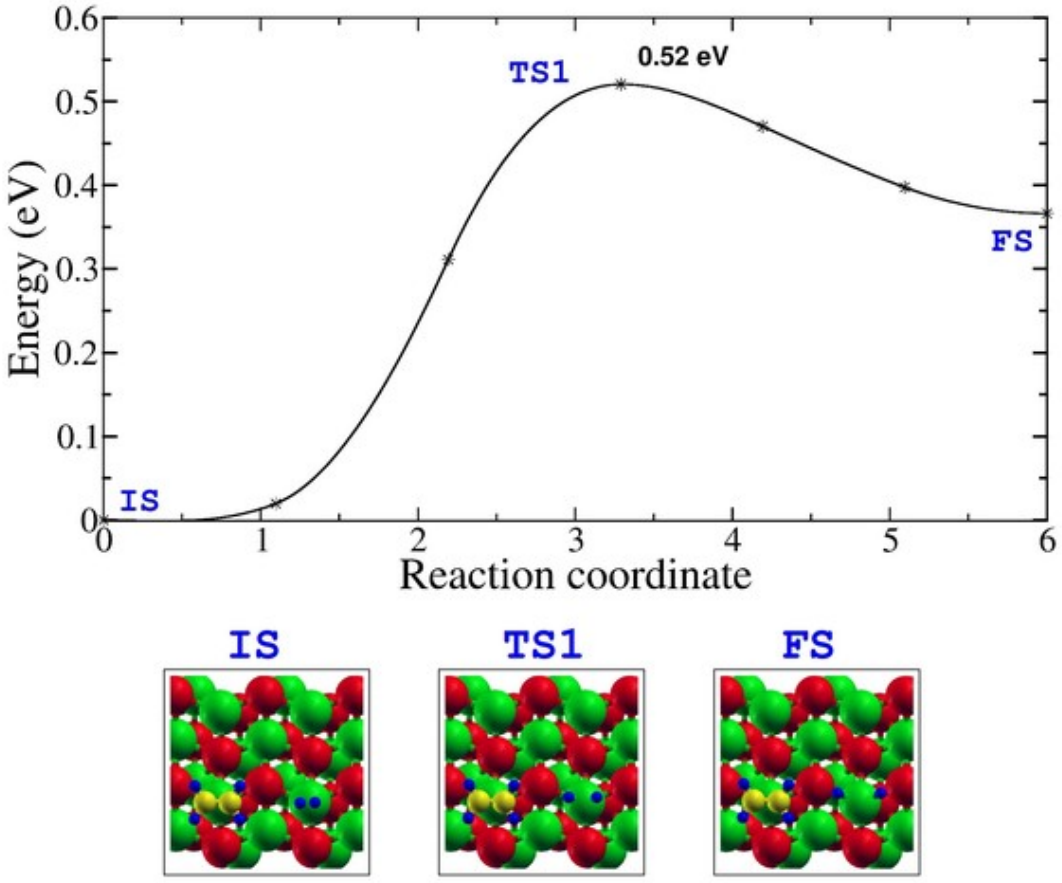

Figure A.8: C_2H_4 + H_2 $\rightarrow$ C_2H_4 + H + H on PG_l : The hydrogen dissociation is endothermic about 0.36 eV and has a barrier of 0.52 eV.

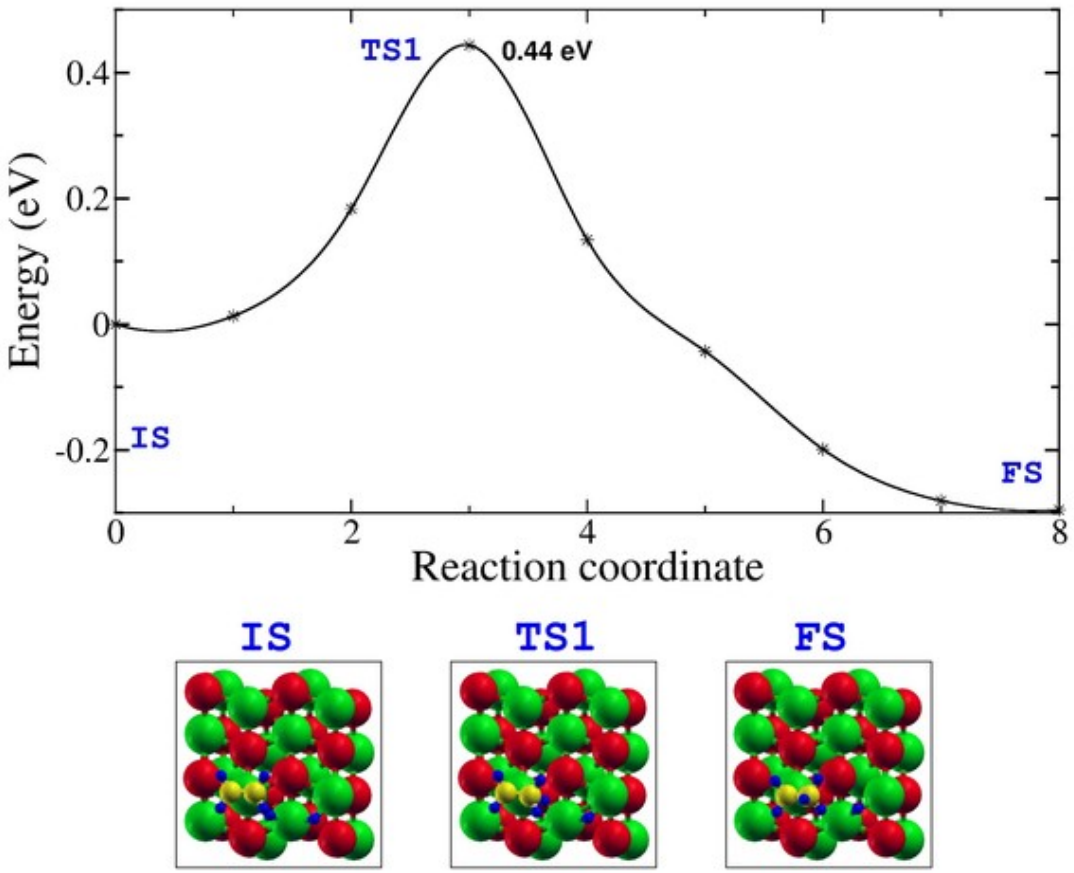

Figure A.9: C_2H_4 + H + H $\rightarrow$ C_2H_5 + H on PG_l : The hydrogenation of ethylene to ethyl on PG_l requires a precedent endothermic (0.26 eV) diffusion of hydrogen into a metastable position (not shown). The hydrogenation of ethylene to ethyl on PG_l from the metastable state has a barrier of 0.44 eV.

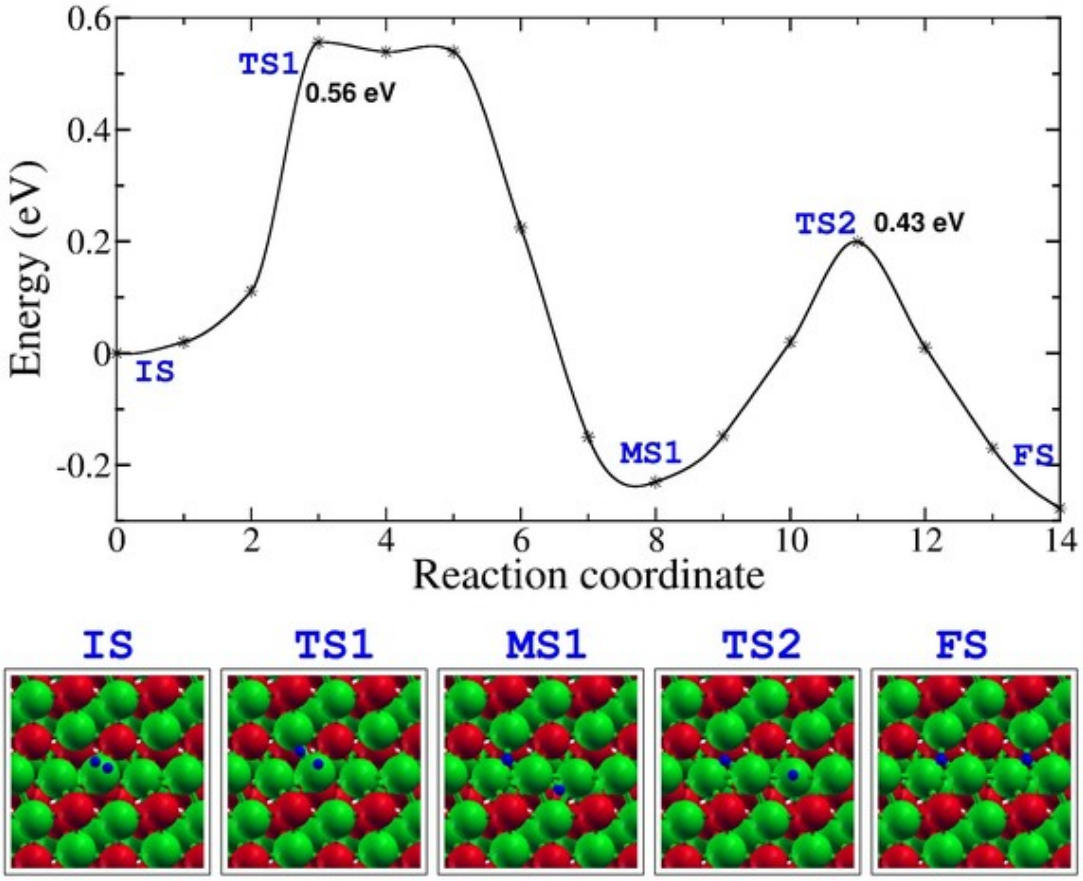

Figure A.10: $H_2 \rightarrow$ H + H on PG_p : The hydrogen dissociation on PGp has a reaction barrier of 0.56 eV. First the hydrogen dissociates into a metastable MS1 state which is -0.23 eV thermodynamically more stable than that of molecular hydrogen. In the next step the metastable hydrogen diffuses to the most stable state with a barrier 0.43 eV, gaining a very small thermodynamic stability of -0.05 eV.

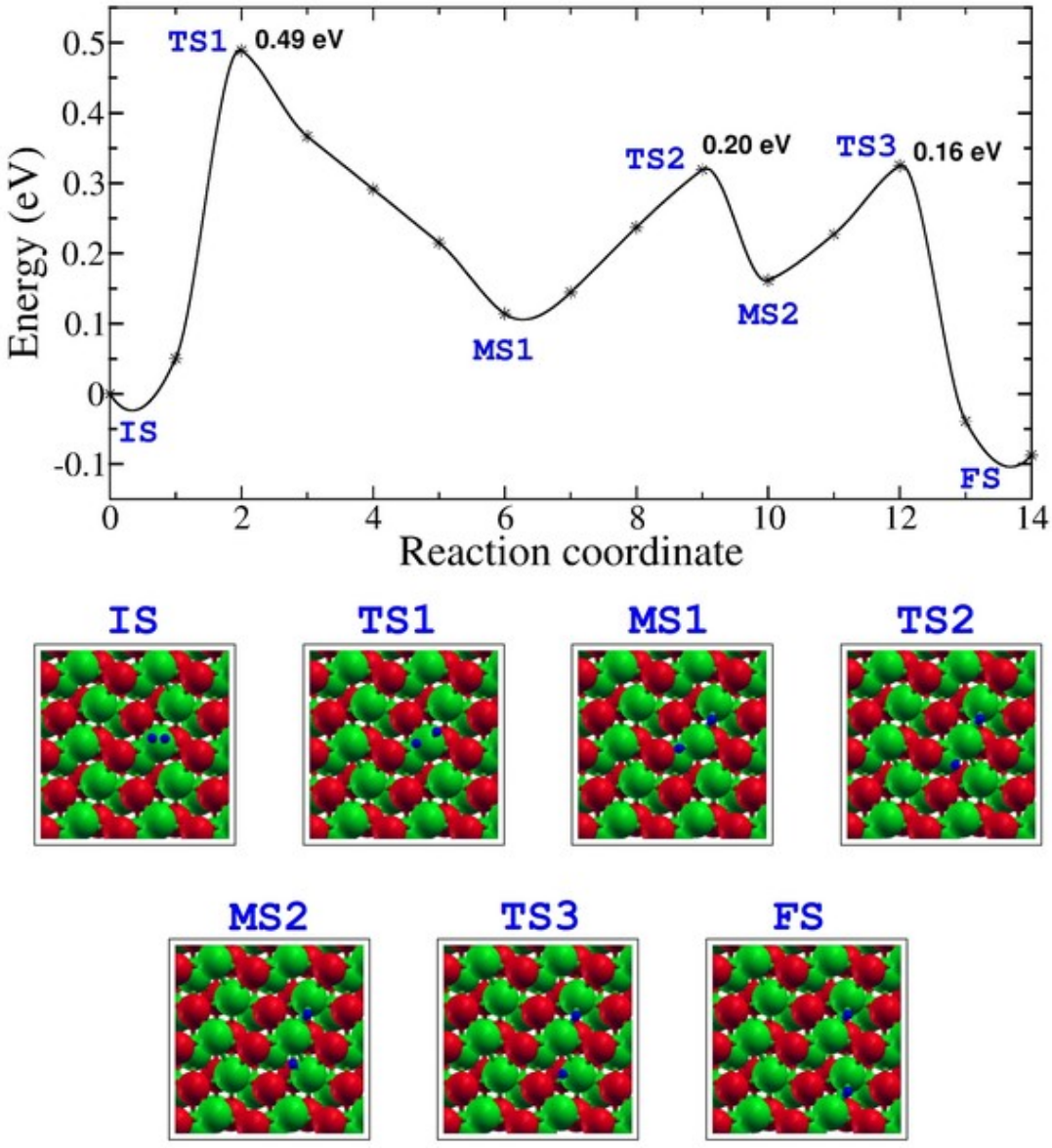

Figure A.11: $H_2 \rightarrow$ H + H on PG_h : The hydrogen dissociates on PG_h with a dissociation barrier of 0.49 eV. In the first step, hydrogen dissociates into a metastable state (labeled as MS1) which is slightly endothermic about 0.11 eV. The metastable hydrogen diffuses to the most stable position through another metastable MS2 state. The hydrogen diffusion results in overall exothermic stability of -0.09 ev. The hydrogen diffusion requires to overcome very small barriers of 0.20 and 0.16 eV.

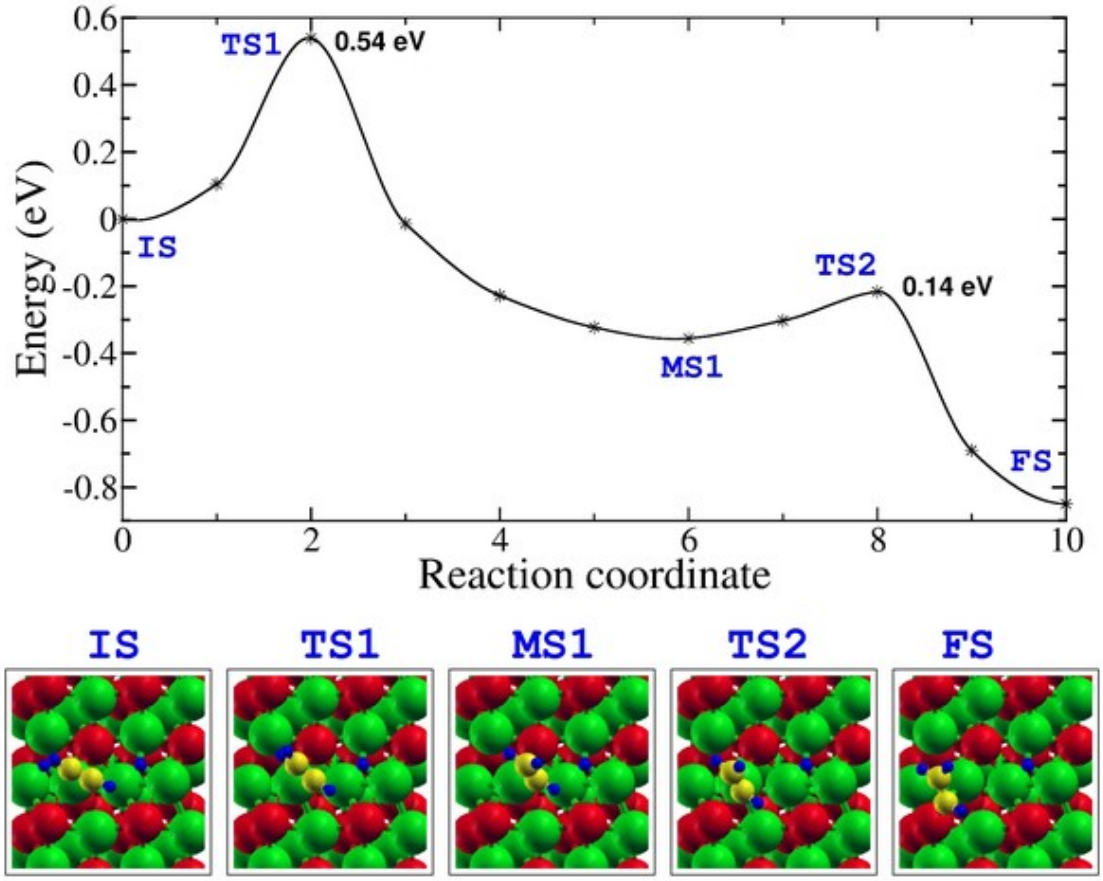

Figure A.12: C_2H_2 + H + H $\rightarrow$ C_2H_3 + H on PGp : The first hydrogenation barrier is about 0.54 eV. The hydrogen directly supplied from Pd-Pd bridge site. At first, hydrogen attacks the C_2H_2 to give a metastable state in which C_2H_3 binds on top of Pd (labeled as MS1). Next the C_2H_3 diffuses to the most stable site, which has very small barrier of only 0.14 eV.

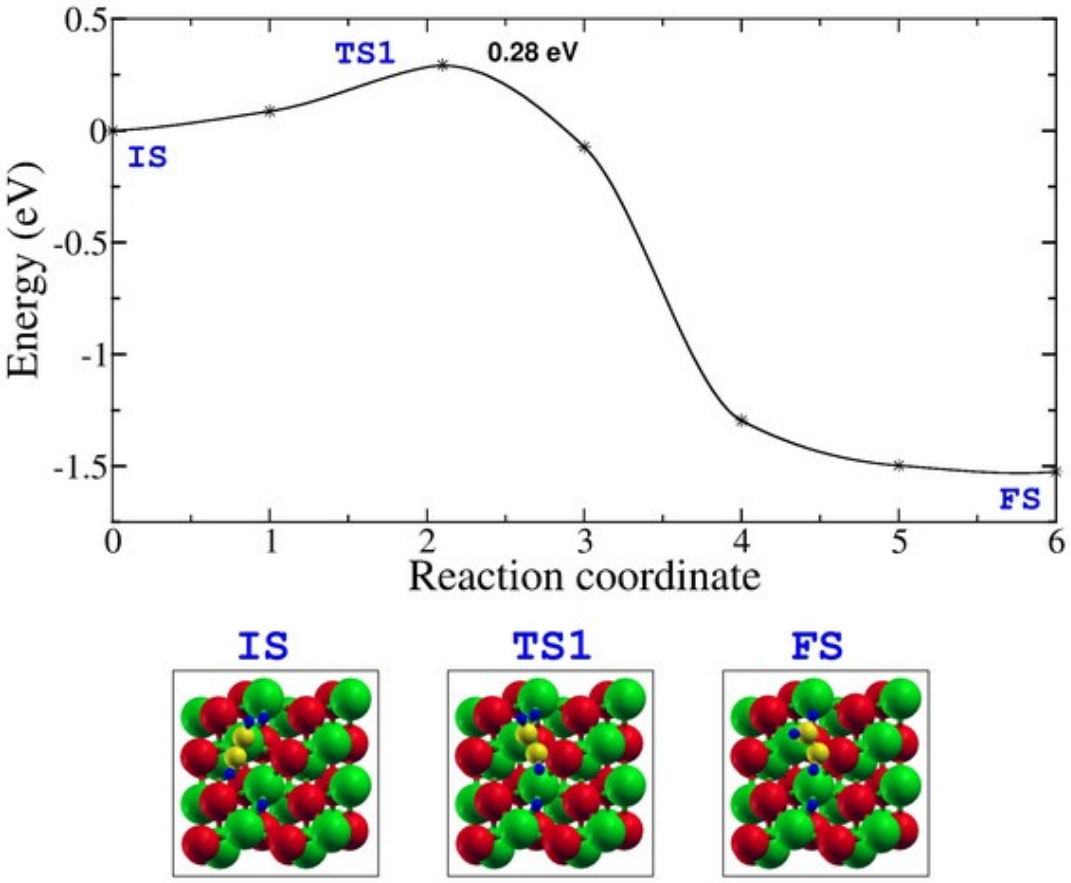

Figure A.13: C_2H_2 **+ H + H** $\rightarrow$ C_2H_3 **+ H on** PG_h **:** The first hydrogenation barrier is very low with 0.28 eV. The hydrogen directly supplied from Pd-Pd bridge site.

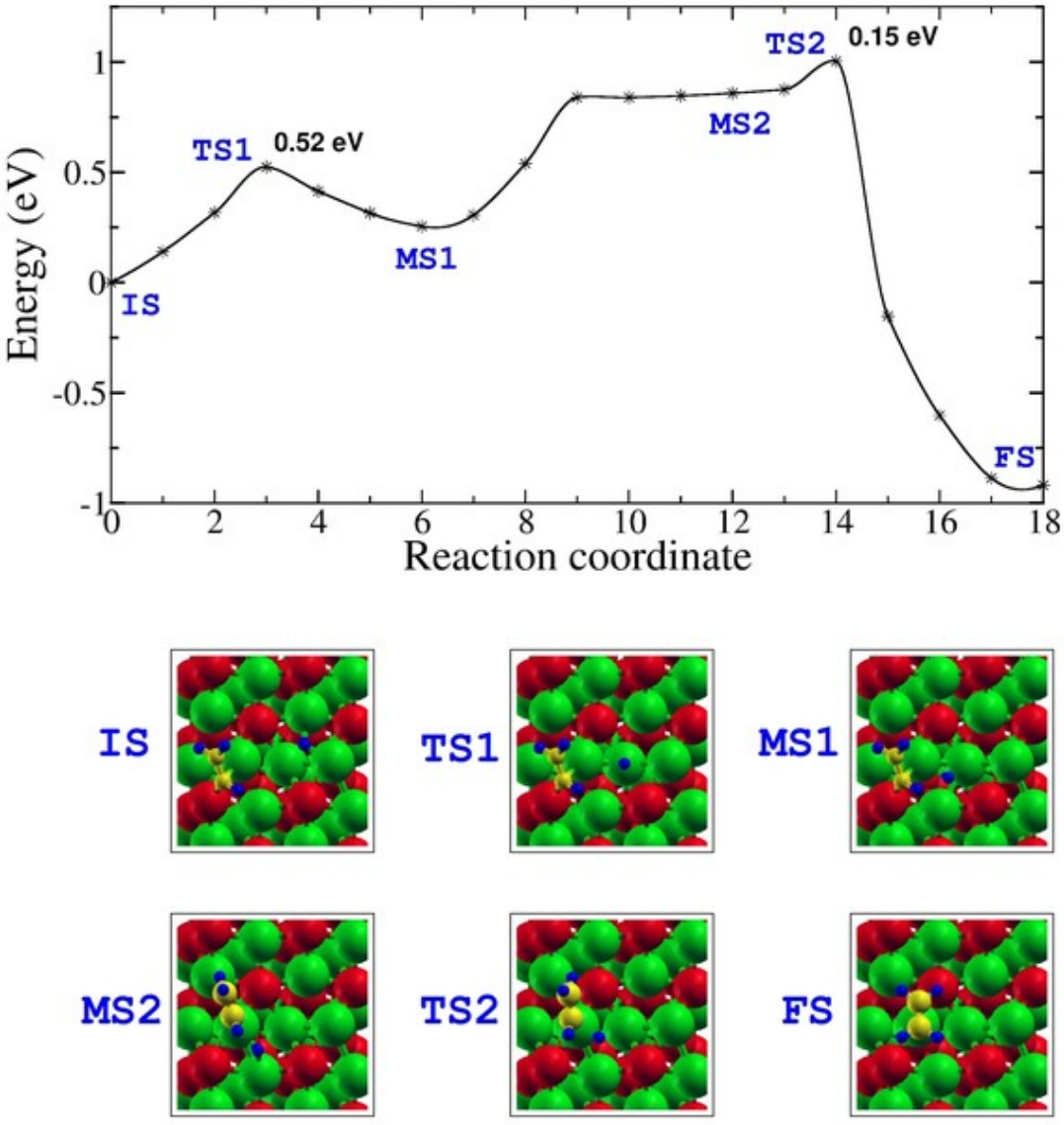

Figure A.14: C_2H_3 + H $\rightarrow$ C_2H_4 on PGp : The hydrogenation of vinyl to ethylene on PGp requires a precedent endothermic (0.86 eV) diffusion of hydrogen and C_2H_3 into a metastable position (labeled as MS2). The hydrogenation barrier from metastable position is very low with 0.15 eV.

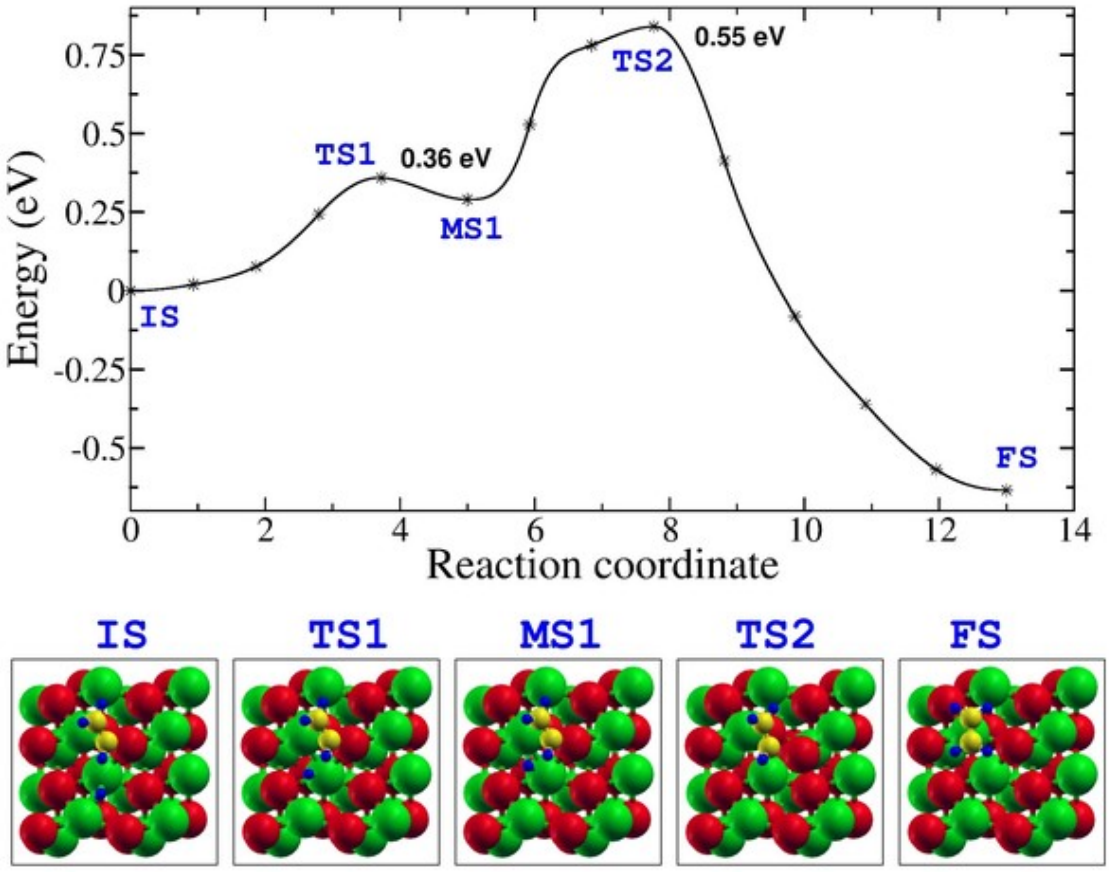

Figure A.15: C_2H_3 + H $\rightarrow$ C_2H_4 on PG_h : The hydrogenation of vinyl to ethylene on PG_h has a total reaction barrier of 0.84 eV. First the hydrogen endothermically diffuses from most stable Pd-Pd bridge to another metastable Pd-Pd bridge (marked as MS1) to attack C_2H_3. Hydrogen supplied from the metastable state attacks the C_2H_3 to give ethylene, this has a barrier of 0.55 eV.

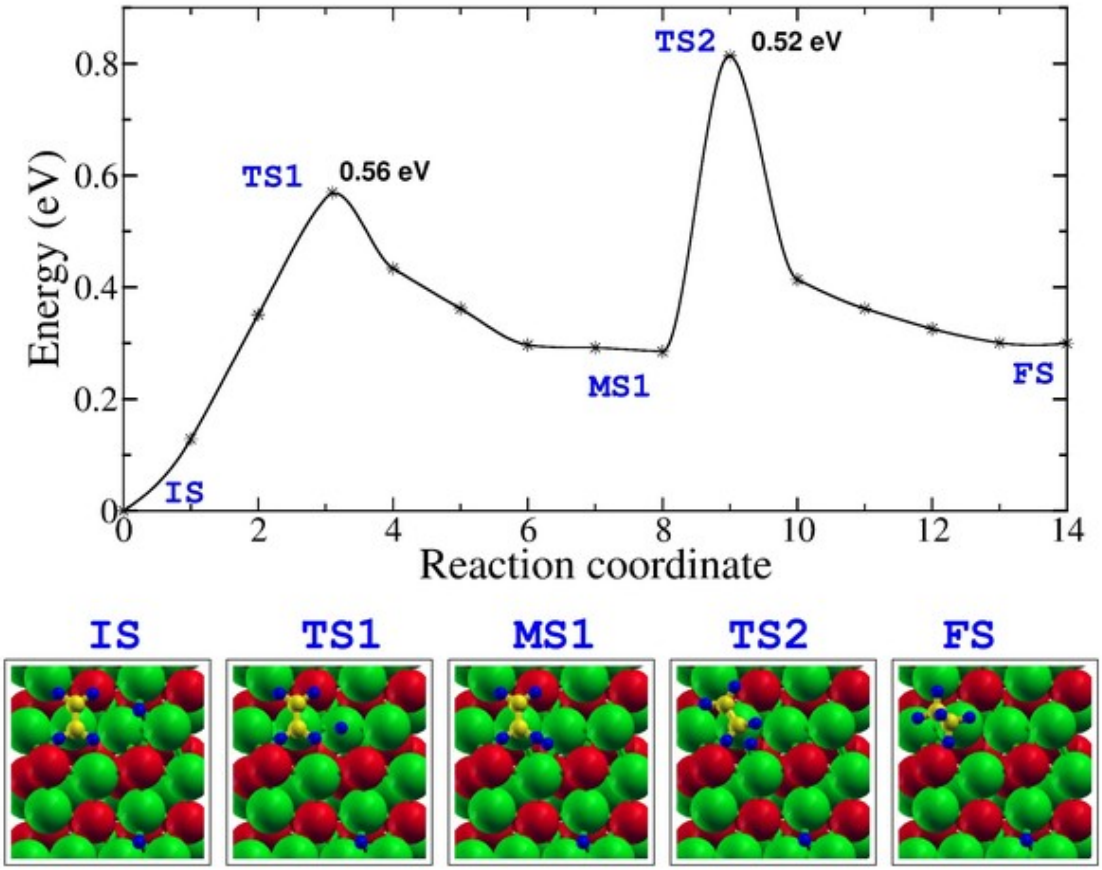

Figure A.16: C_2H_4 + H + H $\rightarrow$ C_2H_5 + H on PGp : The hydrogenation of ethylene to ethyl on PGp requires a precedent endothermic (0.29) diffusion of hydrogen to the metastable MS1 state. The hydrogen diffusion has a barrier of 0.56 eV. Further, the hydrogen attacks to the ethylene to give ethyl and this has a barrier of 0.52 eV, which results in a total reaction barrier of 0.81 eV.

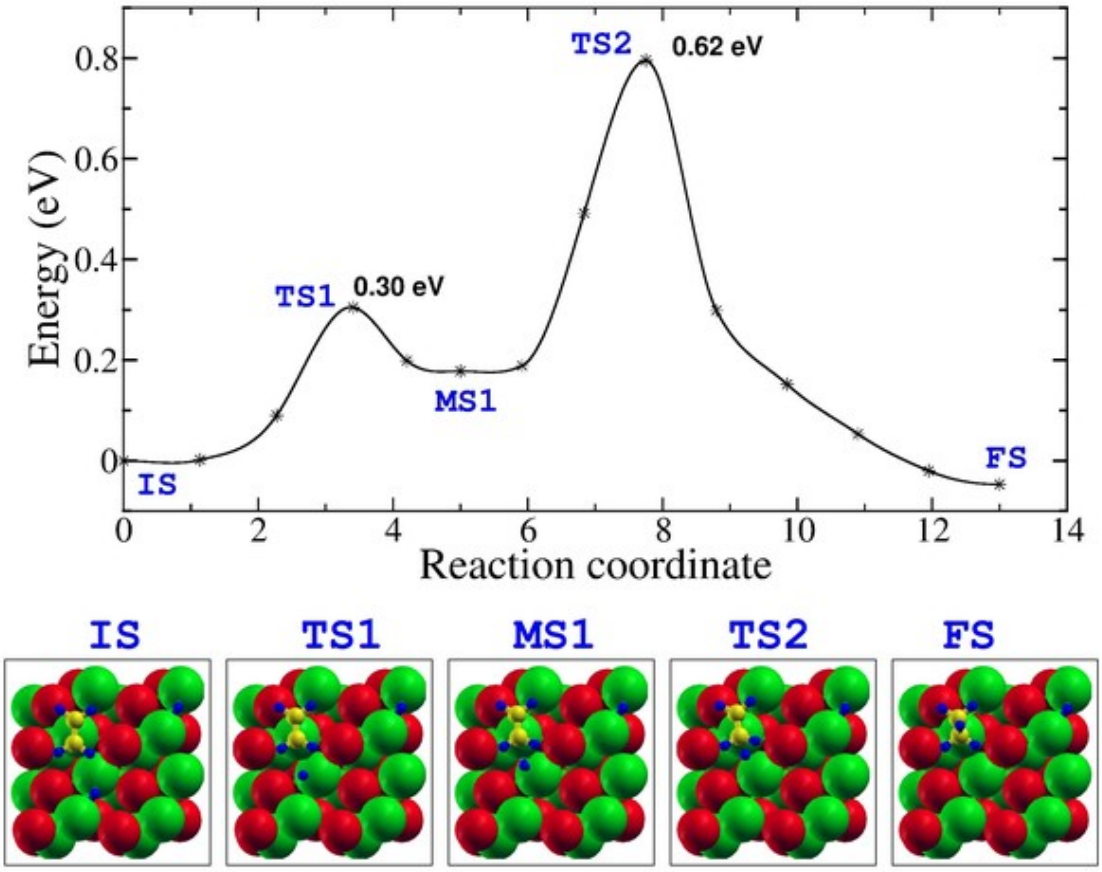

Figure A.17: C_2H_4 + H + H $\rightarrow$ C_2H_5 + H on PG_h : The hydrogenation of ethylene to ethyl on PG_h has a total reaction barrier of 0.80 eV. First the hydrogen endothermically diffuses from most stable Pd-Pd bridge to another metastable Pd-Pd bridge (marked as MS1) to attack C_2H_4. Hydrogen supplied from the metastable state attacks the C_2H_4, this has a barrier of 0.62 eV.

Appendix B

List of reaction steps used in the KMC simulations

The elementary reaction steps accounted for in the KMC simulation are given in Table B.1

Table B.1: Elementary reaction steps accounted for in the KMC simulation.

Index	Elementary step	Reaction site	Reaction
1	Pd_1 diffusion	Terrace	$Pd_1 \rightarrow Pd_1$
2	Pd_2 diffusion	Terrace	$Pd_2 \rightarrow Pd_2$
3	Pd_3 diffusion	Terrace	$Pd_3 \rightarrow Pd_3$
4	Pd_4 diffusion	Terrace	$Pd_4 \rightarrow Pd_4$
5	Ga_1 diffusion	Terrace	$Ga_1 \rightarrow Ga_1$
6	Ga_2 diffusion	Terrace	$Ga_2 \rightarrow Ga_2$
7	Ga_3 diffusion	Terrace	$Ga_3 \rightarrow Ga_3$
8	Ga_4 diffusion	Terrace	$Ga_4 \rightarrow Ga_4$
9	Pd_1Ga_1 diffusion	Terrace	$Pd_1Ga_1 \rightarrow Pd_1Ga_1$
10	Pd_2Ga_1 diffusion	Terrace	$Pd_2Ga_1 \rightarrow Pd_2Ga_1$
11	Pd_1Ga_2 diffusion	Terrace	$Pd_1Ga_2 \rightarrow Pd_1Ga_2$
12	Pd_3Ga_1 diffusion	Terrace	$Pd_3Ga_1 \rightarrow Pd_3Ga_1$
13	Pd_2Ga_2 diffusion	Terrace	$Pd_2Ga_2 \rightarrow Pd_2Ga_2$
14	Pd_1Ga_3 diffusion	Terrace	$Pd_1Ga_3 \rightarrow Pd_1Ga_3$
15	Pd_2 formation	Terrace	$Pd_1 + Pd_1 \rightarrow Pd_2$
16	Pd_3 formation	Terrace	$Pd_1 + Pd_2 \rightarrow Pd_3$
17	Pd_4 formation	Terrace	$Pd_1 + Pd_3 \rightarrow Pd_4$
18	Pd_4 formation	Terrace	$Pd_2 + Pd_2 \rightarrow Pd_4$
19	Ga_2 formation	Terrace	$Ga_1 + Ga_1 \rightarrow Ga_2$
20	Ga_3 formation	Terrace	$Ga_1 + Ga_2 \rightarrow Ga_3$

Continued on next page

Table B.1 – *Continued from previous page*

Index	Elementary step	Reaction site	Reaction
21	Ga_4 formation	Terrace	$Ga_1 + Ga_3 \rightarrow Ga_4$
22	Ga_4 formation	Terrace	$Ga_2 + Ga_2 \rightarrow Ga_4$
23	Pd_1Ga_1 formation	Terrace	$Pd_1 + Ga_1 \rightarrow Pd_1Ga_1$
24	Pd_2Ga_1 formation	Terrace	$Pd_2 + Ga_1 \rightarrow Pd_2Ga_1$
25	Pd_2Ga_1 formation	Terrace	$Pd_1 + Pd_1Ga_1 \rightarrow Pd_2Ga_1$
26	Pd_1Ga_2 formation	Terrace	$Pd_1 + Ga_2 \rightarrow Pd_1Ga_2$
27	Pd_1Ga_2 formation	Terrace	$Ga_1 + Pd_1Ga_1 \rightarrow Pd_1Ga_2$
28	Pd_3Ga_1 formation	Terrace	$Pd_3 + Ga_1 \rightarrow Pd_3Ga_1$
29	Pd_3Ga_1 formation	Terrace	$Pd_2 + Pd_1Ga_1 \rightarrow Pd_3Ga_1$
30	Pd_3Ga_1 formation	Terrace	$Pd_1 + Pd_2Ga_1 \rightarrow Pd_3Ga_1$
31	Pd_2Ga_2 formation	Terrace	$Pd_1 + Pd_1Ga_2 \rightarrow Pd_2Ga_2$
32	Pd_2Ga_2 formation	Terrace	$Pd_2 + Ga_2 \rightarrow Pd_2Ga_2$
33	Pd_2Ga_2 formation	Terrace	$Ga_1 + Pd_2Ga_1 \rightarrow Pd_2Ga_2$
34	Pd_2Ga_2 formation	Terrace	$Pd_1Ga_1 + Pd_1Ga_1 \rightarrow Pd_2Ga_2$
35	Pd_1Ga_3 formation	Terrace	$Pd_1 + Ga_3 \rightarrow Pd_1Ga_3$
36	Pd_1Ga_3 formation	Terrace	$Pd_1Ga_1 + Ga_2 \rightarrow Pd_1Ga_3$
37	Pd_1Ga_3 formation	Terrace	$Pd_1Ga_2 + Ga_1 \rightarrow Pd_1Ga_3$
38	Pd_1 trapping	F-center	$Pd_1 + F^* \rightarrow Pd_1/F$
39	Pd_2 formation	F-center	$Pd_2 + F^* \rightarrow Pd_2/F$
40	Pd_2 formation	F-center	$Pd_1 + Pd_1/F \rightarrow Pd_2/F$
41	Pd_3 formation	F-center	$Pd_3 + F^* \rightarrow Pd_3/F$
42	Pd_3 formation	F-center	$Pd_2 + Pd_1/F \rightarrow Pd_3/F$
43	Pd_3 formation	F-center	$Pd_1 + Pd_2/F \rightarrow Pd_3/F$
44	Pd_4 formation	F-center	$Pd_4 + F^* \rightarrow Pd_4/F$
45	Pd_4 formation	F-center	$Pd_3 + Pd_1/F \rightarrow Pd_4/F$
46	Pd_4 formation	F-center	$Pd_2 + Pd_2/F \rightarrow Pd_4/F$
47	Pd_4 formation	F-center	$Pd_1 + Pd_3/F \rightarrow Pd_4/F$
48	Ga_1 trapping	F-center	$Ga_1 + F^* \rightarrow Ga_1/F$
49	Ga_2 formation	F-center	$Ga_2 + F^* \rightarrow Ga_2/F$
50	Ga_2 formation	F-center	$Ga_1 + Ga_1/F \rightarrow Ga_2/F$
51	Ga_3 formation	F-center	$Ga_3 + F^* \rightarrow Ga_3/F$
52	Ga_3 formation	F-center	$Ga_2 + Ga_1/F \rightarrow Ga_3/F$

Continued on next page

Table B.1 – *Continued from previous page*

Index	Elementary step	Reaction site	Reaction
53	Ga_3 formation	F-center	$Ga_1 + Ga_2/F \rightarrow Ga_3/F$
54	Ga_4 formation	F-center	$Ga_4 + F^* \rightarrow Ga_4/F$
55	Ga_4 formation	F-center	$Ga_3 + Ga_1/F \rightarrow Ga_4/F$
56	Ga_4 formation	F-center	$Ga_2 + Ga_2/F \rightarrow Ga_4/F$
57	Ga_4 formation	F-center	$Ga_1 + Ga_3/F \rightarrow Ga_4/F$
58	Pd_1Ga_1 formation	F-center	$Pd_1Ga_1 + F^* \rightarrow Pd_1Ga_1/F$
59	Pd_1Ga_1 formation	F-center	$Pd_1 + Ga_1/F \rightarrow Pd_1Ga_1/F$
60	Pd_1Ga_1 formation	F-center	$Ga_1 + Pd_1/F \rightarrow Pd_1Ga_1/F$
61	Pd_2Ga_1 formation	F-center	$Pd_2Ga_1 + F^* \rightarrow Pd_2Ga_1/F$
62	Pd_2Ga_1 formation	F-center	$Pd_2 + Ga_1/F \rightarrow Pd_2Ga_1/F$
63	Pd_2Ga_1 formation	F-center	$Pd_1Ga_1 + Pd_1/F \rightarrow Pd_2Ga_1/F$
64	Pd_2Ga_1 formation	F-center	$Ga_1 + Pd_2/F \rightarrow Pd_2Ga_1/F$
65	Pd_2Ga_1 formation	F-center	$Pd_1 + Pd_1Ga_1/F \rightarrow Pd_2Ga_1/F$
66	Pd_1Ga_2 formation	F-center	$Pd_1Ga_2 + F^* \rightarrow Pd_1Ga_2/F$
67	Pd_1Ga_2 formation	F-center	$Pd_1Ga_1 + Ga_1/F \rightarrow Pd_1Ga_2/F$
68	Pd_1Ga_2 formation	F-center	$Pd_1 + Ga_2/F \rightarrow Pd_1Ga_2/F$
69	Pd_1Ga_2 formation	F-center	$Ga_2 + Pd_1/F \rightarrow Pd_1Ga_2/F$
70	Pd_1Ga_2 formation	F-center	$Ga_1 + Pd_1Ga_1/F \rightarrow Pd_1Ga_2/F$
71	Pd_3Ga_1 formation	F-center	$Pd_3Ga_1 + F^* \rightarrow Pd_3Ga_1/F$
72	Pd_3Ga_1 formation	F-center	$Pd_3 + Ga_1/F \rightarrow Pd_3Ga_1/F$
73	Pd_3Ga_1 formation	F-center	$Pd_2Ga_1 + Pd_1/F \rightarrow Pd_3Ga_1/F$
74	Pd_3Ga_1 formation	F-center	$Pd_1Ga_1 + Pd_2/F \rightarrow Pd_3Ga_1/F$
75	Pd_3Ga_1 formation	F-center	$Ga_1 + Pd_3/F \rightarrow Pd_3Ga_1/F$
76	Pd_3Ga_1 formation	F-center	$Pd_2 + Pd_1Ga_1/F \rightarrow Pd_3Ga_1/F$
77	Pd_3Ga_1 formation	F-center	$Pd_1 + Pd_2Ga_1/F \rightarrow Pd_3Ga_1/F$
78	Pd_2Ga_2 formation	F-center	$Pd_2Ga_2 + F^* \rightarrow Pd_2Ga_2/F$
79	Pd_2Ga_2 formation	F-center	$Pd_2Ga_1 + Ga_1/F \rightarrow Pd_2Ga_2/F$
80	Pd_2Ga_2 formation	F-center	$Pd_2 + Ga_2/F \rightarrow Pd_2Ga_2/F$
81	Pd_2Ga_2 formation	F-center	$Pd_1Ga_2 + Pd_1/F \rightarrow Pd_2Ga_2/F$
82	Pd_2Ga_2 formation	F-center	$Ga_2 + Pd_2/F \rightarrow Pd_2Ga_2/F$
83	Pd_2Ga_2 formation	F-center	$Pd_1Ga_1 + Pd_1Ga_1/F \rightarrow Pd_2Ga_2/F$
84	Pd_2Ga_2 formation	F-center	$Pd_1 + Pd_1Ga_2/F \rightarrow Pd_2Ga_2/F$

Continued on next page

Table B.1 – *Continued from previous page*

Index	Elementary step	Reaction site	Reaction
85	Pd_2Ga_2 formation	F-center	$Ga_1 + Pd_2Ga_1/F \rightarrow Pd_2Ga_2/F$
86	Pd_1Ga_3 formation	F-center	$Pd_1Ga_3 + F^* \rightarrow Pd_1Ga_3/F$
87	Pd_1Ga_3 formation	F-center	$Pd_1Ga_2 + Ga_1/F \rightarrow Pd_1Ga_3/F$
88	Pd_1Ga_3 formation	F-center	$Pd_1Ga_1 + Ga_2/F \rightarrow Pd_1Ga_3/F$
89	Pd_1Ga_3 formation	F-center	$Pd_1 + Ga_3/F \rightarrow Pd_1Ga_3/F$
90	Pd_1Ga_3 formation	F-center	$Ga_3 + Pd_1/F \rightarrow Pd_1Ga_3/F$
91	Pd_1Ga_3 formation	F-center	$Ga_2 + Pd_1Ga_1/F \rightarrow Pd_1Ga_3/F$
92	Pd_1Ga_3 formation	F-center	$Ga_1 + Pd_1Ga_2/F \rightarrow Pd_1Ga_3/F$
93	Pd_2 decomposition	Terrace	$Pd_2 \rightarrow Pd_1 + Pd_1$
94	Pd_3 decomposition	Terrace	$Pd_3 \rightarrow Pd_1 + Pd_2$
95	Pd_4 decomposition	Terrace	$Pd_4 \rightarrow Pd_1 + Pd_3$
96	Pd_4 decomposition	Terrace	$Pd_4 \rightarrow Pd_2 + Pd_2$
97	Ga_2 decomposition	Terrace	$Ga_2 \rightarrow Ga_1 + Ga_1$
98	Ga_3 decomposition	Terrace	$Ga_3 \rightarrow Ga_1 + Ga_2$
99	Ga_4 decomposition	Terrace	$Ga_4 \rightarrow Ga_1 + Ga_3$
100	Ga_4 decomposition	Terrace	$Ga_4 \rightarrow Ga_2 + Ga_2$
101	Pd_1Ga_1 decomposition	Terrace	$Pd_1Ga_1 \rightarrow Pd_1 + Ga_1$
102	Pd_2Ga_1 decomposition	Terrace	$Pd_2Ga_1 \rightarrow Pd_2 + Ga_1$
103	Pd_2Ga_1 decomposition	Terrace	$Pd_2Ga_1 \rightarrow Pd_1 + Pd_1Ga_1$
104	Pd_1Ga_2 decomposition	Terrace	$Pd_1Ga_2 \rightarrow Pd_1 + Ga_2$
105	Pd_1Ga_2 decomposition	Terrace	$Pd_1Ga_2 \rightarrow Ga_1 + Pd_1Ga_1$
106	Pd_3Ga_1 decomposition	Terrace	$Pd_3Ga_1 \rightarrow Pd_3 + Ga_1$
107	Pd_3Ga_1 decomposition	Terrace	$Pd_3Ga_1 \rightarrow Pd_2 + Pd_1Ga_1$
108	Pd_3Ga_1 decomposition	Terrace	$Pd_3Ga_1 \rightarrow Pd_1 + Pd_2Ga_1$
109	Pd_2Ga_2 decomposition	Terrace	$Pd_2Ga_2 \rightarrow Pd_1 + Pd_1Ga_2$
110	Pd_2Ga_2 decomposition	Terrace	$Pd_2Ga_2 \rightarrow Pd_2 + Ga_2$
111	Pd_2Ga_2 decomposition	Terrace	$Pd_2Ga_2 \rightarrow Ga_1 + Pd_2Ga_1$
112	Pd_2Ga_2 decomposition	Terrace	$Pd_2Ga_2 \rightarrow Pd_1Ga_1 + Pd_1Ga_1$
113	Pd_1Ga_3 decomposition	Terrace	$Pd_1Ga_3 \rightarrow Pd_1 + Ga_3$
114	Pd_1Ga_3 decomposition	Terrace	$Pd_1Ga_3 \rightarrow Pd_1Ga_1 + Ga_2$
115	Pd_1Ga_3 decomposition	Terrace	$Pd_1Ga_3 \rightarrow Pd_1Ga_2 + Ga_1$
116	Pd_1 escaping	F-center	$Pd_1/F \rightarrow Pd_1 + F^*$

Continued on next page

Table B.1 – *Continued from previous page*

Index	Elementary step	Reaction site	Reaction
117	Pd_2 escaping	F-center	$Pd_2/F \rightarrow Pd_2 + F^*$
118	Pd_2 decomposition	F-center	$Pd_2/F \rightarrow Pd_1 + Pd_1/F$
119	Pd_3 escaping	F-center	$Pd_3/F \rightarrow Pd_3 + F^*$
120	Pd_3 decomposition	F-center	$Pd_3/F \rightarrow Pd_2 + Pd_1/F$
121	Pd_3 decomposition	F-center	$Pd_3/F \rightarrow Pd_1 + Pd_2/F$
122	Pd_4 escaping	F-center	$Pd_4/F \rightarrow Pd_4 + F^*$
123	Pd_4 decomposition	F-center	$Pd_4/F \rightarrow Pd_3 + Pd_1/F$
124	Pd_4 decomposition	F-center	$Pd_4/F \rightarrow Pd_2 + Pd_2/F$
125	Pd_4 decomposition	F-center	$Pd_4/F \rightarrow Pd_1 + Pd_3/F$
126	Ga_1 escaping	F-center	$Ga_1/F \rightarrow Ga_1 + F^*$
127	Ga_2 escaping	F-center	$Ga_2/F \rightarrow Ga_2 + F^*$
128	Ga_2 decomposition	F-center	$Ga_2/F \rightarrow Ga_1 + Ga_1/F$
129	Ga_3 escaping	F-center	$Ga_3/F \rightarrow Ga_3 + F^*$
130	Ga_3 decomposition	F-center	$Ga_3/F \rightarrow Ga_2 + Ga_1/F$
131	Ga_3 decomposition	F-center	$Ga_3/F \rightarrow Ga_1 + Ga_2/F$
132	Ga_4 escaping	F-center	$Ga_4/F \rightarrow Ga_4 + F^*$
133	Ga_4 decomposition	F-center	$Ga_4/F \rightarrow Ga_3 + Ga_1/F$
134	Ga_4 decomposition	F-center	$Ga_4/F \rightarrow Ga_2 + Ga_2/F$
135	Ga_4 decomposition	F-center	$Ga_4/F \rightarrow Ga_1 + Ga_3/F$
136	Pd_1Ga_1 escaping	F-center	$Pd_1Ga_1/F \rightarrow Pd_1Ga_1 + F^*$
137	Pd_1Ga_1 decomposition	F-center	$Pd_1Ga_1/F \rightarrow Pd_1 + Ga_1/F$
138	Pd_1Ga_1 decomposition	F-center	$Pd_1Ga_1/F \rightarrow Ga_1 + Pd_1/F$
139	Pd_2Ga_1 escaping	F-center	$Pd_2Ga_1/F \rightarrow Pd_2Ga_1 + F^*$
140	Pd_2Ga_1 decomposition	F-center	$Pd_2Ga_1/F \rightarrow Pd_2 + Ga_1/F$
141	Pd_2Ga_1 decomposition	F-center	$Pd_2Ga_1/F \rightarrow Pd_1Ga_1 + Pd_1/F$
142	Pd_2Ga_1 decomposition	F-center	$Pd_2Ga_1/F \rightarrow Ga_1 + Pd_2/F$
143	Pd_2Ga_1 decomposition	F-center	$Pd_2Ga_1/F \rightarrow Pd_1 + Pd_1Ga_1/F$
144	Pd_1Ga_2 escaping	F-center	$Pd_1Ga_2/F \rightarrow Pd_1Ga_2 + F^*$
145	Pd_1Ga_2 decomposition	F-center	$Pd_1Ga_2/F \rightarrow Pd_1Ga_1 + Ga_1/F$
146	Pd_1Ga_2 decomposition	F-center	$Pd_1Ga_2/F \rightarrow Pd_1 + Ga_2/F$
147	Pd_1Ga_2 decomposition	F-center	$Pd_1Ga_2/F \rightarrow Ga_2 + Pd_1/F$
148	Pd_1Ga_2 decomposition	F-center	$Pd_1Ga_2/F \rightarrow Ga_1 + Pd_1Ga_1/F$

Continued on next page

Table B.1 – *Continued from previous page*

Index	Elementary step	Reaction site	Reaction
149	Pd_3Ga_1 escaping	F-center	$Pd_3Ga_1/F \rightarrow Pd_3Ga_1 + F^*$
150	Pd_3Ga_1 decomposition	F-center	$Pd_3Ga_1/F \rightarrow Pd_3 + Ga_1/F$
151	Pd_3Ga_1 decomposition	F-center	$Pd_3Ga_1/F \rightarrow Pd_2Ga_1 + Pd_1/F$
152	Pd_3Ga_1 decomposition	F-center	$Pd_3Ga_1/F \rightarrow Pd_1Ga_1 + Pd_2/F$
153	Pd_3Ga_1 decomposition	F-center	$Pd_3Ga_1/F \rightarrow Ga_1 + Pd_3/F$
154	Pd_3Ga_1 decomposition	F-center	$Pd_3Ga_1/F \rightarrow Pd_2 + Pd_1Ga_1/F$
155	Pd_3Ga_1 decomposition	F-center	$Pd_3Ga_1/F \rightarrow Pd_1 + Pd_2Ga_1/F$
156	Pd_2Ga_2 escaping	F-center	$Pd_2Ga_2/F \rightarrow Pd_2Ga_2 + F^*$
157	Pd_2Ga_2 decomposition	F-center	$Pd_2Ga_2/F \rightarrow Pd_2Ga_1 + Ga_1/F$
158	Pd_2Ga_2 decomposition	F-center	$Pd_2Ga_2/F \rightarrow Pd_2 + Ga_2/F$
159	Pd_2Ga_2 decomposition	F-center	$Pd_2Ga_2/F \rightarrow Pd_1Ga_2 + Pd_1/F$
160	Pd_2Ga_2 decomposition	F-center	$Pd_2Ga_2/F \rightarrow Ga_2 + Pd_2/F$
161	Pd_2Ga_2 decomposition	F-center	$Pd_2Ga_2/F \rightarrow Pd_1Ga_1 + Pd_1Ga_1/F$
162	Pd_2Ga_2 decomposition	F-center	$Pd_2Ga_2/F \rightarrow Pd_1 + Pd_1Ga_2/F$
163	Pd_2Ga_2 decomposition	F-center	$Pd_2Ga_2/F \rightarrow Ga_1 + Pd_2Ga_1/F$
164	Pd_1Ga_3 escaping	F-center	$Pd_1Ga_3/F \rightarrow Pd_1Ga_3 + F^*$
165	Pd_1Ga_3 decomposition	F-center	$Pd_1Ga_3/F \rightarrow Pd_1Ga_2 + Ga_1/F$
166	Pd_1Ga_3 decomposition	F-center	$Pd_1Ga_3/F \rightarrow Pd_1Ga_1 + Ga_2/F$
167	Pd_1Ga_3 decomposition	F-center	$Pd_1Ga_3/F \rightarrow Pd_1 + Ga_3/F$
168	Pd_1Ga_3 decomposition	F-center	$Pd_1Ga_3/F \rightarrow Ga_3 + Pd_1/F$
169	Pd_1Ga_3 decomposition	F-center	$Pd_1Ga_3/F \rightarrow Ga_2 + Pd_1Ga_1/F$
170	Pd_1Ga_3 decomposition	F-center	$Pd_1Ga_3/F \rightarrow Ga_1 + Pd_1Ga_2/F$

Appendix C

Stable structures of small clusters on MgO(100) surface

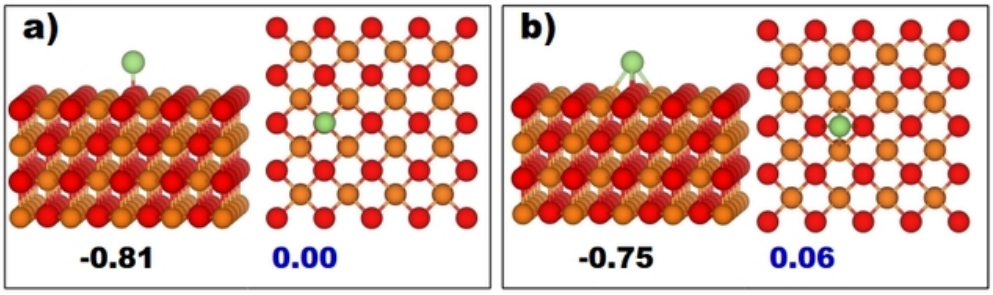

Figure C.1: a)-b) Adsorption configurations for Ga adatom on MgO(100) terrace. Ga atoms are represented by green color balls. The values given in black color are the binding energies of clusters in eV, which is calculated using Equation-2. The values given in blue color are the relative energy in eV with respect to the most stable configuration.

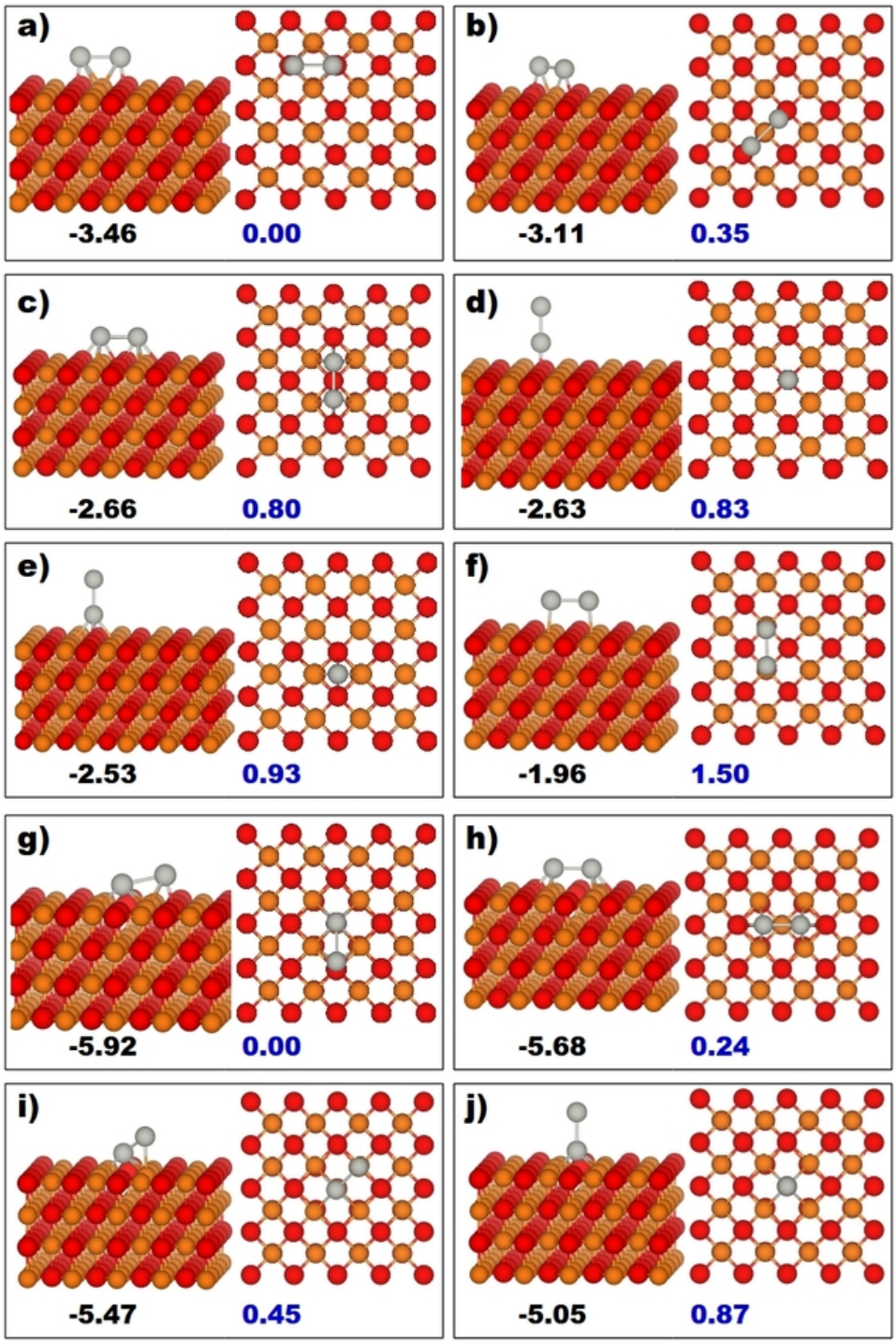

Figure C.2: a)-f) Adsorption configurations for Pd_2 clusters on MgO(100) terrace. g)-j) Adsorption configurations for Pd_2 clusters at the oxygen vacancy site.

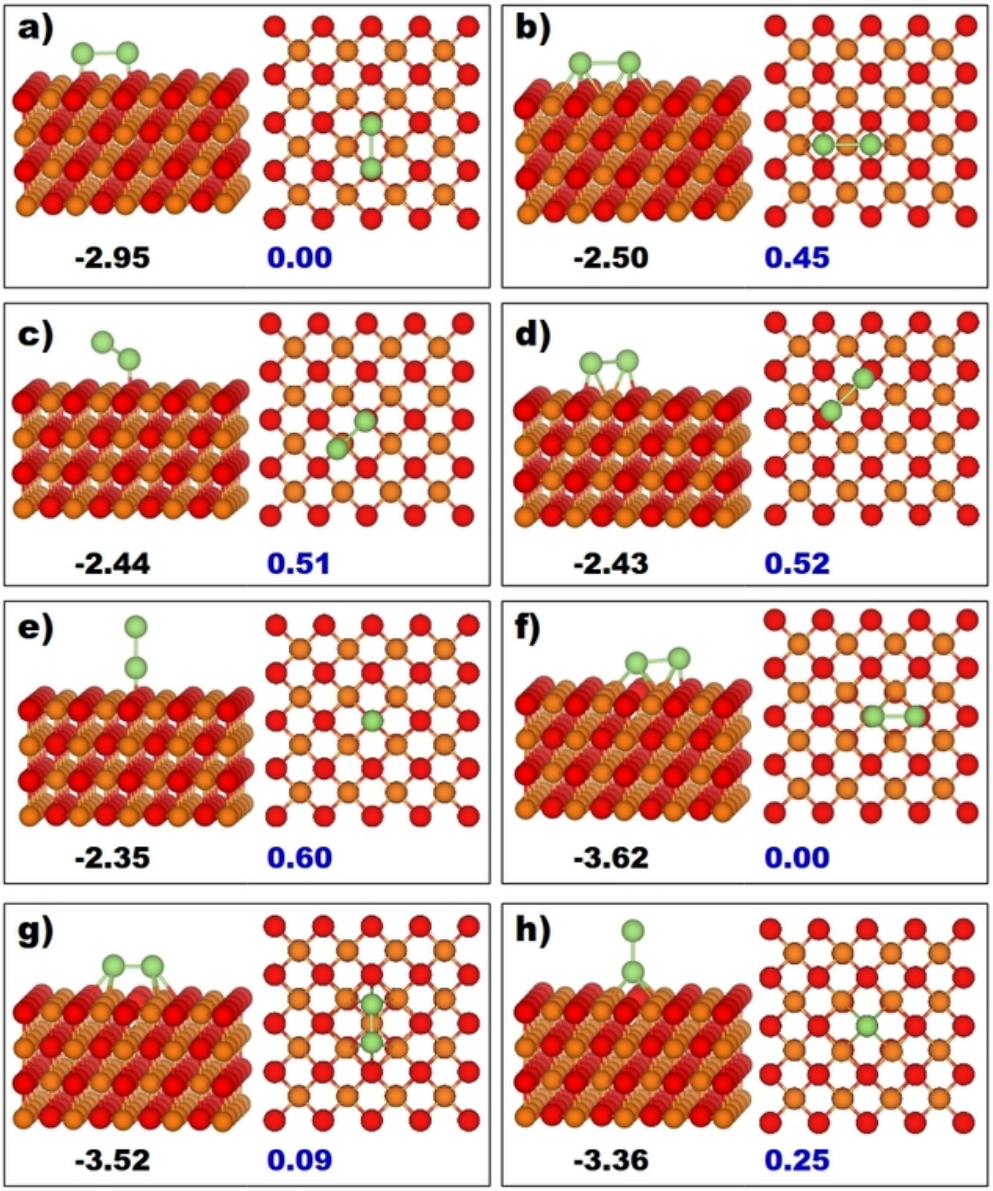

Figure C.3: a)-e) Adsorption configurations for Ga dimer clusters on MgO(100) terrace. f)-h) Adsorption configurations for Ga dimer clusters at the oxygen vacancy site.

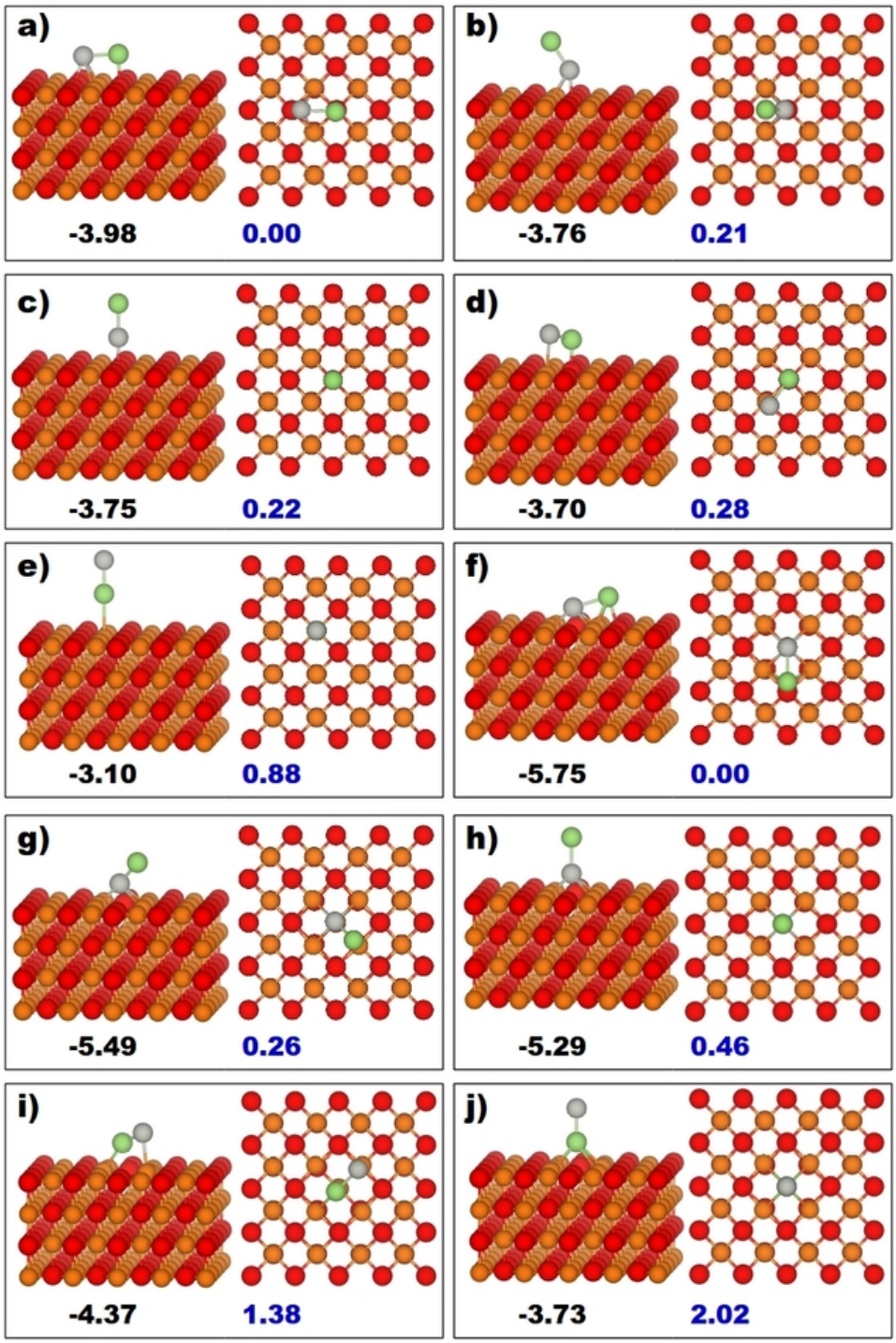

Figure C.4: a)-e) Adsorption configurations for Pd_1Ga_1 clusters on MgO(100) terrace. f)-j) Adsorption configurations for Pd_1Ga_1 clusters at the oxygen vacancy site.

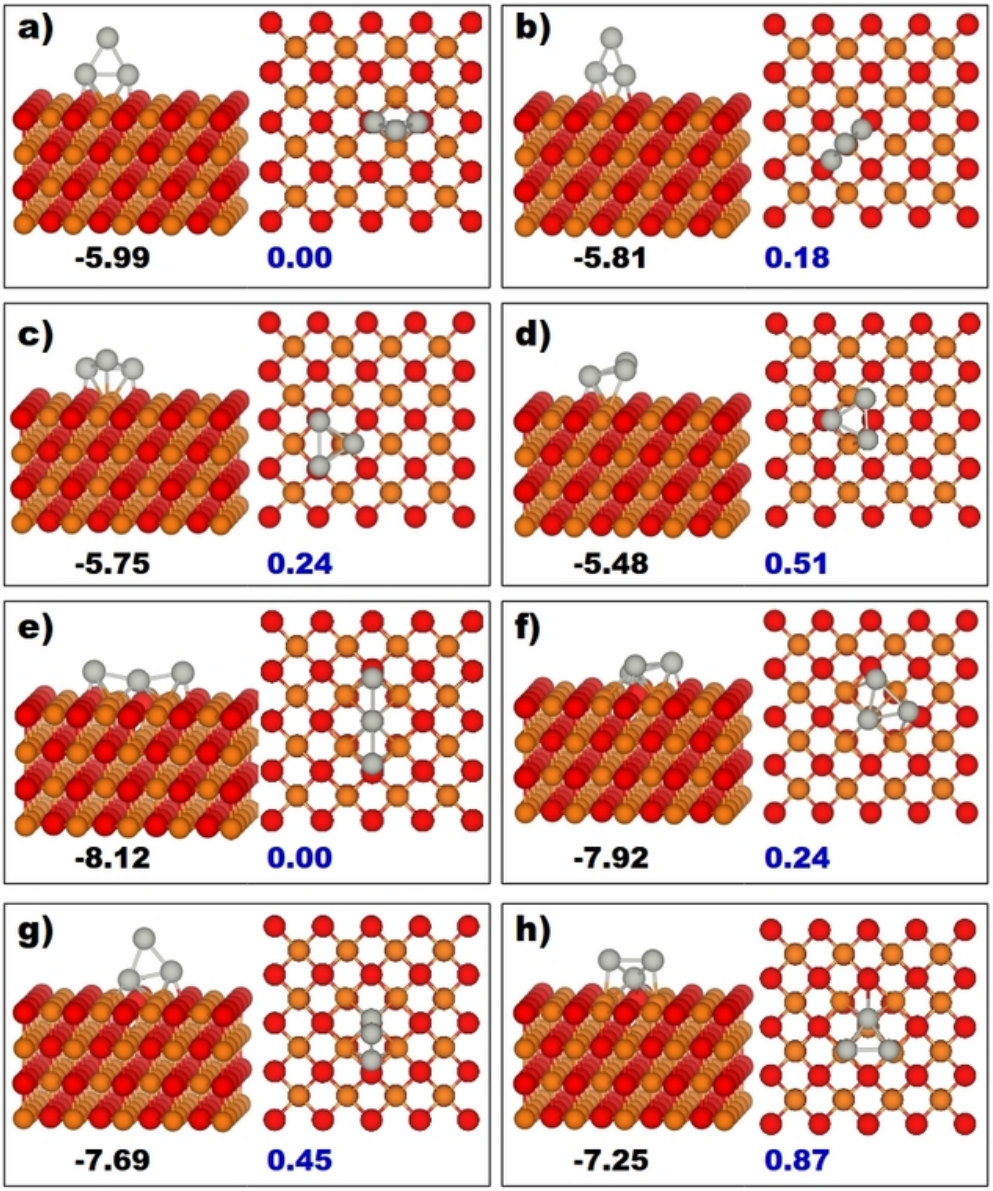

Figure C.5: a)-d) Adsorption configurations for Pd_3 clusters on MgO(100) terrace. e)-h) Adsorption configurations for Pd_3 clusters at the oxygen vacancy site.

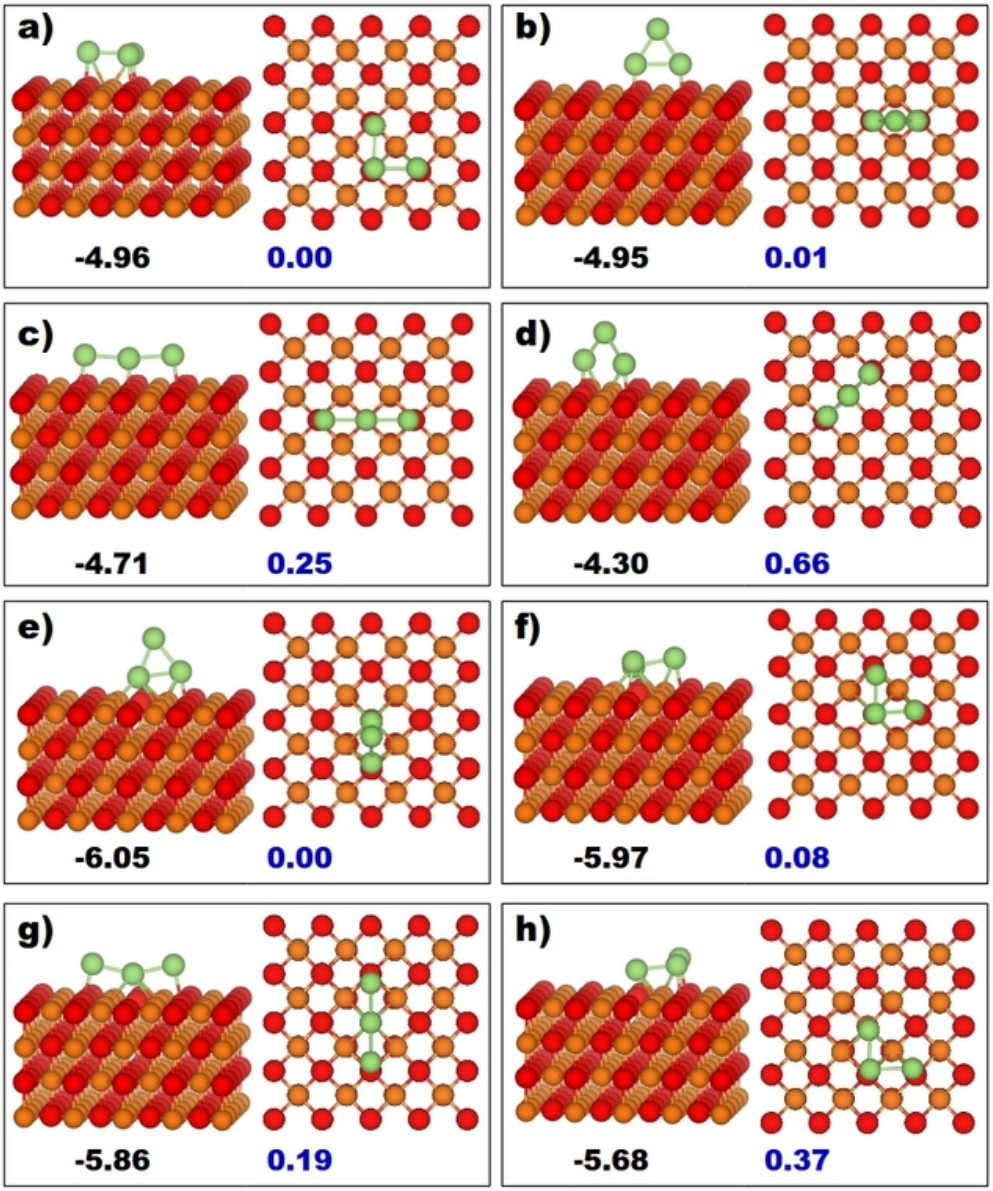

Figure C.6: a)-d) Adsorption configurations for Ga_3 clusters on MgO(100) terrace. e)-h) Adsorption configurations for Ga_3 clusters at the oxygen vacancy site.

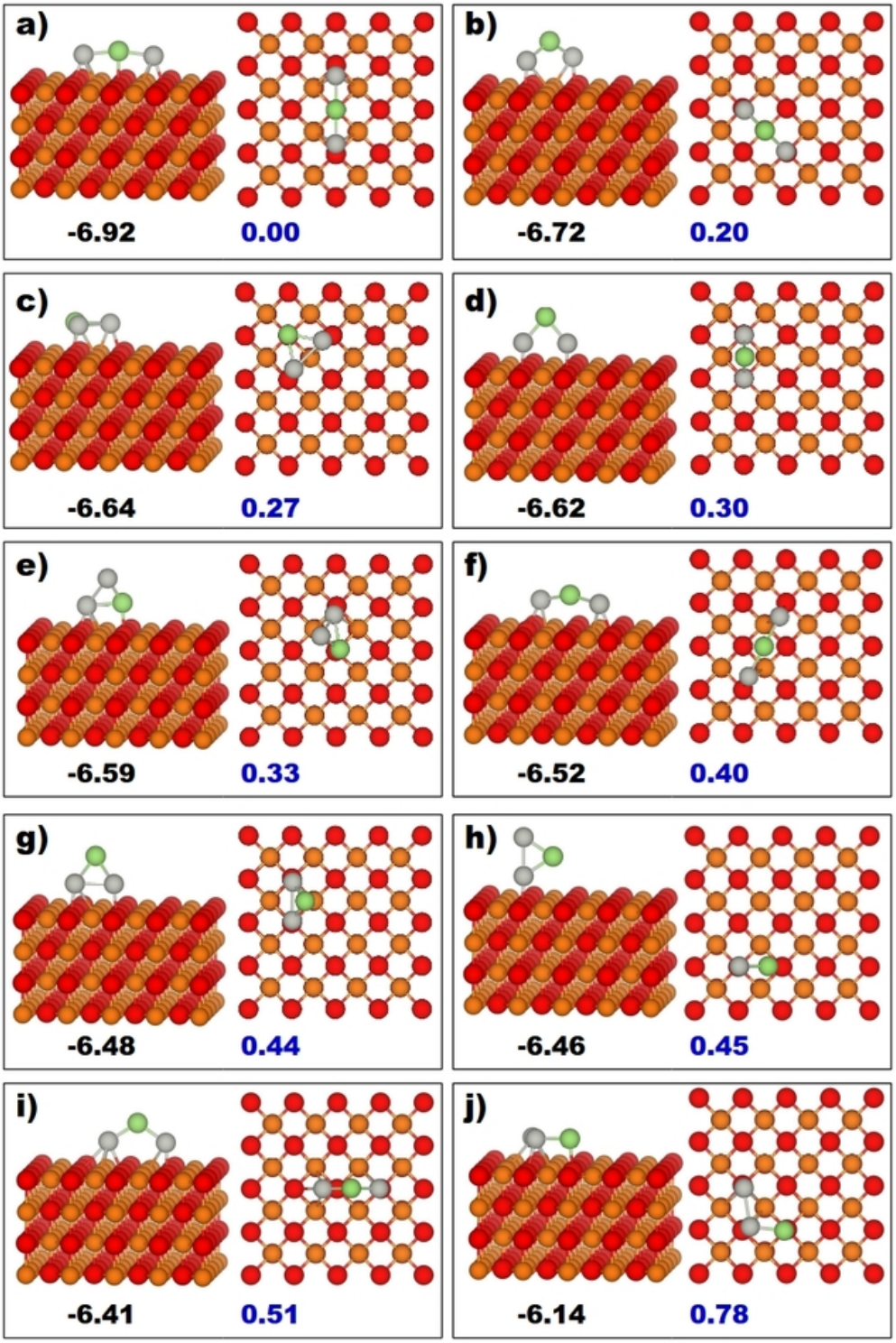

Figure C.7: a)-j) Adsorption configurations for Pd_2Ga_1 clusters on MgO(100) terrace.

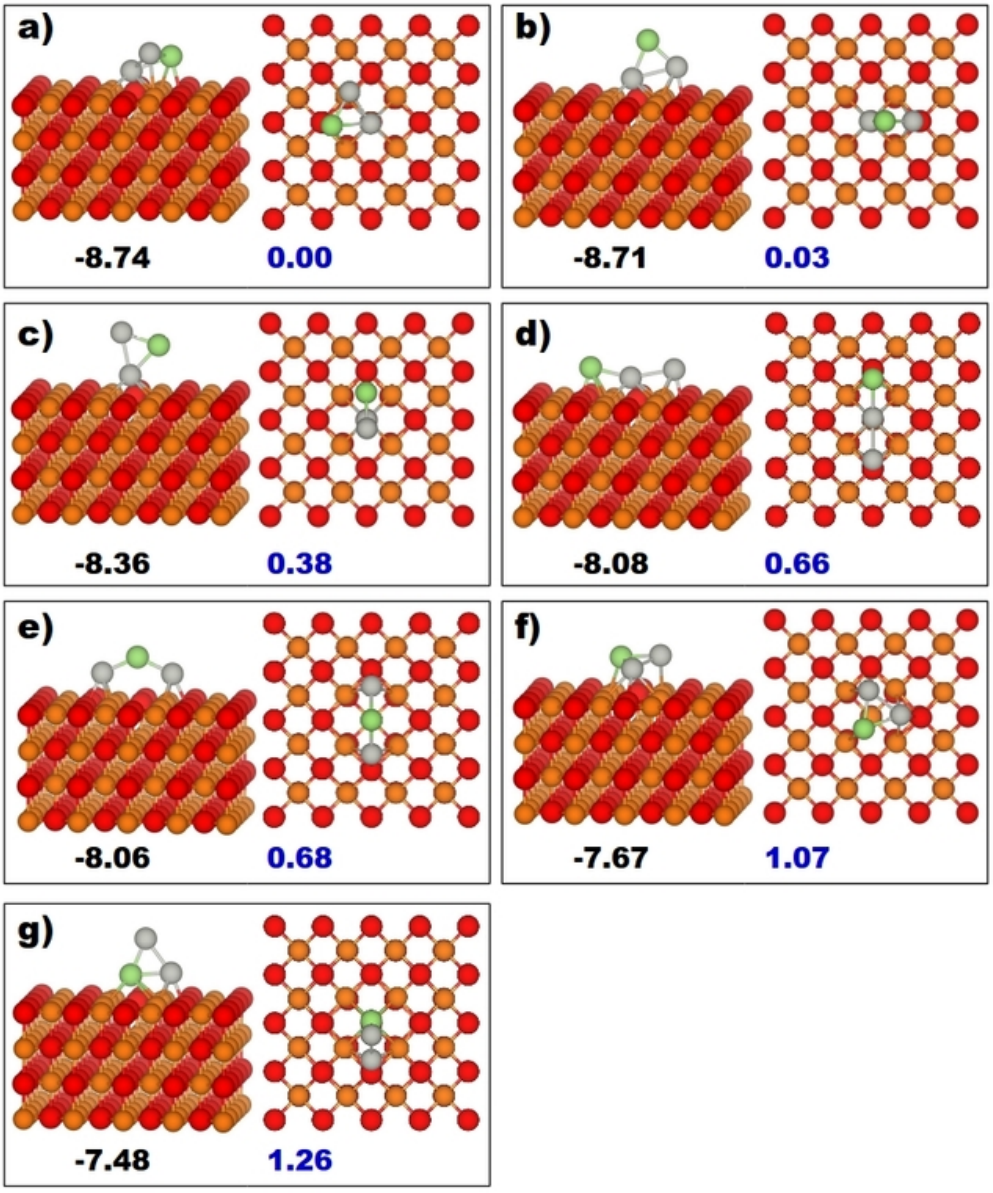

Figure C.8: a)-g) Adsorption configurations for Pd_2Ga_1 clusters at the oxygen vacancy site.

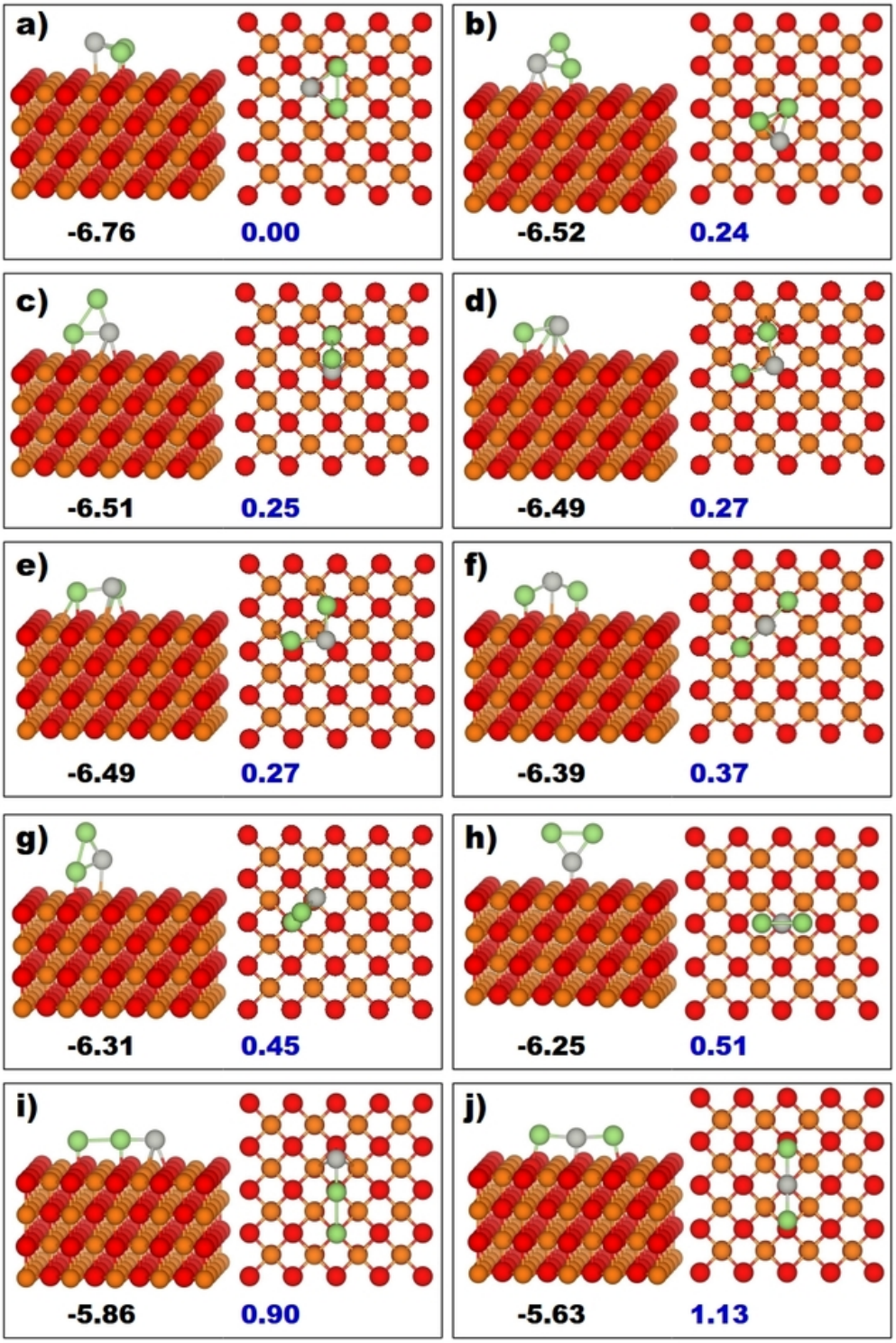

Figure C.9: a)-j) Adsorption configurations for Pd_1Ga_2 clusters on MgO(100) terrace.

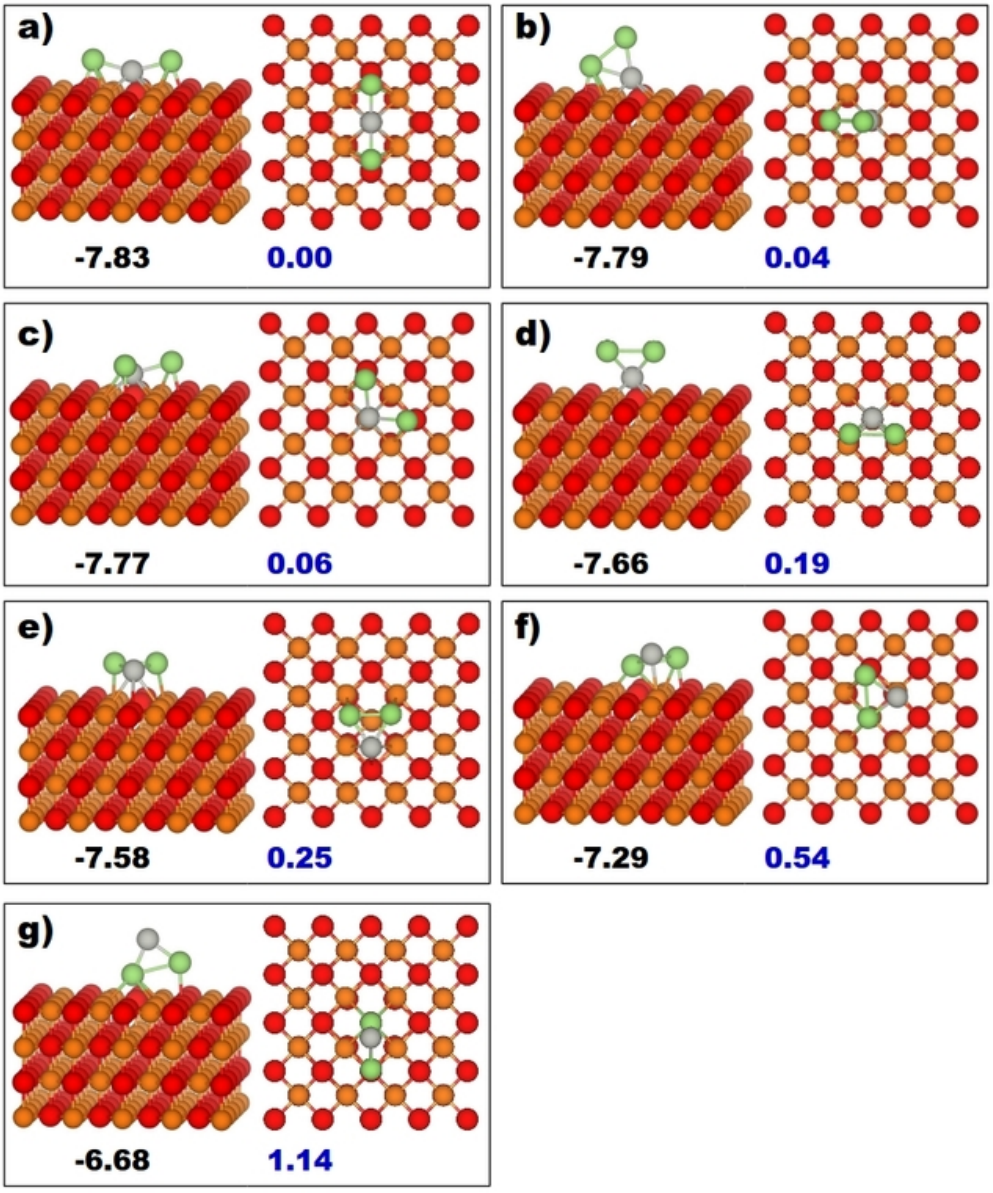

Figure C.10: a)-g) Adsorption configurations for Pd_1Ga_2 clusters at the oxygen vacancy site.

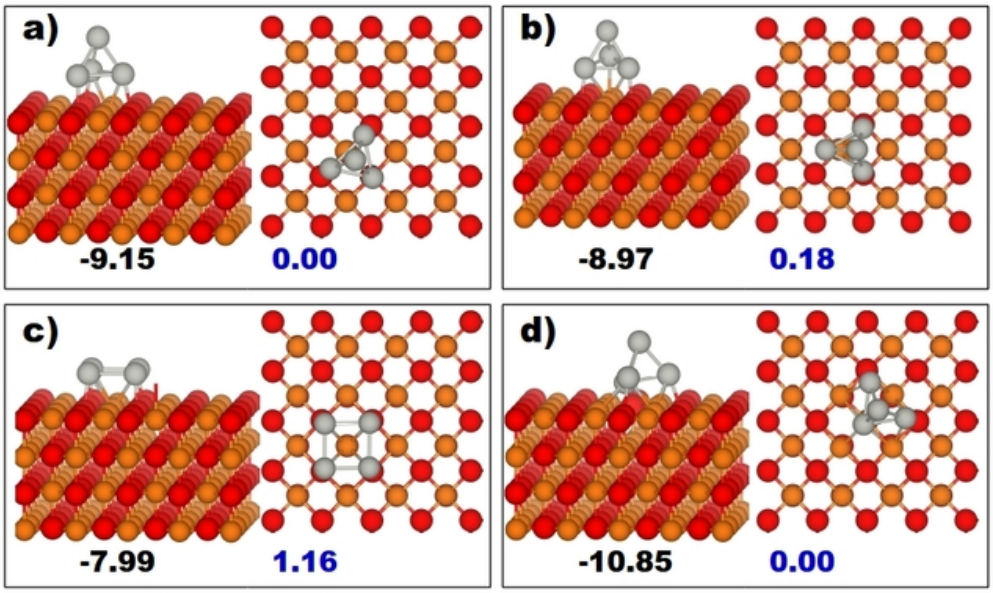

Figure C.11: a)-c) Adsorption configurations for Pd_4 clusters on MgO(100) terrace. d)Most stable adsorption configuration for Pd_4 cluster at the oxygen vacancy site.

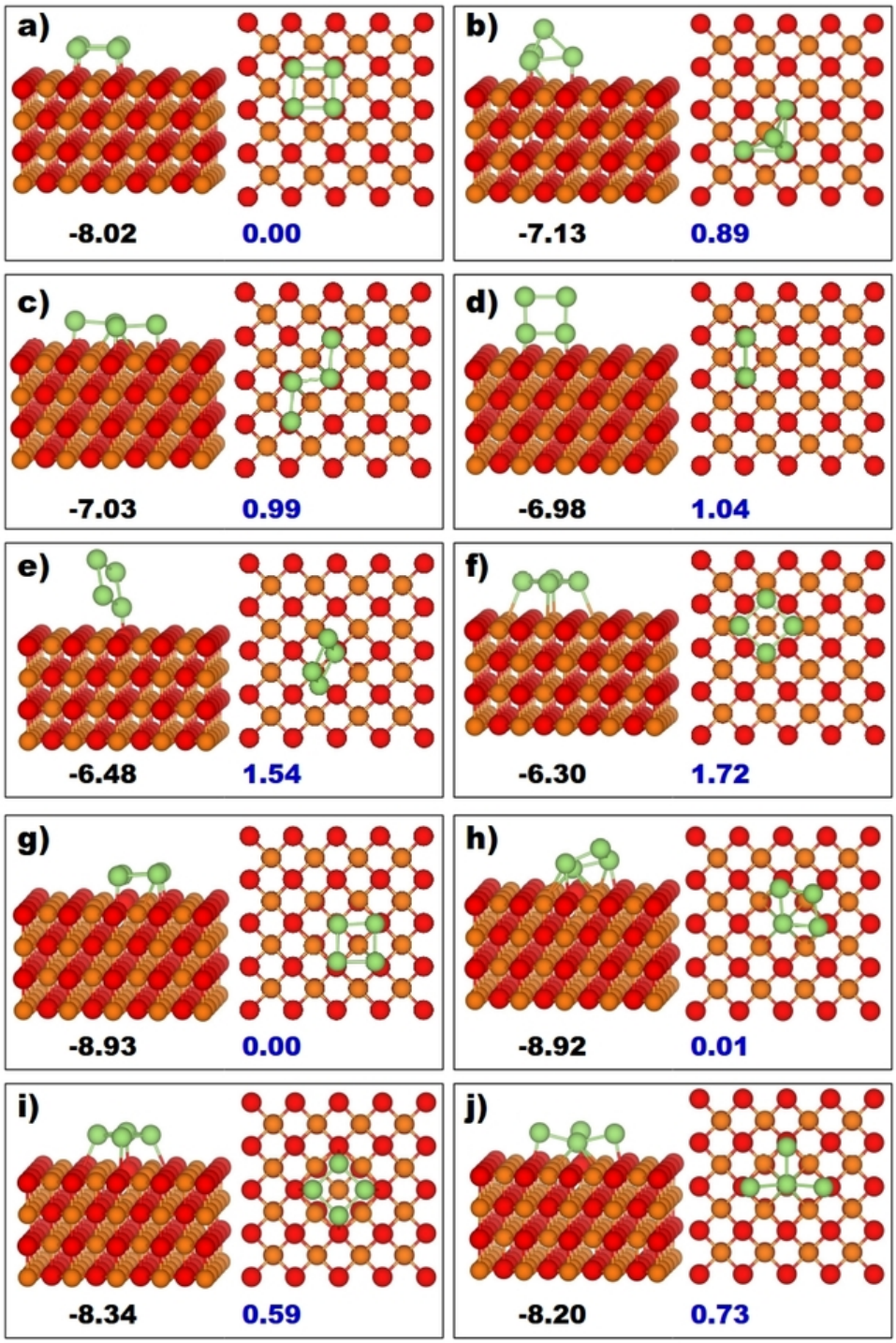

Figure C.12: a)-f) Adsorption configurations for Ga_4 clusters on MgO(100) terrace. g)-j) Adsorption configurations for Ga_4 clusters at the oxygen vacancy site.

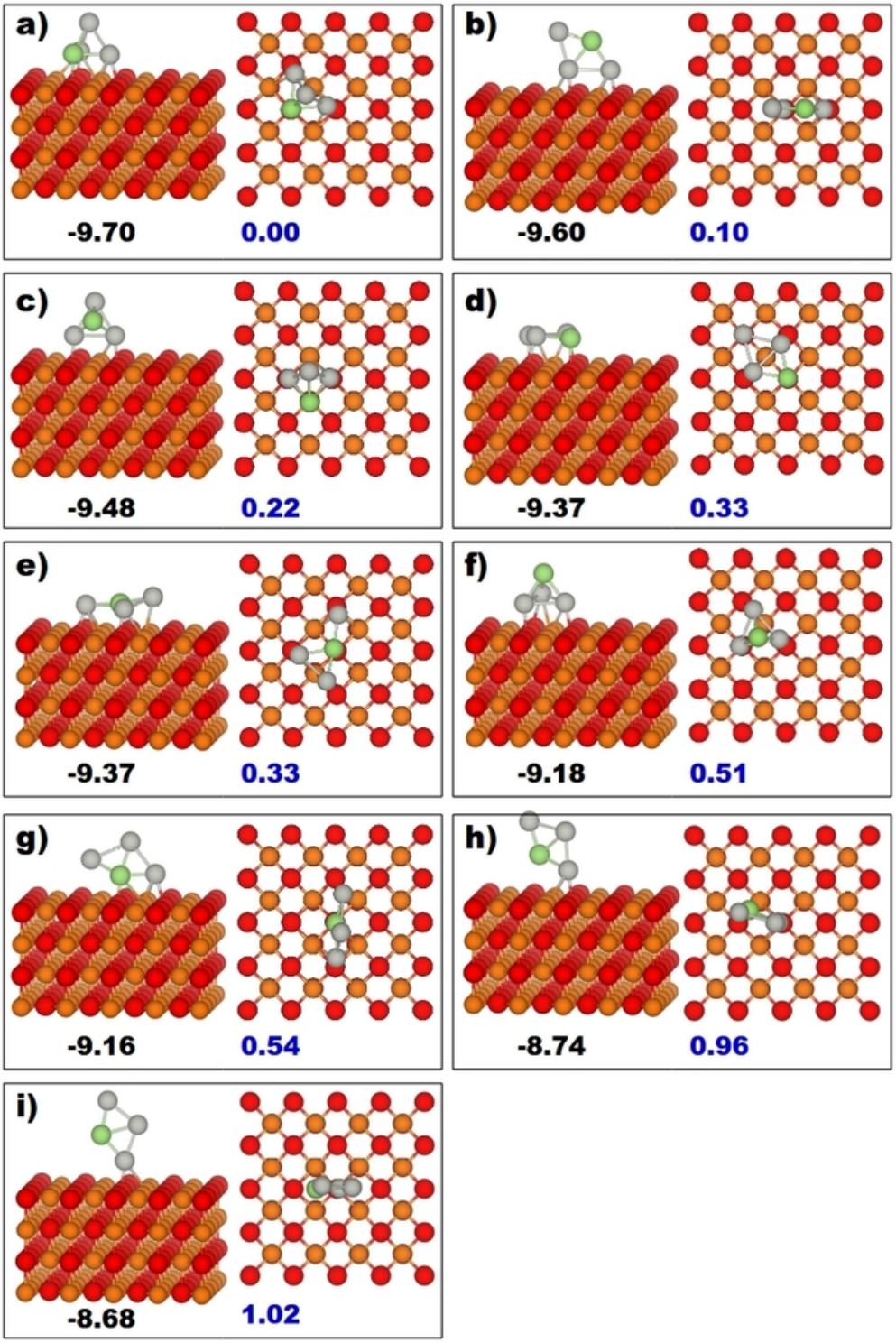

Figure C.13: a)-i) Adsorption configurations for Pd_3Ga_1 clusters on MgO(100) terrace.

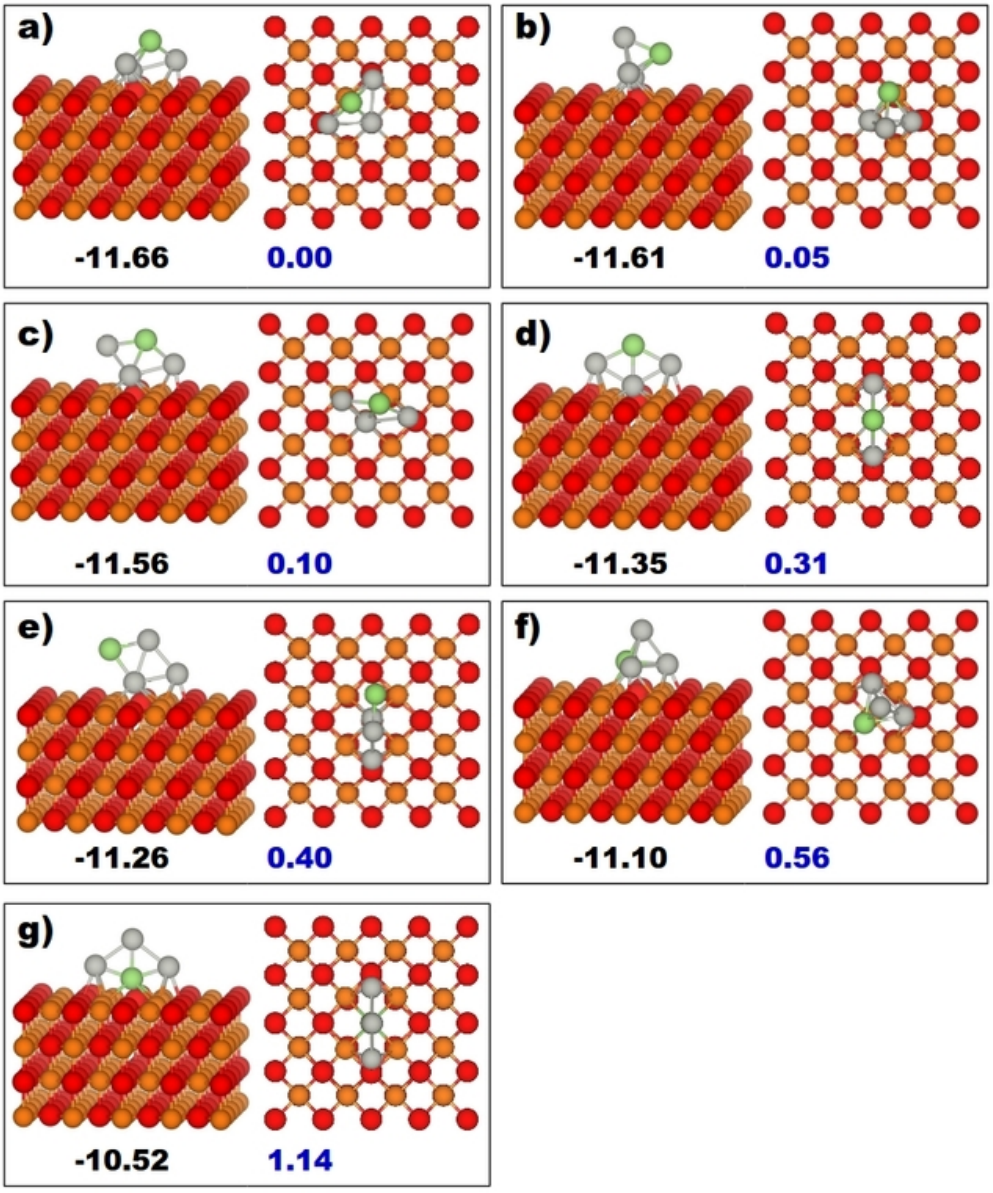

Figure C.14: a)-g) Adsorption configurations for Pd_3Ga_1 clusters at the oxygen vacancy site.

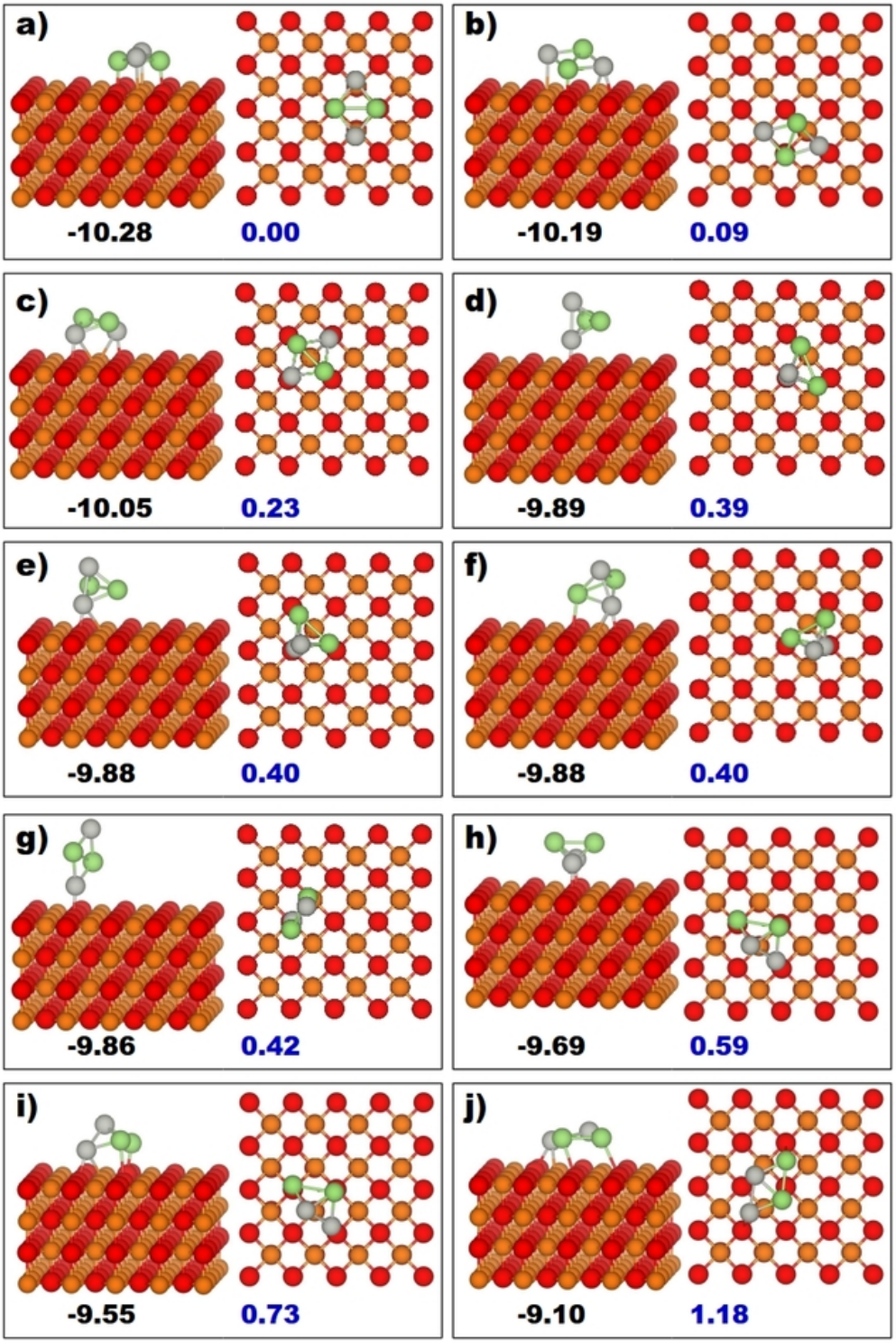

Figure C.15: a)-j) Adsorption configurations for Pd_2Ga_2 clusters on MgO(100) terrace.

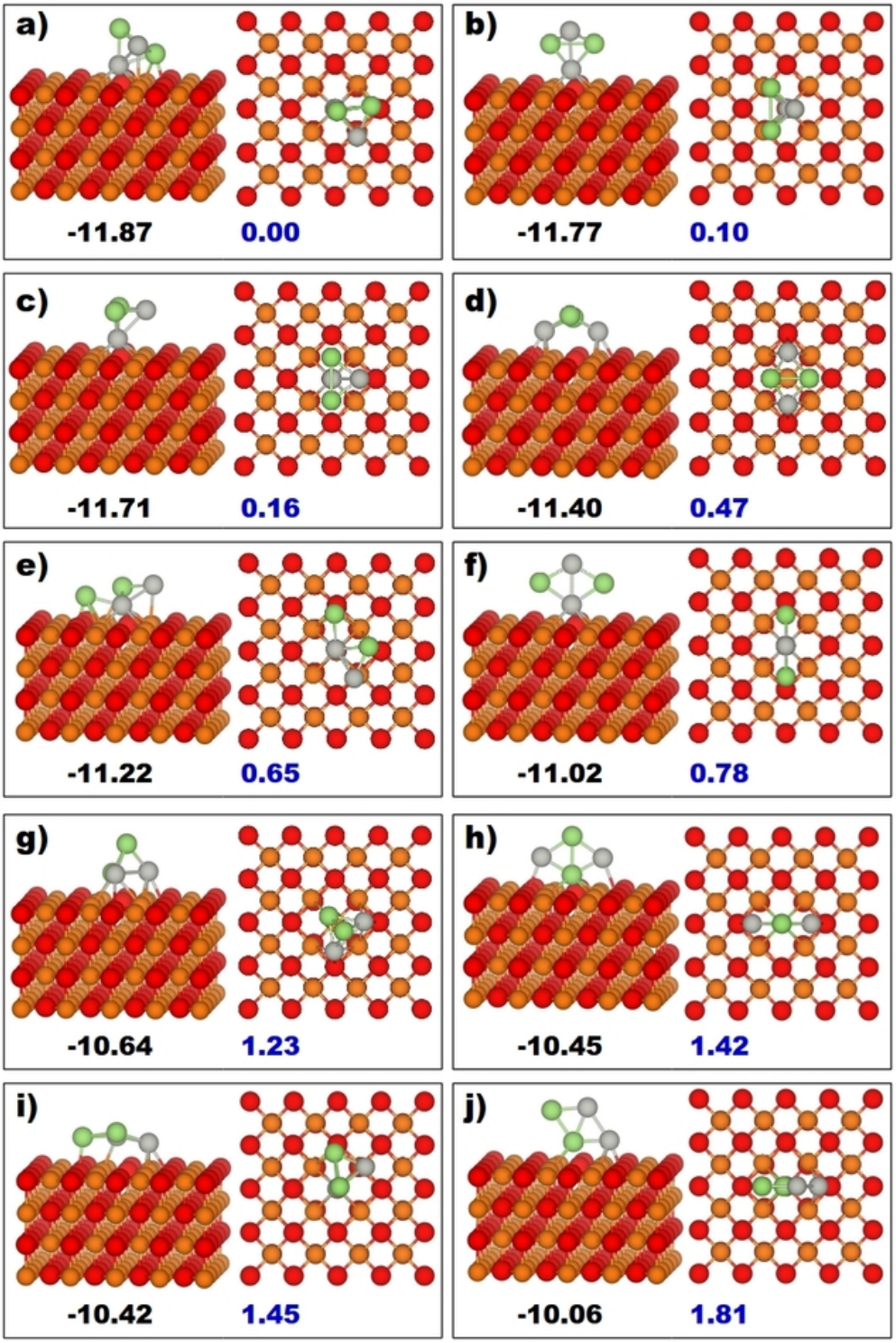

Figure C.16: a)-j) Adsorption configurations for Pd_2Ga_2 clusters at the oxygen vacancy site.

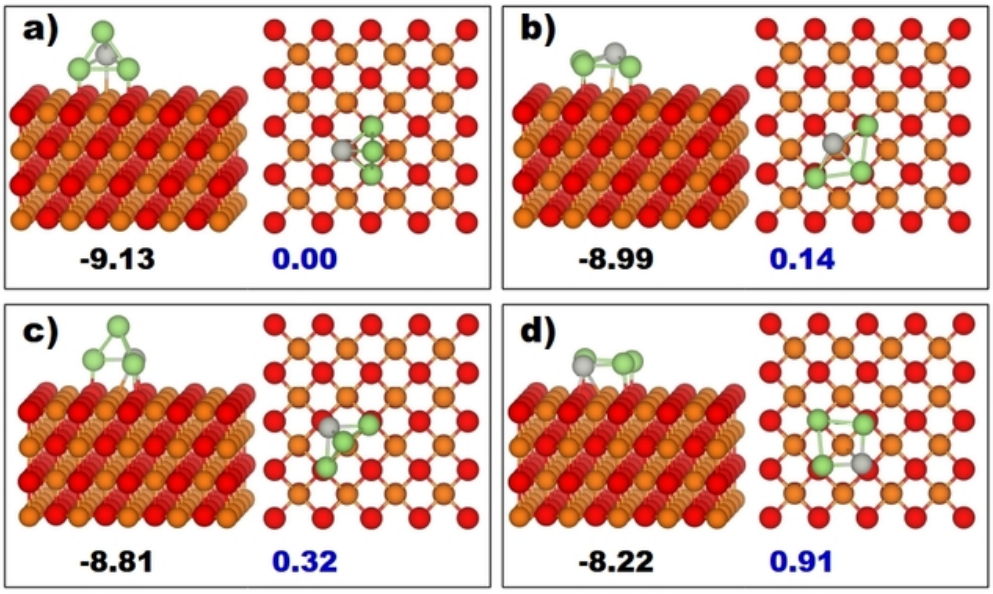

Figure C.17: a)-d) Adsorption configurations for Pd_1Ga_3 clusters on MgO(100) terrace.

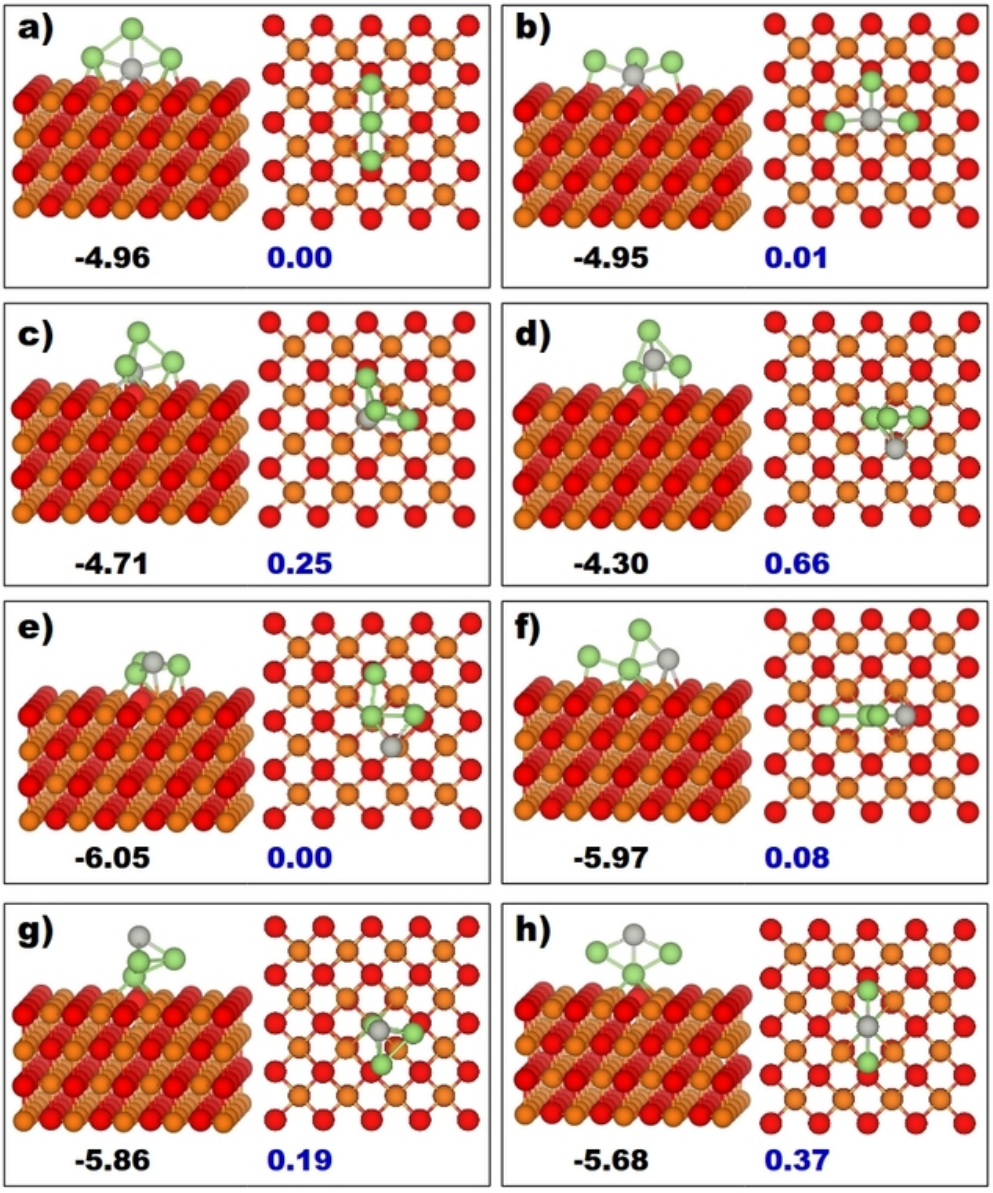

Figure C.18: a)-h) Adsorption configurations for Pd_1Ga_3 clusters at the oxygen vacancy site.

Appendix D

Diffusion of small clusters on MgO(100) surface

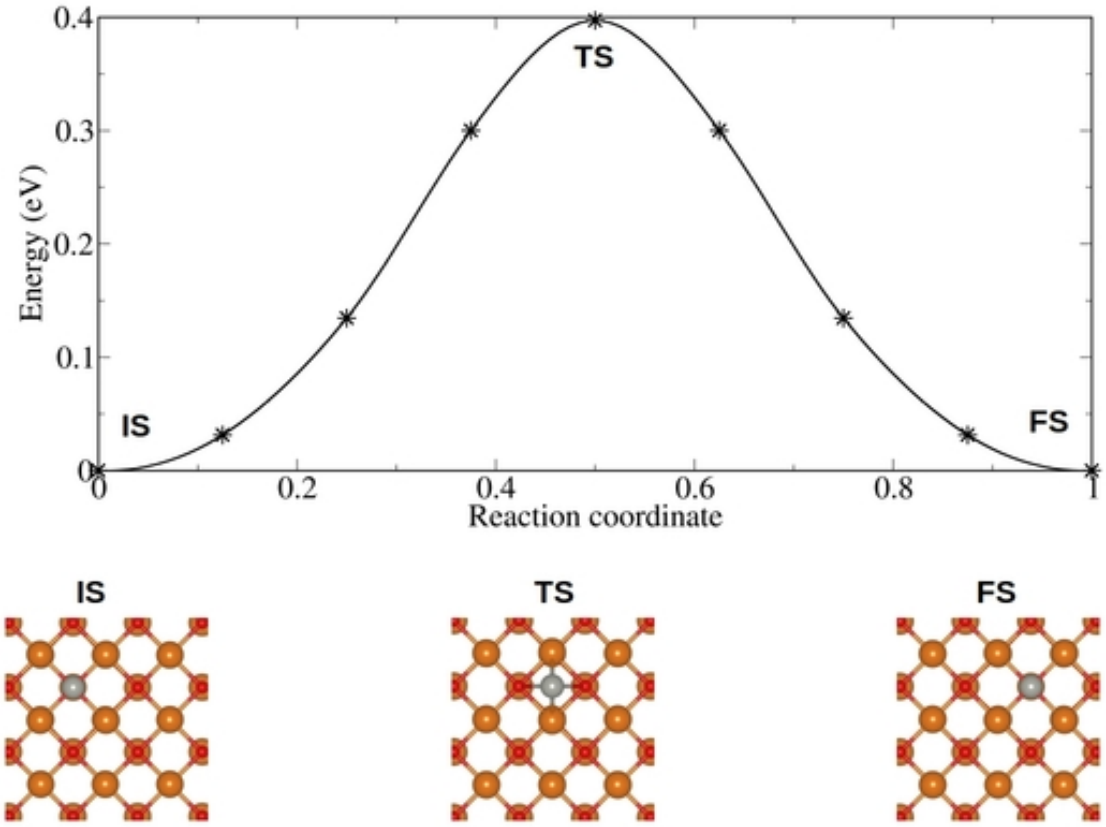

Figure D.1: Diffusion of Pd_1 on the MgO terrace: Hopping The Pd adatom adsorbed on top of oxygen site of MgO terrace diffuses to the next neighboring oxygen site by direct hopping. The diffusion barrier associated with this process is found to be 0.40 eV. At the saddle point, the Pd adatom sits above the hollow site.

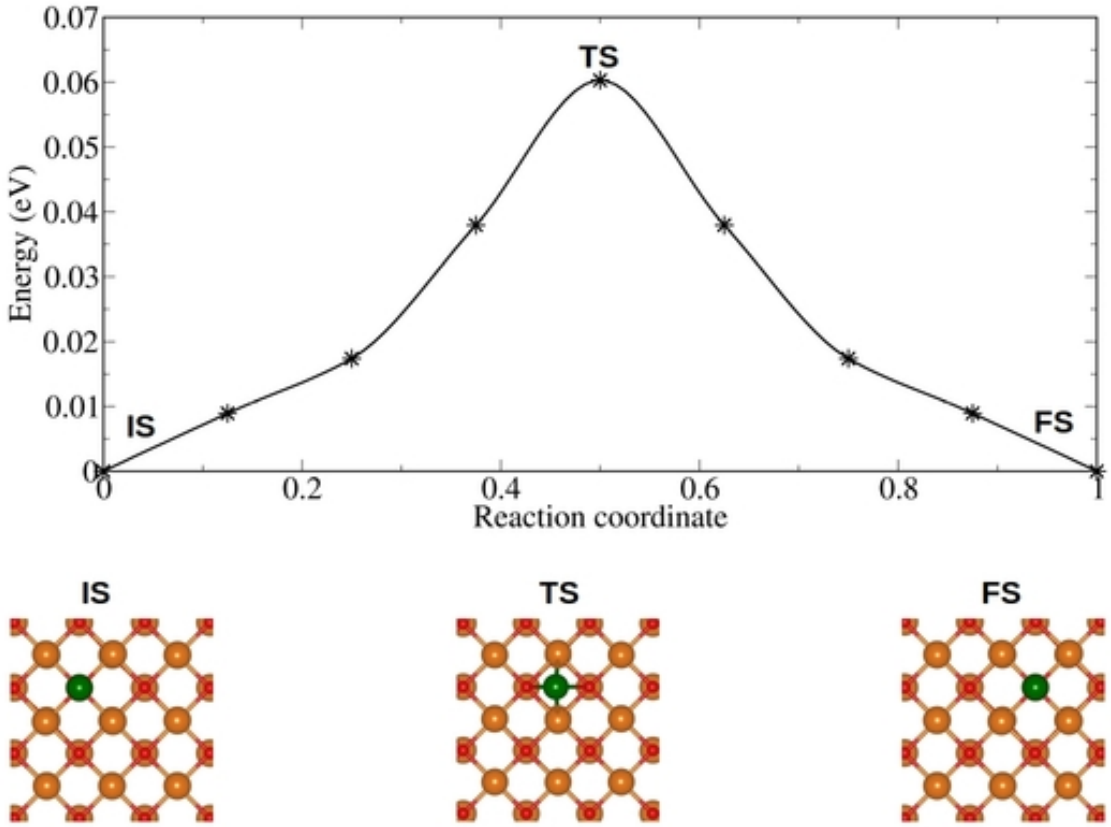

Figure D.2: Diffusion of Ga_1 on the MgO terrace: Hopping The Ga adatom requires to overcome a small barrier of 0.06 eV to between two oxygen sites on the MgO terrace. At the saddle point, the Ga sits above the hollow site.

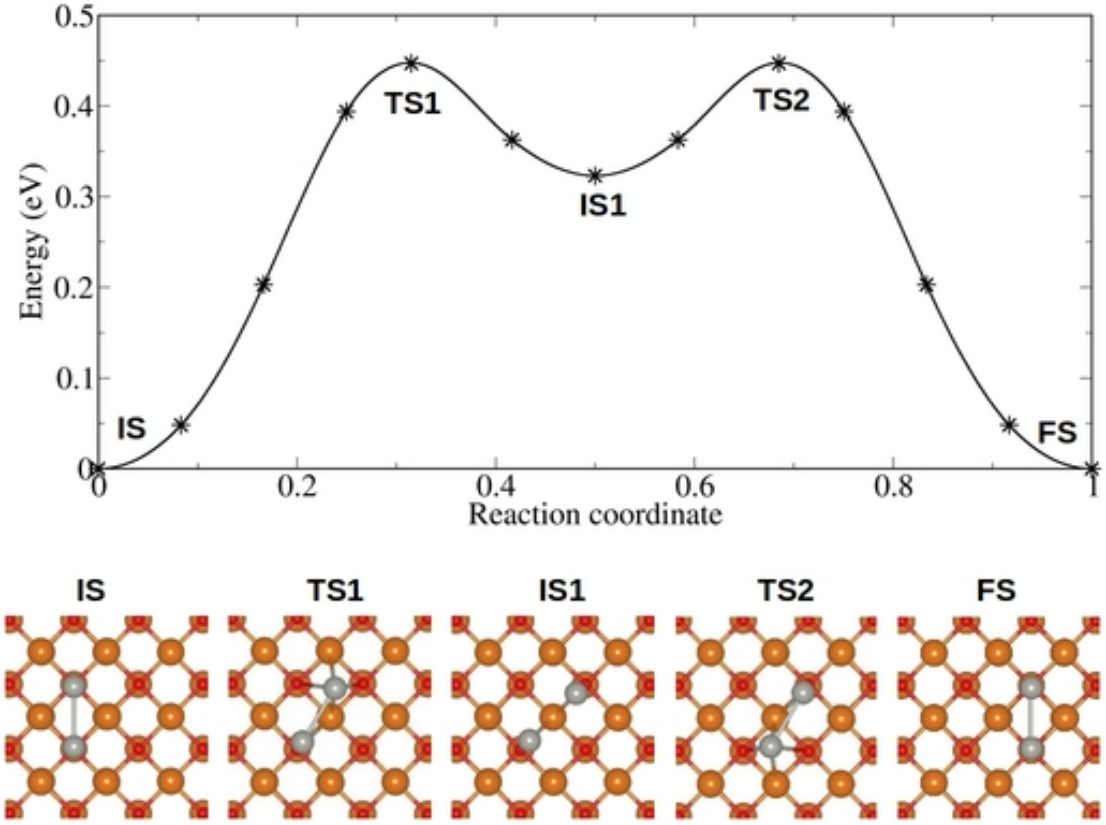

Figure D.3: Diffusion of Pd_2 on the MgO terrace: Partial dissociates The Pd_2 cluster diffuses on MgO terrace through partial dissociation and association mechanism and this involves two steps. In the first step the Pd dimer sitting on top of two neighboring oxygen sites (IS) partially dissociates to form an intermediate state (IS1) where the Pd-Pd bond distance is increased from 2.81 Å at the initial state to 3.10 Å at the intermediate state. The barrier associated with the partial dissociation of Pd dimer is calculated to be 0.44 eV. The second step is reverse of the first one; in this step the partially dissociated Pd dimer reassociates to form the stable Pd dimer (FS). The barrier associated with the reassociation of the dimer is found to be 0.12 eV.

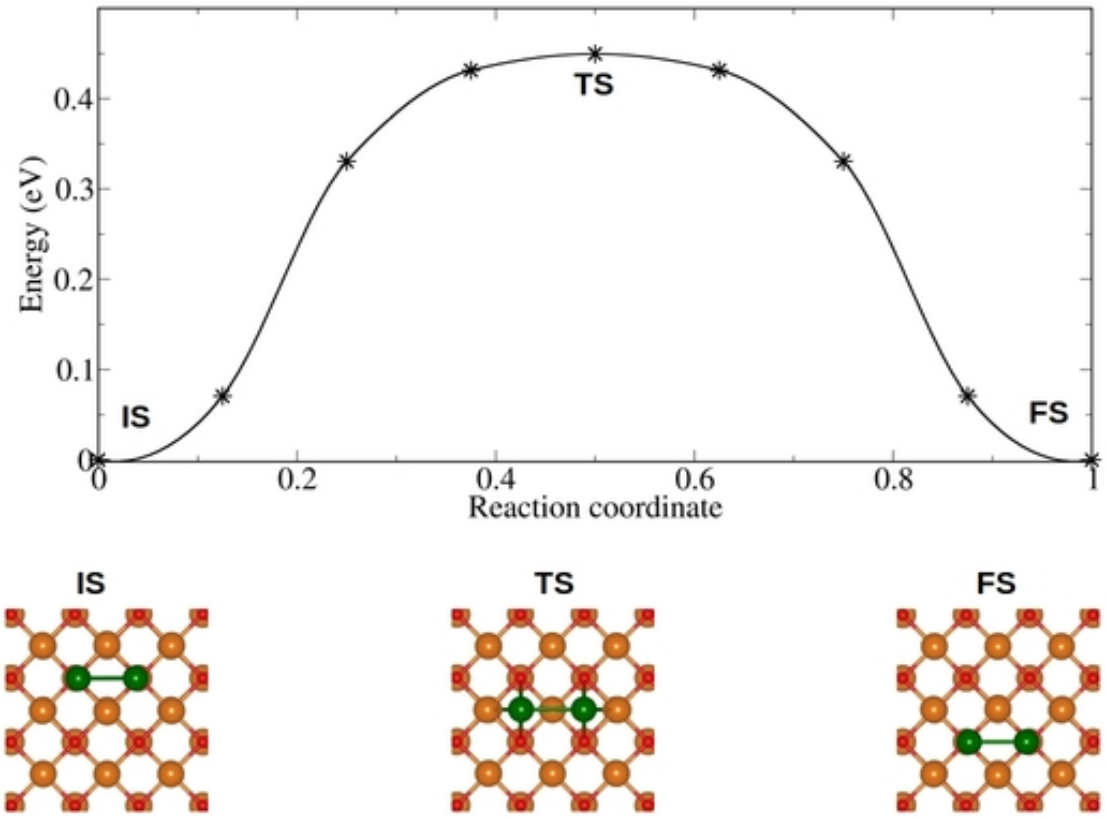

Figure D.4: Diffusion of Ga_2 on the MgO terrace: Sliding (Path 1) The Ga dimer sitting on top of two neighboring surface oxygen sites on MgO terrace diffuses to the next site through a sliding mechanism. For the dimer to slide on the surface, it needs overcome a barrier of 0.45 eV. At the saddle point both the Ga atoms are sitting above the hollow site with the Ga-Ga bond stretched to 2.96 Å from 2.72 Å at the initial state.

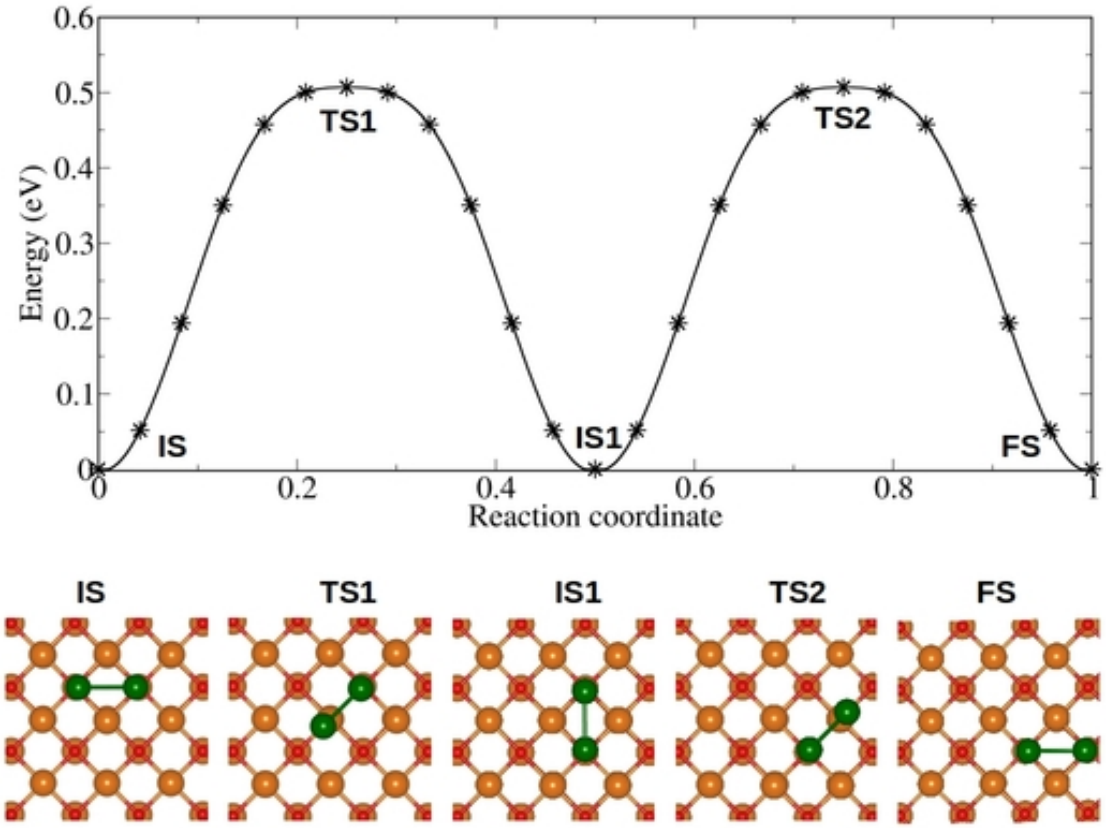

Figure D.5: Diffusion of Ga_2 on the MgO terrace: Walking (Path 2) This involves two steps. The Ga_2 walks on the surface by combined anti-clockwise and clockwise rotation by 90°. In the first step the cluster rotates anti-clockwise about 90° and it requires to overcome a barrier of 0.51 eV. The second step is similar to the first one, however in this step the cluster rotates clockwise.

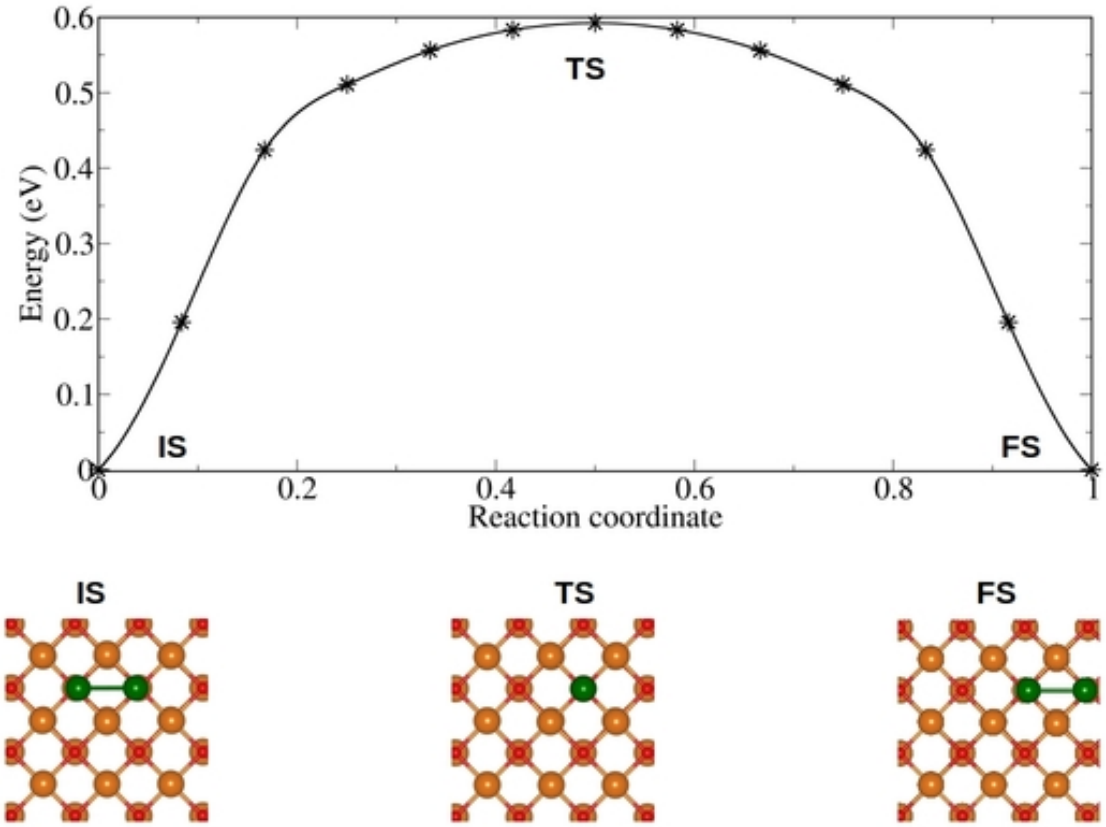

Figure D.6: Diffusion of Ga_2 on the MgO terrace: Cartwheeling (Path 3) The Ga_2 requires to overcome a barrier of 0.59 eV to diffuse by this mechanism. At the saddle point, the Ga_2 cluster stands upright on top of one oxygen site.

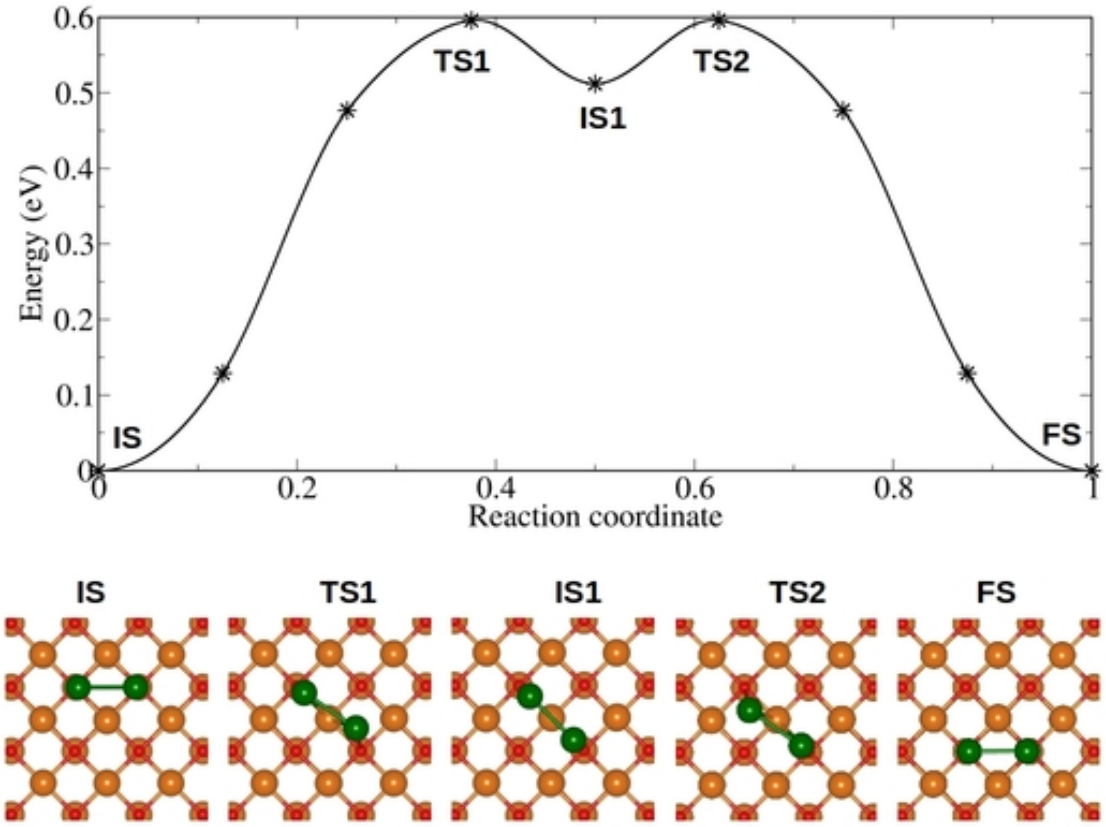

Figure D.7: Diffusion of Ga_2 on the MgO terrace: Walking (Path 4) This involves two steps. In the first step, the Ga_2 binding to the surface rotates clockwise about 45° to form a intermediate state (IS1), and this requires to overcome a barrier of 0.60 eV. Energetically the second step is mirror image of the first step. In the second step, the Ga_2 rotates anti-clockwise about 45° to form the final state (FS).

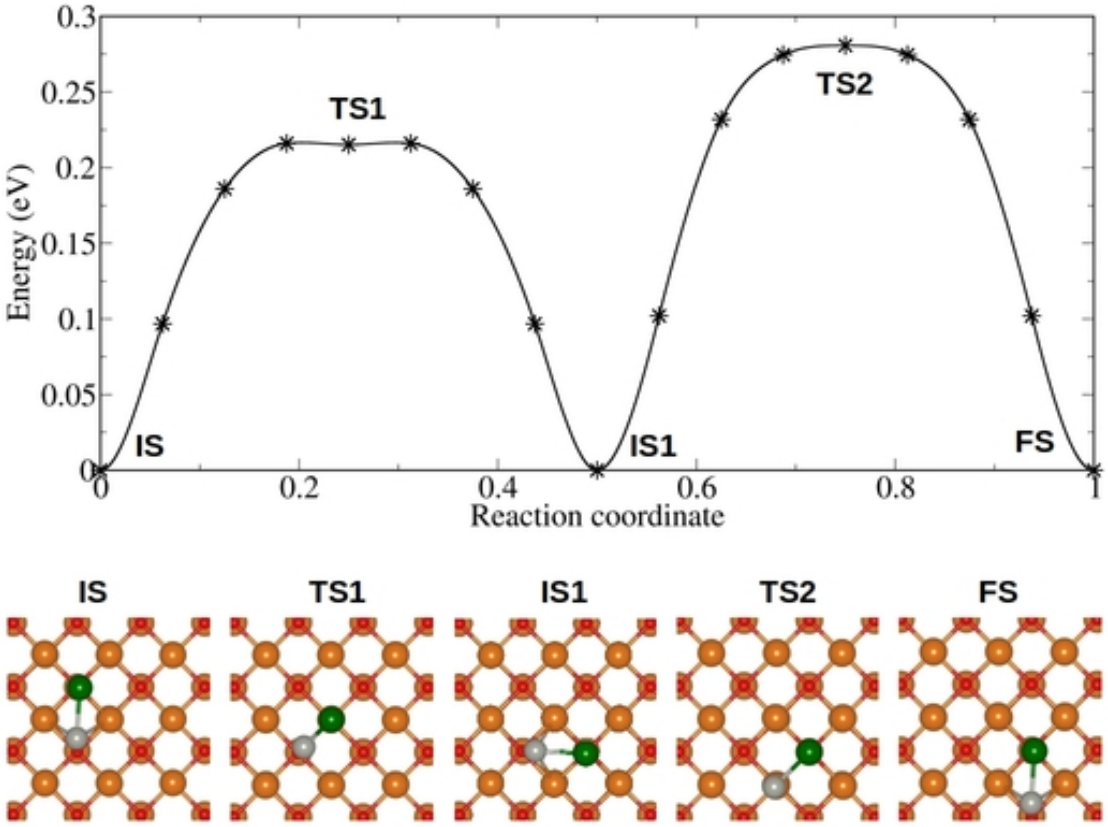

Figure D.8: Diffusion of Pd_1Ga_1 on the MgO terrace: Walking (Path 1) The Pd_1Ga_1 cluster sitting on top of two oxygen sites on MgO terrace diffuses to the next site by walking mechanism. This walking mechanism involves two steps. The first step involves a 90° rotation of Pd_1Ga_1 about the Pd atom. The barrier associated with this rotation is about 0.22 eV. At the saddle point, the Pd sits on top of oxygen site while the Ga sits on top of surface Mg site. However, only the Pd atom is interacting to the surface with a O-Pd distance of 2.21 Å while the Mg-Ga distance is found to be 3.66 Å. This strengthens the Pd-Ga interaction. In contrast to the pure dimers, for which the metal-metal bond distance increases at the saddle point compared with initial state, for bimetallic Pd_1Ga_1 we found a shortening of Pd-Ga bond at the saddle point (from 2.39 Å at the initial state to 2.32 Å at the saddle point). The second step is also a 90° rotation; however, in this step the cluster rotates in the reverse direction about the Ga atom of the cluster. This 90° rotation involves a diffusion barrier of 0.28 eV. At this second saddle point the Ga sits on top of the oxygen atom while the Pd sits on top of surface Mg. The Pd-Ga bond distance decreases to 2.35 Å at the saddle point from 2.39 Å at the initial state.

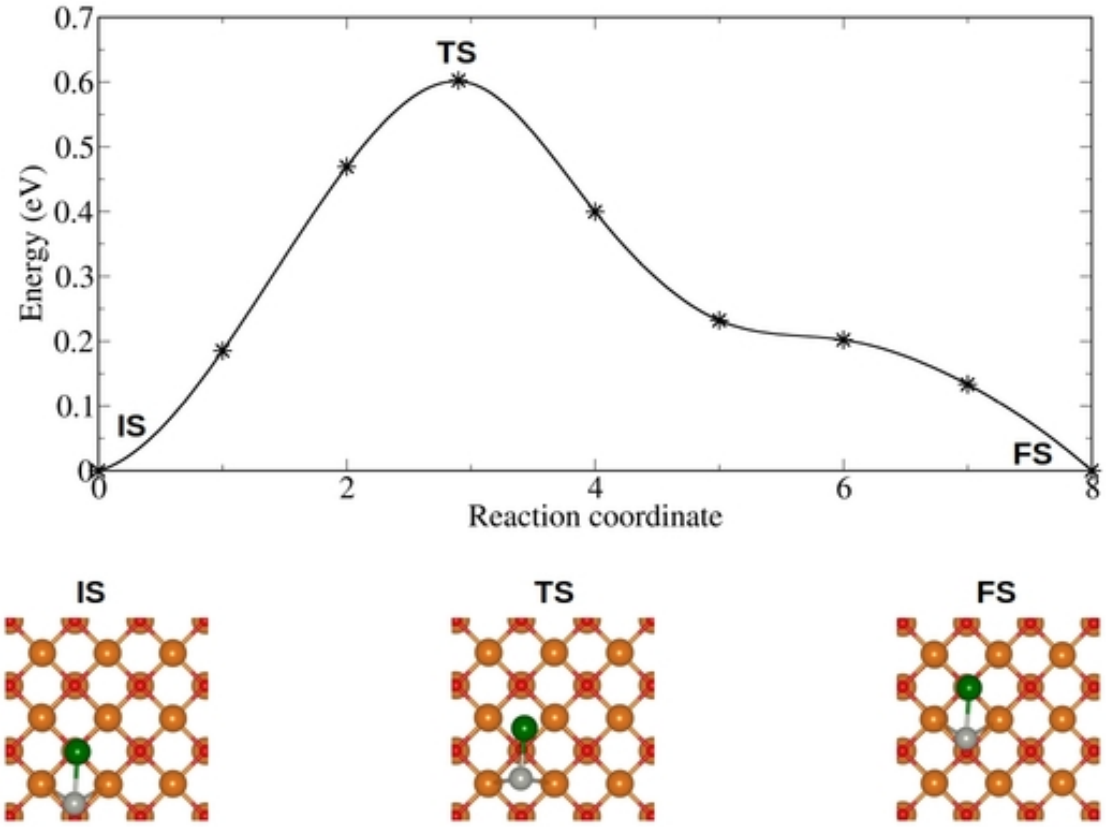

Figure D.9: Diffusion of Pd_1Ga_1 on the MgO terrace: Sliding (Path 2) In this mechanism, the Pd_1Ga_1 cluster sitting on top of two oxygen sites on MgO terrace slides to the next site. The barrier associated with this sliding is about 0.60 eV. At the saddle point both Pd and Ga atoms are sitting on top of two neighboring hollow sites with a Pd-Ga bond length of 2.32 Å.

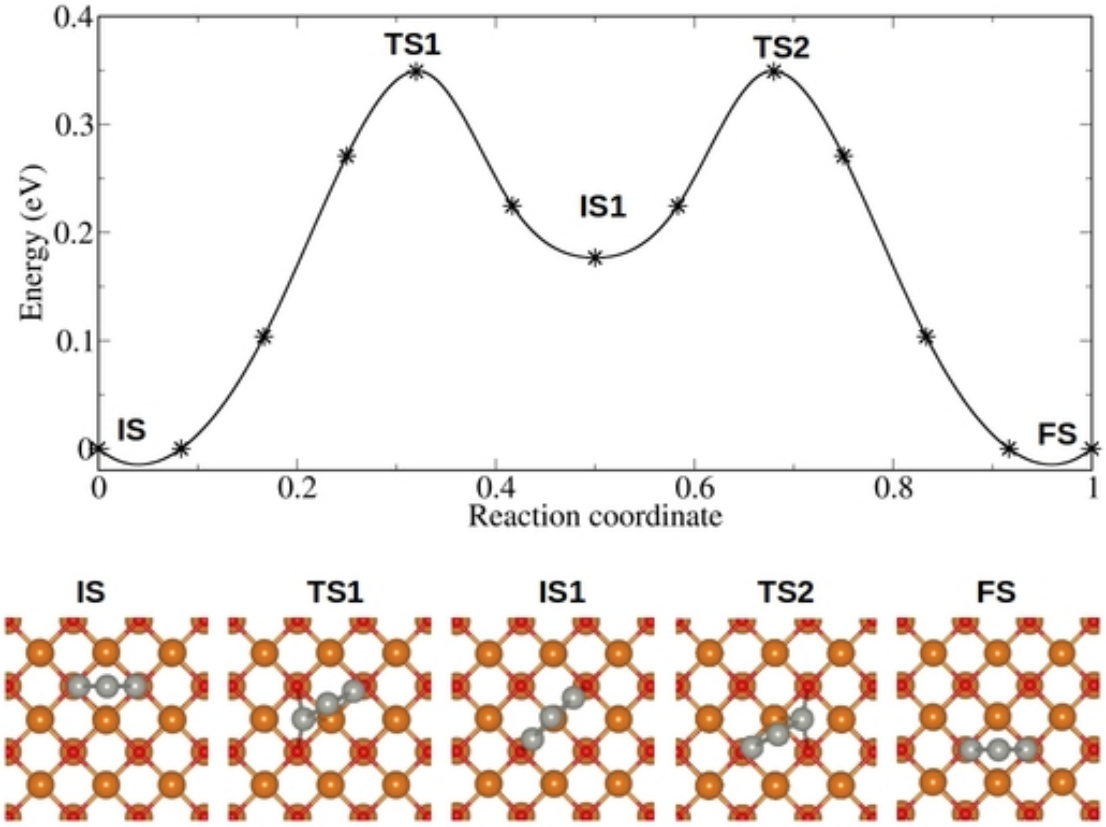

Figure D.10: Diffusion of Pd_3 on the MgO terrace: Walking The Pd_3 cluster diffuses on MgO(100) surface through a two step skating (walking) mechanism. Initially the Pd_3 is bound vertically to the terrace where two of the Pd atoms are on top of two surface oxygen atoms. In the first diffusion step the cluster diffuses to an intermediate state (about 0.18 eV higher in energy than the most stable initial state) in which the Pd atoms that are interacting with the surface is bound to two O atoms, the later having a Mg atom between them. In order to reach this intermediate the cluster rotates by about 45° about one of the Pd atoms anchored to the surface oxygen site. At the saddle point, the Pd atom that moves occupy the hollow site. This diffusion process has a barrier of 0.34 eV associated with it. In the second step the cluster diffuses from the intermediate to the final state through a further rotation of 45°. However, the direction of rotation is reverse to that of the first step and the Pd atom that was mobile in the previous step is now fixed while the fixed Pd atom in the previous step is now mobile. The diffusion barrier associated with this process is calculated to be 0.17 eV.

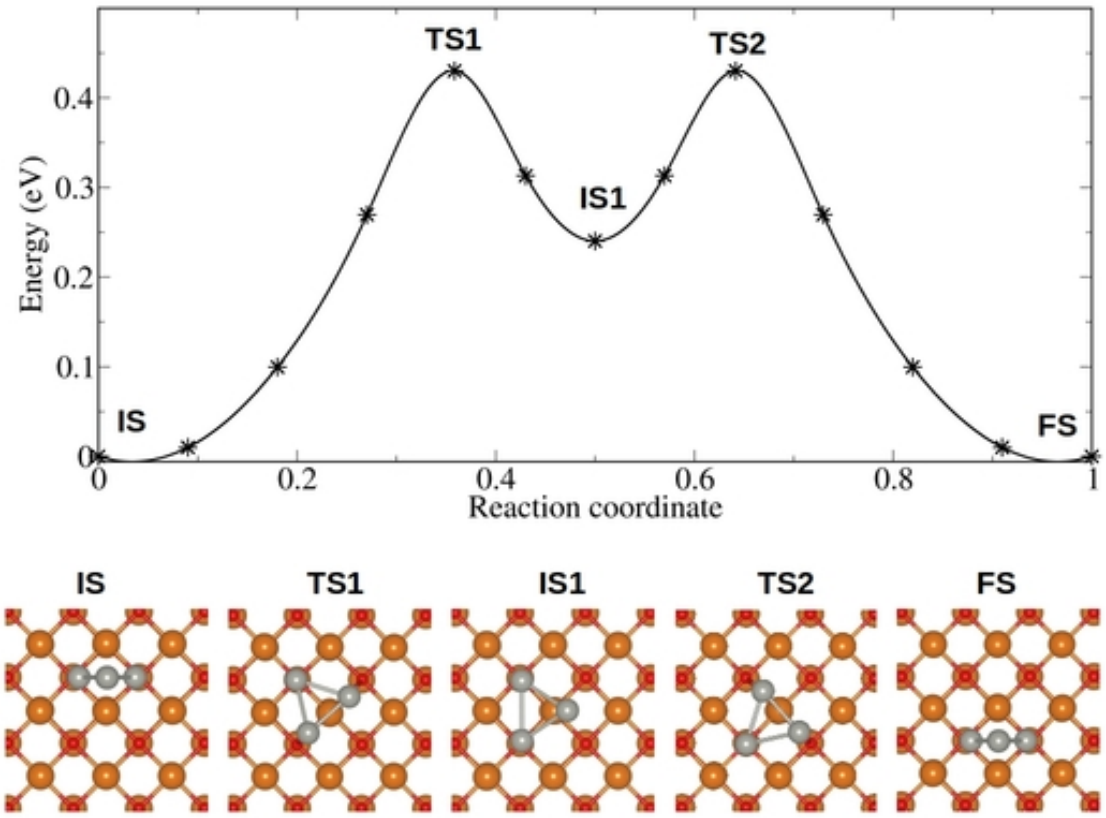

Figure D.11: Diffusion of Pd_3 on the MgO terrace: Flipping Initially the Pd_3 is bound vertically to the terrace where two of the Pd atoms are on top of two surface oxygen atoms. In the first diffusion step the cluster flips to an intermediate state (about 0.24 eV higher in energy than the most stable initial state) in which the cluster binds to the surface in a horizontal geometry. This diffusion process has a barrier of 0.43 eV associated with it. In the second step the cluster flips from the horizontal geometry to the vertical geometry (final state). The diffusion barrier associated with this process is calculated to be 0.19 eV.

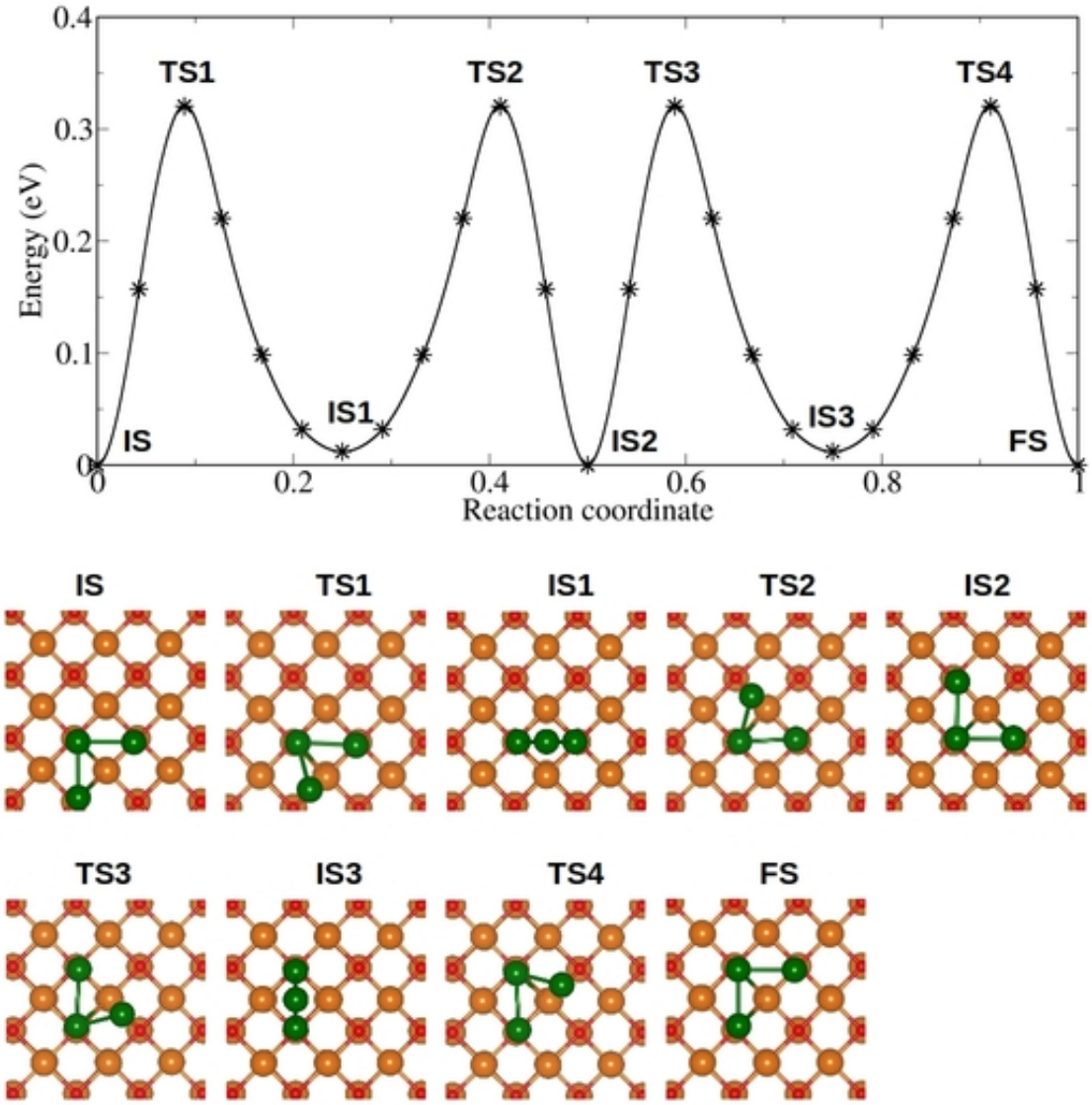

Figure D.12: Diffusion of Ga_3 on the MgO terrace: Rolling (Path 1) In the initial state all three Ga atoms are on top of three surface oxygen atoms making a 'L' shape. In the first step, the cluster moves to an intermediate (about 0.01 eV higher in energy than the initial state) where it is vertically on top of two surface O atoms and forms an isosceles triangle (IS1). This involves a barrier of about 0.32 eV. In the next step, the Ga atom (that is not interacting with the surface) of this vertical cluster falls on the O atom at the other side. The barrier of "toppling" of this cluster is about 0.31 eV. The next two steps are similar to the first two. However, in this case the orientation of the vertical cluster is rotated by 90 ° with respect to that observed in the first intermediate.

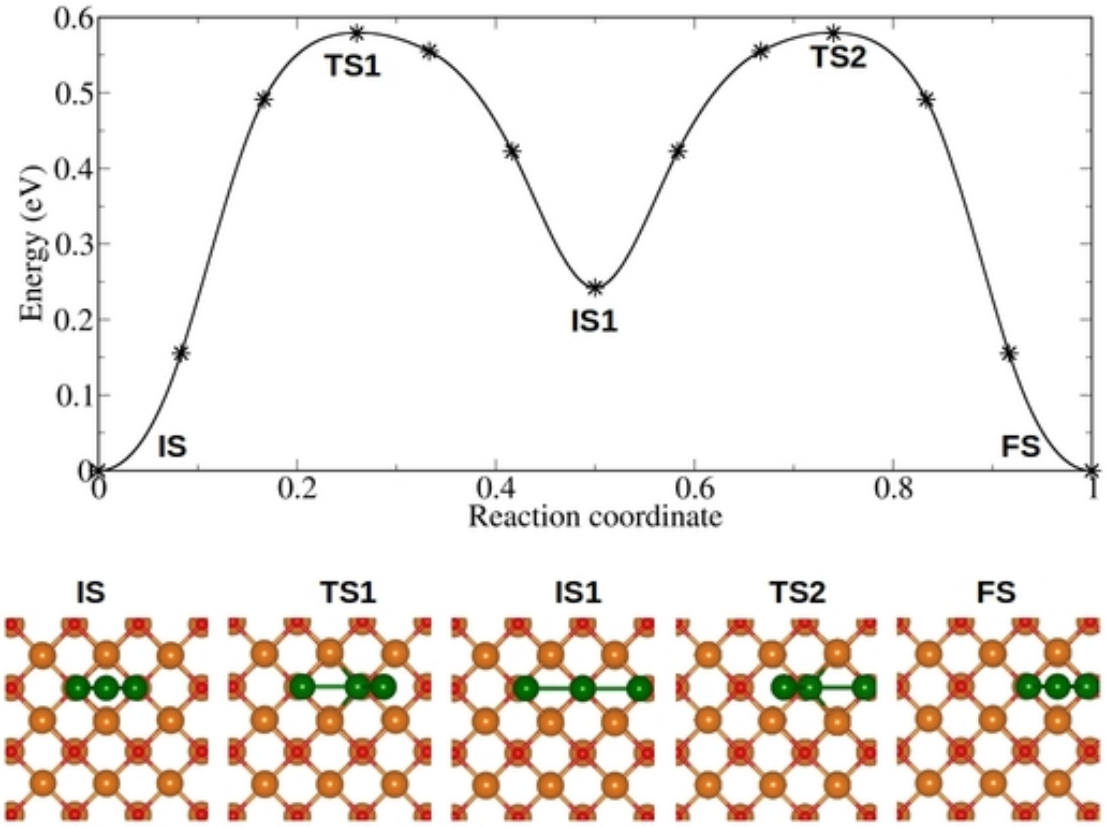

Figure D.13: Diffusion of Ga_3 on the MgO terrace: (Path 2) This mechanism involves two steps. The initial state for this mechanism (IS) is about 0.01 eV less stable than the most stable adsorption geometry. The Ga_3 cluster has a isosceles triangle structure and binding to the surface with two atom interacting to the surface and the third one is standing upright. In the first step, the Ga atom standing upright falls on the oxygen site and forms a intermediate state where all three Ga atoms are binding to surface oxygen in a linear structure (IS1). This step has a diffusion barrier of 0.58 eV. The second step is opposite of the first step, the terminal Ga atom binding to the surface oxygen standing upright to form a isosceles triangle. This has a barrier of 0.34 eV associated with it.

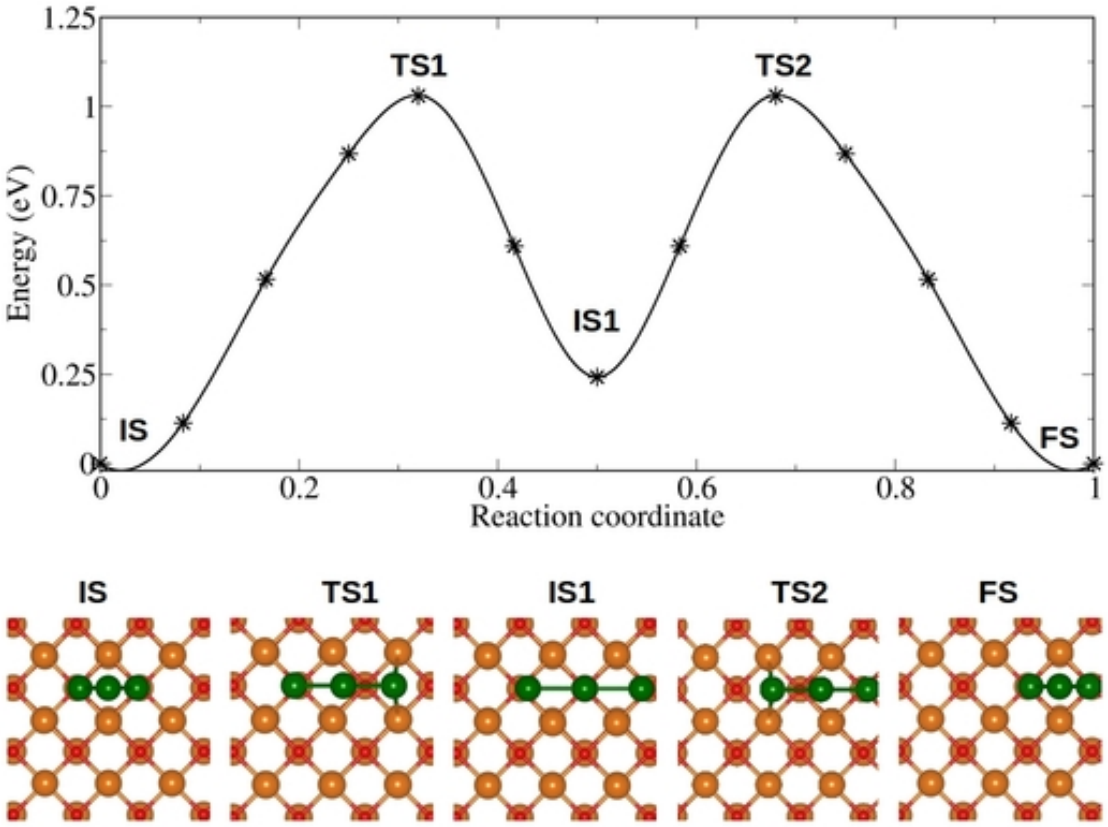

Figure D.14: Diffusion of Ga_3 on the MgO terrace: (Path 3) This mechanism involves two steps. The initial state for this mechanism is same as the initial state of Path 2. In the first step the isosceles triangle structure of Ga_3 (IS) becomes a linear one (IS1). Among the Ga atoms interacting to the surface, one of the Ga is intact and the Ga-Ga bond breaks as the other Ga atom moves to the next oxygen site while the third Ga standing upright comes close to the surface and bind to the surface oxygen. This process has a barrier of 1.02 eV. The second step is reverse of the first one, the linear structure becomes the isosceles triangular structure and has a barrier of 0.78 eV.

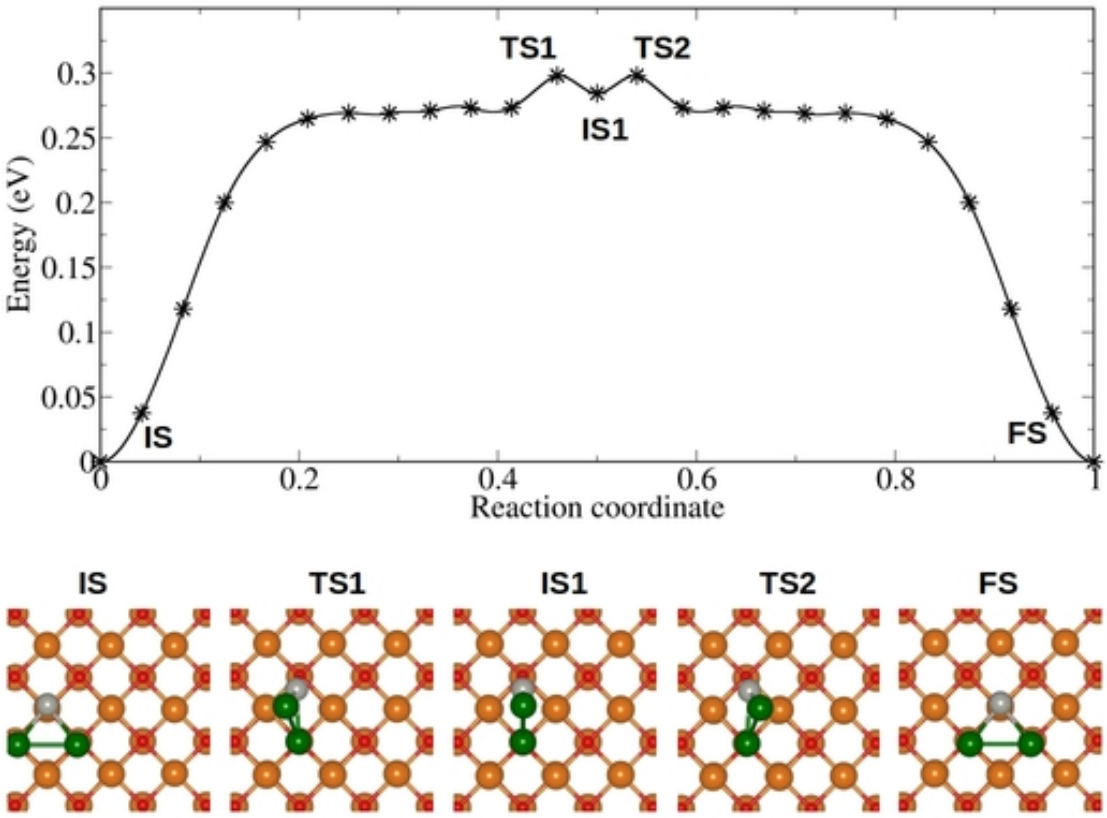

Figure D.15: Diffusion of Pd_1Ga_2 on the MgO terrace: Rolling (Path 1) The Pd_1Ga_2 clusters diffuses on the MgO terrace by rolling mechanism. This involves two steps. In the first step, the Pd_1Ga_2 cluster binding to the surface in horizontal configuration in the initial state (IS) rolls to an intermediate state where the cluster is binding in a vertical geometry (IS1). This intermediate state is bout 0.28 eV higher in energy than the initial state. The barrier associated with this step is about 0.30 eV. In the next step the cluster rolls from the intermediate state to the final state and for this process the cluster requires to overcome a very small barrier of 0.02 eV.

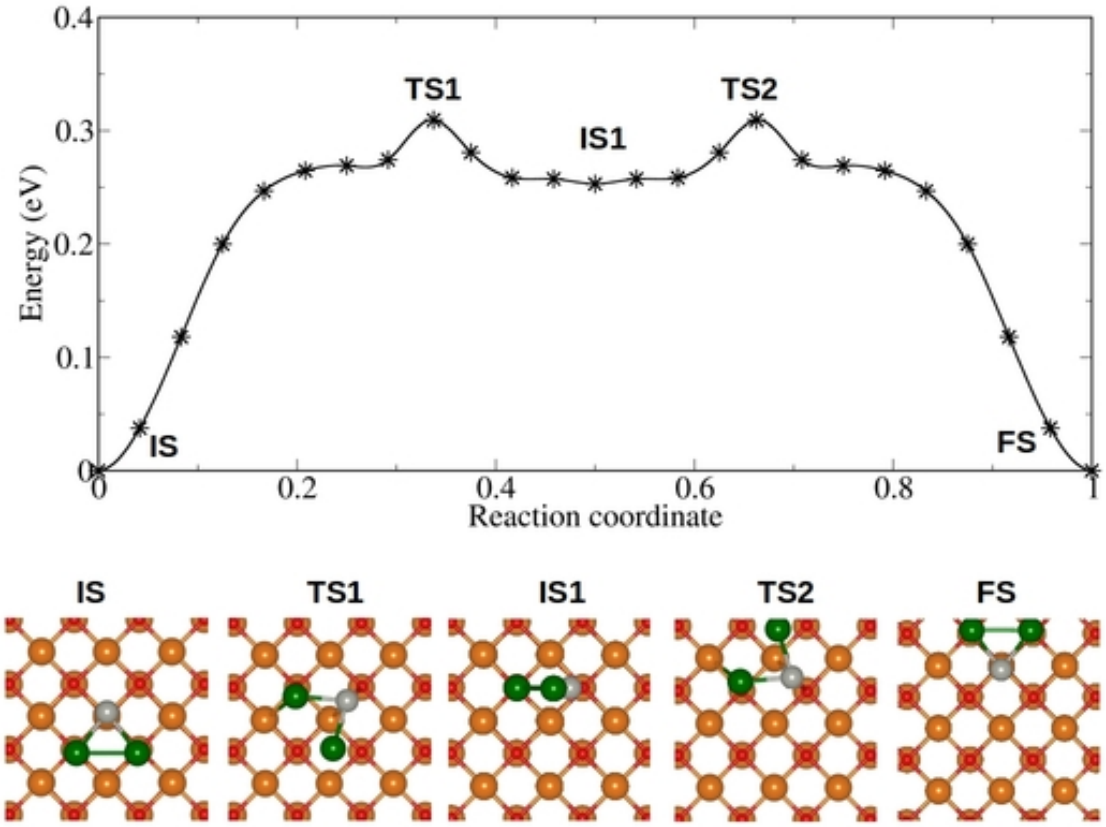

Figure D.16: Diffusion of Pd_1Ga_2 on the MgO terrace: Rolling (Path 2) This mechanism involves two steps. In the first step, the cluster binding ina horizontal geometry (IS) rotates about 90° and one of the Ga atom stands upright to a vertical geometry (IS1). This process has a barrier of 0.31 eV. The second step is reverse of the first step the cluster binding in a vertical geometry rolls to a horizontal final geometry. This requires to overcome a barrier of 0.06 eV.

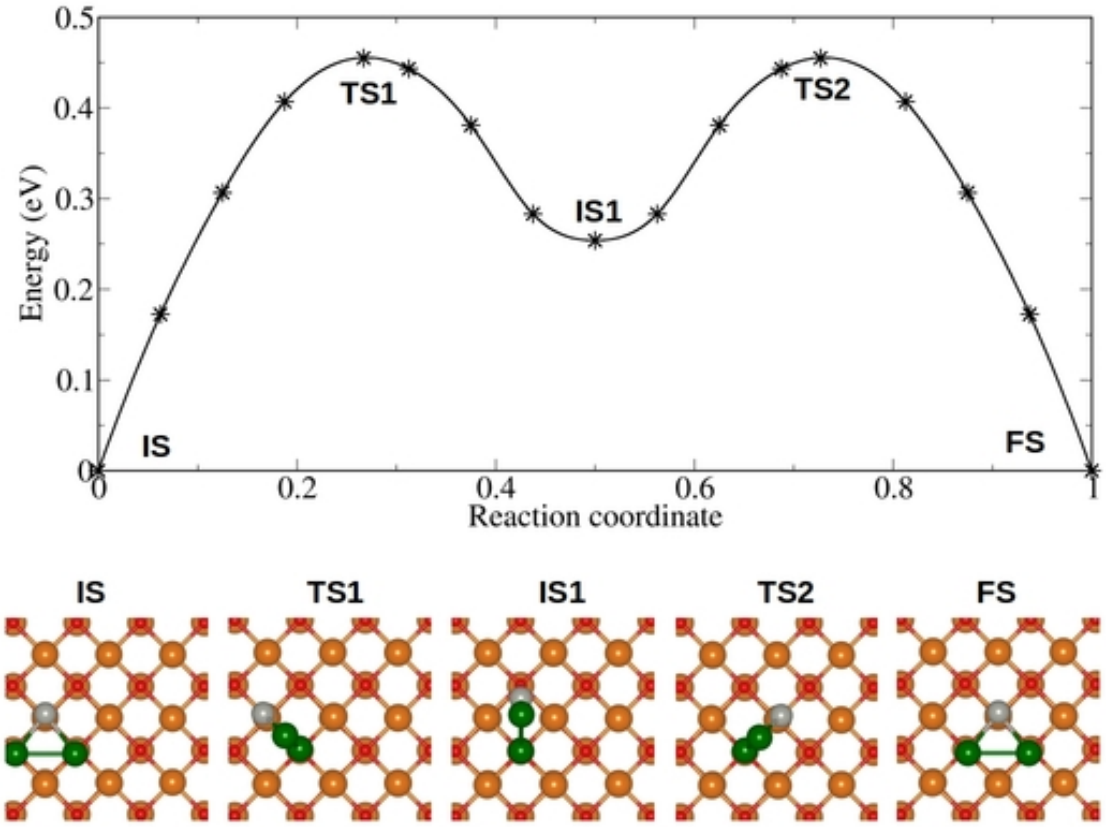

Figure D.17: Diffusion of Pd_1Ga_2 on the MgO terrace: Rolling (Path 3) Similar to other rolling mechanism of Pd_1Ga_2 on MgO terrace, this also involves two steps. In the first step the cluster binding in a horizontal geometry (IS) rolls to a vertical geometry (IS1) through a saddle point (TS1) where the cluster is binding vertically to the surface such that one Ga is binding to the oxygen site and the Pd is binding to the Mg site. For this diffusion process, the cluster requires to overcome a barrier of 0.45 eV. The second step is the reverse of the first step, the cluster binding in the vertical geometry rolls to a horizontal geometry.

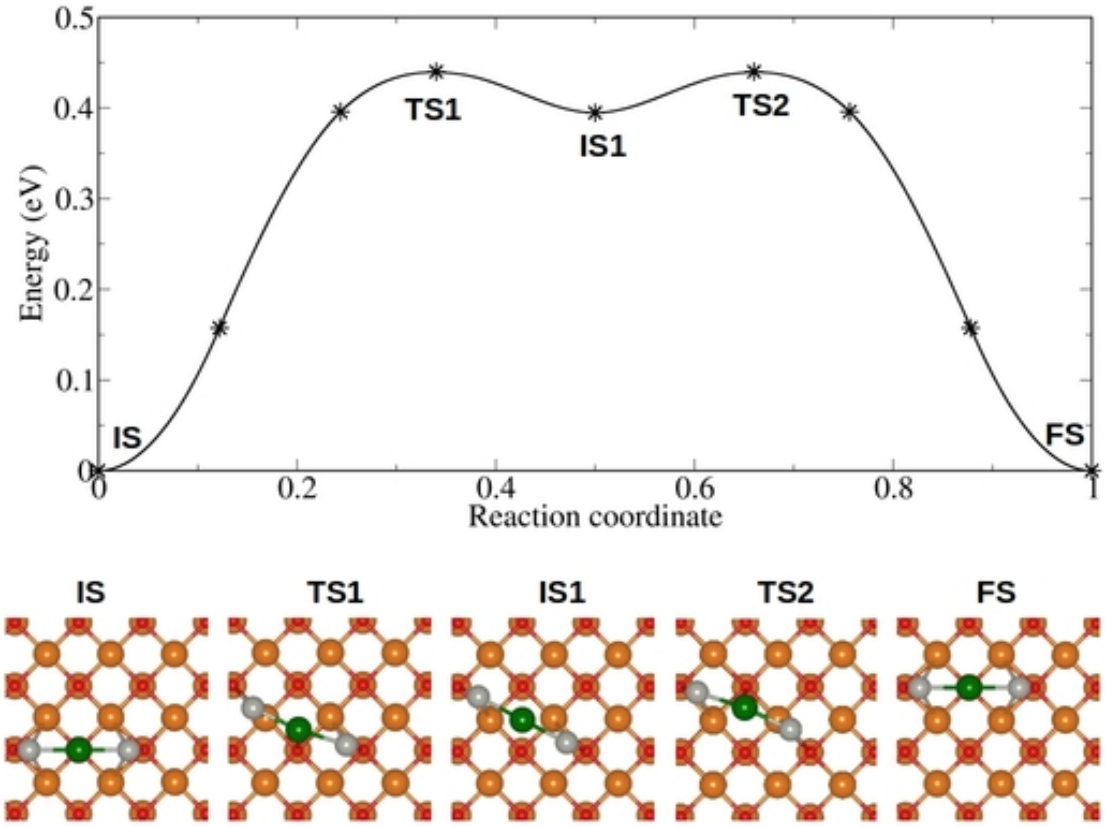

Figure D.18: Diffusion of Pd_2Ga_1 on the MgO terrace: Walking (Path 1) In the initial state, all three atoms of the Pd_2Ga_1 cluster are sitting on top of the three surface oxygen sites, such that the Ga atom is at the center and both the Pd atoms occupy two sides. In the first step, one of the Pd atoms moves to the next neighboring oxygen site and the Ga adjusts its position accordingly to form an intermediate state. At the intermediate state the Ga occupies the hollow site. This intermediate state is 0.39 eV less stable than the most stable initial state. The Pd_2Ga_1 cluster requires to overcome a diffusion barrier of 0.44 eV for this process to occur. The second step is the mirror image of the first process, in this step the Pd_2Ga_1 cluster at the intermediate step diffuses to the final state.

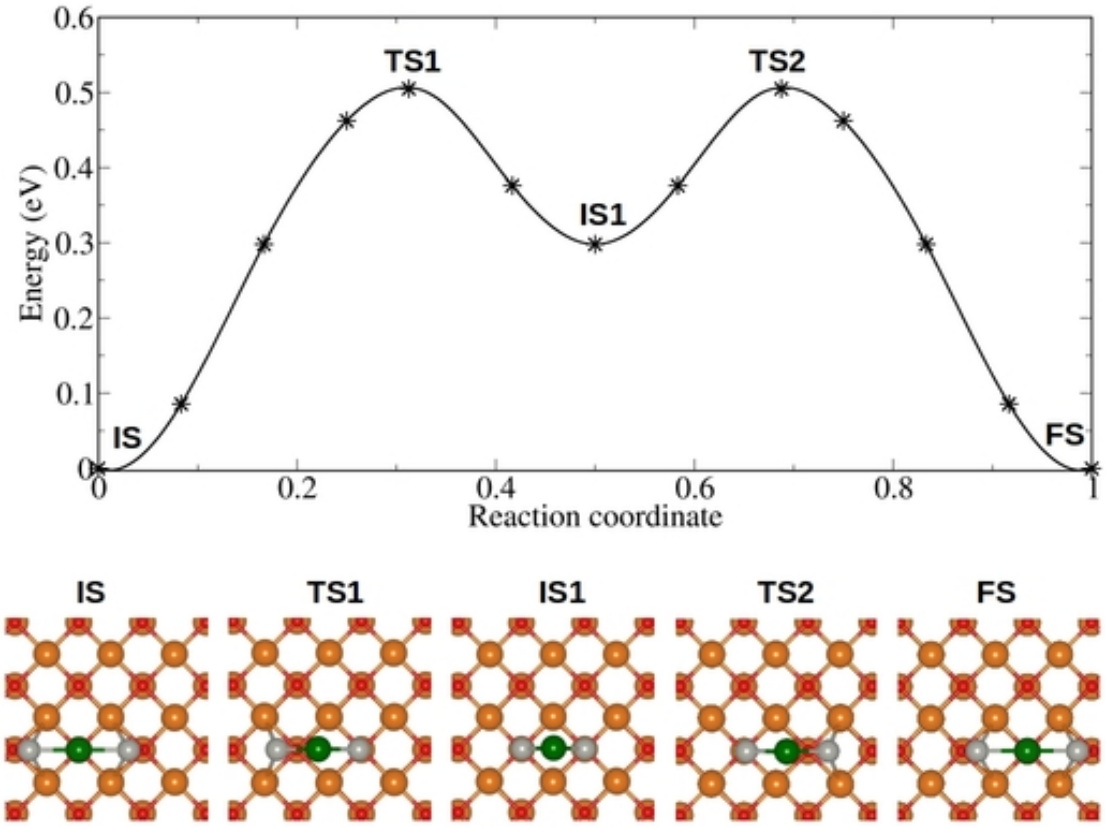

Figure D.19: Diffusion of Pd_2Ga_1 on the MgO terrace: (Path 2) This path involves two steps. In the initial state the Pd_2Ga_1 binds in a linear structure with Ga occupying the center and Pd atoms occupy the sides. In the first step one of the Pd atom stays intact while other Pd moves towards it and subsequently the Ga is uplifted to form a isosceles triangular structure binding vertically to the surface. This intermediate state (IS1) is about 0.30 eV higher in energy than the initial state. The first step has a barrier of 0.50 eV. The second step is reverse of the first step, the isosceles triangular structure becomes a linear one and this requires to overcome a barrier of 0.20 eV.

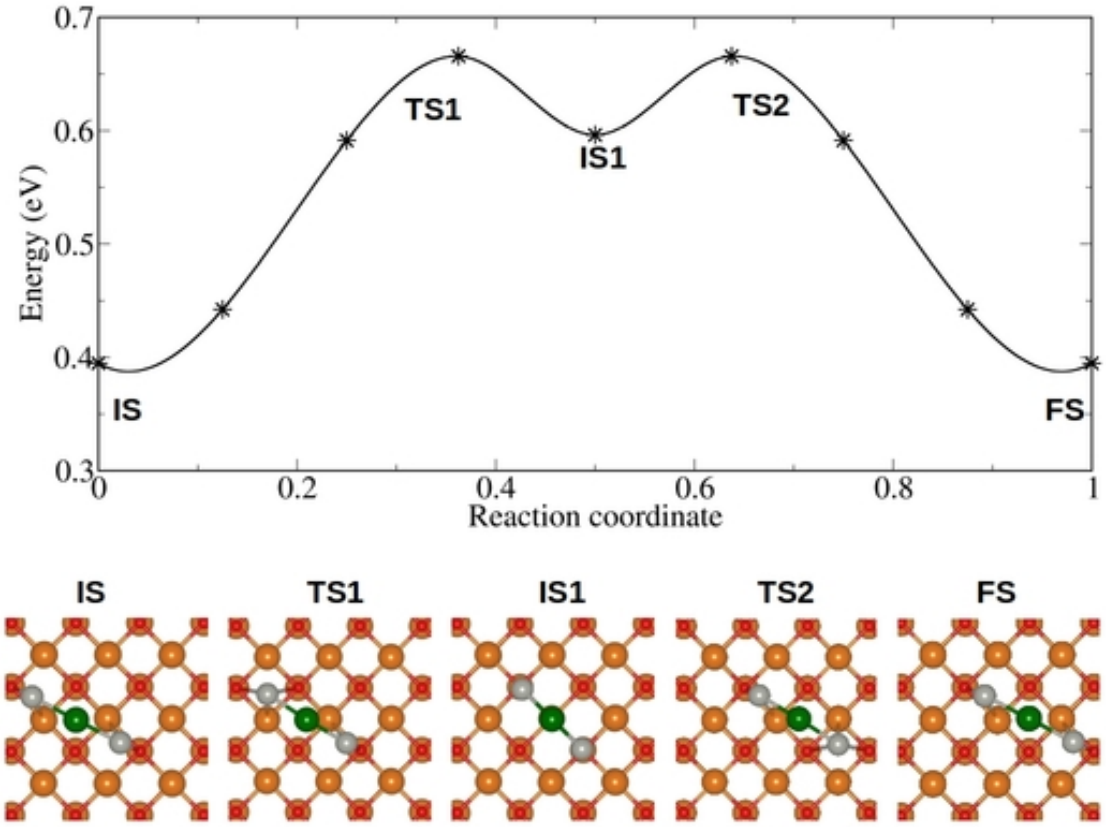

Figure D.20: Diffusion of Pd_2Ga_1 on the MgO terrace: Sliding (Path 3) This path involves two steps. The initial state for this path is about 0.39 eV higher in energy than that of the most stable structure. In the first step, the cluster slides to an intermediate state (IS1), which is about 0.20 eV higher in energy than the initial state. The cluster has to overcome a barrier of 0.27 eV. The second step is energetically mirror image of the first step. The cluster in the intermediate state slides to the final state and this has a barrier of 0.07 eV.

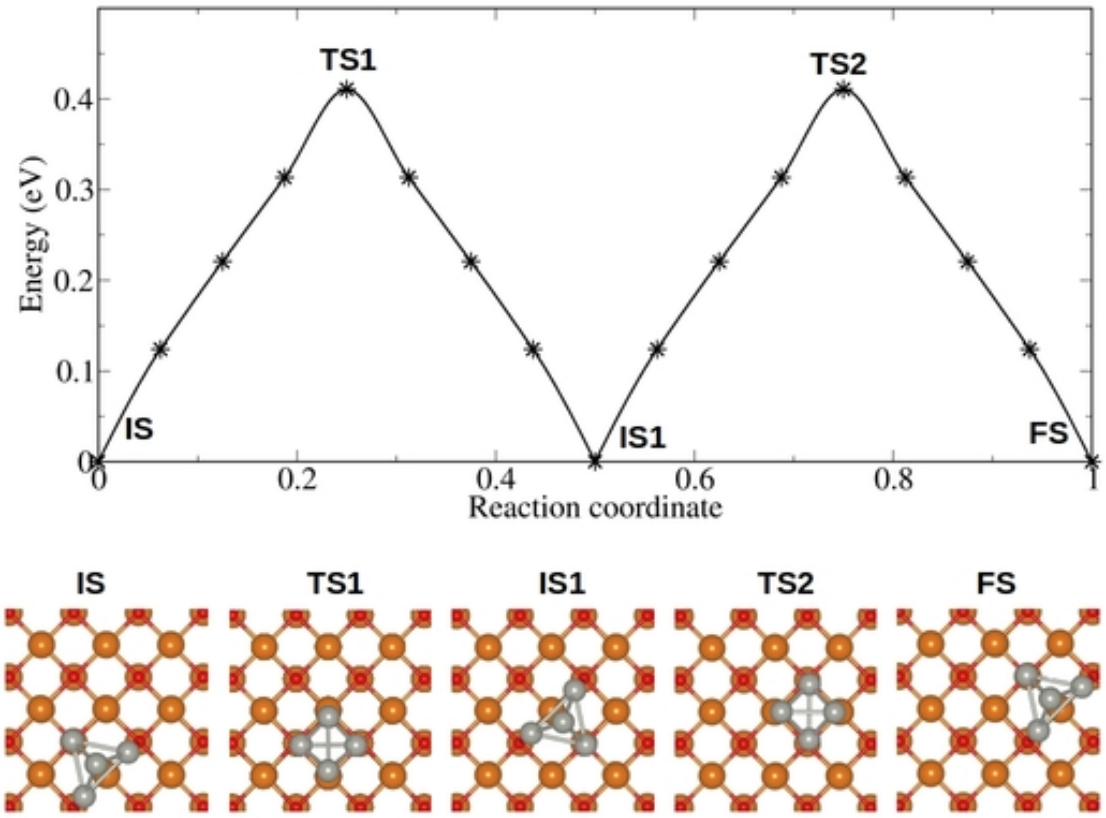

Figure D.21: Diffusion of Pd_4 on the MgO terrace: Rolling The Pd_4 clusters diffuses on MgO surface by following rolling mechanism. In the initial state, one of the Pd atoms is sitting on top of surface O site and two of the Pd atoms are sitting on the bridge site. These three atoms forms the base for the tetrahedron and the fourth Pd atom is standing upright. In the first step, the cluster rolls to the next nearest site with a barrier of 0.41 eV. At the saddle point, two of the Pd atoms are binding on top of two nearby surface oxygen sites and other two Pd atoms are standing upright thereby retaining the tetrahedron structure.

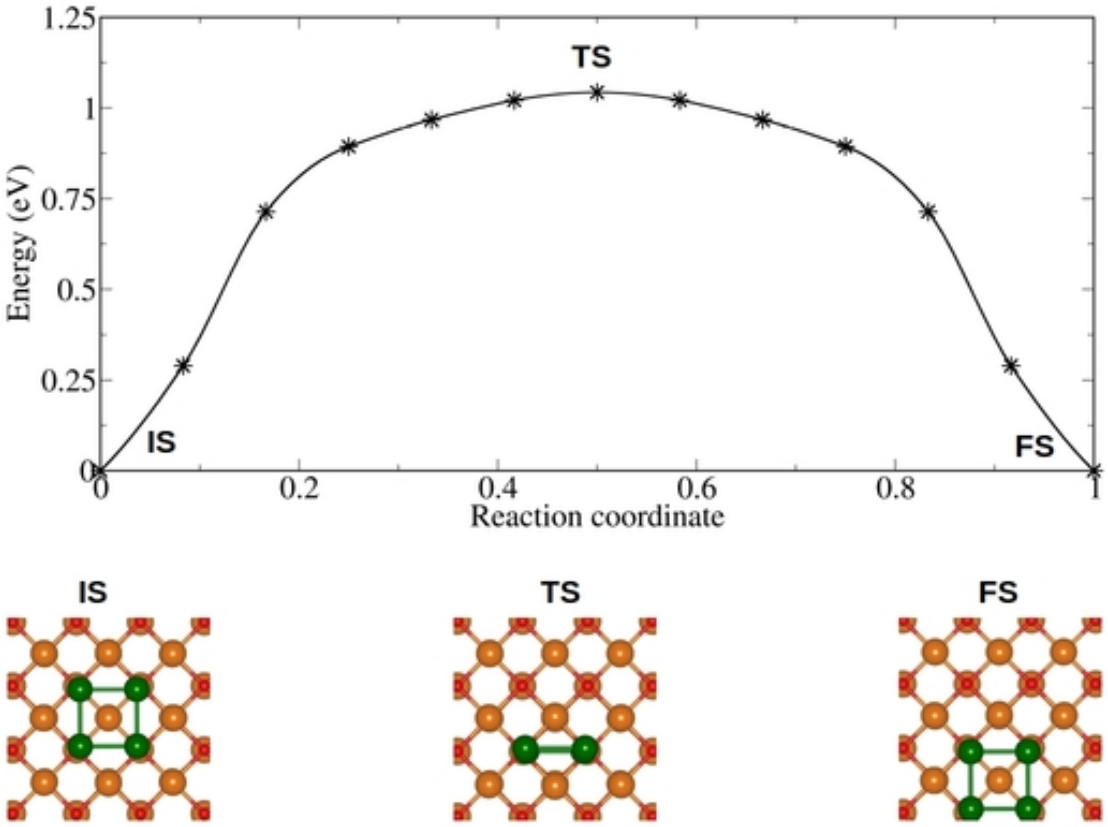

Figure D.22: Diffusion of Ga_4 on the MgO terrace: Rolling (Path 1) The Ga_4 cluster sitting on top of four oxygen sites of the MgO terrace in a planar geometry rolls to the next sites retaining the planar geometry. At the saddle point, the cluster moves to a vertical position retaining the original square geometry. The Ga_4 cluster requires to overcome a barrier of 1.04 eV for this rolling process.

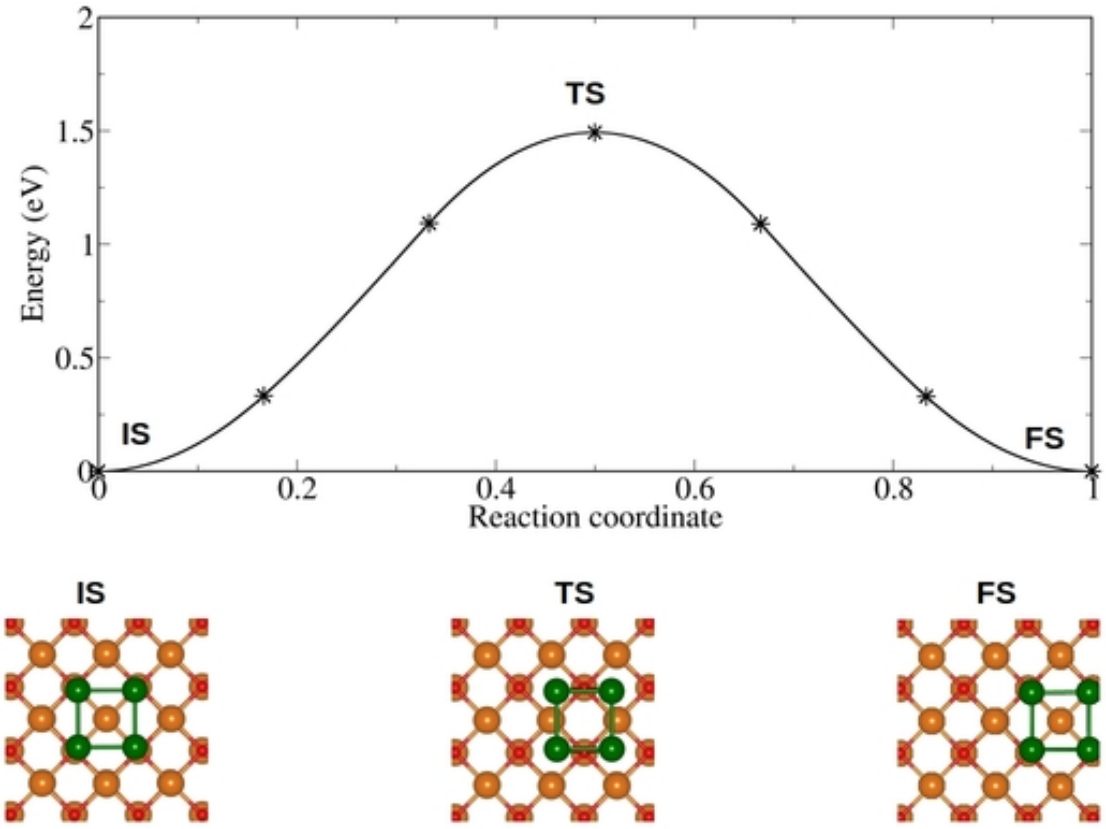

Figure D.23: Diffusion of Ga_4 on the MgO terrace: Sliding (Path 2) Sliding of Ga_4 on the MgO terrace requires to overcome a barrier of 1.49 eV. At the saddle point all the Ga atoms are sitting on top of the hollow sites.

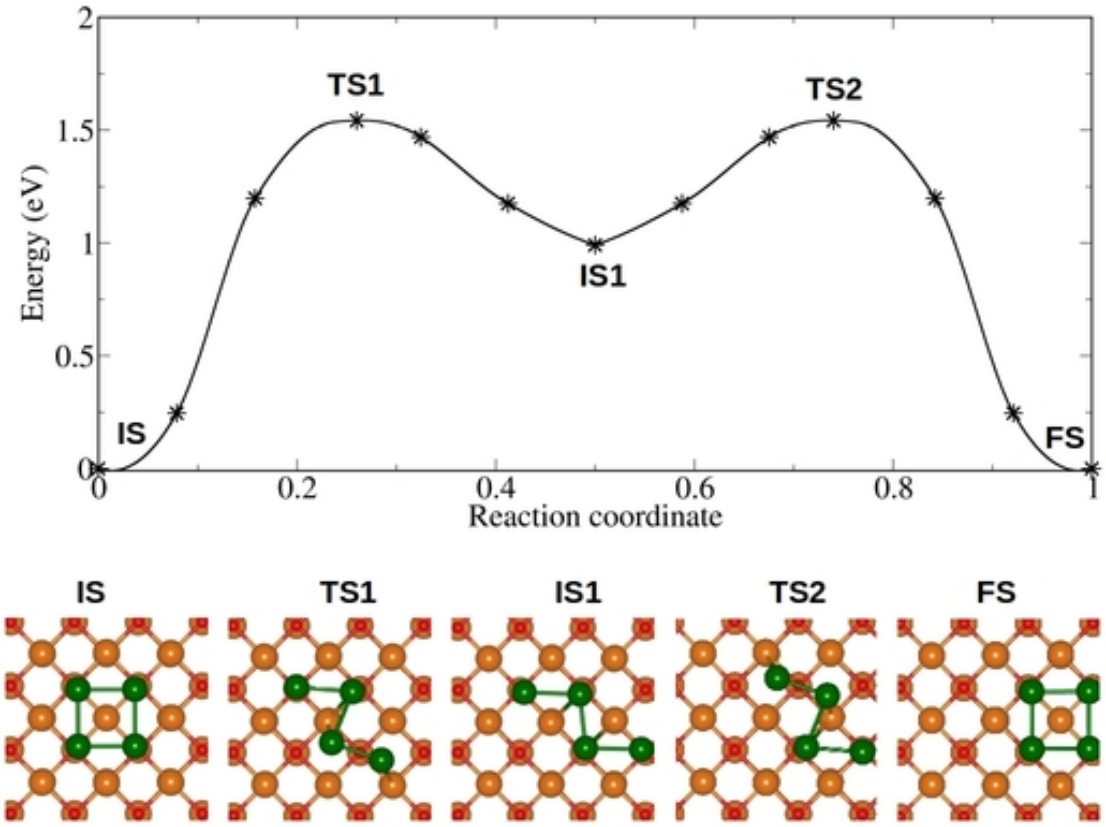

Figure D.24: Diffusion of Ga_4 on the MgO terrace: Partial dissociation (Path 3) This involves two steps. In the first step the Ga_4 binding to the MgO surface partially dissociates (two of the Ga atoms moves to the next site) to form the intermediate state (IS1). The intermediate state is about 0.99 eV higher in energy than the initial state. This requires to overcome a barrier of 1.54 eV. The next step is energetically mirror image of the first step, in this step other two Ga atoms move to form a square structure.

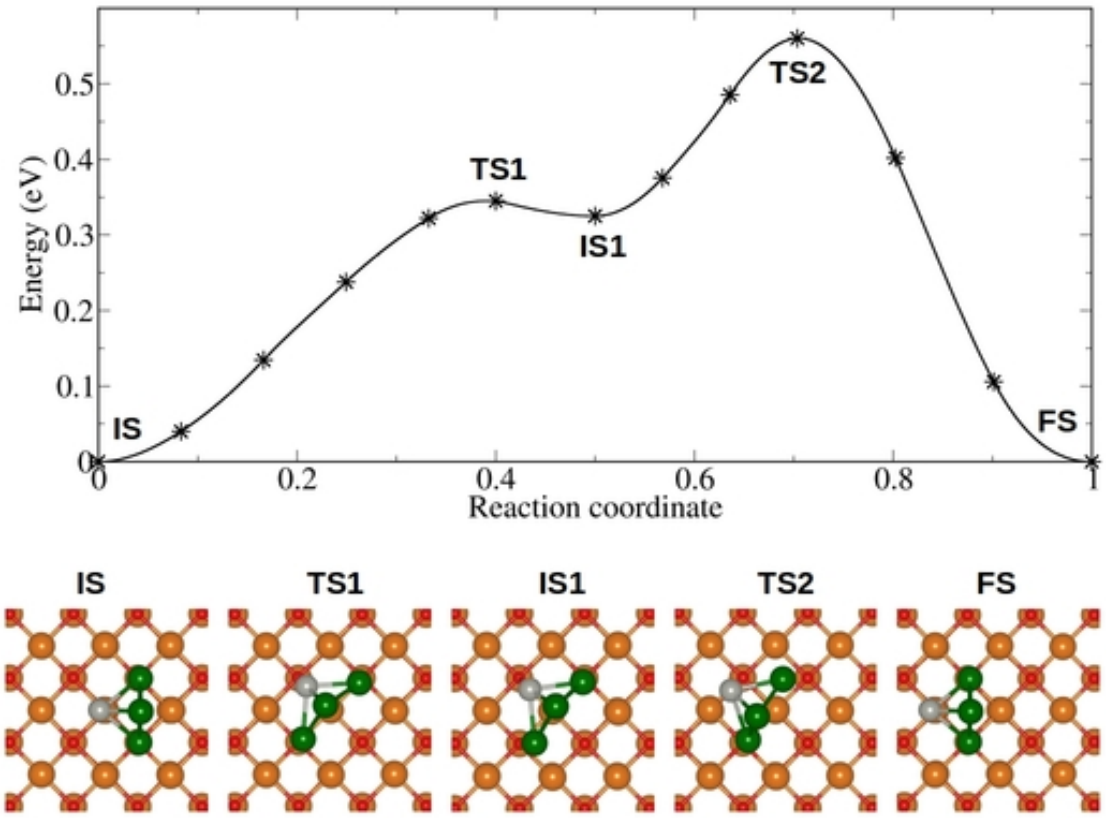

Figure D.25: Diffusion of Pd_1Ga_3 on the MgO terrace: Sliding (Path 1) The Pd_1Ga_3 cluster diffuses on MgO(100) surface by a combined clockwise-anticlockwise rotation of the cluster by 45 ° about one of the Ga atoms that is interacting with the surface. profile of the diffusion process. The clockwise rotation to an intermediate involves a barrier of about 0.34 eV. The anticlockwise rotation of the cluster from this intermediate to the final one involves a barrier of about 0.23 eV. The overall diffusion barrier associated with sliding mechanism is calculated to be 0.56 eV.

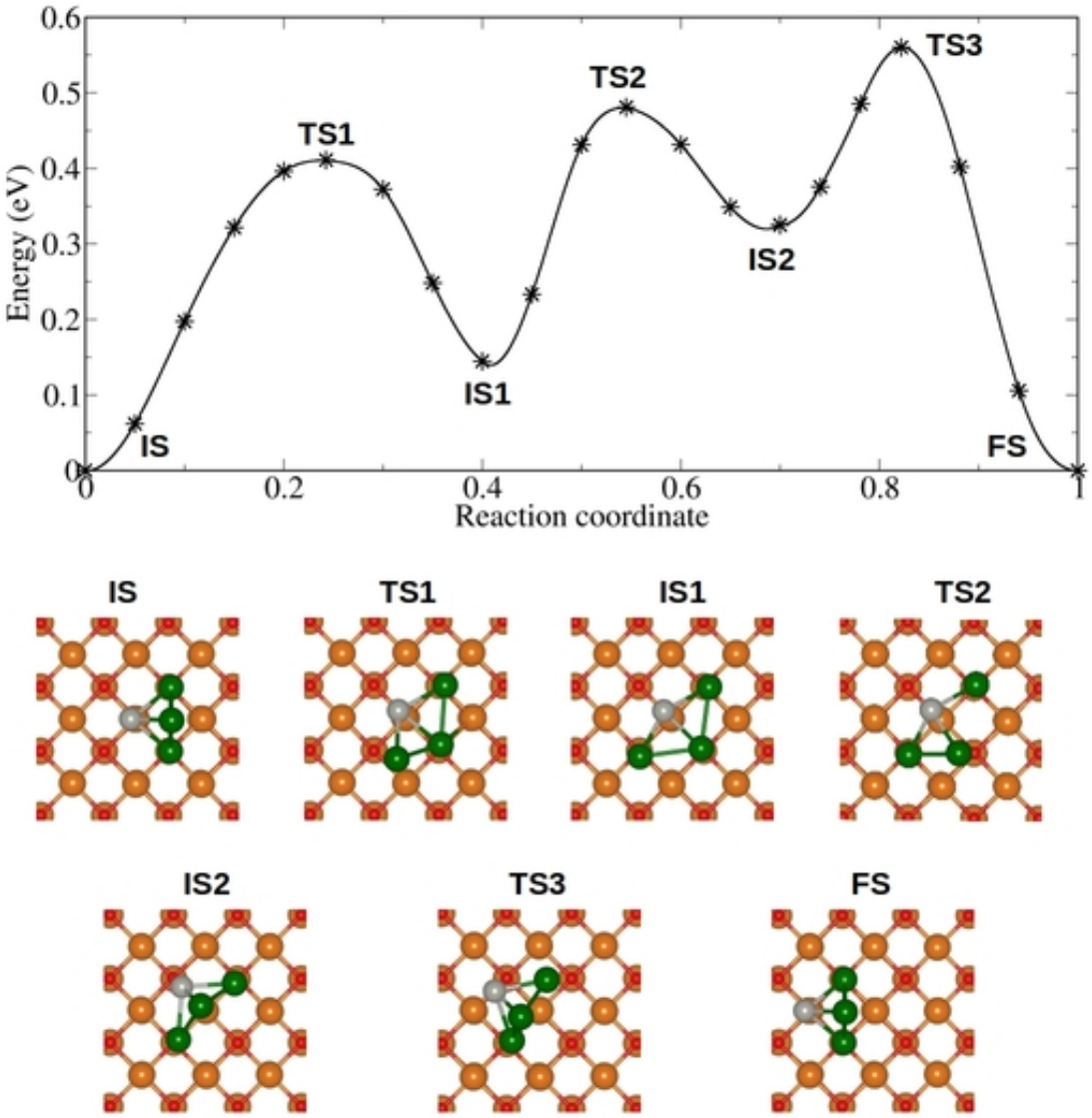

Figure D.26: Diffusion of Pd_1Ga_3 on the MgO terrace: (Path 2) Diffusion of Pd_1Ga_3 following this path involves three steps. In the first step, the Ga sitting on top of the Pd_1Ga_2 base falls on the oxygen site (IS1). This intermediate state is about 0.14 eV higher in energy than initial state and this process has a barrier of 0.41 eV. In the second step, the cluster slides such that the Pd atom binds to the oxygen site and the Ga atom in the middle binds to the Mg site (IS2). This intermediate state (IS2) is about 0.32 eV higher in energy than the initial state and this sliding requires to overcome a barrier of 0.33 eV. The last step is same as the second step in the Path 1. The over of barrier associated with the diffusion of Pd_1Ga_3 following this path is about 0.59 eV.

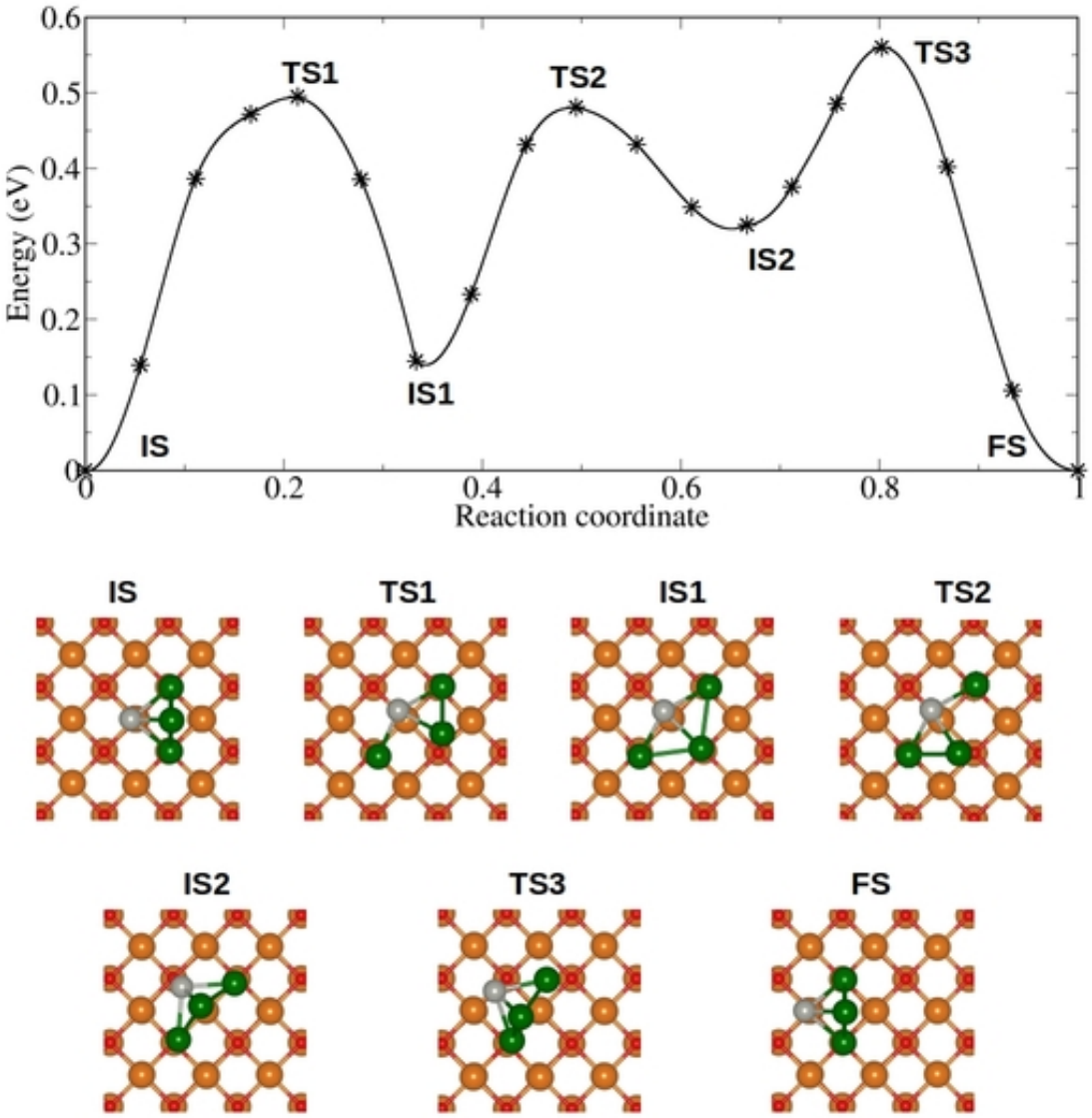

Figure D.27: Diffusion of Pd_1Ga_3 on the MgO terrace: (Path 3) This path involves three steps. In the first path, one of the Ga atom binding to the surface oxygen site moves to the next oxygen site and subsequently the Ga atom sitting on the base triangle binds to the oxygen site on which the moving Ga atom was initially binding. This has a barrier of 0.49 eV. The other two steps are same as the Path 2. The over of barrier associated with the diffusion of Pd_1Ga_3 following this path is about 0.59 eV.

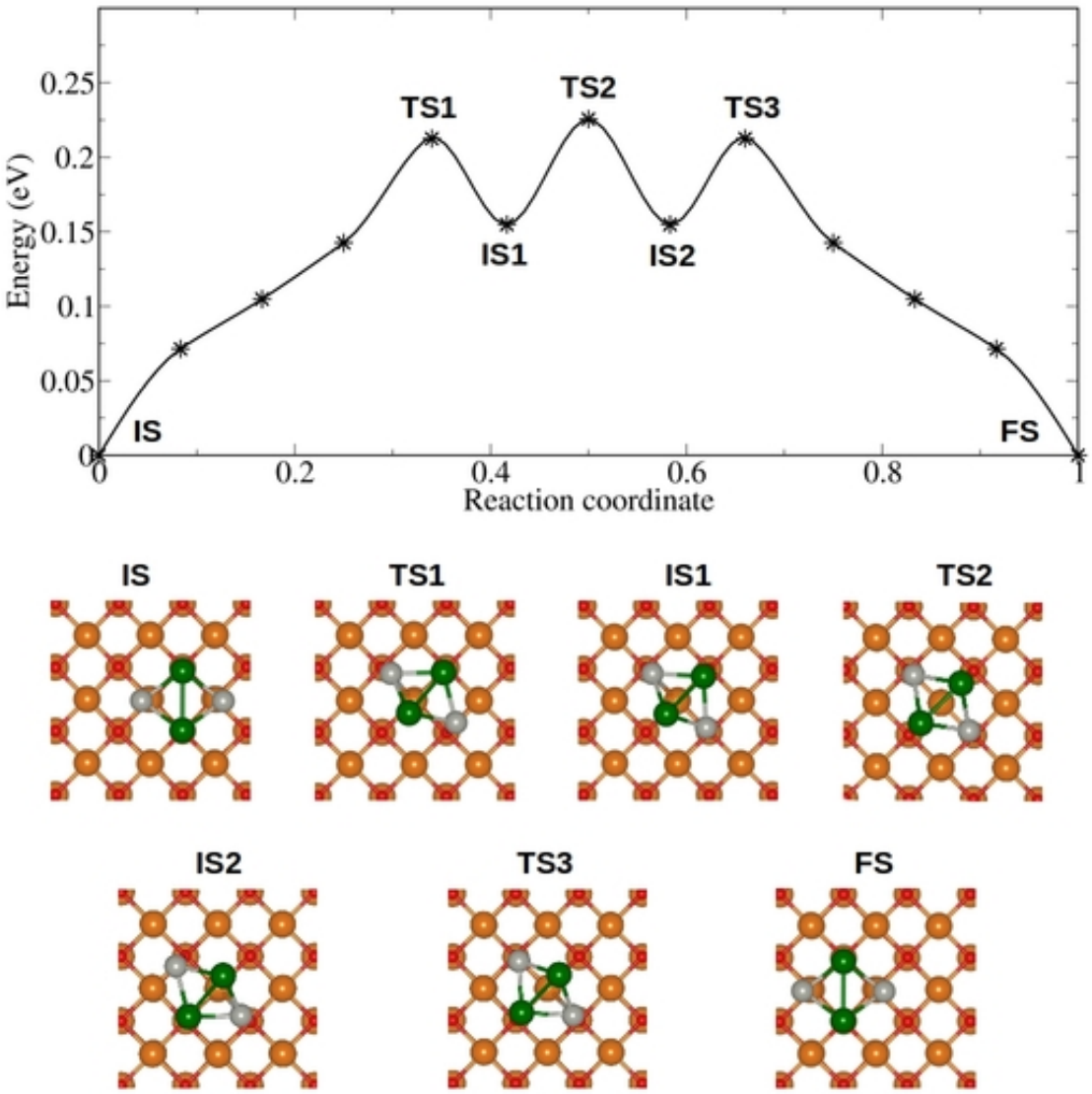

Figure D.28: Diffusion of Pd_2Ga_2 on the MgO terrace: Sliding (Path 1) The diffusion of Pd_2Ga_2 cluster on MgO(100) also involves a combined clockwise-anticlockwise rotation by 45 °. In this mechanism, the whole Pd_2Ga_2 cluster rotates about the surface normal. After the first rotation the cluster reaches a saddle point in which the mid-point of the Pd-Pd/ Ga-Ga bond is atop a Mg atom. The process involves a barrier of 0.22 eV.

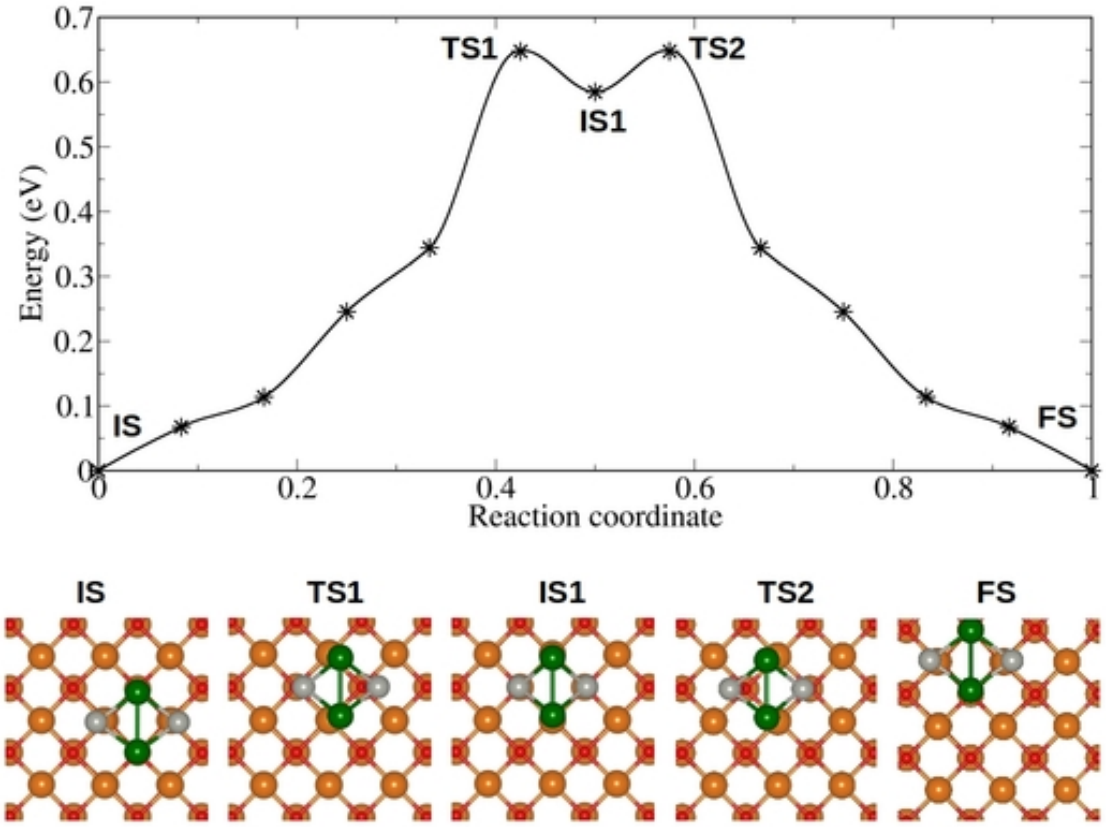

Figure D.29: Diffusion of Pd_2Ga_2 on the MgO terrace: Sliding(Path 2) In the initial state the Pd atoms are sitting on top of the Mg sites and the Ga atoms are sitting on top of the oxygen atoms (IS). This path involves two steps. In the first step, the Pd_2Ga_2 cluster slides to an intermediate state in which the Ga atoms are sitting on top of the Mg sites and the Pd atoms are sitting on top of the oxygen sites (IS1). The intermediate state is about 0.58 eV higher in energy than the initial state and this diffusion requires to overcome a barrier of 0.64 eV. The energetics of the second step is mirror image of the first step, where the cluster slides from the intermediate state to the next stable site.

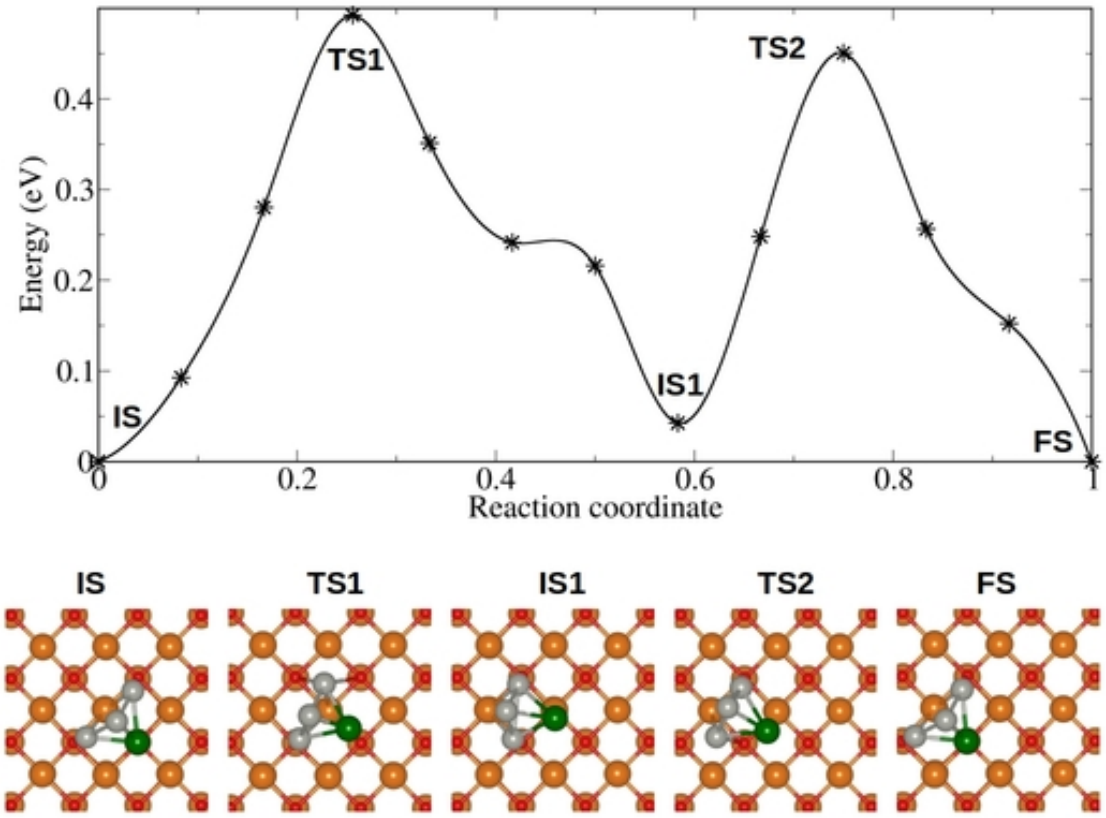

Figure D.30: Diffusion of Pd_3Ga_1 on the MgO terrace: Sliding (Path 1) The diffusion of Pd_3Ga_1 on the MgO terrace involves two steps in which the cluster rotates in opposite direction in each step to slide. In the initial state, the Ga atom sitting on top of oxygen site and two Pd atoms on the bridge sites make the base triangle of the tetrahedron geometry and the third Pd is sitting on top of the base triangle and connected with all three atoms. First the cluster diffuses to a intermediate state in which both the Pd atoms of the base triangle sitting on top of the surface oxygen sites and the Ga is on top of Mg site. This process has a diffusion barrier of 0.49 eV associated with it. In the next step the cluster in the intermediate state diffuses to the next nearest stable site with a barrier of 0.45 eV.

Bibliography

[1] G. Henkelman, "Atomistic simulations of activated processes in materials", *Annu. Rev. Mater. Res.* **47**, pp. 199–216 (2017). 1, 2, 3, 4, 23

[2] Arthur F. Voter, *Introduction to the Kinetic Monte Carlo Method* , pp. 1–23, Springer,Dordrecht (2007), Chapter Number: 1. 1, 168

[3] Reuter Karsten, *First-Principles Kinetic Monte Carlo Simulations for Heterogeneous Catalysis: Concepts, Status, and Frontiers* chapter 3, , pp. 71–111, Wiley-Blackwell (2011). 2, 28

[4] J. Kohanoff and N.I. Gidopoulos, *Density Functional Theory: Basics, New Trends and Applications* , pp. 532–568, Wiley-Blackwell (2003), Chapter Number: 26. 7

[5] W. Hohenberg and P. Kohn, "Inhomogeneous electron gas", *Phys. Rev.* **136**, pp. 864–871 (1964). 9, 20

[6] R. M. Martin, editor, *Electronic Structure: Basic Theory and Practical Methods*, Cambridge University Press, New York 2 edition (2004). 9, 11, 16, 17, 20

[7] W. Kohn and L. J. Sham, "Self-consistent equations including exchange and correlation effects.", *Phys. Rev.* **140(4A)**, pp. A1133–A1138 (1965). 11, 20

[8] D. M. Ceperley and B. J. Alder, "Ground state of the electron gas by a stochastic method", *Phys. Rev. Lett.* **45**, pp. 566–569 (1980). 15

[9] J. P. Perdew and Alex Zunger, "Self-interaction correction to density-functional approximations for many-electron systems", *Phys. Rev. B* **23**, pp. 5048–5079 (1981). 15

[10] A. D. Becke, "Density-functional exchange-energy approximation with correct asymptotic behavior", *Phys. Rev. A* **38**, pp. 3098–3100 (1988). 15

[11] Yue Wang and John P. Perdew, "Spin scaling of the electron-gas correlation energy in the high-density limit", *Phys. Rev. B* **43**, pp. 8911–8916 (1991). 15

[12] John P. Perdew, Kieron Burke, and Matthias Ernzerhof, "Generalized Gradient Approximation made simple", *Phys. Rev. Lett.* **77**(18), pp. 3865–3868 (1996). 15, 35, 65, 91, 183

[13] P. P. Ewald, *Ann. Phys (Leipzig)* **54**, pp. 519 (1917). 16

[14] P. P. Ewald, *Ann. Phys (Leipzig)* **54**, pp. 557 (1917). 16

[15] P. P. Ewald, *Ann. Phys (Leipzig)* **64**, pp. 253 (1921). 16

[16] P. Pulay, "Ab initio calculation of force constants and equilibrium geometries in polyatomic molecules. i. theory", *Mol. Phys.* **17**, pp. 197–204 (1969). 17

[17] R. P. Feynman, "Forces in molecules", *Physical Review* **56**, pp. 340–343 (1939). 17, 20

[18] M. C. Payne, M. P. Teter, D. C. Allan, T. A. Arias, and J. D. Joannopoulos, "Iterative minimization techniques for ab initio total-energy calculations: molecular dynamics and conjugate gradients", *Rev. Mod. Phys.* **64**, pp. 1045–1097 (1992). 18

[19] D. Vanderbilt, "Soft self-consistent pseudopotentials in a generalized eigenvalue formalism", *Phys. Rev. B* **41**, pp. 7892–7895 (1990). 18, 35, 65, 91, 183

[20] J. D. Monkhorst, H. J.; Pack, "Special points for Brillouin-Zone Integrations.", *Phys. Rev. B* **13**, pp. 5188–5192 (1976). 19, 35, 65, 183

[21] C. L. Fu and K. M. Ho, "First-principles calculation of the equilibrium ground-state properties of transition metals: Applications to Nb and Mo", *Phys. Rev. B* **28**, pp. 5480–5486 (1983). 19

[22] M. Methfessel and A. T. Paxton, "High-precision sampling for brillouin-zone integration in metals", *Phys. Rev. B* **40**, pp. 3616–3621 (1989). 19

[23] N. Marzari, D. Vanderbilt, A. DeVita, and M. C. Payne, "Thermal contraction and disordering of the Al(110) surface", *Phys. Rev. Lett.* **82**, pp. 3296–3299 (1999). 19, 35, 65, 91, 183

[24] O. H. Nielsen and Richard M. Martin, "First-principles calculation of stress", *Phys. Rev. Lett.* **50**, pp. 697–700 (1983). 20

[25] O. H. Nielsen and Richard M. Martin, "Quantum-mechanical theory of stress and force", *Phys. Rev. B* **32**, pp. 3780–3791 (1985). 20

[26] M. Born and K. Huang, editors, *Dynamical theory of crystal lattices*, Oxford University Press (1954). 20

[27] Stefano Baroni, Stefano de Gironcoli, Andrea Dal Corso, and Paolo Giannozzi, "Phonons and related crystal properties from density-functional perturbation theory", *Rev. Mod. Phys.* **73**, pp. 515–562 (2001). 20, 94, 183

[28] Stefano Baroni, Paolo Giannozzi, and Andrea Testa, "Green's-function approach to linear response in solids", *Phys. Rev. Lett.* **58**, pp. 1861–1864 (1987). 20

[29] P.D. De Cicco and F. A. Johnson, *Proc. R. Soc. London;Ser. A* **310**, pp. 111 (1969). 21

[30] Robert M. Pick, Morrel H. Cohen, and Richard M. Martin, "Microscopic theory of force constants in the adiabatic approximation", *Phys. Rev. B* **1**, pp. 910–920 (1970). 21

[31] Graeme Henkelman, Gísli Jóhannesson, and Hannes Jónsson, *Methods for Finding Saddle Points and Minimum Energy Paths* , pp. 269–302, Springer Netherlands Dordrecht (2002). 24, 26, 27

[32] Graeme Henkelman, Blas P. Uberuaga, and Hannes Jónsson, "A climbing image nudged elastic band method for finding saddle points and minimum energy paths", *J. Chem. Phys.* **113**, pp. 9901 (2000). 24, 66, 91, 183

[33] Daniel Sheppard, Rye Terrell, and Graeme Henkelman, "Optimization methods for finding minimum energy paths", *The Journal of Chemical Physics* **128**(13), pp. 134106 (2008). 25, 27

[34] Paolo Giannozzi, Stefano Baroni, Nicola Bonini, Matteo Calandra, Roberto Car, Carlo Cavazzoni, Davide Ceresoli, Guido L Chiarotti, Matteo Cococcioni, Ismaila Dabo, Andrea Dal Corso, Stefano de Gironcoli, Stefano Fabris, Guido Fratesi, Ralph Gebauer, Uwe Gerstmann, Christos Gougoussis, Anton Kokalj, Michele

Lazzeri, Layla Martin-Samos, Nicola Marzari, Francesco Mauri, Riccardo Mazzarello, Stefano Paolini, Alfredo Pasquarello, Lorenzo Paulatto, Carlo Sbraccia, Sandro Scandolo, Gabriele Sclauzero, Ari P Seitsonen, Alexander Smogunov, Paolo Umari, and Renata M Wentzcovitch, "QUANTUM ESPRESSO:a modular and open-source software project for quantum simulations of materials", *J. Phys. Condens. Matter* **21**, pp. 395502 (2009). 26, 35, 65, 91, 183

[35] Michail Stamatakis and Dionisios G. Vlachos, "A graph-theoretical kinetic monte carlo framework for on-lattice chemical kinetics", *J. Chem. Phys.* **134**, pp. 214115 (2011). 29, 30, 31, 93

[36] Charlas T Campbell, "Bimetallic surface chemistry", *Annu. Rev. Phys. Chem.* **41**, pp. 775–837 (1990). 33

[37] Andrzej Borodziński and Geoffrey C. Bond, "Selective hydrogenation of ethyne in rthene-rich streams on palladium catalysts. part 1. effect of changes to the catalyst during reaction", *Catal. Rev. Sci. Eng.* **48**(2), pp. 91–144 (2006). 33, 62

[38] Marc Armbrüster, Kirill Kovnir, Malte Behrens, Detre Teschner, Yuri Grin, , and Robert Schlögl, "Pd-ga intermetallic compounds as highly selective semihydrogenation catalysts", *J. Am. Chem. Soc.* **132**(42), pp. 14745–14747 (2010). 33, 58, 62, 84, 90, 174

[39] Dirk Rosenthal, Roland Widmer, Ronald Wagner, Peter Gille, Marc Armbrüster, Yuri Grin, Robert Schlögl, and Oliver Gröning, "Surface investigation of intermetallic pdga($\bar{1}\bar{1}\bar{1}$)", *Langmuir* **28**(17), pp. 6848–6856 (2012). 34, 36, 44

[40] Jan Prinz, Roberto Gaspari, Carlo A. Pignedoli, Jochen Vogt, Peter Gille, Marc Armbrüster, Harald Brune, Oliver Gröning, Daniele Passerone, and Roland Widmer, "Isolated pd sites on the intermetallic pdga(111) and pdga($\bar{1}\bar{1}\bar{1}$) model catalyst surfaces", *Angew. Chem. Int. Ed.* **51**, pp. 9339–9343 (2012). 34, 43, 46, 67

[41] M. Krajĉì and J. Hafner, "Structure and chemical reactivity of the polar threefold surfaces of GaPd: A density-functional study", *J. Chem. Phys.* **138**(12), pp. 124703–124720 (2013). 34, 36, 64, 84

[42] M. Krajĉì and J. Hafner, "The (210) surface of intermetallic B20 compound GaPd as a selective hydrogenation catalyst: A dft study", *J. Catal.* **295**, pp. 70–80 (2012). 34, 36, 50, 63, 67, 68, 71, 82

[43] Jan Prinz, Carlo A. Pignedoli, Quirin S. Stöckl, Marc Armbrüster, Harald Brune, Oliver Gröning, Roland Widmer, and Daniele Passerone, "Adsorption of small hydrocarbons on the three-fold PdGa surfaces: The road to selective hydrogenation", *J. Am. Chem. Soc.* **136**(33), pp. 11792–11798 (2014). 34, 50, 63, 67, 68, 71, 75, 84, 85, 86, 90, 174

[44] B. H. Verbeek, P. K. Larsen, and W. M. Gerits, "Electronic structure of PdGa(110) by photoemission spectroscopy", *Vacuum* **33**, pp. 813–814 (1983). 34, 36, 44

[45] P. Bechthold, P. Jasen, E. González, and A. Juan, "Hydrogen adsorption on pdga(110): A dft study", *J. Phys. Chem. C* **116**(33), pp. 17518–17524 (2012). 34, 36

[46] P. Bechthold, P.V. Jasen, J.S. Ardenghi, E.A. González, and A. Juan, "Ab initio study of co adsorption on pdga(1 1 0)", *Computational Materials Science* **71**, pp. 192–196 (2013). 34

[47] P. Bechthold, J.S. Ardenghi, O. Nagel, A. Juan, E.A. González, and P.V. Jasen, "Hydrogen adsorption on pdga(100), (111) and $(\bar{1}\bar{1}\bar{1})$ surfaces: A dft study", *Int. J. Hydrogen Energ.* **39**(5), pp. 2093–2103 (2014). 34

[48] P. Bechthold, J.S. Ardhengi, A. Juan, E.A. González, and P.V. Jasen, "Co adsorption on pdga(1 0 0), (1 1 1) and $(\bar{1}\bar{1}\bar{1})$ surfaces: A dft study", *Appl. Surf. Sci.* **315**, pp. 467–474 (2014). 34

[49] F. D. Manchester, A. San-Martin, and J. M. Pitre, "The h-pd (hydrogen-palladium) system", *J. Phase Equilib.* **15**(1), pp. 62–83 (1994). 35, 36

[50] V. Heine, "Crystal structure of gallium metal", *J. Phys. C (Proc. Phys. Soc.)* **1**(2), pp. 222–232 (1968). 35, 36

[51] Marc Armbrüster, Horst Borrmann, Michael Wedel, Yurii Prots, Rainer Giedigkeit, and Peter Gille, "Refinement of the crystal structure of palladium gallium (1:1), PdGa", *Z. Kristallogr. NCS* **225**, pp. 617–618 (2010). 35, 36

[52] Nicholas E. Singh-Miller and Nicola Marzari, "Surface energies, work functions, and surface relaxations of low-index metallic surfaces from first principles", *Phys. Rev. B* **80**, pp. 235407 (2009). 36

[53] Juarez L.F. Da Silva, Catherine Stampfl, and Matthias Scheffler, "Converged properties of clean metal surfaces by all-electron first-principles calculations", *Surf. Sci.* **600**, pp. 703–715 (2006). 36

[54] S.V. Meschel and O.J. Kleppa, "Determination of the standard enthalpies of formation of pd2ga and pdga by high-temperature direct synthesis calorimetry", *Thermochimica Acta* **292**, pp. 13–17 (1997). 43

[55] D. R. Lide, editor, *CRC Handbook of Chemistry and Physics*, CRC, Boca Raton 84 edition (2004). 43, 185, 187

[56] M. Krajĉì and J. Hafner, "Selective semi-hydrogenation of acetylene: Atomistic scenario for reactions on the polar threefold surfaces of GaPd", *J. Catal.* **312**, pp. 232–248 (2014). 48, 50, 85

[57] Raghani Pushpa, Prasenjit Ghosh, Shobhana Narasimhan, and Stefano de Gironcoli, "Effective coordination as a predictor of adsorption energies: A model study of no on rh(100) and rh/mgo(100) surfaces", *Phys. Rev. B* **79**, pp. 165406 (2009). 50

[58] J. Osswald, R. Giedigkeit, R. E. Jentoft, M. Armbrüster, F. Girgsdies, K. Kovnir, T. Ressler, Y. Grin, and R. Schlögl, "Palladium-gallium intermetallic compounds for the selective hydrogenation of acetylene: Part i: Preparation and structural investigation under reaction conditions", *J. Catal.* **258**, pp. 210–218 (2008). 56

[59] J. Osswald, K. Kovnir, M. Armbrüster, R. Giedigkeit, R. E. Jentoft, U. Wild, Y. Grin, and R. Schlögl, "Palladium-gallium intermetallic compounds for the selective hydrogenation of acetylene: Part ii: Surface characterization and catalytic performance", *J. Catal.* **258**, pp. 219–227 (2008). 56, 62, 90

[60] P Gille, T Ziemer, M Schmidt, K Kovnir, U Burkhardt, and M Ambrüster, "Growth of large pdga single crystals from the melt", *Intermetallics* **18**, pp. 1663–1668 (2010). 58

[61] Árpád Molnár, Antal Sárkány, and Mónika Varga, "Hydrogenation of carbon-carbon multiple bonds: chemo-, regio- and stereo-selectivity", *J. Mol. Catal. A: Chem.* **173**(1-2), pp. 185 – 221 (2001). 62

[62] Peter Albers, Jörg Pietsch, and Stewart F Parker, "Poisoning and deactivation of palladium catalysts", *J. Mol. Catal. A: Chem.* **173**(1-2), pp. 275 – 286 (2001), Catlaysis with supported palladium metal at the turn of the 21st century. 62

[63] Nuria Lopez and Crisa Vargas-Fuentes, "Promoters in the hydrogenation of alkynes in mixtures: insights from density functional theory", *Chem. Commun.* **48**, pp. 1379–1391 (2012). 62

[64] Priyam A. Sheth, Matthew Neurock, and C. Michael Smith, "A first-principles analysis of acetylene hydrogenation over pd(111)", *The Journal of Physical Chemistry B* **107**(9), pp. 2009–2017 (2003). 62, 68, 71, 85

[65] Priyam A. Sheth, Matthew Neurock, and C. Michael Smith, "First-principles analysis of the effects of alloying pd with ag for the catalytic hydrogenation of acetylene and ethylene mixtures", *J. Phys. Chem. B* **109**(25), pp. 12449–12466 (2005). 62, 71

[66] M García-Mota, J. Gómez-Díaz, G. Novell-Leruth, C. Vargas-Fuentes, L. Bellarosa, B. Bridier, J. Pérez-Ramírez, and N. López, "A density functional theory study of the mythical lindlar hydrogenation catalyst", *Theor. Chem. Acc.* **128**(4-6), pp. 663–673 (2011). 62

[67] K. Kovnir, M. Armbrüster, D. Teschner, T.V. Venkovb, L. Szentmiklósi, F.C. Jentoft, A. Knop-Gerickeb, Yu. Grin, and R. Schlögl, "In situ surface characterization of the intermetallic compound pdga - a highly selective hydrogenation catalyst", *Surf. Sci.* **603**(10), pp. 1784–1792 (2009). 62

[68] Armbrüster Marc, Behrens Malte, Cinquini Fabrizio, Föttinger Karin, Grin Yuri, Haghofer Andreas, Klötzer Bernhard, Knop-Gericke Axel, Lorenz Harald, Ota Antje, Penner Simon, Prinz Jan, Rameshan Christoph, Révay Zsolt, Rosenthal Dirk, Rupprechter Günther, Sautet Philippe, Schlögl Robert, Shao Lidong, Szentmiklósi László, Teschner Detre, Torres Daniel, Wagner Ronald, Widmer Roland, and Gregor Wowsnick, "How to control the selectivity of palladium-based catalysts in hydrogenation reactions: The role of subsurface chemistry", *Chem. Cat. Chem* **4**(8), pp. 1048–1063 (2012). 62

[69] K. Kovnir, M. Armbrüster, D. Teschner, T.V. Venkov, F.C. Jentoft, A. Knop-Gericke, Yu. Grin, and R. Schlögl, "A new approach to well-defined, stable and site-isolated catalysts", *Sci. Technol. Adv. Mater.* **8**(5), pp. 420–427 (2007). 62, 90

[70] K. Kovnir, J. Osswald, M. Armbrüster, D. Teschner, G. Weinberg, U. Wild, A. Knop-Gericke, T. Ressler, Yu. Grin, and R. Schlögl, "Etching of the intermetallic compounds pdga and pd3ga7: An effective way to increase catalytic activity?", *J. Catal.* **264**, pp. 93–103 (2009). 62

[71] Marc Armbrüster, Robert Schlögl, and Yuri Grin, "Intermetallic compounds in heterogeneous catalysis- a quickly developing field", *Sci. Technol. Adv. Mater.* **15**, pp. 034803 (2014). 62

[72] W. M. H. Sachtler, "Chemisorption complexes on alloy surfaces", *Catal. Rev.: Sci. Eng.* **14**(1), pp. 193–210 (1976). 63

[73] A.M Doyle, Sh.K Shaikhutdinov, and H.-J Freund, "Alkene chemistry on the palladium surface: nanoparticles vs single crystals", *J. Catal.* **223**(2), pp. 444–453 (2004). 63

[74] Sh Shaikhutdinov, M Heemeier, M Bäumer, T Lear, D Lennon, R.J Oldman, S.D Jackson, and H.-J Freund, "Structure-reactivity relationships on supported metal model catalysts: Adsorption and reaction of ethene and hydrogen on pd/al2o3/nial(110)", *J. Catal.* **200**(2), pp. 330–339 (2001). 63

[75] P. Bechthold, M. Sandoval, E. A. González, G. Brizuela, A. Bonivardi, and P. V. Jasen, "The electronic structure and bonding of acetylene on pdga(110)", *The Journal of Physical Chemistry C* **119**(32), pp. 18229–18238 (2015). 64, 75

[76] M. Krajčí and J. Hafner, "Intermetallic compounds as selective heterogeneous catalysts: Insights from dft", *Chem. Cat. Chem.* **8**, pp. 34–48 (2016). 64, 68, 84

[77] Nandha Kumar and Prasenjit Ghosh, "Structure and stability of clean and adsorbate covered intermetallic pdga surfaces: A first principles study", *Surf. Sci.* **644**, pp. 69 – 79 (2016). 64, 66, 67, 84, 174

[78] K P Huber and G Hertzberg, *Molecular spectra and molecular structure IV: Constants of diatomic molecules*, Van Norstrand Reinhold New York (1979). 65, 66

[79] D. R. Lide, editor, *CRC handbook of chemistry and physics*, CRC, Boca Raton 90 edition (2010). 65, 66

[80] Graeme Henkelman and Hannes Jónsson, "Improved tangent estimate in the nudged elastic band method for finding minimum energy paths and saddle points", *J. Chem. Phys.* **113**(22), pp. 9978–9985 (2000). 66, 91, 183

[81] W. Sesselmann, B. Woratschek, G. Ertl, and J. Küppers, "Low temperature formation of benzene from acetylene on a pd(111) surface", *Sur. Sci.* **130**(2), pp. 245–258 (1983). 68

[82] L. L. Kesmodel, "Acetylene chemisorption on pd(100): Evidence for a strongly distorted species", *The Journal of Chemical Physics* **79**(9), pp. 4646–4648 (1983). 68

[83] S. Wilke and M. Scheffler, "Potential-energy surface for h_2 dissociation over pd(100)", *Phys. Rev. B* **53**, pp. 4926–4932 (1996). 75

[84] A. Eichler, G. Kresse, and J. Hafner, "Ab-initio calculations of the 6d potential energy surfaces for the dissociative adsorption of h_2 on the (100) surfaces of rh, pd and ag", *Sur. Sci.* **397**, pp. 116–136 (1998). 75

[85] H.-J. Freund, M. Bäumer, and H. Kuhlenbeck, "Catalysis and surface science: What do we learn from studies of oxide-supported cluster model systems?", In *Impact of Surface Science on Catalysis* volume 45 of *Advances in Catalysis* , pp. 333 – 384. Academic Press (2000). 90

[86] Charles T. Campbell, "Ultrathin metal films and particles on oxide surfaces: structural, electronic and chemisorptive properties", *Surface Science Reports* **27**(1–3), pp. 1 – 111 (1997). 90

[87] Claude R. Henry, "Surface studies of supported model catalysts", *Surface Science Reports* **31**(7–8), pp. 231 – 325 (1998). 90

[88] M. Moseler, H. Häkkinen, and U. Landman, "Supported magnetic nanoclusters: Soft landing of pd clusters on a mgo surface", *Phys. Rev. Lett.* **89**, pp. 176103 (2002). 90

[89] M. Valden, X. Lai, and D. W. Goodman, "Onset of catalytic activity of gold clusters on titania with the appearance of nonmetallic properties", *Science* **281**(5383), pp. 1647–1650 (1998). 90

[90] Lijun Xu, Graeme Henkelman, Charles T. Campbell, and Hannes Jónsson, "Small pd clusters, up to the tetramer at least, are highly mobile on the mgo(100) surface", *Phys. Rev. Lett.* **95**, pp. 146103 (2005). 90, 126, 144, 148, 149, 152, 155, 162

[91] Lijun Xu, Graeme Henkelman, Charles T. Campbell, and Hannes Jónsson, "Pd diffusion on mgo(1 0 0): The role of defects and small cluster mobility", *Surface Science* **600**(6), pp. 1351 – 1362 (2006). 90, 97, 100, 103, 104, 115, 126, 128, 144, 148, 149, 152, 155, 162, 165

[92] G. Haas, A. Menck, H. Brune, and J. V. Barth, "Nucleation and growth of supported clusters at defect sites: Pd/mgo(001)", *Phys. Rev. B* **61**, pp. 11105–11108 (2000). 90, 95, 162, 165

[93] Igor A. Pasti, Milos R. Baljozovic, Laura P. Granda-Marulanda, and Natalia V. Skorodumova, "Bimetallic dimers adsorbed on a defect-free mgo(001) surface: Bonding, structure and reactivity", *Phys. Chem. Chem. Phys.* **17**, pp. 9666–9679 (2015). 90

[94] Christopher J. Heard, Sven Heiles, Stefan Vajda, and Roy L. Johnston, "Pdnag(4-n) and pdnpt(4-n) clusters on mgo (100): A density functional surface genetic algorithm investigation", *Nanoscale* **6**, pp. 11777–11788 (2014). 90

[95] Elizabeth Florez, Fanor Mondragon, and Francesc Illas, "Theoretical study of the structure and reactivity descriptors of cunm (m=ni, pd, pt; n = 1–4) bimetallic nanoparticles supported on mgo(001)", *Surf. Sci.* **606**, pp. 1010–1018 (2012). 90

[96] Fabio R. Negreiros, Giovanni Barcaro, Zdenka Kuntova, Giulia Rossi, Riccardo Ferrando, and Alessandro Fortunelli, "Structures of agpd nanoclusters adsorbed on mgo(100): A computational study", *Surf. Sci.* **605**, pp. 483–488 (2011). 90

[97] Giovanni Barcaro and Alessandro Fortunelli, "A study of bimetallic cu–ag, au–ag and pd–ag clusters adsorbed on a double-vacancy-defected mgo(100) terrace", *Faraday Discuss.* **138**, pp. 37–47 (2008). 90

[98] Indu Kaul and Prasenjit Ghosh, "First principles investigations of small bimetallic pdga clusters as catalysts for hydrogen dissociation", *Chem. Phys.* **487**, pp. 87–96 (2017). 90, 103, 107, 110, 112, 115, 117, 121, 122, 126, 131, 133, 135, 137, 174

[99] Jens Nielsen, Mayeul d'Avezac, James Hetherington, and Michail Stamatakis, "Parallel kinetic monte carlo simulation framework incorporating accurate models of adsorbate lateral interactions", *J. Chem. Phys.* **139**, pp. 224706 (2013). 93

[100] G. Barcaro, A. Fortunelli, F. Nita, and R. Ferrando, "Diffusion of palladium clusters on magnesium oxide", *Phys. Rev. Lett.* **95**, pp. 246103 (2005). 100, 144, 148, 152, 162

[101] Livia Giordano, Cristiana Di Valentin, Jacek Goniakowski, and Gianfranco Pacchioni, "Nucleation of pd dimers at defect sites of the mgo(100) surface", *Phys. Rev. Lett.* **92**, pp. 096105 (2004). 100

[102] Ilya V. Yudanov, Stefan Vent, Konstantin Neyman, Gianfranco Pacchioni, and Notker Rösch, "Adsorption of pd atoms and pd4 clusters on the mgo(001) surface: a density functional study", *Chemical Physics Letters* **275**(3–4), pp. 245 – 252 (1997). 100

[103] Alexei V. Matveev, Konstantin M. Neyman, Gianfranco Pacchioni, and Notker Rösch, "Density functional study of {M4} clusters (m=cu, ag, ni, pd) deposited on the regular mgo(001) surface", *Chemical Physics Letters* **299**(6), pp. 603 – 612 (1999). 100

[104] Ilya V. Yudanov, Vladimir A. Nasluzov, Konstantin M. Neyman, and Notker Rösch, "Density functional cluster description of ionic materials: Improved boundary conditions for mgo clusters with the help of cation model potentials", *International Journal of Quantum Chemistry* **65**(5), pp. 975–986 (1997). 100

[105] Gianfranco Pacchioni and Notker Rösch, "Supported nickel and copper clusters on mgo(100): A first-principles calculation on the metal/oxide interface", *The Journal of Chemical Physics* **104**(18), pp. 7329–7337 (1996). 100

[106] Lijun Xu, Charles T. Campbell, Hannes Jónsson, and Graeme Henkelman, "Kinetic monte carlo simulations of pd deposition and island growth on mgo(100)", *Surface Science* **601**(14), pp. 3133 – 3142 (2007). 107, 148, 149, 155, 162, 165, 166

[107] Igor A. Paśti, Miloš R. Baljozović, Laura P. Granda-Marulanda, and Natalia V. Skorodumova, "Bimetallic dimers adsorbed on a defect-free mgo(001) surface: bonding, structure and reactivity", *Phys. Chem. Chem. Phys.* **17**(9666-9679) (2015). 109

[108] Riccardo Ferrando and Alessandro Fortunelli, "Diffusion of adatoms and small clusters on magnesium oxide surfaces", *J. Phys.: Condens. Matter* **21**, pp. 264001 (2009). 144, 148, 149, 155

[109] Livia Giordano and Gianfranco Pacchioni, "Pd nanoclusters at the mgo(1 0 0) surface", *Surface Science* **575**(1–2), pp. 197 – 209 (2005). 148

[110] Ming-Cheng Wu, Charles M. Truong, and D. Wayne Goodman, "Electron-energy-loss-spectroscopy studies of thermally generated defects in pure and lithium-doped mgo(100) films on mo(100)", *Phys. Rev. B* **46**, pp. 12688–12694 (1992). 162

[111] Ram Ramachandran and Raghu K. Menon, "An overview of industrial uses of hydrogen", *Int. J. Hydrogen Energy* **23**(7), pp. 593–598 (1998). 179

[112] A. G. Knapton, "Palladium alloys for hydrogen diffusion membranes", *Platinum Met. Rev.* **21**(2), pp. 44–50 (1977). 180

[113] S. N. Paglieri and J. D. Way, "Innovations in palladium membrane research", *Sep. Purif. Rev.* **31**(1), pp. 1–169 (2002). 180

[114] M. De Falco, editor, *Membrane reactors for hydrogen production processes*, Springer-Verlag London Limited 84 edition (2011). 180

[115] S. Yun and S.T. Oyama, "Correlations in palladium membranes for hydrogen separation", *J Membr. Sci.* **375**, pp. 28–45 (2011). 180

[116] Volker Höllein, Matthew Thorntona, Peter Quicker, and Roland Dittmeyer, "Preparation and characterization of palladium composite membranes for hydrogen removal in hydrocarbon dehydrogenation membrane reactors", *Catal. Today* **67**, pp. 33–42 (2001). 180

[117] Ames Kulprathipanja, Gökhan O Alptekin, John L Falconer, and J Douglas Way, "Pd and pd-cu membranes: Inhibition of H_2 permeation by H_2S", *J. Membr. Sci.* **254**, pp. 49–62 (2005). 180

[118] Huiyuan Gao, Y. S. Lin, Yongdan Li, and Baoquan Zhang, "Chemical stability and its improvement of palladium-based metallic membranes", *Ind. Eng. Chem. Res.* **43**, pp. 6920–6930 (2004). 180

[119] F. A. Lewis, editor, *The palladium hydrogen system*, Academic Press The University of Michigan (1967). 180

[120] L. W. McKeehan, "The crystal structures of the system palladium-hydrogen", *Phys. Rev.* **21**, pp. 334–342 (1923). 180

[121] Oyvind Hatlevik, Sabina K. Gade, Matthew K. Keeling, Paul M. Thoen, A.P. Davidson, and J. Douglas Way, "Palladium and palladium alloy membranes for hydrogen separation and production: History, fabrication strategies, and current performance", *Sep. Purif. Technol.* **73**, pp. 59–64 (2010). 180

[122] Kent E. Coulter, J. Douglas Way, Sabina K. Gade, Saurabh Chaudhari, David S. Sholl, and Lymarie Semidey-Flecha, "Predicting, fabricating, and permeability testing of free-standing ternary palladium-copper-gold membranes for hydrogen separation", *J. Phys. Chem. C* **114**, pp. 17173–17180 (2010). 180

[123] Fernando Roa, Michael J Block, and J Douglas Way, "The influence of alloy composition on the H_2 flux of composite pd-cu membranes", *Desalination* **147**, pp. 411–416 (2002). 180, 181

[124] Ana M. Tarditi and Laura M. Cornaglia, "Novel pdagcu ternary alloy as promising materials for hydrogen separation membranes: Synthesis and characterization", *Surf. Sci.* **605**, pp. 62–71 (2011). 180

[125] N.S. Anand, Subhasis Pati, Ram Avtar Jat, S.C. Parida, and S.K. Mukerjee, "Thermodynamics and kinetics of hydrogen/deuterium absorption-desorption in $Pd_{0.77}Ag_{0.23}$ alloy", *Int. J. Hydrogen Energy.* **40**, pp. 444–450 (2015). 180

[126] Preeti Kamakoti and David S. Sholl, "Towards first principles-based identification of ternary alloys for hydrogen purification membranes", *J. Membr. Sci.* **279**, pp. 94–99 (2006). 180

[127] Shiqiang Hao and David S. Sholl, "Using first-principles calculations to accelerate materials discovery for hydrogen purification membranes by modeling amorphous metals", *Energy Environ. Sci.* **1**, pp. 175–183 (2008). 180

[128] Lymarie Semidey-Flecha and David S. Sholl, "Combining density functional theory and cluster expansion methods to predict H_2 permeance through pd-based binary alloy membranes", *J. Chem. Phys.* **128**, pp. 144701 (2008). 180, 181, 203

[129] Lymarie Semidey-Flecha, Chen Ling, and David S. Sholl, "Detailed first-principles models of hydrogen permeation through pdcu-based ternary alloys", *J. Membr. Sci.* **362**, pp. 384–392 (2010). 180, 181

[130] R.C. Benn, S.M. Opalka, and T.H. Vamderspurt, "Durable pd-based alloy and hydrogen generation membrane thereof", *US Patent No.* , pp. 7,655,183 (2007). 180

[131] Preeti Kamakoti, Bryan D. Morreale, Michael V. Ciocco, Bret H. Howard, Richard P. Killmeyer, Anthony V. Cugini, and David S. Sholl, "Prediction of hydrogen flux through sulfur-tolerant binary alloy membranes", *Science* **307**, pp. 569–573 (2005). 180, 181, 182, 199, 202, 211, 212

[132] M.V. Mundschau, X. Xie, C.R. Evenson IV, and A.F. Sammells, "Dense inorganic membranes for production of hydrogen from methane and coal with carbon dioxide sequestration", *Catal. Today* **118**, pp. 12–23 (2006). 180

[133] M Kajiwara, S Uemiya, and T Kojima, "Stability and hydrogen permeation behavior of supported platinum membranes in presence of hydrogen sulfide", *Int. J. Hydrogen Energy* **24**, pp. 839–844 (1999). 180

[134] Xiulian Pan, Mirjam Kilgus, and Andreas Goldbach, "Low-temperature H_2 and N_2 transport through thin $Pd_{66}Cu_{34}H_x$ layers", *Catal. Today* **104**, pp. 225–230 (2005). 180

[135] David L McKinley, "Method for hydrogen separation and purification", *US Pat.* , pp. 3,439,474 (1969). 181

[136] P.R Subramanian and D.E Laughlin, "Cu-pd (copper-palladium)", *J. Phase Equilib.* **12**, pp. 231–243 (1991). 181

[137] John Piper, "Diffusion of hydrogen in copper-palladium alloys", *J. Appl. Phys.* **37**, pp. 715–721 (1966). 181, 202, 211, 212

[138] Preeti Kamakoti and David S. Sholl, "A comparison of hydrogen diffusivities in pd and cupd alloys using density functional theory", *J. Membr. Sci.* **225**, pp. 145–154 (2003). 181, 182, 202

[139] Preeti Kamakoti and David S. Sholl, "Ab initio lattice-gas modeling of interstitial hydrogen diffusion in cupd alloys", *Phys. Rev. B* **71**, pp. 014301 (2005). 181, 203

[140] Michael C. Gao, Lizhi Ouyang, and Ömer N. Doǵan, "First principles screening of b2 stabilizers in cupd-based hydrogen separation membranes: (1) substitution for pd", *J. Alloys Compd.* **574**, pp. 368–376 (2013). 181

[141] Jacob R. Boes, Gamze Gumuslu, James B. Miller, Andrew J. Gellman, and John R. Kitchin, "Estimating bulk-composition-dependent H_2 adsorption energies on Cu_xPd_{1-x} alloy (111) surfaces", *ACS Catal.* **5**, pp. 1020–1026 (2015). 181

[142] Y.T. Hu and H. Gong, "First principles study of thermodynamic and mechanical properties of $Pd_{50}Cu_{50}$", *J. Alloys Compd.* **639**, pp. 635–641 (2015). 181

[143] Nathan W. Ockwig and Tina M. Nenoff, "Membranes for hydrogen separation", *Chem. Rev.* **107**, pp. 4078–4110 (2007). 182

[144] Carmen Sousa, Virineya Bertin, and Francesc Illas, "Theoretical study of the interaction of molecular hydrogen with pdcu(111) bimetallic surfaces", *J. Phys. Chem. B* **105**, pp. 1817–1822 (2001). 182

[145] Graeme W. Watson, Richard P. K. Wells, David J. Willock, and Graham J. Hutchings, "A comparison of the adsorption and diffusion of hydrogen on the 111 surfaces of ni, pd, and pt from density functional theory calculations", *J. Phys. Chem. B* **105**, pp. 4889–4894 (2001). 182

[146] M. Blanco-Rey and J. C. Tremblay, "Diffusion of hydrogen interstitials in the near-surface region of pd(111) under the influence of surface coverage and external static electric fields", *J. Chem. Phys.* **142**, pp. 154704 (2015). 182

[147] Linda L. Jewell and Burtron H. Davis, "Review of absorption and adsorption in the hydrogen–palladium system", *Appl. Catal., A* **310**, pp. 1–15 (2006). 182

[148] Preeti Kamakoti and David S. Sholl, "Density functional theory studies of hydrogen diffusion in cupd alloys", *Fuel Chemistry Division Preprints* **42**(2), pp. 818–819 (2002). 182

[149] A. Yu. Volkov, O. S. Novikova, and B. D. Antonov, "Formation of an ordered structure in the cu-49 at % pd alloy", *Inorg. Mater.* **49**, pp. 43–48 (2013). 183

[150] Miho Yamauchi and Tatsuya Tsukuda, "Production of an ordered (b2) cupd nanoalloy by low-temperature annealing under hydrogen atmosphere", *Dalton Trans.* **40**, pp. 4842–4845 (2011). 183

[151] Cai Wei, F.T. Kong, and H.R. Gong, "Phase stability and elastic property of pdh and pdcuh phases", *Int. J. Hydrogen Energy* **38**, pp. 16485–16494 (2013). 183

[152] S.M. Opalka, W. Huang, D. Wang, T.B. Flanagan, O.M. Lovvik, S.C. Emerson, Y. She, and T.H. Vanderspurt, "Hydrogen interactions with the pdcu ordered b2 alloy", *J. Alloys Compd.* **446**, pp. 583–587 (2007). 191, 192, 195, 198, 199, 203, 211, 214

[153] J. Völkl and G. Alefeld, *Diffusion of hydrogen in metals, in G. Alefeld, J. Völkl (Eds), Hydrogen in metals I*, Springer Berlin hydrogen in metals i edition (1978). 202, 211

[154] Shahrouz Nayebossadri, John Speight, and David Book, "Effects of low ag additions on the hydrogen permeability of pd-cu-ag hydrogen separation membranes", *J. Membr. Sci.* **451**, pp. 216–225 (2014). 202, 211, 212

[155] L.C. Liu, J.W. Wang, Y.H. He, and H.R. Gong, "Solubility, diffusivity, and permeability of hydrogen at pdcu phases", *J. Membr. Sci.* **542**, pp. 24–30 (2017). 203, 211, 212, 213

[156] C. Decaux, R. Ngameni, D. Solas, S. Grigoriev, and P. Millet, "Time and frequency domain analysis of hydrogen permeation across pdcu metallic membranes for hydrogen purification", *Int. J. Hydrogen Energ.* **35**, pp. 4883–4892 (2010). 211, 214

[157] Chenyang Zhao, Andreas Goldbach, and Hengyong Xu, "Low-temperature stability of body-centered cubic pdcu membranes", *J. Membr. Sci.* **542**, pp. 60–67 (2017). 213, 214

[158] Timothy L. Ward and Tien Dao, "Model of hydrogen permeation behavior in palladium membranes", *J. Membr. Sci.* **153**, pp. 211–231 (1999). 214, 216

[159] Chen Ling and David S. Sholl, "Using first-principles calculations to predict surface resistances to H_2 transport through metal alloy membranes", *J. Membr. Sci.* **303**, pp. 162–172 (2007). 214

SPRINGER NATURE

Title: INTRODUCTION TO THE KINETIC MONTE CARLO METHOD
Author: Arthur F. Voter
Publication: Springer eBook
Publisher: Springer Nature
Date: Jan 1, 2007

Order Completed

Thank you for your order.

This Agreement between Indian Institute of Science Education and Research, Pune -- Nandhakumar Velankanni ("You") and Springer Nature ("Springer Nature") consists of your license details and the terms and conditions provided by Springer Nature and Copyright Clearance Center.

Your confirmation email will contain your order number for future reference.

printable details

License Number	4393761102907
License date	Jul 21, 2018
Licensed Content Publisher	Springer Nature
Licensed Content Publication	Springer eBook
Licensed Content Title	INTRODUCTION TO THE KINETIC MONTE CARLO METHOD
Licensed Content Author	Arthur F. Voter
Licensed Content Date	Jan 1, 2007
Type of Use	Thesis/Dissertation
Requestor type	academic/university or research institute
Format	print and electronic
Portion	figures/tables/illustrations
Number of figures/tables/illustrations	2
Will you be translating?	no
Circulation/distribution	<501
Author of this Springer Nature content	no
Title	Dr.
Instructor name	Prasenjit Ghosh
Institution name	Indian Institute of Science Education and Research, Pune
Expected presentation date	Jul 2018
Portions	Fig. 1, Fig.2
Requestor Location	Indian Institute of Science Education and Research, Pune Dr. Homi Bhabha Road, Ward No. 8, NCL Colony, Pashan, Pune,, Maharashtra 411008 India Attn: Indian Institute of Science Education and Research, Pune
Billing Type	Invoice
Billing address	Indian Institute of Science Education and Research, Pune Dr. Homi Bhabha Road, Ward No. 8, NCL Colony, Pashan, Pune,, India 411008 Attn: Indian Institute of Science Education and Research, Pune

Total	0.00 USD

ORDER MORE CLOSE WINDOW

Copyright Clearance Center

Confirmation Number: 11732360
Order Date: 07/21/2018

Customer Information

Customer: Nandhakumar Velankanni
Account Number: 3001312364
Organization: Indian Institute of Science Education and Research, Pune
Email: nandha.kumar@students.iiserpune.ac.in
Phone: +91 7972991012
Payment Method: Invoice

This is not an invoice

Order Details

Annual review of materials research

Billing Status: **N/A**

Order detail ID:	71321941
ISSN:	1545-4118
Publication Type:	e-Journal
Volume:	
Issue:	
Start page:	
Publisher:	ANNUAL REVIEWS

Permission Status: **Granted**

Permission type: Republish or display content
Type of use: Thesis/Dissertation
Order License Id: 4393770485463

Requestor type	Academic institution
Format	Print, Electronic
Portion	chart/graph/table/figure
Number of charts/graphs/tables/figures	1
The requesting person/organization	Indian Institute of Science Education and Research, Pune
Title or numeric reference of the portion(s)	Fig 2
Title of the article or chapter the portion is from	Atomistic Simulations of Activated Processes in Materials
Editor of portion(s)	N/A
Author of portion(s)	G. Henkelman
Volume of serial or monograph	Annu. Rev. Mater. Res. 2017. 47:199–216
Page range of portion	199-216
Publication date of portion	2017
Rights for	Main product
Duration of use	Life of current edition
Creation of copies for the disabled	no
With minor editing privileges	no
For distribution to	Worldwide
In the following language(s)	Original language of publication
With incidental promotional use	no
Lifetime unit quantity of new product	Up to 499

Title	Dr.
Instructor name	Prasenjit Ghosh
Institution name	Indian Institute of Science Education and Research, Pune
Expected presentation date	Jul 2018

Note: This item was invoiced separately through our **RightsLink service.** More info **$ 0.00**

Total order items: 1 **Order Total: $0.00**

American Physical Society
Reuse and Permissions License

06-Aug-2018

This license agreement between the American Physical Society ("APS") and Nandhakumar Velankanni ("You") consists of your license details and the terms and conditions provided by the American Physical Society and SciPris.

Licensed Content Information

License Number:	**RNP/18/AUG/006646**
License date:	06-Aug-2018
DOI:	10.1103/RevModPhys.64.1045
Title:	Iterative minimization techniques for ab initio total-energy calculations: molecular dynamics and conjugate gradients
Author:	M. C. Payne et al.
Publication:	Reviews of Modern Physics
Publisher:	American Physical Society
Cost:	USD $ 0.00

Request Details

Does your reuse require significant modifications: No

Specify intended distribution locations:	Worldwide
Reuse Category:	Reuse in a thesis/dissertation
Requestor Type:	Student
Items for Reuse:	Figures/Tables
Number of Figure/Tables:	1
Figure/Tables Details:	Figure-5
Format for Reuse:	Print and Electronic
Total number of print copies:	Up to 1000

Information about New Publication:

University/Publisher:	Indian institute of science education and research, Pune
Title of dissertation/thesis:	First Principles Investigations of Thermally Activated Processes in Pd-based Materials
Author(s):	Nandha Kumar V
Expected completion date:	Aug. 2018

License Requestor Information

Name:	Nandhakumar Velankanni
Affiliation:	Individual
Email Id:	nandha.kumar@students.iiserpune.ac.in
Country:	India

American Physical Society
Reuse and Permissions License

TERMS AND CONDITIONS

The American Physical Society (APS) is pleased to grant the Requestor of this license a non-exclusive, non-transferable permission, limited to Print and Electronic format, provided all criteria outlined below are followed.

1. You must also obtain permission from at least one of the lead authors for each separate work, if you haven't done so already. The author's name and affiliation can be found on the first page of the published Article.

2. For electronic format permissions, Requestor agrees to provide a hyperlink from the reprinted APS material using the source material's DOI on the web page where the work appears. The hyperlink should use the standard DOI resolution URL, http://dx.doi.org/{DOI}. The hyperlink may be embedded in the copyright credit line.

3. For print format permissions, Requestor agrees to print the required copyright credit line on the first page where the material appears: "Reprinted (abstract/excerpt/figure) with permission from [(FULL REFERENCE CITATION) as follows: Author's Names, APS Journal Title, Volume Number, Page Number and Year of Publication.] Copyright (YEAR) by the American Physical Society."

4. Permission granted in this license is for a one-time use and does not include permission for any future editions, updates, databases, formats or other matters. Permission must be sought for any additional use.

5. Use of the material does not and must not imply any endorsement by APS.

6. APS does not imply, purport or intend to grant permission to reuse materials to which it does not hold copyright. It is the requestor's sole responsibility to ensure the licensed material is original to APS and does not contain the copyright of another entity, and that the copyright notice of the figure, photograph, cover or table does not indicate it was reprinted by APS with permission from another source.

7. The permission granted herein is personal to the Requestor for the use specified and is not transferable or assignable without express written permission of APS. This license may not be amended except in writing by APS.

8. You may not alter, edit or modify the material in any manner.

9. You may translate the materials only when translation rights have been granted.

10. APS is not responsible for any errors or omissions due to translation.

11. You may not use the material for promotional, sales, advertising or marketing purposes.

12. The foregoing license shall not take effect unless and until APS or its agent, Aptara, receives payment in full in accordance with Aptara Billing and Payment Terms and Conditions, which are incorporated herein by reference.

13. Should the terms of this license be violated at any time, APS or Aptara may revoke the license with no refund to you and seek relief to the fullest extent of the laws of the USA. Official written notice will be made using the contact information provided with the permission request. Failure to receive such notice will not nullify revocation of the permission.

14. APS reserves all rights not specifically granted herein.

15. This document, including the Aptara Billing and Payment Terms and Conditions, shall be the entire agreement between the parties relating to the subject matter hereof.

Title: Selectivity and Reactivity of Pd-Rich PdGa Surfaces toward Selective Hydrogenation of Acetylene: Interplay of Surface Roughness and Ensemble Effect

Author: Nandha Kumar, Prasenjit Ghosh

Publication: The Journal of Physical Chemistry C

Publisher: American Chemical Society

Date: Dec 1, 2016

PERMISSION/LICENSE IS GRANTED FOR YOUR ORDER AT NO CHARGE

This type of permission/license, instead of the standard Terms & Conditions, is sent to you because no fee is being charged for your order. Please note the following:

- Permission is granted for your request in both print and electronic formats, and translations.
- If figures and/or tables were requested, they may be adapted or used in part.
- Please print this page for your records and send a copy of it to your publisher/graduate school.
- Appropriate credit for the requested material should be given as follows: "Reprinted (adapted) with permission from (COMPLETE REFERENCE CITATION). Copyright (YEAR) American Chemical Society." Insert appropriate information in place of the capitalized words.
- One-time permission is granted only for the use specified in your request. No additional uses are granted (such as derivative works or other editions). For any other uses, please submit a new request.

BACK CLOSE WINDOW

Title: Microscopic Insights into Hydrogen Permeation Through a Model PdCu Membrane from First-Principles Investigations

Author: Nandha Kumar, Debabrata Chattaraj, Prasenjit Ghosh, et al

Publication: The Journal of Physical Chemistry C

Publisher: American Chemical Society

Date: Jun 1, 2018

PERMISSION/LICENSE IS GRANTED FOR YOUR ORDER AT NO CHARGE

This type of permission/license, instead of the standard Terms & Conditions, is sent to you because no fee is being charged for your order. Please note the following:

- Permission is granted for your request in both print and electronic formats, and translations.
- If figures and/or tables were requested, they may be adapted or used in part.
- Please print this page for your records and send a copy of it to your publisher/graduate school.
- Appropriate credit for the requested material should be given as follows: "Reprinted (adapted) with permission from (COMPLETE REFERENCE CITATION). Copyright (YEAR) American Chemical Society." Insert appropriate information in place of the capitalized words.
- One-time permission is granted only for the use specified in your request. No additional uses are granted (such as derivative works or other editions). For any other uses, please submit a new request.